Carbon-enhanced photocatalysts for visible light induced detoxification and disinfection

Joanne Gamage McEvoy

Thesis submitted to the
Faculty of Graduate and Postdoctoral Studies
in partial fulfillment of the requirements
for the Doctorate in Philosophy degree in Chemical Engineering

Department of Chemical and Biological Engineering
Faculty of Engineering
University of Ottawa

Abstract

Photocatalysis is an advanced oxidation process for the purification and remediation of contaminated waters and wastewaters, and is advantageous over conventional treatment technologies due to its ability to degrade emerging and recalcitrant pollutants. In addition, photocatalytic disinfection is less chemical-intensive than other methods such as chlorination, and can inactivate even highly resistant microorganisms with good efficacy. Process sustainability and cost-effectiveness may be improved by utilizing solar irradiation as the source of necessary photons for photocatalyst excitation. However, solar-induced activity of the traditionally-used titania is poor due to its inefficient visible light absorption, and recombination of photo-excited species is problematic. Additionally, mass transfer limitations and difficulties separating the catalyst from the post-treatment slurry hinder conversions and efficiencies obtainable in practice. In this research, various strategies were explored to address these issues using novel visible light active photocatalysts. Two classes of carbon-enhanced photocatalytic materials were studied: activated carbon adsorbent photocatalyst composites, and carbon-doped TiO_2. Adsorbent photocatalyst composites based on activated carbon and plasmonic silver/silver chloride structures were synthesized, characterized, and experimentally investigated for their photocatalytic activity towards the degradation of model organic pollutants (methyl orange dye, phenol) and the inactivation of a model microorganism (*Escherichia coli* K-12) under visible light. The adsorptive behaviour of the composites towards methyl orange dye was also studied and described according to appropriate models. Photocatalytic bacterial inactivation induced by the prepared composites was investigated, and the inactivation mechanisms and roles of incorporated antimicrobial silver on disinfection were probed and discussed. These composites were extended towards magnetic removal strategies for post-use separation through the incorporation of magnetic nanoparticles to prepare Ag/AgCl-magnetic activated carbon composites, and the effect of nanoparticles addition on the properties and photoactivities of the resulting materials was explored. Another silver/silver halide adsorbent photocatalyst composite based on activated carbon and Ag/AgBr exhibiting visible light absorption due to both localized surface plasmon resonance and optical band gap absorption was synthesized and its photocatalytic activity towards organics degradation and microbial

inactivation was studied. Carbon-doped mixed-phase titania was also prepared and experimentally investigated.

Résumé

La photo-catalyse est un processus d'oxydation avancé utilisé pour la purification et l'assainissement des eaux usées ou contaminées, qui, grâce à sa capacité de dégrader des polluants récalcitrant, possè de d'importants avantages par rapport aux méthodes de traitements plus conventionnelles. De plus, la désinfection photo-catalytique implique moins de produits chimiques que d'autres méthodes tel que la chlorination et peut efficacement neutraliser les microorganismes les plus résistants. La viabilité et le coût du procédé peuvent être améliorés en utilisant le rayonnement solaire comme source des photons pour l'excitation photo-catalytique. Par contre, cette approche n'est pas efficace lors de l'utilisation d'oxyde de titane, couramment utilisé comme catalyseur, dû à son absorption inefficace de lumière dans le spectre visible, ainsi que des complications associées à la recombinaison d'espèces photo-excitées. Les limites de transfert de matière et la difficulté du processus de séparation du catalyseur de la suspension traitée affectent aussi l'efficacité du procédé. Au long de cette recherche, différentes stratégies visant à résoudre ces difficultés furent explorées. Deux classes de photo-catalyseurs carbonisés furent étudiés : des composés photo-catalytiques adsorbants à base de charbon actif et du TiO_2 dopé au carbone. Des composés adsorbants photo-catalytiques à base de charbon actif et de structures plasmoniques Ag/AgCl furent synthétisés, caractérisés et leur activité photo-catalytique pour la dégradation de polluants organiques (méthylorange et phénol) et l'inactivation de microorganismes (*Escherichia coli* K-12) lors d'exposition à de la lumière du spectre visible fut étudiée. Les caractéristiques d'adsorption de méthylorange des composés furent aussi étudiées en utilisant les modèles appropriés. L'inactivation photo-catalytique de microorganismes par les composites charbon actif-Ag/AgCl fut étudiée et les mécanismes d'inactivation ainsi que le rôle joué par l'agent antimicrobien lors de la désinfection sont discutés. Une approche basée sur la récupération magnétique des photo-catalyseurs fut investiguée en incorporant des nanoparticules magnétiques aux matériaux composites et leur effet sur l'activité photo-catalytique des matériaux composites fut caractérisé. Un autre adsorbent photo-catalytique à base de charbon actif et composite Ag/AgBr, capable d'absorber la lumière visible grâce à une résonance plasmique de surface et à son écart de bandes d'absorption optiques, fut synthétisé et son activité photo-catalytique pour la

dégradation de composés organiques et pour l'inactivation de microorganismes fut étudiée. De l'oxyde de titane multi-phase dopé au carbone fut également préparé et caractérisé.

Statement of Contributions of Collaborators

I hereby declare that I am the sole author of this thesis. I independently designed all experimental studies, performed all data analyses, and wrote all of the chapters and appendices presented in this work. I also conducted all of the experimental work, with the exception of select disinfection experiments presented in Chapter 5, which were performed with the help of Didier Alexandre Bilodeau, a COOP student under my supervision. Didier appears as a co-author on the paper and conference presentation associated to this chapter. In addition, Travis Comeau, an undergraduate thesis student under my supervision, helped develop and troubleshoot the oxidative annealing method described in Chapter 8 to prepare carbon-doped TiO_2, and was listed as a co-author in the three conference presentations related to this study. I have acknowledged other sources of assistance in analyses where applicable.

Dr. Zisheng (Jason) Zhang supervised this thesis project and provided guidance throughout. He also made editorial contributions to the written work presented. Guidance and editorial contributions were also made by Dr. Wenquan Cui of Hebei United University (Tangshan, PR China), who was a visiting professor in Dr. Zhang's research group from May 2011 – May 2012. Dr. Cui is listed as a co-author on papers and conference presentations associated to the work given in Chapters 3 – 5, Chapter 8, and Appendix C, respectively.

Acknowledgments

I would first like to acknowledge my supervisor, Dr. Zisheng (Jason) Zhang, for allowing me to work on this project, and for his guidance, mentorship, and support over the duration of my doctoral studies.

I would also like to acknowledge the Natural Sciences and Engineering Research Council of Canada, the Canadian Federation of University Women, and the University of Ottawa for financial support.

I am indebted to a number of people who provided immense help throughout this project. I would like to acknowledge with gratitude Dr. Wenquan Cui of Hebei United University for invaluable training and technical advice. I am also grateful to everyone at the Centre for Catalysis Research and Innovation (CCRI) at the University of Ottawa, and all others who were involved with materials characterizations and auxiliary testing: Dr. Tara Kell (XRD, Dept. Earth Sciences), Dr. Sander Mommers (XPS, CCRI), Dr. Yong Yang (surface area and porosimetry, CCRI), Dr. Yun Liu (SEM, CCRI), Dr. Sadok Latief (TGA-DSC, CCRI), Dr. Nimal De Silva (ICP, Dept. Earth Sciences), Dr. Jianqun Wang (SEM/TEM, Carleton University), Dr. Paul Dubé (SQUID, McMaster University), and Qi Yueli and coworkers at Hebei United University. I would also like to thank the technical support staff in CHG who helped maintain the photoreactors and lab equipment, especially Louis Tremblay.

I would like to acknowledge also the work of undergraduate students who participated in this project, Travis Comeau and Didier Alexandre Bilodeau. Thank you also to Melissa Elliot, who provided grammar and style editing of the dissertation.

I am grateful to all of the friends I have met during my graduate studies who provided me with both research insights and light-hearted relief. I would like to mention specifically my D218 colleagues past and present, as well as my current and former group mates. A special thanks to Alison Reiche, Gabriel Potvin, and Rong Ran for all of their help, and for always making me laugh.

Finally, I would like to thank the wonderful family members and close personal friends in my life who constantly inspired, challenged, and humbled me with their unwavering and undeserved patience, kindness, wisdom, and love throughout these years. Above all, I would like to thank my husband Matthew McEvoy, without whom none of this would have been possible.

To my family

Table of Contents

List of Figures

List of Tables

Nomenclature, Abbreviations, and Symbols

Photocatalyst nomenclature

AC: activated carbon

Ag/AgBr: metallic silver on silver bromide (also Ag@AgBr)

Ag/AgBr-AC: metallic silver on silver bromide - activated carbon composite

Ag/AgCl: metallic silver on silver chloride (also Ag@AgCl)

Ag/AgCl-AC: metallic silver on silver chloride - activated carbon composite (also A-AC)

Ag/AgX: metallic silver on silver halide

A-MAC: metallic silver on silver chloride - magnetic activated carbon composite

C-TiO_2: carbon-doped TiO_2

P25: Degussa P25 TiO_2

Abbreviations

ACS: American Chemical Society

AFM: atomic force microscopy

AOP: advanced oxidation process

ATP: adenosine triphosphate

ATR: attenuated total reflection

BET: Brunauer, Emmett, and Teller

CB: conduction band

CFU: colony forming units

CNT: carbon nanotube

COD: chemical oxygen demand

CPC: compound parabolic collector

CVD: chemical vapor deposition

DCA: dichloroacetic acid

DFT: density functional theory

DNA: deoxyribonucleic acid

EDS: energy dispersive X-ray spectrometry

EDT: effective disinfection time

EDTA: ethylenediaminetetraacetic acid

FTIR: Fourier Transform Infrared

FWHM: full line width at half maximum

HEPA: high-efficiency particulate absorption

ICDD: International Center for Diffraction Data

ICP: inductively coupled plasma

IF: impact factor

INCO: European Union International Cooperation program

IUPAC: International Union of Pure and Applied Chemistry

JCPDS: Joint Committee on Powder Diffraction Standards (now ICDD)

LB: Luria-Bertani

LED: light-emitting diode

MAC: magnetic activated carbon

MB: methylene blue

MO: methyl orange

MPMS: magnetic properties measurement system

MS: mass spectrometry

NHE: normal hydrogen electrode

NP: nanoparticle

OES: optical emission spectroscopy

PAC: powdered activated carbon

ppb: parts per billion ($\mu g\ L^{-1}$ in aqueous solutions)

ppm: parts per million ($mg\ L^{-1}$ in aqueous solutions)

PVD: physical vapour deposition

PVP: poly(vinyl pyrrolidone)

R-P: Redlich-Peterson

ROS: reactive oxygen species

rpm: revolutions per minute

SAED: selected area electron diffraction

SE: standard error

SEM: scanning electron microscopy

SODIS: solar water disinfection

SPR: surface plasmon resonance

SQUID: superconducting quantum interference device

SSE: sum of square errors

TEM: transmission electron microscopy

TOC: total organic carbon

UV: ultraviolet

UV-Vis: ultraviolet - visible light absorption spectroscopy

VB: valence band

VOC: volatile organic compound

XPS: X-ray photoelectron spectroscopy

XRD: X-ray diffraction

Symbols

Roman

A: irradiated area (m^2)

a_s: Redlich-Peterson equilibrium constant (L mg^{-1})

C: concentration of reactant (mg L^{-1})

C_e: equilibrium pollutant concentration after adsorption (mg L^{-1})

C_f: final pollutant concentration (mg L^{-1})

C_o: initial pollutant concentration (mg L^{-1})

C_t: pollutant concentration at time t (m L^{-1})

D: grain size in Scherrer equation (nm)

E_{bg}: band gap energy (eV)

h: initial adsorption rate (mg pollutant g $catalyst^{-1}$ min^{-1})

Hc: coercive field (Oe)

I_A: intensity for strongest reflection for anatase phase in TiO_2 (-)

I_R: intensity for strongest reflection for rutile phase in TiO_2 (-)

J: flux of photons (Einstein m^{-2} s^{-1})

K: adsorption coefficient of reactant in Langmuir-Hinshelwood expression (L mg^{-1})

k': pseudo-first order rate constant in Langmuir-Hinshelwood expression (min^{-1})

k_1: pseudo-first order rate constant in the Lagergren equation (min^{-1})

k_1, k_2, k_3: kinetic constants in the modified Hom equation (-)

k_2: pseudo-second order rate constant in the McKay and Ho equation (g catalyst mg $pollutant^{-1}$ min^{-1})

K_F: sorption capacity constant in Freundlich equation (mg g^{-1})

k_{id}: intraparticle diffusion rate constant (mg g^{-1} $min^{-0.5}$)

K_L: sorption equilibrium constant in the Langmuir equation (L mg^{-})

$k_{photo,\ 1}$: rate constant for first order photocatalytic reaction (min^{-1})

$k_{photo,\ 2}$: rate constant for second order photocatalytic reaction (L mg^{-1} min^{-1})

k_r: reaction rate constant in Langmuir-Hinshelwood expression (mg L^{-1} min^{-1})

K_S: sorption capacity in Redlich-Peterson equation (mg g^{-1})

K_{sph}: sphericity constant in Scherrer equation (-)

m: number of observations in experimental data set (-)

Mr: remanent magnetization (emu g^{-1})

Ms: saturation magnetization (emu g^{-1})

n: sorption intensity (or heterogeneity) constant in Freundlich equation (-)

N_o: initial bacterial population (CFU mL^{-1})

N_t: bacterial population remaining at time t (CFU mL^{-1})

p: number of parameters in the regression model (-)

P: pressure (mm Hg)

P_o: initial pressure (mm Hg)

q_e: equilibrium sorption capacity of the composites (mg pollutant g $composite^{-1}$)

q_t: sorption capacity of the composites at time t (mg pollutant g $composite^{-1}$)

R: synergy factor (-)

R^2: coefficient of determination (-)

R_L: separation factor based on Langmuir equation (-)

t: elapsed reaction time (min)

V: volume of pollutant solution (L)

W: weight of catalyst loading (g)

x: weight fraction (-)

Greek

β: surface heterogeneity constant in the Redlich-Peterson equation (-)

θ: Bragg angle (^{o})

λ: wavelength of electromagnetic radiation (nm)

ξ: apparent photonic efficiency (mol $Einstein^{-1}$)

Φ: work function (eV)

ϕ: boundary layer thickness parameter in Weber-Morris intraparticle diffusion model (mg g^{-1})

SECTION I: INTRODUCTION

Chapter 1:
Introduction

1.1 Introduction

Heterogeneous photocatalysis is a photo-assisted catalytic process that involves the generation and subsequent reaction of electron-hole pairs in a photocatalyst when excited by light. The photoexcited species can react with oxygen and water to produce reactive species such as hydroxyl radicals and superoxide, which can readily interact with many organic pollutants to effect their degradation, and can also interfere with biological microorganisms to cause their inactivation [1]. This process has been researched as a treatment technology for many applications, including potable water production, domestic and industrial wastewater remediation, indoor air purification, and for the development of self-cleaning surfaces [2].

Photocatalysis belongs to the family of Advanced Oxidation Processes (AOPs), which are advantageous over conventional treatment technologies primarily due to their ability to degrade emerging pollutants such as pharmaceuticals and personal care products, as well as recalcitrant pollutants such as textile dyes and polyhalogenated aromatics [3]. In addition, photocatalytic inactivation of microbial species is a chlorine-free disinfection technique, eliminating the need for storage and transport of large volumes of reactive chemicals, in accordance with the principles of green engineering. Photocatalytic systems can implement solar irradiation as the photoexcitation source, facilitating sustainability and reducing associated operating costs [4].

A major limitation of this process lies in the low solar quantum efficiencies realized with the traditional TiO_2 catalyst, since it is only excited by ultraviolet (UV) light, which is not abundant in solar radiation (~3–5%) [5]. The separation of nanosized catalysts from the reaction medium and efficiency losses due to electron-hole recombination are also problematic [6]. Recently, the development of highly efficient photocatalysts engineered to improve solar utilization and prevent electron-hole recombination has been undertaken through extensive research in advanced and so-called "second-generation" photocatalysts, and materials such as element-doped TiO_2 [7], and silver/silver halide [8] photocatalysts exhibiting enhanced visible light activity have been investigated. Other approaches for improving photocatalytic efficiency and reusability have also been reported, including: the use of bifunctional activated carbon adsorbent photocatalysts to promote pollutant transfer to active sites [9] and the development of magnetic photocatalysts [10] to facilitate post-use separation.

In this thesis, the further exploration of these strategies for enhancement of visible light-induced photocatalysis is proposed, and novel multifunctional photocatalysts are designed, synthesized, and investigated. These hybrid photocatalysts are specifically tailored to possess high visible light efficiency and good applicability for implementation in solar photocatalytic water treatment systems. Mechanistic perspectives associated to the proposed photocatalysts and their implications for future use are discussed.

1.2 Objectives

The broad objective of this project was to prepare novel carbon-enhanced photocatalytic materials with improved visible light response for application to solar photocatalytic degradation of organic compounds and inactivation of microbial species in water. Two major classes of carbon-enhanced photocatalysts were concurrently investigated, namely: adsorbent photocatalyst composites based on activated carbon, and carbon-doped TiO_2. A central objective of this project was to synthesize and characterize novel plasmonic silver/silver chloride - activated carbon adsorbent photocatalyst composites and to study their photocatalytic activity for the degradation of model organic pollutants under visible light.

Description of the adsorptive and photocatalytic behaviour of these composites using appropriate models from literature was defined as a sub-objective. The experimental investigation of the composites as antibacterial and photocatalytic disinfection agents for the inactivation of a model microorganism, *Escherichia coli* K-12 (*E. coli* K-12), was also defined as a sub-objective. Another sub-objective was to extend the prepared novel silver/silver chloride - activated carbon composites towards magnetic removal strategies through incorporation of magnetic activated carbon. As such, the synthesis, characterization, and experimental investigation of photocatalytic activity for model organics degradation and model microorganism inactivation using novel silver/silver chloride - magnetic activated carbon composites was studied. The effect of the incorporated silver halide was also studied as a sub-objective, and novel silver/silver bromide - activated carbon composites were prepared, characterized, and their photocatalytic activity for degradation and disinfection experimentally investigated. Finally, the synthesis, characterization, and visible light induced photocatalytic activity for degradation and disinfection of another class of carbon-enhanced photocatalyst, carbon-doped TiO_2, was also studied as a project objective.

This research contributes to the development of carbon-enhanced visible light active photocatalysts with improved efficiency and applicability to solar photocatalytic treatment schemes. A main novelty of the design approach and work undertaken was in hybridizing existing strategies for the enhancement of visible light photocatalysis to prepare novel multifunctional photocatalytic materials. This was done through combining current research in surface plasmon resonance enhanced photocatalysts, adsorbent photocatalysts, and magnetic photocatalysts to prepare novel plasmonic adsorbent photocatalysts and their magnetic counterparts.

1.3 Thesis structure

1.3.1 General structure

The body of this thesis is divided into six major sections which, apart from introductory, background, and conclusion materials, represent various facets of the project scope that were undertaken and their associated key findings and discussions. These chapters are written in

journal article format, and together cover the project scope and objectives. They can be read independently of one another. There are six research articles contained in the main body, of which four are published in scholarly journals. The four published articles appear in this thesis with permission from the co-authors and respective publishers holding the copyrights. The remaining articles have been submitted for publication. In addition, there are two published review articles, and a published refereed conference paper contained in the Appendices that are associated to the scope of this research.

1.3.2 Description of chapter contents

Further discussion concerning thesis structure, including a detailed description of the contents of each chapter, is presented below. The associated scientific contributions are also listed, including the impact factor (IF) of the relevant journals in which publications were made.

Chapter 1: Introduction

A general overview and discussion related to the research is provided, and the thesis scope and objectives are defined. A framework for the thesis is outlined.

Chapter 2: Background and literature review

Specific background and literature pertinent to the undertaken scope and objectives are summarized with the goal of framing the current project in the context of the state of the art in photocatalysis research.

Chapter 3: Synthesis and characterization of Ag/AgCl-activated carbon composites for enhanced visible light photocatalysis

A novel adsorbent photocatalyst composite based on Ag/AgCl-AC is proposed, synthesized, characterized, and studied for the degradation of aqueous organic pollutants (methyl orange (MO) and phenol) under visible light. In addition to experimental observations of photocatalysis, detailed composite structural information is obtained and interpreted, and mechanistic considerations are made.

Contributions:

a) Published paper

J. Gamage McEvoy, W. Cui, Z. Zhang, Synthesis and characterization of Ag/AgCl-activated carbon composites for enhanced visible light photocatalysis, Applied Catalysis B: Environmental 144 (2014) pp. 702–712. (IF, 2012 = 5.825).

b) Conference presentations

i) J. Gamage McEvoy, W. Cui, Z. Zhang, Visible light induced degradation and disinfection using multifunctional Ag/AgCl activated carbon composite photocatalysts, American Institute of Chemical Engineers Annual Meeting, San Francisco, California, Nov. 3–8, 2013.

ii) J. Gamage McEvoy, W. Cui, Z. Zhang, Degradation of methyl orange by a plasmonic photocatalyst-adsorbent: Ag/AgCl on activated carbon, 7th International Conference on Environmental Catalysis, Lyon, France, Sept. 2–6, 2012.

Chapter 4: Adsorption and visible light degradation of methyl orange by Ag/AgCl-activated carbon composites

The adsorptive and photocatalytic behaviour of the novel Ag/AgCl-AC composites prepared are studied in detail. The sorption of methyl orange is explored and modeled with respect to kinetics and equilibrium, and a detailed description of photocatalytic degradation of methyl orange is provided, and photocatalytic kinetics modeled.

Contributions:

a) Submitted paper

J. Gamage McEvoy, W. Cui, Z. Zhang, Adsorption and visible light degradation of methyl orange by Ag/AgCl-activated carbon, Chemical Engineering Journal, *under review*. (IF, 2012 = 3.743).

Chapter 5: Visible-light-driven inactivation of *Escherichia coli* K-12 using an Ag/AgCl-activated carbon composite photocatalyst

Use of the developed Ag/AgCl-AC composites is extended towards bacterial inactivation, and photocatalytic disinfection of a model microorganism (*E. coli* K-12) is studied. In addition to qualitative and quantitative analyses of inactivation, changes to cell structure and morphology are probed to elucidate the mechanism of action of photo-produced radicals on the cells. Additionally, effects of silver ion elution on inactivation observed in dark and light conditions are discussed, respectively.

Contributions:

a) Published paper

J. Gamage McEvoy, D.A. Bilodeau, W. Cui, Z. Zhang, Visible-light-driven inactivation of *Escherichia coli* K-12 using an Ag/AgCl-activated carbon composite photocatalyst, Journal of Photochemistry & Photobiology A: Chemistry 267 (2013) pp. 25–34. (IF, 2012 = 2.416).

b) Conference presentation

J. Gamage McEvoy, D.A. Bilodeau, W. Cui, Z. Zhang, Photocatalytic inactivation of *Escherichia coli* K12 using Ag/AgCl-AC under visible light, 14th Canadian Society for Chemical Engineering Ontario-Québec Biotechnology Meeting, Ottawa, ON, May 30–31, 2012.

Chapter 6: Synthesis and characterization of magnetically separable Ag/AgCl-magnetic activated carbon composites for visible light induced photocatalytic detoxification and disinfection

Novel adsorbent photocatalysts Ag/AgCl-magnetic AC composites are developed in analogy to Ag/AgCl-AC, and investigated for use with magnetic removal strategies for post-treatment catalyst recovery. The Ag/AgCl-MAC composites are synthesized, characterized, and experimentally studied for their visible light induced photodegradation activities against methyl orange and phenol organic pollutants. The effect of the magnetic component to adsorbent ratio is investigated on the resulting photoactivity and magnetism observed. The disinfective capabilities of the prepared materials are explored for the inactivation of *E. coli* K-12.

Contributions:

a) Accepted paper

J. Gamage McEvoy, Z. Zhang, Synthesis and characterization of magnetically separable Ag/AgCl-magnetic activated carbon composites for visible light induced photocatalytic detoxification and disinfection, Applied Catalysis B: Environmental, *in press*. (IF, 2012 = 5.825).

Chapter 7: Synthesis and characterization of Ag/AgBr-activated carbon composites for visible light induced photocatalytic detoxification and disinfection

A novel adsorbent photocatalyst Ag/AgBr-AC composite is prepared in analogy to Ag/AgCl-AC, and is characterized and experimentally investigated for the visible light induced degradation of organic pollutants, MO dye and phenol. Disinfective capabilities of the prepared composite are also studied for the inactivation of *E. coli* K-12. Mechanistic insights

and photostability are discussed.

Contributions:

a) Submitted paper

J. Gamage McEvoy, Z. Zhang, Synthesis and characterization of Ag/AgBr-activated carbon composites for visible light induced photocatalytic detoxification and disinfection, Journal of Photochemistry & Photobiology A: Chemistry, *under review* (IF, 2012 = 2.416).

Chapter 8: Degradative and disinfective properties of carbon-doped anatase-rutile TiO_2 mixtures under visible light irradiation

A carbon doping strategy for visible light enhancement is explored, and carbon-doped TiO_2 photocatalysts are prepared by oxidative annealing. The obtained materials are characterized and studied for degradation of a model organic dye, methylene blue, and inactivation of a model microorganism, *E. coli* K-12. The effects of synthesis parameters on resulting structure and activity are studied, and a mechanism of visible light activity proposed.

Contributions:

a) Published paper

J. Gamage McEvoy, W. Cui, Z. Zhang, Degradative and disinfective properties of carbon-doped anatase-rutile TiO_2 mixtures under visible light irradiation, Catalysis Today 207 (2012) pp. 191–199. (IF, 2012 = 2.98).

b) Conference presentations

i) J. Gamage McEvoy, W. Cui, T. Comeau, Z. Zhang, Visible-light photocatalysis using carbon-doped TiO_2. 61st Canadian Chemical Engineering Conference, London, ON, Oct. 23–26, 2011.

ii) J. Gamage McEvoy, T. Comeau, Z. Zhang, Visible-light photocatalysis using carbon-modified TiO_2: Degradation of methylene blue model wastewater. International Conference on Environmental Pollution and Remediation 2011, Ottawa, ON, Aug. 17–19, 2011.

iii) J. Gamage McEvoy, T. Comeau, Z. Zhang, Visible-light photocatalysis using carbon-modified TiO_2: Disinfection of *Escherichia coli*, 13th Canadian Society for Chemical Engineering Ontario-Québec Biotechnology Meeting, Kingston, ON, May 12–13, 2011.

Chapter 9: General discussion and conclusions

General discussion and conclusions are made based on the work presented. The novelty of the research conducted and original contributions to knowledge are highlighted, and recommendations for future work outlined.

Appendix A: Antimicrobial and photocatalytic disinfection mechanisms in silver-modified photocatalysts under dark and light conditions

The effect of silver-modification on various classes of photocatalysts reported in literature is discussed with respect to antimicrobial and photocatalytic activities in the absence and presence of light, respectively. Synergistic and respective roles of silver ion elution and photocatalytic activity are considered, and new mechanistic perspectives offered. The emergence of antimicrobial photocatalysts as a novel class of disinfection materials is discussed.

Contributions:

a) Published paper

J. Gamage McEvoy, Z. Zhang, Antimicrobial and photocatalytic disinfection mechanisms in silver-modified photocatalysts under dark and light conditions. Journal of Photochemistry and Photobiology C: Photochemistry Reviews 19 (2014) pp. 62-75. (IF, 2012 = 8.069).

Appendix B: Applications of photocatalytic disinfection: A review

The use of photocatalysis as an alternative disinfection technology is reviewed with respect to its various applications.

Contributions:

a) Published paper

J. Gamage, Z. Zhang, Applications of photocatalytic disinfection: A review, International Journal of Photoenergy vol. 2010 (2010) Article ID 764870 (11 pages). (IF, 2012 = 2.663).

Appendix C: Visible light induced degradation and disinfection using multifunctional Ag/AgCl-AC composite photocatalysts

Select results from the studies presented in Chapters 3 to 5 are discussed in a conference paper detailing the degradative and disinfective properties of prepared Ag/AgCl-AC composites.

Contributions:

a) Published conference proceedings

J. Gamage McEvoy, W. Cui, Z. Zhang, Visible light induced degradation and disinfection using multifunctional Ag/AgCl activated carbon composite photocatalysts, *Proceedings of the 2013 American Institute of Chemical Engineers Annual Meeting*, San Francisco, CA, Nov. 3–8, 2013, paper 405g.

Appendix D: Scholarly contributions

Scholarly contributions made during the course of this doctoral research are detailed, and include the following metrics (excluding submitted papers): publication of 16 peer-reviewed articles in scholarly journals, publication of 2 refereed conference proceedings, participation in 12 conference presentations, and delivery of one invited presentation and two seminars. These contributions include collaborative research that was conducted in parallel to the scope of the current thesis.

1.4 References

[1] J. Anthony Byrne, P.A. Fernandez-Ibañez, P.S.M. Dunlop, D.M.A. Alrousan, J.W.J. Hamilton, Photocatalytic enhancement for solar disinfection of water: A Review, Int. J. Photoenergy 2011 (2011) Article ID 798051.

[2] J. Gamage, Z. Zhang, Applications of photocatalytic disinfection: A review, Int. J. Photoenergy 2010 (2010) Article ID 764870. *(also given in Appendix B)*

[3] S. Malato, J. Blanco, D.C. Alarcón, M.I. Maldonado, P. Fernández-Ibáñez, W. Gernjak, Photocatalytic decontamination and disinfection of water with solar collectors, Catal. Today 122, 1–2 (2007) 137–149.

[4] R.J. Braham, A.T. Harris, Review of major design and scale-up considerations for solar photocatalytic reactors, Ind. Eng. Chem. Res. 48, 19 (2009) 8890–8905.

[5] A. Fujishima, T.N. Rao, D.A. Tryk, Titanium dioxide photocatalysis, J. Photochem. Photobiol., C. 1 (2000) 1–21.

[6] I. Sopyan, M. Watanabe, S. Murasawa, K. Hashimoto, A. Fujishima, An efficient TiO_2 thin-film photocatalyst: photocatalytic properties in gas-phase acetaldehyde degradation, J. Photochem. Photobiol., A. 98, 1–2 (1996) 79–86.

[7] A. Zaleska, Doped-TiO_2: A review, Recent Pat. Eng. 2 (2008) 157–164.

[8] P. Wang, B. Huang, X. Zhang, X. Qin, H. Jin, Y. Dai, Z Wang, J. Wei, J., Zhan, S. Wang, J. Wang, M.-H. Whangbo, Highly efficient visible-light plasmonic photocatalyst Ag@AgBr, Chem. Eur. J. 15 (2009) 1821–1824.

[9] T.-T. Lim, P.-S. Yap, M. Srinivasan, A.G. Fane, TiO_2/AC composites for synergistic adsorption-photocatalysis processes: Present challenges and further developments for water treatment and reclamation, Crit. Rev. Environ. Sci. Technol. 41, 13 (2011) 1173–1230.

[10] S.-Q. Liu (2012). Chapter 4: Magnetic nano-photocatalysts: Preparation, structure, and application, In: E. Lichtfouse et al. [editors], Environmental Chemistry for a Sustainable World: Volume 1: Nanotechnology and Health Risk, doi: 10.1007/978-94-007-2442-6_4., Springer Science + Business Media, B.V.

Chapter 2:
Background and literature review

2.1 Background

2.1.1 General description of photocatalysis

Research in photocatalysis has been pursued since discovery of the photocatalytic water splitting effect by Fujishima and Honda [1]. Photocatalytic processes involve the generation of electron-hole pairs upon excitation of a photocatalytic material (generally a semiconductor), and the negatively charged electrons and positively charged holes can interact with water, oxygen, and adsorbed pollutants to initiate a series of chemical reduction and oxidation reactions that can cause the degradation and eventual mineralization of pollutants [2]. The process is often shown schematically for a semiconductor photodegrading an organic pollutant according to Figure 2.1, where photons exceeding the band gap energy (E_{bg}) of the photocatalyst are absorbed by electrons in the filled valence band (VB), causing them to be promoted to the empty conduction band (CB), leaving behind positively charged holes. Another possible fate of the photoproduced electrons and holes is their recombination, which is reported to be one of the major factors limiting photocatalytic efficiency [3].

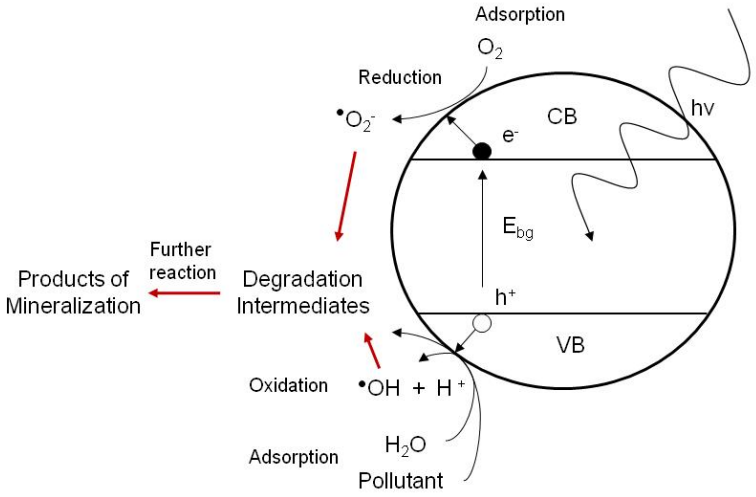

Figure 2.1: Photocatalytic degradation of a pollutant by a semiconductor

The photogenerated radical and reactive oxygen species produced are highly reactive, and can readily interfere with normal biological functions in a number of microorganisms, leading to inactivation. For example, in TiO_2-mediated disinfection of *E. coli*, the mechanism of photocatalytic inactivation has been linked to the action of reactive oxygen species attacking polyunsaturated phospholipids, causing breakdown of the cell membrane through lipid peroxidation [4]. TiO_2 is the most widely used photocatalyst due to its chemical stability, availability, and low cost [5].

2.1.2 Applications of photocatalytic systems

Due to the versatility of photocatalysis to degrade a wide range of organic contaminants; inactivate bacteria, fungi, viruses, and spores; and reduce heavy metals in both air and water matrices, this process has received attention for application to many systems. Photocatalysis has been studied in water treatment for contaminant destruction and removal, heavy metals reduction, and sterilization and disinfection; and in air treatment for purification, decontamination, deodorization, bioaerosol removal, and self-cleaning applications (as reviewed in [6]). Key applications of photocatalytic disinfection were previously highlighted in a publication authored by the PhD candidate, as provided in Appendix B.

2.1.3 Current challenges in photocatalysis

A major challenge in photocatalysis, which is cited to be the main barrier to large-scale

commercialization, lies in the low quantum efficiencies (typically below 5%) of TiO_2-mediated systems. This low efficiency is related to many factors, including: inefficient use of solar radiation, electron-hole recombination, and difficulties in development and scale-up of multi-phase photocatalytic reactors. The reactor design aspect is particularly difficult, since immobilized-bed reactors have been widely used for ease of separation of the treated fluid and nanosized catalyst in large scale systems, resulting in the coupled consideration of mixing regimes, mass transfer effects, reaction kinetics, catalyst immobilization, and optimal illuminated specific surface area [7]. Emission and radiation modeling must also frequently be undertaken for unusual reactor geometries designed to optimize irradiated areas and surface contact such as the corrugated drum reactor developed in our group [8, 9].

Low photocatalytic efficiencies are also related to the use of TiO_2 because of its relatively high band gap energy of 3.2 eV, which leads to the ineffective use of solar radiation. TiO_2 may only be excited by light of wavelengths in the ultraviolet (UV) range ($\lambda < 400$ nm); however, as shown in the solar spectral distribution in Figure 2.2, a large portion (~43%) lies in the visible light region. Only approximately 3–5% of solar radiation contains UV. Other practical issues are associated with TiO_2, such as difficulty in catalyst separation from the treated slurry, due to its nanosized structure [10]. Defects and inefficient pollutant transfer to photogenerated species also lead to the rapid rate of recombination observed experimentally [11].

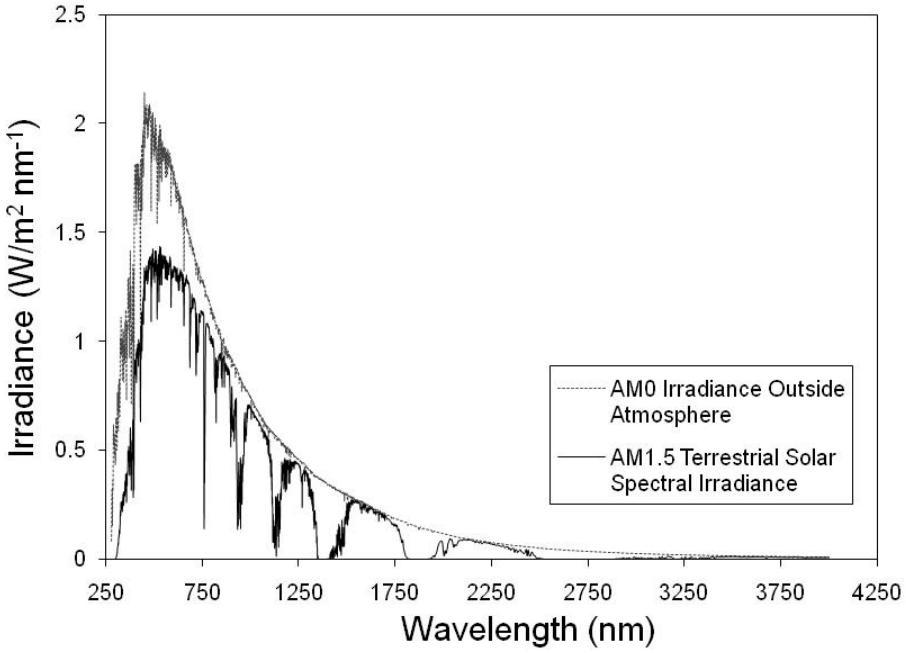

Figure 2.2: Solar spectral distribution (adapted from [12])

2.1.4 Strategies for increasing photocatalytic efficiencies

2.1.4.1 General strategies

Two main categories of research in increasing solar photocatalytic efficiencies exist:

1. Increasing efficiency through photoreactor design and optimization (to better distribute and utilize incoming UV in solar radiation), and
2. Increasing efficiency through photocatalyst development (to utilize a greater fraction of incoming solar radiation).

Photocatalytic reactor design and optimization have led to the development of many novel photoreactors whose structure and function borrow heavily from traditional solar collectors, including: parabolic trough, compound parabolic, and falling film reactors [13]. Other configurations such as packed bed [14] and rotating reactors [8, 9] have also been studied to address the need for effective mixing of the catalyst and reactant medium, and to ensure appropriate exposure to illumination.

Some general approaches for increasing photocatalytic activity through photocatalyst development and modification have been identified in literature, namely: band gap tuning

(altering electronic structure) or extension of excitation wavelengths through the use of photosensitizers; minimizing charge carrier (electron-hole) recombination; and promoting forward reaction by trapping of reactants by adsorption, and facilitating reactant transfer to active sites [15]. Additionally, to address the practical issue of separability, incorporation of magnetic components has also been investigated [16]. These strategies related to photocatalyst improvement are further detailed in subsequent sections.

2.1.4.2 Altering photocatalyst electronic structure and sensitization

Many approaches can be used to shift photocatalyst absorption into the visible light region, including: metal ion implantation using transition metal cations such as V^{+} or Cr^{+} to substitute the lattice Ti^{4+} positions in TiO_2 [17, 18]; anion-doping of TiO_2 to obtain N-doped [19], C-doped [20, 21], or S-doped materials [22, 23]; C, N co-doping of TiO_2 [24]; and the use of dispersions of noble metals such as Pt, Rh, or Au on TiO_2 to act as surface absorption centres, substitutional, and interstitial impurities that lead to band gap narrowing [25, 26]. Other approaches involve the deposition of narrow band gap semiconductors such as CdS (E_{bg} = 0.5 eV) onto TiO_2, to sensitize the larger band gap carrier by injection of photoexcited electrons from the conduction band of CdS into that of TiO_2 [27], or the incorporation of a similar charge injection mechanism by dye-sensitization of TiO_2 [28]. Some proposed mechanisms of alteration of band gap structure upon the addition of dopants and sensitizers are given schematically in Figure 2.3.

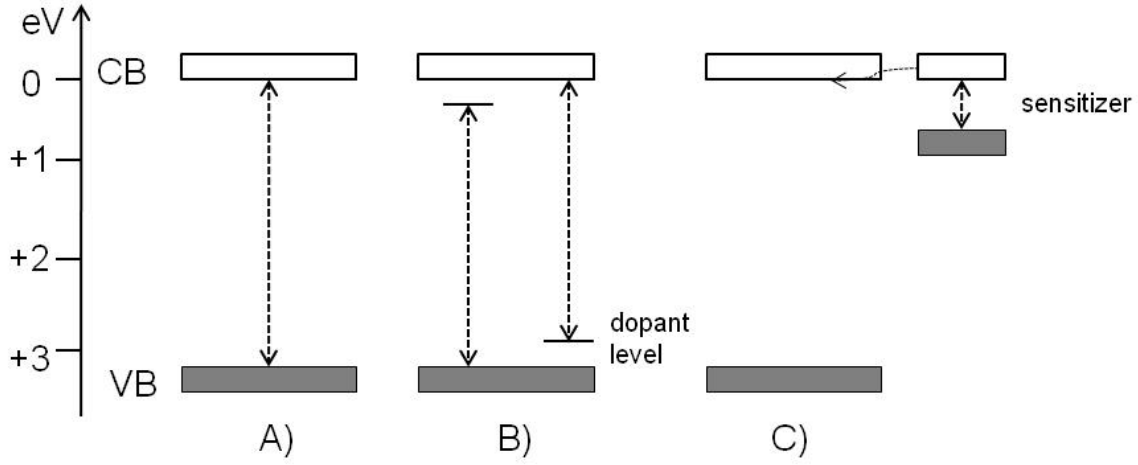

Figure 2.3: Proposed changes to band gap structure of a pure semiconductor photocatalyst A), upon doping B), and upon addition of a sensitizer C); (adapted from [15, 29])

2.1.4.3 Minimizing charge carrier recombination

Research in band engineering of photocatalysts can involve the use of binary metal oxides with various crystal structures such as perovskites (of the form ABO_3, where A and B are metals), pyrochlores ($A_2B_2O_7$), spinels (AB_2O_4), and delafossites (ABO_2), which show good photoactivity due to the orientation of atoms in a layered structure, and effect the mobility of photogenerated charges by incorporation of various elements, thus preventing electron-hole recombination by charge separation mechanisms [30]. Another approach reported is the combination of photoactive crystal structures of TiO_2 (anatase and rutile) having different energy levels, which may promote charge separation by the internal electric field driving force created [31, 32]. Some other methods of minimizing recombination include: deposition of metals on the surface of TiO_2 to act as electron traps [33–35]; carbon nanotube [36–39] and graphene-based semiconductor composites providing high electron mobility [40]; and heterostructure photocatalysts based on semiconductor combination such as mixing of BiOI/BiOBr [41], and AgI/BiOI [42] to separate photogenerated charges at the heterojunction between catalysts.

2.1.4.4 Promoting forward reaction by increased surface areas and synergistic adsorption

Since photocatalysis is a surface reaction, increasing the catalyst surface area can directly influence the reaction rate. This can be accomplished through many different approaches, such as: decreasing photocatalyst size [43]; incorporating the photocatalyst into various high surface area nanostructures such as nanotubes, graphenes, and fullerenes [15]; preparing porous photocatalysts through template methods and self-organization [44]; and immobilizing photocatalysts on high surface area substrates such as activated carbon [45], zeolites [46], glass fibers [47, 48], silica [49–51], pumice stone [52], and clays [53].

For photocatalyst composites fabricated using highly adsorbent substrates, such as activated carbons and fullerenes, a synergistic increase in the photocatalytic rate was reported [54-57]. This synergy was attributed to the presence of a common contact interface between solids, where the pollutants were adsorbed by the substrate and migrated continuously to the supported photocatalyst [58].

2.1.4.5 Improving catalyst separability

The development of porous photocatalysts with high surface areas by dispersion of nanosized materials onto porous solids is also focused on improving the technical feasibility of catalyst separation and reuse. In addition, addressing issues related to nanoparticle aggregation and concerns over biocompatibility and toxicity of these materials as their particle size is decreased also provides motivation for research along this stream [44]. Another approach to improving catalyst separability is through development of magnetically recoverable photocatalysts [59]. These may be two-component magnetic core@photocatalyst shell structures (such as Fe_3O_4@TiO_2 [60], γ-Fe_2O_3@TiO_2 [61]) or three component core@insulating interlayer@shell to prevent reaction between the photocatalyst and magnetic component itself (such as in Fe_3O_4@SiO_2@TiO_2 [62], and Fe_3O_4@SiO_2@AgCl:Ag [63]). Recently, single-component magnetic photocatalysts such as bismuth ferrites ($BiFeO_3Bi_{25}FeO_{40}$, $Bi_{25}FeO_{40}$-$BiFeO_3$ [64]) have also been explored, which act as both photocatalyst and magnetic components.

2.2 Literature review

2.2.1 Overview of carbon-enhanced photocatalysts

As discussed by Leary and Westwood in their review on carbonaceous nanomaterials for the enhancement of TiO_2 photocatalysis [15], development of carbon-enhanced photocatalysts represents an important field of research in visible light photocatalysis. The carbon-enhanced photocatalysts can be grouped according to the following general categories for improving photocatalytic activity: activated carbon adsorption enhancement; carbon-doping; and the incorporation of carbon nanotubes, fullerenes, thin layer carbon coating, and nanometric carbon black. In this project, the first two approaches were investigated concurrently, and are discussed further in subsequent sections with respect to the defined project objectives.

Specifically, literature pertinent to the development of surface plasmon resonance (SPR) photocatalyst-adsorbent composites based on activated carbon and their magnetic counterparts, and the development of carbon-doped TiO_2 is presented. Mechanistic considerations regarding the modes of photocatalysis enhancement, as well as notable

studies, are highlighted with the goal of reviewing the state of the art as relevant to the project undertaken.

2.2.2 Development of SPR photocatalyst-adsorbent composites based on activated carbon and their extension towards magnetic removal strategies

The development of SPR photocatalyst-adsorbent composites, and their extension towards magnetic removal strategies integrates three main streams of current research in improving photocatalytic efficiencies and feasibilities, namely the design of SPR photocatalysts, bifunctional adsorbent photocatalysts, and magnetic photocatalysts.

2.2.2.1 SPR photocatalysts

2.2.2.1.1 Mechanism of photocatalytic enhancement

Nanoparticles of noble metals have been found to exhibit unique optical properties, namely localized SPR, which is a phenomenon arising from the collective oscillation of conduction electrons upon interaction with electromagnetic radiation [65]. The shape, amplitude, and frequency of the localized SPR absorption band is strongly dependent on the effective dielectric constant in the surrounding medium of the nanoparticles and their respective morphologies and size distributions [66]. This SPR can dramatically amplify visible light absorption, and is therefore of interest to photocatalyst development. For example, silver nanoparticles exhibiting SPR in the visible light region have been implemented for the production of photocatalysts such as Ag-TiO_2 [67, 68]. However, having the highly reactive nanoparticles in direct contact with TiO_2 in these catalysts can lead to oxidation of silver at the interface, necessitating introduction of a protective layer of passive material such as SiO_2 to improve stability [67].

Another approach to increasing stability of silver nanoparticles for photocatalysis is through the use of silver halides, which are photosensitive materials widely employed in photographic films. In photographic processes, silver halides absorb photons to liberate electron-hole pairs. The free electrons can combine with mobile interstitial silver ions to cause the separation of a silver atom, and upon continued absorption of photons, clusters of silver atoms are formed [69]. Due to their instability under light, silver halides have not traditionally been used as photocatalysts.

However, when silver halides are partially surface reduced to silver nanoparticles, the two components in the silver/silver halide composite structure can act in concert as an efficient and stable visible light active photocatalyst [70]. The synthesis of silver/silver halides (mainly Ag/AgCl and Ag/AgBr) has been reported in literature using a variety of techniques such as deposition-precipitation-photoreduction [68, 70, 71], one-pot synthesis with poly(vinyl pyrrolidone) (PVP) and ethylene glycol at elevated temperature [72], ionic-liquid synthesis using 1-octyl-3-methylimidazolium chloride as chlorine source and reducing agent [73], double-jet method [74], and microwave-assisted non-aqueous growth [75]. In all cases, strong absorption in the visible light region was observed, due to SPR of the incorporated silver nanoparticles.

In a system such as Ag/AgCl, visible light photons can be absorbed by silver nanoparticles, generating holes and electrons. These can be effectively polarized by the surface plasmon resonance state of nanosilver, causing efficient separation of the charge carriers such that the electrons are transferred to the silver surfaces furthest away from the interface with AgCl (because AgCl is terminated by Cl^- ions, and is negatively charged), and the holes transferred to the AgCl particle surface [70]. The photostability of silver/silver halides has been attributed to this charge separation mechanism, which prevents the generated electrons from being transferred to Ag^+ ions in AgCl [73]. Instead, the electrons are transferred to molecular oxygen present at the surface, forming active species such as superoxide anions, which can facilitate degradation of pollutants [76]. The positive holes generated can oxidize Cl^- ions into chlorine atoms (Cl^o), which are themselves powerful oxidizing agents that can attack organic pollutants near the surface of the catalyst, and be reduced back to their ionic state [70, 74]. The process is shown schematically in Figure 2.4.

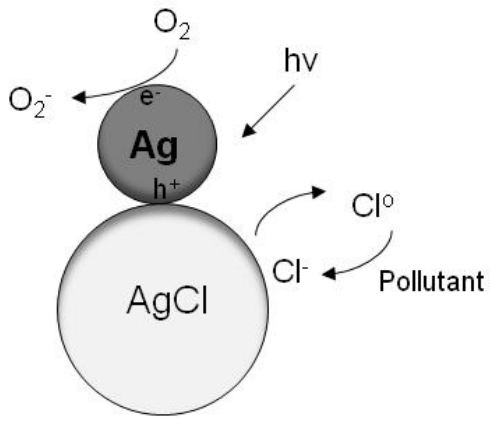

Figure 2.4: Mechanism of photoexcitation and charge separation in Ag/AgCl

Silver/silver halides such as Ag/AgCl therefore represent an important class of photocatalyst because they are highly visible light active due to SPR, and they incorporate a charge separation mechanism that improves catalyst stability and prevents recombination of the photoinduced electrons and holes. Among various silver/silver halide systems reported, Ag/AgCl is the most widely studied, although Ag/AgBr is also of interest due to its increased visible light absorption, attributed to both SPR and band gap absorption of AgBr in the visible light range [77]. The Ag/AgI system is of less interest due to its decreased observed photocatalytic activity arising from the weak oxidation power of iodine [78]. Although research in silver/silver halides and other SPR-enhanced photocatalysts is ongoing and has increased in recent years, it should be noted that understandings of the mechanisms of SPR-enhancement in photocatalytic processes under visible light are still being developed. For example, recent efforts have been made to rationalize, classify, and generalize experimental results based on physical mechanisms and the structure of the prepared photocatalysts according to the formation of Schottky junctions, localized SPR-powered electron-hole generation through sensitization or bandgap breaking, and the localized enhancement of local electric fields [77]. Despite this, conflicting results in literature and debate as to the dominant mechanisms that take place in plasmonic photocatalysis still exist and prevent such generalizations for mechanistic analysis from gaining widespread acceptance to date. However, the mechanism presented in the previous discussion is in accordance with the original 2008 study on Ag@AgCl published by Whangbo's group [70], which carries nearly

400 citations as of 2014, and represents the most widely-used analysis of Ag/AgCl photocatalysis.

2.2.2.1.2 Incorporation of silver/silver halides onto other photocatalysts and onto supports

The incorporation of Ag/AgCl and Ag/AgBr onto other photocatalysts, such as TiO_2 particles [69, 79], TiO_2 nanotubes [80], or layered Bi_2WO_6 [81] has been reported to increase the photocatalytic efficiency over that observed using the carrier catalyst alone, due to the introduction of the plasmonic effect, and the formation of heterojunctions. Deposition of silver/silver halides onto various supports such as such as graphene sheets [71], graphene oxides [40, 82], mesoporous alumina [78], and zeolites [83, 84] has also been reported, where the role of the host material is to increase the surface area and dispersion of Ag/AgCl. The nanocarbon carriers also affected the mobility of photoinduced charges. Another approach to increasing the surface area of Ag/AgCl was reported through the development of porous Ag/AgCl nanocomposites [85], which were found to exhibit high photocatalytic activity for the degradation of methyl orange under visible light.

2.2.2.1.3 Applications to degradation and disinfection

Studies involving the screening and investigation of photocatalytic activity commonly use dyes such as methyl orange, methylene blue, and Rhodamine B as model organic pollutants for photodegradation to maintain a common basis for comparison between catalysts, and to establish a baseline photoreactivity. The degradation of other organics by silver/silver halides was also explored in other studies, such as for model pesticide pentachlorophenol by Ag/AgBr [75].

The disinfective capability of $Ag/AgBr/TiO_2$ was investigated by Hu et al. [69] for inactivation of *E. coli* under visible light irradiation. They studied the mechanism of cell death through transmission electroscope microscopy (TEM) imaging, and confirmed inactivation to be caused by radical decomposition of the cell membrane. The mechanism of *E. coli* photocatalytic cell death was also studied by Zhang et al. [81], and a dominant role of diffusing hydroxyl radicals was found using $Ag/AgBr/Bi_2WO_6$ plasmonic nanojunction catalysts. Photocatalytic disinfection of *E. coli* was also studied by Hu et al. [86] using

AgI/TiO_2, by Elahifard et al. [87] using apatite coated $Ag/AgBr/TiO_2$, and by Wang et al. [88] using $Ag/AgBr/WO_3 \cdot H_2O$ under visible light. The plasmon-induced photocatalytic killing of enteric microorganisms *Shingella dysenteriae*, *E. coli*, and human rotavirus type 2 Wa under visible light was reported using $Ag\text{-}AgI/Al_2O_3$ by Hu et al. [78].

Select studies reported bactericidal effects of silver and silver/silver halides in the absence of any photo-initiated processes. Nanosilver is a well-known antibacterial agent, and has been commercialized for a number of applications including use in consumer products such as clothing, respirators, cosmetics, detergents, socks, shoes, and mobile phones [89]. It has also been implemented into commercial water filters and impregnated into activated carbon to reduce the biocompatibility of these materials [90]. The mode of bactericidal action was proposed to be due to sorption of silver ions onto the negatively charged bacterial cell wall, causing deactivation of cellular enzymes, disruption of the permeability of the membrane, and eventual cell lysis and death [91, 92].

The bactericidal effect of Ag/AgCl only (in the absence of light) was reported using *E. coli* K-12 as a model microorganism [93]. In this case, the bactericidal action observed was due to the effects of incorporated nanosilver. A similar disinfection was observed using AgCl only in the dark [94, 95], was and attributed to the diffusion of Ag^+ ions. Nano-AgBr deposited on activated carbon filters were prepared by Pal et al. [96], and were found to exhibit a bactericidal effect on *E. coli*, however the use of this material as a photocatalyst was not discussed.

2.2.2.2 Bifunctional adsorbent photocatalyst composites

2.2.2.2.1 Mechanism of photocatalytic enhancement

"Bifunctional" adsorbent photocatalyst composites, possessing dual adsorbent and photocatalytic functions [97], have been prepared and investigated for the enhancement of photocatalysis due to their reported synergistic increase in photoactivity attributed to the incorporated adsorbent [56]. Another motivation for their development is to address separability issues associated with the use of nanosized TiO_2 in slurry, while still maintaining high surface areas, which are not attainable using immobilized catalyst films [98].

Adsorbent photocatalysts can achieve high rates and efficiences of photocatalytic degradation, caused in part by the concentration of pollutant around the photocatalyst active sites by the adsorbent. This is an important factor for enhancing reaction rate, due to the short-lived nature of photogenerated radicals (e.g. average lifespan of 10 μs for hydroxyl radicals in the presence of scavengers) [99]. Additionally, the retention of photocatalytic reaction intermediates to undergo further degradation on the active surface is a significant advantage of these composites, where reaction intermediates may be retained by adsorption to undergo subsequent reactions leading to more complete degradation and mineralization, as opposed to being desorbed and diffused away from the surface (as in conventional photocatalysts). In the conventional scheme, further reaction of these chemical intermediates relies upon their diffusion from solution back to the active sites of the photocatalyst [15, 100]. It should also be noted that not all reactants colliding with the conventional unsupported photocatalyst will be adsorbed due to surface area limitations, however, this becomes much more likely with an adsorbent photocatalyst [100].

2.2.2.2.2 Activated carbon-based composites

Activated carbon (AC) has been identified as an attractive material for the preparation of adsorbent photocatalysts because it has a large adsorption capability for a wide range of organic compounds and non-organic matter, is cost effective and available in various particle sizes, and can adsorb most photocatalysis intermediates and byproducts. Additionally, its use is well- established in conventional water treatment schemes and technologies, making it a suitable support or composite material when blended with photocatalysts [101].

There has been a number of studies on TiO_2-AC composites, fabricated using a variety of techniques for synthesis and deposition of the photocatalyst including: chemical methods (e.g. sol-gel, chemical vapor deposition, hydrothermal, molecular adsorption-deposition), and physical methods (e.g. ionized cluster beam). The incorporated activated carbon has been studied in many of its available forms, including as powdered, granular, and fibrous materials [101]. Physical methods have also been reported for the preparation of TiO_2-AC composites, where mixing of TiO_2 and AC is performed in the reaction suspension, and a

synergistic effect is still realized [102–108] although practical issues may occur with the dislodgement of TiO_2 upon abrasion.

Consideration towards the type of AC particle size, activation or pre-treatment, raw materials, and porosity must also be considered in the preparation of adsorbent photocatalyst composites. For example, it is desirable to use a small AC particle size to limit the intraparticle diffusion path, reduce the radical migration path to the internally adsorbed pollutants, and facilitate regeneration by reducing diffusion path of desorbed pollutants to the surface [101]. A limitation of these composites is that the incorporated TiO_2 photocatalyst may cause pore-blocking in activated carbon, as the catalyst often resides on the outer surface and macropores of the composite material [54, 109].

In addition to confirmation and quantification of photoactivity by degradation of indicator dyes as model organic pollutants (methyl orange, methylene blue, Rhodamine B), these composites have been studied for the removal of pollutants in real waste effluents, such as those from paper mills [110], and sewage treatment plants [111]. It should be noted that the majority of studies in literature report the photoactivity under artificial UV irradiation, due to the large required energy to excite the TiO_2 photocatalyst.

Photocatalytic regeneration in TiO_2-AC composites has been reported with some success for the complete destruction of adsorbed materials by the photocatalyst to regenerate the spent activated carbon [112], as well as in studies employing ultrasound-enhanced photocatalytic regeneration (sonophotocatalysis) [111, 113].

2.2.2.2.3 Visible light active photocatalyst-AC composites

A knowledge gap identified in research on adsorbent photocatalysts based on activated carbon lies in the development and incorporation of visible light active photocatalysts into the composites [15], which allows for the better utilization of solar irradiation for photocatalytic treatment and remediation applications. Some research has been conducted along these lines, such as through the preparation of Ag-TiO_2/AC [114], which has improved efficiency over TiO_2 alone due to the electron-trap mechanism of the incorporated silver, and

through the incorporation of CdS-modified TiO_2 into AC fibers, which act through sensitization and charge injection from the smaller band gap photocatalyst [115]. Recent efforts have also been made in the development of N-doped TiO_2-AC composites that are visible light active by a band gap narrowing mechanism [116, 117], where the authors highlighted the need for further development of synergistic AC composite catalysts that can be activated by visible light.

Potential for microbial biofouling and biofilm formation on activated carbon in practical applications of adsorptive photocatalytic treatment of water and wastewater streams can also limit the applicability of these adsorbent photocatalyst composites and should therefore be investigated [101]. Select studies have been performed on photocatalytic inactivation of bacteria by photocatalyst-AC composites, such as the adsorption of *E. coli* cells and their photosterilization over TiO_2-AC granules reported by Horie et al. [118], photosterilization of *E. coli* using TiO_2-AC by Li et al. [119], and inactivation of *Penicillium expansum* fungus using TiO_2-AC fiber film by Ye et al. [120], however the topic of disinfection is not widely reported.

2.2.2.3 Magnetically separable photocatalysts

2.2.2.3.1 Overview of magnetically separable photocatalysts

Suspended photocatalysts possess unique advantages for photocatalysis such as high specific surface area, effective light absorption for solar energy utilization, and ease of transport between powder surfaces and reactants in solution [16]. To facilitate the recovery and cyclic utilization of these suspended particles, immobilization on supports such as glass beads [121–123], lamp walls [124, 125], and glass plates [126] has been studied. However, the photocatalytic activity suffers a decrease upon immobilization due to the low specific surface area provided by the support and limitations in mass transfer. High surface areas and the synergistic effects provided by activated carbon-based adsorbent photocatalyst composites can help overcome these limitations, but it has been reported that even these composite materials are difficult to recover fully [107, 127]. This emphasizes the need for magnetic photocatalysts that can undergo simple separation using an external magnetic force.

Development of magnetic photocatalysts has been ongoing since the first report of a photocatalytic magnetic material consisting of TiO_2 deposited onto a magnetite core was made by Hiroshi et al. [128]. A number of magnetic photocatalysts have been proposed and tested since, mainly having either magnetite (Fe_3O_4), maghemite (γ-Fe_2O_3), or MFe_2O_4 (where M is Ba^{2+}, Ni^{2+}, Co^{2+}, or Zn^{2+} divalent metallic cations) as the functional magnetic component [16].

2.2.2.3.2 Core-shell magnetic photocatalysts

Early magnetic photocatalysts were composed of a two layer core-shell structure, where the photocatalyst was in direct contact with the magnetic component, such as in TiO_2 on Fe_3O_4 [60], TiO_2 on $BaFe_2O_4$ [129], and $NiFe_2O_4$ on TiO_2 [130]. These photocatalysts suffered from a decreased activity and stability because of the direct contact between the two components, causing recombination of photogenerated electrons and holes, and photodissolution of the magnetic iron oxide particles under irradiation. Recombination of photogenerated holes and electrons in systems such as TiO_2/magnetite is thought to occur through hole transfer from the VB of TiO_2 to the VB of magnetite and electron transfer from the CB of TiO_2 to the CB of magnetite, since the energy level of the CB in TiO_2 is higher than of magnetite, and vice versa for the VB. Transfer of these electrons and holes effectively prevents interaction with adsorbed oxygen and water to form reactive species, decreasing the photocatalytic efficiency observed [16].

The introduction of a passivation interlayer between the magnetic core and photocatalyst shell to prevent photodissociation was first proposed by Chen and Zhao [131] in a γ-Fe_2O_3-SiO_2-TiO_2 three-component photocatalyst, where an SiO_2 layer was used as an insulator due to its relatively large band gap energy of ~9.0 eV, which effectively prevented electrical contact of the photocatalyst with the magnetic core. The three-component catalysts have since been widely reported, with both magnetite [62, 132, 133] and maghemite [131, 134–137] magnetic cores studied, as well as nickel [138–140], cobalt [141, 142], and barium ferrites [143, 144]. Other passivation layers, such as poly(methyl methacrylate) [145] have also been investigated. A schematic representation of various three-component magnetic photocatalysts is given in Figure 2.5.

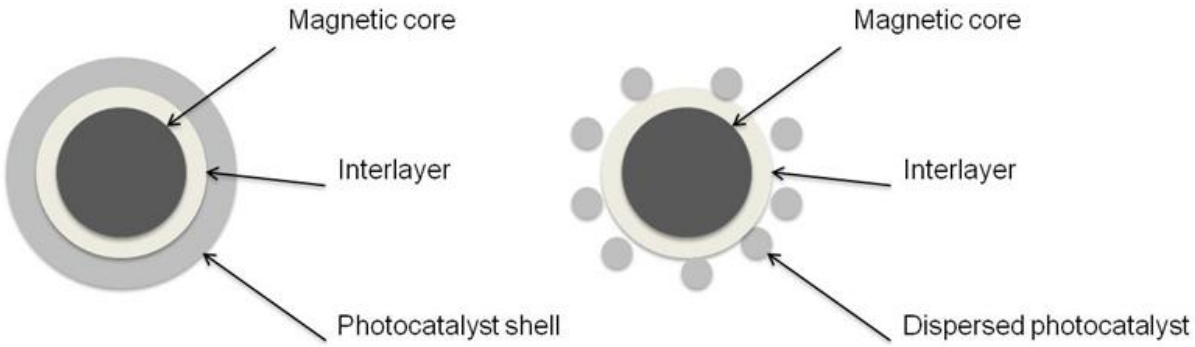

Figure 2.5: Three component core-shell magnetic photocatalysts; two configurations of photocatalyst shown

2.2.2.3.3 Visible light active magnetic photocatalysts

The replacement or modification of TiO_2 in conventional magnetic photocatalysts with materials of higher visible light activity has been studied. While some of these materials contain the core-shell type structure incorporating a passivation layer, early hybrids were reported as simple composites with magnetic iron oxides. Reported strategies for improving visible light activity of magnetic photocatalysts include: modification of TiO_2 by S-doping [146], B-, F- co-doping [147], V-doping [148], Cl-doping [149], N-doping [140, 150, 151], Ce-doping [152], La-doping [153], Cu-doping [154]; and replacement of TiO_2 with visible light active photocatalysts such as $B_{12}TiO_{20}$ [155], $BiVO_4$ [156], Ag_3VO_4 [157], and ZnS [158].

The use of plasmonic enhancement has also been reported for the improvement of visible light activities in core-shell magnetic photocatalysts. Li et al. deposited Ag/AgBr onto an SiO_2-covered magnetite core using a deposition-precipitation-calcination procedure, and evaluated the visible light induced photodegradation of Acid Orange 7 dye as an indicator of photocatalytic activity [159]. Similarly, Ag/AgI was deposited onto SiO_2-coated magnetite using deposition-precipitation-photoreduction, and evaluated for the visible light degradation of Rhodamine B and 4-chlorophenol [160]. An et al. [63] extended this synthesis using AgCl prepared by polyol precipitation, followed by photoreduction to form Ag/AgCl on SiO_2-

coated magnetite. They also tested the degradation of Rhodamine B under visible light irradiation.

Disinfection of bacterial species using magnetic photocatalysts has also been reported to some extent. Rana and Misra [161] investigated the inactivation of *E. coli* using magnetic photocatalyst TiO_2-$NiFe_2O_4$ under UV irradiation. Fast inactivation kinetics of *E. coli* under UV were observed by Chin et al. [162] using commercial P25 TiO_2 (mixed-phase anatase and rutile) coated magnetite nanoparticles, although Coleman et al. [163] previously reported these kinetics to be slower than those of pure P25 in their system consisting of a spiral tube reactor wrapped around a UV lamp with the catalyst in slurry. Bacterial inactivation of *E. coli* was also reported for a magnetic plasmon photocatalyst, Au-AgCl nanotubes decorated with magnetite nanoparticles, under natural sunlight (varying from 400–700 W/m^3) [164].

2.2.2.3.4 Magnetic activated carbon photocatalysts

The preparation of magnetic AC can be performed to improve the separability of the adsorbent, and magnetic activated carbons have been studied for use in precious metals recovery such as gold adsorption from alkaline cyanide solutions [165], or for the adsorption of organic dyes [166], pesticides such as imidacloprid [167], and aqueous organic compounds such as chloroform, phenol, and chlorobenzene [168]. Some representative examples of magnetic activated carbons prepared in literature are presented in Table 2.1.

In these materials, a passivation layer was not considered, since a photoreactive system was not used. As such, SiO_2 coating of the magnetic nanoparticles incorporated into AC was not necessary.

Table 2.1: Comparison of select magnetic activated carbons reported in literature

Magnetic Adsorbent	Adsorbent	Magnetic Component	Preparation Method	Target Adsorbate(s)	Reference
Magnetic charcoal	Knife-milled charcoal beans (0.2–1.5 mm diameter)	Mixed iron oxides (not characterized)	Precipitation of $FeSO_4 \cdot 7H_2O$ in the presence of AC	Organic dyes aniline blue, Bismarck brown Y, methylene blue	[166]
Magnetite-loaded activated carbon	Commercial activated carbon	Magnetite nanoparticles (19–124 nm)	Co-precipitation to form magnetite and subsequent doping into AC; heterogeneous method based on refluxing goethite, AC, and $FeCl_2 \cdot 4H_2O$	Gold as $Au(CN)_2$ in cyanide solution	[165]
Magnetite-AC nanocomposite	Activated carbon black (Vulcan XC-72)	Magnetite nanoparticles (~8 nm diameter)	Co-precipitation to form magnetite, sonication in the presence of AC to deposit magnetite	Methylene blue	[169]
Magnetic powdered activated carbon (PAC)	Norit powdered activated carbon	Mixed phase magnetite, maghemite (non-magnetic hematite and goethite present)	Co-precipitation of $FeCl_3$ and $FeSO_4$ by dropwise addition of NaOH in the presence of PAC	Imidacloprid	[167]
Maghemite-AC spheres	Carbon microspheres (formed during hydrothermal synthesis)	Single-phase maghemite	Hydrothermal reaction of glucose, $Fe(NO_3)_3 \cdot 9H_2O$, followed by CO_2 activation at 700°C for 2 hours	Methyl orange	[170]
Magnetic PAC	Dried Calgon WPH PAC	Mixed phase magnetite, maghemite (non-magnetic hematite present)	Heterogeneous nucleation: co-precipitation of iron (II) and (III) salts in the presence of carbon by rapid alkaline hydrolysis	Mercury (II)	[171]

The extension of magnetic activated carbon to photocatalytic applications by introduction of a photocatalyst to form a composite was first investigated by Ao et al. in 2008 [172]. In this

study, sol-gel synthesis was used to deposit TiO_2 onto magnetic activated carbon, which contained mixed magnetite and maghemite nanoparticles. The weight ratio of magnetic activated carbon to titania was held at 1:2 in all samples, and the iron was present in concentrations up to 30 weight percent. Some pore-blocking and reduction in surface area was observed upon addition of iron and TiO_2. The photocatalytic activity of the composite was evaluated by the degradation of phenol under UV irradiation. While phenol degradation was possible using this catalyst, a photodissociation of magnetite (E_{bg} = 0.1 eV) and maghemite (E_{bg} = 2.3 eV) phases under irradiation was observed [60, 132]. In another study by Ao et al. [173], maghemite-AC was prepared, and was used at weight ratios of 1:7 (γ-Fe_2O_3: AC) and 1:3 (magnetic AC: TiO_2). The lower iron concentration, and dominance of the maghemite phase prevented photodissolution of magnetic nanoparticles, although a small portion was still found to be degraded, as quantified by inductively coupled plasma - atomic emission spectroscopic analysis of the Fe content in the processed water. Subsequently, Ao et al. investigated the degradation of an azo dye X-3B using titania-coated magnetic activated carbon under visible and UV irradiation. The visible light activity observed was attributable to the dye-sensitization effect of X-3B [174]. Ao et al. also incorporated N-doped TiO_2 into the magnetic AC adsorbent, and tested this composite under solar irradiation [175]. An increased visible light absorption due to band gap narrowing was observed in the N-doped titania compared to neat TiO_2, and degradation of X-3B dye was studied. It should be noted that a self-sensitization mechanism may have also played a role in this system, due to visible light absorption by the dye. In addition, some incorporated iron was found to be degraded.

Another TiO_2 magnetic activated carbon was prepared by Wang and Zhou [137] based on a soft magnetic ferrite (Mn_{1-x}-$Zn_xFe_2O_4$) material integrated into activated carbon, and dip-coated in TiO_2 sol. The composite was found to possess good degradation activity for methyl orange under UV irradiation. Photodissolution of the incorporated magnetic particles was not addressed in this study, but the material was recyclable, and was able to perform well in up to 5 cycles. TiO_2-magnetic activated carbon was also investigated in a photocatalytic ozonation-intensified process for degradation of a model pharmaceutical compound, metoprolol tartrate, using a solar simulator and oxygen addition [176]. The prepared composite was

found to degrade the model compound in two hours for up to five consecutive runs. In this study, minor amounts of iron and titanium were found to leach from the catalyst into solution. Another report involving the preparation of TiO_2-AC incorporated nickel nanoparticles as the magnetic component, and studied the material for the degradation of methyl orange under UV [177].

2.2.3 Development of mixed-phase carbon-doped TiO_2

The following sections address literature pertinent to the investigation of carbon-doped TiO_2.

2.2.3.1 Mechanism of photocatalytic enhancement

Although TiO_2 doping has been studied using a variety of metallic and non-metallic dopants, nitrogen- and carbon-doping are of particular interest due to their low associated costs and band-gap narrowing, which significantly improve visible light absorption [15]. Carbon doping has been shown to be more effective than nitrogen doping [21, 178–180], although such catalysts are cited to be more difficult to prepare and have been less widely applied [179]. Synthesis has been performed via many routes, including simple mixing of a carbon nanomaterial with TiO_2 [37], direct oxidation of Ti metal in a burner flame [181, 182], sol-gel synthesis [183], hydrothermal synthesis [184], and deposition techniques such as physical vapor deposition, chemical vapor deposition, and electrophoretic deposition [15]. Due to the many variations in synthesis routes and results, conflicting findings in the literature have often been reported, spurring debate and controversy over the mechanism of visible light enhancement [185–189]. In general, it is accepted that band gap narrowing occurs in the presence of carbon dopant, which causes a red-shift in the photoactive wavelengths. Carbon-doping can alter the band gap from 0.1–1.5 eV [15]. However, the state of the carbon dopant has been reported and interpreted differently in various studies. Specifically, it is sometimes present as a substitutional anion due to the Ti-C bond in carbide [190–193], or as an interstitial cation due to the C-O bond in carbonates [21, 184, 194–196]. Despite this variation in findings for carbon-doped TiO_2, a widely supported view for the mechanism of band gap narrowing by carbon addition suggests the creation of mid-gap states (as shown in Figure 2.3) caused by mixing of the C 2p and O 2p states [19, 180, 197–199].

2.2.3.2 Oxidative annealing

Oxidative annealing of TiC in air to form carbon-doped TiO_2 is a facile one-step approach for obtaining visible light active photocatalysts. First introduced by Irie et al. [192] as a two-step oxidation procedure, Choi et al. used a variation of this synthesis based on one-step oxidation of TiC in air [190]. They tested the carbon-doped material semi-qualitatively for the degradation of methylene blue dye under visible light irradiation by monitoring changes in dye absorption spectra subject to photocatalytic degradation for 20 minutes. Shen et al. also investigated the one-step oxidation synthesis in air to produce carbon-doped TiO_2 (C-TiO_2), which was able to photocatalytically degrade trichloroacetic acid under visible light irradiation [199]. In addition, Cong et al. prepared carbon-doped TiO_2 loaded onto multiwalled carbon nanotubes using a two-step oxidative annealing process [200]. The addition of dopants such as carbon, nitrogen, and sulfur have been found to favour transformation of the anatase to rutile crystal phase in TiO_2 [201], while a synergistic effect between the anatase and rutile forms of TiO_2 has been reported to increase the photocatalytic activity of such mixtures [102]. Carbon-doped mixed-phase titania powders have been investigated previously [201], however the emphasis in oxidative annealing methods has been on the production of a pure anatase phase carbon-doped powder.

There have also been select reports on bacterial inactivation using carbon-doped TiO_2, including: inactivation of *E. coli* under visible light using C-TiO_2 prepared by ion-assisted electron beam evaporation [203], inactivation of *E. coli* under fluorescent light using C-TiO_2 prepared by aerosol flame deposition [204], and inactivation of *E. coli, Staphylococcus aureus, Enterococcus faecalis,* and fungi *Candida albicans* and *Aspergillus niger* under visible light by C-TiO_2 prepared using a sol-gel method [205]. However, since the synthesis method of preparation of doped powders has a strong effect on the final product and corresponding photocatalytic activity [15], it is difficult to elucidate the photocatalytic antimicrobial activity of C-TiO_2 prepared by oxidative annealing based on literature precedent alone.

2.3 Conclusions

In this chapter, specific features, advantages, and current challenges in photocatalytic processes were highlighted to provide a background and framework for the scope of the undertaken project. General strategies for improving photocatalytic efficiencies were presented and discussed, and a focused literature review of topics related to carbon-enhanced photocatalysts for visible light induced detoxification and disinfection was subsequently provided with the goal of framing the project objectives in the context of the current state of the art in photocatalysis research.

2.4 References

[1] A. Fujishima, K. Honda, Electrochemical photolysis of water at a semiconductor electrode, Nature 238 (1972) 37–38.

[2] C. Turchi, D.F. Ollis, Heterogeneous photocatalysis for water purification – contaminant mineralization, kinetics, and elementary reactor analysis, Environ. Prog. 9, 4 (1990) 229–234.

[3] J. Hagen (2006). Photocatalysis In: Industrial Catalysis: A practical approach, Second edition, Wiley-WCH Verlag GmbH & Co. KGaA, Weinheim, FRG.

[4] P.-C. Maness, S. Smolinski, D.-M. Blake, Z. Huang, E.J. Wolfrum, W.A. Jacoby, Bactericidal activity of photocatalytic TiO_2 reaction: Toward an understanding of its killing mechanism, Appl. Environ. Microbiol. 65 (1999) 4094–4098.

[5] S. Hager, R. Bauer, G. Kudielka, Photocatalytic oxidation of gaseous chlorinated organics over titanium dioxide, Chemosphere 41, 8 (2000) 1219–1225.

[6] D.F. Ollis, Photocatalytic purification and remediation of contaminated air and water, C.R. Acad. Sci. Paris, Série IIc, Chemie/Chemistry 3 (2000) 405–411.

[7] D. Devilliers, Semiconductor photocatalysis: Still an active research area despite barriers to commercialization, Energeia (CAER – University of Kentucky Center for Applied Energy Research) 17, 3 (2006) 1–3.

[8] S.M. Meunier, J. Gamage, Z. Duvnjak, Z. Zhang, Design and characterization of a novel rotating corrugated drum reactor for wastewater treatment, Int. J. Photoenergy 2010 (2010) Article ID A146743.

[9] A.A. Donaldson, A. Ye, J. Gamage McEvoy, Z. Zhang, Rotating corrugated photoreactor design: Experimental and computation analysis of TiO_2-based photocatalysis, AIChE J. 59, 2 (2012) 560–570.

[10] I. Sopyan, M. Watanabe, S. Murasawa, K. Hashimoto, A. Fujishima, An efficient TiO_2 thin-film photocatalyst: photocatalytic properties in gas-phase acetaldehyde degradation, J. Photochem. Photobiol., A. 98, 1–2 (1996) 79–86.

[11] B. Liu, K. Nakata, X. Zhao, T. Ochiai, T. Murakami, A. Fujishima, Theoretical kinetic analysis of heterogeneous photocatalysis: The effects of surface trapping and bulk recombination through defects, J. Phys. Chem. C 115, 32 (2011) 16037–16042.

[12] ASTM International (2008). ASTM Standard G173-03, Standard tables for reference solar spectral irradiances: Direct normal and hemispherical on 37^{o} tilted surface, doi: 10.1520/G0173-03R08.

[13] R.J. Braham, A.T. Harris, Review of major design and scale-up considerations for solar photocatalytic reactors, Ind. Eng. Chem. Res. 48, 19 (2009) 8890–8905.

[14] H.A. Irazoqui, M.A. Isla, R.J. Brandi, A.E. Cassano, Packed-bed photocatalytic reactors. A packing structure model and its experimental validation with computerized tomography, Ind. Eng. Chem. Res. 43, 6 (2004) 1430–1442.

[15] R. Leary, A. Westwood, Carbonaceous nanomaterials for the enhancement of TiO_2 photocatalysis, Carbon 49, 3 (2011) 741–772.

[16] S.-Q. Liu (2012). Chapter 4: Magnetic nano-photocatalysts: Preparation, structure, and application In: E. Lichtfouse et al. [editors], Environmental Chemistry for a Sustainable World: Volume 1: Nanotechnology and Health Risk, doi: 10.1007/978-94-007-2442-6_4., Springer Science + Business Media, B.V.

[17] M. Anpo, Utilization of TiO_2 photocatalysts in green chemistry, Pure Appl. Chem. 72, 7 (2000) 1265–1270.

[18] M. Anpo, M. Takeuchi, The design and development of highly reactive titanium dioxide photocatalysts operating under visible light irradiation, J. Catal. 216, 1–2 (2003) 505–516.

[19] R. Asahi, T. Morikawa, T. Ohwaki, K. Aoki, Y. Taga, Visible-light photocatalysis in nitrogen-doped titanium oxides, Science 293 (2001) 269–271.

[20] S.U.M. Khan, M. Al-Shahry, W.B. Ingler, Efficient photochemical water splitting by a chemically modified n-TiO_2. Science 297 (2002) 2243–2245.

[21] S. Sakthivel, H. Kisch, Daylight photocatalysis by carbon-modified titanium dioxide, Angew. Chem. Int. Ed. 42, 40 (2003) 4908–4911.

[22] T. Umebayashi, T. Yamaki, H. Itok, K. Asai, Band gap narrowing of titanium dioxide by sulphur doping, Appl. Phys. Lett. 81, 3 (2002) 454–456.

[23] T. Umebayashi, T. Yamaki, S. Yamamoto, A. Miyashita, S. Tanaka, T. Sumita, K. Asai, Sulfur-doping of rutile-titanium dioxide by ion implantation: Photocurrent spectroscopy and first-principles band calculation studies, J. Appl. Phys. 93, 9 (2003) 5156–5160.

[24] Y. Cong, F. Chen, J.L. Zhang, M. Anpo, Carbon and nitrogen-codoped TiO_2 with high visible light photocatalytic activity, Chem. Lett. 35, 7 (2006) 800–801.

[25] H. Kisch, L. Zang, C. Lange, W.F. Maier, C. Antonius, D. Meissnew, Modified, amorphous titania – A hybrid semiconductor for detoxification and current generation by visible light, Angew. Chem. Int. Ed. 37, 21 (1998) 3034–3036

[26] L. Zang, W. Macyk, C. Lange, W.F. Maier, C. Antonius, D. Meissnew, H. Kisch, Visible-light detoxification and charge generation by transition metal chloride modified titania, Chem. Eur. J. 6, 2 (2000) 379–384.

[27] S.S. Srinivasan, J. Wade, E.K. Stefankos, Visible light photocatalysis via CdS/TiO_2 nanocomposite materials, J. Nanomater. 2006 (2006) Article ID 87326.

[28] B. O'Regan, M. Grätzel, A low-cost, high-efficiency solar cell based on dye-sensitized colloidal TiO_2 films, Nature 353 (1991) 737–740.

[29] N. Serpone, Is the band gap of pristine TiO_2 narrowed by anion- and cation-doping of titanium dioxide in second-generation photocatalysts?, J. Phys. Chem. B 110, 48 (2006) 15287–24293.

[30] S. Murugesan, M.N. Huda, Y. Yan, M.M. Al-Jassim, V.R. Subramanian, Band-engineering bismuth titanate pyrochlores for visible light photocatalysis, J. Phys. Chem. C 114, 23 (2010) 10598–10605.

[31] Z. Liu, Z.-G. Zhao, M. Miyauchi, Efficient visible light active $CaFe_2O_4/WO_3$ based composite photocatalysts: Effect of interfacial modification, J. Phys. Chem. C 113, 39 (2009) 17132–17137.

[32] J. Yu, H. Yu, B. Cheng, M. Zhou, X. Zhao, Enhanced photocatalytic activity of TiO_2 powder (P25) by hydrothermal treatment, J. Mol. Catal. A: Chem. 253, 1–2 (2006) 112–118.

[33] D. Behar, J. Rabani, Kinetics of hydrogen production upon reduction of aqueous TiO_2 nanoparticles catalyzed by Pd^o, Pt^o, or Au^o coatings and an unusual hydrogen abstraction; steady state and pulse radiolysis study, J. Phys. Chem. B 110, 17 (2006) 8750–8755.

[34] S. Kim, S.-J. Hwang, W. Choi, Visible light active platinum-ion-doped TiO_2 photocatalyst, J. Phys. Chem. B 109, 51 (2005) 24260–24267.

[35] X. You, F. Chen, J. Zhang, M. Anpo, A novel deposition precipitation method for preparation of Ag-loaded titanium dioxide, Catal. Lett. 102, 3–4 (2005) 247–250.

[36] B. Ahmmad, Y. Kusumoto, S. Somekawa, M. Ikeda, M. Carbon nanotubes synergistically enhance photocatalytic activity of TiO_2, Catal. Commun. 9, 6 (2008) 1410–1413.

[37] Y. Yao, G. Li, S. Ciston, R.M. Lueptow, K.A. Gray, Photoreactive TiO_2/carbon nanotube composites: Synthesis and reactivity, Environ. Sci. Technol. 42, 13 (2008) 4952–4957.

[38] Y. Yu, J.C. Yu, C.-Y. Chan, Y.-K., Che, J.-C. Zhao, L. Ding, W.-K. Ge, P.-K. Wong, Enhancement of adsorption and photocatalytic activity of TiO_2 by using carbon nanotubes for the treatment of azo dye, Appl. Catal., B. 61, 1–2 (2005) 1–11.

[39] C.-Y. Kuo, Prevenient dye-degradation mechanisms using UV-TiO_2/carbon nanotubes process, J. Hazard. Mater. 163, 1 (2009) 239–244.

[40] Q. Xiang, J. Yu, M. Jaroniec, Graphene-based semiconductor photocatalysts, Chem. Soc. Rev. 41 (2012) 782–796.

[41] J. Cao, B. Xu, B. Luo, H. Lin, S. Chen, Novel BiOI/BiOBr heterojunction photocatalysts with enhanced visible light photocatalytic properties, Catal. Commun. 13, 1 (2011) 63–68

[42] H. Cheng, B.B. Huang, Y. Dai, X.Y. Qin, X.Y. Zhang, One-step synthesis of the nanostructured AgI/BiOI composites with highly enhanced visible-light photocatalytic performances, Langmuir 26, 9 (2010) 6618–6624.

[43] M. Ni, M.K.H. Leung, D.Y.C. Leung, K. Sumathy, A review and recent developments in photocatalytic water-splitting using TiO_2 for hydrogen production, Renewable Sustainable Energy Rev. 11, 3 (2007) 401–425.

[44] J.H. Pan, H. Dou, Z. Xiong, C. Xu, J. Ma, X.S. Zhao, Porous photocatalysts for advanced water purifications, J. Mater. Chem. 20, 22 (2010) 4512–4528.

[45] T. Torimoto, S. Ito, S. Kuwabata, H. Yoneyama, Effects of adsorbents used as supports for titanium dioxide loading on photocatalytic degradation of propyzamide, Environ. Sci. Technol. 30, 4 (1996) 1275–1281.

[46] H. Wang, B. Yang, W. Zhang, Photocatalytic degradation of methyl orange on Y zeolite supported TiO_2, Adv. Mater. Res. 129–131 (2010) 733–737.

[47] A. Rachel, M. Subrahmanyam, P. Boule, Comparison of photocatalytic efficiencies of TiO_2 in suspended and immobilised form for the photocatalytic degradation of nitrobenzenesulfonic acids, Appl. Catal., B. 37, 4 (2002) 301–308.

[48] H. Yu, S.C. Lee, J. Yu, C.H. Ao, Photocatalytic activity of dispersed TiO_2 particles deposited on glass fibers, J. Mol. Catal. A: Chem. 246, 1–2 (2006) 206–211.

[49] E. Beyers, E. Biermans, S. Ribbens, K. De Witte, M. Mertens, V. Meynen, S. Bals, G. Van Tendeloo, E.F. Vansant, P. Cool, Combined TiO_2/SiO_2 mesoporous photocatalysts with location and phase controllable TiO_2 nanoparticles, Appl. Catal., B. 88, 3–4 (2009) 515–524.

[50] H.-J. Kim, Y.-G. Shul, H. Han, Photocatalytic properties of silica-supported TiO_2, Top. Catal. 35, 3–4 (2005) 287–293.

[51] L. Zou, Y. Luo, M. Hooper, E. Hu, Removal of VOCs by photocatalysis process using adsorption enhanced TiO_2-SiO_2 catalyst, Chem. Eng. Process. 45 (2006) 959–964.

[52] K. Venkata Subba Rao, A. Rachel, M. Subrahmanyam, P. Boule, Immobilization of TiO_2 on pumice stone for the photocatalytic degradation of dyes and dye industry pollutants, Appl. Catal., B. 46, 1 (2003) 77–85.

[53] E. Manova, P. Aranda, M. Angeles Martín-Luengo, S. Letaïf, E. Ruiz-Hitzky, New titania-clay nanostructured porous materials, Microporous Mesoporous Mater. 131, 1–3 (2010) 252–260.

[54] D.-K. Lee, S.-C. Kim, S.-J. Kim, I.-S. Chung, S.-W. Kim, Photocatalytic oxidation of microcystin-LR with TiO_2-coated activated carbon, Chem. Eng. J. 102, 1 (2004) 93–98.

[55] S.X. Liu, X.Y. Chen, X. Chen, A TiO_2/AC composite photocatalyst with high activity and easy separation prepared by a hydrothermal method, J. Hazard. Mater. 143 (2007) 257–263.

[56] J. Matos, J. Laine, J.M. Herrmann, Synergy effect in the photocatalytic degradation of phenol on a suspended mixture of titania and activated carbon, Appl. Catal., B. 18, 3–4 (1998) 281–291.

[57] B. Tryba, A.W. Morawski, M. Inagaki, Application of TiO_2-mounted activated carbon to the removal of phenol from water, Appl. Catal., B. 41, 4 (2003) 427–433.

[58] X. Wang, Y. Liu, Z. Hu, Y. Chen, W. Liu, G. Zhao, Degradation of methyl orange by composite photocatalysts nano-TiO_2 immobilized on activated carbons of different porosities, J. Hazard. Mater. 169 (2009) 1061–1067.

[59] V. Polshettiwar, R. Luque, A. Fihri, H. Zhu, M. Bouhrara, J.-M. Basset, Magnetically recoverable nanocatalysts, Chem. Rev. 111, 5 (2011) 3036–3075.

[60] D. Beydoun, R. Amal, G.K.C. Low, S. McEvoy, Novel photocatalyst: titania-coated magnetite, activity and photodissolution, J. Phys. Chem. B 104, 18 (2000) 4387–4396.

[61] R. Buonsanti, V. Grillo, R. Carlino, C. Giannini, M.L. Curri, C. Innocenti, C. Sangregorio, K. Achterhold, F.G. Parak, A. Agostiano, P.D. Cozzoli, Seeded growth of asymmetric binary nanocrystals made of a semiconductor TiO_2 rodlike section and a magnetic γ-Fe_2O_3 spherical domain, J. Am. Chem. Soc. 128, 51 (2006) 16953–16970.

[62] M. Ye, Q. Zhang, X. Hu, J. Ge, Z. Lu, L. He, Z. Chen, Y. Yin, Magnetically recoverable core-shell nanocomposites with enhanced photocatalytic activity, Chem. Eur. J. 16, 21 (2010) 6243–4250.

[63] C. An, X. Ming, J. Wang, S. Wang, Construction of magnetic visible-light driven plasmonic Fe_3O_4@SiO_2@AgCl:Ag nanophotocatalyst, J. Mater. Chem. 22, 11 (2012) 5171–5176.

[64] G.Q. Tan, Y.Q. Zheng, H.Y. Miao, A. Xia, H.J. Ren, Controllable microwave hydrothermal synthesis of bismuth ferrites and photocatalytic characterization, J. Am. Ceram. Soc. 95, 1 (2012) 280–289.

[65] X. Huang, I.H. El-Sayed, W. Qian, M.A. El-Sayed, Cancer cell imaging and photothermal therapy in the near-infrared region by using gold nanorods, J. Am. Chem. Soc. 128, 6 (2006) 2115–2129.

[66] K.L. Kelly, E. Coronado, L.L. Zhao, G.C. Schatz, The optical properties of metal nanoparticles: The influence of size, shape, and dielectric environment, J. Phys. Chem. B 107, 3 (2003) 668–677.

[67] K. Awazu, M. Fujimaki, C. Rockstuhl, J. Tominaga, H. Murakami, Y. Ohki, N. Yoshida, T. Watanabe, A plasmonic photocatalyst consisting of silver nanoparticles embedded in titanium dioxide, J. Am. Chem. Soc. 130, 5 (2008) 1676–1680.

[68] P. Wang, B. Huang, X. Zhang, X. Qin, H. Jin, Y. Dai, Z. Wang, J. Wei, J. Zhan, S. Wang, J. Wang, M.-H. Whangbo, Highly efficient visible-light plasmonic photocatalyst Ag@AgBr, Chem. Eur. J. 15 (2009) 1821–1824.

[69] C. Hu, Y. Lan, J. Qu, X. Hu, A. Wang, Ag/AgBr/TiO_2 visible light photocatalyst for destruction of azodyes and bacteria, J. Phys. Chem. B 110, 9 (2006) 4066–4072.

[70] P. Wang, B. Huang, X. Qin, X. Zhang, Y. Dai, J. Wei, M.-H. Whangbo, Ag@AgCl: A highly efficient and stable photocatalyst active under visible light, Angew. Chem. Int. Ed. 47 (2008) 7931–7933.

[71] H. Zhang, X. Fan, X. Quan, S. Chen, H. Yu, Graphene sheets grafted Ag@AgCl hybrid with enhanced photocatalytic activity under visible light, Environ. Sci. Technol. 45, 13 (2011) 5731–5736.

[72] X. An, S. Pen, Y. Sun, Facile synthesis of sunlight-driven AgCl:Ag plasmonic nanophotocatalyst, Adv. Mater. 22, 23 (2010) 2570–2574.

[73] H. Xu, H. Li, J. Xia, S. Yin, Z. Luo, L. Liu, L. Xu, One-pot synthesis of visible-light-driven plasmonic photocatalyst Ag/AgCl in ionic liquid, ACS Appl. Mater. Interfaces 3, 1 (2011) 22–29.

[74] D. Wang, Y. Duan, Q. Luo, X. Li, L. Bao, Visible light photocatalytic activities of plasmonic Ag/AgBr particles synthesized by a double jet method, Desalination 270, 1–3 (2011) 174–180.

[75] J. Jiang, H. Li, L. Zhang, New insight into daylight photocatalysis of AgBr @Ag: Synergistic effect between semiconductor photocatalysis and plasmonic photocatalysis, Chem. Eur. J. 18, 20 (2012) 6360–6369.

[76] J. Yu, G. Dai, B. Huang, Fabrication and characterization of visible-light-driven plasmonic photocatalyst Ag/AgCl/TiO_2 nanotube arrays, J. Phys. Chem. C 113, 37 (2009) 16394–16401.

[77] X. Zhang, Y.L. Chen, R.-S. Liu, D.P. Tsai, Plasmonic photocatalysis, Rep. Prog. Phys. 76 (2013) 046401 (1)–046401 (41).

[78] C. Hu, T. Peng, X. Hu, Y. Nie, X. Zhou, J. Qu, H. He, Plasmon-induced photodegradation of toxic pollutants with Ag-AgI/Al_2O_3 under visible-light irradiation, J. Am. Chem. Soc. 132 (2010) 857–862.

[79] J.-F. Guo, B. Ma, A. Yin, K. Fan, W.-L. Dai, Highly stable and efficient Ag/AgCl@TiO_2 photocatalyst: Preparation, characterization, and application in the treatment of aqueous hazardous pollutants, J. Hazard. Mater. 211–212 (2012) 77–82.

[80] Y. Wen, H. Ding, Preparation and photocatalytic activity of Ag@AgCl modified anatase TiO_2 nanotubes, Chin. J. Catal. 32 (2011) 36–45.

[81] L. Zhang, K.-H. Wong, Z. Chen, J.C. Yu, J. Zhao, C. Hu, C.-Y. Chan, P.-K. Wong, AgBr-Ag-Bi_2WO_6 nanojunction system: A novel and efficient photocatalyst with double visible-light active components, Appl. Catal., A. 363, 1–2 (2009) 221–229.

[82] M. Zhu, P. Chen, M. Liu, Graphene oxide enwrapped Ag/AgX (X= Br, Cl) nanocomposite as a highly efficient visible light plasmonic photocatalyst, ACS Nano 5, 6 (2011) 4529–4536.

[83] M. Padervand, M. Tasviri, M.R. Gholami, Effective photocatalytic degradation of an azo dye over nanosized Ag/AgBr modified TiO_2 loaded on zeolite, Chem. Pap. 65, 3 (2011) 280–288.

[84] V.R. Reddy, A. Currao, G. Calzaferri, Zeolite A and zeolite L monolayers modified with AgCl as photocatalyst for water oxidation to O_2, J. Mater. Chem. 17, 34 (2007) 3603–3609.

[85] Y. Li, Y. Ding, Porous AgCl/Ag nanocomposites with enhanced visible light photocatalytic properties, J. Phys. Chem. C 114, 7 (2010) 3175–3179.

[86] C. Hu, J. Guo, J. Qu, X. Hu, Photocatalytic degradation of pathogenic bacteria with AgI/TiO_2 under visible light irradiation, Langmuir 23, 9 (2007) 4982–4987.

[87] M.R. Elahifard, S. Rahimnejad, S. Haghighi, M.R. Gholami, Apatite-coated $Ag/AgBr/TiO_2$ visible-light photocatalyst for destruction of bacteria, J. Am. Chem. Soc. 129, 31 (2007) 9552–9553.

[88] P. Wang, B. Huang, X. Qin, X. Zhang, Y. Dai, M.-H. Whangbo, $Ag/AgBr/WO_3{\cdot}H_2O$: Visible-light photocatalyst for bacteria destruction, Inorg. Chem. 48, 22 (2009) 10697–10702.

[89] D. Rejeski, (2009). Nanotechnology and consumer products, http://www.nanotechproject.org/publications/archive/nanotechnology_consumer_products/, 5 June 2012.

[90] C. Marambio-Jones, E.M.V. Hoek, A review of the antibacterial effects of silver nanomaterials and potential implications for human health and the environment, J. Nanopart. Res. 12, 5 (2010) 1531–1551.

[91] H.T. Ratte, Bioaccumulation and toxicity of silver compounds: A review, Environ. Toxicol. Chem. 18, 1 (1999) 89–108.

[92] V. Sambhy, M.M. MacBride, B.R. Peterson, Silver bromide nanoparticle/polymer composites: Dual action tunable antimicrobial materials, J. Am. Chem. Soc. 128, 30 (2006) 9798–9808.

[93] B. Naik, V. Desai, M. Kowshik, V.S. Prasad, G.F. Fernando, N.N. Ghosh, Synthesis of Ag/AgCl-mesoporous silica nanocomposites using a simple aqueous solution-based chemical method and a study of their antibacterial activity on *E. coli*, Particulology 9, 3 (2011) pp 243–247.

[94] M.A. Butkus, L. Edling, M.P. Labare, The efficacy of silver as a bactericidal agent: Advantages, limitations and considerations for future use, J. Water Supply Res. Technol. AQUA 52 (2003) 407–416.

[95] O. Choi, K.K. Deng, N.-J. Kim, L. Ross, R.Y. Surampalli, Z. Hu, The inhibitory effects of silver nanoparticles, silver ions, and silver chloride colloids on microbial growth, Water Res. 42, 12 (2008) 3066–3074.

[96] S. Pal, J. Joardar, J.M. Song, Removal of *E. coli* from water using surface-modified activated carbon filter media and its performance over an extended use, Environ. Sci. Technol. 40, 19 (2006) 6091–6097.

[97] W. Li, S. Liu, Bifunctional activated carbon with dual photocatalysis and adsorption capabilities for efficient phenol removal, Adsorption 18 (2012) 67–74.

[98] S. Malato, J. Blanco, D.C. Alarcón, M.I. Maldonado, P. Fernández-Ibáñez, W. Gernjak, Photocatalytic decontamination and disinfection of water with solar collectors, Catal. Today 122, 1–2 (2007) 137–149.

[99] J. Hoigne, (1998). Chemistry of aqueous ozone and transformation of pollutants by ozonation and advanced oxidation processes In O. Hutzinger [editors], The Handbook of Environmental Chemistry (pp. 83–141), Springer-Verlag, Berlin, Germany.

[100] X. Zhang, M. Zhou, L. Lei, Preparation of photocatalytic TiO_2 coatings of nanosized particles on activated carbon by AP-MOCVD, Carbon 43, 8 (2005) 1700–1708.

[101] T.-T. Lim, P.-S. Yap, M. Srinivasan, A.G. Fane, TiO_2/AC composites for synergistic adsorption-photocatalysis processes: Present challenges and further developments for water treament and reclamation, Crit. Rev. Environ. Sci. Technol. 41, 13 (2011) 1173–1230.

[102] J. Araña, J.A. Herrera Melián, J.M. Doña Rodríguez, O. González Diaz, A. Viera, J. Pérez Peña, P.M. Marrero Sosa, V. Espino Jimẽnez, TiO_2-photocatalysis as a tertiary treatment of naturally treated wastewater, Catal. Today 76, 2–4 (2002) 279–289.

[103] J. Araña, J.M. Doña-Rodríguez, E. Tello Rendón, C. Garriga i Cabo, O. González-Díaz, O., J.A. Herrera-Melián, J. Pérez-Peña, G. Colón, J.A. Navío, TiO_2 activation by using activated carbon as a support: Part I. Surface characterization and decantability study, Appl. Catal., B. 44, 2 (2003) 161–172.

[104] J. Araña, J.M. Doña Rodríguez, E. Tello Rendón, C. Garriga i Cabo, O. González-Diáz, J.A. Herrera-Melián, J. Pérez Peña, G. Colón, J.A. Navío, TiO_2 activation by using activated carbon as a support: Part II. Photoreactivity and FTIR study, Appl. Catal., B. 44, 2 (2003) 153–160.

[105] T. Cordero, J.-M. Chovelon, C. Duchamp, C. Ferronato, J. Matos, Surface nano-aggregation and photocatalytic activity of TiO_2 on H-type activated carbons, Appl. Catal., B. 73, 3–4 (2007) 227–235.

[106] T. Cordero, C. Duchamp, J.-M Chovelon, C. Ferronato, J. Matos, Influence of L-type activated carbons on photocatalytic activity of TiO_2 in 4-chlorophenol photodegradation, J. Photochem. Photobiol., A. 191, 2–3 (2007) 122–131.

[107] J. Matos, J. Laine, J.M. Herrmann, Effect of the type of activated carbons on the photocatalytic degradation of aqueous organic pollutants by UV irradiated titania, J. Catal. 200, 1 (2001) 10–20.

[108] J. Matos, J. Laine, J.M. Herrmann, D. Uzcategui, J.L. Brito, Influence of activated carbon upon titania on aqueous photocatalytic consecutive runs of phenol photodegradation, Appl. Catal., B. 70, 1–4 (2007) 461–469.

[109] L.F. Valsco, J.B. Parra, C.O. Ania, Role of activated carbon features on the photocatalytic degradation of phenol, Appl. Surf. Sci. 256, 17 (2010) 5254–5258.

[110] R. Yuan, R. Guan, P. Liu, J. Zheng, Photocatalytic treatment of wastewater from paper mill by TiO_2 loaded on activated carbon fibers, Colloids Surf., A 293, 1–3 (2007) 80–86.

[111] B. Zhu, L. Zou, Trapping and decomposing of color compounds from recycled water by TiO_2 coated activated carbon, J. Environ. Manage. 90, 11 (2009) 3217–3225.

[112] S. Nottakun, J.C. Crittenden, D.W. Hand, D.L. Perram, M.E. Mullins, Regeneration of adsorbents using heterogenous advanced oxidation, J. Environ. Eng. 119, 4 (1993) 695–714.

[113] S.C. Panchangam, A.Y.-C. Lin, J.H. Tsai, C.-F. Lin, Sonication-assisted photocatalytic decomposition of perfluorooctanoic acid, Chemosphere 75, 5 (2009) 654–660.

[114] X. Zhang, M. Zhou, L. Lei, Preparation of an Ag-TiO_2 photocatalyst loaded on activated carbon by MOCVD, Mat. Chem. Phys. 91, 1 (2005) 73–79.

[115] W. Zhao, Z. Bai, A. Ren, B. Guo, C. Wu, Sunlight photocatalytic activity of CdS modified TiO_2 loaded on activated carbon, Appl. Surf. Sci. 256, 11 (2010) 3493–3498.

[116] P.-S. Yap, T.-T. Lim, Effect of aqueous matrix species on synergistic removal of bisphenol-A under solar irradiation using nitrogen-doped TiO_2/AC composite, Appl. Catal., B. 101, 3–4 (2011) 709–717.

[117] P.-S. Yap, T.-T. Lim, M. Srinivasan, Nitrogen-doped TiO_2/AC bifunctional composite prepared by two-stage calcination for enhanced synergistic removal of hydrophobic pollutant using solar irradiation, Catal. Today 161, 1 (2011) 46–52.

[118] Y. Horie, M. Taya, S. Tone, Evaluation of photocatalytic sterilization rates of *Escherichia coli* cells in titanium dioxide slurry irradiated with various light sources, J. Chem. Eng. Jpn. 31, 6 (1998) 922–929.

[119] Y. Li, M. Ma, X. Wang, X. Wang, Inactivated properties of activated carbon supported TiO_2 nanoparticles for bacteria and kinetic study, J. Environ. Sci. 20, 12 (2008) 1527–1533.

[120] S.-Y. Ye, M.-L. Fan, X.-L. Song, S.-C. Luo, Enhanced photocatalytic disinfection of *P. expansum* in cold storage using a TiO_2/ACF film, Int. J. Food Microbiol. 136, 3 (2010) 332–339.

[121] H. Al-Ekabi, N. Serpone, Kinetics studies in heterogeneous photocatalysis. I. Photocatalytic degradation of chlorinated phenols in aerated aqueous solutions over titania supported on a glass matrix, J. Phys. Chem. 92, 20 (1988) 5726–5731.

[122] S. Sakthivel, M.V. Shankar, P. Palinichamy, B. Arabindoo, V. Murugesan, Photocatalytic decomposition of leather dye: Comparative study of TiO_2 supported on alumina and glass beads, J. Photochem. Photobiol., A. 148, 1–3 (2002) 153–159.

[123] N. Serpone, E. Borgarello, R. Harris, P. Cahill, M. Borgarella, E. Pelizzetti, Photocatalyis over TiO_2 supported on a glass substrate, Sol. Energy Mater. 14, 2 (1986) 121–126.

[124] J. Sabate, M.A. Anderson, M.A. Aguado, J. Giminez, S. Cerveramarch, C.G. Hill, Comparison of TiO_2 powder suspensions and TiO_2 ceramic membranes supported on glass as photocatalytic systems in the reduction of chromium(VI), J. Mol. Catal. 71, 1 (1992) 57–68.

[125] J. Sabate, M.A. Anderson, H. Kikkawa, M. Edwards, C.G. Hill, A kinetic study of the photocatalytic degradation of 3-chlorosalicylic acid over TiO_2 membranes supported on glass, J. Catal. 127, 1 (1991) 167–177.

[126] M.A. Anderson, M.J. Gieselmann, Q.Y. Xu, Titania and alumina ceramic membranes, J. Membr. Sci. 39, 3 (1988) 243–258.

[127] T. Tsumura, N. Kojitani, H. Umemura, M. Toyoda, M. Inagaki, Composites between photoactive anatase-type TiO_2 and adsorptive carbon, Appl. Surf. Sci. 196, 1–4 (2002) 429–436.

[128] R. Hiroshi, H. Yukiko, Y. Michichiro, A. Shoichi, (1994). Magnetic photocatalyst, JP 615420 (A).

[129] S. Lee, J. Drwiega, C.-Y. Wu, D. Mazyck, W.M. Sigmund, Anatase TiO_2 nanoparticle coating on barium ferrite using titanium bis-ammonium lactate dihydroxide and its use as a magnetic photocatalyst, Chem. Mater. 16, 6 (2004) 1160–1164.

[130] S. Rana, J. Rawat, R.D.K. Misra, Anti-microbial active composite nanoparticles with magnetic core and photocatalytic shell: TiO_2-$NiFe_2O_4$ biomaterial system, Acta. Biomater. 1, 6 (2005) 691–703.

[131] F. Chen, C. Zhao, Preparation and photocatalytic properties of a novel kind of loaded photocatalyst of $TiO_2/SiO_2/\gamma$-Fe_2O_3, Catal. Lett. 58, 4 (1999) 246–247.

[132] D. Beydoun, R. Amal, G. Low, S. McEvoy, Occurrence and prevention of photodissolution at the phase junction of magnetite and titanium dioxide, J. Mol. Catal. A: Chem. 180, 1–2 (2002) 193–200.

[133] S. Watson, J. Scott, D. Beydoun, R. Amal, Studies on the preparation of magnetic photocatalysts, J. Nanopart. Res. 7, 6 (2005) 691–705.

[134] S. Abrahamson, L. Srithammavanh, J.M. Siaugue, O. Horner, X. Xu, V. Cabuil, Nanometric core-shell-shell γ-$Fe_2O_3/SiO_2/TiO_2$ particles, J. Nanopart. Res. 11, 2 (2009) 459–465.

[135] F. Chen, Y. Xie, J. Zhao, G. Lu, Photocatalytic degradation of dyes on a magnetically separated photocatalyst under visible and UV irradiation, Chemosphere 44, 5 (2001) 1159–1168.

[136] Y. Gao, B. Chen, H. Li, Y. Ma, Preparation and characterization of a magnetically separated photocatalyst and its catalytic properties, Mater. Chem. Phys. 80, 1 (2003) 348–355.

[137] S. Wang, S. Zhou, Titania deposited on soft magnetic activated carbon as a magnetically separable photocatalyst with enhanced activity, Appl. Surf. Sci. 256, 21 (2010) 6191–6198.

[138] Y.S. Chung, S.B. Park, D.W. Kang, Magnetically separable titania-coated nickel ferrite photocatalyst, Mater. Chem. Phys. 86, 2–3 (2004) 375–381.

[139] S. Xu, W. Shangguan, J. Yuan, M. Chen, J. Shi, Preparation and photocatalytic properties of magnetically separable TiO_2 supported on nickel ferrite, Chin. J. Chem. Eng. 15 (2007) 190–195.

[140] S. Xu, W. Shangguan, J. Yuan, M. Chen, J. Shi, Preparations and photocatalytic properties of magnetically separable nitrogen-doped TiO_2 supported on nickel ferrite, Appl. Catal., B. 71, 3–4 (2007) 177–184.

[141] W. Fu, H. Yang, M. Li, M. Li, N. Yang, G. Zou, Anatase TiO_2 nanolayer coating on cobalt ferrite nanoparticles for magnetic photocatalyst, Mater. Lett. 59, 27 (2005) 3530–3534.

[142] H. Zhang, R. Hou, Z. Lu, X. Duan, A novel magnetic nanocomposite involving anatase titania coating on silica-modified cobalt ferrite via lower temperature hydrolysis of a water-soluble titania precursor, Mater. Res. Bull. 44, 10 (2009) 2000–2008.

[143] W.L. Kostedt, H.E. Byrne, D.W. Mazyck, A high surface area magnetic photocatalyst with controlled pore size, Environ. Prog. Sustain. Energy 29, 1 (2010) 10–16.

[144] S.-W. Lee, J. Drwiega, D. Mazyck, C.Y. Wu, W.M. Sigmund, Synthesis and characterization of hard magnetic composite photocatalyst (barium ferrite silica titania) and its photoactivity, Mater. Chem. Phys. 96, 2–3 (2006) 483–488.

[145] Y. Chen, L. Chen, N. Shang, Photocatalytic degradation of dimethyl phthalate in an aqueous solution with Pt-doped TiO_2-coated magnetic PMMA microspheres, J. Hazard. Mater. 172, 1 (2009) 20–29.

[146] H. Li, X. Zhang, Y. Hup, J. Zhu, Supercritical preparation of a highly active S-doped TiO_2 photocatalyst for methylene blue mineralization, Environ. Sci. Technol. 41, 12 (2007) 4410–4414.

[147] E.A. Reyez-Garcia, Y. Sun, D. Raftery, Solid-state characterization of the nuclear and electronic environments in a boron-fluoride co-doped TiO_2 visible-light photocatalyst, J. Phys. Chem. C 111, 45 (2007) 17146–17154.

[148] S. Klosek, D. Raftery, Visible light driven V-doped TiO_2 photocatalyst and its photooxidation of ethanol, J. Phys. Chem. B 105, 14 (2001) 2815–2819.

[149] H. Xu, Z. Zheng, L. Zhang, H. Zhang, F. Deng, Hierarchical chlorine-doped rutile TiO_2 spherical clusters of nanorods: Large-scale synthesis and high photocatalytic activity, J. Solid State Chem. 181, 9 (2008) 2518–2522.

[150] A.A. Aziz, K.S. Yong, S. Ibrahim, S. Pichiah, Enhanced magnetic separation and photocatalytic activity of nitrogen doped titania photocatalyst supported on strontium ferrite, J. Hazard. Mater. 199–200 (2012) 143–150.

[151] Y. Nosaka, M. Matsushita, J. Nishino, A.Y. Nosaka, Nitrogen-doped titanium dioxide photocatalysts for visible response prepared by using organic compounds, Sci. Technol. Adv. Mater. 6, 2 (2005) 143–148.

[152] M. He, D. Li, D. Jiang, M. Chen, Magnetically separable γ-Fe_2O_3@SiO_2@Ce-doped TiO_2 core-shell nanocomposites: Fabrication and visible-light driven photocatalytic activity, J. Solid State Chem. 192 (2012) 139–143.

[153] Z. Shi, X. Zhang, S. Yao, Synthesis and photocatalytic properties of lanthanum doped anatase TiO_2 coated Fe_3O_4 composites, Rare Met. 30, 3 (2011) 252–257.

[154] H.Y. Chen, B.S. Zhao, Z.H. Li, The preparation of magnetically separated Cu doped TiO_2 by coating-calcining method, Adv. Mater. Res. 197–198 (2011) 857–860.

[155] S. Xu, W. Shangguan, J. Yuan, J. Shi, M. Chen, Preparations and photocatalytic degradation of methyl orange in water on magnetically separable $Bi_{12}TiO_{20}$ supported on nickel ferrite, Sci. Technol. Adv. Mater. 8, 1–2 (2007) 40–46.

[156] K.-J. Liu, Z.-D. Chang, W.-J. Li, P. Che, H.-L. Zhou, Visible-light-driven magnetic $BiVO_4$ photocatalyst: Synthesis and photocatalytic performance, Chin. J. Inorg. Chem. 27, 8 (2011) 1465–1470.

[157] L. Nie, Y. Meng, B. Yang, Z. Xiao, L. Fang, S. Li, A novel magnetically separable photocatalyst silver vanadate@SiO_2/Fe_3O_4, Adv. Mater. Res. 356–360 (2012) 455–458.

[158] Y. Li, H.-Y. Xu, L. Xu, L. Xu, Preparation and photocatalytic activity of ZnS/nickel-zinc ferrite magnetic photocatalyst, J. Synth. Cryst. 40, 4 (2011) 995–999.

[159] G. Li, K.H. Wong, X. Zhang, C. Hu, J.C. Yu, R.C.Y. Chan, P.K. Wong, Degradation of acid orange 7 using magnetic AgBr under visible light: The roles of oxidizing species, Chemosphere 76, 9 (2009) 1185–1191.

[160] J.-F. Guo, B. Ma, A. Yin, K. Fan, W.-L. Dai, Photodegradation of rhodamine B and 4-chlorophenol using plasmonic photocatalyst of Ag-AgI/Fe_2O_3@SiO_2 magnetic nanoparticle under visible light irradiation, Appl. Catal., B. 101, 3–4 (2011) 580–586.

[161] S. Rana, R.D.K. Misra, The anti-microbial activity of titania-nickel ferrite composite nanoparticles, J. Miner. Mater. Soc. 57, 12 (2005) 65–69.

[162] C.-J.M. Chin, Y.-J. Chang, G.-J. Weng, C.-Y. Shen, Synthesis of magnetic TiO_2 nanoparticles as bactericidal photocatalyst, Adv. Mater. Res. 123–125 (2010) 260–263.

[163] H.M. Coleman, C.P. Marquis, J.A. Scott, S.-S. Chin, R. Amal, Bactericidal effects of titanium dioxide-based photocatalysts, Chem. Eng. J. 113, 1 (2005) 55–63.

[164] Y. Zhai, L. Han, P. Wang, G. Li, W. Ren, L. Liu, E. Wang, S. Dong, Superparamagnetic plasmonic nanohybrids: Shape-controlled synthesis, TEM-induced structure evolution, and efficient sunlight-driven inactivation of bacteria, ACS Nano 5, 11 (2011) 8562–8570.

[165] S.A. Kahani, M. Hamadanian, O. Vandadi, Deposition of magnetite nanoparticles in activated carbons and preparation of magnetic activated carbons, AIP Conf. Proc. 929, 183 (2007), doi:10.1063/1.2776712

[166] I. Šafařík, K. Nymburská, M. Šafařiková, Adsorption of water-soluble organic dyes on magnetic charcoal, J. Chem. Tech. Biotechol. 69, 1 (1997) 1–4.

[167] M. Zahoor, M. Magramlioglu, Adsorption of imidacloprid on powdered activated carbon and magnetic activated carbon, Chem. Biochem. Eng. Q. 25, 1 (2011) 55–63.

[168] L.C.A. Oliveira, R.V.R.A. Rios, J.D. Fabris, V. Garg, K. Sapag, R.M. Lago, Activated carbon/iron oxide magnetic composites for the adsorption of contaminants in water, Carbon 40, 12 (2002) 2177–2183.

[169] P. Thakuria, P.A. Joy, Superparamagnetic nanocomposite of magnetite and activated carbon for removal of dyes from waste water, Nanosci. Nanotechnol. Lett. 1, 3 (2009) 171–175.

[170] Z. Jia, K. Peng, Y. Li, R. Zhu, Preparation and application of novel magnetically separable γ-Fe_2O_3/activated carbon sphere adsorbent, Mater. Sci. Eng. B. 176, 11 (2011) 861–865.

[171] E.K. Faulconer, N.V. Hoosgesteijn von Reitzenstein, D.W. Mazyck, Optimization of magnetic powdered activated carbon for aqueous Hg (II) removal and magnetic recovery, J. Hazard. Mater. 199–200 (2012) 9–14.

[172] Y. Ao, J. Xu, D. Fu, C. Yuan, A simple route for the preparation of anatase titania-coated magnetic porous carbons with enhanced photocatalytic activity, Carbon 46, 4 (2008) 596–603.

[173] Y. Ao, J. Xu, D. Fu, X. Shen, C. Yuan, A novel magnetically separable composite photocatalyst: Titania-coated magnetic activated carbon, Sep. Purif. Technol. 61, 3 (2008) 436–441.

[174] Y. Ao, J. Xu, D. Fu, C. Yuan, Photocatalytic degradation of X-3B by titania-coated magnetic activated carbon under UV and visible irradiation, J. Alloys Compd. 471, 1–2 (2009) 33–38.

[175] Y. Ao, J. Xu, S. Zhang, D. Fu, Synthesis of a magnetically separable composite photocatalyst with high photocatalytic activity under sunlight, J. Phys. Chem. Solids 70, 6 (2009) 1042–1047.

[176] A. Rey, D.H. Quiñones, P.M. Álvarez, F.J. Beltrán, P.K. Plucinski, Simulated solar-light assisted photocatalytic ozonation of metoprolol over titania-coated magnetic activated carbon, Appl. Catal., B. 111–112 (2012) 246–253.

[177] M.A. Gondal, C. Li, X. Chang, L. Sikong, Z.H. Yamani, Q. Zhou, F. Yang, Q. Lin, Facile preparation of magnetic C/TiO_2/Ni composites and their photocatalytic performance for removal of a dye from water under UV light irradiation, J. Environ. Sci. Health A. Tox. Hazard. Subst. Environ. Eng. 47, 4 (2012) 570–576.

[178] D. Chen, Z. Jiang, J. Geng, Q. Wang, D. Yang, Carbon and nitrogen co-doped TiO_2 with enhanced visible-light photocatalytic activity, Ind. Eng. Chem. Res. 46, 9 (2007) 2741–2746.

[179] F. Dong, H. Wang, Z. Wu, One-step "green" synthetic approach for mesoporous C-doped titanium dioxide with efficient visible light activity, J. Phys. Chem. C 113, 38 (2009) 16717–16723.

[180] J.H. Park, S. Kim, A.J. Bard, Novel carbon-doped TiO_2 nanotube arrays with high aspect ratios for efficient solar water splitting, Nano Lett. 6, 1 (2006) 24–28.

[181] A. Fujishima, K. Kohayakawa, K. Honda, Hydrogen production under sunlight with an electrochemical photocell, J. Electrochem. Soc. 122, 11 (1975) 1487–1489.

[182] K. Noworyta, J. Augustynski, Spectral photoresponses of carbon-doped TiO_2 film electrodes, Electrochem. Solid-State Lett. 7, 6 (2004) E31–E33.

[183] A.C. Pierre, (1998). Introduction to Sol-gel Processing, Kluwer, Boston.

[184] W. Ren, Z. Ai, F. Jia, L. Zhang, X. Fan, Z. Zou, Low temperature preparation and visible light photocatalytic activity of mesoporous carbon-doped crystalline TiO_2, Appl. Catal., B. 69, 3–4 (2007) 138–144.

[185] A. Fujishima, Comment on "Efficient photochemical water splitting by a chemically modified n-TiO_2" (I), Science 301 (2003) 1673a.

[186] C. Hagglund, M. Grätzel, B. Kasemo, Comment on "Efficient photochemical water splitting by a chemically modified n-TiO_2" (II), Science 301 (2003) 1763b.

[187] S.U.M. Khan, M. Al-Shahry, W.B. Inger, Response to comments on "Efficient photochemical water splitting by a chemically modified n-TiO_2", Science 301 (2003) 1673d.

[188] K.S. Lackner, Comment on "efficient photochemical water splitting by a chemically modified n-TiO_2" (III), Science 301 (2003) 1673c.

[189] A.B. Murphy, Does carbon doping of TiO_2 allow water splitting in visible light? Comments on "Nanotube enhanced photoresponse of carbon modified (CM)-n-TiO_2 for efficient water splitting, Sol. Energy Mater. Sol. Cells 92, 3 (2008) 363–367.

[190] Y. Choi, T. Umebayashi, M. Yoshikawa, Fabrication and characterization of C-doped anatase TiO_2 photocatalysts, J. Mater. Sci. 39, 5 (2004) 18737–1839.

[191] S.-W. Hsu, T.-S. Yang, T.-K. Chen, M.-S. Wong, Ion-assisted electron-beam evaporation of carbon-doped titanium dioxide films as visible-light photocatalyst, Thin Solid Films 515, 7–8 (2007) 3521–3526.

[192] H. Irie, Y. Watanabe, K. Hashimoto, Carbon-doped anatase TiO_2 powders as a visible-light sensitive photocatalyst, Chem. Lett. 32, 8 (2003) 772–773.

[193] H. Wang, J.P. Lewis, Effects of dopant states on photoactivity in carbon-doped TiO_2, J. Phys. Condens. Matter. 17 (2005) L209–L213.

[194] Y. Li, D.-S. Hwang, N.H. Lee, S.-J. Kim, Synthesis and characterization of carbon-doped titania as an artificial solar light sensitive photocatalyst, Chem. Phys. Lett. 404, 1–3 (2005) 25–29.

[195] T. Ohno, T. Tsubota, K. Nishijima, Z. Miyamoto, Degradation of methylene blue on carbonate species-doped TiO_2 photocatalysts under visible light, Chem. Lett. 33, 6 (2004) 750–751.

[196] T. Tachikawa, S. Tojo, K. Kawai, M. Endo, M. Fujitsuka, T. Ohno, K. Nishijima, Z. Miyamoto, T. Majima, Photocatalytic oxidation reactivity of holes in the sulphur- and carbon-doped TiO_2 powders studied by time-resolved diffuse reflectance spectroscopy, J. Phys. Chem. B 108, 50 (2004) 19299–19306.

[197] C. Di Valentin, G. Pacchioni, A. Selloni, Theory of carbon doping of titanium dioxide, Chem. Mater. 17, 26 (2005) 6656–6665.

[198] H. Liu, A. Imanishi, Y. Nakato, Mechanisms for photooxidation reactions of water and organic compounds on carbon-doped titanium dioxide, as student by photocurrent measurements, J. Phys. Chem. C 111, 24 (2007) 8603–8610.

[199] M. Shen, Z. Wu, H. Huang, Y. Du, Z. Zou, P. Yang, Carbon-doped anatase TiO_2 obtained from TiC for photocatalysis under visible light irradiation, Mater. Lett. 60, 5 (2006) 693–697.

[200] Y. Cong, X. Li, Y. Dun, Z. Dong, G. Yuan, Z. Cui, X. Lai, Carbon-doped TiO_2 coating on multiwalled carbon nanotubes with higher visible light photocatalytic activity, Appl. Catal., B. 107, 1–2 (2011) 128–134.

[201] A. Chatterjee, S.-B. Wu, P.-W. Chou, M.-S. Wong, C.-L. Cheng, Observation of carbon-facilitated phase transformation of titanium dioxide forming mixed-phase titania by confocal Raman microscopy, Appl. Phys. Lett. 42, 5 (2011) 1075–1080.

[202] J.M. Kroon, N.J. Bakker, J.P. Smit, P. Liska, K.R. Thampi, P. Wang, S.M. Zakeeruddin, M. Grätzel, A. Hinsch, S. Hore, U. Wurfel, R. Sastrawan, J.R. Durrant, R. Palomares, H. Pettersson, T. Gruszecki, J. Walter, K. Skupien, G.E. Tulloch, Nanocrystalline dye-sensitized solar cells having maximum performance, Prog. Photovoltaics Res. Appl. 15, 1 (2007) 1–18.

[203] M.-S. Wong, W.-C. Chu, D.-S. Sun, H.-S. Huang, J.-H. Chen, P.-J. Tsai, N.-T. Lin, M.-S. Yu, S.-F. Hsu, S.-L. Wang, H.-H. Chang, Visible-light-induced bactericidal activity of a nitrogen-doped titanium photocatalyst against human pathogens, Appl. Environ. Microbiol. 72, 9 (2006) 6111–6116.

[204] G.-T. Lim, K.H. Kim, J. Park, S.-H. Ohk, J.-H. Kim, J.-L. Cho, Synthesis of carbon-doped photocatalytic TiO_2 nano-powders by AFD process, J. Ind. Eng. Chem. 16, 5 (2010) 723–727.

[205] D. Mitoraj, A. Jañczyk, M. Strus, H. Kisch, G. Stochel, P.B. Heczko, W. Macyk, Visible light inactivation of bacteria and fungi by modified titanium dioxide, Photochem. Photobiol. Sci. 6, 6 (2007) 642–648.

SECTION II: ENHANCED ADSORBENT PHOTOCATALYSTS BASED ON ACTIVATED CARBON

Chapter 3:
Synthesis and characterization of Ag/AgCl-activated carbon composites for enhanced visible light photocatalysis

Joanne Gamage McEvoy, Wenquan Cui, Zisheng Zhang

Applied Catalysis B: Environmental 144 (2014) 702–712.

Abstract

Adsorptive photocatalyst composites based on Ag/AgCl and activated carbon were proposed and investigated. The Ag/AgCl-AC composites were synthesized using impregnation-precipitation-photoreduction, and characterized by X-ray diffraction, transmission and scanning electron microscopies, respectively, X-ray photoelectron spectroscopy, N_2 sorption, and ultraviolet-visible diffuse reflectance spectrophotometry. The photoactivities of the prepared materials were studied for the degradation of methyl orange and phenol under visible light. A mechanism for synergistic adsorption and photocatalysis by Ag/AgCl-AC was proposed, where silver acts by surface plasmon resonance to generate electrons and holes, and polarization of the photoinduced charges relative to AgCl facilitates charge carrier separation, while AC concentrates the pollutant around the active sites.

Keywords: plasmon photocatalyst, Ag/AgCl, visible light photocatalysis, activated carbon

3.1 Introduction

Strategies for overcoming the low solar photocatalytic efficiencies realized with traditional TiO_2 photocatalysts have been developed through the design and fabrication of advanced and so-called "second generation" photocatalytic materials, which have greater visible light responses and are engineered to reduce the rates of electron-hole recombination during photocatalysis. Some approaches proposed are through impurity doping [1], metals deposition [2–4], or sensitization [5, 6].

An interesting phenomenon that has been exploited to prepare high efficiency visible light active photocatalysts is the localized surface plasmon resonance (SPR) exhibited by nanoparticles (NPs) of noble metals. This results in unique optical properties arising from collective oscillation of conduction electrons upon interaction with electromagnetic radiation, and can cause amplified visible light absorption by photocatalysts depending on the size and morphology of the NPs [7]. Silver NPs exhibiting SPR incorporated on silver halide structures (Ag/AgX; X = Cl, Br, I) have been used as plasmonic photocatalysts with extended visible light absorption, where the nanosilver and silver halide also act in concert to polarize the photoinduced charges, facilitating electron-hole separation. The incorporated silver halide can also generate oxidizing species, such as Cl^o or Br^o (for Ag/AgCl and Ag/AgBr, respectively) [8].

Another approach for improving the efficiency of photocatalytic processes is through the immobilization on or incorporation of porous media with the catalyst [9, 10]. Composite materials based on silver/silver halide plasmonic photocatalysts and carbonaceous nanostructures (such as graphene oxides [11, 12], and graphene sheets [13]) have been previously explored, and were shown to exhibit enhanced visible light induced photoactivity. Activated carbon can also be used in photocatalyst composites, and is well-suited to practical applications for water treatment systems due to the following reasons [14]: (1) AC is able to adsorb a wide range of organic compounds as well as natural organic matter, (2) it is widely available in many particle sizes at competitive costs, (3) its use and application in water and wastewater treatment is well-established compared to other support materials, and (4) AC-

containing composites facilitate the ease of separation of nanosized photocatalysts from solution.

A synergistic increase in the photocatalytic activity of TiO_2-AC composites has been observed [10], and is attributed to the presence of a common contact interface between solids, where the pollutants are adsorbed by AC, and migrate continuously to the supported photocatalyst [15]. The AC support may also affect the dynamics of photo-induced charges [16]. However, the need for incorporation of visible light active photocatalysts into AC-photocatalyst composites has been emphasized in literature [14].

In this study, enhanced visible light active Ag/AgCl-AC composite photocatalysts are synthesized and characterized, and their activity is investigated for the degradation of methyl orange dye (MO) and phenol organic pollutants. The prepared composites combine the enhanced visible light absorption and photocatalytic efficiency gained using silver/silver halide plasmonic photocatalysts with the synergy of adsorption obtained through incorporation within an AC matrix to create hybrid photocatalysts.

3.2 Experimental

3.2.1 Synthesis of Ag/AgCl-AC composites

Ag/AgCl-AC composites were prepared using an impregnation-precipitation-photoreduction method. Typically, 1 g of unmodified Darco G60 activated carbon (100 mesh, Sigma-Aldrich) was impregnated in 20 mL of aqueous $AgNO_3$ (ACS grade, MP Biomedicals) of a certain concentration. The mixture was sonicated for 10 minutes, and then stirred magnetically for 6 hours. 20 mL of HCl (reagent-grade, Fisher Scientific) was then added in a 50% stoichiometric excess under magnetic stirring for 2 hours to induce the precipitation of deposited $AgNO_3$ into AgCl. The partial reduction of AgCl was then carried out via irradiation by a 300 W UV-Vis light source (Ushio ELH) for 1 hour. The mixture was filtered and dried in air overnight. The prepared Ag/AgCl-AC composite powders were gently ground in an agate mortar before use, and are denoted by weight ratio of Ag to AC (Ag: AC), calculated as if all of the AgCl was reduced to Ag. Reference Ag/AgCl was prepared using

the same synthesis procedure omitting the AC impregnation step, and AgCl was prepared similarly without photoreduction.

3.2.2 Characterization

X-ray diffraction (XRD) patterns of all prepared powders were collected using a Rigaku Ultima IV XRD with a Cu K(α) source (λ = 0.15418 nm) operating at 40 kV and 44 mA. Transmission electron microscopy imaging was performed using a FEI (formerly Phillips) Tecnai F20 G2 field emission transmission electron microscope (TEM) at an acceleration voltage of 200 keV. The samples were dispersed in water and dropped onto a copper grid for observation. Morphology was studied by a Tescan VegaII XMU field emission scanning electron microscope (SEM) after coating the samples in Au/Pd alloy using an Anatech Hummer VII sputter coater. The chemical states of the photocatalysts were analyzed by XSAM800 X-ray photoelectron spectroscopy (XPS), and the patterns were deconvoluted using XPSPEAK41 software. The surface areas, total pore volumes, and microporosity data were obtained from N_2 sorption isotherms collected at 77 K using an automatic adsorption apparatus (Nova 4200E, Quantachrome). The samples were outgassed at 50^{o}C under N_2 flow for 1 hour at a pressure of 760 – 770 mm Hg. The Brunauer, Emmett, and Teller (BET) surface areas were calculated using the adsorption isotherms in the range of P/Po < 0.015. The total pore volumes of the samples were calculated using the volume of adsorbed N_2 at P/Po = 0.975, and the *t*-plot method was used to calculate micropore volumes and external surface areas. Ultraviolet-visible (UV-Vis) diffuse reflectance spectra were measured on a UV-Vis spectrophotometer (Puxi, UV 1901) equipped with an integrating sphere attachment and on a Thermo Evolution 300 spectrophotometer equipped with a Praying Mantis diffuse reflectance accessory over the range of 230 – 800 nm.

3.2.3 Photocatalytic degradation experiments

3.2.3.1 Photoreactor

To quantify the photocatalytic degradation of organic pollutants using the composite Ag/AgCl-AC, a slurry reactor was placed in a constructed reflective housing to prevent outside light from entering the system. Illumination was provided by a 300 W ELH tungsten halide bulb (Ushio) with a UV filter (Kenko Zeta, λ > 410 nm, transmittance > 90%) at a

distance of 10 cm from the beaker. The irradiation was measured using a quantum meter (Biospherical QSL-2100; 400 nm < λ < 700 nm), and was found to be approximately 4.7×10^{-3} Einstein m^{-2} s^{-1}. The light source chosen simplistically simulated visible light present in solar irradiation, and the intensity was maintained sufficiently high to prevent the dependence of reaction rate on the formation or recombination of electron-hole pairs. Accordingly, the photocatalytic reactions studied were thought to occur in the mass transport-controlled regime. Cooling was provided by an external cooling jacket, and the temperature of the reaction was controlled to 20 ± 2°C.

3.2.3.2 MO adsorption and photodegradation

For the combined adsorption-photocatalysis screening experiments, 0.5 g L^{-1} catalyst was added to a 200 mL solution containing reagent-grade MO (Fisher Scientific) and immediately exposed to illumination under constant magnetic stirring at 180 rpm for 2 hours. The adsorption-only tests were performed using the same procedure in the absence of light. For the prolonged photocatalysis tests, 200 mL of MO solution was allowed to equilibriate in the dark with 0.5 g L^{-1} of catalyst under constant magnetic stirring at 180 rpm for 2 hours prior to each experiment. The photocatalytic degradation was then performed for 2.5 hours in the presence of visible light irradiation. For all trials, samples were drawn periodically and centrifuged, and the supernatant analyzed using a spectrophometer (Genesys 10UV, ThermoScientific). The peak absorbance used for MO was λ = 463 nm for pH > 4 and λ = 505 for pH < 3. The initial MO concentration was kept at 25 mg L^{-1}, except in the concentration studies. The initial pH of the solution was left unadjusted at pH 5.5, except in the pH studies. For the pH studies, the initial pH was adjusted with either 0.5 M HCl or 0.5 M NaOH (reagent-grade, Fisher Scientific), and was measured with a benchtop pH probe (accumet AB15+ Basic, Fisher Scientific). Recyclability tests were performed by centrifuging the MO-catalyst slurry between trials at 3500 rpm for 3 minutes in a Hermle Z400K centrifuge (Hermle Labortechnik GmbH), removing the supernatant, and redispersing the catalyst in fresh 25 g L^{-1} MO solution. The quenching experiments were performed by the addition of appropriate radical scavengers. 0.01 M isopropanol (reagent-grade, Fisher Scientific**)** was used as the radical scavenger, 0.01 M ethylenediaminetetraacetate disodium salt dihydrate (EDTA) (99%, Sigma-Aldrich) was used as the holes scavenger, and N_2

bubbling was used to suppress the formation of superoxide radicals. The removal efficiency was calculated using the following formula:

$$Removal\ Efficiency\ (\%) = (C_o - C_t)/C_o \times 100 \qquad (3.1)$$

Where C_o denotes the initial pollutant concentration (mg L^{-1}), and C_t is the concentration at time *t* (mg L^{-1}). For prolonged runs including a dark adsorption time, C_o for photocatalysis was taken as the adsorption equilibrium concentration. Control runs were performed in the absence of light and catalyst, respectively. The error associated to the experiments was estimated as the standard deviation between triplicate runs.

3.2.3.3 Phenol adsorption and photodegradation

Adsorption and photodegradation of phenol (98%, Fisher Chemical) was also studied in the photosystem using a composite loading of 0.5 g L^{-1} in 200 mL solution with an initial concentration of 13 mg L^{-1}, using a magnetic stir speed of 180 rpm. The supernatant from the periodically withdrawn samples was analyzed at a peak absorbance of λ = 270 nm. Phenol degradation was studied for 3 hours after the 2 hour dark adsorption period.

3.3 Results and discussion

3.3.1 Catalyst characterization

The phase structure and crystallinity of the prepared materials were investigated by XRD, and the obtained patterns for the composites and for pure AC and Ag/AgCl are shown in Figure 3.1, respectively. The pure AC exhibited mainly amorphous structure, with the exception of a wide, shallow hexagonal (002) graphitic peak, which indicated small regions of crystallinity were present as in other commercial activated carbons [17]. The prepared composites exhibited similar patterns and crystallinities to pure Ag/AgCl, as indicated by peak positions and intensities. The diffraction peaks were indexed to the face centered cubic AgCl phase (JCPDS card # 31-1238) with lattice constants of *a* = 5.545 – 5.549 Å, in good agreement with literature for AgCl (*a* = 5.549 Å[18]). From the enlarged patterns shown in Figure 3.2, main diffraction peaks for the (111) plane at 38.1^o and for the (200) plane at 44.3^o for metallic Ag (JCPDS card #01-087-0597) were observed in the pure Ag/AgCl prepared, implying that the *in situ* reduction was able to promote the transformation of some AgCl to

Ag. However, peaks associated to metallic silver could not be observed in the pattern for a representative Ag/AgCl-AC composite (2.5:1), which may have been due to the low content, small particle sizes, and high dispersion of silver on the surface of Ag/AgCl-AC, as was previously reported for Ag/AgI-Al_2O_3 prepared using deposition-precipitation-photoreduction synthesis [19].

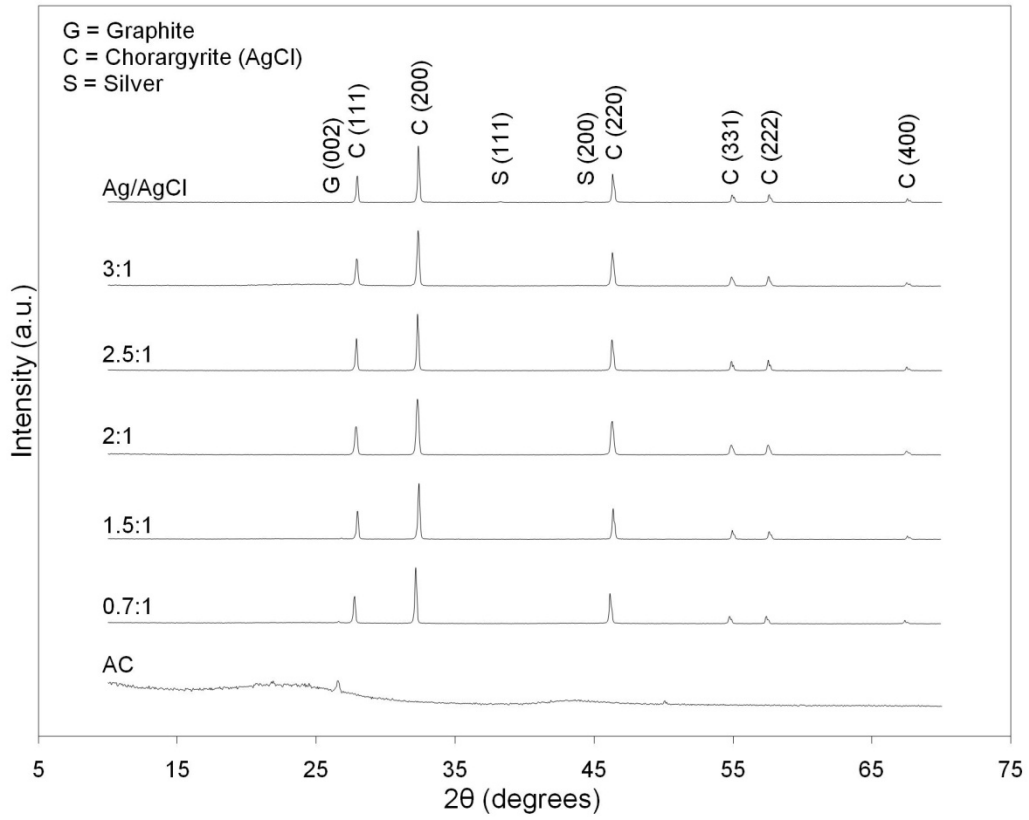

Figure 3.1: XRD patterns for Ag/AgCl, AC, and various Ag/AgCl-AC composites

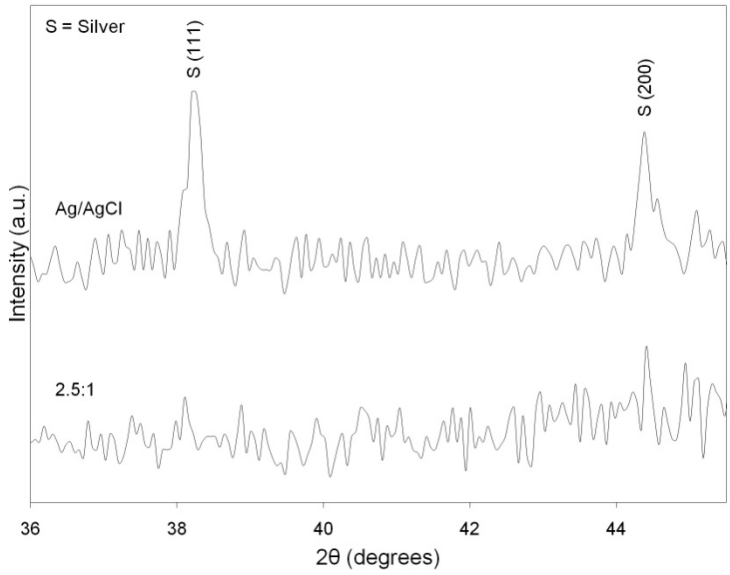

Figure 3.2: XRD patterns for Ag/AgCl and 2.5:1 Ag/AgCl-AC composite

The structure of the composites was studied by TEM, and images of a representative Ag/AgCl-AC (2.5:1), and the as-prepared Ag/AgCl are shown in Figure 3.3. For pure Ag/AgCl, AgCl particles ranging from approximately 1.7 – 2.1 μm were observed, and were decorated with smaller metallic silver clusters (~120 – 160 nm) on their exterior. The high-resolution TEM of the silver clusters formed indicated an interlayer *d*-spacing of 0.24 nm, which corresponded well to the Ag (111) plane of silver. The selected area diffraction pattern (SAED) shown in the inset of Fig. 3.3b indicated that the sample was polycrystalline in nature, and the observed rings were attributed to diffraction from the (111), (200), and (220) reflections of fcc silver (JCPDS card #01-087-0597), based on calculated *d*-spacings of 2.47 Å, 2.12 Å, and 1.45 Å, respectively. For the Ag/AgCl-AC composite, the TEM images indicated that photocatalyst deposition occurred mainly on the exterior surface of activated carbon (which was identifiable by the large, light, grainy structures in Figures 3.3c and 3.3.d), and the darker, more electron-dense regions attributable to silver/silver halides formed heterogeneous clusters on its outer surface.

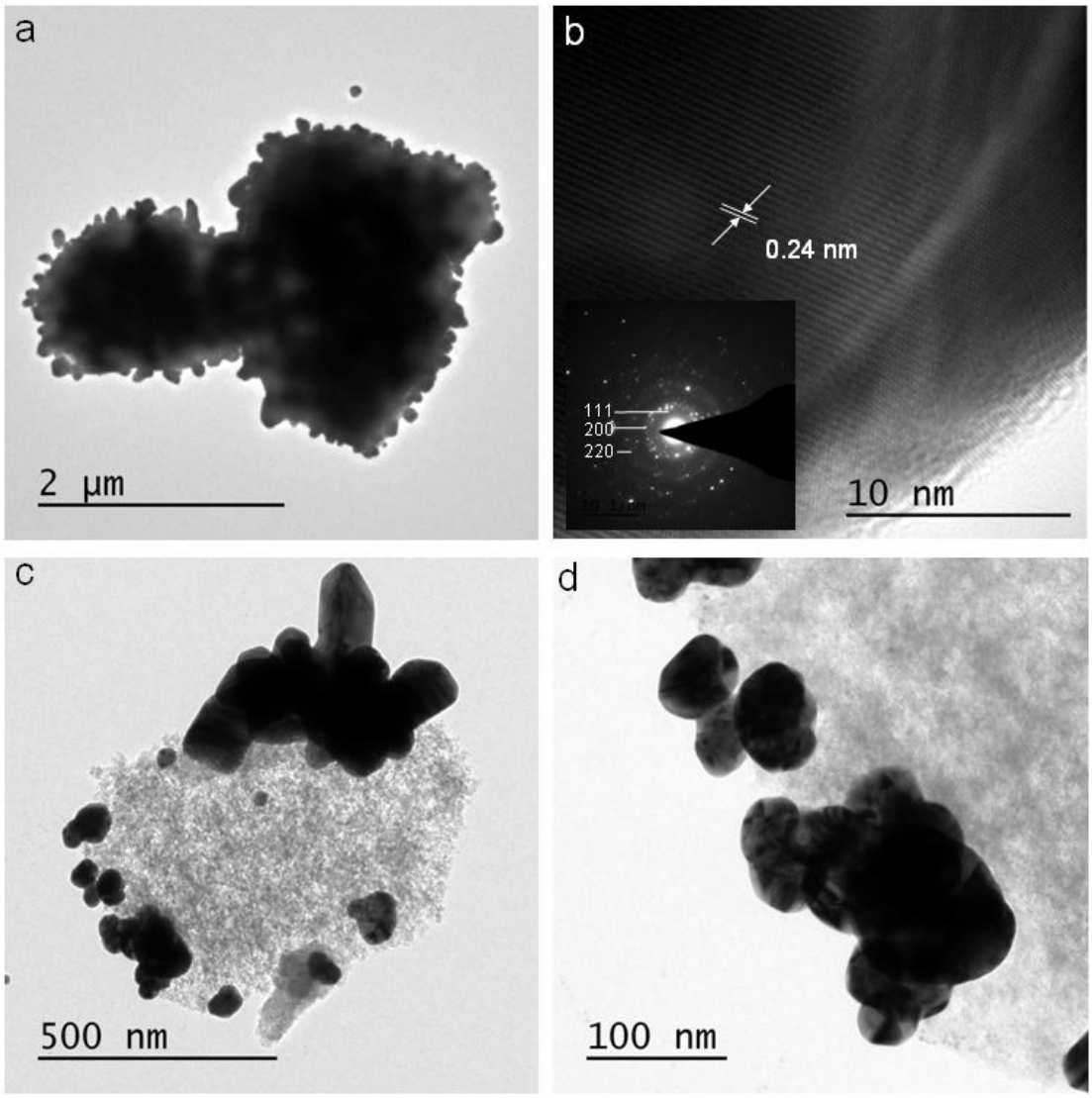

Figure 3.3: TEM images of a) Ag/AgCl; b) high-resolution TEM of Ag in Ag/AgCl; SAED pattern inset; and c), d) as-prepared Ag/AgCl-AC composite (2.5:1)

To further investigate the morphology of the prepared Ag/AgCl-AC composites, SEM imaging was performed, and the results are presented in Figure 3.4. The deposition of Ag/AgCl onto AC resulted in the formation of heterogeneous clusters with high surface coverage, although some exposed surfaces of the textured carbon host material were observed. Metallic silver was also seen on the surface of the silver halides, although it was not easily observed by TEM imaging due to the thickness and three dimensional nature of Ag/AgCl clusters formed in the composites. AgCl particles in Ag/AgCl-AC were found by

SEM to range from 470 nm to 1.06 µm, and the reduced Ag were approximately 110 nm to 150 nm in size. Photochemical reduction of AgCl *in situ* has been reported to generate Ag atoms that aggregate to form silver nanograins, which deposit on the surface of the silver halide particles [13], in good agreement with the results obtained in this study.

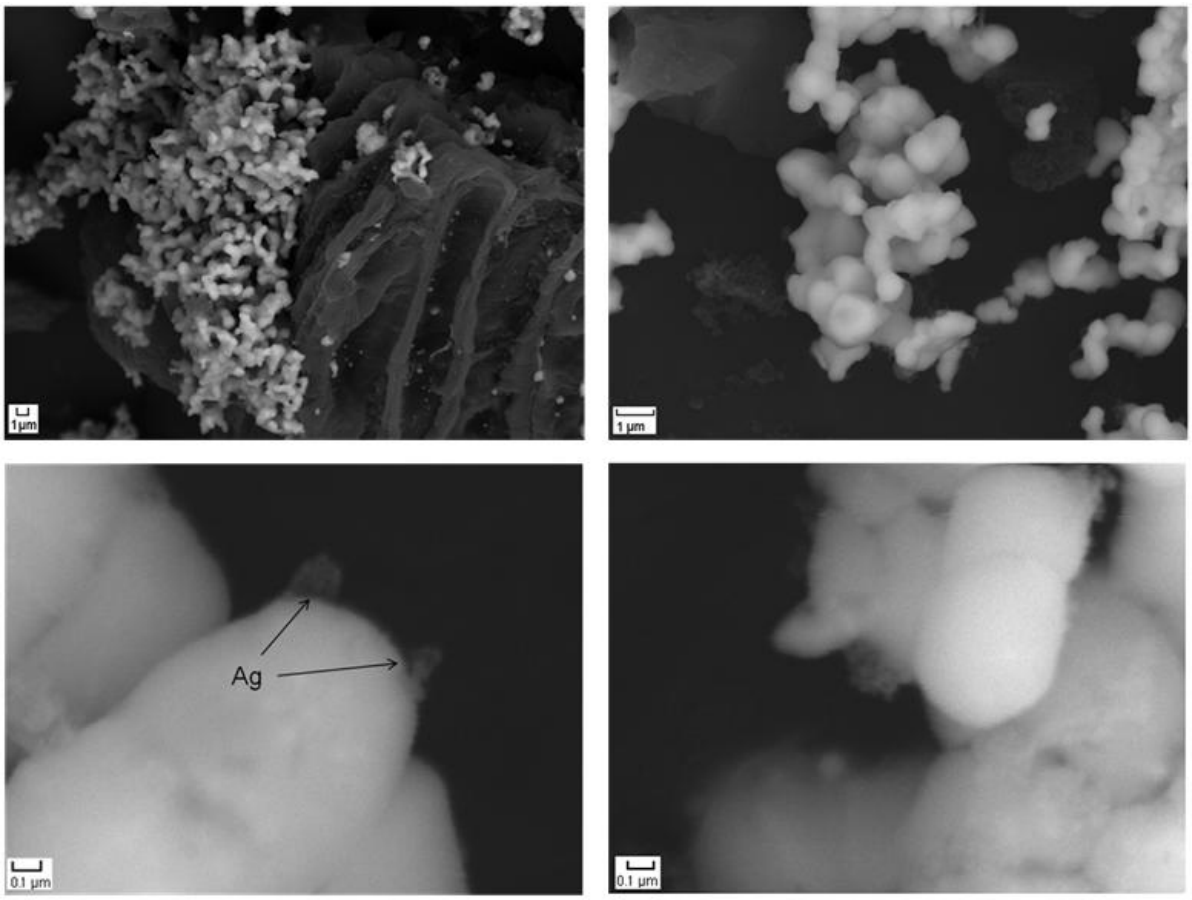

Figure 3.4: SEM images of Ag/AgCl-AC composite (2.5:1)

The surface chemical states of the samples were investigated by XPS. Spectra from the high-resolution scans of Cl 2p and Ag 3d orbits are given for Ag/AgCl and for a representative Ag/AgCl-AC composite (2.5:1) in Figures 3.5a, and 3.5b, respectively. The deconvoluted peaks for the Cl 2p orbits were centered at approximately 197.6 eV and 199.2 eV for both Ag/AgCl and the prepared composite. These peaks corresponded well to Cl 2p 3/2 and Cl 2p 1/2, indicating the presence of chlorine as ionic Cl^- [20, 21]. The silver peaks at approximately 366.8 eV and 372.8 eV were ascribed to binding energies of Ag 3d 5/2 and Ag

3d 3/2, respectively, for Ag^{+} present in AgCl [20, 22]. Smaller peaks obtained at 367.7 eV and 373.8 were assigned to binding energies of Ag 3d 5/2 and Ag 3d 3/2, respectively, for metallic Ag [23]. This indicated that silver was present in the samples as Ag^{+} in AgCl and as Ag^{o} in metallic Ag, further evidencing the photoreduction of some AgCl to Ag under UV-Vis irradiation.

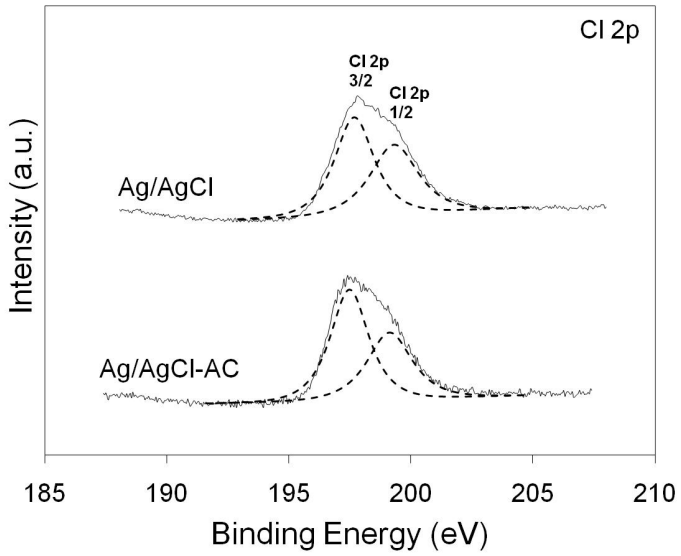

Figure 3.5a: Cl 2p XPS spectra for Ag/AgCl and 2.5:1 Ag/AgCl-AC composite

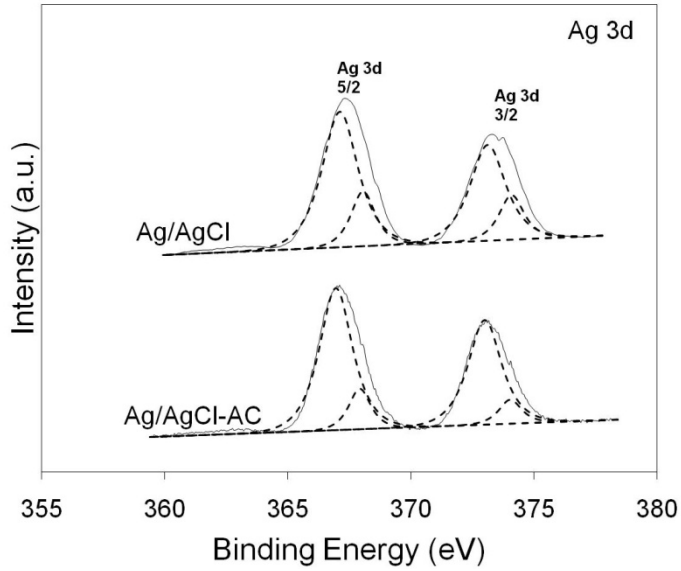

Figure 3.5b: Ag 3d XPS spectra for Ag/AgCl and 2.5:1 Ag/AgCl-AC composite

BET surface areas calculated by N_2 sorption are summarized in Table 3.1, and were found to vary between 63.0 and 279.3 $m^2\ g^{-1}$ for the Ag/AgCl-AC composites. The BET range used was P/Po < 0.015, and was chosen based on a criterion proposed by Rouquérol et al. [24] for materials possessing microporosity. The composite surface areas were also expressed relative to activated carbon, and were found to consistently decrease with increasing Ag/AgCl content. This was thought to be due to pore-blocking by the Ag/AgCl particles. The surface areas of the composites were all smaller than that of activated carbon, but were all larger than that of pure Ag/AgCl, suggesting an increased adsorptive capability of the composites compared to the bare photocatalyst alone.

Table 3.1: Surface areas of Ag/AgCl, AC, and Ag/AgCl-AC composites

Catalyst	**BET surface area ($m^2\ g^{-1}$)**	**Relative surface area (%)**
AC	810.9	100
0.7:1 composite	279.3	34
1.5:1 composite	149.2	18
2:1 composite	105.5	13
2.5:1 composite	77.1	9.5
3:1 composite	63.0	7.8
Ag/AgCl	2.1	2.6

The structure and porosity of the composites were studied, and the nitrogen sorption isotherm for a representative sample (2.5:1) is given in Figure 3.6, with that of AC shown for comparison. Both isotherms observed were Type IV according to IUPAC classifications [25], with H4 hysteresis in the desorption branch due to the presence of mesopores [26].

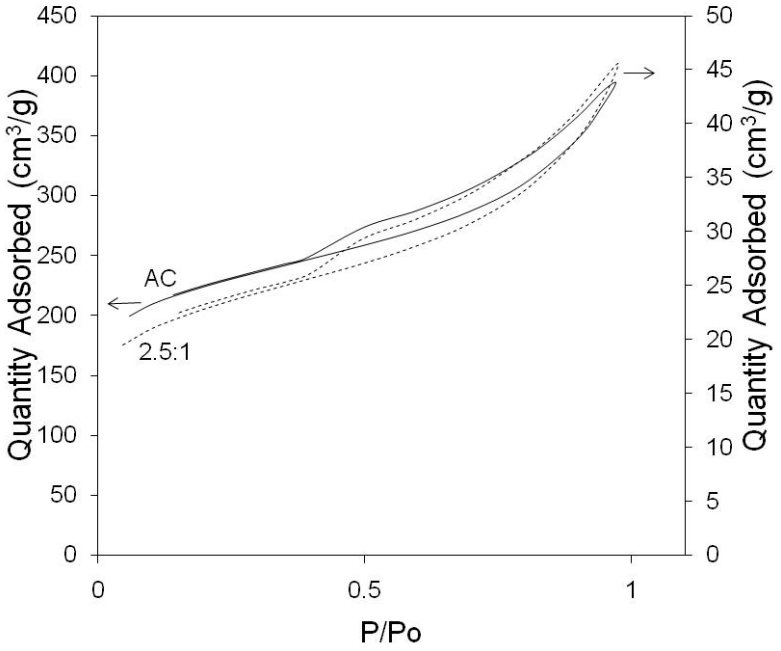

Figure 3.6: N_2 sorption isotherms for AC and 2.5:1 Ag/AgCl-AC composite

Table 3.2: Porosity characteristics of AC and 2.5:1 Ag/AgCl-AC

Catalyst	Total pore volume (cm^3/g)	Micropore volume (cm^3/g)	Micropore Area (m^2/g)	Mesopore Volume (cm^3/g)	Mesopore Area (m^2/g)
AC	0.61	0.27	510	0.34	201
Ag/AgCl-AC	0.070	0.025	48.0	0.045	26.1

*calculated by difference

The total pore volumes, microporosity and mesoporosity data are summarized in Table 3.2. The total pore volume, as well as the micro- and mesopore volumes (and consequently, areas) all decreased significantly upon addition of Ag/AgCl into the AC composites. The constructed *t*-plots indicated that microporosity significantly contributed to the total pore volume. For AC, micropores contributed 44% of the total pore volume, while this decreased to approximately 36% in the Ag/AgCl-AC composite. Based on the sizes of Ag/AgCl particles observed in the composite, the photocatalyst was not thought to penetrate the micropores of AC (<2 nm), but instead formed an "egg-shell" structure, where heterogeneous clusters of photocatalyst deposited onto the outer surface of AC [27]. These clusters decreased the pore volume and surface area of the resulting composite by blocking

mesopores and pore entrances present on the AC surface. This pore blockage also caused a reduction in micropore volume, since mesopores in AC were the main thoroughfares to micropores for sorption [27]. Based on the trend in BET surface areas, increasing Ag/AgCl content in the composites was thought to enhance this pore-blocking effect.

UV-Vis diffuse reflectance absorption data for a representative Ag/AgCl-AC composite (2.5:1), as-prepared Ag/AgCl, and unreduced AgCl are given in Figure 3.7, respectively. For all the samples, an absorbance edge at ~385 nm was observed due to the band gap of AgCl ($E_{bg,\ indirect}$ = 3.25 eV [28]). Compared to unreduced AgCl, the prepared Ag/AgCl catalyst exhibited a broad absorption band in the range of 400 – 800 nm, which was attributed to the surface plasmon resonance of Ag NPs produced during photoreduction. The broadness of the peak was due to multiple plasmonic oscillation frequencies present because of variation in the shapes and diameters of Ag NP clusters formed [7, 29, 30]. The Ag/AgCl-AC composite prepared also showed broad, strong absorbance in the visible light region, which indicated that it possessed good applicability as a visible light active photocatalyst.

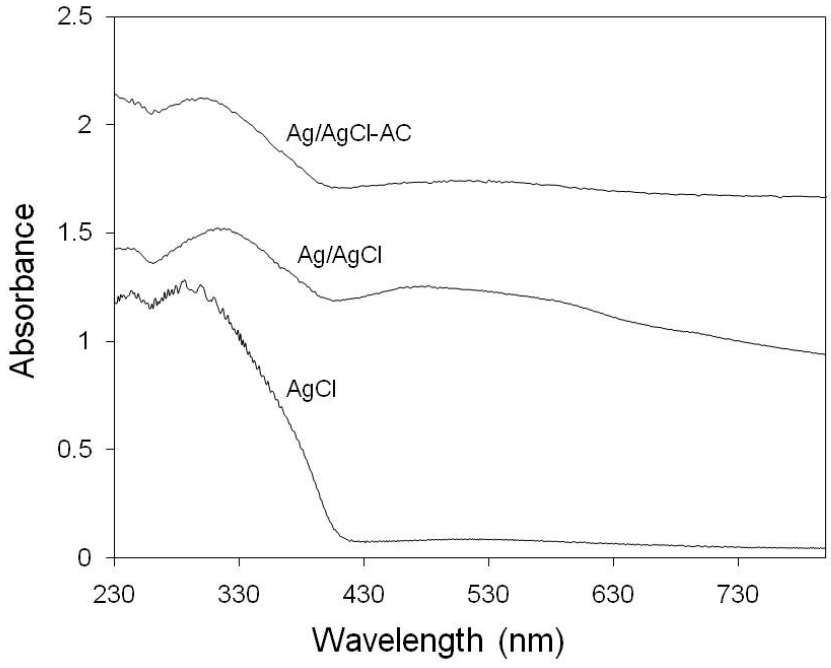

Figure 3.7: UV-Vis absorption spectra of 2.5:1 Ag/AgCl-AC composite, as-prepared Ag/AgCl, and unreduced AgCl, respectively

3.3.2 Photocatalytic activity

3.3.2.1 MO adsorption and photodegradation

Preliminary activity screening for the prepared composites was performed by comparing the MO removal observed using a combined adsorption-photocatalysis process to that obtained by dark adsorption only [31, 32]. The results from the rapid screening tests are given in Figure 3.8. Preliminary trials using pure Ag/AgCl indicated a negligible removal under dark adsorption conditions, and a 15.1% MO removal under visible light irradiation, while the unmodified AC was able to completely adsorb MO from solution in under 10 minutes. Additionally, MO removal in the absence of catalyst was found to be less than 1.5%, and the effects of photolysis were therefore thought to be negligible.

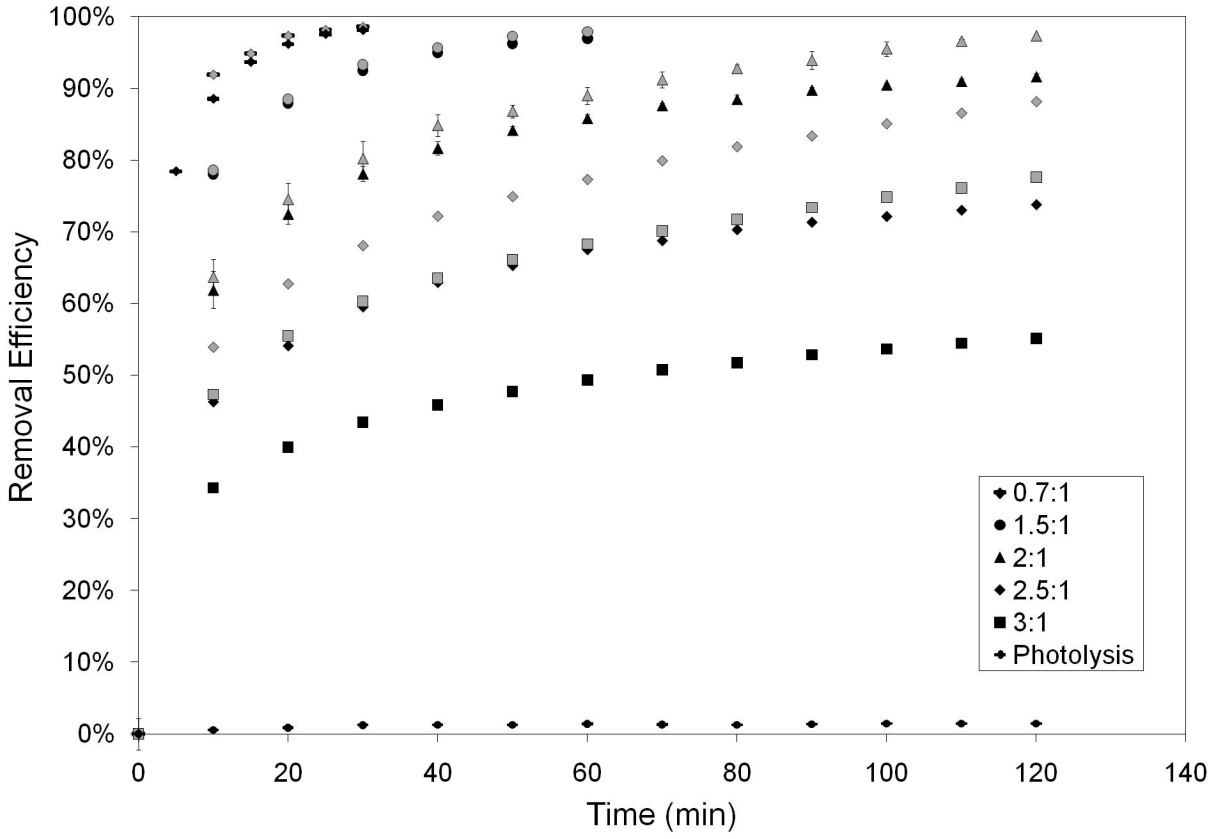

Figure 3.8: Comparison of adsorptive and combined adsorptive-photocatalytic MO removal for Ag/AgCl-AC composite powders, where black and grey markers represent adsorption and combined photocatalysis-adsorption, respectively. (C_o = 25 mg L^{-1}, loading = 0.5 g L^{-1}, pH = 5.5) – *average of three trials, representative error bars shown*

Final MO removal efficiencies were calculated and are given in Table 3.3. The Ag/AgCl-AC composites exhibited much higher adsorptive capacities towards MO than pure Ag/AgCl, and this was thought to be due to their larger available surface areas. The prepared composites also had very strong adsorptive capabilities compared to other Ag/AgX-based carbon composites reported in literature such as Ag/AgCl-reduced graphene oxide sheets [13]. A noticeable enhancement in final removal efficiency between the dark adsorption and combined adsorption-photocatalysis processes was realized for the composites containing high loadings of Ag/AgCl (2:1, 2.5:1, 3:1 ratios, respectively). This increased efficiency under irradiation was thought to be due to production of photoexcited species by the Ag/AgCl photocatalytic component of the composites. The increase was not proportional to the additive effects of adsorption and photocatalysis, since the efficiency observed for a full loading (0.5 g L^{-1}) of Ag/AgCl was 15.1%, and the composites contained the photocatalyst in lower proportions (a nominal loading of 0.5 g composite L^{-1} was used). This suggested the presence of a synergistic effect of adsorption on the photocatalytic removal efficiency, as reported for other adsorbent photocatalysts such as TiO_2 on AC [33]. Although there may have been photoinduced radical generation at lower Ag/AgCl compositions (0.7:1, 1.5:1) under irradiation, the enhancement was not observed using the present conditions due to the stronger removal of MO by adsorption only.

Table 3.3: MO removal efficiencies obtained using Ag/AgCl-AC composites

Catalyst	**Removal Efficiency: $(C_o-C_f)/C_o$ (%)**
Pure Ag/AgCl (adsorption only)	Negligible
Pure Ag/AgCl (adsorption + photocatalysis)	15.1
0.7:1 (adsorption only)	98.6
0.7:1 (adsorption + photocatalysis)	98.1
1.5:1 (adsorption only)	98.0
1.5:1 (adsorption + photocatalysis)	97.9
2:1 (adsorption only)	91.7
2:1 (adsorption + photocatalysis)	97.3
2.5:1 (adsorption only)	73.8
2.5:1 (adsorption + photocatalysis)	88.1
3:1 (adsorption only)	55.1
3:1 (adsorption + photocatalysis)	77.6

To further investigate photocatalysis mediated by the Ag/AgCl-AC composites, prolonged runs were carried out by allowing the catalyst and MO to equilibriate in the dark for 2 hours, followed by visible light irradiation for 2.5 hours. The results obtained are shown in Figure 3.9 as amount of MO removed from solution per weight of catalyst used (or catalyst equivalent, in the case of AC).

The presence of irradiation has been found in some cases to result in an increase of pollutant adsorption onto AC in TiO_2-AC composites, as studied for methylene blue dye under UV [34]. To investigate this in the current system, a control experiment was performed using AC only, at an equivalent loading as that contained in the 2.5:1 composite. From the results shown in Figure 3.9, the provided irradiation did not induce a significant change in the adsorption of dye onto activated carbon. In contrast, the composite catalysts exhibited a noticeable increase in the removal rate of MO upon illumination, after the adsorption pseudo-equilibrium was reached. This was thought to be due to visible light absorption and consequent photocatalytic action by the composites, removing the MO pollutant by photodegradation, and by a dynamic adsorption-photocatalysis mechanism under visible light.

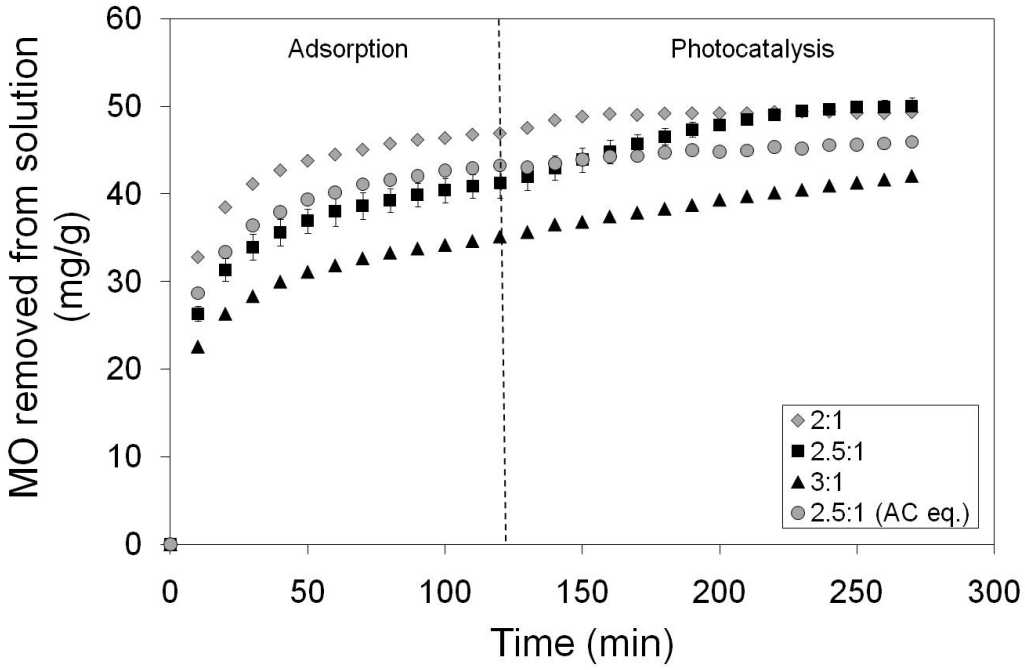

Figure 3.9: Adsorption and subsequent photocatalysis using 2:1, 2.5:1, and 3:1 Ag/AgCl-AC, respectively. The prolonged test using an equivalent AC loading as that incorporated into the 2.5:1 composite is shown for comparison. (C_o = 25 mg L^{-1}, loading = 0.5 g L^{-1}, pH = 5.5) – *representative error bars shown*

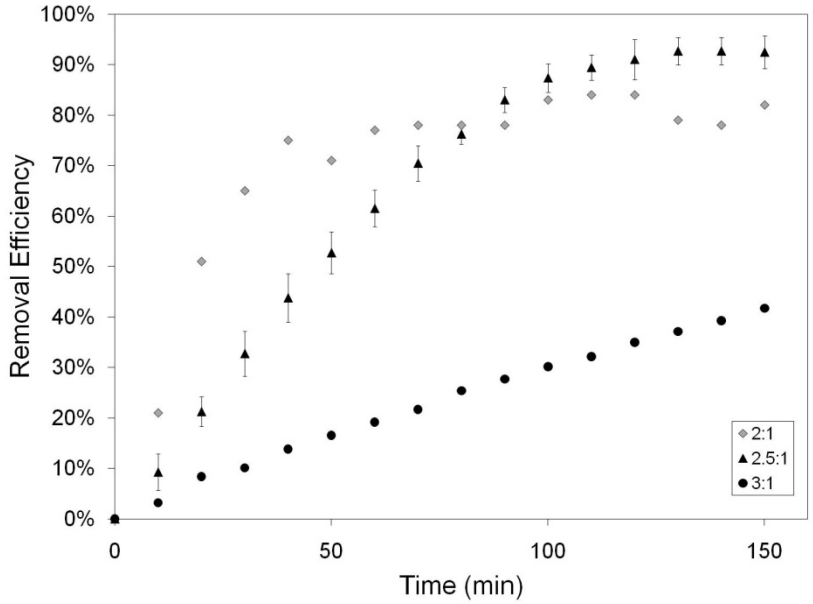

Figure 3.10: Photocatalytic removal efficiency as a function of time for 2:1, 2.5:1, and 3:1 Ag/AgCl-AC composites, respectively. (C_o = 25 mg L^{-1}, loading = 0.5 g L^{-1}, pH = 5.5) – *representative error bars shown*

The data from the prolonged adsorption-photocatalysis studies shown in Figure 3.9 were normalized using the concentrations at the end of dark adsorption as the initial concentrations for photocatalytic reaction, and the calculated temporal removal efficiencies for photocatalysis are given in Figure 3.10. The Langmuir-Hinshelwood kinetic expression for heterogeneous surface reactions was used to describe the data, where the reaction rate is described by the following expression.

$$-dC/dt = K k_r C/(1+KC) \qquad (3.2a)$$

Where K is the Langmuir-Hinshelwood adsorption coefficient (L mg^{-1}), and k_r is the reaction rate constant (mg L^{-1} min^{-1}). Simplification of this kinetic expression into a pseudo-first order equation is frequently employed for photocatalysis in cases where the initial concentration used is sufficiently small (< 10^{-3} mol L^{-1} [35]). The simplified, integrated rate expression is given by:

$$ln(C_o/C) = k't \qquad (3.2b)$$

Where k' denotes the pseudo-first order rate constant (min^{-1}). This apparent rate constant has been cited to be appropriate for the quantitative comparison of different photocatalytic systems, since it enables the calculation of photocatalytic activity independently of dark adsorption [36]. To compare kinetic rates obtained using various catalysts, the rate constants were calculated using equation (3.2b) for the initial linear portion of the reaction, and the fitted data is shown in comparison with the experimental values in Figure 3.11.

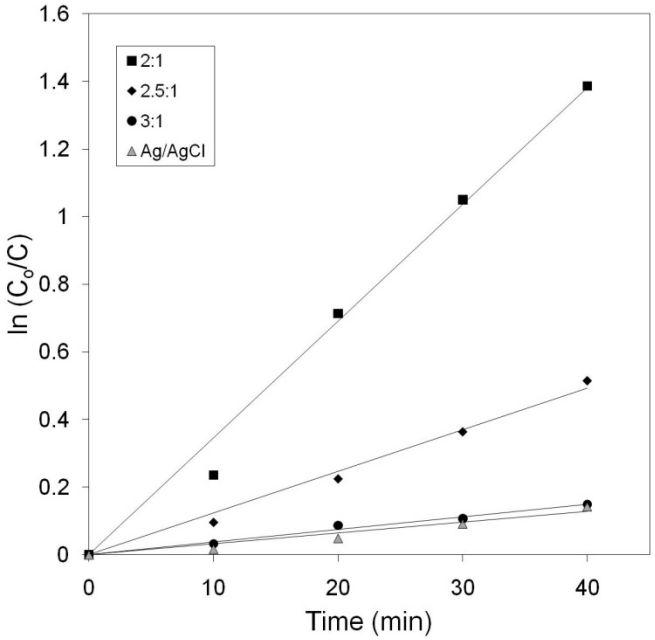

Figure 3.11: Photodegradation kinetics for 2:1, 2.5:1, and 3:1 Ag/AgCl-AC composites and Ag/AgCl, respectively. (loading = 0.5 g L^{-1}, pH = 5.5)

The rate constants obtained from the slopes of fitted lines for the 2:1, 2.5:1, and 3:1 composites were 0.0345, 0.0128, and 0.0037 min^{-1}, respectively, and was 0.0032 min^{-1} for an Ag/AgCl prolonged run control. The R^2 values associated to the fitted data ranged from 0.948 – 0.997, and the fit was thought to be appropriate to model the initial stages of degradation. The synergy factor (R) for activated carbon composite photocatalysts, defined by Matos et al. [10] and adapted in this case for a pure Ag/AgCl reference catalyst, was calculated by equation (3.3):

$$R = k'(Ag/AgCl\text{-}AC)/k'(Ag/AgCl) \qquad (3.3)$$

Where R was essentially a ratio of the pseudo-first order kinetic constants. This yielded synergy factors of 10.8, 4, and 1.2 for the 2:1, 2.5:1, and 3:1 composites, respectively. The synergy factor for the 3:1 composite was near unity because the loss of adsorptive capacity caused a decrease in removal rate severe enough to cause its activity to become comparable to that obtained using a full (i.e. 0.5 g L^{-1}) loading of pure Ag/AgCl alone. However, for the lower-loaded composites, the calculated synergy factors were much greater than 1, indicating that the presence of AC enhanced the overall pollutant removal efficiency.

The removal behaviour upon irradiation was thought to be strongly influenced by the sorptive capability of the composites, where the powder with high surface area (2:1), exhibited a fast removal rate due to its high sorptive capability, and vice versa for the low surface area composite (3:1). While an increased MO removal rate from solution did not necessarily mean all of the pollutant was being degraded photocatalytically, a higher sorptive capability of the composite was presumed to promote faster pollutant transfer from solution to the reactive sites. It should be noted that increasing the Ag/AgCl ratio in the composite may have provided a greater number of photocatalytic reaction sites, but also decreased the total adsorption by reducing the available sorptive surface area, so a trade-off was required between the desired adsorptive and photocatalytic activities. As a temporary optimum, the 2.5:1 powder was chosen for further study to illustrate the dynamic adsorption-photocatalysis behaviour of the designed catalysts.

3.3.2.2 Effect of initial MO concentration

The effect of initial MO concentration on activity was investigated in the range of 25 – 50 mg L^{-1}, and the results obtained are shown in Figure 3.12. While all of the trials performed exhibited some photodegradation using the composite catalyst, the activity observed tended to decrease with increasing MO concentration. The lowest final degradation (13.2%) was realized using an initial concentration of 50 mg L^{-1}, while the highest degradation (93.8%) was achieved at 25 mg L^{-1}. The observed difference may have been due to the effect of pollutant concentration on the light penetration into solution [37]. The solution transmittance decreased with increasing concentration, resulting in fewer photons reaching the catalyst surface, and a consequent reduction in degradation activity. This was consistent with literature for the effect of initial MO concentration on photocatalysis [37–40]. To investigate whether increased light penetration at lower initial concentrations affected MO photolysis, the photolytic conversion at an initial concentration of 5 ppm was measured, and was found to be negligible, as shown in Figure 3.12.

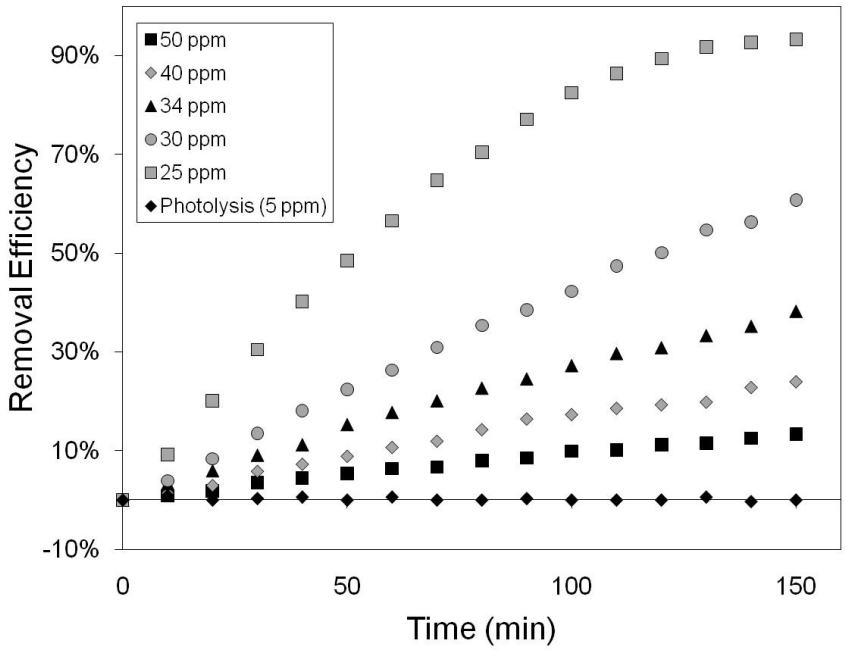

Figure 3.12: Effect of initial concentration on photodegradation using 2.5:1 composite. (loading = 0.5 g L^{-1}, pH = 5.5)

3.3.2.3 Effect of pH

Solution pH has been reported to be a very important parameter in photocatalytic processes [35, 41, 42]. The pH can affect catalyst-pollutant interactions and the generation of redox species during irradiation [39, 43]. The initial solution pH was investigated between the range of pH 2 –9.5 by adjustment with HCl or NaOH, and the results obtained from degradation are shown in Figure 3.13. It should be noted that photolytic MO degradation did not change significantly between acidic and basic media, and was thought to have a negligible contribution on the changes in degradation observed.

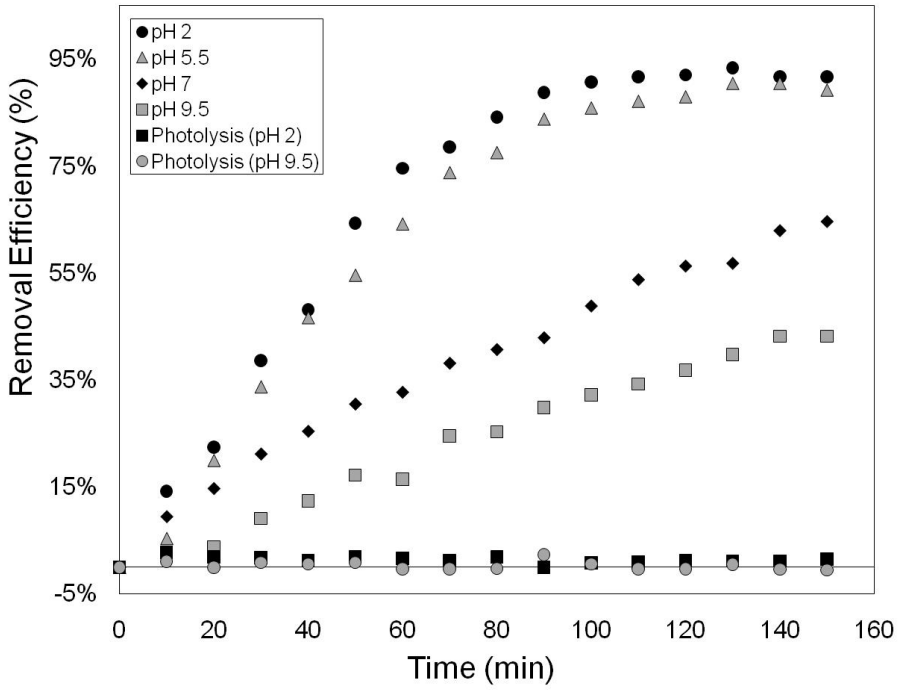

Figure 3.13: Effect of pH on photodegradation using 2.5:1 composite. (C_o = 25 mg L^{-1}, loading = 0.5 g L^{-1})

The pH was found to strongly affect the photocatalytic process, with degradation taking place more rapidly in acidic solution, and decreasing with increasing pH. This may have been due to changes in surface charge properties with changes in pH for methyl orange and the consequent changes in adsorption affinity towards the catalyst. MO existed in its anionic state in water at pH 7 and above due to the sodium ion dissociation. In acidic conditions, amphoteric MO formed from hydrogen becoming attached to nitrogen in the azo bond associated with the ring structure [44]. The change is shown schematically in Figure 3.14.

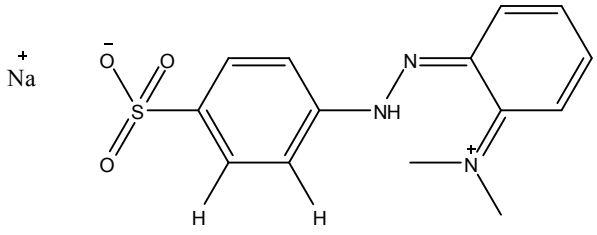

(a)

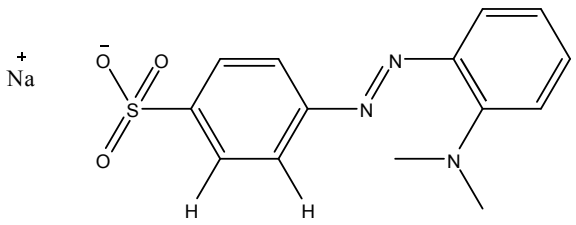

(b)

Figure 3.14: Methyl orange structure in a) acidic and b) basic media

The surfaces of AgCl particles were likely terminated by Cl^- ions [45], and were therefore negatively charged. Additionally, polarization of electron distribution within metallic Ag on the surface was thought to lead to regions of its negative and positive charges being far from and close to the Ag/AgCl interface, respectively [45]. Therefore, the surface of Ag/AgCl was likely negatively charged. The interaction of these negatively charged catalyst surfaces with anionic MO in alkaline solution may have induced Coulombic repulsion, resulting in a decreased amount of substrate adsorbed. This effect was not present in acidic media, where the MO took on an amphoteric structure. The photocatalytic degradation of anionic (mainly sulphonated) dyes was found in other literature to be optimized in acidic conditions, and decrease in the pH range of 7–11 [46], in good agreement with the results obtained in this study.

While electrostatic attractions and repulsions between pollutant and catalyst affect activity, the interpretation of data at variable pH is difficult in practice due to the different redox species present. At low pH values, positive holes are considered the major oxidation species, while at neutral or high pH, hydroxyl radicals are predominant [42, 43, 47–50]. Elucidation of degradation mechanism therefore becomes difficult, since the dye could be degraded through hydroxyl radical attack, directly oxidized by positive holes, or reduced by negative electrons or superoxides. These factors also influenced the activity results observed at various pH values.

3.3.2.4 Recyclability

To evaluate the recyclability of Ag/AgCl-AC, the 2.5:1 composite was used in four consecutive trials, recovering the catalyst between runs by centrifuging and decanting. The

MO removal by adsorption and degradation in the sequential runs is shown in Figure 3.15.

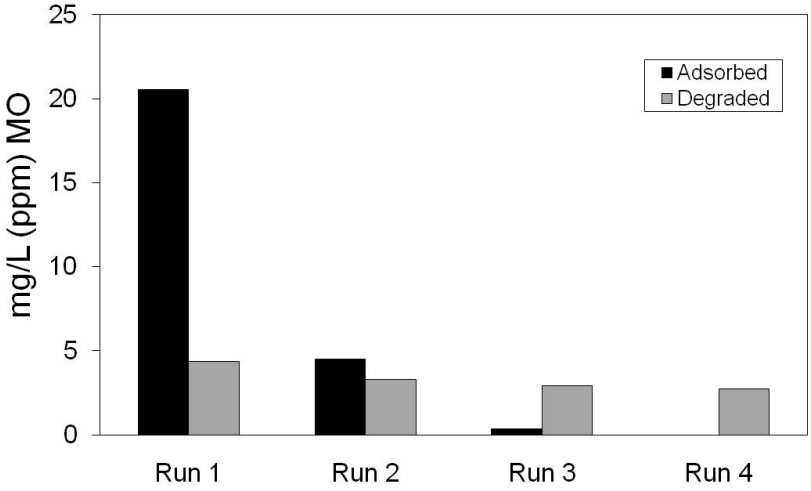

Figure 3.15: Adsorption and photodegradation performance of 2.5:1 composite over four consecutive cycles (C_o = 25 mg L^{-1}, loading = 0.5 g L^{-1}, pH = 5.5)

MO adsorption using the composite catalyst was found to decrease between consecutive runs. This was due to the limited sorption capacity of the recycled composite, and an inability of the photocatalyst portion to fully regenerate the incorporated AC by degrading all of the adsorbed MO. The latter effect also resulted in a decrease in photocatalytic activity with repeated use because the rate of degradation was low compared to the rate of substrate accumulation. This may have caused saturation at the surface of the photocatalyst, diminishing its photonic efficiency [51]. A gradual decrease in efficiency could be observed with repeated use of the composite, and in the second to fourth trials, the photocatalyst was able to degrade 75%, 67%, and 62% of the total MO degraded in the first run, respectively. This decreased efficiency with increased cycle number may have also been due to the formation of reaction intermediates and their subsequent adsorption and accumulation on the photocatalyst surface [52, 53], or limitations in diffusion of the pollutant from the micropores of the composite to the actual catalytic sites on its outer surface [54].

The XRD pattern for the composite catalyst after use in four consecutive trials is shown in Figure 3.16, with the pattern of the fresh material for comparison. Spectral patterns observed before and after recycling were nearly identical, indicating good stability of the catalyst.

Weak reflections at 38.1^{o} and 44.3^{o} attributable to the (111) and (200) faces of metallic silver, respectively, were observed in the used sample. The appearance of these peaks was thought to be due to an increase of Ag nanoparticle sizes during visible light induced photocatalysis, caused by aggregation and photodecomposition of some AgCl to form additional metallic Ag clusters. However, this decomposition was previously found to have only a minor effect on the total surface contents of Ag and AgCl, as per reports in literature using similar experimental conditions [45, 21, 55], confirming the overall stability of such catalysts in repeated use.

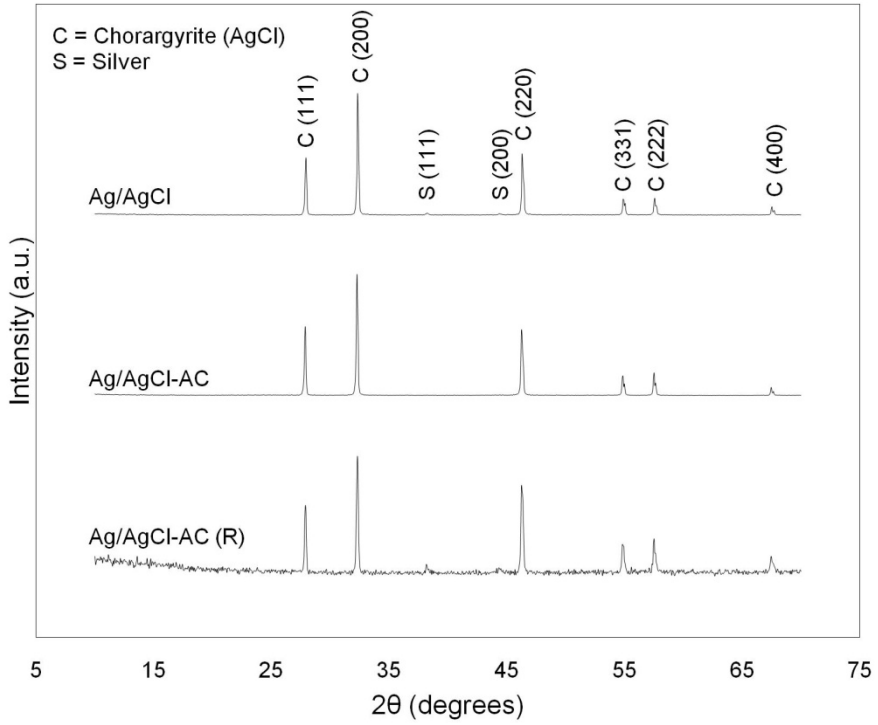

Figure 3.16: XRD patterns for as-prepared Ag/AgCl, 2.5:1 Ag/AgCl-AC composite, and recycled 2.5:1 Ag/AgCl-AC composite after four adsorption-photocatalysis cycles, respectively

3.3.2.5 Role of radical species

Radical and hole trapping experiments were designed to investigate the roles of the photo-induced species in the prepared composites through the use of appropriate quenchers. The quenching effect of scavengers can be used as a diagnostic tool to discern relative importances of various photo-induced species present [56], where the rate of photocatalytic

reaction may be partially suppressed by the employed quencher, resulting in a lowered apparent rate constant (*k'*). The magnitude of this reaction suppression is indicative of the relative role of the quenched species in the reaction. Nitrogen bubbling was used to reduce the dissolved oxygen concentration in solution, limiting the capture of photoinduced electrons by molecular oxygen to generate superoxide radicals. EDTA was used as a hole scavenger, while isopropanol was used as a hydroxyl radical scavenger. The EDTA itself had a negligible effect on the adsorption capacity of AC, as previously reported [57]. The kinetic data obtained using various suppressants are given in Table 3.4.

Table 3.4: Kinetic data in the presence of various scavengers for 2.5:1 composite

	Species suppressed	***k'*** **($x10^{-2}$ min^{-1})**	**R^2**	***k'/k'*** **(no quenching) (%)**
N_2 bubbling	Superoxide radical ($^{\bullet}O_2^-$)	0.28	0.99	21.9
Isopropanol	Hydroxyl radical ($^{\bullet}OH$)	0.11	0.99	85.9
EDTA	Positive charge vacancy (hole, h^+)	0.31	0.96	24.2

From the observed changes in kinetics, the hydroxyl radical was thought to not play a dominant role in photocatalytic oxidation due to its weak quenching effect, consistent with other studies on Ag/AgX-type catalysts [20, 56, 58]. The holes were found to have a more pronounced effect, as indicated by the observed decrease in reaction rate upon addition of EDTA. Holes were thought to act by two pathways, namely through direct surface reaction with the dye, or by oxidation of chloride ions in AgCl to form chlorine species, which subsequently oxidized the dye. Superoxide radicals formed by molecular oxygen were also found to play a significant role in the photocatalytic oxidation. The predominance of these two species in photocatalytic dye degradation using an Ag/AgCl-modified catalyst was also found by Xiong et al. [58].

3.3.2.6 Activity for phenol degradation

The photocatalytic activity for degradation of a colorless organic compound, phenol, was investigated to confirm that a surface plasmon resonance induced photocatalytic process took place using the Ag/AgCl-AC composite, and not merely a photosensitization of organic MO dye under visible light irradiation [59]. The results from the adsorption and subsequent photocatalysis, as well as calculated degradation kinetics are shown in Figure 3.17. The

composite exhibited good activity for phenol degradation, converting approximately 13 mg phenol per gram composite under illumination, where the photolytic conversion was found to be negligible. The photocatalysis-induced transformation was greater than phenol adsorption observed in the dark. The pseudo-first order rate constant was calculated using eq. (3.2b), and was found to be 0.0103 min^{-1}. These phenol photodegradation results confirmed that the Ag/AgCl-AC composites prepared possessed visible light activity.

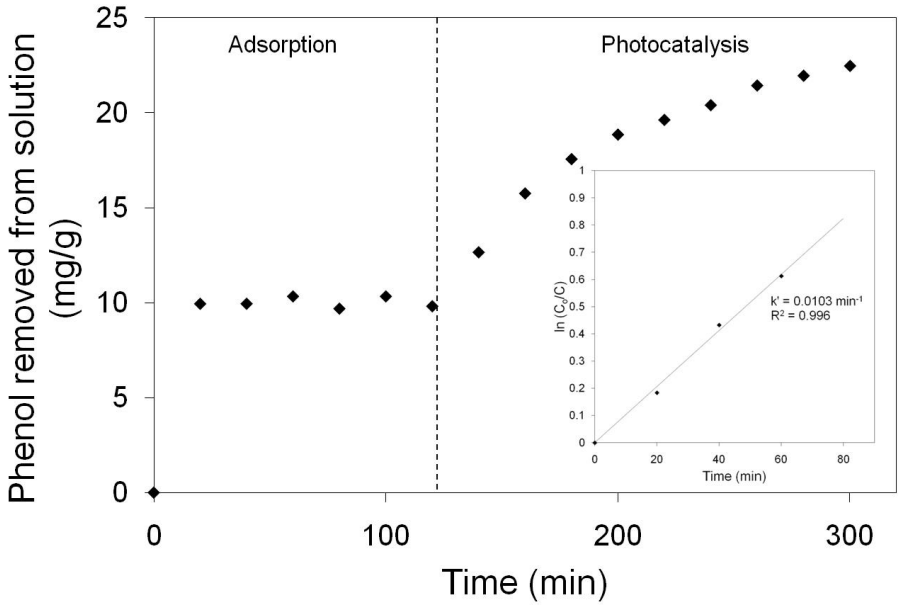

Figure 3.17: Adsorption and subsequent photocatalysis using 2.5:1 Ag/AgCl-AC in phenol. Photocatalytic degradation kinetics shown inset. (C_o = 13 mg L^{-1}, loading = 0.5 g L^{-1})

3.3.3 Mechanism

The mechanism of photocatalytic action of the Ag/AgCl-AC composites was thought to be related to the localized surface plasmon resonance of silver nanoparticles on the surface of the incorporated AgCl. In this system, visible light photons were absorbed by the silver nanoparticles, generating holes and electrons. These were effectively polarized by the surface plasmon resonance state of the silver, causing efficient separation of the holes and electrons such that the electrons were transferred to the silver surfaces furthest away from the interfaces with AgCl, and the holes transferred to the AgCl particle surfaces [45]. The stability of silver on silver halides was attributed to this charge separation, which prevented

the generated electrons from being transferred to Ag^+ ions in AgCl [60]. The electrons were instead transferred to molecular oxygen present at the surface, forming active species such as superoxide anions, which could facilitate the degradation of organic pollutants (MO, phenol) [61]. The positive holes generated could oxidize Cl^- ions into Cl^o, which were themselves powerful oxidizing agents that could attack organic pollutants near the surface of the catalyst [40] to reduce the Cl^o atoms back to their ionic state.

Activated carbon in the composites provided adsorption sites for the pollutant. The adsorbed pollutant could then migrate to Ag/AgCl decomposition centers located on the AC surface, due to the concentration gradients present [62]. In the absence of this highly adsorbent AC support, the pollutant had to collide with the photocatalyst and maintain efficient contact for the reaction to occur. If this contact was not maintained, the reactants or intermediates would be desorbed back into solution. The AC also played a role in allowing chain photocatalytic reactions to proceed more easily by retaining intermediate products on its surface through adsorption. Additionally, the AC surface had many more adsorption sites than neat Ag/AgCl, which reduced the likelihood of pollutant molecules colliding with the catalyst but not being adsorbed due to surface area limitations [63]. The process is shown schematically in Figure 3.18.

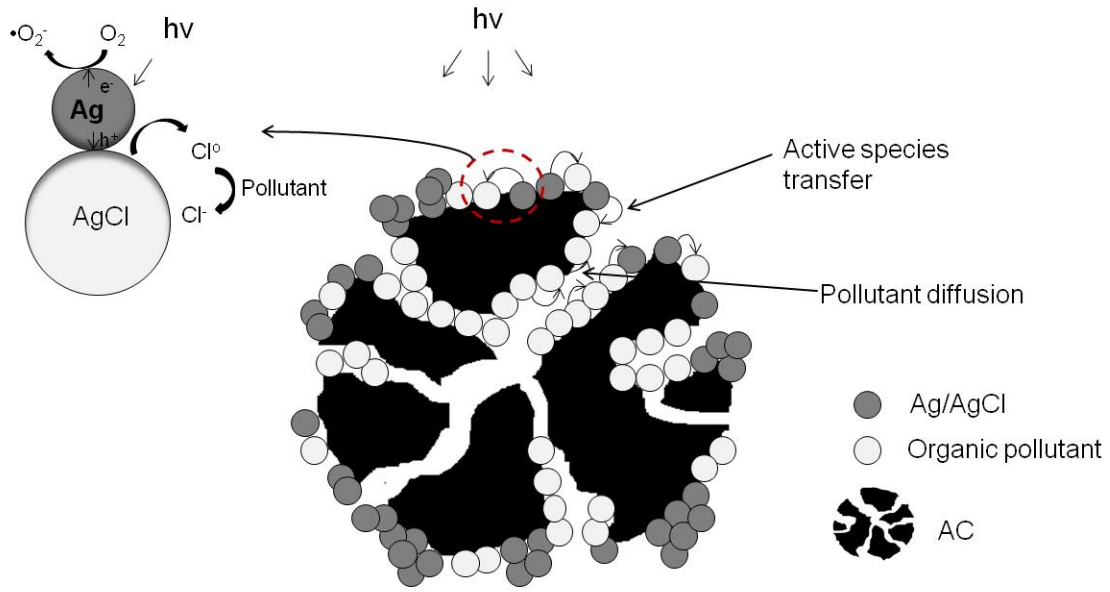

Figure 3.18: Mechanism of Ag/AgCl-AC photocatalysis on the degradation of an organic pollutant (adapted from [64])

3.4 Conclusions

In this work, novel composite photocatalysts based on Ag/AgCl and activated carbon were synthesized by an impregnation-precipitation-photoreduction method. The prepared composites possessed an "egg-shell" structure, although some pore-blocking of AC occurred due to the incorporated Ag/AgCl. The composites exhibited good photocatalytic activity for the degradation of MO and phenol under visible light. The role of the radical species was elucidated through quenching experiments, and holes and oxygen species were found to be dominant for photodegradation. Some decrease in activity was observed with cyclic use, so future work on this catalyst should include investigations in improving its recyclability, such as through prolonged light exposure to regenerate the activated carbon surface [62]. The effect of the activated carbon in the composite should also be studied, and parameters such as particle size, porosity, and pre-treatment investigated with respect to the structural and morphological characteristics of the resulting Ag/AgCl-AC. For example, it has been proposed that smaller particle sizes can facilitate AC regeneration, since desorbed pollutants

may have shorter diffusion paths to the photocatalytic active sites on the exterior surface of the composite [14]. The effect of light intensity on the composite should also be explored, and the material tested under real sun conditions, to validate its applicability to solar systems, such as for use in solar AC regeneration schemes [65]. Due to the high adsorption capacity observed towards aqueous organic MO dye, adsorptive characteristics of the composites should also be described according to appropriate mechanistic considerations.

3.5 Acknowledgments

This work was supported by the Natural Sciences and Engineering Research Council of Canada and the National Natural Science Foundation of China (Grant No. 50972037 and 51172063). The authors would like to acknowledge the Centre for Catalysis Research and Innovation and the Department of Earth Sciences (University of Ottawa), Qi Yueli and colleagues at the College of Chemical Engineering (Hebei United University), and Dr. Jianqun Wang (Carleton University) for help with sample characterizations.

3.6 References

[1] W.Y. Choi, A. Termin, M.R. Hoffmann, Role of metal-ion dopants in quantum-sized TiO_2 – correlation between photoreactivity and charge-carrier recombination dynamics, J. Phys. Chem. 98 (1994) 13669–13679.

[2] G. Zhao, H. Kozuka, T. Yoko, Sol-gel preparation and photoelectrochemical properties of TiO_2 films containing Au and Ag metal particles, Thin Solid Films 277 (1996) 147–154.

[3] C.M. Wang, A. Heller, H. Gerischer, Palladium catalysis of O_2 reduction by electrons accumulated on TiO_2 particles during photoassisted oxidation of organic compounds, J. Am. Chem. Soc. 114 (1992) 5230–5234.

[4] I.M. Arabatzis, T. Stergiopoulos, M.C. Bernard, D. Labou, S.G. Neophytides, P. Falaras, Silver-modified titanium dioxide thin films for efficient photodegradation of methyl orange, Appl. Catal., B. 42 (2003) 187–201.

[5] R. W. Fessenden, P.V. Kamat, Rate constants for charge injection from excited sensitizer into SnO_2, ZnO, and TiO_2 semiconductor nanocrystallites, J. Phys. Chem. 99 (1995) 12902–12906.

[6] J.M. Stipkala, F.N. Castellano, T.A. Heimer, C.A. Kelly, K.J.T. Livi, G.J. Meyer, Light-induced charge separation at sensitized sol-gel processed semiconductors, Chem. Mater. 99 (1997) 2341–2353.

[7] P. Wang, B. Huang, X. Zhang, X. Qin, H. Jin, Y. Dai, Z. Wang, J. Wei, J. Zhan, S. Wang,

J. Wang, M.-H. Whangbo, Highly efficient visible-light plasmonic photocatalyst Ag@AgBr, Chem. Eur. J. 15 (2009) 1821–1824.

[8] A. Pourahmad, S. Sohrabnezhad, E. Kashefian, AgBr/nano AlMCM-41 visible light photocatalyst for degradation of methylene blue dye, Spectrochim. Acta Part A. 77 (2010) 1108–1114.

[9] H. Slimen, A. Houas, J.P. Nogier, Elaboration of stable anatase TiO_2 through activated carbon addition with high photocatalytic activity under visible light, J. Photochem. Photobiol., A. 221 (2011) 13–21.

[10] J. Matos, J. Laine, J.M. Herrmann, Synergy effect in the photocatalytic degradation of phenol on a suspended mixture of titania and activated carbon, Appl. Catal., B. 18 (1998) 281–291.

[11] M. Zhu, P. Chen, M. Liu, Sunlight-driven plasmonic photocatalysts based on Ag/AgCl nanostructures synthesized *via* an oil-in-water medium: Enhanced catalytic performance by morphology selection, J. Mater. Chem. 21 (2011) 16413–16419.

[12] M. Zhu, P. Chen, M. Liu, Graphene oxide enwrapped Ag/AgX (X = Br, Cl) nanocomposite as a highly efficient visible-light plasmonic photocatalyst, ACS Nano 5 (2011) 4529–4536.

[13] H. Zhang, X. Fan, X. Quan, S. Chen, H. Yu, Graphene sheets grafted Ag@AgCl hybrid with enhanced plasmonic photocatalytic acitivty under visible light, Environ. Sci. Technol. 45 (2011) 5731–5736.

[14] T.-T. Lim, P.-S. Yap, M. Srinivasan, A.G. Fane, TiO_2/AC composites for synergistic adsorption-photocatalysis processes: Present challenges and further developments for water treatment and reclamation, Crit. Rev. Env. Sci. Technol. 41 (2011) 1173–1230.

[15] X. Wang, Y. Liu, Z. Hu, Y. Chen, W. Liu, G. Zhao, Degradation of methyl orange by composite photocatalysts nano-TiO_2 immobilized on activated carbons of different porosities, J. Hazard. Mater. 169 (2009) 1061–1067.

[16] S. Basha, D. Keane, A. Morrissey, K. Nolan, M. Oelgemöller, J. Tobin, Studies on the adsorption and kinetics of photodegradation of pharmaceutical compound, indomethacin using novel photocatalytic adsorbents (IPCAs), Ind. Eng. Chem. Res. 49 (2009) 11302–11309.

[17] W. Li, C. Liang, W. Zhou, J. Qiu, Z. Zhou, G. Sun, Q. Xin, Preparation and characterization of multiwalled carbon nanotube-supported platinum for cathode catalysts of direct methanol fuel cells, J. Phys. Chem. B 107 (2003) 6292–6299.

[18] D. Chen, S.H. Yoo, Q. Huang, G. Ali, S.O. Cho, Sonochemical synthesis of Ag/AgCl nanocubes and their efficient visible-light-driven photocatalytic performance, Chem. Eur. J. 18 (2012) 5192–5200.

[19] C. Hu, T. Peng, X. Hu, Y. Nie, X. Zhou, J. Qu, H. He, Plasmon-induced photodegradation of toxic pollutants with Ag-AgI/Al_2O_3 under visible-light irradiation, J. Am. Chem. Soc. 132 (2010) 857–862.

[20] J. Jiang, L. Zhang, Rapid microwave-assisted nonaqueous synthesis and growth mechanism of AgCl/Ag, and its daylight-driven plasmonic photocatalysis, Chem. Eur. J. 17 (2011) 3710–3717.

[21] P. Wang, B. Huang, Z. Lou, X. Zhang, X. Qin, Y. Dai, Z. Zheng, X. Wang, Synthesis of highly efficient Ag@AgCl plasmonic photocatalysts with various structures, Chem. Eur. J. 16 (2010) 538–544.

[22] M. Zayat, D. Einot, R. Reisfeld, Reversible photochromism of sol-gel SiO_2: AgCl films, J. Sol-Gel Sci. Technol. 10 (1997) 203–211.

[23] P. Gangopaghyay, R. Kesavamoorthy, S. Bera, P. Magudapathy, K.G.M. Nair, B.K. Panigrahi, S.V. Narasimnhan, Optical absorption and photoluminescence spectroscopy of the growth of silver nanoparticles, Phys. Rev. Lett. 94 (2005) 047403 (1)–047403 (4).

[24] J. Rouquérol, P. Llewellyn, F. Rouquérol, Is the BET equation applicable to microporous adsorbents?, Stu. Surf. Sci. Catal. 160 (2007) 49–56.

[25] K.S.W. Sing, D.H. Everett, R.A.W. Haul, L. Moscou, R.A. Pierotti, J. Rouquérol, T. Siemieniewska, Reporting physisorption data for gas/solid systems with special reference to the determination of surface area and porosity, Pure Appl. Chem. 57 (1985) 603–619.

[26] J. Rouquérol, D. Avnir, C.W. Fairbridge, D.H. Everett, J.H. Haynes, N. Pernicone, J.D.F. Ramsay, K.S.W. Sing, K.K. Unger, IUPAC Recommendations for the characterization of porous solids, Pure Appl. Chem. 66 (1994) 1739–1758.

[27] X. Zhang, L. Lei, Effect of preparation methods on the structure and catalytic performance of TiO_2/AC photocatalysts, J. Hazard. Mater. 153 (2008) 827–833.

[28] S. Glaus, G. Calzaferri, The band structures of the silver halides AgF, AgCl, and AgBr: A comparative study, Photochem. Photobiol. Sci. 2 (2003) 398–401.

[29] P. Jain, W. Huang, M. El-Sayed, On the universal scaling behaviour of the distance decay of plasmon coupling in metal nanoparticle pairs: A plasmon ruler equation, Nano Lett. 7 (2007) 2080–2088.

[30] J.-F. Guo, B. Ma, A. Yin, K. Fan, W.-L. Dai, Highly stable and efficient Ag/AgCl@TiO_2 photocatalyst: Preparation, characterization, and application in the treatment of aqueous hazardous pollutants, J. Hazard. Mater. 211–212 (2012) 77–82.

[31] R. Jiang, H.-Y. Zhu, G.-M. Zeng, L. Xiao, Y.-J. Guan, Synergy of adsorption and visible light photocatalysis to decolour methyl orange by activated carbon/nanosized CdS/chitosan composite, J. Cent. South Univ. Technol. 17 (2010) 1223–1229.

[32] Y. Tang, Z. Jiang, Q. Tay, J. Deng, Y. Lai, D. Gong, Z. Dong, Z. Chen, Visible-light plasmonic photocatalysts anchored on titanate nanotubes: A novel nanohybrid with synergistic effects of adsorption and degradation, RSC Adv. 2 (2012) 9406–9414.

[33] J. Matos, J. Laine, J.-M. Herrmann, D. Uzcategui, J.L. Brito, Influence of activated carbon upon titania on aqueous photocatalytic consecutive runs of phenol photodegradation, Appl. Catal., B 70 (2007) 461–469.

[34] A.Y. Khan, D.W. Mazyck. The effect of UV irradiation on adsorption by activated

carbon/TiO_2 composites, Carbon 44 (2006) 182–184.

[35] J.-M. Herrmann, Heterogeneous photocatalysis: fundamentals and applications to the removal of various types of aqueous pollutants, Catal. Today 53 (1999) 115–129.

[36] J. Matos, J. Laine, J.-M. Herrmann, Effect of the type of activated carbons on the photocatalytic degradation of aqueous organic pollutants by UV-irradiated titania, J. Catal. 200 (2001) 10–20.

[37] F. Akbal, Photocatalytic degradation of organic dyes in the presence of titanium dioxide under UV and solar light: Effect of operational parameters, Environ. Prog. 24 (2005) 317–322.

[38] V. Nam, J. Kim, G. Han, Photocatalytic oxidation of methyl orange in a three-phase fluidized bed reactor, Chemosphere 47 (2002) 1019–1024.

[39] N. Guettai, H. Ait Amar, Photocatalytic oxidation of methyl orange in presence of titanium dioxide in aqueous suspension. Part I: Parametric study, Desalination 185 (2005) 427–437.

[40] D. Wang, Y. Duan, Q. Luo, X. Li, L. Bao, Visible light photocatalytic activities of plasmonic Ag/AgBr particles synthesized by a double jet method, Desalination 270 (2011) 174–180.

[41] Y. Wang, Solar photocatalytic degradation of eight commercial dyes in TiO_2 suspension, Water Res. 34 (2000) 990–994.

[42] H. Lachheb, E. Puzenat, A. Houas, M. Ksibi, E. Elaloui, C. Guillard, J.M. Herrmann, Photocatalytic degradation of various types of dyes (Alizarin S, Crocein Orange G, Methyl Red, Congo Red, Methylene Blue) in water by UV-irradiated titania, Appl. Catal., B. 39 (2002) 75–90.

[43] W.Z. Tang, Z. Zhang, H. An, M.O. Quintana, D.F. Torres, TiO_2/UV photodegradation of azo dyes in aqueous solutions, Environ. Technol. 18 (1997) 1–12.

[44] E. Akama, A.J. Tong, M. Ito, S. Tanaka, The study of the partitioning mechanism of methyl orange in an aqueous two-phase system, Talanta 48 (1999) 1133–1137.

[45] P. Wang, B. Huang, X. Qin, X. Zhang, Y. Dai, J. Wei, M.-H. Whangbo, Ag@AgCl: A highly efficient and stable photocatalyst active under visible light, Angew. Chem. Int. Ed. 47 (2008) 7931–7933.

[46] I.K. Konstantinou, T.A. Albanis, TiO_2-assisted photocatalytic degradation of azo dyes in aqueous solution: Kinetic and mechanistic investigations: A Review, Appl. Catal., B. 49 (2004) 1–14.

[47] C. Guillard, H. Lachheb, A. Houas, M. Ksibi, E. Elaloui, J.M. Herrmann, Influence of chemical structure of dyes, of pH and of inorganic salts on their photocatalytic degradation by TiO_2 comparison for the efficiency of powder and supported TiO_2, J. Photochem. Photobiol., A. 158 (2003) 27–36.

[48] I. Poulios, I. Tsachpinis, Photodegradation of the textile dye Reactive Black 5 in the presence of semiconducting oxides, J. Chem. Technol. Biotechnol. 74 (1999) 349–357.

[49] V. Augugliaro, C. Baiocchi, A.B. Prevot, E. García-López, V. Loddo, S. Malato, G. Marcí, L. Palmisano, M. Pazzi, E. Pramauro, Azo-dyes photocatalytic degradation in aqueous suspension of TiO_2 under solar irradiation, Chemosphere 49 (2002) 1223–1230.

[50] A. Epling, C. Lin, Photoassisted bleaching of dyes utilizing TiO_2 and visible light, Chemosphere 46 (2002) 561–570.

[51] J. Araña, J.L. Martínez Nieto, J.A. Herrera Melián, J.M. Doña Rodríguez, O. Gondález Díaz, J. Pérez Peñam, O. Bergasa, C. Alvarez, J. Méndez, Photocatalytic degradation of formaldehyde containing wastewater from veterinarian laboratories, Chemosphere 55 (2004) 893–904.

[52] S.X. Liu, X.Y. Chen, X. Chen, A TiO_2/AC composite photocatalyst with high activity and easy separation prepared by a hydrothermal method, J. Hazard. Mater. 143 (2007) 257–263.

[53] Y.H. Ao, J.J. Xu, D.G. Fu, X.W. Shen, C.W. Yuan, Low temperature preparation of anatase TiO_2-coated activated carbon, Colloids Surf., A 312 (2008) 125–130.

[54] C.-C. Mao, H.-S. Went, Effect of heat treatment on photocatalytic activity of titania incorporated with carbon black for degradation of methyl orange, Environ. Prog. Sustainable Energy 31 (2011) 306–317.

[55] D. Wang, Y. Duan, Q. Luo, X. Li, J. An, L. Bao, L. Shi, Novel preparation method for a new visible light photocatalyst: mesoporous TiO_2 supported Ag/AgBr, J. Mater. Chem. 22 (2012) 4847–4854.

[56] G. Li, K.H. Wong, X. Zhang, C. Hu, J.C. Yu, R.C.Y. Chan, P.K. Wong, Degradation of acid orange 7 using magnetic AgBr under visible light: The roles of oxidizing species, Chemosphere 76 (2009) 1185–1191.

[57] S. Mukherjee, S. Kumar, A.K. Misra, M. Fan, Removal of phenols from water environment by activated carbon, bagasse ash and wood charcoal, Chem. Eng. J. (2007) 133–142.

[58] W. Xiong, Q. Zhao, X. Li, D. Zhang, One-step synthesis of flower-like Ag/AgCl/BiOCl composite with enhanced visible-light photocatalytic activity, Catal. Commun. 16 (2011) 229–233.

[59] T. Wu, G. Liu, J. Zhao, H. Hidaka, N. Serpone, Photoassisted degradation of dye pollutants vs. self-photosensitized oxidation transformation of *Rhodamine B* under visible light irradiation in aqueous TiO_2 suspensions, J. Phys. Chem. B 102, 30 (1998) 5845–5851.

[60] H. Xu, H. Li, J. Xia, S. Yin, Z. Luo, L. Liu, L. Xu, One-pot synthesis of visible-light driven plasmonic photocatalyst Ag/AgCl in ionic liquid, ACS Appl. Mater. Interfaces 3 (2011) 22–29.

[61] J. Yu, G. Dai, B. Huang, Fabrication and characterization of visible-light-driven plasmonic photocatalyst Ag/AgCl/TiO_2 nanotube arrays, J. Phys. Chem. C 113 (2009) 16394–16401.

[62] W. Li, S. Liu, Bifunctional activated carbon with dual photocatalysis and adsorption capabilities for efficient phenol removal, Adsorption 18 (2012) 67–74.

[63] R. Leary, A. Westwood, Carbonaceous nanomaterials for the enhancement of TiO_2 photocatalysis, Carbon 49 (2011) 741–772.

[64] K.Y. Foo, B.H. Hameed, Decontamination of textile wastewater via TiO_2/activated carbon composite materials, Adv. Colloid Interface Sci. 159 (2010) 130–143.

[65] P.-S. Yap, T.-T. Lim, Solar regeneration of powdered activated carbon impregnated with visible-light responsive photocatalyst: Factors affecting performances and predictive model, Water Res. 46 (2012) 3054–3064.

Chapter 4:
Adsorption and visible light degradation of methyl orange by Ag/AgCl-activated carbon composites

Joanne Gamage McEvoy, Wenquan Cui, Zisheng Zhang

Abstract

Adsorption and visible light induced photocatalytic degradation of methyl orange (MO) dye was investigated in a slurry system using plasmonic adsorbent photocatalysts, Ag/AgCl-activated carbon (AC) composites. The dark adsorption kinetics and isotherms were studied, and a nonlinear optimization strategy and defined error functions as goodness-of-fit criteria were used to assess appropriateness of various models to describe the experimental data. Using this approach, the adsorption kinetics were found to follow second order behaviour, and the isotherms obtained were Langmuirian. The intraparticle diffusion model was used to study the sorption mechanism, and it was found that internal diffusion was not the only limiting factor present. The enhancement of MO removal by Ag/AgCl-AC composites due to the incorporated photocatalyst was quantified under visible light irradiation, and the photocatalytic activity was found to follow Langmuir-Hinshelwood kinetics with adsorption constants of 0.523 and 0.039 L mg^{-1} and reaction constants of 0.0695 and 0.117 mg L^{-1} min^{-1} for adsorbent photocatalysts prepared at ratios of 2:5 and 3:1, respectively.

Keywords: adsorption, visible light photocatalysis, activated carbon, Ag/AgCl, adsorbent photocatalyst

4.1 Introduction

Since the discovery of the photocatalytic effect by Fujishima and Honda in 1972 [1], photocatalytic processes have been widely studied and characterized for potential applications in many fields, including: environmental remediation [2], water and wastewater treatment [3], antimicrobial applications [4], and self-cleaning systems [5]. An attractive feature of such processes is that they can utilize solar energy as a source of irradiation to effect the degradation of contaminants by photocatalysis-mediated redox reactions, increasing their sustainability and lowering operating costs. However, the photonic efficiencies realized with photocatalysis are still very low, impeding the commercial development of this process [6].

Contributing to these low efficiencies is the use of the traditional TiO_2 catalyst, which has a band gap corresponding to ultraviolet (UV) light not abundant in solar radiation. Efforts to improve the efficiency of solar photocatalysis have been undertaken through the design and fabrication of visible light active catalysts, such as those based on impurity doping [7], metals deposition [8], or sensitization [9, 10]. Highly efficient and stable visible light active photocatalysts based on metallic nanosilver on silver halides (Ag/AgCl, Ag/AgBr) have been reported in literature [11–13], where the enhanced visible light absorption is based on the surface plasmon resonance (SPR) effect of the incorporated metallic silver nanostructures. The host silver halides help facilitate charge separation, and can also produce halide oxidizing species, which contribute to degradation.

Another difficulty in photocatalysis lies in the use, separation, and recovery of nano-sized TiO_2 [14]. To address concerns related to the nano-sized photocatalyst, the incorporation of activated carbon as a catalyst support, or as a composite with TiO_2 has been proposed and investigated [15]. These composite materials have also been found to exhibit a synergistic increase in photocatalytic activity compared to pure TiO_2 [15–17], attributable to the presence of a common contact interface between solids, where the pollutants can be adsorbed by AC, and migrate continuously to the supported photocatalyst [18].

In our previous research, novel Ag/AgCl-AC composites were synthesized and characterized. These hybrid composites combined the SPR-induced visible light enhancement and adsorption synergy strategies for photocatalysis efficiency improvement. In order to further characterize such bifunctional materials for future optimization and scale-up, the adsorptive and photocatalytic behaviours must also be appropriately described [19]. Accordingly, in this study, adsorption and photocatalysis using the prepared composites is further explored, and the appropriateness of various kinetic and equilibrium models for description of these processes is systematically investigated.

4.2 Experimental

4.2.1 Synthesis of Ag/AgCl-AC composites

Ag/AgCl-AC composites were prepared using an impregnation-precipitation-photoreduction method. Typically, 1 g of unmodified Darco G60 activated carbon (100 mesh, Sigma-Aldrich) was impregnated in 20 mL of aqueous $AgNO_3$ (ACS grade, MP Biomedicals) of a certain concentration. The mixture was sonicated for 10 minutes, and then stirred magnetically for 6 hours. 20 mL of HCl (reagent-grade, Fisher Scientific) was then added in a 50% stoichiometric excess under magnetic stirring for 2 hours to induce the precipitation of deposited $AgNO_3$ into AgCl. The reduction of some AgCl was carried out via irradiation by a 300 W UV-Vis light source (Ushio ELH) for 1 hour, and the mixture was then filtered and dried in air overnight. The prepared Ag/AgCl-AC composite powders were gently ground in an agate mortar before use. The samples are denoted by weight ratio of Ag to AC (Ag: AC), calculated as if all of the AgCl was reduced to Ag.

4.2.2 Characterization

X-ray diffraction (XRD) patterns of all prepared powders were collected using a Rigaku Ultima IV XRD apparatus with a Cu K(α) source ($\lambda = 0.15418$ nm) operating at 40 kV and 44 mA. The surface areas were obtained from N_2 sorption isotherms collected at 77 K using an automatic adsorption apparatus (Nova 4200E, Quantachrome). The samples were outgassed at 50^oC under N_2 flow for 1 hour at a pressure of 760 – 770 mm Hg. The Brunauer, Emmett, and Teller (BET) surface areas of the samples were calculated using the adsorption isotherms in the range of $P/Po < 0.015$. This range was chosen based on a criterion proposed

by Rouquérol et al. [20] for materials containing microporosity.

4.2.3 Adsorption batch experiments

Adsorption equilibrium studies were conducted using 500 mL Erlenmeyer flasks in the dark at ambient temperature (22^{o}C). The initial concentration of methyl orange (MO) was varied between 13 and 108 mg L^{-1} at the natural pH of the solutions, and a catalyst loading of 0.5 g L^{-1} in 200 mL MO was used. The solutions were kept under magnetic stirring at 180 rpm for approximately 4 hours, or until the concentration did not decrease further over a period of 1 hour. 1 mL aliquots of the samples were withdrawn periodically, and were centrifuged at 12 000 rpm for 3 minutes in an accuSpin Micro 17 (Fisher Scientific) microcentrifuge. The peak absorbance of the supernatant (at λ = 463) was then measured using a Genysys 10-UV spectrophotometer (ThermoScientific.). This absorbance was correlated to concentration using the Beer-Lambert Law and a prepared standard curve.

4.2.4 Photocatalytic degradation experiments

To quantify the photocatalytic degradation of MO using the composite powders, a slurry reactor was used in a constructed reflective housing to prevent outside light from entering the system. Illumination was provided by a 300 W ELH tungsten halide bulb (Ushio) with a UV filter (Kenko Zeta, λ > 410 nm, transmittance > 90%) at a distance of 10 cm from the beaker. The irradiation was measured using a quantum meter (Biospherical QSL-2100; 400 nm < λ < 700 nm), and was found to be approximately $4.7x10^{-3}$ Einstein m^{-2} s^{-1}. Cooling was provided by an external cooling jacket, and the temperature of the reaction was controlled to 20^{o}C ± 2. For the combined adsorption-photocatalysis tests, 0.5 g L^{-1} catalyst was added to a 200 mL solution containing reagent-grade MO (Fisher Scientific) and immediately exposed to illumination under constant magnetic stirring at 180 rpm for 2 hours. The adsorption kinetic tests were performed using the same procedure in the absence of light. For the prolonged photocatalysis and recyclability tests, 200 mL of MO solution was allowed to equilibriate in the dark with 0.5 g L^{-1} of catalyst under constant magnetic stirring at 180 rpm for 2 hours prior to each experiment. The photocatalytic degradation was then studied for 2.5 hours in the presence of visible light irradiation. For all tests, samples were withdrawn every 10 minutes and centrifuged, and the supernatant analyzed using a spectrophometer. The initial concentration was kept at 25 mg L^{-1}, and the initial pH of the solution was left unadjusted.

Control runs were performed in the absence of light and catalyst, respectively.

4.2.5 Analysis

The sorption capacity, q_t (mg MO g composite^{-1}) of the composite powders was determined from equation (4.1):

$$q_t = V(C_o - C_t)/W \qquad (4.1)$$

where the initial MO concentration in the aqueous phase, and that at time t (min) are denoted by C_o and C_t, respectively (mg L^{-1}), V is the volume of MO solution (L), and W is the mass of composite used (g). For the equilibrium sorption capacity, q_e, (mg g^{-1}), the difference was taken between the initial concentration and the equilibrium concentration (C_e).

Parameters associated to various adsorption and photodegradation models were estimated using nonlinear optimization by assessment of an error function evaluating the goodness-of-fit of the model to the experimental data. The optimization procedure involved minimization of this error function, and was performed using the Solver add-in in Microsoft Excel. Nonlinear optimization using error function minimization has been suggested to be advantageous over traditional assessments of sorption model parameters and their respective goodness-of-fit criterion (R^2) based on linear regression because the linearizing transformations used to estimate the sorption isotherms implicitly alters their error structure, violating the error variance and normality assumptions of standard least squares analysis [21, 22].

In the current analysis, the sum of square errors (SSE) was used for the optimization procedure, where:

$$\mathrm{SSE} = \Sigma\,(q_{,\,calc} - q_{,exp})_i^{\,2} \qquad (4.2)$$

Where the subscript “calc” and “exp” denote the calculated and experimental values, respectively, and the sum is taken over the entire range of data. The standard error (SE) is defined by:

$$\mathrm{SE} = \sqrt{(1/m-p)}\;\Sigma\,(q_{,\,calc} - q_{,exp})_i^{\,2} \qquad (4.3)$$

Where m is the number of observations in the experimental data set and p is the number of parameters in the regression model. The coefficient of determination for the model was calculated using equations (4.4) and (4.5), where:

$$R^2 = 1 - SSE/SST \quad (4.4)$$

$$SST = \Sigma (q_{i,\,calc} - q_{avg,calc})^2 \quad (4.5)$$

And the total sum of squares (SST) is the sum of the square difference between each model-fitted value and the predicted sample mean. The SE and coefficient of determination (R^2) of the models were used in addition to the SSE to gauge the goodness-of-fit. Smaller SSE and SE values, and regression coefficients approaching 1 indicated better fit of the model to the experimental data.

4.3 Results and discussion

4.3.1 Catalyst characterization

The prepared catalysts were characterized by XRD to determine their phase structure and crystallinity. The patterns obtained are shown in Figures 4.1a and 4.1b, respectively, with those of pure Ag/AgCl and unmodified AC given for comparison. AC exhibited a mainly amorphous structure, however a wide, shallow hexagonal (002) graphitic peak was observed due to the small regions of crystallinity present [23]. All of the prepared composites exhibited similarity in phase and crystallinity to the pure Ag/AgCl pattern. The patterns were indexed to face centered cubic AgCl (JCPDS card #31-1238). From the enlarged patterns shown in Figure 4.1b for the prepared Ag/AgCl and a representative composite (2.5:1), the main diffraction peaks for (111) and (200) planes of metallic silver were observable at angles of 38.1^o and 44.3^o for the pure synthesized Ag/AgCl, corresponding to the major reflections for metallic silver according to JCPDS card #01-087-0597. This indicated that the *in situ* reduction could successfully reduce some AgCl to Ag, and confirmed the presence of metallic silver in Ag/AgCl. However, the peaks were not observed for the composite, which may have been due to the low content, small particle sizes, and high dispersion of metallic silver on the Ag/AgCl-AC surface [24].

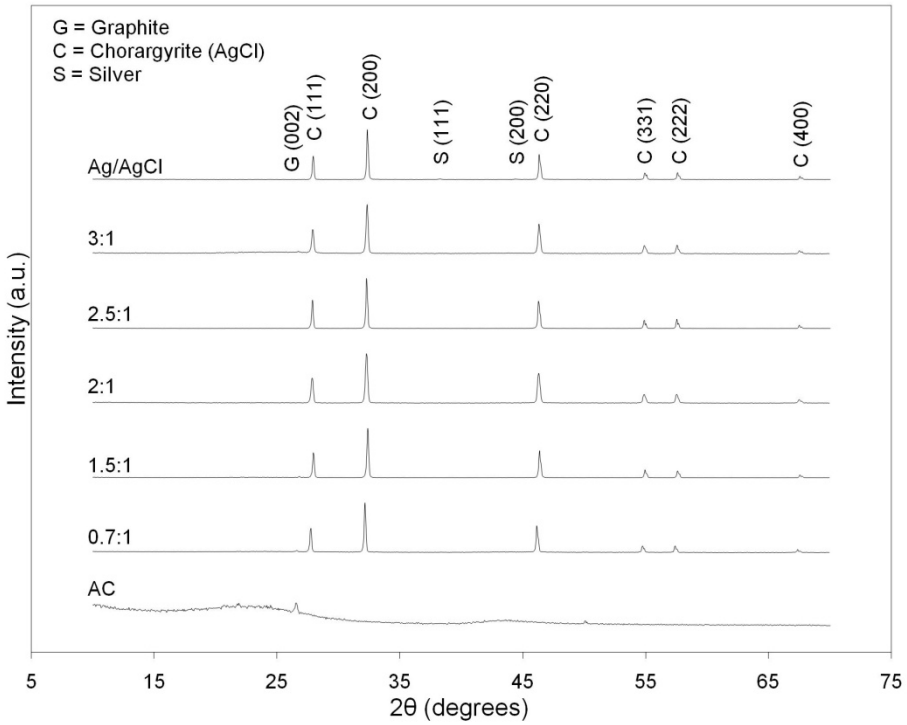

Figure 4.1a: XRD patterns for AC, Ag/AgCl, and Ag/AgCl-AC composites prepared at various photocatalyst: adsorbent ratios

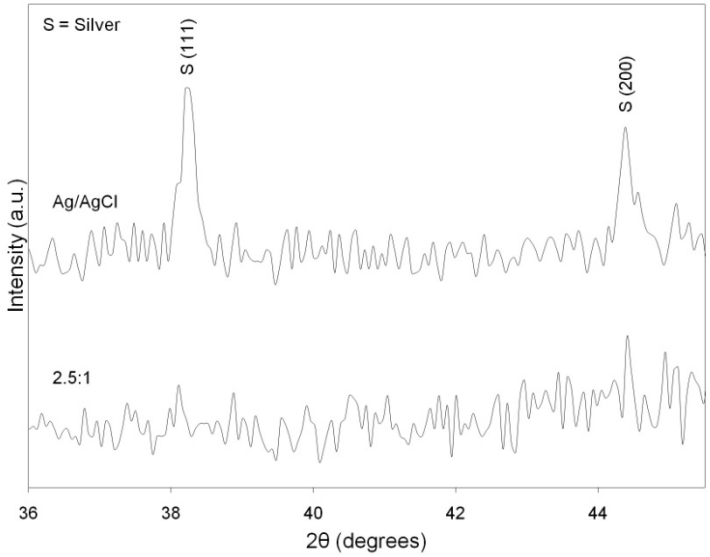

Figure 4.1b: Enlarged XRD patterns for Ag/AgCl, and 2.5:1 Ag/AgCl-AC composite

The surface areas of the prepared composites were calculated using a multi-point Brunauer, Emmett, and Teller (BET) estimation, and are given in Table 4.1, respectively, with calculated surface areas for AC and pure Ag/AgCl shown for reference. The surface areas of the composites were found to consistently decrease with increasing Ag/AgCl content, but were all larger than that of pure Ag/AgCl. This decrease in surface area was thought to be attributable to pore-blocking by deposited Ag/AgCl, forming "egg-shell" composites, where the photocatalyst was restricted to the outer surface of the AC adsorbent [25].

Table 4.1: Surface areas of prepared Ag/AgCl-AC composites and reference materials

Catalyst	**BET surface area (m^2/g)**	**Relative surface area (%)**
AC	810.9	100
0.7:1 composite	279.3	34
1.5:1 composite	149.2	18
2:1 composite	105.5	13
2.5:1 composite	77.1	9.5
3:1 composite	63.0	7.8
Ag/AgCl	2.1	2.6

4.3.2 Adsorption studies

4.3.2.1 Adsorption kinetics

Adsorption kinetics are important for the description of solute uptake rate and for understanding dynamic sorption behaviour of the system, and are strongly dependent on adsorbate-adsorbent interactions [26]. In this study, the pseudo-first and pseudo-second order adsorption models were compared for the description of experimentally observed adsorption kinetics, as shown in Figure 4.2. Both of these models use a lumped analysis, where the adsorption steps such as external diffusion, internal diffusion, and adsorptive uptake were described as an overall adsorption rate [27–30].

The pseudo-first order model, introduced by Lagergren in 1898 for liquid/solid systems [27], is given by:

$$dq_t/dt = k_1(q_e - q_t) \qquad (4.6)$$

Where q_e is the equilibrium sorption capacity (mg g^{-1}), k_1 is the pseudo-first order sorption

rate constant (min^{-1}), and q_t denotes the amount sorbed at contact time t (mg g^{-1}). When q_t = 0 at t = 0, the pseudo-first order model may be integrated from t = 0 to t to yield eq. (4.7).

$$q_t = q_e[1-exp(-k_1 t)] \quad (4.7)$$

The pseudo-second order kinetic model, proposed by McKay and Ho [28] is given as follows, where dynamic adsorption is described by:

$$dq_t/dt = k_2(q_e-q_t)^2 \quad (4.8)$$

Where k_2 is the pseudo-second order rate constant (g mg^{-1} min^{-1}). The pseudo-second order rate equation can also be integrated when q_t = 0 at t = 0 to yield:

$$q_t = k_2 q_e^2 t / (1+k_2 q_e t) \quad (4.9)$$

The initial adsorption rate can be defined based on the pseudo-second order equation:

$$h = k_2 q_e^2 \quad (4.10)$$

Where h is the initial uptake rate (mg g^{-1} min^{-1}). The kinetic parameters for the pseudo-first and pseudo-second order models estimated using nonlinear regression are shown for each of the prepared catalysts with their respective goodness-of-fit criteria and calculated errors in Table 4.2. A comparison of the experimental data and the model-predicted values is given in Figure 4.2.

Table 4.2: Kinetic parameters for MO adsorption onto various Ag/AgCl-AC composites

	Composite				
Models	**0.7:1**	**1.5:1**	**2:1**	**2.5:1**	**3:1**
Experimental sorption capacity/ mg g^{-1}	50.73	50.34	46.89	38.17	29.6
Pseudo-first order					
k_1 /min^{-1}	0.27	0.16	0.10	0.085	0.079
q_e /mg g^{-1}	50.39	49.28	44.83	36.06	27.56
R^2	0.999	0.996	0.980	0.970	0.961
SE	0.431	1.13	1.89	1.87	1.64
SSE	0.744	8.99	39.3	38.3	29.6
Pseudo-second order					
q_e /mg g^{-1}	52.83	52.42	48.60	39.71	30.62
k_2 /g min^{-1} mg^{-1}	0.016	0.0062	0.0035	0.0033	0.0039
h / mg g^{-1} min^{-1}	44.85	17.00	8.30	5.27	3.65
R^2	0.999	0.999	0.998	0.996	0.991
SE	0.146	0.115	0.540	0.734	0.768
SSE	0.08528	0.0932	3.20	5.97	6.50

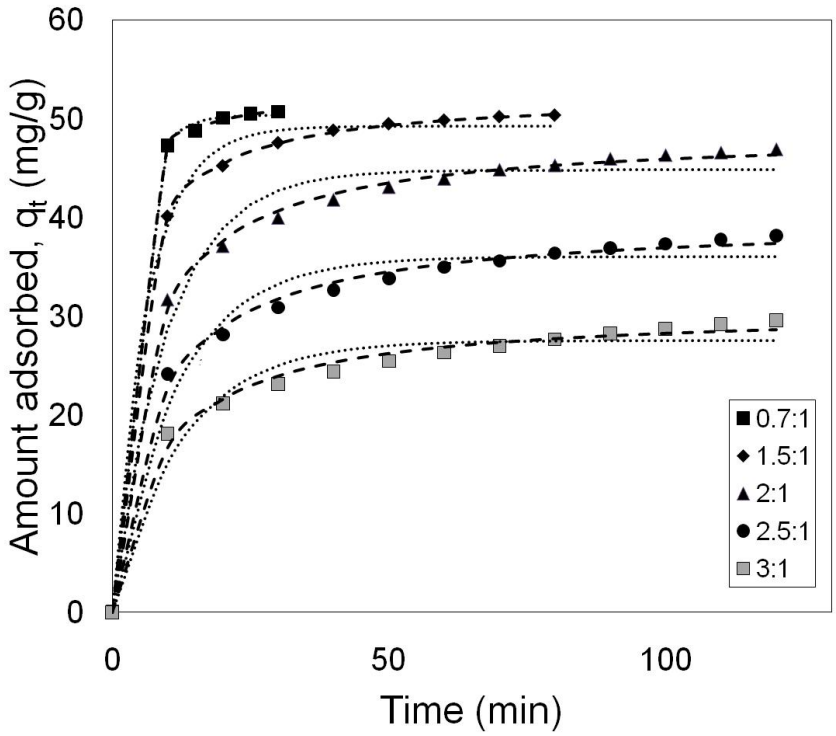

Figure 4.2: MO adsorption kinetics: Comparison of experimental data with model-predicted values, where dotted and dashed lines represent first and second order models, respectively. (C_o = 25 mg L^{-1}, composite loading = 0.5 g L^{-1})

As seen in Figure 4.2, the data correlated well with the second order modeled values, and the SE and SSE goodness-of-fit criteria were much lower than those calculated for the first order model. The R^2 values were also in good agreement with the SE and SSE criteria, confirming that the second order model adequately described the observed behaviour. Appropriateness of this model implied that the dynamic adsorption process occurred upon interaction of the MO adsorbate and two adsorption sites in the composite. The kinetics of adsorption for other composite adsorbent photocatalysts have also been shown in literature to follow second order behaviour [31].

The calculated values of the equilibrium sorption capacities (52.83 – 30.62 mg g^{-1} for 0.7:1 to 3:1 composites, respectively) were slightly higher than the experimentally observed values (50.73 – 29.60 mg g^{-1} for 0.7:1 to 3:1 composites, respectively). The equilibrium sorption capacity was found to generally decrease with increasing Ag/AgCl content, which was thought to be due to the effects of pore-blocking and agglomeration decreasing the available surface area for adsorption at higher Ag/AgCl loadings. There was a rapid decrease in sorption capacity observed upon increasing the catalyst loading past 2:1, which may have been due to increased agglomeration and formation of particle aggregates at loadings past this value. The sorption rate constant generally decreased with increasing Ag/AgCl content between 0.7:1 and 2:1 composites, but beyond this, there was negligible change (considering the increased error at higher concentrations). The initial uptake rate also generally decreased with increasing Ag/AgCl content due to the decreased available surface area.

4.3.2.2 Adsorption mechanism

The sorption rate may be controlled by factors such as: solute diffusion from solution to the film surrounding the particle, solute diffusion from the film to the particle surface (external diffusion), diffusion from the surface to the internal sites (intraparticle or pore diffusion), or uptake by the sorbent [32]. This uptake can involve mechanisms such as physico-chemical sorption, ion exchange, precipitation, or complexation [33, 34]. The Weber-Morris intraparticle diffusion model can be used to identify the adsorption mechanism, where the following relationship describes the effect of intraparticle diffusion resistance on adsorption [35]:

$$q_t = k_{id}\, t^{1/2} + \varphi \qquad (4.11)$$

Where k_{id} is the intraparticle diffusion rate constant (mg g^{-1} $min^{-0.5}$) and φ (mg g^{-1}) is a parameter indicative of the boundary layer thickness. According to the Weber-Morris intraparticle diffusion model, a plot of q_t with $t^{0.5}$ is linear if intraparticle diffusion plays a role in the adsorption process. Additionally, if the plot passes through the origin, this intraparticle diffusion can be considered to be the only rate-limiting step present.

The calculated intraparticle diffusion parameters are given in Table 4.3 with their respective errors, and intraparticle diffusion plots are shown in Figure 4.3.

Table 4.3: Intraparticle diffusion model parameters for dynamic adsorption on various Ag/AgCl-AC composites

	Composite				
	0.7:1	**1.5:1**	**2:1**	**2.5:1**	**3:1**
Intraparticle diffusion parameter					
k_i / mg g^{-1} $min^{-0.5}$	2.13	1.64	1.70	1.70	1.33
Φ / mg g^{-1}	40.6	38.2	30.5	21.4	15.7
R^2	1	0.960	0.946	0.971	0.981
SE	0.00476	0.449	0.666	0.544	0.411
SSE	2.3E-06	0.404	2.66	1.776	1.519

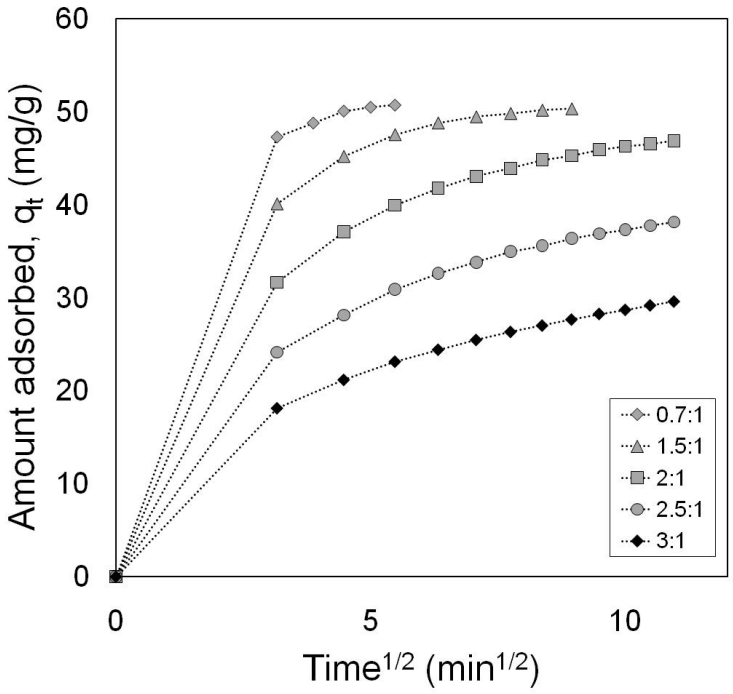

Figure 4.3: Intraparticle diffusion plots for Ag/AgCl-AC composite (C_o = 25 mg L^{-1}, loading = 0.5 g L^{-1})

The kinetic data obtained all exhibited similar features of a steeper region with increased sorption initially, followed by a secondary linear region describing the intraparticle diffusion, followed by a third region as equilibrium was reached. The presence of multilinearity in the intraparticle diffusion plots was indicative that two or more steps governed the adsorption process [36, 37]. The initial steeper portion was attributable to bulk and surface of film diffusion (boundary layer diffusion), while the second linear section was indicative of a gradual adsorption stage where the intraparticle or pore diffusion was involved, and the third stage was representative of equilibrium. Since extrapolation of the second linear region also did not pass through the origin, other mechanisms such as simultaneous boundary layer diffusion, complexation or ion-exchange were thought to also control the rate of adsorption during this stage [38, 39].

The intraparticle diffusion rate constants were calculated from the slope of the second linear portion and ranged from 2.13 – 1.33 mg g^{-1} $min^{-0.5}$ for the 0.7:1 to 3:1 composites,

respectively. The calculated k_i values were found to generally decrease with increasing Ag/AgCl content. This was thought to be indicative of changes to internal diffusion rate related to changes in surface chemistry at different loadings [29, 30], or more likely, from lower accessibility to micropores due to pore-blocking and surface coverage of AC by Ag/AgCl at higher loadings. The intercept values (φ) were also calculated, and ranged from 40.6 – 15.7 mg g^{-1} for 0.7:1 to 3:1 composites, respectively. These intercepts were reflective of the boundary layer thicknesses, with larger values indicating a greater role of bulk or external diffusion as the rate-limiting step [40, 41]. The calculated boundary layer parameters were found to decrease with increasing photocatalyst loading, and external diffusion was thought to become less limiting as the photocatalyst content of the composites increased, since there was less external surface area available due to increased surface coverage of the AC structure with Ag/AgCl agglomerates.

4.3.2.3 Adsorption equilibrium

Adsorption equilibrium describes the ratio between the adsorbed pollutant and that remaining in solution when the adsorbate-containing phase has been sufficiently contacted with the adsorbent and the bulk solution adsorbate concentration reaches a dynamic balance with the interface concentration [42, 43]. Adsorption isotherms may be used to describe equilibrium behaviour, but can also be used to elucidate the sorption mechanism, surface properties, and sorbent affinity by interpretation of the equation parameters and underlying thermodynamic assumptions of the adsorption models [21]. The most widely used models are the Langmuir [44] and Freundlich isotherms [45].

The Langmuir equation is given by:

$$\text{Langmuir: } q_e = K_L q_m C_e/(1+K_L C_e) \qquad (4.12)$$

Where q_m is the theoretical monolayer capacity (mg g^{-1}), K_L is the sorption equilibrium constant, which is related to the energy of adsorption (L mg^{-1}), and C_e is the equilibrium concentration in solution (mg L^{-1}). The Langmuir model assumes monolayer adsorption, with adsorption occurring only at a fixed number of homogeneous sites.

The Freundlich equation can be described by:

$$\text{Freundlich: } q_e = K_F C_e^{1/n} \qquad (4.13)$$

Where K_F and n are constants that describe the adsorption capacity (mg g^{-1}) and intensity (or heterogeneity), respectively. The Freundlich empirical model describes non-ideal and reversible adsorption, and is not restricted to monolayer adsorption. It can be applied to multilayer adsorption, where the non-uniform distribution of adsorption heat and affinity is accounted for in the model over a heterogeneous surface [46]. The Freundlich isotherm is criticized for lacking a fundamental thermodynamic basis, because it does not approach Henry's law at low concentrations [47].

The Redlich-Peterson (R-P) isotherm is a three-parameter hybrid isotherm that combines features of the Langmuir and Freundlich isotherm into an empirical equation [48]:

$$\text{Redlich-Peterson: } q_e = K_s C_e / (1 + a_s C_e^{\beta}) \qquad (4.14)$$

Where K_S is the R-P adsorption capacity (mg g^{-1}), a_s is the R-P equilibrium constant (L mg^{-1}), and β is an exponent describing the surface heterogeneity, which lies between 0 and 1. In the limit when β = 1, the R-P equation reduces to the Langmuir equation, while in the limit when β = 0, the Freundlich equation results. The Redlich-Peterson model has been studied in addition to Langmuir and Freundlich isotherms for the adsorption of aqueous dyes onto activated carbons [48].

The Langmuir, Freundlich, and Redlich-Peterson isotherms were fitted to equilibrium data for various composites using the nonlinear optimization procedure described. The isotherm parameters and their respective errors are given in Table 4.4. The experimental and modeled data for a representative composite is compared to that for AC in Figure 4.4, and the isotherms for various compositions of Ag/AgCl-AC are shown in Figure 4.5.

Table 4.4: Adsorption isotherm parameters for MO adsorption equilibrium onto Ag/AgCl-AC

	Adsorbent/Composite					
Models	**AC**	**0.7:1**	**1.5:1**	**2:1**	**2.5:1**	**3:1**
Langmuir						
q_m/mg g^{-1}	219.81	121.52	68.75	60.91	55.42	42.01
K_L /L mg^{-1}	0.986	4.58	3.39	4.79	4.28	3.68
R^2	0.989	0.992	0.897	0.870	0.984	0.889
SE	6.75	2.84	5.20	3.48	1.66	3.43
SSE	182	32.4	108	48.5	11.0	47.1
Freundlich						
K_F /L mg^{-1}	106.8	80.70	46.72	46.25	39.44	28.47
N	3.29	6.99	7.51	11.0	9.57	7.20
R^2	0.794	0.979	0.724	0.857	0.751	0.754
SE	26.4	4.47	7.91	3.63	5.75	4.60
SSE	2780.6	79.87	251	52.7	132	84.7
Redlich-Peterson						
K_S /L mg^{-1}	216.7	581.9	257.7	247.1	262.1	199.1
a_s/ L mg^{-1}	0.986	4.92	3.94	4.02	4.93	5.36
β	1.00	0.989	0.982	1.00	0.987	0.953
R^2	0.989	0.992	0.899	0.884	0.987	0.910
SE	7.79	2.77	5.92	4.02	1.75	3.55
SSE	182	30.8	105	46	9.15	37.7

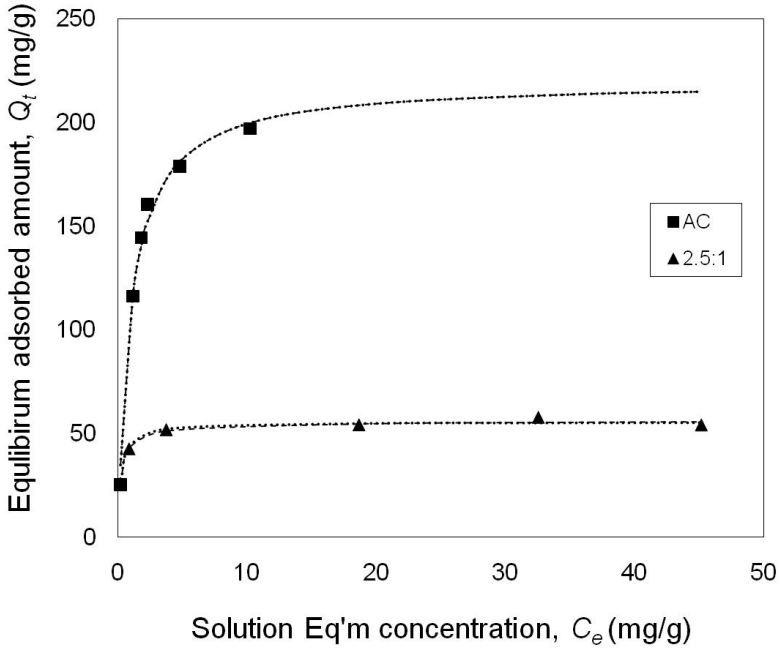

Figure 4.4: MO adsorption isotherms for Darco G60 AC and 2.5:1 Ag/AgCl composite, where dotted and dashed lines represent Langmuir and Redlich-Peterson modeled isotherms, respectively. (loading = 0.5 g L^{-1})

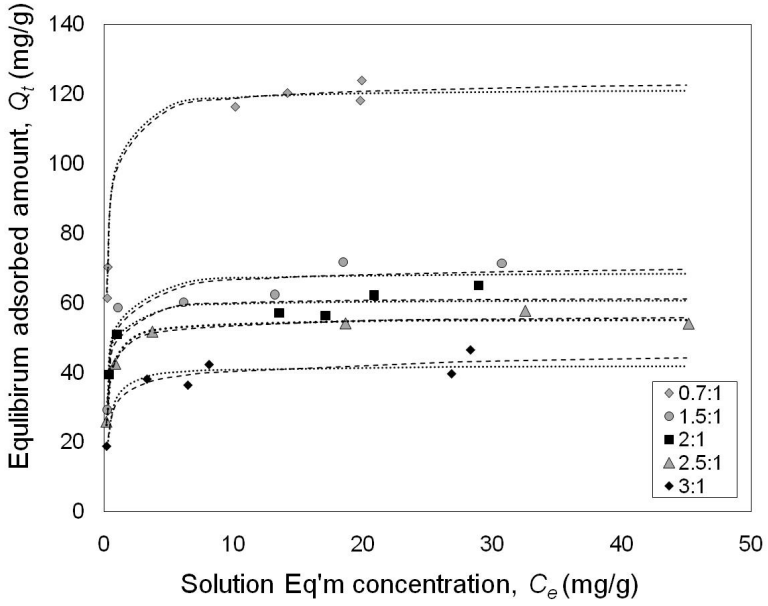

Figure 4.5: MO adsorption isotherms for Ag/AgCl-AC composites of various composition, where dotted and dashed lines represent Langmuir and Redlich-Peterson modeled isotherms, respectively. (loading = 0.5 g L^{-1})

The Langmuir model was found to exhibit appropriate fit to the isotherm data, since the SE and SSE values were generally lower than those of the Freundlich model, and the R^2 values ranged from 0.87 – 0.99. From the Langmuir model parameters, the monolayer capacity was found to decrease with increasing Ag/AgCl amount, which was consistent with the expected results due to the effects of pore-blocking and surface coverage by Ag/AgCl. The sorption equilibrium constants calculated for the composite powders were greater than that found for pure activated carbon, indicating that the adsorption energy for the composites was higher than that for pure AC.

Based on the calculated Langmuir constant and initial adsorbate concentration, a dimensionless separation factor, R_L, can be defined [49]:

$$\text{Separation factor: } R_L = 1/(1+K_L C_o) \qquad (4.15)$$

Where the value of R_L is related to the nature of adsorption, with $R_L > 1$ indicating unfavourable adsorption, $R_L = 1$ indicating linear adsorption, $0 < R_L < 1$ indicating favourable adsorption, and $R_L = 0$ indicating irreversible adsorption. The calculated values of R_L calculated were found to vary between 0.0088 and 0.070 for pure AC, and between 0.0027 and 0.028 for all of the composites, indicating that adsorption was favourable in all cases. This also indicated that the prepared Ag/AgCl-AC was an appropriate adsorbent of methyl orange. The adsorption was more favourable at higher concentrations, since the calculated R_L values decreased with increasing initial solution concentrations.

The Redlich-Peterson model also fit the data well, with marginally different values of SE and SSE compared to the Langmuir model, and regression coefficients of 0.884 or greater. The Redlich-Peterson surface heterogeneity term was found to be close to one (ranging from 0.953 - 1.00). In the R-P model, a greater deviation of this value from unity was indicative of a highly heterogeneous system [50]. The near-unity values obtained using the R-P model further indicated good agreement of the data with Langmuir-type behaviour. The adsorption was therefore interpreted as monolayer coverage of a homogeneous surface (in terms of surface bonding energy and functional groups).

4.3.3 Photocatalysis studies

4.3.3.1 Preliminary screening of photocatalytic activity

Preliminary tests on the photocatalytic activity of the prepared composites were carried out using a combined adsorption-photocatalysis process and comparing the MO removal observed to that attained using dark adsorption only. The results of these screening trials are given in Figure 4.6.

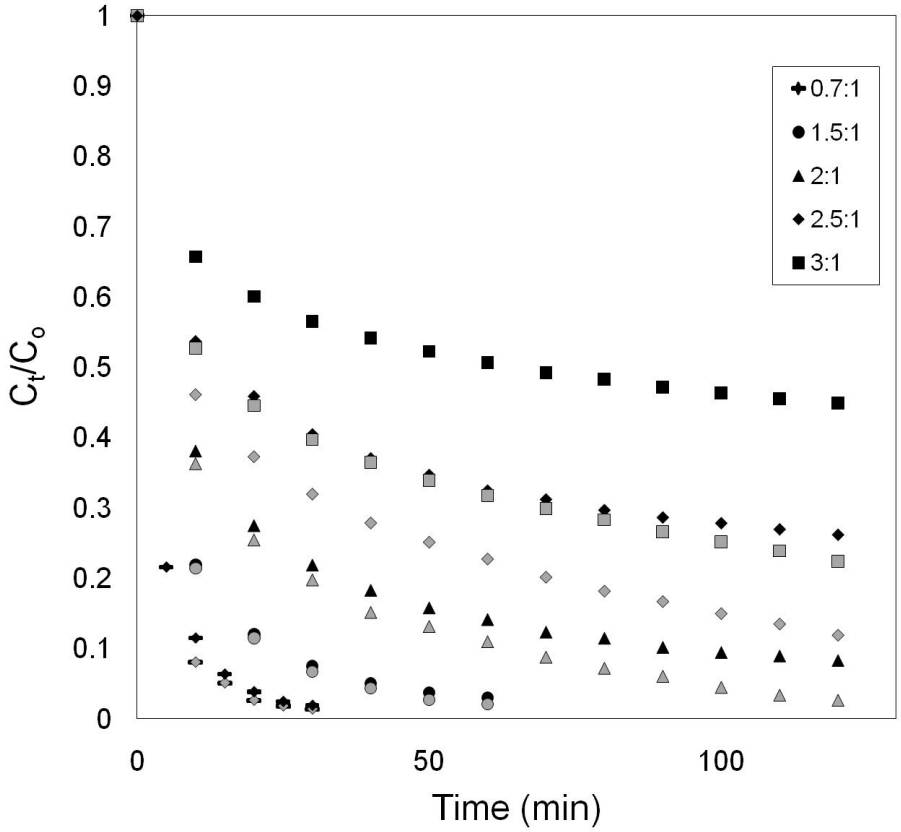

Figure 4.6: Comparison of adsorptive and combined adsorptive-photocatalytic MO removal for Ag/AgCl-AC composite powders, where black and grey markers represent adsorption and combined photocatalysis-adsorption, respectively. (C_o = 25 mg L^{-1}, composite loading = 0.5 g L^{-1}) – *average of three trials shown*

Preliminary runs were also performed using pure Ag/AgCl in the dark and under irradiation, respectively. The catalyst showed negligible adsorption towards MO in the dark, and was able to degrade 15.1% when irradiated for 2 hours. Tests conducted using Darco G60 AC only indicated a complete removal of the MO from solution in under 10 minutes, and

negligible enhancement of adsorption under irradiation. From the results obtained, the composite powders containing a high loading of Ag/AgCl (2:1, 2.5:1, 3:1 compositions) showed considerable enhancement in the removal of MO from solution for the combined photocatalysis-adsorption process over the dark adsorption alone. For the composites containing less photocatalyst (0.7:1, 1.5:1), there was negligible increase observed when irradiation was provided due to the slower rate of photocatalysis compared to the rate of adsorptive removal by AC. A summary of the removal efficiencies are given in Table 4.5 for comparison.

Table 4.5: MO removal efficiencies for various Ag/AgCl-AC composites

Catalyst	**Removal Efficiency: $(1 - C_f/C_o) \times 100$ (%)**
Pure Ag/AgCl (adsorption only)	Negligible
Pure Ag/AgCl (adsorption + photocatalysis)	15.1
0.7:1 (adsorption only)	98.6
0.7:1 (adsorption + photocatalysis)	98.1
1.5:1 (adsorption only)	98.0
1.5:1 (adsorption + photocatalysis)	97.9
2:1 (adsorption only)	91.7
2:1 (adsorption + photocatalysis)	97.3
2.5:1 (adsorption only)	73.8
2.5:1 (adsorption + photocatalysis)	88.1
3:1 (adsorption only)	55.1
3:1 (adsorption + photocatalysis)	77.6

The increase in removal efficiency observed for the 2:1, 2.5:1, 3:1 composites was thought to be due to the production of photocatalytic radicals and reactive species by the incorporated Ag/AgCl, and the synergistic effect of photocatalysis and adsorption on removal efficiency. This synergy was observed for other photocatalysts such as TiO_2 supported on AC [16], and was attributed to the common contact interface between solids promoting mass transfer, as well as the adsorbent support facilitating photocatalytic chain reactions by intermediates retention to promote more complete degradation and mineralization of the pollutant [18]. Deposition of the photocatalyst onto activated carbon was thought to result in intimate contact, which led to a stronger interphase interaction between the AC and Ag/AgCl in the prepared composites compared to physical mixtures of photocatalyst and AC [51]. The weak

physical bonding of photocatalyst on the surface of AC in mechanical mixtures may cause the photocatalyst to become dislodged from AC in solution, removing the common contact interface, and decreasing the synergy observed [15]. The decreased size of Ag/AgCl on the composite compared to the pure Ag/AgCl synthesized also likely played a role in improving the photocatalytic activity observed, since deposition onto AC was advantageous for producing smaller grains of the catalytic material. Preparation of bulk Ag/AgCl resulted in particle aggregation, which increased the effective particle size, reducing the available surface area for photocatalytic reaction. Additionally, in the case of Ag/AgCl-AC composites, the adsorbed MO molecules could move (desorb and transfer) directly to the deposited Ag/AgCl, which was adhered to AC.

An increased enhancement in MO removal upon irradiation was observed with increasing Ag/AgCl content, and was thought to be due to the increased production of radicals and reactive species at higher loadings due to greater photocatalyst concentrations. It should be noted that, at lower Ag/AgCl contents, adsorption dominated the process since the kinetics of adsorption were much faster than those observed for photocatalysis. Therefore, although there may have been some radical generation by the photocatalyst in these cases, enhancement of the process was difficult to observe at the given conditions, since there was almost full removal of the pollutant by adsorption only.

4.3.3.2 Photocatalytic degradation of MO

To further characterize the photocatalytic process using Ag/AgCl-AC composites, prolonged runs were carried out using a dark adsorption period of 2 hours, followed by visible light photocatalysis. The results are given in Figure 4.7.

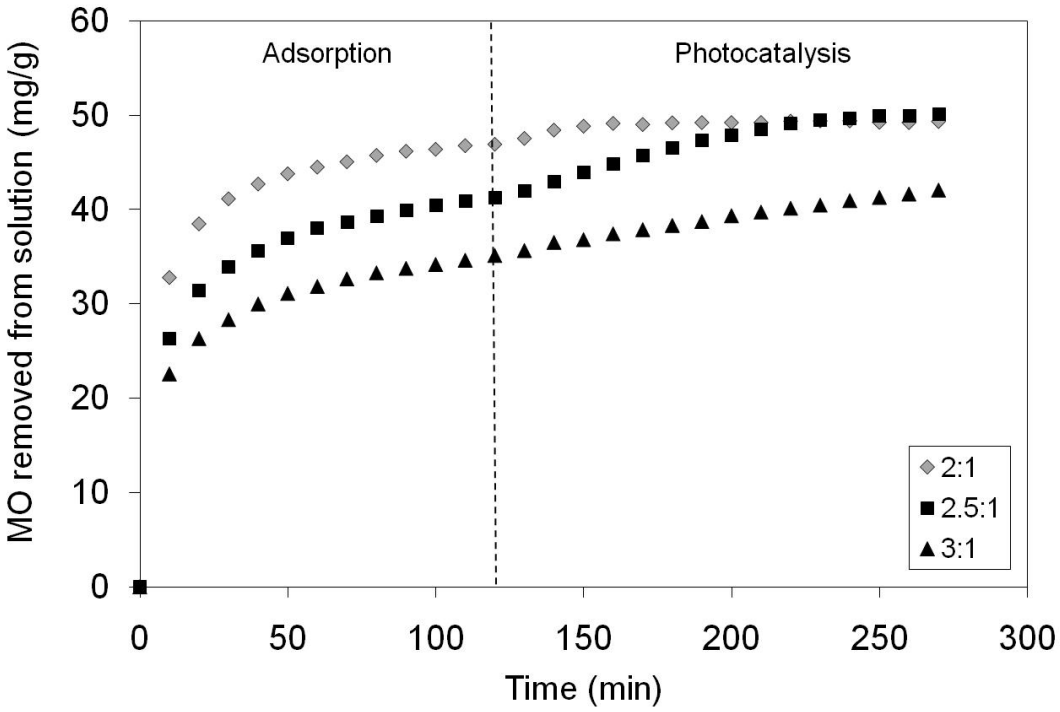

Figure 4.7: Adsorption and subsequent photocatalysis using 2:1, 2.5:1, and 3:1 Ag/AgCl-AC composites, respectively (C_o = 25 mg L^{-1}, loading = 0.5 g L^{-1})

The adsorption process was found from the experimental data to reach a pseudo-equilibrium after approximately 2 hours. Upon irradiation, there was a gradual change in the rate of MO removal from solution, due to the photocatalytic process. The photocatalysis data can be given in the conventional normalized manner, as shown in Figure 4.8. Further discussion of the comparative activities between the prepared composites is provided in subsequent sections, with respect to their kinetic descriptions.

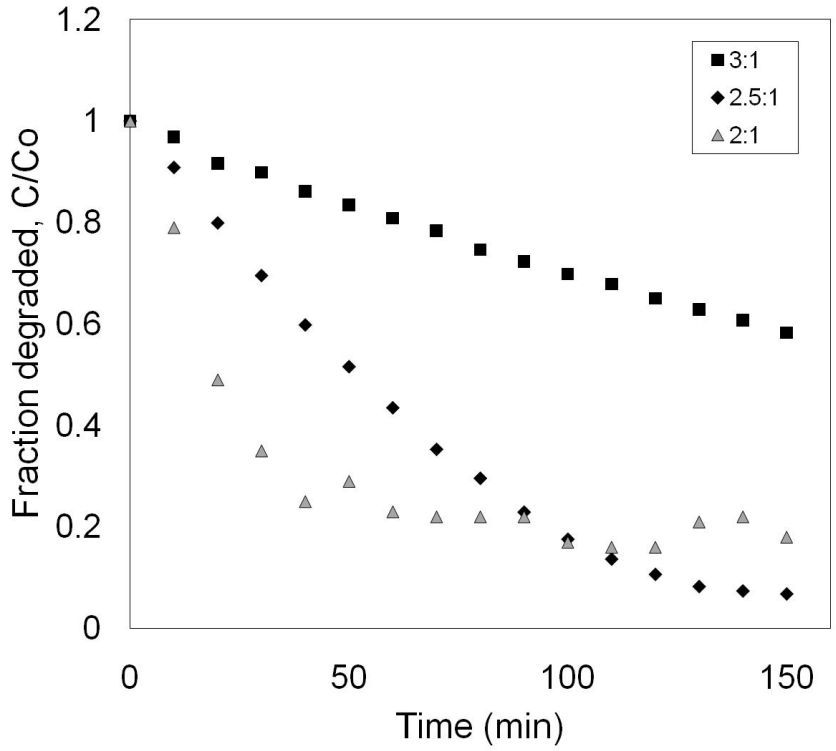

Figure 4.8: MO photodegradation using Ag/AgCl-AC composites (loading = 0.5 g L^{-1})

4.3.3.3 Kinetics of photodegradation

To quantify the kinetics of photodegradation, the first order, second order, and Langmuir-Hinshelwood models were fitted to the experimental data [52]. These kinetic models are expressed by the following equations, respectively:

$$\text{First order:} \quad r = -dC/dt = k_{photo,1}C \qquad (4.16)$$

$$\text{Second order:} \quad r = -dC/dt = k_{photo,2}C^2 \qquad (4.17)$$

$$\text{Langmuir-Hinshelwood:} \quad r = -dC/dt = K k_r C/(1+KC) \qquad (4.18)$$

Where r is the rate of MO photodegradation (mg L^{-1} min^{-1}), C is the concentration of MO (mg L^{-1}), $k_{photo,1}$ is the first order rate constant (min^{-1}), $k_{photo,\ 2}$ is the second order rate constant (L mg^{-1} min^{-1}), K is the Langmuir-Hinshelwood adsorption coefficient (L mg^{-1}) and k_r is the Langmuir-Hinshelwood rate constant (mg L^{-1} min^{-1}).

The first and second order equations follow traditional rate equations for chemical reactions, where the rate of reaction is either proportional to the concentration or its square. The

Langmuir-Hinshelwood kinetic analysis, however, considers the adsorption of pollutants and subsequent surface reaction. The Langmuir-Hinshelwood analysis is frequently employed for the study of heterogeneous photocatalysis, but is usually reduced to an apparent first order model when the concentrations are sufficiently small [53].

The three kinetic models can be integrated with respect to the limits $C = C_e$ at time $t = 0$ and $C = C$ at time t, to obtain the follow nonlinearized forms:

$$\text{First order:} \quad C = C_e \exp(-k_{photo,1}\, t) \quad (4.19)$$

$$\text{Second order:} \quad C = C_e / (k_{photo,2}\, C_e\, t + 1) \quad (4.20)$$

$$\text{Langmuir-Hinshelwood:} \quad C = C_e - (K k_r\, t - \ln(C_e/C))/K \quad (4.21)$$

It should be noted that the initial concentration for the photocatalytic reaction is the equilibrium concentration after dark adsorption (i.e. $C_{o,\ photocatalysis} = C_{e,\ adsorption}$). Nonlinear regression was used to estimate the first and second order model parameters, and the Langmuir-Hinshelwood parameters, respectively. For the Langmuir-Hinshelwood solution procedure, a script was written for Ridder's method root-finding algorithm using Visual Basic for Applications. This was then used simultaneously with the Microsoft Excel Solver add-in during the optimization procedure. The regressed parameters are given in Table 4.6, and comparison of the experimental data with the model-predicted values is given in Figure 4.9. The photoactivity data for the 2:1 composite was not modeled using these approaches, due to its inability to degrade the equilibrium concentration significantly past 40 minutes, which led to deviations in the modeled data. The discrepancy observed was thought to be due to the formation of photoreaction intermediates, which were degraded at a much slower rates than the original parent dye compound, as investigated and discussed in subsequent chapters.

Table 4.6: Photocatalysis kinetic parameters for MO photodegradation by Ag/AgCl-AC

	Composite	
Models	**2.5:1**	**3:1**
First order		
$k_{photo,1}$ / min^{-1}	0.0147	0.00359
R^2	0.965	0.999
SE	0.0517	0.0046
SSE	0.0400	0.00032
Second order		
$k_{photo,2}$ / L mg^{-1} min^{-1}	0.0053	0.00052
R^2	0.751	0.991
SE	0.114	0.0115
SSE	0.195	0.00198
Langmuir-Hinshelwood		
K_{ad} /L mg^{-1}	0.523	0.039
k_{L-H} / mg L^{-1} min^{-1}	0.0695	0.117
R^2	0.997	0.998
SE	0.0169	0.0061
SSE	0.0040	0.0005

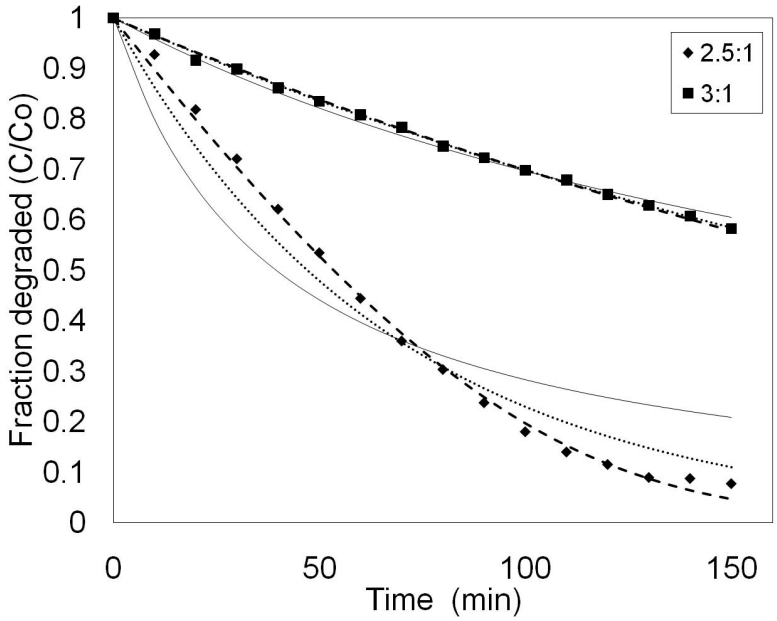

Figure 4.9: Photocatalysis kinetics for Ag/AgCl-AC composite powders, where dotted, solid, and dashed lines represent first order, second order, and L-H modeled values, respectively. (loading = 0.5 g L^{-1})

From comparison of the experimental and model-predicted data, the Langmuir-Hinshelwood kinetics were found in general to best describe the degradation behaviour, with K_{ad} values of

0.523 L mg^{-1} and 0.039 L mg^{-1}, and k_{L-H} values of 0.0695 mg L^{-1} min^{-1} and 0.117 mg L^{-1} observed for the 2.5:1 and 3:1 Ag/AgCl-AC composites, respectively. The goodness-of-fit criteria also indicated that the errors were very low using the first order model, especially for the 3:1 composite, where the model followed the L-H data very closely. The Langmuir-Hinshelwood parameters indicated that the rate of pollutant adsorption decreased with increasing Ag/AgCl content, while the rate of photodegradation (i.e. reaction) increased with increased loading. In light of the adsorption kinetics investigated in previous sections, this analysis was seemingly appropriate for description of the photocatalytic system dynamics with respect to the adsorptive nature of the composites. For example, the 3:1 composite was expected to exhibit an increased photoactivity due to its higher photocatalyst loading and capacity to generate reactive species, but its overall rate of degradation was also thought to be limited by its lessened ability to effectively transfer pollutants onto its surface by adsorption. The inverse was true for the 2.5:1 composite, as it had a higher sorption capacity, but less Ag/AgCl content. Exact optimization in the future should be subject to quantitative modeling of the physical processes and the definition of an objective function, such as a weighted trade-off between the desired adsorptive and photocatalytic pollutant removal.

The Langmuir-Hinshelwood adsorption constant was found to be much smaller than that calculated using the adsorption isotherm. In the isotherm model, the adsorption constant was dependent on number of adsorptive sites available on the composite surface, however, during photodegradation, both the dye molecule and its degradation products were thought to be adsorbed, so the number of available adsorptive sites was effectively decreased.

4.4 Conclusions

The adsorptive and photocatalytic properties of a novel visible light active Ag/AgCl-AC composite plasmonic adsorbent photocatalyst were investigated. Using a nonlinear optimization strategy with defined error functions as goodness-of-fit criteria, the adsorption kinetics were found to follow second order behaviour, and the equilibrium isotherms were found to be Langmuir-type. The intraparticle diffusion plots were constructed, and for all compositions of Ag/AgCl-AC studied, internal diffusion was not the only rate limiting step

for adsorption. The incorporation of Ag/AgCl photocatalyst into the AC composite was found to increase the removal efficiency of MO under visible light over adsorption only, and the photodegradation process followed Langmuir-Hinshelwood kinetics.

4.5 Acknowledgments

This work was supported by the Natural Sciences and Engineering Research Council of Canada and the National Natural Science Foundation of China (Grant No. 50972037 and 51172063). The authors would like to acknowledge the Department of Earth Sciences (University of Ottawa) and the College of Chemical Engineering at Hebei United University for help with sample characterization.

4.6 References

[1] A. Fujishima, K. Honda, Electrochemical photolysis of water at a semiconductor electrode, Nature 238 (1972) 37–38.

[2] D.S. Bhatkhande, V.G. Pangarkar, A.A.C.M. Beenackers, Photocatalytic degradation for environmental applications – a review, J. Chem. Technol. Biotechnol. 77 (2001) 102–116.

[3] D. Bahnemann, Photocatalytic water treatment: Solar energy applications, Solar Energy 77 (2004) 445–459.

[4] J. Gamage, Z. Zhang, Applications of photocatalytic disinfection: A review, Int. J. Photoenergy 2010 (2010) Article ID 764871. *(also given in Appendix B)*

[5] A. Fujishima, T.N. Rao, D.A. Tryk, Titanium dioxide photocatalysis, J. Photochem. Photobiol., C. 29 (2000) 1–21.

[6] Z. Wang, B. Huang, Y. Dai, P. Wang, Z. Zheng, H. Cheng, Relationship between microstructure and photocatalytic properties of nanomaterials, Z. Kristallogr. 225 (2010) 520–527.

[7] W.Y. Choi, A. Termin, M.R. Hoffmann, Role of metal-ion dopants in quantum-sized TiO_2 – correlation between photoreactivity and charge-carrier recombination dynamics, J. Phys. Chem. 98 (1994) 13669–13679.

[8] G. Zhao, H. Kozuka, T. Yoko, Sol-gel preparation and photoelectrochemical properties of TiO_2 films containing Au and Ag metal particles, Thin Solid Films (1996) 147–154.

[9] R. W. Fessenden, P.V. Kamat, Rate constants for charge injection from excited sensitizer into SnO_2, ZnO, and TiO_2 semiconductor nanocrystallites, J. Phys. Chem. (1995) 12902–12906.

[10] J.M. Stipkala, F.N. Castellano, T.A. Heimer, C.A. Kelly, K.J.T. Livi, G.J. Meyer, Light-induced charge separation at sensitized sol-gel processed semiconductors, J. Chem. Mater. (1997) 2341–2353.

[11] P. Wang, B. Huang, X. Qin, X. Zhang, Y. Dai, J. Wei, M.-H. Whangbo, Ag@AgCl: A highly efficient and stable photocatalyst active under visible light, Angew. Chem. Int. Ed. 47 (2008) 7931–7933.

[12] P. Wang, B. Huang, X. Zhang, X. Qin, H. Jin, Y. Dai, Z. Wang, J. Wei, J. Zhan, S. Wang, J. Wang, M.-H. Whangbo, Highly efficient visible-light plasmonic photocatalyst Ag@AgBr, Chem. Eur. J. 15 (2009) 1821–1824.

[13] H. Xu, H. Li, J. Xia, S. Yin, Z. Luo, L. Liu, L. Xu, One-pot synthesis of visible-light driven plasmonic photocatalyst Ag/AgCl in ionic liquid, ACS Appl. Mater. Interfaces 3 (2011) 22–29.

[14] I. Sopyan, M. Watanabe, S. Murasawa, K. Hashimoto, A. Fujishima, An efficient TiO_2 thin-film photocatalyst: photocatalytic properties in gas-phase acetaldehyde degradation, J. Photochem. Photobiol., A. 98, 1–2 (1996) 79–86.

[15] T.-T. Lim, P.-S. Yap, M. Srinivasan, A.G. Fane, TiO_2/AC composites for synergistic adsorption-photocatalysis processes: Present challenges and further developments for water treatment and reclamation, Crit. Rev. Environ. Sci. Technol. 41 (2011) 1173–1230.

[16] J. Matos, J. Laine, J.-M. Herrmann, Synergy effect in the photocatalytic degradation of phenol on a suspended mixture of titania and activated carbon, Appl. Catal., B. 18 (1998) 281–291.

[17] J. Matos, J. Laine, J.-M. Herrmann, D. Uzcategui, J.L. Brito, Influence of activated carbon upon titania on aqueous photocatalytic consecutive runs of phenol photodegradation, Appl. Catal., B. 70 (2007) 461–469.

[18] X. Wang, Y. Liu, Z. Hu, Y. Chen, W. Liu, G. Zhao, Degradation of methyl orange by composite photocatalysts nano-TiO_2 immobilized on activated carbons of different porosities, J. Hazard. Mater. 169 (2009) 1061–1067.

[19] W. Li, S. Liu, Bifunctional activated carbon with dual photocatalysis and adsorption capabilities for efficient phenol removal, Adsorption 18 (2012) 67–74.

[20] J. Rouquérol, P. Llewellyn, F. Rouquérol, Is the BET equation applicable to microporous adsorbents?, Stu. Surf. Sci. Catal. 160 (2007) 49–56.

[21] S. Kundu, A.K. Gupta, Arsenic adsorption onto iron oxide-coated cement (IOCC): Regression analysis of equilibrium data with several isotherm models and their optimization, Chem. Eng. J. 122 (2006) 93–106.

[22] J.F. Porter, G. McKay, K.H. Choy, The prediction of sorption from a binary mixture of acidic dyes using single- and mixed-isotherm variants of the ideal adsorbed solute theory, Chem. Eng. Sci. 54 (1999) 5863–5885.

[23] W. Li, C. Liang, W. Zhou, J. Qiu, Z. Zhou, G. Sun, Q. Xin, Preparation and characterization of multiwalled carbon nanotube-supported platinum for cathode catalysts of direct methanol fuel cells, J. Phys. Chem. B 107 (2003) 6292–6299.

[24] C. Hu, T. Peng, X. Hu, Y. Nie, X. Zhou, J. Qu, H. He, Plasmon-induced photodegradation of toxic pollutants with Ag-AgI/Al_2O_3 under visible-light irradiation, J. Am. Chem. Soc. 132 (2010) 857–862.

[25] X. Zhang, L. Lei, Effect of preparation methods on the structure and catalytic performance of TiO_2/AC photocatalysts, J. Hazard. Mater. 153 (2008) 827–833.

[26] Y.-S. Ho, Citation review of Lagergren kinetic rate equation on adsorption reactions, Scientometrics, 59 (2004) 171–177.

[27] S. Largergren, Zur theorie der sogenannten adsorption gelöster stoffe (*About the theory of so-called adsorption of soluble substances)*, K. Sven. Vetenskapsakad. Handl., Band 24, 4 (1898) 1–39.

[28] G. McKay, Y.-S. Ho, Pseudo-second-order model for sorption processes, J. Process Biochem. 34 (1999) 451–465.

[29] L. Li, P.A. Quinlivan, D.R.U. Knappe, Effects of activated carbon surface chemistry and pore structure on the adsorption of organic contaminants from aqueous solution, Carbon 49 (2002) 2085–2100.

[30] F. Villacanas, M.F.R. Pereira, J.J.M. Orfao, J.L. Figueiredo, Adsorption of simple aromatic compounds on activated carbons, J. Colloid Interface Sci. 293 (2006) 128–136.

[31] S. Basha, C. Barr, D. Keane, K. Nolan, A. Morrissey, M. Oelgemöller, J.M. Tobin, On the adsorption/photodegradation of amoxicillin in aqueous solutions by an integrated photocatalytic adsorbent (IPCA): Experimental studies and kinetics analysis, Photochem. Photobiol. Sci. 10 (2011) 1014–1022.

[32] J.C. Igwe, A.A. Abia, Adsorption kinetics and intraparticulate diffusivities for bioremediation of Co (II), Fe (II) and Cu (II) ions from waste water using modified and unmodified maize cob, Int. J. Phys. Sci. 2 (2007) 119–127.

[33] A. Findon, O. Mckay, N.S. Blair, Transport studies for the sorption of copper ions by chitosan, J. Environ. Sci. Health Part. A. 28 (1993) 173–185.

[34] W.J. Weber, F.A. Digiano, Process dynamics in environmental systems, Wiley and Sons, New York, 1996, pp.89–94.

[35] W. J. Weber, J.C. Morris, Kinetics of adsorption on carbon from solution, J. Sanit. Eng. Div. Am. Soc. Civ. Eng. 89 (1963) 31–60.

[36] E.I. Unuabonah, K.O. Adebowale, B.I. Olu-Owolabi, Kinetic and thermodynamic studies of the adsorption of lead (II) ions onto phosphate-modified kaolinite clay, J. Hazard. Mater. 144 (2007) 386–395.

[37] F.C. Wu, R.L. Tseng, R.S. Juang, Initial behaviour of intraparticle diffusion model used in the description of adsorption kinetics, Chem. Eng. J. 153 (2009) 1–8.

[38] A.S. Özcan, B. Erdem, A. Özcan, Adsorption of Acid Blue 193 from aqueous solutions onto BTMA-bentonite, Colloids Surf. A: Physicochem. Eng. Aspects 266 (2005) 73–81.

[39] V.J.P. Poot, G. McKay, J.J. Healy, Removal of basic dye from effluent using wood as an adsorbent, J. Water Pollut. Control. Fed. 50 (1978) 926–935.

[40] D. Kavitha, C. Namasivayam, Experimental and kinetic studies on methylene blue adsorption by coir pith carbon, Bioresour. Technol. 98 (2007) 14–21.

[41] H.K. Boparai, M. Joseph, D.M. O'Carroll, Kinetics and thermodynamics of cadmium ion removal by adsorption onto nano zerovalent iron particles, J. Hazardous Mater. 186 (2011) 458–465.

[42] K.V. Kumar, S. Sivanesan, Sorption isotherm for safranin onto rice husk: Comparison of linear and non-linear methods, Dyes Pigments 72 (2007) 130-133.

[43] M. Ghiaci, A. Abbaspur, R. Kia, F. Seyedeyn-Azad, Equilibrium isotherm studies for the sorption of benzene, toluene, and phenol onto organo-zeolites and as-synthesized MCM-41, Sep. Purif. Technol. 40 (2004) 217–229.

[44] I. Langmuir, The constitution and fundamental properties of solids and liquids, J. Am. Chem. Soc. 38 (1916) 2221–2295.

[45] H.M.F. Freundlich, Über die adsorption in lösungen *(On the adsorption in solutions)*, Z. Phys. Chem. 57 (1906) 385–470.

[46] A.W. Adamson, A.P. Gast, Physical Chemistry of Surfaces, Sixth Ed. Wiley-Interscience, New York, 1997

[47] O. Redlich, D.L. Peterson, A useful adsorption isotherm, J. Phys. Chem. 63 (1959) 1024–1026.

[48] K.Y. Foo, B.H. Hameed, Insights into the modeling of adsorption isotherm systems, Chem. Eng. J. 156 (2010) 2–10.

[49] K.R. Hall, L.C. Eagleton, A. Acrivos, T. Vermeulen, Pore- and solid-diffusion kinetics in fixed-bed adsorption under constant-pattern conditions, Ind. End. Chem. Fundam. 5 (1966) 212–223.

[50] K.V. Kumar, M. Monteiro de Castro, M. Martinez-Escandell, M. Molina-Sabio, J. Silvestre-Albero, F. Rodriguez-Reinoso, A continuous site energy distribution function from Redlich-Peterson isotherm for adsorption on heterogeneous surfaces, Chem. Phys. Lett. 492 (2010) 187–192.

[51] W. Wang, P. Serp, P. Kalck, J. L. Faria, Visible light photodegradation of phenol on MWNT-TiO_2 composite catalysts prepared by a modified sol-gel method, J. Mol. Catal. A: Chem. 235 (2005) 194–199.

[52] S. Basha, D. Keane, A. Morrissey, K. Nolan, M. Oelgemöller, J. Tobin, Studies on the adsorption and kinetics of photodegradation of pharmaceutical compounds, indomethacin using novel photocatalytic adsorbents (IPCAs), Ind. Eng. Chem. 49 (2010) 11302–11309.

[53] J.-M. Herrmann, Heterogeneous photocatalysis: fundamentals and applications to the removal of various types of aqueous pollutants, Catal. Today 53 (1999) 115–129.

Chapter 5:
Visible-light-driven inactivation of *Escherichia coli* K-12 using an Ag/AgCl-activated carbon composite photocatalyst

Joanne Gamage McEvoy, Didier Alexandre Bilodeau, Wenquan Cui, Zisheng Zhang

Journal of Photochemistry and Photobiology A: Chemistry, 267 (2013) 25–34.

Abstract

The inactivation of *Escherichia coli* K-12 was investigated using a novel Ag/AgCl-activated carbon composite photocatalyst under visible light irradiation. The photocatalyst was found to effect a 97 ± 2.5% inactivation of bacteria under irradiation for sixty minutes in a 5 g L^{-1} slurry. The composite also possessed some biocidal action in the absence of light due to the incorporated silver; however, the action of photoproduced reactive oxygen species (ROS) on the bacteria dominated the disinfection process under irradiation. The mechanism of photocatalytic cell death was thought to be attributed to ROS attack causing cell wall damage, and was probed by indirect observations of changes to cell membrane structure and permeability upon photocatalytic treatment.

Keywords: activated carbon, plasmon photocatalyst, *Escherichia coli* K-12, inactivation

5.1 Introduction

Photocatalysis has been investigated as an alternative disinfection method since the first report of its antimicrobial efficacy by Matsunaga et al. in 1985 [1]. This semiconductor-mediated process possesses advantages over traditional treatments, such as chlorination, which can be associated with the production of toxic disinfection byproducts [2]. Photocatalytic disinfection has been investigated for the inactivation of a wide variety of bacteria, spores, and viruses; and for application to many uses, such as for potable water production, air filtration, and the development of antimicrobial surfaces (as reviewed by Gamage and Zhang [3]).

A limitation of the traditional TiO_2 semiconductor used in photocatalytic processes lies in the low quantum efficiency due to its large band gap and consequent inability to effectively utilize solar irradiation, which contains only a small portion (~3–5%) of high-energy ultraviolet (UV) light. To address this, many efforts have been made in the development of novel photocatalysts with enhanced visible light response, since a large fraction (~43%) of the incoming global irradiation is comprised of these components. Other considerations in designing high-efficiency photocatalytic materials involve the prevention of electron-hole recombination during the photoinitiated process, and the improvement of mass transfer through increasing photocatalyst surface area [4] or developing composites containing adsorbent components [5, 6].

A novel hybrid plasmonic photocatalyst-adsorbent composite, Ag/AgCl-activated carbon (AC), was previously proposed by our group. This material combines the surface plasmon resonance effect of nano-scale noble metals, causing them to have enhanced visible light response [7], and the adsorption synergy observed in composites containing photocatalysts and adsorbents such as AC [5]. In the Ag/AgCl-AC composite, the role of nanosilver is in the visible light induced generation of electron-hole pairs, while Ag and AgCl act in concert to provide photocatalyst stability by polarizing the photoinduced charges, preventing electron-hole recombination and reduction of Ag^+ in AgCl [7]. The incorporated AC acts by adsorption to facilitate continuous transfer between the pollutant and the photocatalytic

active sites [8].

An identified problem with these adsorbent photocatalyst composites is in the potential biofouling and biofilm formation that may occur on the AC matrix, which is highly biocompatible. Silver/silver halide materials such as Ag/AgCl and Ag/AgBr-based catalysts have been found to be effective antibacterial agents and can act photocatalytically to inactivate microbial targets [9]. The antimicrobial activity of these materials was also reported in the absence of photocatalytic mechanisms [9–11]. In addition, nanosilver has been widely investigated for incorporation into AC as an antibacterial agent due to its desirable controlled ionic silver release properties [12–14]. Accordingly, in this study we investigated the antibacterial and photocatalytic disinfection properties of surface plasmon resonance enhanced Ag/AgCl-activated carbon composites on the inactivation of a model microorganism, *Escherichia coli* K-12. Bacterial inactivation using this composite may address the issue of AC biofouling through the incorporated antimicrobial activity, while also offering potential for use as a visible light active photocatalyst in applications such as solar photocatalytic disinfection.

5.2 Experimental

5.2.1 Materials

5.2.1.1 Ag/AgCl-AC composites

Ag/AgCl-AC composites were prepared using an impregnation-precipitation-photoreduction method. Briefly, unmodified AC (Darco G60, 100 mesh, Sigma-Aldrich) was loaded with a certain amount of $AgNO_3$ (ACS grade, MP Biomedicals), and precipitated using HCl (reagent-grade, Fisher Scientific), followed by photoreduction by an unfiltered 300 W tungsten halide bulb (Ushio ELH) for one hour, and subsequent filtration and drying. The catalyst was prepared at a weight ratio of 2.5:1 (Ag:AC). This ratio was calculated assuming that all AgCl was reduced to Ag, for simplicity. In reality, only a partial reduction took place [7]. Additionally, the batch-to-batch variation of the composite was thought to have a minimal effect on the experimental error, as antimicrobial and photocatalytic efficiencies observed were comparable using different batches of the catalyst. Pure Ag/AgCl was also

prepared using a similar synthesis, but omitting the AC impregnation step.

5.2.1.2 Bacterial strain

Wild-type *Escherichia coli* K-12 (TG1 strain) was used as a standard strain for all bacterial inactivation studies. *E. coli* K-12 was chosen because it is known to be non-pathogenic and is a common model used in laboratory experiments. It was obtained from Dr. Christopher Q. Lan in the Department of Chemical and Biological Engineering at the University of Ottawa, and was maintained as a laboratory strain.

5.2.2 Photocatalytic inactivation

5.2.2.1 Source of irradiation

Irradiation for photocatalytic inactivation studies was provided by a 300 W ELH tungsten halide bulb (Ushio) equipped with a UV filter (Kenko Zeta, $\lambda > 410$ nm, transmittance > 90%). The irradiation was measured using a quantum meter (Biospherical QSL-2100; 400 nm $< \lambda <$ 700 nm), and was found to be approximately 4.7×10^{-3} Einstein m^{-2} s^{-1}.

5.2.2.2 Cell culture and enumeration

All inactivation trials were performed in triplicate, and all materials were sterilized for 20 minutes at 121°C prior to use. For all studies, the inactivation was quantified as loss of culturability of the bacteria. Cultures were prepared by growing *E. coli* K-12 (TG1) aerobically in Luria-Bertani medium (Difco LB broth, Miller; containing 10 g L^{-1} tryptone, 5 g L^{-1} yeast extract, and 10 g L^{-1} NaCl) on a rotary shaker at 37°C for 14 hours overnight until the stationary phase was reached, as determined by a prepared growth curve. The initial concentration from the overnight culture was found by serial dilution and plating. Plated aliquots of 25 μL were spread in triplicate on LB agar plates for each dilution, and incubated at 37°C for 18 hours. Bacterial enumeration was performed using standard plate counts (for viable and cultivable bacteria), where counts in the range of 30 – 300 colony forming units (CFU) per plate were considered statistically significant and were used to calculate the cell concentration.

5.2.2.3 Zone of inhibition

Zone of inhibition studies were performed by immobilization of the synthesized powders on thin glass substrates [15] (Fisherbrand microscope cover glass; 22x22 mm, 0.17 - 0.25 mm

thick). According to the procedure modified from Zhang et al. [16], catalyst slurry (150 g L^{-1}) in 70 vol% ethanol was painted uniformly to form an opaque film on the substrates, and allowed to dry in air overnight.

The immobilized catalyst was then contacted with LB agar plates containing 125 µL of diluted stationary phase *E. coli*, prepared using a spread plate method. The following experiments were performed: negative (no substrate), glass substrate only (no catalyst), AC-coated substrate, and Ag/AgCl-AC coated substrate. For each experiment, one set of plates was kept in the dark and another set was irradiated for 10 minutes. Cooling was provided by a fan. The prepared bacterial samples were incubated for 18 hours at 37°C, and then imaged using an AlphaImager MultiImage light cabinet (Alpha Innotech) interfaced with Alphaview software. The images were further processed using Canon MeasureIT software to quantify the zone of inhibition. The equivalent radius was taken as the shortest distance between the centre of the catalyst-containing substrate to the edge of the no-growth region observed. To minimize measurement error, an average was taken between 4 symmetric points of the antibacterial region for each plate. The radius of the zone of inhibition was calculated by subtracting the catalyst equivalent radius from the measured radius, which included the no-growth region.

5.2.2.4 Multi-blot technique

To perform qualitative analysis of photocatalytic inactivation, a multi-blot technique was used, employing 12-well cell culture plates inoculated with 5 mL per well of an *E. coli* suspension in saline (0.9 wt% NaCl). The initial bacterial suspension was prepared by centrifuging 1 mL of liquid culture at 14 800 rpm for 5 minutes and resuspending in saline. This centrifugation and washing procedure was repeated three times to remove the growth media. The initial concentration of the prepared *E. coli* suspension in each well was controlled to ~10^6 CFU mL^{-1}. The appropriate amount of catalyst was then added to the wells, and the plate was exposed to visible light irradiation. Cooling was provided by a fan, and the wells were manually stirred every 3 minutes. After irradiation, blots from each well were made onto an LB agar plate using a multi-blot replicator tool with 12 pins of 3.18 mm diameter, delivering a 3 µL hanging drop from each well to the plate (VP Scientific). The plates were blotted in duplicate, and incubated at 37°C for 18 hours prior to imaging using a

light cabinet. The images were taken using white light in transillumination mode. The bactericidal activity was qualitatively estimated by the bacterial growth on the incubated plate, corresponding to various conditions in the respective wells. The runs were performed in triplicate for each set of conditions studied.

5.2.2.5 Temporal course of inactivation

The temporal course of inactivation was studied using 50 mL of saline solution spiked with 10^6 CFU mL^{-1} bacteria in a 100 mL Pyrex beaker. This initial bacterial suspension was prepared using the same centrifugation and washing procedure described for the multi-blot assay. The catalyst was then added to the bacterial suspension at a loading of 5 g L^{-1}, and the mixture was magnetically stirred at 160 rpm under irradiation. During disinfection, the temperature was maintained constant at $20^oC \pm 2$ using a water bath, and samples were collected periodically. The collected samples were serially diluted in saline and spread onto LB agar plates using aliquot volumes ranging from 25 – 100 µL. The plates were then incubated and bacteria enumerated using a standard plate count method.

5.2.2.6 Cell membrane permeability studies

To determine the extent of damage to bacterial permeability, bacterial cultivability on modified growth medium was monitored, using sodium cholate as a supplement as per Pigeot-Rémy et al. [17]. These trials were performed using identical procedures as in the previous temporal course of disinfection studies, however, the samples were spread onto LB agar plates supplemented with 10 g L^{-1} sodium cholate (BioXtra, > 99% purity).

Potassium ion (K^+) leakage from the inactivated bacteria was also used to indicate changes to cell membrane permeability, and was measured through inductively coupled plasma optical emission spectroscopy (ICP-OES) using a Varian Vista-Pro CCD spectrometer. For given time intervals during the photocatalytic reaction, 1 mL of illuminated bacterial suspension was removed and centrifuged at 14 800 rpm for 5 minutes. The supernatant was then withdrawn and stabilized with 5 vol% nitric acid (reagent-grade, Fisher Scientific) prior to analysis.

5.2.2.7 ATR-FTIR

To investigate changes to cell envelope structure upon photocatalytic inactivation, attenuated total reflection - Fourier transform infrared measurements (ATR-FTIR) were performed on a Bruker Tensor 37 spectrophotometer (Bruker Optics GmbH) equipped with a Bruker Platinum ATR accessory with a single reflection diamond crystal. Interferograms from 16 scans were averaged to obtain one spectrum, and a 4 cm^{-1} resolution was used in the spectral range of 4000–600 cm^{-1}. The background measurement was taken to be air, and the interferograms were transformed to ATR-FTIR spectra using OPUS 6.5 software. It was shown previously in photocatalyst - *E. coli* aqueous mixtures that hydrated and vacuum-dried samples exhibited the same ATR-FTIR peaks irrespective of degree of hydration [18]. For ATR-FTIR analysis, the photocatalyst was separated from the samples by gravity settling for 10 minutes, and a 5 μL aliquot was taken from the supernatant. The aliquot was then dropped onto the ATR crystal, and the interferograms were measured. The spectrum of pure deionized water was also recorded, and served as a reference for water subtraction. The slight contributions from water vapor and CO_2 in each spectrum were completely removed by subtracting the water vapor and CO_2 spectrum, respectively, using the OPUS software. To eliminate the contributions of water from the spectrum of the sample in aqueous solution, the solvent spectrum was subtracted from the sample spectrum after multiplication by an appropriate factor, which was chosen such that the spectral line in the region 2600 – 1800 cm^{-1} approached zero [19–21].

5.2.2.8 Silver ion diffusion

The diffusion of silver ions (Ag^{+}) from the prepared photocatalyst was measured using inductively coupled plasma mass spectrometry (ICP-MS) on an Agilent HP 4500. 5 g L^{-1} of Ag/AgCl-AC in distilled deionized water was magnetically stirred at 160 rpm in the dark for 7 days, and 1 mL samples were withdrawn periodically. The samples were centrifuged and the supernatant acidified before analysis. For all ICP measurements, the analyses were performed for triplicate samples.

5.3 Results and discussion

5.3.1 Qualitative analysis of bactericidal action

5.3.1.1 Zone of inhibition

The antibacterial and photocatalytic inactivation properties of the composite were evaluated using Gram-negative *E. coli* as a model microorganism, since it is an indicator of faecal contamination [22]. The zone of inhibition assay, similar to the Kirby-Bauer disc diffusion assay, was used to screen bactericidal and photocatalytic activities. In this assay, a 22 millimetre thin glass square substrate saturated with Ag/AgCl-AC composite was placed onto an agar plate that had been seeded with bacteria. The glass substrates were chosen to promote the penetration of light when probing photoactivity. The observed zones of inhibition (regions around the substrate where no growth occurred) were then quantified in the digital images of the plates after incubation.

A typical result from the zone of inhibition study using the prepared composite under visible light irradiation is given in Figure 5.1a, and characteristic features of the assay are shown. In this analysis, a larger no-growth region (dark region around the immobilized catalyst) was indicative of a larger zone of inhibition, and evidenced a stronger antibacterial effect. Figures 5.1b and 5.1c show the appropriate controls for the glass cover slide and AC only, after irradiation. As observed in these figures, neither the irradiated slide nor AC possessed any amount of biocidal activity. The same controls, performed in the dark, also confirmed the biocompatibility of these materials. However, upon exposure of the bacteria to the composite-containing substrate, a distinct biocidal activity and resulting zone of inhibition were observed for both the dark and irradiated cases. This indicated that incorporation of Ag/AgCl into the activated carbon composite decreased the resulting biocompatibility, which agreed with the expected results based on literature for the biocidal activity of Ag/AgCl on *E. coli* [10, 11, 23].

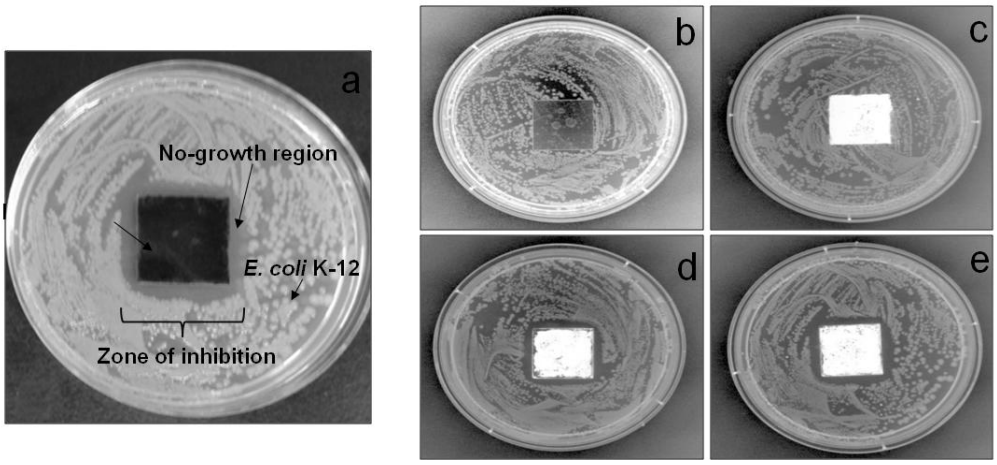

Figure 5.1: Representative zone of inhibition results for samples: a) and e) prepared composite + irradiation; b) cover slide only + irradiation; c) activated carbon + irradiation; and d) prepared composite, no irradiation. Figure 5.1a shows the photographed plate with characteristic features of the assay indicated. Figures b) through e) were taken using an imaging cabinet and are shown in reverse color for clarity.

To further investigate the presence of a photo-induced process caused by irradiation of the composite, a comparison was made between the biocidal activity in the dark (due to the antibacterial effect only) and after irradiation (due to the antibacterial effect and photocatalytic inactivation). The comparison was made based on measurements of the equivalent diameter of the zone of inhibition observed in 10 samples from 3 independent trials for the dark and light runs, respectively, and the results are presented in Figure 5.2. The average zone of inhibition observed in the dark was found to be 1.729 ± 0.226 mm, while that observed under irradiation was 2.564 ± 0.476 mm. Using a paired *t*-test with a 5% level of significance on the two samples, a statistically significant difference ($P < 0.0004$; two-tailed) was found between the bacterial inactivation observed in the dark and light samples.

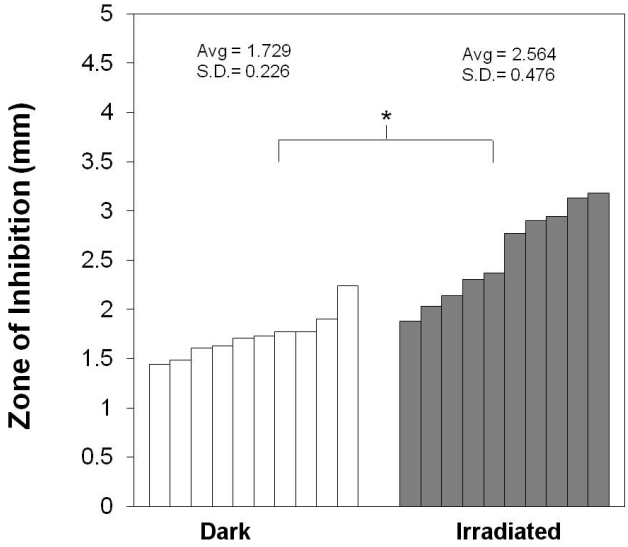

Figure 5.2: Size of zone of inhibition observed in dark and light trials, $*P < 0.0004$

The observed increase in inactivation with the irradiated samples was thought to be attributable to the production of reactive radical species by the photocatalyst upon illumination. From the results obtained, multiple inactivation mechanisms were thought to have simultaneously taken place due to the composite, where the antibacterial action of Ag/AgCl and photocatalytic disinfection may have both played a role. The presence of multiple mechanisms was recently reported by Dong et al. for Ag/AgCl nanocomposites used for the inactivation of *E. coli, Staphylococcus aureus,* and *Bacillus subtilis* [23]. In this study, they proposed that the bacterial inactivation observed under irradiation may have been due to combined effects of the biocidal action of Ag nanoparticles, formation of Ag^+ ions, and generation of reactive oxygen species (ROS) by the photocatalyst. However, the dark-only inactivation using the prepared Ag/AgCl was not reported. Improvement of the dark biocidal activity by photocatalytic action of a composite catalyst under irradiation was studied for Ag/TiO_2 thin films for the inactivation of *E. coli* [24]. Additionally, the synergistic bactericidal activity of $Ag\text{-}TiO_2$ (P25) nanoparticles in both light and dark conditions was reported by Li et al. [25]. They attributed the mechanism of dark biocidal action to direct contact of the bacteria with Ag nanoparticles, and the formation of toxic Ag species such as Ag^+, Ag(0), AgCl, and $AgCl_2^-$, while the mechanism for UV-induced inactivation was

thought to be largely due to generation of ROS by the composite photocatalyst. Ag/AgBr-based materials have similarly been reported as having multiple mechanisms for effecting cell death, such as in Ag/AgBr-TiO_2 composite, where the dark biocidal activity was attributed to the effects of incorporated nanosilver, and the photocatalytic enhancement under visible light was due to ROS generation [9].

5.3.1.2 Multi-blot technique

To confirm and further investigate the photocatalytic effect, a qualitative multi-blot technique was performed using the catalysts in slurry. In this assay, various conditions were used in each well of a 12-well plate, and the growth in each well was observed by transferring equal volumes to a plate containing growth media, incubating, and imaging the bacterial colonies formed. The absence of growth in a position on the plate after transfer was therefore indicative of total or severe loss of culturability of the bacterial population in the corresponding well. Preliminary trials were performed using various catalyst concentrations and irradiation times. Loadings from 0 g L^{-1} (blank) to 20 g L^{-1} were investigated for 15 and 60 minutes, respectively, and the results are given in Figure 5.3.

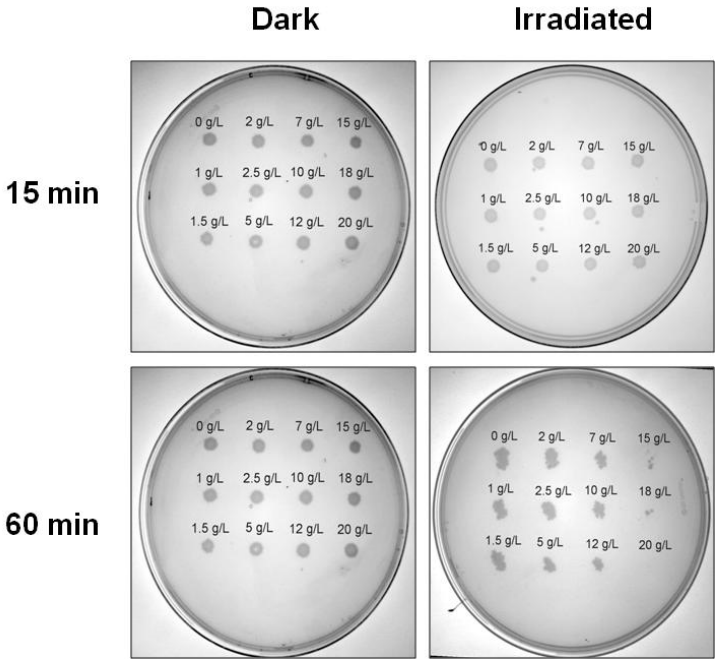

Figure 5.3: Comparison of bacterial growth in 12-well plates for dark and irradiated slurries, respectively, at composite concentrations of 0 to 20 g L^{-1} and irradiation times of 15 & 60 minutes, respectively – *results from a representative trial shown*

No inactivation was observable in the absence of irradiation for all of the dark trials performed (at both 15 and 60 minutes). Additionally, for short irradiation times (15 minutes), no inactivation was observable for all concentrations of composite used, regardless of the irradiation provided. It should be noted that, in all of these cases, there may have been some amount of inactivation occurring in the wells, but it was not enough to severely affect the total culturability of the bacterial population. Therefore growth still occurred on the plates, so the inactivation was not visually observable. When the irradiation period was increased to 60 minutes, the slurries containing high composite concentrations (> 12 g L^{-1}) became severely inactivated, and little or no growth was observed after incubation of the transferred droplets from these wells onto the growth medium. The same result was observed in three independent trials under each condition, confirming the efficacy of cell death observed.

The results alluded to the role of photogenerated radicals and reactive oxygen species in the inactivation mediated by the composite, since the biocidal effects due to the release of ionic silver alone could not cause complete inactivation. Additionally, the absence of noticeable inhibition in the dark indicated that adsorption of the bacteria onto the AC-containing composite photocatalyst did not cause the complete removal of bacteria from solution, even at loadings up to 20 g L^{-1} and exposure times up to 60 minutes. Prolonged exposure times and higher catalyst loadings were found to be necessary to observe the photocatalytic inactivation, since the initial bacterial concentration was high (10^6 CFU mL^{-1}), the contact period was short, and near-complete loss of culturability was required to produce a qualitative effect. However, from the results of the dark and irradiated samples, the photogenerated species were thought to likely play a significant role in the mechanism of inactivation.

The multi-blot assay was then used for comparison of various catalyst performances and investigation of the effect of irradiation on photoinactivation. The bacterial growth observed for the dark and irradiated trials comparing catalysts is shown in Figure 5.4. On each plate, the following catalysts were added to the wells (in vertical triplicates; from left to right): blank (no catalyst addition), activated carbon, neat Ag/AgCl, and prepared Ag/AgCl-AC

composite. The catalyst loading used was 20 mg L^{-1} for the composite, and calculated equivalents of Ag/AgCl and AC were used in their respective wells. The 12-well plates were irradiated for 60 minutes. The triplicate wells indicated the same results in three independent trials, which showed that this assay possessed good repeatability.

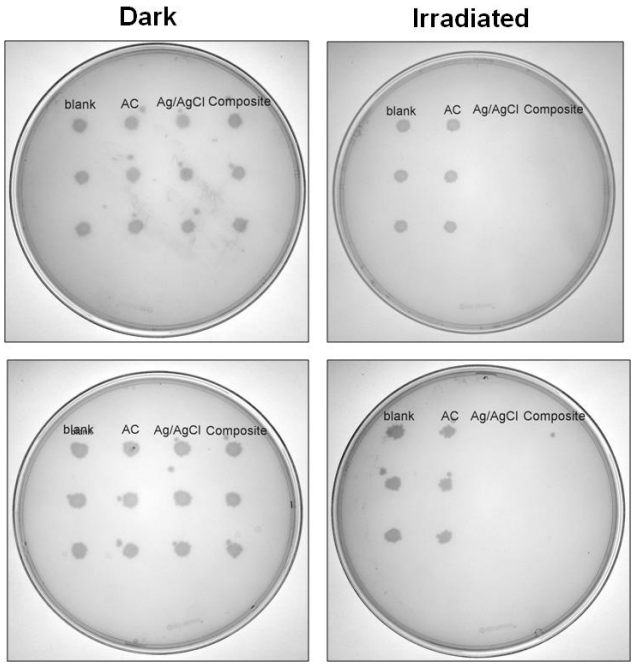

Figure 5.4: Comparison of bacterial growth in 12-well plates for dark and irradiated slurries using various catalysts (60 minutes, 20 mg L^{-1}) – *results from two representative trials shown*

In agreement with the zone of inhibition controls and with literature, the AC was found to be highly biocompatible. Bacterial adsorption onto the carbon in slurry also did not dominate the process, since bacterial growth was still observed after exposure for 60 minutes in the AC-containing wells. As expected, the neat Ag/AgCl and the Ag/AgCl-AC composite did not noticeably inhibit bacterial growth in the dark, however upon irradiation, both of these materials were able to cause complete inactivation. The photolysis, or photo-induced cell death in the absence of catalyst, was found to be negligible, indicating that the contribution to biocidal activity from the light source at was not significant. There were also no noticeable photo-induced effects from using unmodified AC. The antibacterial and photocatalytic effects of the composite photocatalyst were therefore thought to be mainly due to the incorporation of Ag/AgCl into the host AC, and both Ag/AgCl and the composite exhibited

qualitatively similar activities.

5.3.2 Temporal course of inactivation

To evaluate the temporal course of inactivation due to photocatalysis, a standard plate count method was used to quantify viable and cultivable bacterial concentration changes with time upon exposure to various treatments. A comparison of inactivation curves for photolysis (no catalyst), AC equivalent, dark control (no light), and the prepared Ag/AgCl-AC composite are given in Figure 5.5, with the final survival ratios shown inset. The final survival ratios were calculated as the ratio of Nt/No, where Nt represents the bacterial concentration after the total inactivation time, t (t = 60) and No is the initial concentration (t = 0).

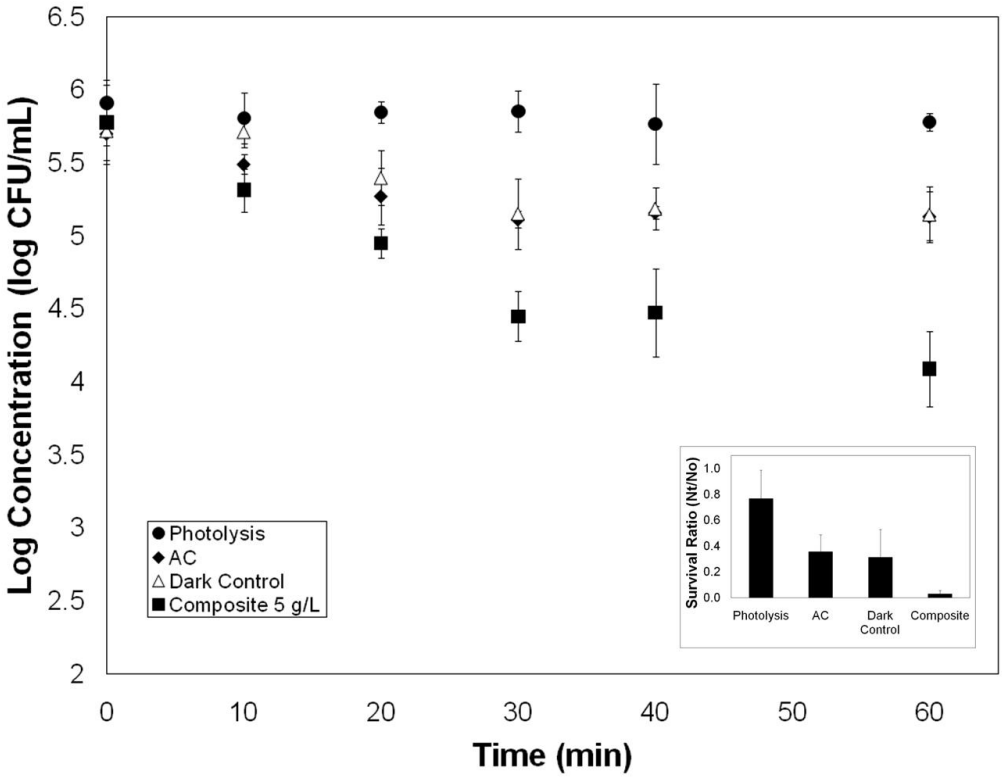

Figure 5.5: Inactivation curves for photolysis, dark control, AC, and irradiated composite; final survival ratios shown inset. (composite loading = 5 g L^{-1}, pH = 5.5)

The photolysis run represented cell death in the absence of any adsorptive, antibacterial, or photocatalytic phenomena. The contribution of the visible light source in inactivating the bacteria was found to be negligible with time, and a final survival ratio of 0.77 ± 0.22 was

observed. The AC trial, performed using equivalent AC as that incorporated into the composite, indicated some bacterial adhesion onto the AC substrate, decreasing the population in solution (where the concentration was quantified). For the AC-only removal, a final survival ratio of 0.36 ± 0.13 was found. The adsorption proceeded gradually for the first 30 minutes, after which no further change was observed. The dark control, which was performed using the composite in the absence of light, showed a similar temporal course as AC, with a final survival ratio of 0.31 ± 0.22. However, using the non-irradiated composite, both the biocidal effect of Ag/AgCl and adsorption were possible mechanisms that were thought to contribute to decreasing concentration.

In terms of adsorption (bacterial adhesion), photocatalyst-activated carbon composites have been found in literature to posses "egg-shell"-type structures [26, 27], where the photocatalyst occupies mainly the outside surface of AC, effectively decreasing the total surface area by pore-blocking. Darco G60 AC possesses a high degree of porosity, and has a pore size distribution in the range of 5–30 nm [27]. Due to the average length of 2–4 μm and average diameter of 0.5–1 μm for rod-shaped *E. coli*, it was assumed that the bacteria was mainly adsorbed on the outer surface of both the AC and the composite in this study, and could not diffuse into the pores.

It was also previously reported that Ag/AgCl carried a mainly negative surface charge due to termination by chlorine ions, and polarization of the metallic Ag electron distribution relative to the AgCl interface [7], while unmodified AC was expected to carry a positive charge at the slightly acidic solution pH used (~5.5). The Gram-negative bacteria used also had a negative surface charge at this pH. This implied that, although the AC adsorption trials contained equivalent mass loadings as those used in the composite, electrostatic interactions between the bacteria and adsorbent materials may have been different between the two trials (AC and composite, respectively) due to the presence of Ag/AgCl photocatalyst on the outer surface of AC. This difference was thought to affect the adsorption dynamics observed. A similar effect was previously reported using a silver-modified TiO_2 catalyst, where the surface characteristics of titania were altered by the incorporation of silver, changing bacterial adhesion properties of *E. coli* on the modified material [28].

Although the adsorption behaviour was not expected to be similar between AC and Ag/AgCl-AC trials, it was also difficult to confirm the presence of biocidal action of the composite in the dark. However, from our previous investigations of zone of inhibition, a biocidal activity was observed using Ag/AgCl-AC in the absence of irradiation, and was thought to be attributable to the effects of the silver contained in the composite catalyst.

The mechanism of biocidal action for silver nanoparticles and for silver-containing compounds has been linked primarily to the release of silver in its ionic form (Ag^+) [11, 29–31]. It was also recently demonstrated that silver nanoparticles do not possess any intrinsic particle-specific bactericidal activity apart from the known antimicrobial toxicity of Ag^+, and that release of this ion in the presence of water and oxygen plays an instrumental role in the observed bactericidal action [29]. The toxicity of Ag^+ ions at sub-micromolar concentrations is due to their interaction with enzymes in the respiratory chain reaction, resulting in uncoupling respiration from the synthesis of ATP [32]. The Ag^+ is also able to bind with transport proteins, leading to proton leakage and induced collapse of proton motive force [33]. The silver ions have a high affinity for thiol groups in cysteine residues present from respiratory and transport proteins [34, 35]. Action on bacterial cells include inducing morphological changes such as cytoplasm shrinkage and detachment of the cell wall membrane, as well as DNA condensation and localization into electron-light regions in the centre of the cell, and cell membrane degradation leading to the leakage of intracellular components [29, 36, 37].

To probe the diffusion of silver ions from the composite catalyst in the dark slurry system, samples were analyzed using ICP-MS. The non-cumulative release of silver ions into 50 mL distilled deionized water under stirring in the dark was recorded, and the concentration was found to be 531 ± 93 ppb, 320 ± 81 ppb, and 121 ± 40 ppb after 1 hour, 24 hours, and 7 days immersion, respectively. These values were thought to represent upper limits on the free silver ion concentration in solution, since the ion release was tested in the absence of anionic ligands such as chlorine or organosulfur compounds such as thiols (–SH). In the experimental inactivation studies, the dissolved ionic silver concentration from the Ag/AgCl-AC composite was thought to be due to contributions of the irreversible oxidation of metallic

Ag to Ag (I), followed by its speciation, as well as the limited solubility of AgCl itself (10^{-5} solubility limit). It was previously found through silver equilibrium speciation and pathway studies that, due to the high affinity binding of thiols ($K_{ads} \sim 10^{12}$), direct thiol transfer could occur at silver ion concentrations lower than the AgCl precipitation threshold and that the thiol targets were typically abundant enough in experimental studies to receive all of the free silver [38]. Additionally, the presence of silver at concentrations at levels as low as 400 ppb were effective against many bacterial species when used alone as a biocide [39]. Therefore, based on the release behaviour observed, the contribution of ionic silver was thought to play some role in the biocidal activity of the photocatalyst.

There was an improved rate of bacterial inactivation upon irradiation of the composite photocatalyst, and a final survival ratio of 0.03 ± 0.025 was observed, corresponding to inactivation of 97 ± 2.5% of the bacterial population. This increased loss of bacterial cultivability was thought to be due to the photocatalytic action on the bacteria when the photocatalyst was irradiated with visible light. Photons in the visible light region were absorbed by the photocatalyst and used to generate electron-hole pairs in metallic silver due to its SPR state. The photogenerated electrons and holes could then undergo further reaction with dissolved oxygen and water to form ROS species, which were thought to interact with *E. coli* bacteria. The inactivation of *E. coli* K-12 using a similar plasmon-enhanced photocatalyst Ag/AgBr-Bi_2WO_6 under visible light was previously attributed to the role of diffusing $^{\bullet}OH$ radical species produced [40]. Cell death due to the action of ROS species has been attributed to the peroxidation of functional groups in cell wall bilayers leading to an increase in bilayer wall disorder. This was found to increase the fluidity of the cell wall [41], and cause eventual lysis through free efflux of intracellular components [41, 42]. In this study, changes to the cell membrane permeability were probed and are discussed in subsequent sections.

5.3.3 Evidence of *E. coli* cell damage

5.3.3.1 Cell membrane permeability studies

The structure of the cell wall of Gram-negative *E. coli* is shown in Figure 5.6 for context. The interaction of Gram-negative bacteria with photocatalytic ROS can induce damage to the

cell envelope integrity, such as by altering the outer membrane permeability to allow the penetration of deleterious substances [17]. For example, lipopolysaccharide, phosphatidylethanolcholine, and peptidoglycan; main wall structural elements, were found to be photocatalytically degraded at the photocatalyst-bacteria interface using TiO_2 and *E. coli* [18]. The loss of membrane structure and function is thought to cause cell death in photocatalytic processes [18, 43].

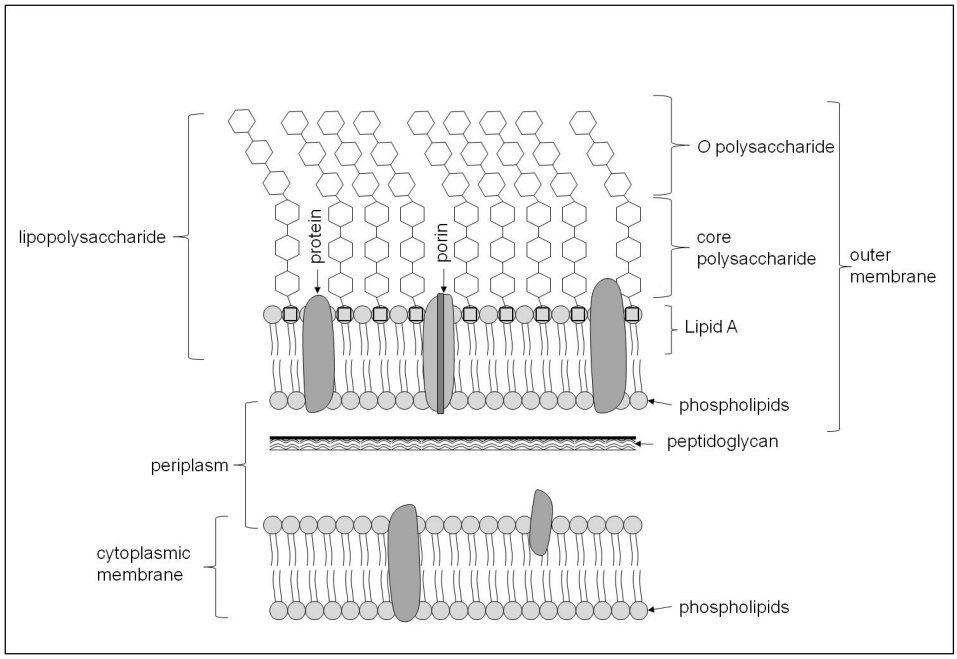

Figure 5.6: Cell wall structure for Gram-negative *E. coli* (adapted from [18])

The cell envelope of Gram-negative bacteria consists of two membranes, which are separated by the periplasm, containing a thin peptidoglycan layer. The outer membrane acts as a selective barrier preventing the entry of toxic molecules into the cell, which plays a major role in bacterial survival in hostile environments [44], such as in enabling *E. coli* to colonize the intestines of mammals due to the impermeability of the outer membrane to bile acids.

To elucidate the effects of photocatalytic damage to the outer membrane permeability, the cultivability of *E. coli* was monitored using LB medium supplemented with sodium cholate,

and the results are shown in Figure 5.7. Sodium cholate is a bile salt, which can be used to indicate the presence of outer membrane damages and bacterial sensitivity to membrane-perturbing agents [17]. It is dehydroxylated by bacteria to form a secondary bile acid, deoxycholate, which is a detergent that can solubilize lipids. It has been shown in literature that bacteria having an altered cell envelope are more sensitive to deoxycholate [45] due to the compromised integrity of their outer membranes.

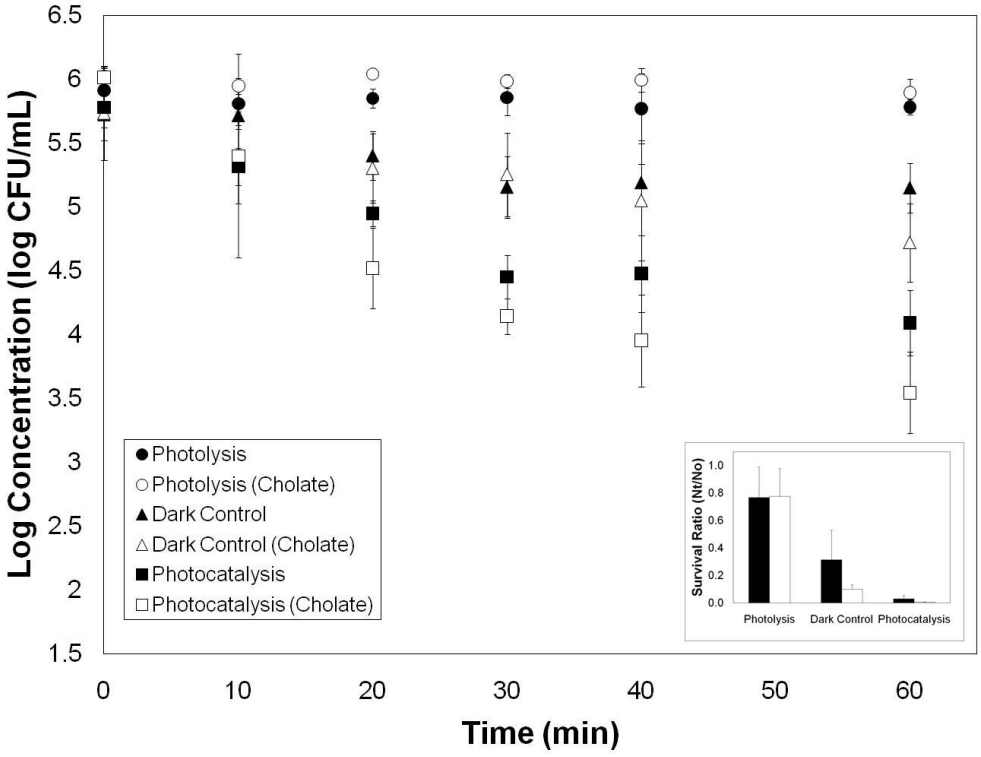

Figure 5.7: Comparison of inactivation curves using unmodified and sodium cholate-supplemented LB plates, respectively; final survival ratios shown inset. (composite loading = 5 g L^{-1}, pH = 5.5)

No modification in bacterial cultivability was observed in the photolytic process (in the absence of photocatalysis) on the sodium cholate-supplemented LB, and the inactivation curve followed closely that obtained using the standard LB medium. The final survival ratios were found to be 0.77 ± 0.22 and 0.77 ± 0.20 using standard LB and the cholate-supplemented medium, respectively. For the dark disinfection process (in the absence of

light), the bacterial cultivability using the supplemented medium was also similar to that using the standard medium, and the curves observed were nearly identical for the first forty minutes. The final survival ratios observed were 0.31 ± 0.22 and 0.10 ± 0.033 using the standard LB and the supplemented medium, respectively.

For photocatalysis-induced disinfection, the bacterial cultivabilities observed were systematically lower on the cholate-supplemented medium than on standard LB. This was hypothesized to be due to induced changes in the outer membrane permeability from the action of photocatalytic ROS, allowing for the penetration of deleterious substances such as the sodium cholate products. The final ratios observed were 0.030 ± 0.025 and 0.0046 ± 0.0045 using standard LB and the supplemented medium, respectively. Although this suggested that membrane permeability changes took place, the observed errors were high, so the results were inconclusive based on this study alone.

Changes to the cell membrane permeability during photocatalytic inactivation were therefore further probed by measuring the potassium ion (K^+) ion leakage from the cells, as per Saito et al. [42]. K^+ is a component that exists universally in bacteria, and is involved in the regulation of polysome content and in protein synthesis. The measurement of K^+ leakage from bacteria has been commonly used as a marker for indicating cell membrane damage in photocatalytic inactivation processes [40, 46–48]. It has been suggested that interaction of bacteria with the catalyst and ROS species may cause some initial changes to cell membrane permeability, which are reversible. However, upon increased attack upon cell wall layers, leakage of ions and small molecules occurs. This stage causes irreversible damage and ultimately leads to cell death [49]. The K^+ levels measured at various time intervals from a control in the absence of photocatalyst (photolysis), and for the photocatalytic process using Ag/AgCl-AC are shown in Figure 5.8.

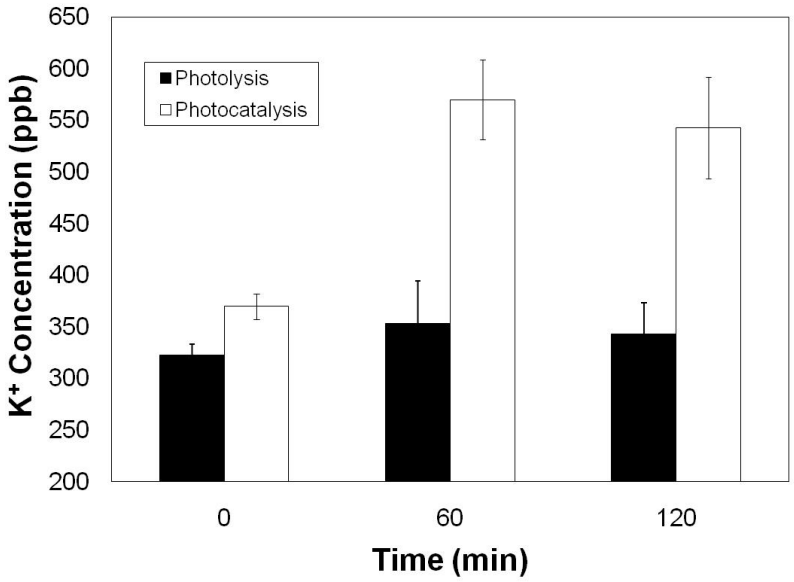

Figure 5.8: Potassium ion leakage from *E. coli* cells under various conditions ($C_o = 10^6$ CFU mL^{-1}, composite loading = 5 g L^{-1}, pH = 5.5)

In the case of irradiation in the absence of photocatalyst (photolysis), used as a baseline for comparison, the potassium ion concentration was found to be stable with time and did not change significantly after two hours. In contrast, the potassium ion concentrations increased markedly with time upon irradiation using the photocatalyst composite, in parallel with the temporal course of inactivation. This potassium ion leakage was in agreement with the results suggested by the sodium cholate assay, and evidenced the presence of changes in the cell membrane pemeability, which led to the leakage of intracellular components such as ionic potassium. The initial increase in potassium ion concentration (in the first sixty minutes) was thought to be due to damages on the outer membrane permeability. Since the concentration reached steady values and did not further increase in the next sixty minutes, the inner membrane may not have been completely eroded by the photogenerated radicals. Longer times may be neccesary to observe this phenomenon, which would cause a further spike in the potassium concentrations in solution, as reported in literature using UV-induced processes [46].

5.3.3.2 ATR-FTIR studies

To monitor changes to the cell structure upon exposure to photocatalytic inactivation, ATR-FTIR absorbances were studied at various time intervals in the reaction. The spectra obtained are given in Figures 5.9 and 5.10, respectively. Functional groups were referenced to the reported values for biomolecules and bacterial cells [18, 50–55].

From Figures 5.9 and 5.10, the characteristic peaks at ~3297 and 3080 cm^{-1} were observed due to amide A and amide B, respectively, while the peaks at 1653 and 1540 cm^{-1} arose from the ν(C=O) stretching vibrations in the amide I and the N–H bending with contributions from the C-N stretching vibrations of the peptide group. These characteristic peaks were found to decrease with increasing irradiation time, indicating changes to the secondary structure of the proteins in *E. coli* due to photocatalytic peroxidation [56]. The peaks observed between 3000–2800 cm^{-1} were assigned to the C–H stretching vibrations of $–CH_3$ and $–CH_2$ groups. This region is of interest for probing changes to cell membrane permeability because approximately 70% of the *E. coli* cell wall mass is composed of these bonds [55]. The peaks observed at 2963, 2921, 2876, and 2851 cm^{-1} were attributed to ν_a (CH_3), ν_a (CH_2), ν_s (CH_3), and ν_s (CH_2), respectively. These peaks decreased or disappeared upon exposure to photocatalytic inactivation, indicating changes to the C–H bonds in the fatty tails of lipid molecules. The bands around ~1242 cm^{-1} were associated with the asymmetric stretching mode of ν_a (PO_2^-) of the phospholipid phospho-diester present [18]. The peak observed at ~1072 was assigned to the vibrations of sugar rings in lipopolysaccharides [57], while other peaks between 1000 and 1200 cm^{-1} were attributed to other groups such as peptidoglycan and exo-polysaccharides [18]. The shapes of the peaks in the oligosaccharide region (1110 – 950 cm^{-1}) were modified upon exposure to photocatalysis. The results suggested that outer leaflet damage of *E. coli* occurred during the inactivation, in agreement with literature [18, 58] and with results obtained from permeability studies.

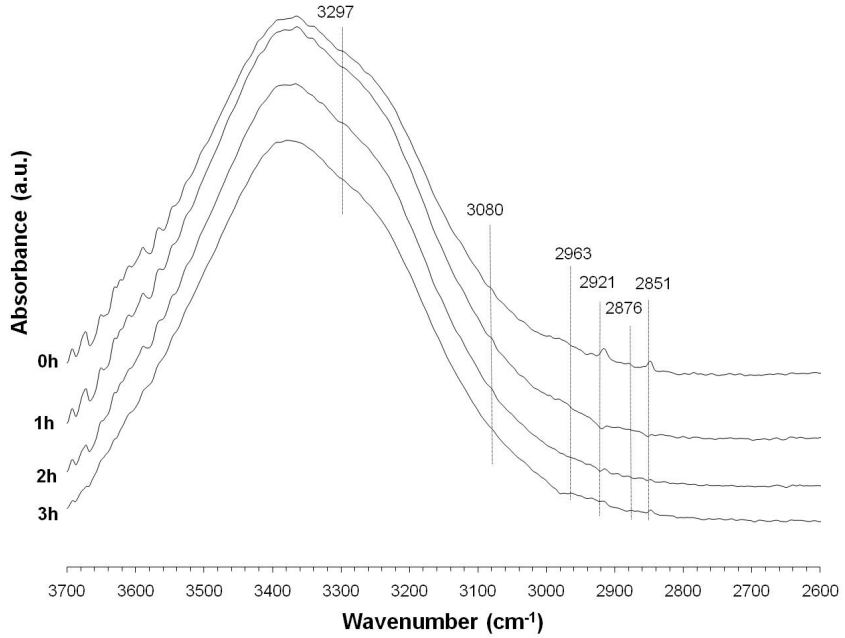

Figure 5.9: Changes to ATR-FTIR spectra of *E. coli* upon photocatalytic inactivation (bands in 3700–2600 cm^{-1} spectral region)

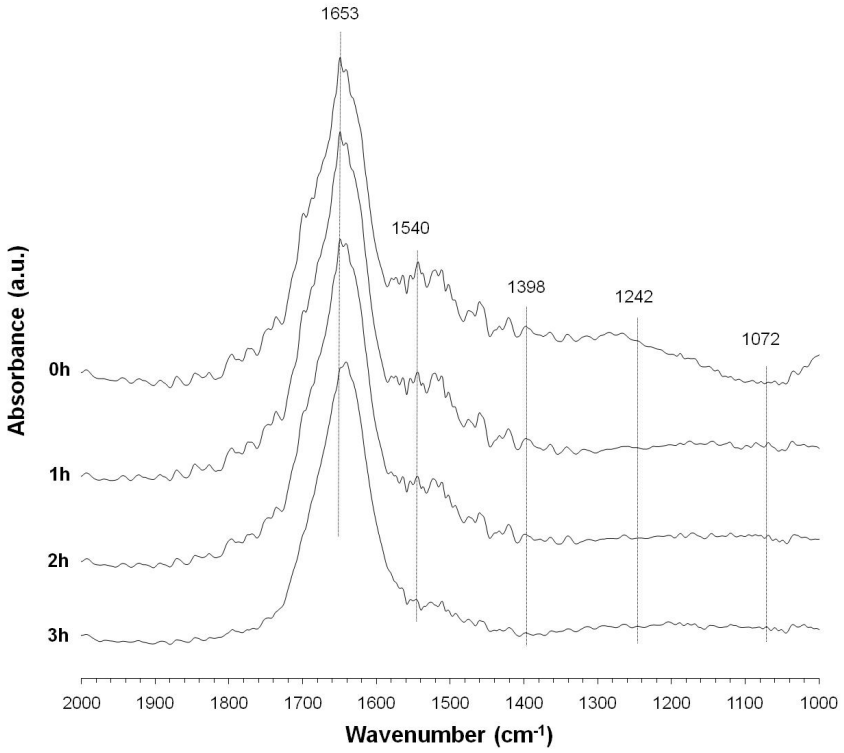

Figure 5.10: Changes to ATR-FTIR spectra of *E. coli* upon photocatalytic inactivation (bands in 2000–1000 cm^{-1} spectral region)

5.3.4 Mechanism of antibacterial and photocatalytic activity

The antibacterial activity of the composite in the absence of light was thought to be caused by elution of silver ions due to the irreversible oxidation of metallic nanosilver and the limited solubility of the AgCl carrier material to form dissolved silver in the form of Ag^{+}, $AgCl_{(aq)}$, or $AgCl_x^{1-x}{}_{(aq)}$ complexes. The free silver ions could then undergo speciation by binding to anionic ligands such as biological thiols or Cl^- present in growth medium or saline. The action of free silver ions and their soluble complexes on thiol-containing proteins is a major cause of silver ion toxicity to biological species [35]. Under irradiation (such as in the photoactivity studies), the silver ion speciation was further complicated by the precipitation of $AgCl_{(s)}$, which could form nanoparticles that could be reduced under photoirradiation [38]. This pathway may have been responsible for the regeneration of some Ag/AgCl species in the current system. The visible light activity of the composite was due to the surface plasmon resonance state of the incorporated nanosilver, which was able to produce electron-hole pairs. This plasmon resonance oscillation could also effectively polarize the charges such that the photo-produced electrons could be transferred to the silver surface farthest away from the AgCl interface, due to the negative surface charge on the latter, preventing reduction of the Ag^{+} species. The positively charged holes could then be transferred to the AgCl surface, promoting the stability of the photocatalyst. Additionally, this charge separation mechanism reduced the rate of electron-hole recombination [7]. The positively charged hole could oxidize water to produce hydroxyl radicals, oxidize Cl^- to produce active Cl^o, or interact with bacteria directly. The negatively charged electron could reduce dissolved oxygen to produce superoxide species and other ROS that participated in the inactivation of *E. coli* through action of photo-produced radicals on the cell membrane. The exposed activated carbon surfaces on the composite were thought to promote adsorption and contribute to bacterial adhesion. The process is shown schematically in Figure 5.11 for some proposed acting mechanisms.

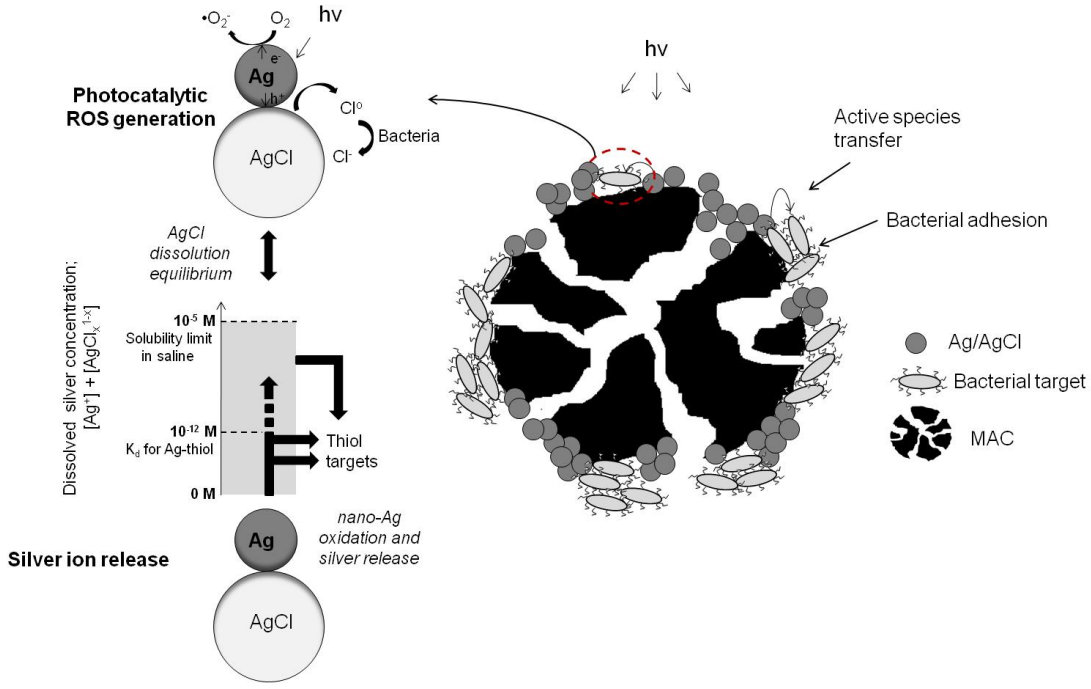

Figure 5.11: Acting mechanisms in bacterial inactivation using Ag/AgCl-AC composite (adapted from [38, 59])

5.4 Conclusions and recommendations

The inactivation of 97 ± 2.5% of *E. coli* K-12 was achieved in one hour under visible light irradiation in the presence of an Ag/AgCl-AC composite photocatalyst. The visible light induced photoactivity of the composite indicated its potential applicability to solar photocatalytic disinfection schemes. Incorporation of Ag/AgCl onto AC decreased the biocompatibility of the composite material, reducing risks of biofilm formation and biofouling in the adsorbent. Some inactivation activity was observed in the absence of light, and this was thought to be due to the effects of silver ion elution arising from oxidation of metallic silver nanoparticles and the limited solubility of AgCl. Under irradiation, the photocatalyst could become efficiently excited due to the surface plasmon resonance state of the nanosilver and electron-hole separation mechanism of the AgCl carrier. The contributions of the photocatalytic ROS species were thought to dominate the inactivation process. The mechanism of cell death was attributed to cell membrane damage and changes to cell permeability due to attack by ROS species. In the future, the presence and role of these photogenerated ROS should be confirmed by anaerobic experiments. Additionally, the

investigation of silver ion release behaviour in the photocatalytic process to determine its relative and synergistic role in relation to ROS generation should be investigated. Since silver-based antimicrobials generally exhibit broad-spectrum disinfection activity, the inactivation of other bacterial targets, such as *Bacillus subtilus* and *Pseudomonas putida* should also be considered.

5.5 Acknowledgments

This work was supported by the Natural Sciences and Engineering Research Council of Canada, the National Natural Science Foundation of China (Grant No. 50972037, 51172063, 5120256), and the Natural Science Foundation of Hebei Province, China (grant No. E2012401070). The authors would like to acknowledge Dr. Elena Baranova and Dr. Nimal De Silva from the University of Ottawa for help with FTIR, and ICP, respectively, and for providing useful discussion.

5.6 References

[1] T. Matsunaga, R. Tomoda, T. Nakajima, H. Wake, Photoelectrochemical sterilization of microbial cells by semiconductor powders, FEMS Microbiol. Lett. 29, 1–2 (1985) 211–214.

[2] P.S.M. Dunlop, J.A. Byrne, N. Manga, B.R. Eggins, Photocatalytic removal of bacterial pollutants from drinking water, J. Photochem. Photobiol., A. 148, 1–3 (2002) 355–363.

[3] J. Gamage, Z. Zhang, Applications of photocatalytic disinfection: A review, Int. J. Photoenergy, 2010 (2010) Article ID 764870. *(also given in Appendix B)*

[4] J.H. Pan, H. Dou, Z. Xiong, C. Xu, J. Ma, X.S. Zhao, Porous photocatalysts for advanced water purifications, J. Mater. Chem. 20 (2010) 4512–4528.

[5] J. Matos, J. Laine, J.-M. Herrmann, D. Uzcategui, J.L. Brito, Influence of activated carbon upon titania on aqueous photocatalytic consecutive runs of phenol photodegradation, Appl. Catal., B. 70 (2007) 461–469.

[6] T.-T. Lim, P.-S. Yap, M. Srinivasan, A.G. Fane, TiO_2/AC composites for synergistic adsorption-photocatalysis processes: Present challenges and further developments for water treatment and reclamation, Crit. Rev. Environ. Sci. Technol. 41 (2011) 1173–1230.

[7] P. Wang, B. Huang, X. Qin, X. Zhang, Y. Dai, J. Wei, M.-H. Whangbo, Ag@AgCl: A highly efficient and stable photocatalyst active under visible light, Angew. Chem. Int. Ed. 47 (2008) 7931–7933.

[8] W. Li, S. Liu, Bifunctional activated carbon with dual photocatalysis and adsorption capabilities for efficient phenol removal, Adsorption 18 (2012) 67–74.

[9] X. Wang, X. Tang, Z. Chen, T.-T. Lim, Highly stable heterostructured Ag/AgBr/TiO_2 composite: a bifunctional visible-light active photocatalyst for destruction of ibuprofen and bacteria, J. Mater. Chem. 22 (2012) 23149–23158.

[10] M. Tuncer, E. Sekey, Single step sol-gel made silver chloride on titania xerogels to inhibit *E. coli* bacteria growth: effect of preparation and chloride ion on bactericidal activity, J. Sol-gel Sci. Technol. 59 (2011) 304–310.

[11] O. Choi, K. Kanjun Deng, N.-J. Kim, L. Ross, R.Y. Surampalli, Z. Hu, The inhibitory effects of silver nanoparticles, silver ions, and silver chloride colloids on microbial growth, Water Res. 42 (2008) 3066–3074.

[12] S.-J. Park, Y.-S. Jang, Preparation and characterization of activated carbon fibers supported with silver metal for antibacterial behaviour, J. Colloid Surf. Sci. 261 (2003) 238–243.

[13] Y.L. Wang, Y.Z. Wan, X.H. Dong, G.X. Cheng, H.M. Tao T.Y. Wen, Preparation and characterization of antibacterial viscose-based activated carbon fiber supporting silver, Carbon 36, 11 (1998) 1567–1571.

[14] H. Le Pape, F. Solano-Serena, P. Contini, C. Devillers, A. Maftah, P. Leprat, Involvement of reactive oxygen species in the bactericidal activity of activated carbon fibre supporting silver: Bactericidal activity of ACF (Ag) mediated by ROS, J. Inorg. Biochem. 98 (2004) 1054–1060.

[15] B.A. Akgun, A.W. Wren, C. Durucan, M.R. Towler, N.P. Mellott, Sol-gel derived silver-incorporated titania thin films on glass: bactericidal and photocatalytic activity, J. Sol-gel Sci. Technol. 59 (2011) 228–238.

[16] Z. Zhang, W.A. Anderson, M. Moo-Young, Experimental analysis of a corrugated plate photocatalytic reactor, Chem. Eng. J. 99, 2 (2004) 145–152.

[17] S. Pigeot-Rémy, F. Simonet, E. Errazuriz-Cerda, J.C. Lazzaroni, D. Atlan, C. Guillard, Photocatalysis and disinfection of water: Identification of potential bacterial targets, Appl. Catal., B. 104 (2011) 390–398.

[18] J. Kiwi, V. Nadtochenko, Evidence for the mechanism of photocatalytic degradation of the bacterial wall membrane at the TiO_2 interface by ATR-FTIR and laser kinetic spectroscopy, Langmuir 21 (2005) 4631–4641.

[19] Y. Etzion, R. Linker, U. Cogan, I. Shmulevich, Determination of protein concentration in raw milk by mid-infrared Fourier transform infrared/attenuated total reflectance spectroscopy, J. Dairy Sci. 87 (2004) 2779–2788.

[20] F. Dousseau, M. Therrien, M. Pézolet, On the spectral subtraction of water from the FT-IR spectra of aqueous solutions of proteins, Appl. Spectrosc. 43, 3 (1989) 538–542.

[21] M. Nara, N. Yonezawa, T. Shimada, K. Takahashi, M. Tanokura, F. Yumoto, H. Nakagawaz, J. Ohashi, S. Hamano, M. Nakano, Fourier transform infrared spectroscopic analysis of the intact zona pellucid of the mammalian egg: Changes in the secondary structure of bovine zona pellucid proteins during fertilization, Exp. Biol. Med. 231 (2006) 166–171.

[22] J. Marugán, R. van Grieken, C. Pablos, C. Sordo, Analogies and differences between photocatalytic oxidation of chemicals and photocatalytic inactivation of microorganisms, Water Res. 44, 3 (2010) 789–796.

[23] L. Dong, D. Liang, R. Gong, In situ photoactivated AgCl/Ag nanocomposites with enhanced visible light photocatalytic and antibacterial activity, Eur. J. Inorg. Chem. 2012, 19 (2012) 3200–3208.

[24] O. Akhavan, Lasting antibacterial activities of Ag - TiO_2/Ag/a-TiO_2 nanocomposite thin film photocatalysts under solar light irradiation, J. Colloid Interface Sci. 336 (2009) 117–124.

[25] M. Li, M.E. Noriega-Trevino, N. Nino-Martinez, C. Marambio-Jones, J. Wang, R. Damoiseaux, F. Ruiz, E.M.V. Hoek, Synergistic bactericidal activity of Ag-TiO_2 nanoparticles in both light and dark conditions, Environ. Sci. Technol. 45 (2011) 8989–8995.

[26] X. Zhang, L. Lei, Effect of preparation methods on the structure and catalytic performance of TiO_2/AC photocatalysts, J. Hazard. Mater. 153 (2008) 827–833.

[27] B. Gao, P.S. Yap, T.M. Lim, T.-T. Lim, Adsorption-photocatalytic degradation of Acid Red 88 supported TiO_2: Effect of activated carbon support and aqueous anions, Chem. Eng. J. 171 (2011) 1098–1107.

[28] A. Kubacka, M. Ferrer, A. Martínez-Arias, M. Fernández-García, Ag promotion of TiO_2 –anatase disinfection capability: Study of *Escherichia coli* inactivation, Appl. Catal., B. 84 (2008) 87–93.

[29] Z.-M. Xiu, Q.-B. Zhang, H.L. Puppala, V.L. Colvin, P.J.J. Alvarez, Negligible particle-specific antibacterial activity of silver nanoparticles, Nano Lett. 12, 8 (2012) 4271–4275.

[30] B. Naik, V. Desai, M. Kowshik, V. S. Prasad, G.F. Fernando, N.N. Ghosh, Synthesis of Ag/AgCl-mesoporous nanocomposites using a simple aqueous solution-based chemical method and a study of their antibacterial activity on *E. coli*, Particuology 9 (2011) 243–247.

[31] C. Marambio-Jones, E.M.V. Hoek, A review of the antibacterial effects of silver nanomaterials and potential implications for human health and the environment, J. Nanopart. Res. 12 (2010) 1531–1551.

[32] K. Holt, A. Bard, Interaction of silver (I) ions with the respiratory chain of *Escherichia coli*: an electrochemical and scanning electrochemical study of the antimicrobial mechanism of micromolar Ag, Biochemistry 44 (2005) 13214–13223.

[33] C. Lok, C. Ho, R. Chen, Q. He, W. Yu, H. Sun, P. Tam, J. Chiu, C. Che, Proteomic analysis of the mode of antibacterial action of silver nanoparticles, J. Proteome Res. 5 (2006) 916–924.

[34] H. Petering, Pharmacology and toxicology of heavy-metal silver, Pharmacol. Ther. A. 1 (1976) 127–130.

[35] S. Liau, D. Read, W. Pugh, J. Furr, A. Russell, Interaction of silver nitrate with readily identifiable groups: relationship to the antibacterial action of silver ions, Lett. Appl. Microbiol. 25 (1997) 279–283.

[36] W. Jung, H. Koo, K. Kim, S. Shin, S. Kim, Y. Park, Antibacterial activity and mechanism of action of the silver ion in *Staphylococcus aureus* and *Escherichia coli*, Appl. Environ. Microbiol. 74 (2008) 2171–2178.

[37] Q. Fend, J. Wu, G. Chen, F. Cui, T. Kim, J. Kim, A mechanistic study of the antibacterial effect of silver ions on *Escherichia coli* and *Staphylococcus aureus*, J. Biomed. Mater. Res. 52 (2000) 662–668.

[38] J. Liu, D.A. Sonshine, S. Shervani, R.H. Hurt, Controlled release of biologically active silver from nanosilver surfaces, ACS Nano 4, 11 (2010) 6903–6913.

[39] M.N. Birmele, L.E. McCoy, M.S. Roberts, Disinfection of spacecraft potable water systems by passivation with ionic silver, NASA Technical Report; available at: http://ntrs.nasa.gov/archive/nasa/casi.ntrs.nasa.gov/20110014435_2011014957.pdf; accessed Dec. 10, 2012.

[40] L.S. Zhang, K.H. Wong, H.Y. Yip, C. Hu, J.C. Yu, C.Y. Chan, P.K. Wong, Effective photocatalytic disinfection of *E. coli* K-12 using AgBr-Ag-Bi_2WO_6 nanojunction system irradiated by visible light: The role of diffusing hydroxyl radicals, Environ. Sci. Technol. 44 (2010) 1392–1398.

[41] C. Pulgarin, J. Kiwi, V. Nadtochenko, Mechanism of photocatalytic bacterial inactivation on TiO_2 films involving cell-wall damage and lysis, Appl. Catal., B. 127, 30 (2012) 179–183.

[42] T. Saito, T. Iwase, J. Horie, T. Morioka, Mode of photocatalytic bactericidal action of powdered semiconductor TiO_2 on mutans streptococci, J. Photochem. Photobiol., B. 14 (1992) 369–379.

[43] P.-C.Maness, S. Smolinski, D.M. Blake, Z. Huang, E.J. Wolfrum, W.A. Jacoby, Bactericidal activity of photocatalytic TiO_2 reaction: Toward and understanding of its killing mechanism, Appl. Environ. Microbiol. 65, 9 (1999) 4094–4098.

[44] M. Vaara, Agents that increase the permeability of the outer membrane, Microbiol. Rev. 56 (1992) 395–411.

[45] J.C. Lazzaroni, R.C. Portalier, Genetic and biochemical characterization of periplasmic-leaky mutants of *Escherichia coli* K-12, J. Bacteriol. 145 (1981) 1351–1358.

[46] Z.-X. Lu, L. Zhou, Z.-L. Zhang, W.-L. Shi, Z.-X. Xie, H.-Y. Xie, D.-W. Pang, P. Shen, Cell damage induced by photocatalysis of TiO_2 thin films, Langmuir 19 (2003) 8765–8768.

[47] C. Hu, J. Guo, J. Qu, X. Hu, Photocatalytic degradation of pathogenic bacteria with AgI/TiO_2 under visible light irradiation, Langmuir 23 (2007) 4982–4987.

[48] J. Ren, W. Wang, L. Zhang, J. Cheng, S. Hu, Photocatalytic inactivation of bacteria by photocatalyst Bi_2WO_6 under visible light, Catal. Commun. 10 (2009) 1940–1943.

[49] H.A. Foster, I.B. Ditta, S. Varghese, A. Steele, Photocatalytic disinfection using titanium dioxide: spectrum and mechanism of antimicrobial activity, Appl. Microbiol. Biotechnol. 90 (2011) 1847–1868.

[50] D. Naumann, Infrared Spectroscopy. In Microbiology Encylopedia of Analytical Chemistry; Meyers, R.A. Ed. John Wiley and Sons Ltd.: Chinchester, UK. 2000 p.102

[51] C. Schultz, D. Naumann, In vivo study of order of the membranes of Gram-negative bacteria by Fourier-transform infrared spectroscopy (FT-IR), FEBS Lett. 294 (1991) 43–46.

[52] D. Helm, D. Naumann, Identicification of some bacterial cell components by FT-IR spectroscopy, FEMS Microbiol. Lett. 126 (1995) 75–79.

[53] W. Zeroual, C. Choisy, S.M. Doglia, H. Bobichon, J.F. Angiboust, M. Manfait, Monitoring of bacterial growth and structural analysis as probed by FT-IR spectroscopy, Biochim. Biophys. Acta 1222 (1994) 171–178.

[54] M. Gué, V. Dupont, A. Dufour, O. Sire, Bacterial swarming: A biochemical time-resolved FTIR-ATR study of *Proteus mirabilis* swarm-cell differentiation, Biochemistry 40 (2001) 11938–11945.

[55] V.A. Nadtochenko, A.G. Rinćon, S.E. Stanca, J. Kiwi, Dynamics of *E. coli* membrane cell peroxidation during TiO_2 photocatalysis studied by ATR-FTIR spectroscopy and AFM microscopy, J. Photochem. Photobiol., A. 169 (2004) 131–137.

[56] G. Vedantham, H. G. Sparks, S.U. Sane, S. Tzannis, T.M. Przybycien, A holistic approach for protein secondary structure estimated from infrared spectra in H_2O solutions, Anal. Biochem. 285 (2000) 33–49.

[57] Y. Hou, X. Li, Q. Zhao, G. Chen, C.L. Raston, Role of hydroxyl radicals and mechanism of *Escherichia coli* inactivation on Ag/AgBr/TiO_2 nanotube array electrode under visible light irradiation, Environ. Sci. Technol. 46, 7 (2012) 4042–4050.

[58] Q. Wang, T. Fan, P. Liu, X. Min, X. Li, Study of the bioeffects of CdTe quantum dots on *Escherichia coli* cells, J. Colloid Interface Sci. 363 (2011) 476–480.

[59] K.Y. Foo, B.H. Hameed, Decontamination of textile wastewater via TiO_2/activated carbon composite materials, Adv. Colloid Interface Sci. 159 (2010) 130–143.

[Editorial note: Select graphics in Chapter 6 appear in the associated journal contribution as supplementary material.]

Chapter 6:

Synthesis and characterization of magnetically separable Ag/AgCl-magnetic activated carbon composites for visible light induced detoxification and disinfection

Joanne Gamage McEvoy, Zisheng Zhang

Applied Catalysis B: Environmental (2014), in press.

Abstract

A magnetic adsorbent photocatalyst composite Ag/AgCl-magnetic activated carbon (A-MAC) was proposed and investigated. Magnetic activated carbon was prepared by impregnation of AC with silica-coated magnetite particles synthesized via chemical co-precipitation and a modified Stöber process, and was then used to synthesize Ag/AgCl-MAC composites by a facile deposition-precipitation-photoreduction method. The prepared composites were characterized by X-ray diffraction, transmission and scanning electron microscopies, respectively, X-ray photoelectron spectroscopy, N_2 sorption, and ultraviolet-visible light diffuse reflectance spectroscopy. The magnetic properties of the composites were studied by superconducting quantum interference device magnetometry, and they were found to exhibit quasi-superparamagnetic behaviour. The visible light induced photoactivities of the samples were studied for the degradation of model organic pollutants, methyl orange and phenol, and cyclic degradation experiments were performed by recovering the composite by magnetic separation between runs. The prepared composites were also found to possess good activity for photocatalytic disinfection, inducing a 3-log reduction in *Escherichia coli* K-12 in 40 minutes under irradiation. The incorporation of silica-coated magnetite into AC was thought to influence morphology in the final photocatalyst-adsorbent composites, and the role of silica in preventing iron oxide dissolution in the photoreactive system was investigated and discussed.

Keywords: Ag/AgCl, magnetic photocatalyst, activated carbon, adsorbent photocatalyst

6.1 Introduction

In recent years, efforts towards the development of solar photocatalysis have been made with the goal of improving process efficiencies in order to realize the scalability and practical utilization of this advanced oxidation process for the abatement of pollutants in a number of environmental effluents, such as for the treatment of recalcitrant dyes and polyhalogenated organics in industrial wastewaters. Of particular interest is the design and fabrication of highly efficient photocatalytic materials that can be excited by visible light abundant in solar irradiation, which are engineered to possess low rates of recombination of the photo-excited electrons and holes [1]. These photocatalysts may overcome some of the difficulties inherent to use of traditional photocatalytic TiO_2, such as its large band gap energy (E_{bg} = 3.2 eV).

One such material explored is the silver/silver halide composite photocatalyst [2], which possesses high efficiency for visible light utilization and low rates of electron-hole recombination due to localized surface plasmon resonance exhibited by the incorporated silver nanoparticles. This phenomenon gives rise to unique optical properties arising from the collective oscillation of conduction electrons upon interaction with electromagnetic radiation, and can result in amplified absorption of visible light depending on size and morphology of the nanoparticles. In the silver/silver halide system, nanosilver and silver halide act in concert to polarize the photoinduced charges, which facilitates electron-hole separation. Additionally, the silver halide can produce oxidizing species such as Cl^o or Br^o (for Ag/AgCl and Ag/AgBr, respectively), which enhance photodegradation [3].

Another approach to increasing photocatalyst efficiency involves the improvement of mass transfer characteristics by immobilization on or incorporation of porous media with the catalyst [4, 5]. Synergistic increases in the activity of TiO_2-activated carbon composites have been reported, and are attributed to the presence of a common contact interface between the solids, where the AC captures the pollutants by adsorption, allowing them to migrate continuously to the supported photocatalyst due to the presence of concentration gradients [6]. However, the need for incorporation of visible light active photocatalysts into these AC composites was emphasized in literature [7]. Additionally, such composites were reported to

suffer from biofouling and the formation of biofilms, due to the biocompatibility of AC.

To address practical issues related to separation of suspended photocatalysts from slurry, the development of magnetically recoverable photocatalysts has become an active field of research. These photocatalysts may be two-component magnetic core@photocatalyst shell structures (such as Fe_3O_4@TiO_2 [8], γ-Fe_2O_3@TiO_2 [9]) or three component core@insulating interlayer@shell to prevent reaction between the photocatalyst and magnetic component itself (such as in Fe_3O_4@SiO_2@TiO_2 [10], and the surface plasmon resonance enhanced Fe_3O_4@SiO_2@AgCl:Ag [11]). Ao et al. first proposed the hybridization of magnetic removal strategies with adsorbent photocatalyst composites by synthesizing TiO_2-magnetic activated carbon composites, prepared by the impregnation of mixed-phase iron oxides into activated carbon, followed by sol-gel synthesis to deposit TiO_2 photocatalyst into the composite [12], and evaluated the photocatalytic activity for phenol degradation under ultraviolet (UV) light. Subsequent studies also investigated the photodegradation of an azo dye under visible and UV irradiation [13], and preparation of the composite using visible light active N-doped TiO_2 as the photocatalyst component [14]. In some cases, a photodissolution of the iron oxides was observed, since no SiO_2 passivation layer was used.

In our previous work, we proposed and developed Ag/AgCl-AC composites to address the need for more efficient visible light utilization of adsorbent photocatalyst materials, and tested their photoactivity for the degradation of organic pollutants, methyl orange dye (MO) and phenol [15]. In these composites, nanosilver acted by surface plasmon resonance to induce enhanced visible light activity, while the silver and silver halide promoted charge separation, and AC concentrated the pollutant around the supported active sites. Due to the reported photocatalytic disinfection activity of silver/silver halide structures [16], and because of interest in impregnated nanosilver for the reduction of AC biocompatibility [17–19], the developed Ag/AgCl-AC composites were also studied for the photocatalytic inactivation of *Escherichia coli (E. coli)* K-12 under visible light, and the antibacterial and photocatalytic disinfective capabilities of the catalyst were confirmed [20]. In the current study, we extend our previous work on the surface plasmon resonance enhanced Ag/AgCl-

AC composites towards magnetic removal strategies by the incorporation of magnetic activated carbon to synthesize Ag/AgCl-magnetic AC composites (Ag/AgCl-MAC) and examine their activity for visible light induced degradation of organic and biological model pollutants.

6.2 Experimental

6.2.1 Materials

All materials were obtained from Fisher Scientific, unless otherwise mentioned, and were of reagent-grade or higher purity.

6.2.2 Synthesis of Ag/AgCl-magnetic activated carbon

6.2.2.1 Synthesis of silica-coated Fe_3O_4 nanoparticles

Magnetic Fe_3O_4 nanoparticles were synthesized by chemical co-precipitation of $FeCl_3 \cdot 6H_2O$ and $FeSO_4 \cdot 7H_2O$ at a molar ratio of 2.6:1. The iron salts were mixed in 100 mL of distilled deionized water at 70^{o}C under vigorous stirring [21, 22]. A 2 M solution of NaOH was added dropwise until the pH was approximately 11. The black solution formed was maintained at 70^{o}C under magnetic stirring for 1 h to ensure growth of the nanoparticles, and the mixture was then cooled to room temperature (~25^{o}C) in ambient air. The precipitate was collected by magnetic separation, and was rinsed with distilled deionized water multiple times to obtain a neutral pH in the product. The black Fe_3O_4 particles were then were rinsed three times with absolute ethanol, filtered, dried overnight, and ground in an agate mortar for 2 minutes.

Silica coating of the obtained Fe_3O_4 nanoparticles was performed using a modified Stöber process [11, 23]. A dispersion of 1 g Fe_3O_4 nanoparticles in 20 mL of 0.1 M sodium dodecyl sulphate was prepared by sonication for 10 minutes. The mixture was vigorously stirred for 30 minutes, followed by the successive addition of 20 mL of absolute ethanol, 6 mL of concentrated ammonia (14 N), and 5 mL of tetraethyl orthosilicate. The reaction was maintained at 50^{o}C for 3 h, and the grey silica-coated Fe_3O_4 nanoparticles obtained were separated magnetically, rinsed with distilled deionized water and absolute ethanol three

times, and dried at room temperature overnight.

6.2.2.2 Synthesis of magnetic activated carbon (MAC)

Magnetic activated carbon was prepared by impregnation of unmodified commercial Darco G60 activated carbon (100 mesh, Sigma-Aldrich) with the silica-coated magnetic iron oxide nanoparticles. Activated carbon was added in a certain amount to a solution of 0.6 g of coated nanoparticles in 200 mL water, which had previously been dispersed by sonication for 10 minutes. The activated carbon-nanoparticle mixture was then stirred for 1 hour, and the solid phase was collected by a magnet and dried at 40^{o}C. The silica-coated nanoparticles and AC were mixed at various weight ratios, as described in Table 6.1.

6.2.2.3 Synthesis of Ag/AgCl-MAC

Ag/AgCl-MAC composites were prepared using an impregnation-precipitation-photoreduction method, as previously reported for the synthesis of Ag/AgCl-AC [15]. The weight ratio of Ag/AgCl to activated carbon was maintained at 2.5:1 in all of the composites, calculated as if all of the AgCl was reduced to Ag. The weight ratios and equivalent weight fractions of the components in the prepared Ag/AgCl-MAC composites are shown in Table 6.1, where Ag/AgCl- MAC is denoted by A-MAC, and Ag/AgCl-AC is denoted A-AC.

Table 6.1: Composition of Ag/AgCl-MAC photocatalysts prepared at various weight ratios

Catalyst	**Weight ratios**		**Equivalent weight fractions**		
	SiO_2-iron oxide: AC	SiO_2-iron oxide: AC: Ag/AgCl	SiO_2-iron oxide	AC	Ag/AgCl
1:3 A-MAC	1:3	0.33: 1: 2.5	0.0862	0.261	0.653
1:5 A-MAC	1:5	0.2: 1: 2.5	0.0541	0.270	0.676
1:7 A-MAC	1:7	0.14: 1: 2.5	0.0385	0.275	0.687
A-AC	-	0: 1: 2.5	0	0.286	0.714

6.2.3 Characterization

X-ray diffraction (XRD) patterns were collected using a Rigaku Ultima IV XRD apparatus with a CuK(α) source (λ = 0.15418 nm) operating at 40 kV and 44 mA. Transmission electron microscopy imaging was performed using a FEI (formerly Phillips) Tecnai F20 G2 field emission transmission electron microscope (TEM) equipped with an energy dispersive X-ray (EDS) detector for spectrometry. Histograms of particle size distributions were

constructed using particle size measurements made on digital TEM images with Canon MeasureIT software. The morphology of the samples was investigated using a Tescan VegaII XMU field emission scanning electron microscope (SEM), with Au/Pd alloy coated samples (coated with an Anatech Hummer VII sputter coater). X-ray photoelectron spectroscopy (XPS) was studied on a Kratos Analytical Axis Ultra DLD instrument, using monochromated Al X-rays at 140 W. The surface areas, total pore volumes, and microporosity data were obtained from N_2 sorption isotherms at 77 K, using automatic adsorption apparatus and measurement systems (ASAP 2020, Micromeritics and Nova 4200E, Quantachrome). The Brunauer, Emmett, and Teller (BET) surface areas of the samples were calculated using a multi-point estimation, the total pore volumes were calculated using the volumes of adsorbed N_2 at P/Po = 0.977, and the *t*-plot method was used to calculate micropore volumes and external surface areas. The Barrett-Joyner-Halenda method was used for the adsorption branch to calculate the pore size data. Ultraviolet-visible (UV-Vis) diffuse reflectance spectra were measured on a Thermo Evolution 300 spectrophotometer (ThermoScientific) equipped with a Praying Mantis diffuse reflectance accessory over the range of 230 – 900 nm. Isothermal magnetization data was collected in the field range from $-4x10^4 – 4x10^4$ Oe at 300 K using a Quantum Design magnetic properties measurement system (MPMS) superconducting quantum interference device (SQUID).

6.2.4 Photocatalytic degradation

6.2.4.1 Photoreactor

To quantify photocatalytic degradation, a slurry reactor was used in a constructed reflective housing to prevent outside light from entering the system. Illumination was provided by a 300 W ELH tungsten halide bulb (Ushio) with a UV filter (Kenko Zeta, $\lambda > 410$ nm, transmittance > 90%) at a distance of 10 cm from the beaker. The irradiation was measured using a quantum meter (Biospherical QSL-2100; 400 nm < λ < 700 nm), and was found to be approximately $4.7x10^{-3}$ Einstein m^{-2} s^{-1}. Cooling was provided by an external cooling jacket, and the temperature of the reaction was controlled to $20^oC \pm 2$.

6.2.4.2 Photodegradation of methyl orange (MO)

For the photocatalysis tests, 200 mL of MO solution was allowed to equilibriate in the dark

with 0.5 g L^{-1} of catalyst under constant magnetic stirring at 180 rpm for 2 hours prior to each experiment. Photocatalytic degradation was then performed for 2.5 hours in the presence of visible light irradiation. For all tests, samples were drawn periodically, centrifuged, and the supernatant was analyzed at a single wavelength using a spectrophometer (Genesys 10UV, ThermoScientific). The peak absorbance used for MO was λ = 463 nm. The initial MO concentration was 25 mg L^{-1}. The MO removal from solution was expressed relative to the catalyst loading, and was given by q_t (mg MO g $catalyst^{-1}$), calculated according to eq. (6.1).

$$q_t = V(C_i - C_t)/W \qquad (6.1)$$

where the initial MO concentration in the aqueous phase, and that at time t (min) are denoted by C_i and C_t, respectively (mg L^{-1}), V is the volume of MO solution (L), and W is the mass of composite used (g). The broad-scan UV-Vis data for MO adsorption and degradation was collected on a Biochrom Ultrospec 60 UV/Vis spectrophotometer. To evaluate the magnetic recovery and recyclability of the composite, cyclic adsorption-photocatalysis runs were performed by recovering the catalyst magnetically between cycles and redispersing it into fresh MO solution before each re-use. Photolysis was measured by MO degradation in the absence of catalyst, and the error associated to the experiments was estimated as the standard deviation between triplicate runs.

6.2.4.3 Photodegradation of phenol

Adsorption and photodegradation of phenol was also studied in the photosystem using the same methodology described for MO experiments (200 mL solution, composite loading of 0.5 g L^{-1}, magnetic stir speed of 180 rpm, unadjusted pH), but the initial concentration used was 13 mg L^{-1}, and the supernatant was analyzed spectrophotometrically at a peak absorbance of λ = 270 nm. The photocatalytic degradation of phenol was carried out for 3 hours after the initial dark adsorption period.

6.2.5 Iron oxide photodissolution

Iron oxide photodissolution was investigated by monitoring Fe^{+} concentration in solution using inductively coupled plasma mass spectrometry (ICP-MS) on an Agilent HP 4500. A 5 g L^{-1} slurry of A-MAC catalyst in 50 mL distilled deionized water was magnetically stirred

under irradiation at 180 rpm for 2.5 hours, and samples were withdrawn periodically. The catalyst was then separated by centrifugation at 14 800 rpm for 5 minutes, and the supernatant was removed and stabilized with 5 vol% nitric acid prior to analysis. The trials were performed for the 1:7 A-MAC composite, and for a reference 1:7 A-MAC material prepared using iron oxide nanoparticles with no silica coating.

6.2.6 Silver ion elution

The elution of silver ions (Ag^{+}) from the prepared A-MAC composite was also measured using ICP-MS. 5 g L^{-1} of catalyst (1:5 A-MAC) in 50 mL distilled deionized water was magnetically stirred at 160 rpm in the dark for 1 hour, and 1 mL samples were withdrawn periodically. The samples were centrifuged and the supernatant was removed and acidified before analysis. For all ICP measurements, the analyses were performed for triplicate samples.

6.2.7 Photocatalytic disinfection

6.2.7.1 Bacterial strain

Wild-type *E. coli* K-12 (TG1 strain) was used for all bacterial inactivation studies, due to its non-pathogenicity and its use as a common model in laboratory experiments. It was obtained from Dr. Christopher Q. Lan in the Department of Chemical and Biological Engineering at the University of Ottawa, and was maintained as a laboratory strain.

6.2.7.2 Cell culture and enumeration

All inactivation trials were performed in triplicate, and all materials were sterilized for 20 minutes at 121^{o}C prior to use. The inactivation was quantified as loss of culturability of the bacteria in the disinfection studies. Bacterial cultures were prepared by growing *E. coli* K-12 (TG1) aerobically in Luria-Bertani medium (Difco LB broth, Miller; containing 10 g L^{-1} tryptone, 5 g L^{-1} yeast extract, and 10 g L^{-1} NaCl) on a rotary shaker at 37^{o}C for 14 hours until the stationary phase was reached. The initial concentration from the overnight culture was determined by serial dilution and plating using a plated volume of 25 µL. Aliquots were spread on solid LB agar plates in triplicate for each dilution, and incubated at 37^{o}C for 18 hours. Bacterial enumeration was performed using standard plate counts for viable and cultivable bacteria, and counts obtained were used to calculate the cell concentration in

colony forming units (CFU) mL^{-1}.

6.2.7.3 Temporal course of inactivation

The temporal course of inactivation was studied using 50 mL of saline (0.9 wt% NaCl) spiked with bacteria in a 100 mL Pyrex beaker. The initial bacterial suspension was prepared by centrifuging 1 mL of bacterial culture at 14 800 rpm for 5 minutes and resuspending the pellet in saline. This centrifugation and washing procedure was repeated three times to remove the growth media. The bacterial suspension was then used to prepare the spiked solution, controlling the initial concentration to ~10^6 CFU mL^{-1}. Catalyst was then added to the bacterial suspension at a loading of 5 g L^{-1}, and the mixture was magnetically stirred at 160 rpm under visible light irradiation (provided by a filtered 300 W Ushio ELH lamp). During the disinfection, the temperature was maintained constant at $20^oC \pm 2$ using a water bath, and samples were collected periodically. The samples were serially diluted in saline and spread onto LB agar plates using aliquot volumes ranging from 25 – 200 μL. The plates were then incubated and bacteria enumerated using the standard plate count method. Control runs were performed in the absence of photocatalyst and light, respectively.

6.3 Results and discussion

6.3.1 Catalyst characterization

6.3.1.1 X-ray diffraction

The phase structure and crystallinity of the prepared materials were investigated by XRD, and the results are given in Figure 6.1 for the prepared iron oxide and magnetic activated carbons, respectively. The diffraction patterns obtained for the pure iron oxide was well-indexed to the cubic spinel structure of magnetite, and characteristic peaks at 18.3^o, 30.1^o, 35.4^o, 37.1^o, 43.1^o, 53.4^o, 56.9^o, 62.5^o were observed, corresponding to the (111), (220), (311), (440), (422), (511), and (440) faces respectively, in good agreement with JCPDS card #19-0629.

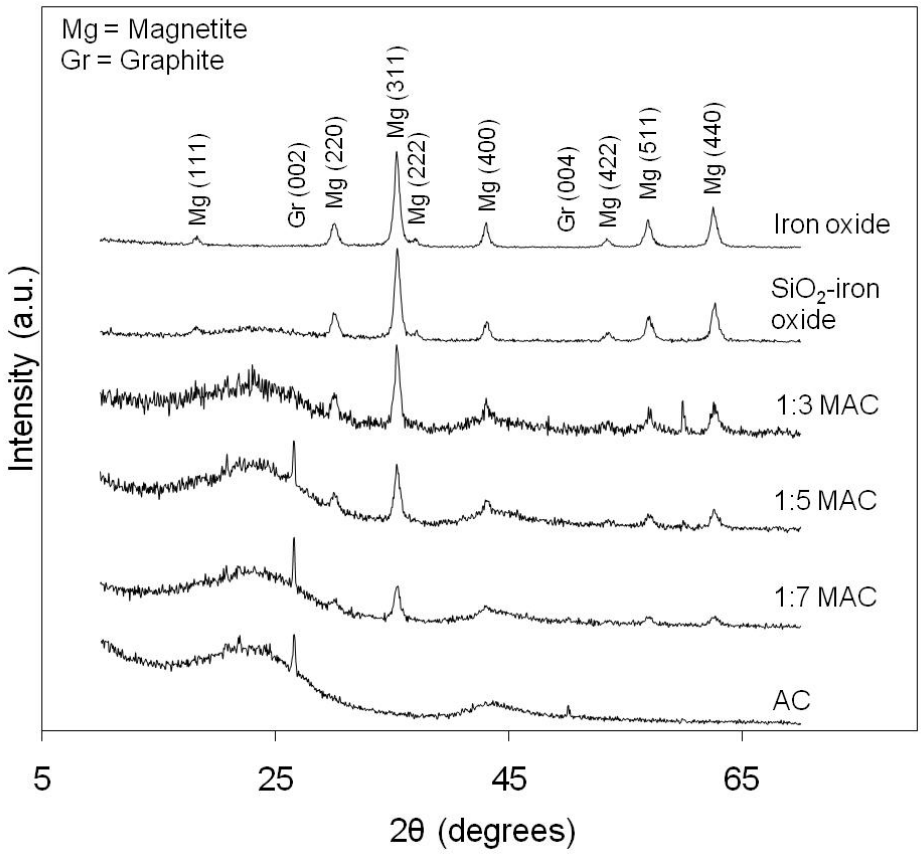

Figure 6.1: XRD patterns for iron oxide, SiO_2-iron oxide, AC, and magnetic AC prepared at various ratios

Upon introduction of the silica coating, the patterns observed contained the same characteristic magnetite peaks, as well as a small broad amorphous halo due to SiO_2 between $20^o – 30^o$. The unmodified AC also exhibited mainly amorphous structure, with the exception of hexagonal (002) and (004) graphitic peaks, which indicated that small regions of crystallinity were present [24]. The XRD patterns for all prepared magnetic AC materials exhibited the characteristic peaks observed for the magnetite phase, as well as the (002) graphite plane, except for the MAC prepared with a magnetic particle loading of 1:3. In the 1:3 MAC pattern, the graphitic peak was not noticeable due to the relatively lower activated carbon content in the magnetic material, in accordance with the compositions given in Table 6.1. The appearance of a peak at ~60^o also suggested the transformation of some magnetite into an impurity phase, such as the less magnetic maghemite, or nonmagnetic goethitic iron

oxide in accordance with JCDPS card #29-0713. The formation of this impurity phase may have been caused by the overloading of activated carbon with magnetite nanoparticles and their subsequent transformations, especially upon prolonged exposure to the oxidative environment used during the drying step in the MAC synthesis. The formation of the less-magnetic maghemite phase from oxidation of magnetite has been found to be dependent on a number of experimental and environmental conditions, such as the particle sizes of magnetite, water content, and temperature [25, 26]. Nonmagnetic goethite may have been formed from this maghemite oxidation product, and the direct formation of goethite from magnetite may have also occurred in this system [27]. These transformations were not as pronounced for the materials prepared using lower iron oxide: AC ratios.

The XRD patterns of composite A-MAC photocatalysts were also investigated, and the results are given in Figure 6.2, with pure Ag/AgCl and the nonmagnetic Ag/AgCl-AC shown for reference. All of the patterns observed exhibited peaks at 27.8^{o}, 32.2^{o}, 46.2^{o}, 54.8^{o}, 57.5^{o}, and 67.5^{o} corresponding to the (110), (200), (220), (331), (222), and (400) reflections of chlorargyrite (JCPDS card #31-1238). The major diffraction peaks for the (111) and (200) planes of silver, at 38.1^{o} and 44.3^{o}, respectively, were not easily observable in the AC composites, and this was thought to be due to the low content, small particle size, and high dispersion of the photo-reduced silver on the surface of Ag/AgCl-AC and on Ag/AgCl-MAC [28].

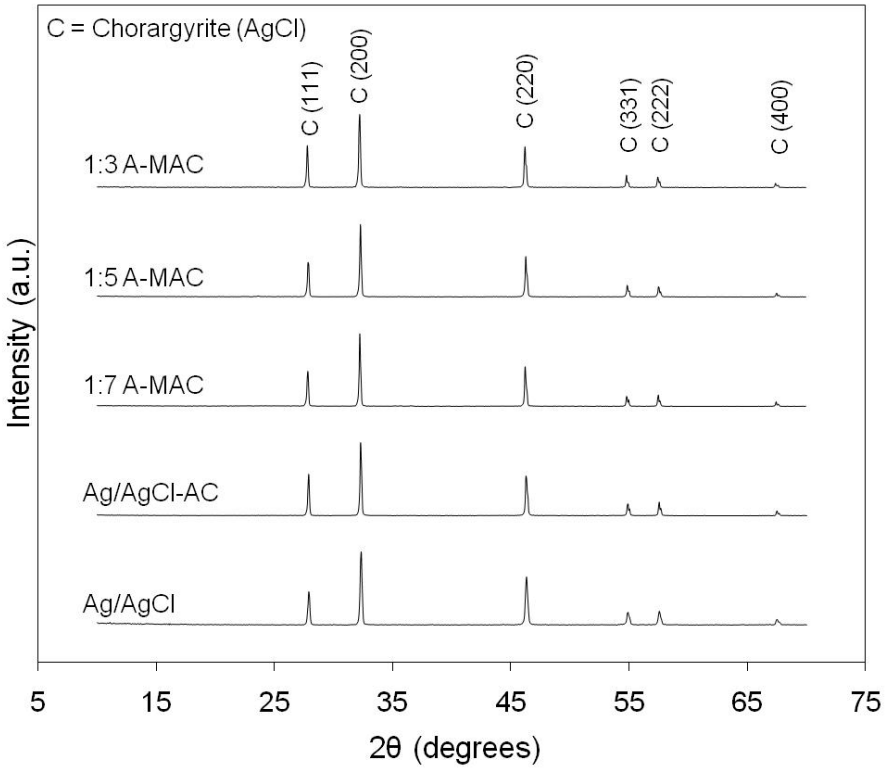

Figure 6.2: XRD patterns for Ag/AgCl, Ag/AgCl-AC, and Ag/AgCl-magnetic AC photocatalysts prepared at various ratios

6.3.1.2 TEM/SEM observation

Typical bright-field TEM images for the prepared iron oxide and SiO_2-coated iron oxide are given in Figure 6.3. From Figures 6.3a and 6.3b, the iron oxide nanoparticles prepared possessed regular spherical shapes, and had an average diameter of 10.5 ± 2.3 nm. The coating procedure yielded SiO_2-coated iron oxides, as seen in Figures 6.3c and 6.3d, where the dark, electron-dense spheres observed were attributable to iron oxide, while the light regions surrounding them were the outer silica layers formed on the magnetic nanoparticles. This implied that a core-shell structure was created through the modified Stöber process, with a silica thickness ~5 nm. The size of the individual core-shell particles observed was ~21–30 nm.

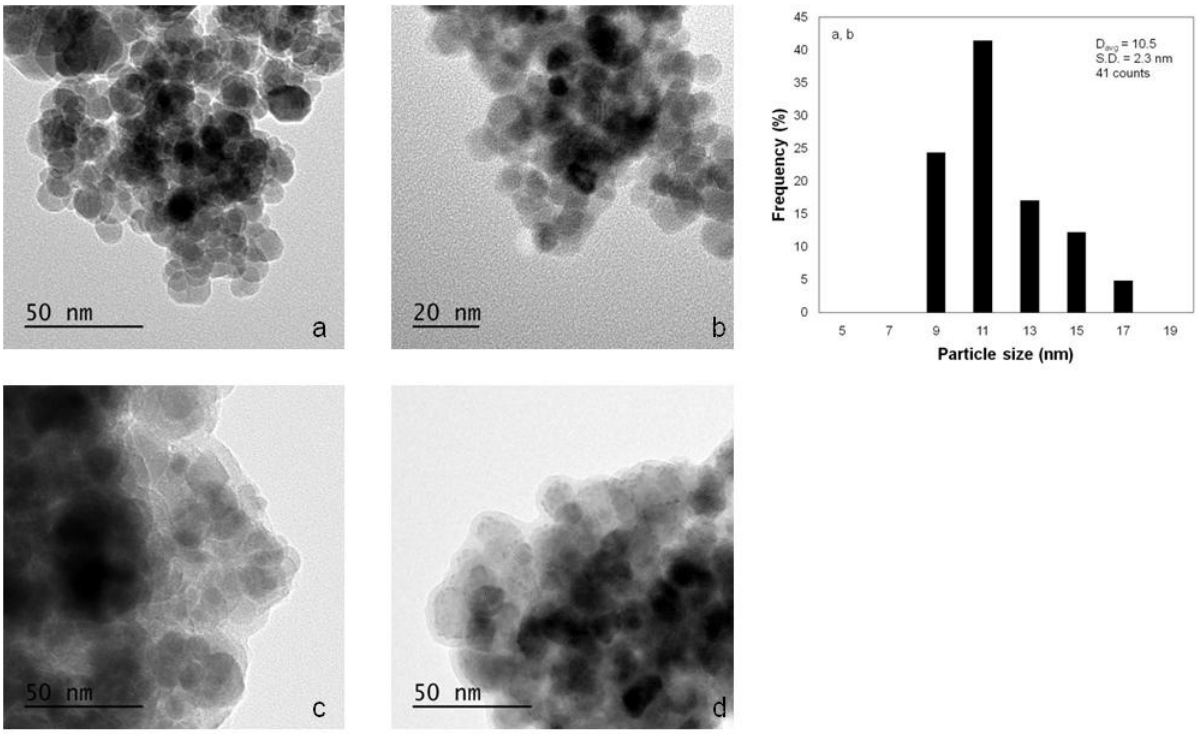

Figure 6.3: TEM images of iron oxide NPs (a, b) and SiO_2-iron oxide (c, d). The histogram for iron oxide NPs is also shown

TEM imaging performed on a typical magnetic activated carbon (1:5 MAC) is shown in Figure 6.4, and the results suggested that the silica-coated iron oxide nanoparticles were well adhered to or incorporated within the larger activated carbon structure, since no free nanoparticle clusters were readily observed. The TEM-EDS pattern shown for the MAC confirmed the presence of carbon, iron, silicon, and oxygen in the μm-scale superstructures shown in Fig. 6.4a, where the presence of copper in the spectra was due to the copper grid used for observation.

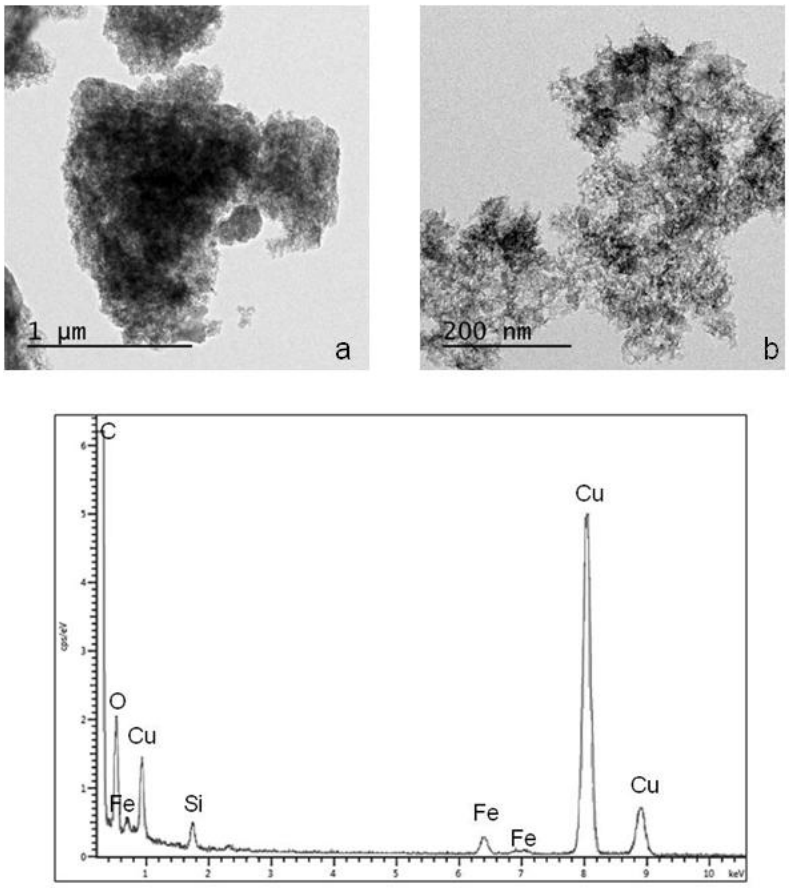

Figure 6.4: TEM images of 1:5 MAC and associated EDS spectra

SEM imaging was also performed to study structure and morphology of the prepared composites, and the results are shown in Figure 6.5 for a representative Ag/AgCl-magnetic AC (1:5 A-MAC), with the morphology of nonmagnetic A-AC shown for reference. The Ag/AgCl was observed to tightly adhere to the surfaces of the magnetic activated carbon to form a dense photocatalyst network, which was not the case for the nonmagnetic AC composite. This was thought to be due to the influence of silica-coated iron oxides incorporated into the AC on the deposition behaviour of AgCl. The silica coating may have affected electrostatic interactions between silver nitrate and activated carbon used in the synthesis by making the magnetic AC composite more negatively charged overall in the aqueous-based impregnation than the pure AC. Silver nitrate was also expected to have a high affinity for SiO_2 in the aqueous synthesis solution [22], so silica-coated iron oxides on the surface of AC may have acted as preferential host sites for silver ion deposition. The

photoreduced metallic silver could be easily observed on the surface of the AgCl particles in the composite, and was found to range from 115–180 nm, while the host AgCl structures were between 1.2 and 1.7 µm.

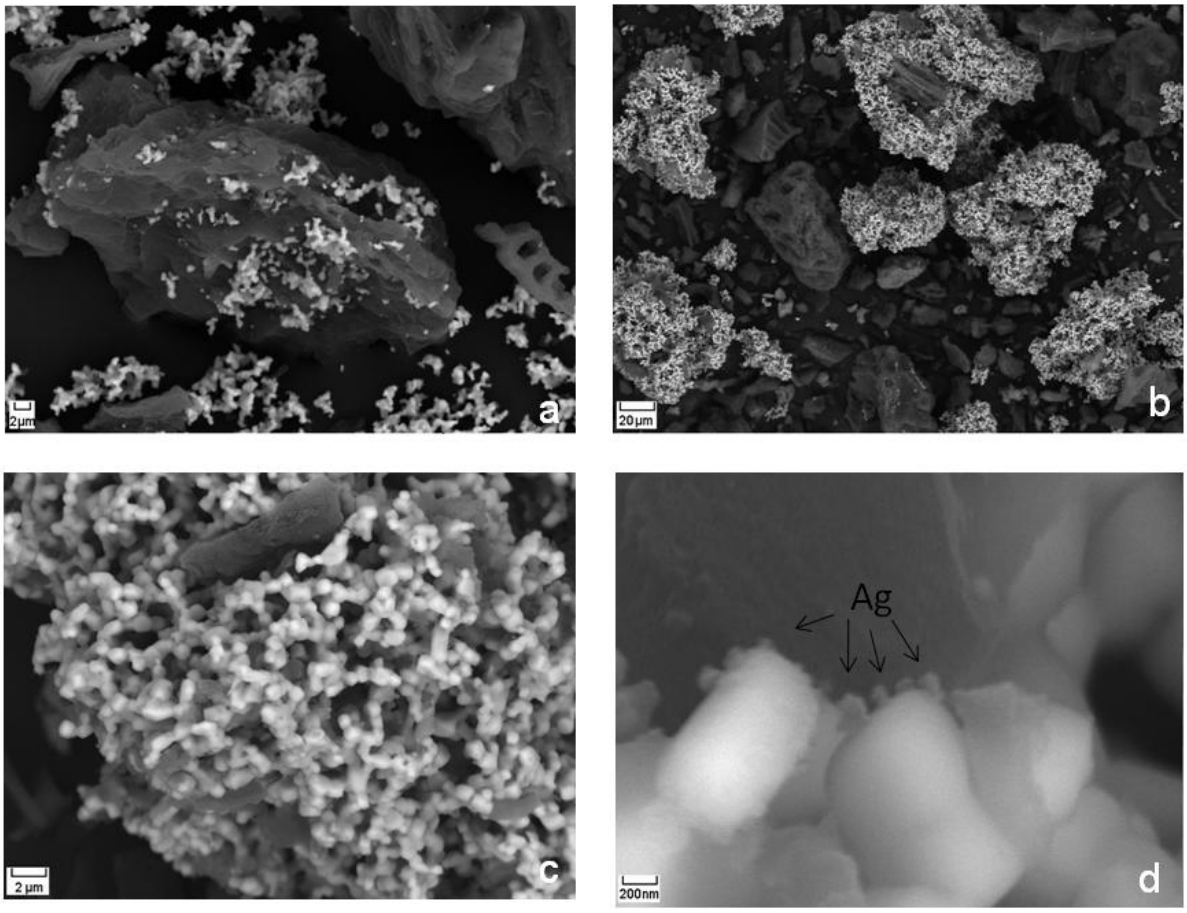

Figure 6.5: SEM images of a) A-AC, b) – d) 1:5 A-MAC

6.3.1.3 X-ray photoelectron spectroscopy

The XPS full-scan spectra for a representative magnetic activated carbon (1:5 MAC) and its corresponding Ag/AgCl composite (1:5 A-MAC) are shown in Figures 6.6a and 6.6b, respectively. In both spectra, peaks assigned to the Fe 2p states at ~714.5 eV were very weak or unobservable relative to the strong Si 2s and 2p states present, indicating that the coating procedure resulted in complete coverage of the iron oxide spheres by the SiO_2 layer [29]. Additionally, the presence of the silicon peaks in both surface XPS spectra indicated that

some of the SiO_2-iron oxide structures incorporated into AC occupied its outer surface, and remained exposed even after AgCl deposition.

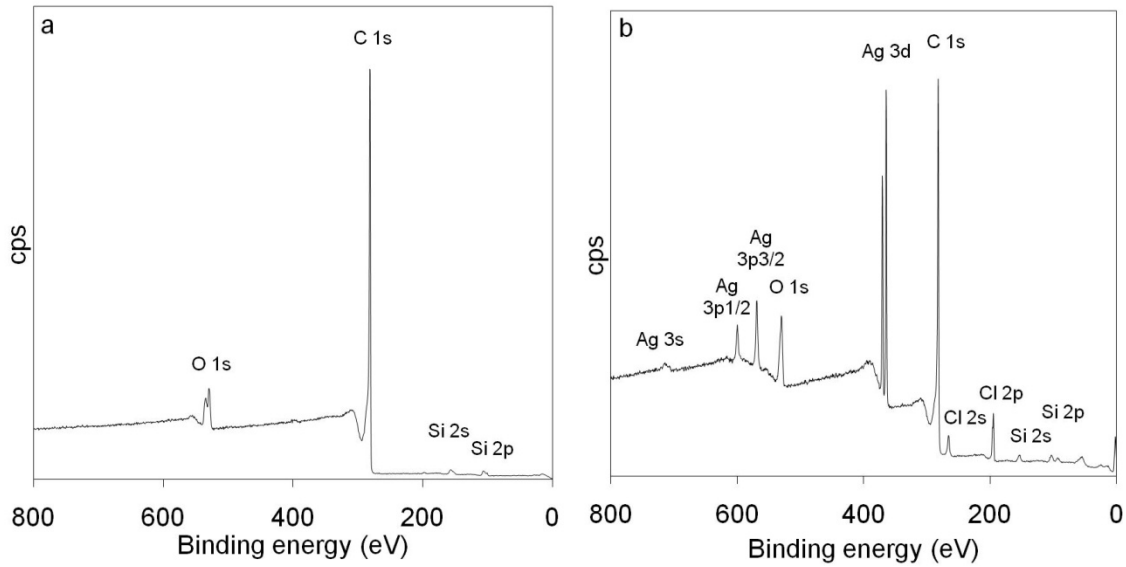

Figure 6.6: XPS spectra for a) 1:5 MAC, and b) 1:5 A-MAC

6.3.1.4 N_2 sorption isotherms

The structure and porosity characteristics of the samples were studied, and nitrogen sorption isotherms obtained are shown in Figure 6.7a for AC and a representative magnetic AC (1:5 A-MAC), and in Figure 6.7b for various prepared Ag/AgCl-magnetic AC composites (1:5 and 1:7 A-MAC, respectively), with the nonmagnetic A-AC shown for reference. All of the isotherms observed were classified as Type IV by IUPAC standards [30], with H4 hysteresis in the desorption branch due to the presence of mesopores [31].

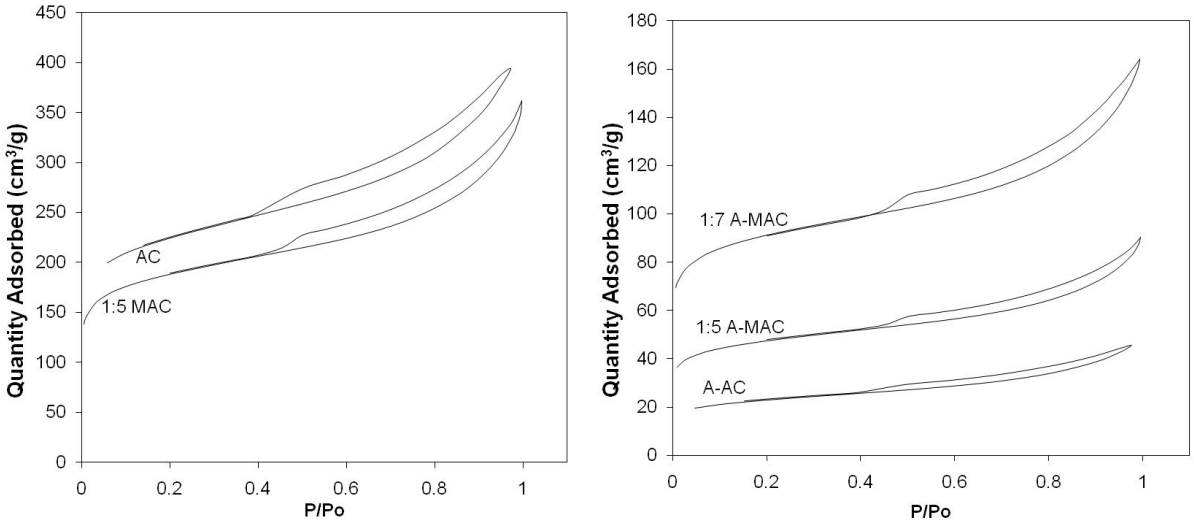

Figure 6.7: N_2 sorption isotherms for a) AC and 1:5 MAC; and b) 1:7 A-MAC, 1:5 A-MAC, and A-AC, respectively

From the isotherms obtained, parameters related to structural and textural characteristics of the synthesized materials were calculated, and are summarized in Table 6.2. Consistent with the results observed for the nonmagnetic A-AC composite with respect to the nonmagnetic AC host material, the BET surface area, total pore volume, as well as micro- and mesopore volumes all decreased upon introduction of Ag/AgCl into the magnetic 1:5 MAC. Interestingly, although the total pore volume and microporosity of pure AC decreased after iron oxide addition, the external surface area increased. This was thought to be due to the creation of mesopores and macropores by silica-coated iron oxide aggregates on the surface of the AC structure, as reflected in the increase in pore diameter. Additionally, deposition of magnetic nanoparticles into the larger mesopores may have also caused pore-blocking of the micropore channels, since mesopores were the main thoroughfares to the microporous regions [32]. Based on SEM observations of the particle sizes of Ag/AgCl formed, they were not thought to enter the pore structure of the MAC host material, but instead formed "egg-shell" composites, where the photocatalyst mainly deposited in clusters on the outside surface of AC [32], causing the observed decreases in surface area and porosity between the 1:5 MAC and A-MAC, respectively. The 1:7 A-MAC composite had a higher BET surface area than 1:5 A-MAC, since the host 1:7 MAC had less magnetic particles incorporated into it and occupying its pore volume and external surface than in the 1:5 MAC. The volume

contribution of micropores to the total pore volume was similar for A-AC and both A-MAC samples studied, and ranged from 32 – 36%.

Table 6.2: Structural and textural characteristics for A-MAC materials calculated from N_2 sorption isotherms

	Property					
Catalyst	BET surface area ($m^2\ g^{-1}$)	Total pore volume ($cm^3\ g^{-1}$)	Micropore volume ($cm^3\ g^{-1}$)	Micropore surface area ($cm^2\ g^{-1}$)	External surface area ($cm^2\ g^{-1}$)	Average pore diameter, BJH ads. (nm)
AC	811	0.609	0.269	510	201	3.624
A-AC	77.1	0.070	0.025	48.0	26.1	3.621
1:5 MAC	645	0.237	0.159	341	304	6.36
1:5 A-MAC	162	0.128	0.041	89.5	72.9	6.59
1:7 A-MAC	344	0.237	0.085	184	127	6.57

6.3.1.5 UV-Vis diffuse reflectance spectroscopy

The UV-Vis absorption spectra for the prepared Ag/AgCl-magnetic activated carbon composites were studied, and are given in Figure 6.8 for a representative sample (1:5 A-MAC), as well as for Ag/AgCl-AC, pure Ag/AgCl, and unreduced AgCl. All of the samples were observed to have an absorbance edge at ~385 nm, corresponding to the band gap of AgCl ($E_{bg,\ indirect}$ = 3.25 eV [33]). Additionally, the photoreduced samples exhibited broad absorption from 400 – 900 nm attributable to surface plasmon resonance of metallic silver nanoparticles produced during irradiation. This broad absorption band was not observed for the unreduced AgCl, evidencing the role and efficacy of photoreduction. The broadness of the absorption band observed in the partially reduced samples was thought to be due to the presence of multiple plasmonic oscillation frequencies, which were caused by a variation in the shapes and diameters of Ag nanoparticle clusters formed [2].

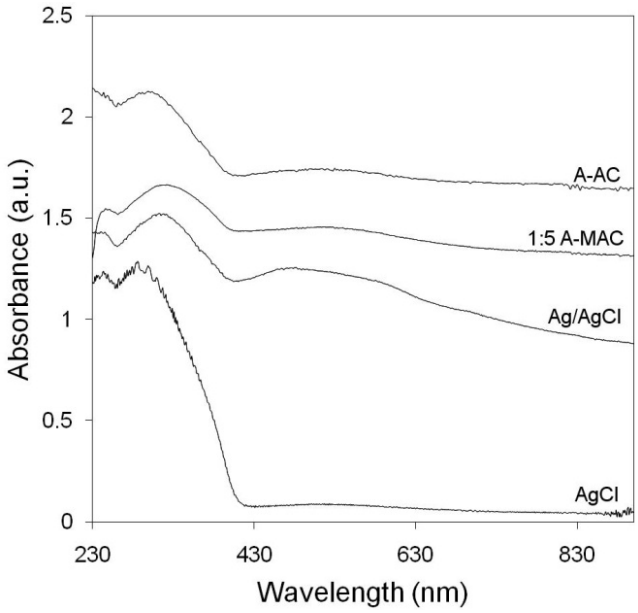

Figure 6.8: UV-Vis absorption spectra for a representative Ag/AgCl-magnetic AC (1:5 A-MAC), A-AC, Ag/AgCl, and unreduced AgCl, respectively

6.3.1.6 SQUID magnetometry and magnetic separation

The magnetic properties of the synthesized materials were probed by SQUID magnetometry, and room temperature magnetic hysteresis loops for synthesized iron oxide, magnetic AC, and Ag/AgCl-magnetic AC composites are shown in Figures 6.9a and 6.9b, respectively. The associated magnetic parameters of saturation magnetization (Ms), coercive field (Hc), and remanant magnetization (Mr) are summarized in Table 6.3.

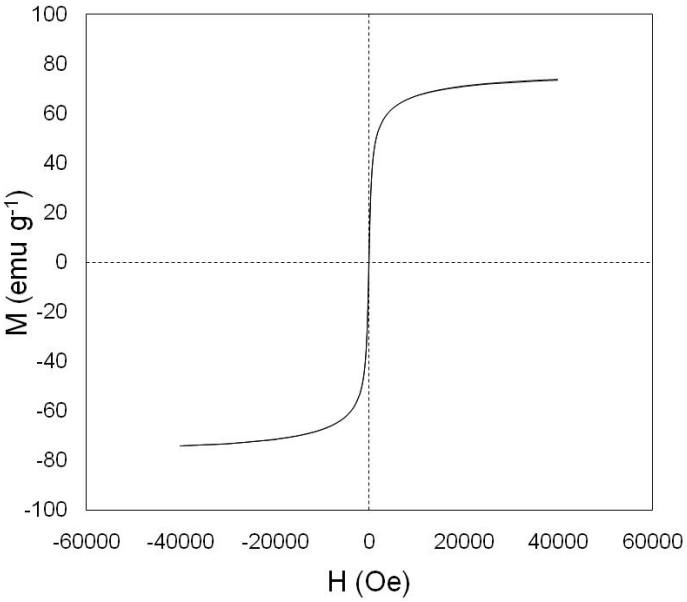

Figure 6.9a: Room temperature magnetization hysteresis loop for synthesized iron oxide nanoparticles

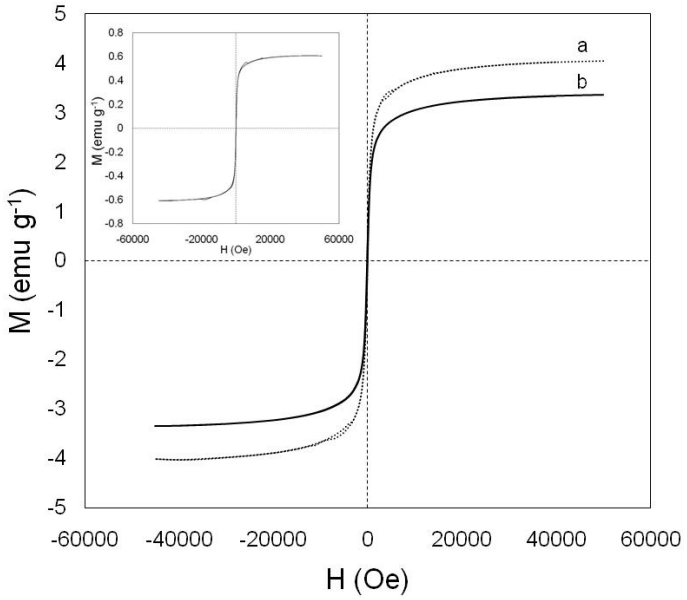

Figure 6.9b: Room temperature magnetization hysteresis loop for a) 1:5 MAC, and b) 1:7 MAC; curve for 1:5 A-MAC shown inset

Table 6.3: Room temperature magnetic properties of iron oxide nanoparticles and representative magnetic composites: 1:7 MAC, 1:5 MAC, and 1:5 A-MAC, respectively

Sample	**Ms (emu g^{-1})**	**Hc (Oe)**	**Mr (emu g^{-1})**
Iron oxide NPs	74.02	26	2.42
1:5 MAC	4.05	45	0.021
1:7 MAC	3.36	45	0.17
1:5 A-MAC	0.61	35	-0.030

The prepared iron oxide nanoparticles exhibited quasi-superparamagnetic behaviour, as evidenced by their low coercive field and remanent magnetization. The prepared magnetic activated carbons (1:5, 1:7) and Ag/AgCl-magnetic AC composite (1:5 A-MAC) also showed similar behaviour, with Hc ranging from 35 – 45 Oe, and Mr from -0.03 – 0.17 emu g^{-1}. The saturation magnetization of magnetic activated carbon increased with increasing iron oxide content, although this value decreased upon introduction of the Ag/AgCl component, due to the large relative weight contribution by the nonmagnetic photocatalyst. However, for all materials prepared, the squareness ratios (Mr/Ms) observed were less than 5.2%, confirming their quasi-superparamagnetic behaviour at room temperature [34, 35]. The acceptable saturation magnetization values indicated that the prepared materials were suited to magnetic removal strategies, as shown in Figure 6.10 for the 1:5 A-MAC exposed to two 12.5mm cubic NdFeB magnets, each having surface field strengths of 5.75×10^3 Gauss**,** for 5 minutes. The low coercivity and remanent magnetization observed also implied that catalyst aggregation could be prevented and that the catalyst could be easily redispersed for recovery or reuse in a suspension [36].

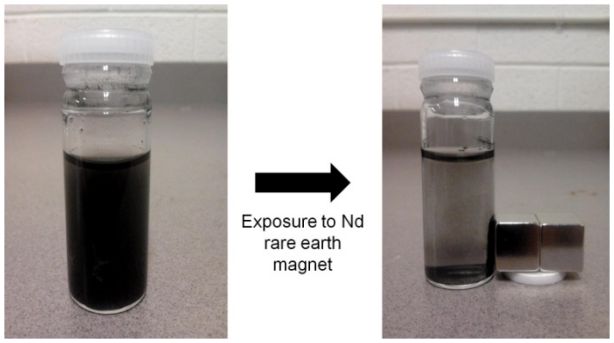

Figure 6.10: Magnetic separation using 1:5 A-MAC exposed to cubic NdFeB magnet

6.3.2 Photocatalytic degradation of organic compounds

6.3.2.1 MO adsorption and photodegradation

Adsorption and photodegradation were studied for a model organic compound, MO dye, which was found to have a negligible photolysis over 2.5 hours under visible light irradiation. The prolonged adsorption-photocatalysis trials consisted of a 2 hour dark adsorption period, followed by illumination for 2.5 hours, and the results obtained are shown in Figure 6.11 as MO removed from solution per weight of catalyst used for the prepared materials, with the nonmagnetic Ag/AgCl-AC composite data shown for reference. The magnetic composites exhibited similar adsorption-photocatalysis behaviour as nonmagnetic Ag/AgCl-AC, where an MO adsorption pseudo-equilibrium was achieved after 2 hours, and a sharp change in MO removal occurred upon irradiation and continued until the pollutant was almost fully removed from solution. This increase in removal upon irradiation was thought to be due to photoexcitation of the catalyst and subsequent photocatalytic action of radicals and reactive species on the dye, initiating a dynamic adsorption-photocatalytic degradation process.

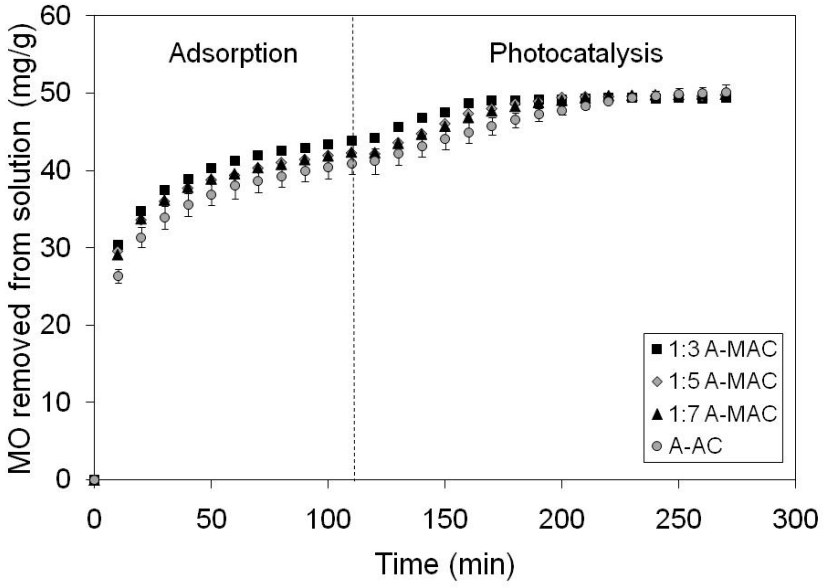

Figure 6.11: Adsorption and subsequent photocatalysis using A-MAC prepared at various weight ratios. (C_o = 25 mg L^{-1}, composite loading = 0.5 g L^{-1}) – *representative error bars shown*

The removal of MO by adsorption from solution was qualitatively similar or within error for the AC and MAC composites, ranging from 41.2 – 44.2 mg MO g composite^{-1} after two hours, and this dark adsorption was thought to be governed by a number of factors. The methyl orange dye adsorbate was considered to be a bulky molecule, with a molecular size of 1.31 x 0.55 x 0.18 nm [37], and it was previously indicated that pores having diameter between 2.5 – 4.5 nm were most suitable to MO adsorption [6], since pores with width or diameter 1.7 – 3 times larger than the adsorbates provided favorable adsorption [38]. Based on this, it followed that although the BET surface area observed for pure A-AC was much lower than that for the prepared A-MAC materials, adsorbate removal was also likely influenced by preferential adsorption of MO into the smaller pores present/accessible in A-AC. Based on the size of MO, it was also implied that much of MO adsorption took place in the external surface area (mesopores, macropores) of the composite catalysts, and that increasing total surface area through increasing microporosity would not be an effective way to improve adsorption for MO. The adsorption characteristics were thought to be further influenced by the structure and morphology of the composites formed, since it was found by SEM that the introduction of silica-coated iron oxides induced the formation of more tightly packed composites with much of their outer surfaces covered in photocatalyst, as opposed to the nonmagnetic counterparts. Additionally, the presence of exposed silica-coated iron oxides on the external surface of the composite after Ag/AgCl deposition was also expected to influence adsorption by changing electrostatic interactions between the dye and A-MAC. For example, silica was present in its negatively charged state, since the isoelectric point was previously found to be pH 2 [36], and the surface of Ag/AgCl was thought to also be negatively charged due to termination by Cl^- ions and the polarization of the electron distribution in silver relative to AgCl [40]. This may have induced a more negative charge on the A-MAC composites, and changed their interaction with the negatively charged sulfonate groups present in MO, although the MO itself carried an overall amphoteric charge at the slightly acidic pH (~5.5) used in the studies.

Data for photocatalytic removal was normalized and presented as a temporal course of MO degraded in Figure 6.12, where initial concentration, C_o (mg L^{-1}), was represented by the

equilibrium concentration achieved after 2 hours of dark adsorption.

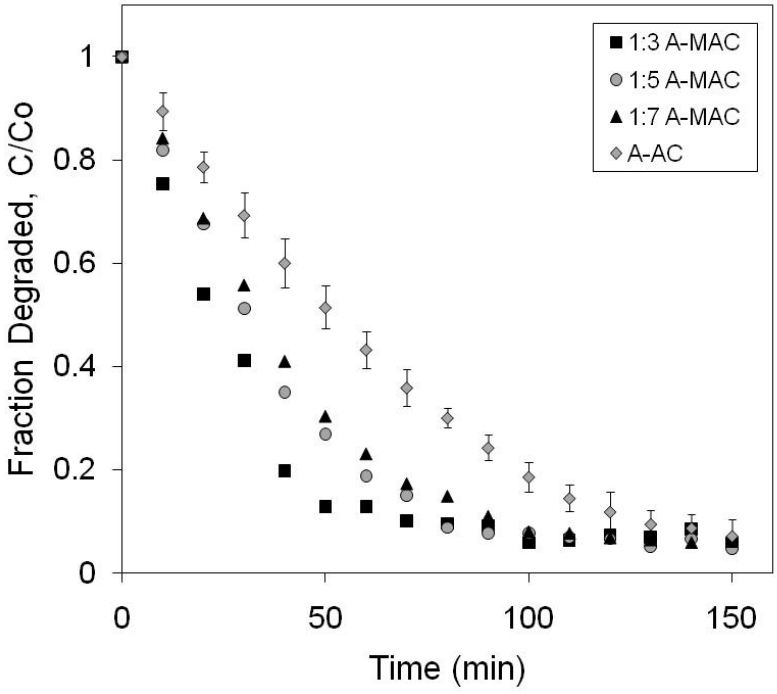

Figure 6.12: MO photodegradation by A-MAC composites and A-AC (loading = 0.5 g L^{-1}) – *representative error bars shown*

The photocatalytic heterogeneous surface reaction could be described using the Langmuir-Hinshelwood kinetic expression, where the following equation defined reaction rate:

$$-dC/dt = K k_r C/(1+KC) \qquad (6.2a)$$

Where K is the Langmuir-Hinshelwood adsorption coefficient (L mg^{-1}), and k_r is the reaction rate constant (mg L^{-1} min^{-1}). This kinetic expression could be simplified into a pseudo-first order equation when the initial concentration used was sufficiently small (< 10^{-3} mol L^{-1} [41]). In this case, $C_o < 7.7x10^{-5}$ mol L^{-1}, so the pseudo-first order approximation was used. The integrated rate expression is given by:

$$ln(C_o/C) = k't \qquad (6.2b)$$

Where k' denotes the pseudo-first order rate constant (min^{-1}), which incorporates both the reaction rate constant and the equilibrium adsorption constant. To quantitatively compare photoactivities of the catalysts for the degradation of MO under visible light, the pseudo-first

order rate constants were calculated for the initial linear portion of the reaction.

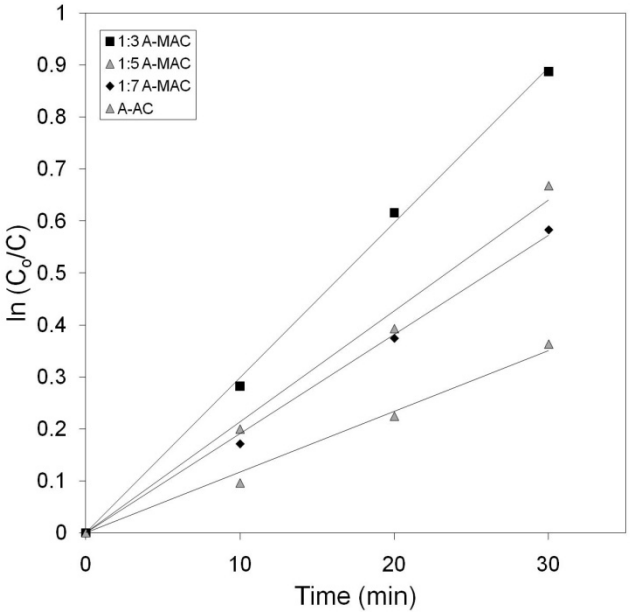

Figure 6.13: Photocatalytic degradation kinetics for A-MAC composites and A-AC, respectively (loading = 0.5 g L^{-1})

Comparison of fitted and experimental data is shown in Figure 6.13, respectively, where the slopes of the fitted lines represented the pseudo-first order rate constants in accordance with equation (6.2b). From the fitted data, the pseudo-first order rate constants were found to be 0.0298, 0.0213, 0.0191, and 0.0124 min^{-1} for the 1:3 A-MAC, 1:5 A-MAC, 1:7 A-MAC, and A-AC composites, respectively, with R^2 values between 0.991 and 0.998. The activity of the magnetic composites was greater than that of nonmagnetic A-AC, which may have been due to competitive adsorption of photons by the exposed activated carbon surfaces in the latter material [42], reducing efficiency of Ag/AgCl excitation. Activity of the magnetic AC composites was found to increase as the proportion of magnetic component increased, which may have also been caused by reduction of this competitive photon adsorption effect due to suspected changes to composite structure and morphology induced by the introduction of silica-coated iron oxide particles, and more efficient mass transfer between adsorbed methyl orange on the AC and surface active sites of Ag/AgCl. Additionally, as discussed in subsequent sections, positive effects of eluted ionic silver under irradiation may have also increased photocatalytic activity for MO degradation by acting as electron traps preventing

electron-hole recombination in the magnetic composites. Although the 1:3 A-MAC composite had the highest photocatalytic activity, its saturation magnetization was thought to decline with respect to the 1:5 and 1:7 catalysts, due to the observed phase change of the contained magnetite to a less magnetic impurity phase. Therefore, the 1:5 A-MAC catalyst was selected for further photoactivity testing as it possessed acceptable magnetization and photoactivity.

6.3.2.2 Evidence for the photocatalytic degradation of MO

Degradation of MO in photocatalytic systems is reported to occur first by attack on the azo bond by photoproduced reactive species to degrade polyaromatic rings in MO and create mono substituted aromatics. These intermediate molecules may then undergo further radical attack to induce aromatic fragment degradation and eventual mineralization [43]. To probe photocatalytic degradation of MO by the A-MAC composites prepared, changes to the UV-Vis absorption spectra of MO were monitored over the course of photodegradation, and results from representative spectra are shown in Figure 6.14. The initial spectrum at time t = 0 (corresponding to the beginning of photocatalysis, after adsorption in the dark) was characterized by a major band around 463 nm due to light absorption by azo bonds in the MO structure, and a smaller peak in the UV range at ~265 nm due to absorption by benzene-like structures. With an increase in the photocatalytic treatment time, the spectral height of the azo peak at 463 nm decreased markedly, while the intensity of the band at 265 nm increased. However, past 60 minutes, this band intensity in the UV range also decreased. These results agreed well with literature, where extended aromatic MO was first degraded by photocatalytic attack to produce benzene-like structures that absorbed in the 200–270 nm range. These intermediates then underwent further degradation as the reaction proceeded [43]. Hydrazine may have also been formed as an intermediate, contributing to the increase in absorbance around 250 nm [44]. The changes in UV-Vis spectra evidenced that MO underwent photocatalytic degradation in the irradiated system. It should be noted that the lack of shift in the major band at 463 nm further confirmed that the effect of self-sensitization on MO degradation was negligible [45].

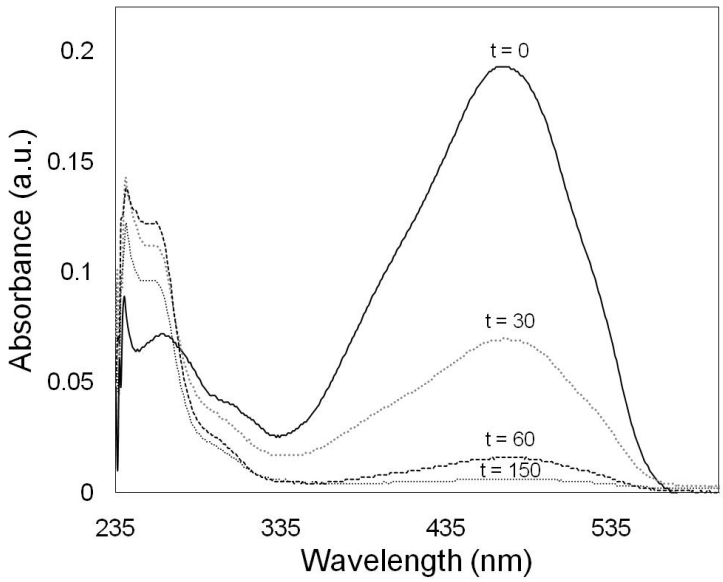

Figure 6.14: UV-Vis solution spectra during MO photodegradation by 1:5 A-MAC composite (C_o = 25 mg L^{-1}, loading = 0.5 g L^{-1})

6.3.2.3 Recyclability

Recyclability of the prepared 1:5 A-MAC composite was studied by performing four consecutive adsorption-photocatalysis cycles, recovering the catalyst between runs by magnetic separation. The photocatalyst performance in these sequential runs is shown in Figure 6.15.

The adsorptive capabilities of the composite decreased with sequential runs, and were exhausted after the second cycle. This was thought to be partially due to inability of the incorporated Ag/AgCl photocatalyst to fully regenerate the adsorptive AC surface during the photocatalysis cycle by degrading all of the adsorbed MO. This also resulted in a decrease in photocatalytic activity with repeated use without regeneration between cycles, since the rate of degradation was lower than rate of accumulation of MO onto the composite, which saturated the photocatalyst surface and decreased its photonic efficiency [46]. In the second to fourth uses of the composite, 70.9%, 63.5%, and 52.6%, of the total MO degraded in the first run were decomposed by the recycled material, respectively. This activity was comparable to that previously described for nonmagnetic Ag/AgCl-AC composites, where the amount of MO degraded in the second to fourth runs was 75.2%, 66.8%, and 62.7% of

that of the first run, respectively [15]. These reported cycling runs were performed using centrifugation to recover the spent catalyst between trials, where in the current case, magnetic separation was used. The observed decreases in photocatalytic activity of magnetic Ag/AgCl-AC composite compared to its nonmagnetic counterpart may have been due to some catalyst washout that occurred with magnetic separation between runs. Despite this, the similarity in cyclic activities observed indicated that magnetic separation could be employed to recover the spent catalyst. As previously discussed, the decreased efficiency with increased cycle number in the absence of regeneration may have also been attributed to the formation of reaction intermediates and their adsorption and accumulation on the photocatalyst [42, 47], as evidenced by Figure 6.14. The presence of these intermediates complicated the analysis and interpretation of recyclability of the composite, since the reactive and nonselective photoproduced reactive species were thought to act both on the parent MO compound and on the produced reaction intermediates.

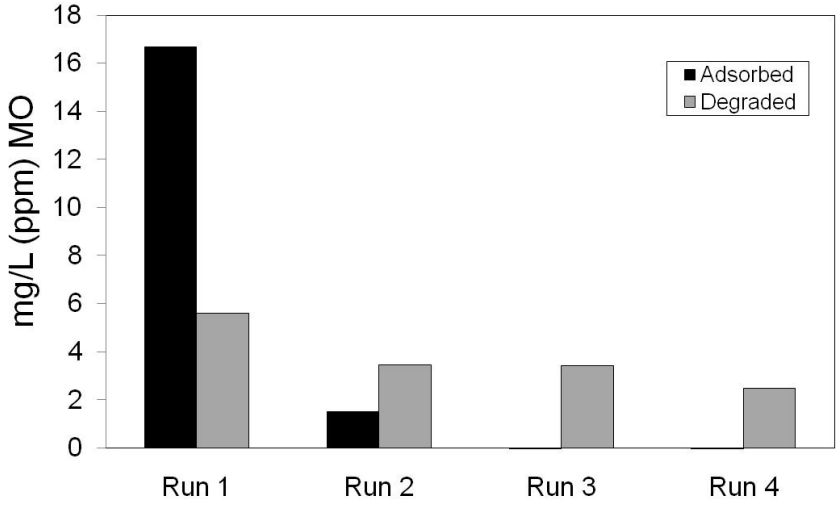

Figure 6.15: Adsorption and photodegradation performance of 1:5 A-MAC composite over four consecutive cycles (C_o = 25 mg L^{-1}, loading = 0.5 g L^{-1})

The XRD pattern for the composite catalyst was collected after its cyclic use, and is shown in Figure 6.16, with the fresh catalyst pattern for comparison. The patterns before and after cyclic use were very similar, although small peaks at 38.1^o and 44.3^o were observed in the recycled material due to the (111) and (200) faces of metallic silver. The presence of these

metallic silver peaks was thought to be due to an increase in the Ag nanoparticle size during visible light photocatalysis, due to aggregation and photoreduction of some AgCl to form additional metallic Ag clusters. This decomposition was reported to have a minor effect on the total surface contents of Ag and AgCl under similar experimental conditions as those used in this study [40, 48, 49], confirming the stability of such catalysts in repeated use.

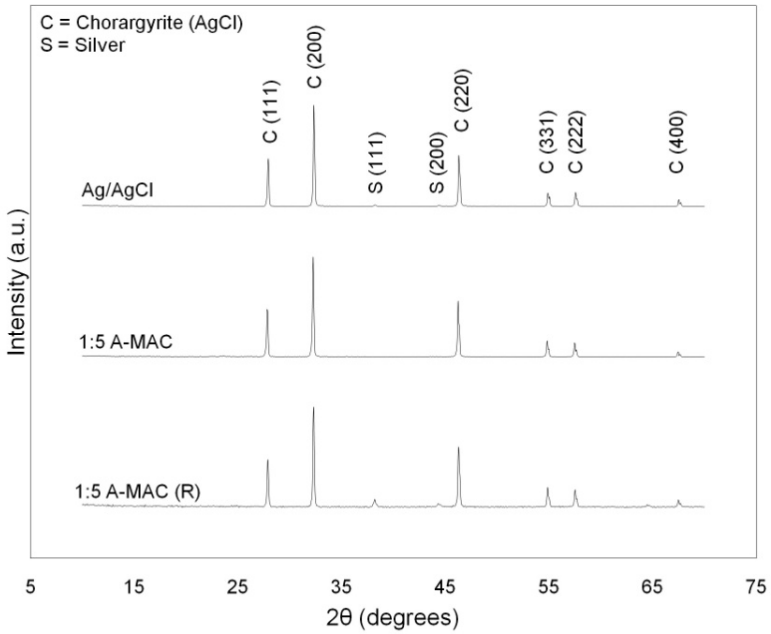

Figure 6.16: XRD patterns for as-prepared Ag/AgCl, fresh 1:5 A-MAC composite, and recycled 1:5 A-MAC composite after four adsorption-photocatalysis cycles

6.3.2.4 Phenol photodegradation

To ensure that the observed activity from the Ag/AgCl-magnetic AC composite was due to surface plasmon resonance induced photocatalysis, and was not only caused by photosensitization of organic MO dye under visible light [50], the photodegradation was tested against phenol, a colorless organic target pollutant. The adsorption and subsequent photocatalysis, and associated pseudo-first order kinetics are shown in Figure 6.17. The photolytic conversion of phenol was found to be negligible, and the composite exhibited good activity for organics degradation in the absence of a dye-sensitized mechanism, converting about 9.5 mg phenol per gram composite with a pseudo-first order rate constant of 0.0052 min^{-1}. Factors such as adsorption affinity of the pollutant for the composite, initial

pollutant concentration, and light penetration in solution were thought to influence the observed differences in photoactivities of A-MAC towards MO and phenol, respectively.

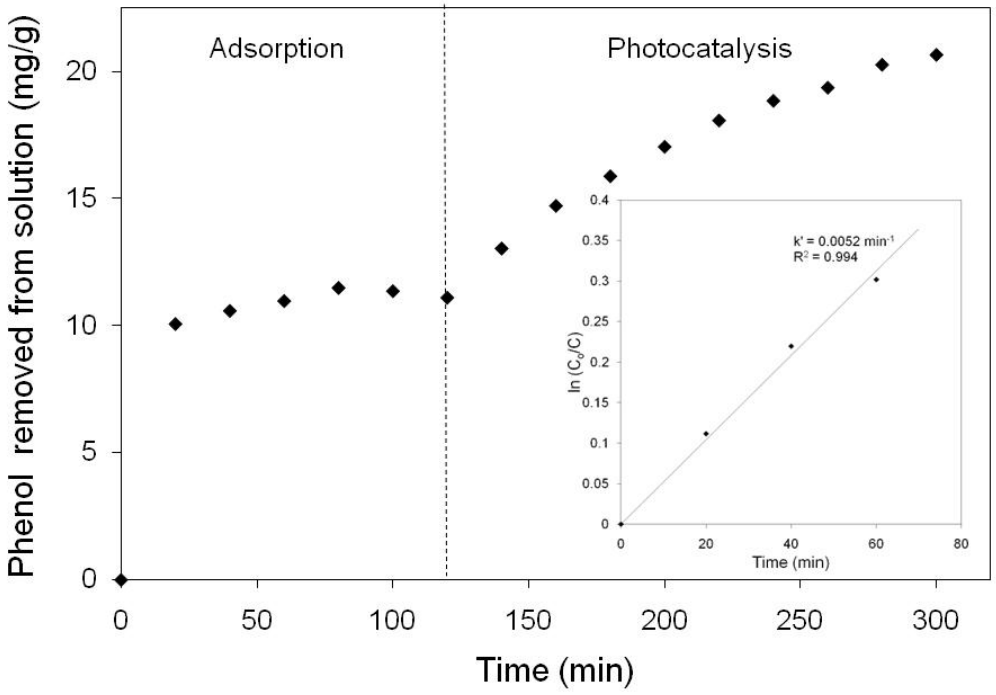

Figure 6.17: Adsorption and subsequent photocatalysis using 1:5 A-MAC in phenol. Photocatalytic degradation kinetics shown inset. (C_o = 13 mg L^{-1}, composite loading = 0.5 g L^{-1})

6.3.3 Iron oxide photodissolution

Based on previous reports of photodissolution of iron oxides in photocatalyst/iron oxide systems [8, 51, 52], the effect of the silica coating was studied in the current A-MAC composites. The concentration of iron ions in a 5 g L^{-1} aqueous catalyst slurry under irradiation was found to be 0.53 ± 0.13 mg L^{-1} after 60 minutes and 0.62 ± 0.021 mg L^{-1} after 150 minutes, respectively, for the 1:7 A-MAC composite prepared with silica-coated iron oxide particles. These values increased to 1.1 ± 0.042 mg L^{-1} after 60 minutes and 1.1 ± 0.033 mg L^{-1} after 150 minutes, respectively, for the same composite prepared using uncoated iron oxides. This implied that the silica coating was effective in decreasing the occurrence of iron oxide photodissolution, since the ionic iron concentration in solution was

lower for the silica-containing material under irradiation. The photo-Fenton reaction was also thought to be negligible in the photoreactive system due to the low concentrations of Fe obtained. The values of ionic iron were thought to be even lower in the actual photocatalytic systems studied for the degradation of MO and phenol, since a composite loading of 0.5 g L^{-1} was used, as opposed to 5 g L^{-1} used in the control tests.

6.3.4 Photocatalytic inactivation of *E. coli* K-12

Photocatalytic inactivation of a Gram-negative model microorganism, *E. coli* K-12 was studied, as it is a common indicator for faecal contamination [53]. The temporal course of inactivation was quantified for the 1:5 A-MAC composite in dark and light conditions, respectively, and for the 1:5 MAC material itself. The results are shown in Figure 6.18, with A-AC for comparison. The photolysis trial performed in the absence of catalyst, indicative of loss of culturability due to damage from the photon source alone, was found to have a negligible effect. Biocompatibility of magnetic AC was tested using an equivalent loading of MAC as that incorporated into the composite, and the final survival ratio was found to be 0.19 ± 0.048, which was comparable to that observed with equivalent neat AC, implying that the incorporation of silica-coated magnetic nanoparticles into the adsorbent did not induce significant toxicity. The population decrease in this case was thought to be due to adsorption of bacteria onto the exposed activated carbon surfaces in MAC. Upon introduction of Ag/AgCl into magnetic AC, an increased loss of cell culturability was observed over that of bacterial adhesion on MAC alone, in both dark and light conditions using the composite photocatalyst, achieving final survival ratios of 0.04 ± 0.029 and 0.00074 ± 0.001 for each case, respectively.

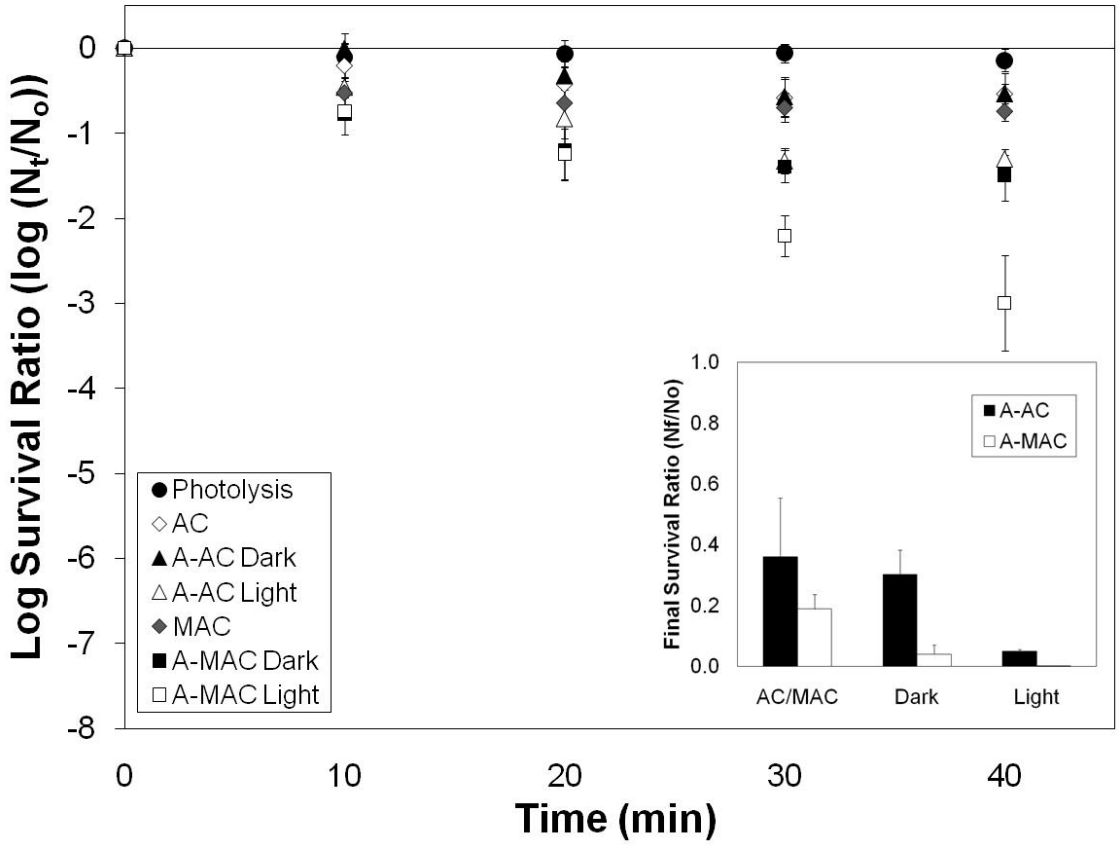

Figure 6.18: Inactivation curves for photolysis, AC, A-AC (dark), A-AC (light), 1:5 MAC, 1:5 A-MAC (dark), and 1:5 A-MAC (light), respectively. Catalyst loading used was 5 g L^{-1} (or calculated equivalent for AC/MAC); final survival ratios shown inset. (N_o = 10^6 CFU mL^{-1}, pH = 5.5)

In the dark, the inactivation was attributed to bacterial adhesion onto the solid catalyst and toxicity of the silver ions eluted. Silver ions are toxic at sub-micromolar concentrations, due to their interaction with enzymes in the respiratory chain reaction, causing the uncoupling of respiration from the synthesis of ATP [54]. Additionally, Ag^+ can bind with transport proteins, leading to proton leakage and inducing collapse of proton motive force [55]. These silver ions were formed in the dark by irreversible oxidation of metallic nanosilver and the limited solubility of the AgCl carrier material in saline to form dissolved ionic silver and silver complexes such as $AgCl_{(aq)}$, or $AgCl_x^{1-x}{}_{(aq)}$, that could interact with thiol-containing proteins [56]. The release of silver ions from 5 g L^{-1} composite into 50 mL distilled deionized

water under stirring in the dark was recorded, and the Ag^+ concentration was found ICP-MS to be 50.8 ± 0.51 mg L^{-1} after 40 minutes, and 52.4 ± 0.19 mg L^{-1} after 60 minutes, respectively. This was much higher than the 0.53 ± 0.09 mg L^{-1} previously observed for the A-AC composite after 60 minutes, and the difference was thought to be due to changes in structure and morphology of the magnetic composite compared to the original A-AC, since the rate of silver ion release was controlled by silver oxidation, which in aqueous medium depended on the rate of water diffusion and the diffusion characteristics [57]. This diffusion was thought to differ between magnetic and nonmagnetic composites, and the increased silver elution by the A-MAC material caused the increase in dark inactivation capability observed in Figure 6.18. It should be noted that the silver ion measurements performed quantified silver ion diffusion into water, which represented an upper limit on the actual diffusion that occurred in saline and in the presence of thiol targets.

This silver ion elution may have also influenced MO adsorption and degradation observed using the magnetic composites, since the effect of silver ions on photocatalytic degradation of organics is generally reported to increase degradation rate due the electron trapping mechanism of Ag^+, which reduces recombination of photogenerated charges [58]. For example, in pure photocatalyst systems such as TiO_2, this enhancement is attributable to the formation of surface adsorbed Ag^+ species, which can become photoreduced and subsequently act as electron traps to prevent recombination [59]. However, the dissolved Ag^+ concentration in the organic degradation studies was expected to be much lower than the value quantified by ICP-MS in the control due to the ten-fold decrease in composite loading used in the photodegradation studies compared to that used for the inactivation studies. In a similar dynamic adsorbent photocatalyst system based on a chitosan-TiO_2 composite [60], doubling the Ag^+ concentration in solution from 100 mg L^{-1} to 200 mg L^{-1} caused a moderate (13.4%) increase in MO photodegradation.

The inactivation capability observed using the magnetic Ag/AgCl-MAC composite increased significantly in the photocatalysis trials, as the production of photoactive species was facilitated by illumination. The results agreed well with the trend observed for nonmagnetic

Ag/AgCl-AC, where some bactericidal activity was observed in the dark, and inactivation was increased under illumination due to the production of radical and reactive oxygen species [20]. The inactivation realized using the magnetic photocatalyst composite was found to effect a greater loss of culturability to the bacteria than nonmagnetic Ag/AgCl-AC, due to its increased silver ion elution, and better photocatalytic efficiency caused by more complete surface coverage of the AC host structure by photocatalyst, reducing competition for photons in the irradiated process. The illumination of the catalyst with visible light was thought to produce electron-hole pairs that could undergo reaction with dissolved oxygen and water to form reactive oxygen species (ROS), which could then interact with *E. coli* bacteria. The action of ROS on bacteria was found in literature to cause a loss of culturability due to peroxidation of cell wall bilayer functional groups, leading to increased disorder in the bilayer, which increased the fluidity of the cell wall and caused eventual lysis through free efflux of intracellular components [61, 62]. The eluted Ag^{+} species may have also reduced the rate of recombination of the photoproduced electrons and holes, increasing the photocatalytic efficiency observed. However, it should be noted that, as previously discussed for the Ag/AgCl-AC composite, complications may arise from the use of silver-eluting catalysts in the presence of saline, since binding with free Cl^{-} may occur past the solubility limit (10^{-5}), causing the formation of AgCl nanoparticles that may then be photoreduced in the irradiated system [63]. Although this may result in the effective regeneration of some Ag/AgCl photocatalyst, its presence is difficult to quantify in the current scheme. Despite this, the approximately 3-log reduction observed in the photocatalytic system indicated that this material possessed good applicability and efficacy for solar photocatalytic disinfection.

6.3.5 Mechanism of photocatalytic action

The composites were thought to act photocatalytically under visible light through participation of localized surface plasmon resonance of the silver nanoparticles formed from partial reduction of AgCl. The generation of holes and electrons occurred in these silver nanoparticles upon the absorption of photons of appropriate wavelengths, and the polarization of charges was induced by the surface plasmon resonance state of the silver. This polarization facilitated effective charge separation of the photogenerated holes and electrons, as the negatively charged electrons were transferred to the silver surface farthest

away from the AgCl interface, and the holes transferred to the surface of AgCl [40]. This charge separation was responsible for the stability of silver/silver halide structures, since the generated electrons were prevented from being transferred to Ag^+ in AgCl [64], but were instead transferred to molecular oxygen to form active species such as superoxide [65]. Simultaneously, the holes generated could also oxidize water to produce hydroxyl radicals, or directly oxidize Cl^- ions into Cl^o, which may have also interacted with target pollutants near the surface of the catalyst [66], and be reduced back to their ionic state. In the adsorbent photocatalyst composites prepared, the role of the activated carbon was to concentrate the pollutant around the photocatalytic active sites, allowing adsorbed pollutant to migrate to the Ag/AgCl decomposition centers present on the adsorbent surface due to concentration gradients [67]. In the absence of adsorbent supports, the pollutant was required to collide with the catalyst and maintain sufficient contact for reaction, after which the intermediates were desorbed back into solution. Additionally, the neat photocatalyst had limited surface area present, which restricted the number of successful collisions with pollutant molecules [68]. In the adsorbent composite, this limitation was overcome, and chain reactions were thought to be promoted since the AC allowed for the retention of reaction intermediates. Mechanistic pathways investigated in literature for the photocatalytic mineralization of MO and phenol were thought to occur to various extents in the irradiated system [69, 70].

6.4 Conclusions

In this work, novel magnetic adsorbent photocatalyst composites were synthesized by the preparation of magnetic AC incorporating silica-coated Fe_3O_4 nanoparticles, and a subsequent deposition-precipitation-photoreduction procedure to obtain "egg-shell" structured Ag/AgCl-magnetic AC. The resulting composites possessed quasi-superparamagnetic behaviour, and exhibited good visible light induced photocatalytic activity towards the degradation of a model dye, methyl orange, and a colorless organic, phenol. The material could be recovered by an external magnetic field, and possessed some photocatalytic activity in up to four cyclic degradation cycles. The prepared Ag/AgCl-magnetic AC composite also exhibited strong activity for *E. coli* K-12 inactivation, and was able to effect a 3-log reduction in 40 minutes under irradiation in a 5 g L^{-1} slurry. The visible

light induced photodegradation and disinfection capabilities of the composite material, as well as its recovery by magnetic separation, indicate its applicability towards solar detoxification and disinfection schemes using slurry photocatalytic reactors. Future work on this catalyst involves improving its performance in cyclic use, such as through prolonged exposure to irradiation to regenerate the activated carbon surface [71]. Additionally, the role of dissolved silver in photocatalytic organics degradation and inactivation should be clarified in both dark and light conditions for the prepared composites. Optimization of the adsorptive, photocatalytic, and magnetic behaviours of the developed composites should also be undertaken. One strategy proposed to improve the magnetic removal efficiency is by improving the photocatalyst activity to reduce the equivalent composite weight, such as through morphology-controlled synthesis of high-performance Ag/AgCl [72]. The effect of operational parameters such as light intensity, solution concentration, and pH on the resulting photoactivity of the prepared composites should also be studied in the future.

6.5 Acknowledgments

This work was supported by the Natural Sciences and Engineering Research Council of Canada. The authors would like to acknowledge Dr. Alexander Mommers and Dr. Yong Yang at the Centre for Catalysis Research and Innovation (University of Ottawa), Dr. Jianqun Wang (Carleton University), and Dr. Paul Dubé from the Brockhouse Institute for Materials Research (McMaster University) for their help with characterizations. Dr. Nimal De Silva from the University of Ottawa is also thanked for help with ICP-MS analysis.

6.6 References

[1] N. Serpone, Is the band gap of pristine TiO_2 narrowed by anion- and cation- doping of titanium dioxide in second-generation photocatalysts?, J. Phys. Chem. B 110 (2006) 24287–24293.

[2] P. Wang, B. Huang, X. Zhang, X. Qin, H. Jin, Y. Dai, Z. Wang, J. Wei, J. Zhan, S. Wang, J. Wang, M.-H. Whangbo, Highly efficient visible-light plasmonic photocatalyst Ag@AgBr, Chem. Eur. J. 15 (2009) 1821–1824.

[3] A. Pourahmad, S. Sohrabnezhad, E. Kashefian, AgBr/nanoAlMCM-41 visible light photocatalyst for degradation of methylene blue dye, Spectrochim. Acta A 77 (2010) 1108–1114.

[4] J. Matos, J. Laine, J.M. Herrmann, Synergy effect in the photocatalytic degradation of phenol on a suspended mixture of titania and activated carbon, Appl. Catal., B. 18 (1998) 281–291.

[5] H. Slimen, A. Houas, J.P. Nogier, Elaboration of stable anatase TiO_2 through activated carbon addition with high photocatalytic activity under visible light, J. Photochem. Photobiol., A. 221 (2011) 13–21.

[6] X. Wang, Y. Liu, Z. Hu, Y. Chen, W. Liu, G. Zhao, Degradation of methyl orange by composite photocatalysts nano-TiO_2 immobilized on activated carbons of different porosities, J. Hazard. Mater. 169 (2009) 1061–1067.

[7] T.-T. Lim, P.-S. Yap, M. Srinivasan, A.G. Fane, TiO_2/AC composites for synergistic adsorption-photocatalysis processes: Present challenges and further developments for water treatment and reclamation, Crit. Rev. Env. Sci. Technol. 41 (2011) 1173–1230.

[8] D. Beydoun, R. Amal, G.K.C. Low, S. McEvoy, Novel photocatalyst: titania-coated magnetite, activity and photodissolution, J. Phys. Chem. B 104, 18 (2000) 4387–4396.

[9] R. Buonsanti, V. Grillo, R. Carlino, C. Giannini, M.L. Curri, C. Innocenti, C. Sangregorio, K. Achterhold, F.G. Parak, A. Agostiano, P.D. Cozzoli, Seeded growth of asymmetric binary nanocrystals made of a semiconductor TiO_2 rodlike section and a magnetic γ-Fe_2O_3 spherical domain, J. Am. Chem. Soc. 128, 51 (2006) 16953–16970

[10] M. Ye, Q. Zhang, X. Hu, J. Ge, Z. Lu, L. He, Z. Chen, Y.Yin, Magnetically recoverable core-shell nanocomposites with enhanced photocatalytic activity, Chem. Eur. J. 16, 21 (2010) 6243–6250.

[11] C. An, X. Ming, J. Wang, S. Wang, Construction of magnetic visible-light driven plasmonic Fe_3O_4@SiO_2@AgCl:Ag nanophotocatalyst, J. Mater. Chem. 22, 11 (2012) 5171–5176.

[12] Y. Ao, J. Xu, D. Fu, C. Yuan, A simple route for the preparation of anatase titania-coated magnetic porous carbons with enhanced photocatalytic activity, Carbon 46, 4 (2008) 596–603.

[13] Y. Ao, J. Xu, D. Fu, X. Shen, C. Yuan, C. A novel magnetically separable composite photocatalyst: Titania-coated magnetic activated carbon, Sep. Purif. Technol. 61, 3 (2008) 436–441.

[14] Y. Ao, J. Xu, D. Fu, C. Yuan, Photocatalytic degradation of X-3B by titania-coated magnetic activated carbon under UV and visible irradiation, J. Alloys Compd. 471, 1–2 (2009) 33–38.

[15] J. Gamage McEvoy, W. Cui, Z. Zhang, Synthesis and characterization of Ag/AgCl-activated carbon composites for enhanced visible light photocatalysis, Appl. Catal., B. 144 (2014) 702–712. *(also given in Chapter 3)*

[16] X. Wang, X. Tang, Z. Chen, T.-T. Lim, Highly stable heterostructured Ag/AgBr/TiO_2 composite: a bifunctional visible-light active photocatalyst for destruction of ibuprofen and bacteria, J. Mater. Chem. 22 (2012) 23149–23158.

[17] S.-J. Park, Y.-S. Jang, Preparation and characterization of activated carbon fibers supported with silver metal for antibacterial behaviour, J. Colloid Surf. Sci. 261 (2003) 238–243.

[18] Y.L. Wang, Y.Z. Wan, X.H. Dong, G.X. Cheng, H.M. Tao T.Y. Wen, Preparation and characterization of antibacterial viscose-based activated carbon fiber supporting silver, Carbon 36, 11 (1998) 1567–1571.

[19] H. Le Pape, F. Solano-Serena, P. Contini, C. Devillers, A. Maftah, P. Leprat, Involvement of reactive oxygen species in the bactericidal activity of activated carbon fibre supporting silver: Bactericidal activity of ACF (Ag) mediated by ROS, J. Inorg. Biochem. 98 (2004) 1054–1060.

[20] J. Gamage McEvoy, D.A. Bilodeau, W. Cui, Z. Zhang, Visible-light-driven inactivation of *Escherichia coli* K-12 using an Ag/AgCl-activated carbon composite photocatalyst. J. Photochem. Photobiol., A. 267 (2013) 25–34. *(also given in Chapter 5)*

[21] J.H. Meng, G.Q. Yang, L.M. Yan, X.Y. Wang, Synthesis and characterization of magnetic nanometer pigment Fe_3O_4, Dyes Pigments 66 (2005) 109–113.

[22] G. Li, K.H. Wong, X. Zhang, C. Hu, J. C. Yu, R.C.Y. Chan, P.K. Wong, Degradation of Acid Orange 7 using magnetic AgBr under visible light: The roles of oxidizing species, Chemosphere 76 (2009) 1185–1191.

[23] W. Stöber, A. Fink, E. Bohn, Controlled growth of monodisperse silica spheres in the micron size range, J. Colloid Interface Sci. 26 (1968) 62–69.

[24] W. Li, C. Liang, W. Zhou, J. Qiu, Z. Zhou, G. Sun, Q. Xin, Preparation and characterization of multiwalled carbon nanotube-supported platinum for cathode catalysts of direct methanol fuel cells, J. Phys. Chem. B 107 (2003) 6292–6299.

[25] R.J. Gilkes, A. Suddhiprakarn, Magnetite alteration in deeply-weathered adamellite, J. Soil Sci. 30 (1979) 357–361.

[26] T.W. Swaddle, P. Oltmann, Kinetics of the magnetite-maghemite-hematite transformation, with special reference to hydrothermal systems, Can. J. Chem. 58 (1980) 1763–1772.

[27] Y.T. He, S.J. Traina, Transformation of magnetite to goethite under alkaline pH conditions, Clay Miner. 42 (2007) 13–19.

[28] C. Hu, T. Peng, X. Hu, Y. Nie, X. Zhou, J. Qu, H. He, Plasmon-induced photodegradation of toxic pollutants with Ag-AgI/Al_2O_3 under visible-light irradiation, J. Am. Chem. Soc. 132 (2010) 857–862.

[29] J.-F. Guo, B. Ma, A. Yin, K. Fan, W.-L. Dai, Photodegradation of rhodamine B and 4-chlorophenol using plasmonic photocatalyst Ag-AgI/Fe_3O_4@SiO_2 magnetic nanoparticle under visible light irradiation, Appl. Catal., B. 101 (2011) 580–586.

[30] K.S.W. Sing, D.H. Everett, R.A.W. Haul, L. Moscou, R.A. Pierotti, J. Rouquérol, T. Siemieniewska, Reporting physisorption data for gas/solid systems with special reference to the determination of surface area and porosity, Pure Appl. Chem. 57 (1985) 603–619.

[31] J. Rouquérol, D. Avnir, C. W. Fairbridge, D.H. Everett, J.H. Haynes, N. Pernicone, J.D.F. Ramsay, K.S.W. Sing, K.K. Unger, IUPAC Recommendations for the characterization of porous solids, Pure Appl. Chem. 66 (1994) 1739–1758.

[32] X. Zhang, L. Lei, Effect of preparation methods on the structure and catalytic performance of TiO_2/AC photocatalysts, J. Hazard. Mater. 153 (2008) 827–833.

[33] S. Glaus, G. Calzaferri, The band structures of the silver halides AgF, AgCl, and AgBr: A comparative study, Photochem. Photobiol. Sci. 2 (2003) 398–401.

[34] B.R.S. Lemos, A.P.C. Teixeira, J.D. Ardisson, W.A.A. Macedo, L.E. Fernandez-Outon, C.C. Amorim, F.C.C. Moura, R.M. Lago, Magnetic amphiphilic composites applied for the treatment of biodiesel wastewaters, Appl. Sci. 2 (2012) 513–524.

[35] M. Villani, T. Rimoldi, D. Calestani, L. Lazzarini, V. Chiesi, F. Casoli, F. Albertini, A. Zappettini, Composite multifunctional nanostructures based on ZnO tetrapods and superparamagnetic Fe_3O_4 nanoparticles, Nanotech. 24 (2013) Article ID# 135601.

[36] Z. He, T. Hong, J. Chen, S. Song, A magnetic TiO_2 photocatalyst doped with iodine for organic pollutant degradation, Sep. Purif. Technol. 96 (2012) 50–57.

[37] X. Zhuang, Y. Wang, C. Feng, Y. Shen, D. Zhao, Highly efficient adsorption of bulky dye molecules in wastewater on ordered mesoporous carbons, Chem. Mater. 21 (2009) 706–716.

[38] C. Pelekani, V.L. Snoeyink, Competitive adsorption in natural water: role of activated carbon pore size, Water Res. 33 (1999) 1209–1219.

[39] M. Luo, D. Bowden, P. Brimblecombe, Removal of dyes from water using a TiO_2 photocatalyst supported on black sand, Water Air Soil Pollut. 198 (2009) 233–241.

[40] P. Wang, B. Huang, X. Qin, X. Zhang, Y. Dai, J. Wei, M.-H. Whangbo, Ag@AgCl: A highly efficient and stable photocatalyst active under visible light, Angew. Chem. Int. Ed. 47 (2008) 7931–7933.

[41] J.-M. Herrmann, Heterogeneous photocatalysis: fundamentals and applications to the removal of various types of aqueous pollutants, Catal. Today 53 (1999) 115–129.

[42] Y.H. Ao, J.J. Xu, D.G. Fu, X.W. Shen, C.W. Yuan, Low temperature preparation of anatase-TiO_2-coated activated carbon, Colloid Suf. A. Physicochem. Eng. Aspects 312 (2008) 125–130.

[43] S. Al-Qaradawi, S.R. Salman, Photocatalytic degradation of methyl orange as a model compound, J. Photochem. Photobiol., A. 148 (2002) 161–168.

[44] L.-C. Chen, F.-R. Tsai, C.-M. Huang, Photocatalytic decolorization of methyl orange in aqueous medium of TiO_2 and Ag-TiO_2 immobilized on γ-Al_2O_3, J. Photochem. Photobiol., A. 170 (2005) 7–14.

[45] Y. Zang, R. Farnood, Photocatalytic activity of AgBr/TiO_2 in water under simulated sunlight irradiation, Appl. Catal., B. 79 (2008) 334–340.

[46] J. Araña, J.L. Martínez Nieto, J.A. Herrera Melián, J.M. Doña Rodríguez, O. Gondález Díaz, J. Pérez Peñam, O. Bergasa, C. Alvarez, J. Méndez, Photocatalytic degradation of

formaldehyde containing wastewater from veterinarian laboratories, Chemosphere 55 (2004) 893–904.

[47] S.X. Liu, X.Y. Chen, X. Chen, A TiO_2/AC composite photocatalyst with high activity and easy separation prepared by a hydrothermal method, J. Hazard. Mater. 143 (2007) 257–263.

[48] P. Wang, B. Huang, Z. Lou, X. Zhang, X. Qin, Y. Dai, Z. Zheng, X. Wang, Synthesis of highly efficient Ag@AgCl plasmonic photocatalysts with various structures, Chem. Eur. J. 16 (2010) 538–544.

[49] D. Wang, Y. Duan, Q. Luo, X. Li, J. An, L. Bao, L. Shi, Novel preparation method for a new visible light photocatalyst: mesoporous TiO_2 supported Ag/AgBr, J. Mater. Chem. 22 (2012) 4847–4854.

[50] T. Wu, G. Liu, J. Zhao, H. Hidaka, N. Serpone, Photoassisted degradation of dye pollutants vs. self-photosensitized oxidation transformation of *Rhodamine B* under visible light irradiation in aqueous TiO_2 suspensions, J. Phys. Chem. B 102, 30 (1998) 5845–5851.

[51] J. Navio, G. Colon, M. Trillas, J. Peral, X. Domenech, J.J. Testa, J. Padron, D. Rodriguez, M.I. Litter, Heterogeneous photocatalytic reactions of nitrite oxidation and Cr(VI) reduction on iron-doped titania prepared by the wet impregnation method, Appl. Catal., B. 16 (1998) 187–196.

[52] M.I. Litter, J.A. Navio, Comparison of photocatalytic efficiency of TiO_2, iron oxides and mixed Ti(IV)-Fe(III) oxides, J. Photochem. Photobiol., A. 84 (1994) 183–193.

[53] J. Marugán, R. van Grieken, C. Pablos, C. Sordo, Analogies and differences between photocatalytic oxidation of chemicals and photocatalytic inactivation of microorganisms, Water Res. 44, 3 (2010) 789–796.

[54] K. Holt, A. Bard, Interaction of silver (I) ions with the respiratory chain of *Escherichia coli*: an electrochemical and scanning electrochemical study of the antimicrobial mechanism of micromolar Ag, Biochemistry 44 (2005) 13214–13223.

[55] C. Lok, C. Ho, R. Chen, Q. He, W. Yu, H. Sun, P. Tam, J. Chiu, C. Che, Proteomic analysis of the mode of antibacterial action of silver nanoparticles, J. Proteome Res. 5 (2006) 916–924.

[56] S. Liau, D. Read, W. Pugh, J. Furr, A. Russell, Interaction of silver nitrate with readily identifiable groups: relationship to the antibacterial action of silver ions, Lett. Appl. Microbiol. 25 (1997) 279–283.

[57] R. Kumar, H. Münstedt, Silver ion release from antimicrobial polyamide/silver composites, Biomater. 26 (2005) 2081–2088.

[58] M.I. Litter, Heterogeneous photocatalysis: transition metal ions in photocatalytic systems, Appl. Catal., B. 23 (1999) 89–114.

[59] A. Dobosz, A. Sobczyński, The influence of silver additives on titania photoactivity in the photooxidation of phenol, Water Res. 37 (2003) 1489–1496.

[60] X. Zhao, Q. Li, X. Zhang, H. Su, K. Lan, A. Chen, Simultaneous removal of metal ions and methyl orange by combined selective adsorption and photocatalysis, Environ. Prog. Sust. Energ. 30, 4 (2011) 567–575.

[61] C. Pulgarin, J. Kiwi, V. Nadtochenko, Mechanism of photocatalytic bacterial inactivation on TiO_2 films involving cell-wall damage and lysis, Appl. Catal., B. 128 (2012) 179–183.

[62] T. Saito, T. Iwase, J. Horie, T. Morioka, Mode of photocatalytic bactericidal action of powdered semiconductor TiO_2 on mutans streptococci, J. Photochem. Photobiol., B. 14 (1992) 369–379.

[63] J. Liu, D.A. Sonshine, S. Shervani, R.H. Hurt, Controlled release of biologically active silver from nanosilver surfaces, ACS Nano 4, 11 (2010) 6903–6913.

[64] H. Xu, H. Li, J. Xia, S. Yin, Z. Luo, L. Liu, L. Xu, One-pot synthesis of visible-light driven plasmonic photocatalyst Ag/AgCl in ionic liquid, ACS Appl. Mater. Interfaces 3 (2011) 22–29.

[65] J. Yu, G. Dai, B. Huang, Fabrication and characterization of visible-light-driven plasmonic photocatalyst Ag/AgCl/TiO_2 nanotube arrays, J. Phys. Chem. C 113 (2009) 16394–16401.

[66] D. Wang, Y. Duan, Q. Luo, X. Li, L. Bao, Visible light photocatalytic activities of plasmonic Ag/AgBr particles synthesized by a double jet method, Desalination 270 (2011) 174–180.

[67] W. Li, S. Liu, Bifunctional activated carbon with dual photocatalysis and adsorption capabilities for efficient phenol removal, Adsorption 18 (2012) 67–74.

[68] R. Leary, A. Westwood, Carbonaceous nanomaterials for the enhancement of TiO_2 photocatalysis, Carbon 49 (2011) 741–772.

[69] C. Baiocchi, M.C. Brussino, E. Pramauro, A.B. Prevot, L. Palmisano, G. Marci, Characterization of methyl orange and its photocatalytic degradation products by HPLC/UV-Vis diode array and atmospheric pressure ionization quadrupole ion trap mass spectrometry, Int. J. Mass Spec. 214 (2002) 247–256.

[70] E. Grabowska, J. Reszczynska, A. Zaleska, Mechanism of phenol photodegradation in the presence of pure and modified-TiO_2: A review, Water Res. 46 (2012) 5453–5471.

[71] P.-S. Yap, T.-T. Lim, Solar regeneration of powdered activated carbon impregnated with visible-light responsive photocatalyst: Factors affecting performances and predictive model, Water Res. 46 (2012) 3054–3064.

[72] M. Zhu, P. Chen, M. Liu, Sunlight-driven plasmonic photocatalysts based on Ag/AgCl nanostructures synthesized *via* an oil-in-water medium: enhanced catalytic performance by morphology selection, J. Mater. Chem. 21 (2011) 16413–16419.

Chapter 7:
Synthesis and characterization of Ag/AgBr-activated carbon composites for visible light induced photocatalytic detoxification and disinfection

Joanne Gamage McEvoy, Zisheng Zhang

Abstract

A novel Ag/AgBr-activated carbon (AC) composite photocatalyst was proposed and investigated. The composite was prepared by impregnation-precipitation-photoreduction, and characterized by X-ray diffraction, scanning electron microscopy, N_2 sorption, and ultraviolet-visible light diffuse reflectance spectroscopy. The prepared material possessed an "egg-shell" structure, where the photocatalyst formed heterogeneous agglomerates on the outside surface of the adsorbent host material. Ag/AgBr-AC exhibited enhanced absorption in the visible light region, and photocatalysis was studied for the degradation of model organic pollutants (methyl orange dye (MO), phenol) and a model microorganism (*Escherichia coli* K-12). Photocatalytic degradation of organic pollutants under visible light occurred with pseudo-first order rate constants of 0.0491 min^{-1} and 0.007 min^{-1} for MO and phenol, respectively using a catalyst loading of 0.5 g L^{-1}. Photocatalytic inactivation of 50 mL of a 10^6 CFU mL^{-1} bacterial suspension induced a 3-log loss of culturability in 60 minutes with a catalyst loading of 5 g L^{-1}. The mechanism of photocatalytic action for Ag/AgBr-AC composites was discussed with respect to the adsorption, localized surface plasmon resonance, and conventional semiconductor photocatalysis processes that took place under visible light.

Keywords: visible light photocatalysis, Ag/AgBr, silver halides, plasmon photocatalyst

7.1 Introduction

Photocatalytic processes involve the creation of electron-hole pairs upon irradiation of a photocatalyst and the subsequent interaction of these charge carriers with oxygen and water to create highly reactive species such as hydroxyl radicals, hydrogen peroxide, and superoxide, which mediate reduction and oxidation reactions causing the degradation of many organic pollutants. The reactive oxygen species produced can also interfere with normal biological processes, and photocatalysis has as such been proposed as a chlorine-free alternative disinfection method [1, 2]. Photocatalysis is advantageous for environmental remediation because it can be driven by solar irradiation, which is a free and abundant renewable resource, however, a major limitation associated to this lies in the low solar efficiencies and high rates of electron-hole recombination caused by use of the traditional TiO_2 photocatalyst, whose band gap falls within the UV range, which is not abundant in sunlight.

Research into visible light active photocatalysts has been ongoing in order to improve the solar response and reduce charge carrier recombination in photocatalytic materials through various approaches. In particular, surface plasmon resonance (SPR) enhanced photocatalysts based on silver/silver halides (Ag/AgX; X = Cl, Br, I) have been proposed as highly efficient and stable photocatalytic materials under visible light [3–5]. In these photocatalysts, the visible light activity is attributed to SPR of the metallic nanosilver, while efficient charge separation occurs due to interaction of the host silver halide with induced charges in the nanosilver. In addition, efforts towards improving mass transfer processes in photocatalysis have been made through the use of composite materials such as TiO_2-AC [6–8], which exhibit enhanced synergistic activity due to the continuous transfer of adsorbed pollutants to the supported photocatalytic active sites and the retention of intermediates on the adsorbent facilitating complete pollutant mineralization by promoting chain reactions. In our previous work, we explored these strategies for improving photocatalytic efficiencies by synthesizing and investigating a surface plasmon resonance enhanced composite adsorbent photocatalyst Ag/AgCl-AC [9], and studying its synergistic adsorption-photocatalysis behaviour for model organic pollutants (methyl orange (MO) dye, phenol) as well as its inactivation capabilities

against a model microorganism *Escherichia coli* K-12 (*E. coli*) [10].

Due to the smaller band gap energy of AgBr compared to AgCl ($E_{bg,\ indirect}$ of 2.6 eV and 3.25 eV, respectively [11]), the former may act by both SPR-enhanced and conventional semiconductor photocatalytic processes under visible light irradiation, since it can be excited by longer wavelength light in the visible range. Based on this dual excitation mechanism upon irradiation, the behaviour of Ag/AgBr differs significantly from that of Ag/AgCl-based materials [12]. In this study, we propose a novel Ag/AgBr-AC composite, which can act through both an SPR-mediated mechanism and by conventional semiconductor photocatalysis under visible light due to the narrow band gap of AgBr. The structure and properties of the prepared photocatalyst are explored, and activity for organics degradation and bacterial inactivation via photocatalysis are investigated.

7.2 Experimental

7.2.1 Materials

All materials were obtained from Fisher Scientific, unless otherwise mentioned, and were of reagent-grade or higher purity.

7.2.2 Synthesis of Ag/AgBr-AC composite

Ag/AgBr-AC composite was prepared using an impregnation-precipitation-photoreduction method. Briefly, unmodified AC (Darco G60, 100 mesh, Sigma-Aldrich) was loaded with a certain amount of $AgNO_3$ (ACS grade, MP Biomedicals), and precipitated with stoichiometric aqueous KBr, followed by photoreduction by an unfiltered 300 W tungsten halide bulb for one hour, and subsequent filtration and drying. The catalyst was prepared at a weight ratio of 2.5:1 (Ag: AC), which was calculated assuming that all of the AgBr was reduced to Ag, for simplicity. Reference AgBr and Ag/AgBr were prepared using the same procedures but eliminating the irradiation and impregnation steps, respectively.

7.2.3 Characterization

X-ray diffraction (XRD) patterns of prepared samples were collected by a Rigaku Ultima IV XRD apparatus with a CuK(α) source (λ = 0.15418 nm) operating at 40 kV and 44 mA. Sample morphology was probed using a Tescan VegaII XMU field emission scanning

electron microscope (SEM), with Au/Pd alloy coated samples (coated with an Anatech Hummer VII sputter coater). The surface areas, total pore volumes, and microporosity data were obtained from N_2 sorption isotherms collected at 77 K, using automatic adsorption apparatus and measurement systems (ASAP 2020, Micromeritics and Nova 4200E, Quantachrome). Brunauer, Emmett, and Teller (BET) surface areas were calculated from the collected sorption isotherms, total pore volumes were estimated using the volume of adsorbed N_2 at P/Po = 0.977, and the *t*-plot method was used to calculate micropore volume and external surface area. The Barrett-Joyner-Halenda method was used for the adsorption branch to calculate pore size data. Ultraviolet-visible (UV-Vis) diffuse reflectance spectra were collected on a Thermo Evolution 300 spectrophotometer (ThermoScientific) equipped with a Praying Mantis diffuse reflectance accessory over the range of 230 – 900 nm.

7.2.4 Photocatalytic degradation

7.2.4.1 Photoreactor

Photocatalytic degradation was studied using a slurry reactor in a constructed reflective housing. Illumination was provided by a 300 W ELH tungsten halide bulb (Ushio) with a UV filter (Kenko Zeta, $\lambda > 410$ nm, transmittance > 90%) at a distance of 10 cm from the beaker. The irradiation intensity was measured by a quantum meter (Biospherical QSL-2100; 400 nm $< \lambda <$ 700 nm), and was found to be approximately 4.7×10^{-3} Einstein m^{-2} s^{-1}. Cooling was provided by an external cooling jacket, and temperature of the reaction was controlled to $20^{o}C \pm 2$.

7.2.4.2 Photodegradation of methyl orange (MO)

Preliminary screening tests were performed to evaluate the adsorptive and photocatalytic behaviours of the prepared materials. Adsorption-only tests were conducted by allowing 200 mL of MO solution to equilibriate in the dark with 0.5 g L^{-1} composite in slurry under constant magnetic stirring at 180 rpm for 2 hours, at a constant temperature of $20\ ^{o}C \pm 2$, at the free solution pH. Combined adsorption-photocatalysis tests were performed using the same procedure in the presence of visible light irradiation. The initial MO concentration used for all tests was 25 mg L^{-1}. To monitor the pollutant concentration with time, samples were removed periodically and were centrifuged to remove suspended catalyst. Optical absorbance

of the supernatant was analyzed using a Genesys 10UV spectrophotometer (ThermoScientific) at a peak wavelength of $\lambda = 463$ nm for MO and was used to calculate concentration by the Beer-Lambert Law and a prepared calibration curve. UV-Vis full-spectrum wave scan data was also collected using a Biochrom Ultrospec 60 UV/Vis spectrophometer. The removal efficiency from these screening tests was calculated according to the following formula:

$$Removal\ Efficiency\ (\%) = (C_o - C_t)/C_o \times 100 \qquad (7.1)$$

Where C_o denotes the initial pollutant concentration (mg L^{-1}), and C_t is the concentration at time t (mg L^{-1}). Prolonged photocatalysis tests were performed using the same conditions, but allowing 200 mL of 25 g L^{-1} MO solution to equilibriate in the dark with 0.5 g L^{-1} catalyst under constant magnetic stirring at 180 rpm for 2 hours prior to each experiment, followed by irradiating the system for 2.5 hours. The pollutant removal from solution was given by the following expression (in mg pollutant per g photocatalyst):

$$q_t = V(C_o - C_t)/W \qquad (7.2)$$

where V is the volume of pollutant solution (L), and W is the mass of photocatalyst used (g). Recyclability tests were performed by centrifuging the reaction medium at 3500 rpm for 3 minutes in a Hermle Z400K centrifuge (Hermle Labortechnik GmbH), removing the supernatant, and redispersing the catalyst in 25 mg L^{-1} fresh MO solution before each re-use. The error associated to the experiments was estimated as the standard deviation between three independent runs.

7.2.4.3 Photodegradation of phenol

The adsorption and photodegradation of phenol was also studied in the slurry photosystem described using the same methodology as in the prolonged photocatalysis tests for MO (200 mL solution, composite loading of 0.5 g L^{-1}, magnetic stir speed of 180 rpm, free pH). However, for phenol, the initial concentration was 13 mg L^{-1}, and a peak wavelength of $\lambda =$ 270 nm was used for spectrophotometric analysis. In addition, irradiation was provided for 3 hours after the initial 2 hour dark adsorption period.

7.2.5 Photocatalytic disinfection

7.2.5.1 Bacterial strain

Bacterial inactivation studies were performed using non-pathogenic, wild-type *E. coli* K-12 (TG1 strain), which was obtained from Dr. Christopher Q. Lan from the Department of Chemical and Biological Engineering at the University of Ottawa and was maintained as a laboratory strain.

7.2.5.2 Cell culture and enumeration

Bacterial inactivation trials were performed in triplicate, and all materials were sterilized for 20 minutes at 121^{o}C prior to use. Inactivation was quantified by loss of bacterial culturability in the disinfection studies performed. Cell cultures were prepared by growing *E. coli* K-12 aerobically in Luria-Bertani medium (Difco LB broth, Miller; containing 10 g L^{-1} tryptone, 5 g L^{-1} yeast extract, and 10 g L^{-1} NaCl) on a rotary shaker maintained at 37 ^{o}C for 14 hours until the stationary phase was reached. The initial concentration from the overnight culture was quantified by plating 25 µL aliquots of serially diluted culture onto solid LB agar plates. Spread plates were prepared in triplicate for each dilution, and were incubated at 37^{o}C for 18 hours. Bacterial enumeration was performed using standard plate count methods for viable and cultivable bacteria, and counts obtained were used to calculate the cell concentration in colony forming units (CFU) mL^{-1}.

7.2.5.3 Temporal course of inactivation

Temporal course of inactivation was studied using 50 mL of saline (0.9 wt% NaCl) solution spiked with bacteria at an initial concentration of ~10^{6} CFU mL^{-1} in a 100 mL Pyrex beaker. The bacterial suspension used to prepare the spiked solution was obtained by centrifuging 1 mL of bacterial culture at 14 800 rpm for 5 minutes and resuspending the pellet in saline. The centrifugation and washing procedure was repeated three times to remove the growth media. The prepared composite was then added to the bacterial suspension at a loading of 5 g L^{-1}, and the mixture was magnetically stirred at 160 rpm under visible light irradiation, which was provided by a filtered 300 W Ushio ELH lamp. The temperature during inactivation was maintained at 20^{o}C ± 2 using a cooling jacket, and samples were collected periodically. The collected samples were serially diluted in saline and spread onto solid LB agar plates using

aliquot volumes ranging from 25 – 100 μL. The plates were incubated for 18 hours and bacteria enumerated using a standard plate count method, where counts in the range of 30 – 300 were considered statistically significant. Controls in the absence of photocatalyst and light were performed, respectively.

7.3 Results and discussion

7.3.1 Catalyst characterization

7.3.1.1 X-ray diffraction

Phase structure and crystallinity of the prepared Ag/AgBr-AC composite were investigated by XRD, and the results are given in Figure 7.1, with the patterns for pure Ag/AgBr and AC shown for reference. The unmodified AC host material possessed a mainly amorphous structure, although (002) and (004) hexagonal graphitic peaks were observed, attributed to small regions of crystallinity in the commercially-obtained adsorbent [13]. The pure Ag/AgBr prepared was well-indexed to cubic bromargyrite according to JCPDS card #06-0438, with characteristic peaks at 2θ (Bragg angle) values of 26.7°, 31.0°, 44.3°, 52.5°, 55.0°, and 64.5° corresponding to the (111), (200), (220), (311), (222), and (400) faces, respectively. Upon introduction of Ag/AgBr, the pattern of the resulting AC composite closely resembled that of the as-prepared Ag/AgBr. Major diffraction peaks for (111) and (200) planes of silver at 38.1° and 44.3°, respectively, were not prominent in any of the patterns, and this was thought to be due to the low content, small particle sizes, and high dispersion of photo-reduced silver in the silver halide composite system, as was previously reported for Ag-AgI/Al_2O_3 [5].

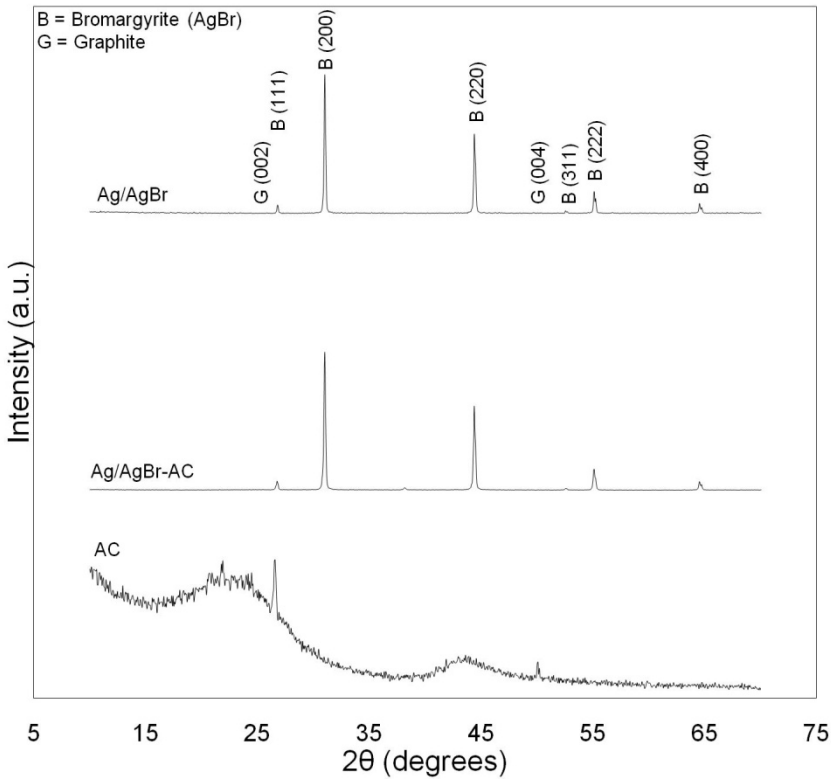

Figure 7.1: XRD patterns for prepared Ag/AgBr-AC composite, pure Ag/AgBr, and unmodified AC, respectively

7.3.1.2 Scanning electron microscopy

To study the structure and morphology of the prepared Ag/AgBr-AC composite, SEM imaging was performed, and the results are shown in Figure 7.2. Similar to the previously reported Ag/AgCl-AC [9], the prepared Ag/AgBr-AC possessed an "egg-shell" composite structure, where photocatalyst mainly occupied the outer surfaces and pore mouths of the host activated carbon, as was also observed for TiO_2-AC composites [14]. The Ag/AgBr-AC composites prepared resulted in a high surface coverage of the adsorbent host material by the photocatalyst, which was thought to affect their overall surface areas and sorption capacities due to AC pore-blockage. Ag/AgBr formed heterogeneous agglomerates on the adsorbent surface, with particle sizes in the range of approximately 250–830 nm.

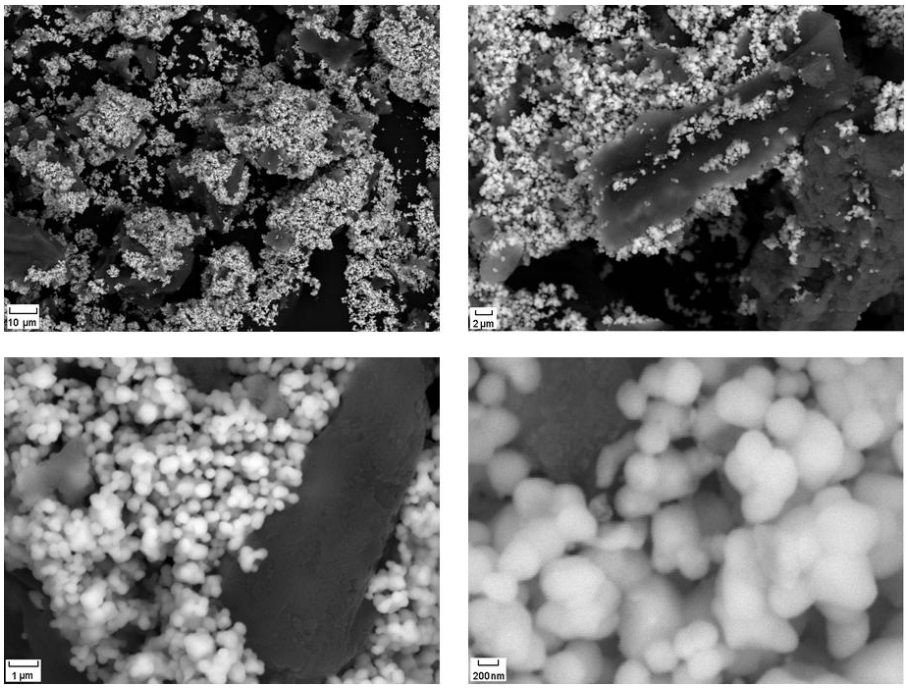

Figure 7.2: SEM images of Ag/AgBr-AC composite

7.3.1.3 N_2 sorption isotherms

Structure and porosity characteristics of the Ag/AgBr-AC composite were studied, and the N_2 sorption isotherm obtained is shown in Figure 7.3, with that of unmodified AC shown for comparison. Both of the isotherms were classified as Type IV according to the IUPAC standards [15], with H4 desorption hysteresis due to the presence of mesopores [16].

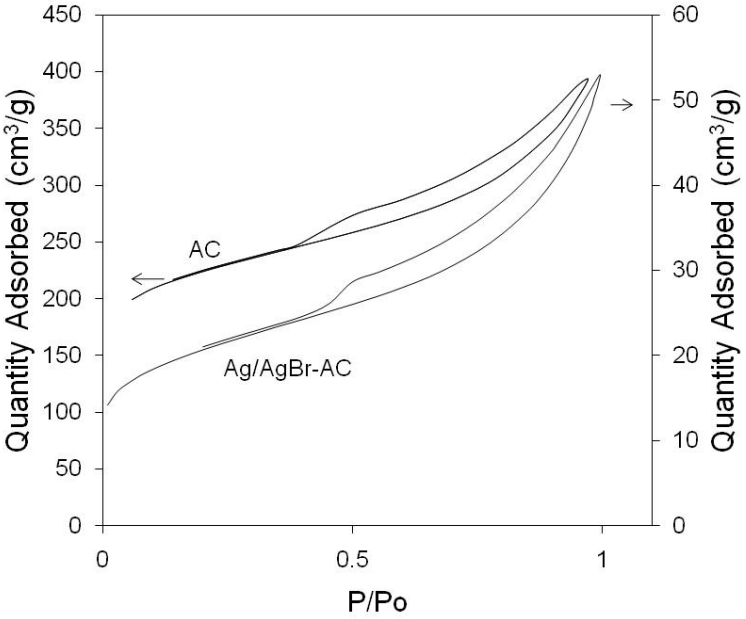

Figure 7.3: N_2 sorption isotherms for AC and Ag/AgBr-AC, respectively

Structural and textural characteristics of the synthesized materials were calculated from the obtained isotherms, and are summarized in Table 7.1. Upon introduction of photocatalyst into the AC matrix, the BET surface area, total pore volume, external surface area, as well as micropore volume and surface area all decreased significantly. The increase in average pore diameter in the composite was thought to be due to the creation of mesopores and macropores in channels between the deposited Ag/AgBr clusters on the surface of AC. The significant decrease in micropore volume in the composite was attributed to the effects of pore-blocking of mesopores by deposited Ag/AgBr, since these mesopores provided the main thoroughfares to microporous regions in the host adsorbent [14].

Table 7.1: Structural and textural characteristics of AC and Ag/AgBr-AC calculated from N_2 sorption isotherms

Material	**Property**					
	BET surface area ($m^2\ g^{-1}$)	Total pore volume ($cm^3\ g^{-1}$)	Micropore volume ($cm^3\ g^{-1}$)	Micropore surface area ($cm^2\ g^{-1}$)	External surface area ($cm^2\ g^{-1}$)	Average pore diameter, BJH ads. (nm)
AC	811	0.609	0.269	510	201	3.624
Ag/AgBr-AC	72.7	0.076	0.0087	19.6	53.1	6.428

7.3.1.4 UV-Vis diffuse reflectance spectroscopy

UV-Vis diffuse reflectance spectroscopy was performed to study the optical absorption behaviour of the prepared Ag/AgBr-AC composite, and the results are shown in Figure 7.4. Unreduced pure AgBr was found to possess an absorption edge at approximately 477 nm, corresponding to its band gap absorption ($E_{bg,\ indirect}$ = 2.6 eV [11]). This absorption edge was also observed for the partially photoreduced Ag/AgBr and Ag/AgBr-AC composite, indicating that the prepared materials possessed absorption in the visible light region due to band gap absorption. The same was not true for AgCl-based photocatalysts, since the absorption edge for AgCl was in the UV range (~385 nm, $E_{bg,\ indirect}$ = 3.25 eV [11]). Upon partial reduction of pure AgBr, enhanced visible light absorption was observed, and a broad absorption band from 480 – 730 nm appeared, which was not present in the unreduced sample. This absorption was attributed to surface plasmon resonance of metallic silver nanoparticles produced from AgBr upon irradiation, where the peak broadness was thought to be due to a variation in the shape and diameters of metallic silver clusters [3]. The prepared Ag/AgBr-AC composite retained both semiconductor and surface plasmon resonance enhanced visible light absorption characteristics exhibited by the incorporated Ag/AgBr, and was therefore appropriate for further investigation as a visible light active photocatalyst.

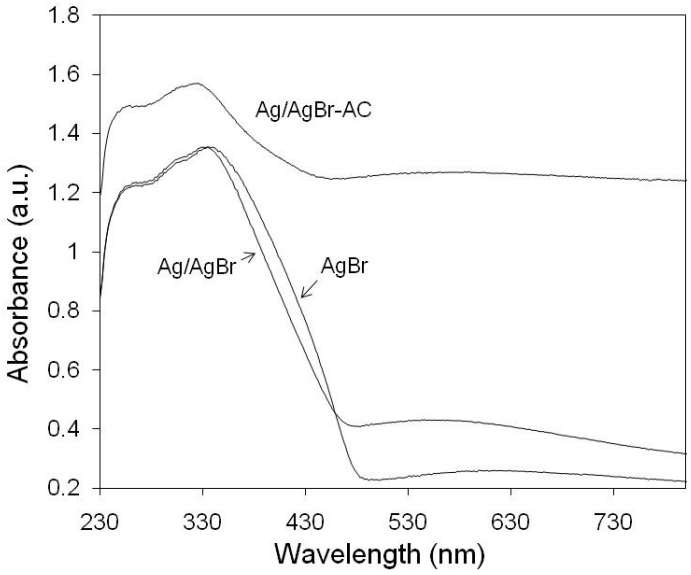

Figure 7.4: UV-Vis absorption spectra for unreduced AgBr, Ag/AgBr, and Ag/AgBr-AC composite, respectively

7.3.2 Photocatalytic degradation of organic compounds

7.3.2.1 Methyl orange adsorption and photodegradation

Preliminary screening tests were performed to evaluate the MO removal behaviour exhibited by the prepared Ag/AgBr-AC composites by adsorption and combined adsorption-photocatalysis processes, respectively, against a model organic dye (MO). The results from these studies are shown in Figure 7.5. In the rapid screening tests, MO adsorption behaviour in the dark was compared to the combined adsorption-photocatalysis process in the presence of visible light irradiation [17, 18].

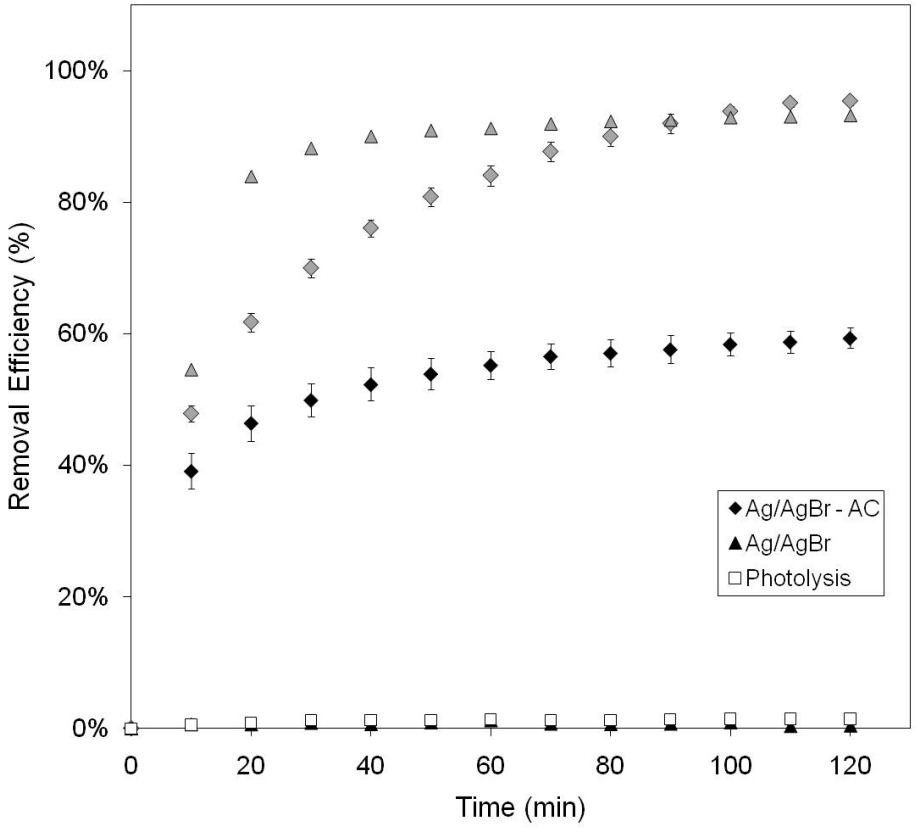

Figure 7.5: Comparison of adsorptive and combined adsorptive-photocatalytic MO removal for Ag/AgBr-AC and Ag/AgBr, where black and grey markers represent adsorption and combined adsorption-photocatalysis, respectively. (C_o = 25 mg L^{-1}, loading = 0.5 g L^{-1}) – *average of three trials, representative error bars shown*

The photolysis of MO was found to be negligible, since its concentration did not change significantly under irradiation due to visible light absorption by the dye. It should also be noted that unmodified AC, used at a loading of 0.5 g L^{-1}, could remove all MO in under 10

minutes, and was not shown in Figure 7.5. The pure Ag/AgBr exhibited negligible adsorptive capabilities at a nominal loading of 0.5 g L^{-1}, removing under 0.4% of MO by adsorption alone. However, upon irradiation, the removal by Ag/AgBr significantly increased due to visible light induced photocatalytic action on the dye, and the MO removal efficiency observed after 2 hours was approximately 93.3%. In contrast to pure Ag/AgBr, the prepared Ag/AgBr-AC composite was able to adsorb MO in the dark, and removed up to 59.3% in the adsorption-only process. Upon irradiation, the composite activity for MO removal also increased markedly, achieving a 95.4% removal efficiency after 2 hours. The enhancement observed was thought to be due to the effect of the incorporated photocatalyst to generate radical species, which could degrade the dye through a dynamic adsorption-photocatalysis mechanism. Although the final removal efficiency obtained with the Ag/AgBr-AC composite was comparable to that of pure Ag/AgBr, the two materials exhibited different temporal removal behaviours, as seen in Figure 7.5. To further investigate the MO removal processes mediated by Ag/AgBr and Ag/AgBr-AC composite photocatalysts, full spectrum UV-Vis data for the MO dye was collected and the results are shown in Figure 7.6.

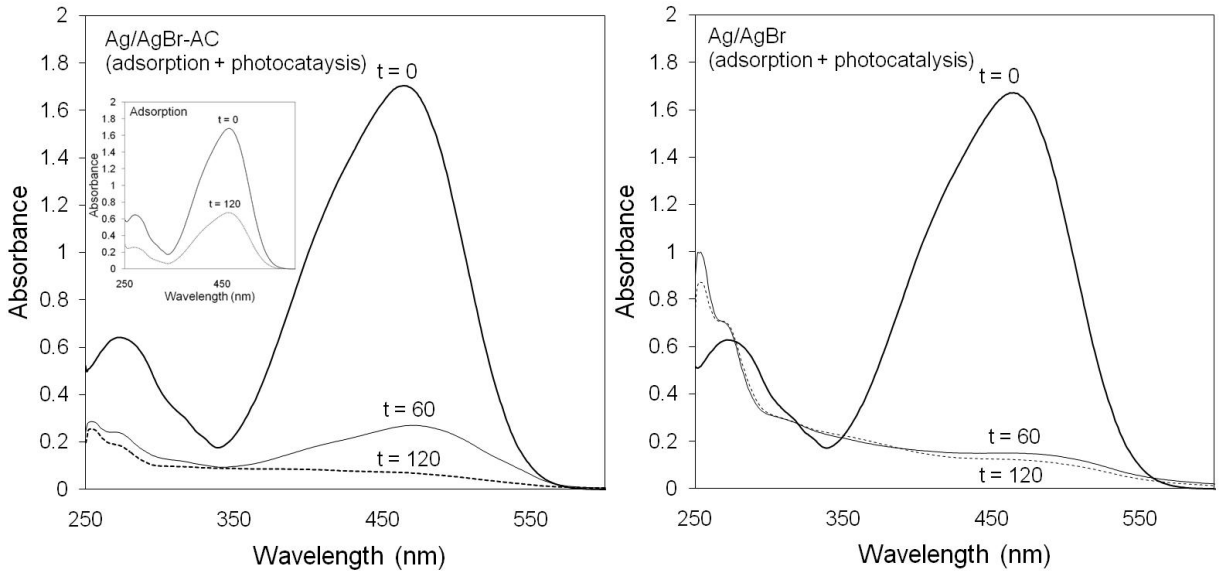

Figure 7.6: UV-Vis solution spectra during combined adsorptive-photocatalytic MO removal processes mediated by Ag/AgBr-AC composite and Ag/AgBr, respectively. Inset: UV-Vis solution spectra for MO removal by adsorption only using Ag/AgBr-AC. (C_o = 25 mg L^{-1}, loading = 0.5 g L^{-1})

The major peak observed at 463 nm in the initial solution spectra (at t = 0) was attributed to light absorption by azo bonds in the extended aromatic ring structure of MO, and the smaller peak around 265 nm occurred due to absorption by benzene-like structures, which absorbed in the 200 – 270 nm range [19]. For the adsorption-only removal by Ag/AgBr-AC (shown inset), these peaks decreased monotonously with treatment time, indicating that dark adsorption did not significantly affect MO structure, since the optical absorption characteristics of the initial solution were preserved. The combined adsorption-photocatalysis process also exhibited similar decreases in spectral intensities, although with increased treatment time, the spectral height of the azo peak became lower than the intensity of the peak attributable to benzene-like structures. In contrast, for adsorption-photodegradation mediated by pure Ag/AgBr, the spectral height for the mono-substituted aromatics initially increased, and then gradually decreased upon increased treatment time. These trends were thought to be due to the initial photodegradation of polyaromatic rings of MO by radical attack on the azo bond to create mono-substituted aromatics causing dramatic reduction in the spectral height at the extended MO peak wavelength. The reaction intermediates formed could then undergo aromatic fragment degradation upon prolonged photocatalytic treatment, causing decay in the mono-aromatic peak intensities. The intensities of peaks observed for the Ag/AgBr and Ag/AgBr-AC materials in the combined adsorption-photocatalysis processes, respectively, suggested that the aromatic organic load in solution at the end of treatment time for removal via the Ag/AgBr-AC composite was lower than that observed for unsupported Ag/AgBr, as evidenced by the lower spectral intensities of reaction intermediate peaks. This reduced aromatic organic load may have been due to the effects of adsorption in the AC composite, transferring the reaction intermediates from the solution phase (where UV-Vis spectra were quantified) to the adsorbent solid. However, it should be noted that the AC adsorbent support was suggested in literature to play a role in the photocatalytic mechanism, where adsorbent-supported photocatalysts caused the formation of different photoreaction intermediates than the unsupported photocatalyst alone, such as for phenol photodegradation by TiO_2-AC [20]. The synergistic effect of the adsorbent support on the observed photocatalytic activity has been attributed to its ability to transfer adsorbed pollutants to the supported photocatalytic active sites due to mass transfer gradients [21], and

to adsorptive intermediate retention facilitating photocatalytic chain reactions leading to more complete mineralization [22, 23]. These observations regarding the role of activated carbon on photocatalytic mechanisms agree with the preliminary screening results obtained in this study.

To further characterize the removal processes, prolonged runs were performed by investigating adsorption and subsequent photocatalytic degradation, and the results are shown in Figure 7.7 as MO removed from solution per weight of catalyst used. The prolonged adsorption-photocatalysis test consisted of a 2 hour dark adsorption period followed by visible light irradiation of the reaction system for 2.5 hours. The Ag/AgBr-AC composite achieved a pseudo-equilibrium after 2 hours of dye adsorption in the dark, and upon irradiation, exhibited a sharp change in the removal behaviour due to photoexcitation of the catalyst and subsequent action of the photo-produced radicals, initiating the dynamic adsorption-photocatalytic degradation process.

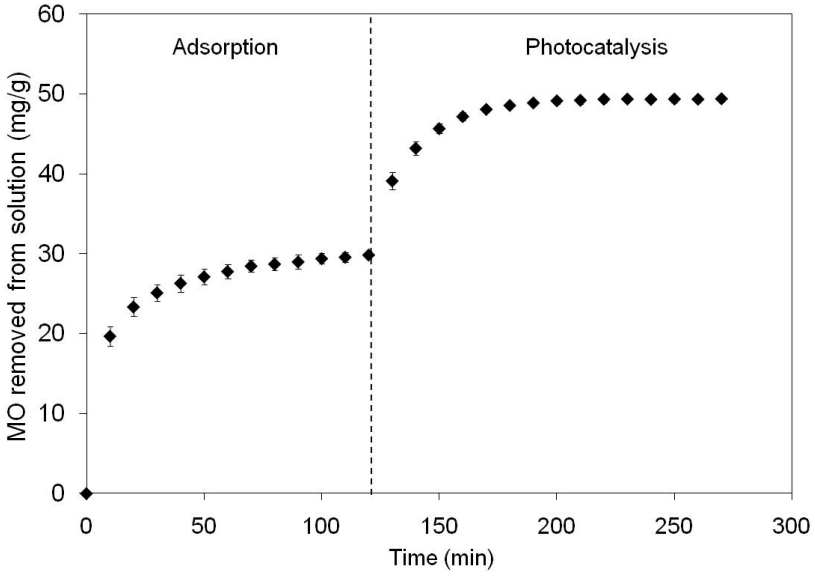

Figure 7.7: Adsorption and subsequent photocatalysis using Ag/AgBr-AC composites. (C_o = 25 mg L^{-1}, loading = 0.5 g L^{-1})

The prepared Ag/AgBr-AC composites were able to remove approximately 29.8 mg MO/g composite via adsorption in the dark. SEM observation of the catalysts revealed that much of

the adsorbent surface was covered by silver halide structures, and this was thought to have a negative influence on its sorption capacity for MO, especially due to pore blockage of interior adsorption sites in the sorbent by the photocatalyst. The increased removal upon irradiation was attributed to photoexcitation of the Ag/AgBr catalyst and production of radical species such as hydroxyl and superoxide radicals, which could interact with MO to cause its degradation.

Concentration data for photocatalytic MO removal was normalized by the initial concentration at the start of irradiation, which was taken as the adsorption pseudo-equilibrium concentration, and presented as fraction degraded (C/C_o) as function of irradiation time in Figure 7.8. The photocatalytic process was described according to Langmuir-Hinshelwood kinetics, given by the following equation:

$$-dC/dt = K k_r C/(1+KC) \quad (7.3a)$$

Where K is the Langmuir Hinshelwood adsorption coefficient (L mg^{-1}), and k_r is the reaction rate constant (mg L^{-1} min^{-1}). This kinetic expression is easily simplified into a pseudo-first order equation when the initial concentration used is sufficiently small (< 10^{-3} mol L^{-1} [24]). In this case, $C_o < 7.7x10^{-5}$ mol L^{-1}, so the first-order approximation was valid. The integrated rate equation is given by:

$$ln(C_o/C) = k't \quad (7.3b)$$

Where k' denotes a pseudo-first order rate constant (min^{-1}). The rate constants were calculated using this method for the initial linear portion of the reaction, and the fitted and experimental data for the Ag/AgBr-AC composites are shown in the inset of Figure 7.8.

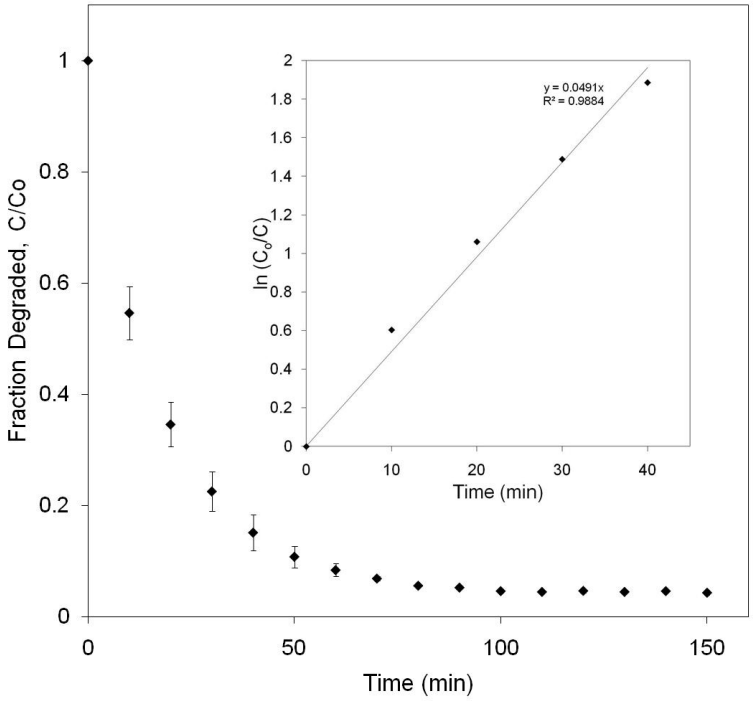

Figure 7.8: MO photodegradation by Ag/AgBr-AC composites. Photocatalytic degradation kinetics shown inset. (loading = 0.5 g L^{-1})

The fitted data yielded a pseudo-first order rate constant of 0.0491 min^{-1} (R^2 = 0.988), and the silver bromide-containing composite possessed a photocatalytic rate more than three times greater than that reported for a similar Ag/AgCl-AC material [9]. This was thought to be partially attributable to improved visible light activity of the Ag/AgBr photocatalytic component over that of Ag/AgCl in the composites prepared. Unlike Ag/AgCl, whose visible light activity was only due to surface plasmon resonance of the incorporated nanosilver, Ag/AgBr was able to generate electron-hole pairs due to visible light induced excitation of the host silver halide itself, since its optical band gap fell within the visible light range. This mechanism was thought to contribute to visible light induced photoactivity in addition to surface plasmon resonance enhancement from metallic silver, as discussed in subsequent sections. Therefore, the combined visible light activity of AgBr and metallic Ag components were thought to contribute to the increased photocatalytic efficiency observed.

7.3.2.2 Recyclability and stability

The recyclability and stability of the prepared Ag/AgBr-AC composite were investigated by conducting four consecutive adsorption-photocatalysis cycles, recovering the catalyst between runs by centrifugation and decanting, and replacing the reaction fluid with fresh 25 g L^{-1} MO solution. The adsorption and photodegradation performance in these sequential runs is given in Figure 7.9 as mg L^{-1} (ppm) MO removed during each cycle by adsorption and photocatalysis, respectively.

The adsorptive MO removal decreased with increasing cycle number, and this was thought to be due to exhaustion of sorption capacity in the composite. Despite this, the incorporated photocatalyst was thought to play a role in partially regenerating some of the adsorptive sites on the AC surface by degrading adsorbed MO and intermediates during the photocatalysis cycles, since the additive MO sorption in the first two runs (~36.4 mg MO g composite^{-1}) was greater than the average total MO sorption capacity observed for the composite (~29.8 mg MO g composite^{-1}, as seen in Figure 7.7). However, beyond the second cycle, the adsorptive capabilities of the composite were exhausted, which was also thought to contribute to the decreased photoactivity observed with increasing cycle number, since the adsorption and accumulation rate of MO was greater than its degradation rate, saturating the surface and resulting in decreased photonic efficiency [25]. The photodegradation of MO observed in the second to fourth uses of the composite were 92.3%, 78.9%, and 65.9% of the total MO degraded in the first run, respectively. The formation of reaction intermediates was also thought to contribute to the decrease in photocatalytic activity observed, since their adsorption and accumulation on the composite could increase the total organic load in the system with increasing cycle number [26, 27].

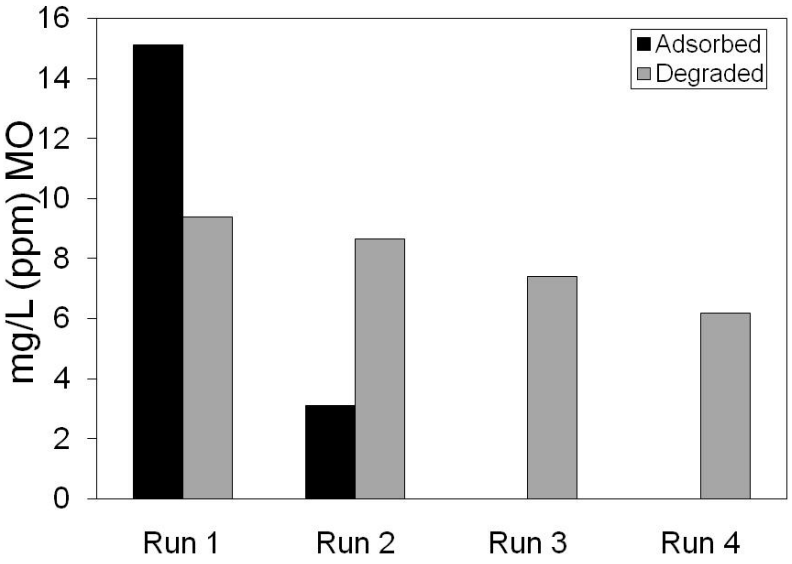

Figure 7.9: Adsorption and photodegradation performance of Ag/AgBr-AC composite over four consecutive cycles. (C_o = 25 mg L^{-1}, loading = 0.5 g L^{-1})

To evaluate stability of the prepared composite in repeated uses, the spent material was characterized by XRD, and the pattern obtained is shown in Figure 7.10, with that of the fresh composite, and of the composite used once shown for comparison.

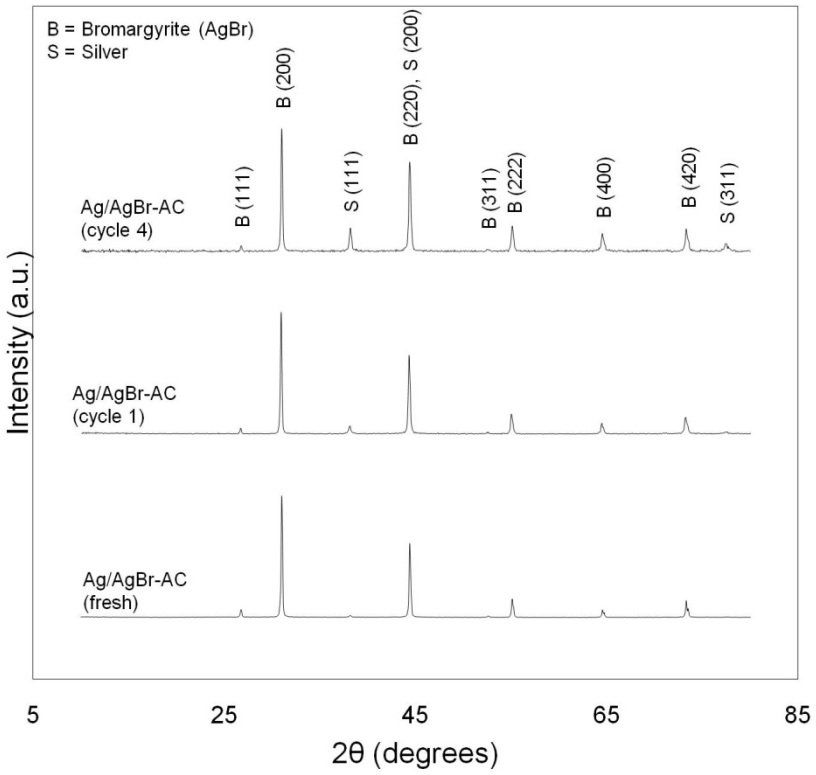

Figure 7.10: XRD patterns for fresh Ag/AgBr-AC and recycled composite after one and four consecutive adsorption-photocatalysis cycles, respectively

The patterns for the recycled materials exhibited similar crystallographic characteristics as the pattern for the fresh composite, in that peaks attributable to bromaragyite were observed in accordance with JCPDS card #06-0438. However, a significant increase in the major (111) peak of metallic silver at 38.1^{o} was observed with increasing cycle number, as well as increases in the heights of the (200) and (311) faces at 44.3^{o} and 64.4^{o}, respectively (JCPDS card #01-087-0597). This indicated that metallic silver was present in increasing amounts as the catalyst was used in repeated cycles, which was thought to be largely influenced by reduction of AgBr in the photosystem under irradiation. This effect was also observed in literature for other AgBr- based photocatalysts such as AgBr/Ag polyhedrons [28] and AgBr-graphene photocatalysts under visible light [29], and AgBr/ZnO photocatalysts under UV [30]. Metallic silver clusters present in the recycled catalyst used four times were thought to be formed during prolonged photoirradiation used in the cycling experiments, and were observed by SEM, as shown in Figure 7.11. The morphology of the Ag/AgBr component in

the recycled AC composite varied from the initial morphology observed, and small clusters on the order of ~100 nm attributable to metallic Ag appeared on the surface of AgBr particles.

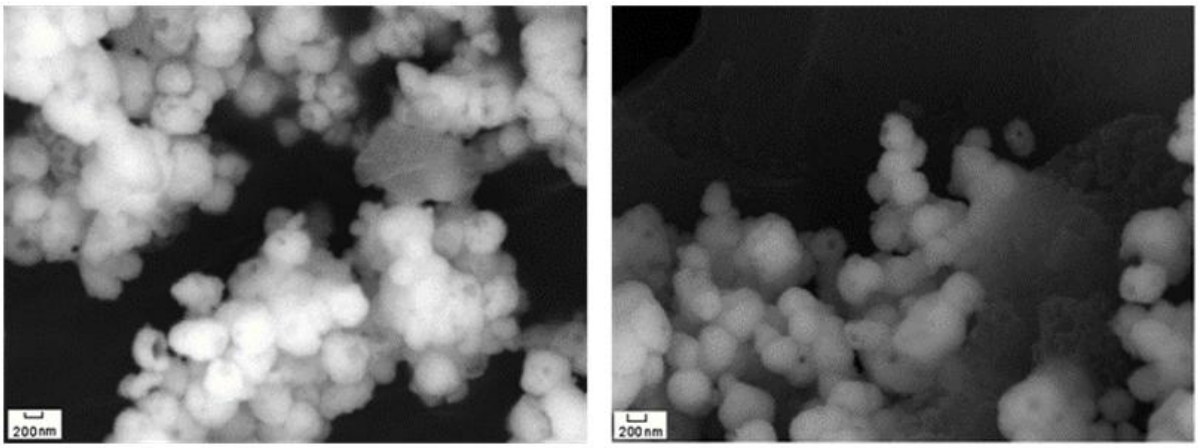

Figure 7.11: SEM images of recycled Ag/AgBr-AC composite after four consecutive adsorption-photocatalysis cycles

This metallic nanosilver was thought to contribute to the surface plasmon resonance enhancement in the recycled composite, and UV-Vis diffuse reflectance spectroscopy was performed to investigate its light absorption behaviour.

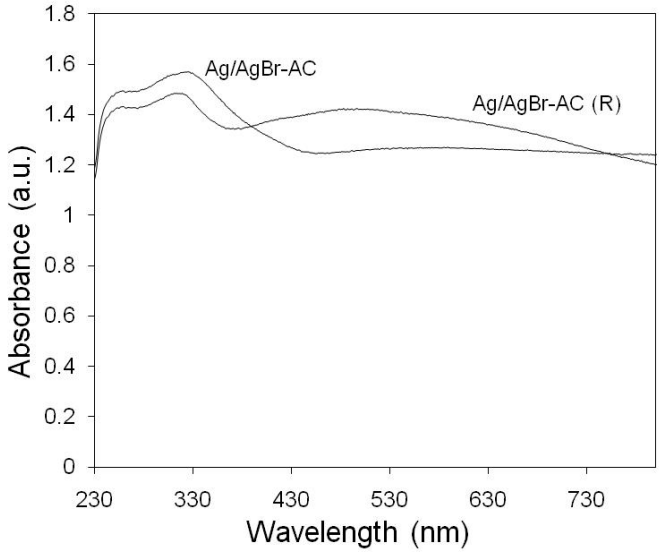

Figure 7.12: UV-Vis spectra for fresh Ag/AgBr-AC and recycled composite after four consecutive adsorption-photocatalysis cycles

As seen from the results in Figure 7.12, the recycled composite exhibited a much stronger SPR band in the visible light region than the fresh material, due to the larger quantity of silver nanoparticles formed on the AgBr surfaces during cycling experiments. This increased visible light absorption was thought to enhance photoactivity observed in subsequent cycles to some extent. It should be noted metallic silver exhibiting SPR in silver/silver halide photocatalysts has been reported to act in concert with the host silver halide to help stabilize photo-induced charges and prevent their recombination, and also helps prevent the generated electrons from being transferred to Ag^+ in AgX [31]. As such, the formed metallic nanosilver may help improve the stability of Ag/AgX-type photocatalysts in subsequent cycles. For example, Wang et al. noted that a large amount of Ag was generated on the surface of prepared AgBr/Ag after one photocatalytic cycle, but that the composition did not vary significantly after the fifth cycle [28], and the stability observed in subsequent cycles was attributed to the electron-hole separation induced in the composite material.

7.3.2.3 Phenol photodegradation

The photodegradation of a colorless organic target pollutant, phenol, was investigated using the prepared Ag/AgBr-AC composite to study the degradation activity in the absence of any photosensitization mechanisms due to visible light absorption from the organic dye [32]. The adsorption and subsequent photocatalysis of phenol is shown in Figure 7.13, with the degradation kinetics given inset. The photolysis of phenol was previously confirmed to be negligible in this system, and the composite was able to convert approximately 7.6 mg phenol per gram of composite in three hours of irradiation, with a pseudo-first order rate constant of 0.007 min^{-1}, indicating that Ag/AgBr-AC possessed activity for organics degradation in the absence of dye-sensitization.

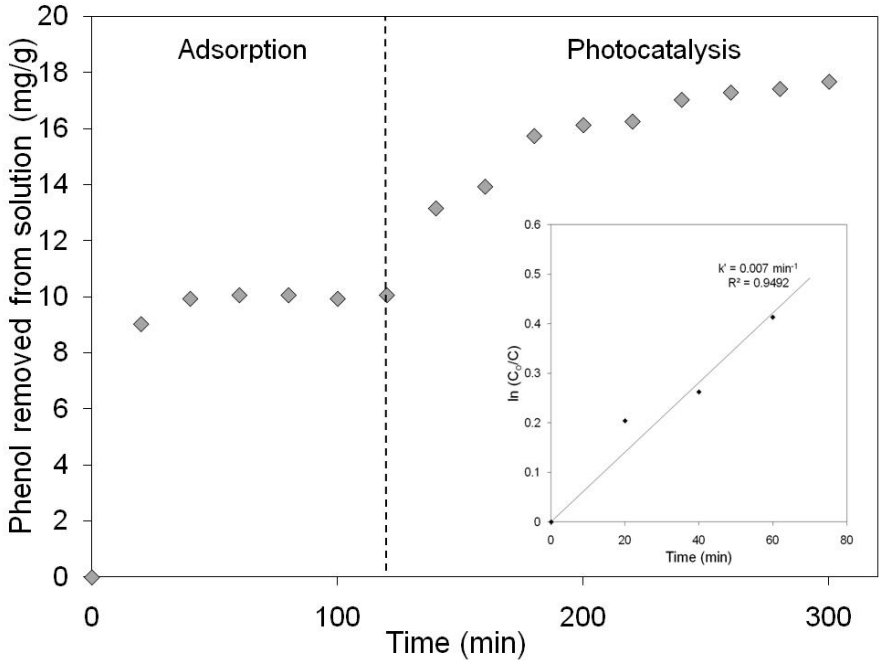

Figure 7.13: Adsorption and subsequent photocatalysis using Ag/AgBr-AC in phenol. Photocatalytic degradation kinetics shown inset. (Co = 13 mg L^{-1}, loading = 0.5 g L^{-1})

7.3.3 Photocatalytic disinfection of *E. coli* K-12

The photocatalytic inactivation Gram-negative *E. coli* K-12 was investigated, since it is a common indicator for faecal contamination [33]. The temporal course of inactivation was studied using standard plate count methods for quantification of loss of culturability, and the results are shown in Figure 7.14 for the Ag/AgBr-AC composite in dark and light conditions, respectively. The inactivation curve obtained for a photolysis control in the absence of catalyst is also shown for comparison.

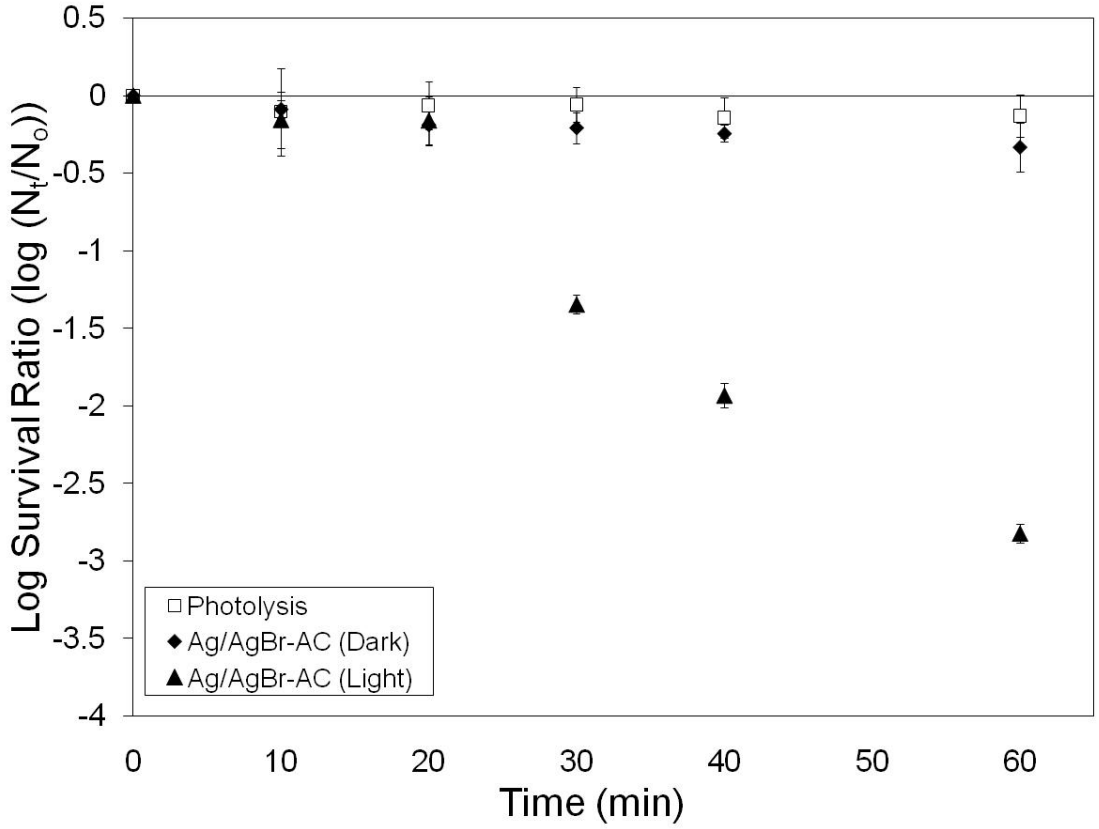

Figure 7.14: Inactivation curves for photolysis and Ag/AgBr-AC composite in dark and light conditions, respectively. (N_o = 10^6 CFU mL^{-1}, composite loading = 5 g L^{-1}, pH = 5.5)

Loss of culturability due to photolytic cell death was found to be negligible in this system, with a final survival ratio (Nt/No at t = 60) of 0.77 ± 0.22. In comparison, the final survival ratios associated to Ag/AgBr-AC in the dark and Ag/AgBr-AC under irradiation were 0.49 ± 0.15, and 0.0015 ± 0.00027, respectively. The loss of culturability in the dark inactivation trial was representative of both bacterial adhesion onto the composite and the bactericidal effects of Ag/AgBr-AC. However, the Ag/AgBr-AC used in the absence of light was not able to induce a significant reduction in the bacterial population, which suggested that the bacterial adhesion onto the composite was not significant, and that silver ion elution from the material in the dark did not occur at high enough concentrations to cause a significant antibacterial effect. The latter observation differed from the results for the previously studied Ag/AgCl-AC composites [10], which exhibited some bactericidal activity in the absence of irradiation, attributed to elution of silver ions from the composite material in the dark. These

silver ions were thought to be present as Ag^+ and dissolved silver complexes, which were reported to have a high affinity to bind to thiol groups in cysteine residues from respiratory and transport proteins [34, 35], and were toxic to *E. coli* at sub-micromolar concentrations [36]. The absence of biocidal effect due to eluted silver for Ag/AgBr-AC in this system was attributed to the lower solubility of AgBr than AgCl to form dissolved silver complexes, and the suspected smaller quantity of oxidizable metallic silver on the surface of prepared Ag/AgBr-AC, since Ag clusters were not easily observed by SEM for the fresh composite. It should also be noted that, although AC itself can induce some bacterial adhesion due to interactions between its positive surface charge at the pH used in these studies (~5.5) and the negatively charge bacterial cell wall, surface coverage by negatively charged Ag/AgBr photocatalyst was thought to impart a more negative overall charge to the Ag/AgBr-AC composite, introducing Coulombic repulsions with the Gram-negative bacteria and preventing significant bacterial adhesion.

In contrast, Ag/AgBr-AC under irradiation was able to induce a significant bacterial inactivation, causing up to 3-log reduction in 60 minutes. This was thought to be due to the formation of oxidative radicals and species such as $^{\bullet}OH$, $^{\bullet}O_2^-$, and H_2O_2 by the interaction of photogenerated electrons and holes from the photocatalyst with dissolved oxygen and water. These reactive species could cause peroxidation of functional groups in the cell wall bilayers of *E. coli*, leading to eventual lysis through efflux of intracellular components, as previously described in literature [37, 38]. The temporal course of inactivation in the irradiated system exhibited a delay during the initial twenty minutes of reaction, and a similar result was reported for visible light photocatalytic destruction of *E. coli* by Ag/AgBr/TiO_2 [39]. The authors further investigated the observed lag by quantifying eluted potassium ion concentration as an indicator of cell membrane permeability, and found that K^+ leakage occurred immediately upon irradiation and continued upon prolonged treatment. During the lag period, the leakage was due to disordering of the outer membrane by lipidperoxidation, although this did not cause bacterial inactivation, since mechanisms to repair cell wall damage may have also played a role during this initial stage [40]. This presence of this "shoulder" region has been discussed with respect to photocatalytic inactivation kinetics as a

single-hit multiple-target or series event phenomenon, where cell damage occurs cumulatively rather than as an instantaneously lethal event [41].

7.3.4 Mechanism of photocatalytic action

For degradation of organic compounds via photocatalysis, the Ag/AgBr-AC composites were thought to act through a dynamic adsorption-photocatalysis process under visible light, where the role of the activated carbon was to concentrate the pollutant around active sites in the catalyst, and the Ag/AgBr acted through combined surface plasmon resonance and semiconductor photocatalysis mechanisms to promote the formation of reactive species such as Br^{o}, superoxide anion, hydroxyl radical, and oxidative holes. The process is shown schematically for the degradation of organic pollutants (MO, phenol) in Figure 7.15. The adsorbed pollutant could migrate to the suspended Ag/AgBr photocatalytic sites via concentration gradients present in the material [42], and the adsorptive composite was thought to promote retention and further reaction of degradation intermediates, reducing the effects of mass transfer limitations on the photocatalytic process.

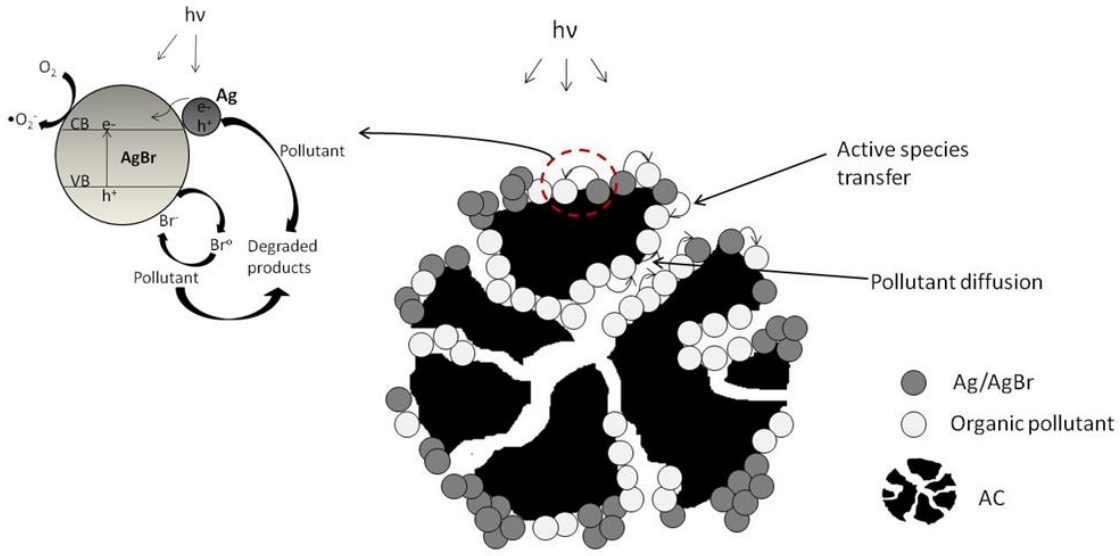

Figure 7.15: Mechanisms of Ag/AgBr-AC photocatalysis on the degradation of an organic pollutant (adapted from [12, 43])

As recently discussed by Jiang et al. [12], the enhanced activity observed using Ag/AgBr photocatalysts may be due to enrichment of surface plasmon resonance excited electrons on the surface of the silver nanoparticles, and their subsequent injection to the conduction band of AgBr due to the formation of a Schottky barrier at the interface of the metal and semiconductor, and the lower work function of Ag than AgBr (Φ_{Ag} = 4.25 eV, Φ_{AgBr} = 5.3 eV) [44]. In addition, AgBr conventional semiconductor photocatalysis also occurred based on the low energy band gap of AgBr, which could be excited by visible light to liberate electrons from its valence band, leaving behind positively charged holes. The electrons and holes produced in the process could then interact with dissolved oxygen and water to produce reactive species necessary for photodegradation. The holes could also induce the formation of Br^o from Br^-, which could oxidize the adsorbed pollutants to regenerate Br^-. The junction between Ag and AgBr promoted charge separation in the Ag/AgBr photocatalyst, and a synergistic effect of SPR and semiconductor photocatalysis may have also occurred due to the SPR-induced local electric field causing an increased generation of electron-hole pairs in the semiconductor [12]. It should be noted that an alternative mechanism for Ag/AgBr photoactivity proposed in literature discussed the polarization of surface plasmon resonance induced charges relative to the Ag/AgBr interface, where electrons accumulated in the metallic silver, and emphasized the importance of electron affinity of the incorporated halide atoms and the formation of oxidizing monovalent halides as the limiting step in the Ag/AgX photoinduced processes [45]. In the case of photocatalytic inactivation, the discussed mechanisms for electron-hole formation were thought to be similar, where the reactive oxygen species formed by photocatalysis could cause lipidperoxidation of the cell envelope in the bacteria studied.

7.4 Conclusions and recommendations

A novel Ag/AgBr-AC adsorbent photocatalyst composite was synthesized via impregnation-precipitation-photoreduction, and possessed enhanced visible light absorption due to the localized surface plasmon resonance of metallic nanosilver, and band gap absorption by AgBr. The prepared composite could be used for the degradation of model organic pollutants (methyl orange dye, phenol) under visible light irradiation in a slurry system with a loading

of 0.5 g L^{-1}. In addition, the Ag/AgBr-AC composite exhibited good activity for the inactivation of *E. coli* bacteria, which was thought to be due to the production of photo-induced radicals and their subsequent action on cells to induce a loss of culturability, where a 3-log reduction was observed in 60 minutes using a 5 g L^{-1} slurry. The catalyst recyclability and stability were investigated, and although the composite exhibited photocatalytic activity in up to 4 cycles, some *in situ* reduction of AgBr to Ag occurred and was evidenced by post-use characterization. The effect of this partial reduction on the long-term stability of the Ag/AgBr-AC composite should be further investigated. In addition, the adsorptive and photocatalytic activities should be optimized through adjusting the adsorbent to photocatalyst ratio, and regeneration strategies investigated in order to improve adsorptive site regeneration during photocatalytic cycles.

7.5 Acknowledgments

This work was supported by the Natural Sciences and Engineering Research Council of Canada. The authors would like to acknowledge Dr. Yong Yang at the Centre for Catalysis Research and Innovation (University of Ottawa) and Dr. Jianqun Wang (Carleton University) for help with sample characterization.

7.6 References

[1] T. Matsunaga, R. Tomoda, T. Nakajima, H. Wake, Photoelectrochemical sterilization of microbial cells by semiconductor powders, FEMS Microbiol. Lett. 29, 1–2 (1985) 211–214.

[2] J. Gamage, Z. Zhang, Applications of photocatalytic disinfection: A review, Int. J. Photoenergy, 2010 (2010) Article ID 764870. *(also given in Appendix B)*

[3] P. Wang, B. Huang, X. Zhang, X. Qin, H. Jin, Y. Dai, Z. Wang, J. Wei, J. Zhan, S. Wang, J. Wang, M.-H. Whangbo, Highly efficient visible-light plasmonic photocatalyst Ag@AgBr, Chem. Eur. J. 15 (2009) 1821–1824.

[4] P. Wang, B. Huang, X. Qin, X. Zhang, Y. Dai, J. Wei, M.-H. Whangbo, Ag@AgCl: A highly efficient and stable photocatalyst active under visible light, Angew. Chem. Int. Ed. 47 (2008) 7931–7933.

[5] C. Hu, T. Peng, X. Hu, Y. Nie, X. Zhou, J. Qu, H. He, Plasmon-induced photodegradation of toxic pollutants with Ag-AgI/Al_2O_3 under visible-light irradiation, J. Am. Chem. Soc. 132 (2010) 857–862.

[6] J. Matos, J. Laine, J.M. Herrmann, Synergy effect in the photocatalytic degradation of

phenol on a suspended mixture of titania and activated carbon, Appl. Catal., B. 18 (1998) 281–291.

[7] J. Matos, J. Laine, J.-M. Herrmann, D. Uzcategui, J.L. Brito, Influence of activated carbon upon titania on aqueous photocatalytic consecutive runs of phenol photodegradation, Appl. Catal., B. 70 (2007) 461–469.

[8] T.-T. Lim, P.-S. Yap, M. Srinivasan, A.G. Fane, TiO_2/AC composites for synergistic adsorption-photocatalysis processes: Present challenges and further developments for water treatment and reclamation, Crit. Rev. Env. Sci. Technol. 41 (2011) 1173–1230.

[9] J. Gamage McEvoy, W. Cui, Z. Zhang, Synthesis and characterization of Ag/AgCl-activated carbon composites for enhanced visible light photocatalysis, Appl. Catal., B. 144 (2014) 702–712. *(also given in Chapter 3)*

[10] J. Gamage McEvoy, D.A. Bilodeau, W. Cui, Z. Zhang, Visible-light-driven inactivation of *Escherichia coli* K-12 using an Ag/AgCl-activated carbon composite photocatalyst. J. Photochem. Photobiol., A. 267 (2013) 25–34. *(also given in Chapter 5)*

[11] S. Glaus, G. Calzaferri, The band structures of the silver halides AgF, AgCl, and AgBr: A comparative study, Photochem. Photobiol. Sci. 2 (2003) 398–401.

[12] J. Jiang, H. Li, L. Zhang, New insight into daylight photocatalysis of AgBr@Ag: Synergistic effect between semiconductor photocatalysis and plasmonic photocatalysis, Chem. Eur. J. 18, 20 (2012) 6360–6369.

[13] W. Li, C. Liang, W. Zhou, J. Qiu, Z. Zhou, G. Sun, Q. Xin, Preparation and characterization of multiwalled carbon nanotube-supported platinum for cathode catalysts of direct methanol fuel cells, J. Phys. Chem. B 107 (2003) 6292–6299.

[14] X. Zhang, L. Lei, Effect of preparation methods on the structure and catalytic performance of TiO_2/AC photocatalysts, J. Hazard. Mater. 153 (2008) 827–833.

[15] K.S.W. Sing, D.H. Everett, R.A.W. Haul, L. Moscou, R.A. Pierotti, J. Rouquérol, T. Siemieniewska, Reporting physisorption data for gas/solid systems with special reference to the determination of surface area and porosity, Pure Appl. Chem. 57 (1985) 603–619.

[16] J. Rouquérol, D. Avnir, C. W. Fairbridge, D.H. Everett, J.H. Haynes, N. Pernicone, J.D.F. Ramsay, K.S.W. Sing, K.K. Unger, IUPAC Recommendations for the characterization of porous solids, Pure Appl. Chem. 66 (1994) 1739–1758.

[17] R. Jiang, H.-Y. Zhu, G.-M. Zeng, L. Xiao, Y.-J. Guan, Synergy of adsorption and visible light photocatalysis to decolour methyl orange by activated carbon/nanosized CdS/chitosan composite, J. Cent. South Univ. Technol. 17 (2010) 1223–1229.

[18] Y. Tang, Z. Jiang, Q. Tay, J. Deng, Y. Lai, D. Gong, Z. Dong, Z. Chen, Visible-light plasmonic photocatalysts anchored on titanate nanotubes: A novel nanohybrid with synergistic effects of adsorption and degradation, RSC Adv. 2 (2012) 9406–9414.

[19] S. Al-Qaradawi, S.R. Salman, Photocatalytic degradation of methyl orange as a model compound, J. Photochem. Photobiol., A. 148 (2002) 161–168.

[20] L.F. Velasco, J.B. Parra, C.O. Ania, Role of activated carbon features on the photocatalytic degradation of phenol, Appl. Surf. Sci. 256, 17 (2010) 5254–5258.

[21] R. Leary, A. Westwood, Carbonaceous nanomaterials for the enhancement of TiO_2 photocatalysis, Carbon 49 (2011) 741–772.

[22] X. Zhang, M. Zhou, L. Lei, Preparation of photocatalytic TiO_2 coatings of nanosized particles on activated carbon by AP-MOCVD, Carbon 43, 8 (2005) 1700–1708.

[23] X. Zhang, M. Zhou, L. Lei, TiO_2 photocatalyst deposition by MOCVD on activated carbon, Carbon 44, 2 (2006) 325–333.

[24] J.-M. Herrmann, Heterogeneous photocatalysis: fundamentals and applications to the removal of various types of aqueous pollutants, Catal. Today 53 (1999) 115–129.

[25] J. Araña, J.L. Martínez Nieto, J.A. Herrera Melián, J.M. Doña Rodríguez, O. Gondález Díaz, J. Pérez Peñam, O. Bergasa, C. Alvarez, J. Méndez, Photocatalytic degradation of formaldehyde containing wastewater from veterinarian laboratories, Chemosphere 55 (2004) 893–904.

[26] Y.H. Ao, J.J. Xu, D.G. Fu, X.W. Shen, C.W. Yuan, Low temperature preparation of anatase-TiO_2-coated activated carbon, Colloid Suf. A. Physicochem. Eng. Aspects 312 (2008) 125–130.

[27] S.X. Liu, X.Y. Chen, X. Chen, A TiO_2/AC composite photocatalyst with high activity and easy separation prepared by a hydrothermal method, J. Hazard. Mater. 143 (2007) 257–263.

[28] H. Wang, X. Lang, J. Gao, W. Liu, D. Wu, Y. Wu, L. Guo, J. Li, Polyhedral AgBr microcrystals with an increased percentage of exposed {111} facets as a highly efficient visible-light photocatalyst, Chem. Eur. J. 18, 15 (2012) 4620–4626.

[29] J. Liang, H. Wang, L. Li, Y. Xu, L. Guo, Well-graphitized graphene as photoinduced charge transport channel for improving the photocatalytic activity of AgBr, New. J. Chem. 37 (2013) 1797–1802.

[30] B. Krishnakumar, B. Subash, M. Swaminathan, AgBr-ZnO – An efficient nano-photocatalyst for the mineralizatin of Acid Black 1 with UV light, Sep. Purif. Technol. 85 (2012) 35–44.

[31] H. Xu, H. Li, J. Xia, S. Yin, Z. Luo, L. Liu, L. Xu, One-pot synthesis of visible-light driven plasmonic photocatalyst Ag/AgCl in ionic liquid, ACS Appl. Mater. Interfaces 3 (2011) 22–29.

[32] T. Wu, G. Liu, J. Zhao, H. Hidaka, N. Serpone, Photoassisted degradation of dye pollutants vs. self-photosensitized oxidation transformation of *Rhodamine B* under visible light irradiation in aqueous TiO_2 suspensions, J. Phys. Chem. B 102, 30 (1998) 5845–5851.

[33] J. Marugán, R. van Grieken, C. Pablos, C. Sordo, Analogies and differences between photocatalytic oxidation of chemicals and photocatalytic inactivation of microorganisms, Water Res. 44, 3 (2010) 789–796.

[34] H. Petering, Pharmacology and toxicology of heavy-metal silver, Pharmacol. Ther. A. 1 (1976) 127–130.

[35] S. Liau, D. Read, W. Pugh, J. Furr, A. Russell, Interaction of silver nitrate with readily identifiable groups: relationship to the antibacterial action of silver ions, Lett. Appl. Microbiol. 25 (1997) 279–283.

[36] K. Holt, A. Bard, Interaction of silver (I) ions with the respiratory chain of *Escherichia coli*: an electrochemical and scanning electrochemical study of the antimicrobial mechanism of micromolar Ag, Biochemistry 44 (2005) 13214–13223.

[37] C. Pulgarin, J. Kiwi, V. Nadtochenko, Mechanism of photocatalytic bacterial inactivation on TiO_2 films involving cell-wall damage and lysis, Appl. Catal., B. 128 (2012) 179–183.

[38] T. Saito, T. Iwase, J. Horie, T. Morioka, Mode of photocatalytic bactericidal action of powdered semiconductor TiO_2 on mutans streptococci, J. Photochem. Photobiol., B. 14 (1992) 369–379.

[39] C. Hu, Y. Lan, J. Qu, X. Hu, Z. Wang, Ag/AgBr/TiO_2 visible light photocatalyst for destruction of azodyes and bacteria, J. Phys. Chem. B 110 (2006) 4066–4072.

[40] H. Zheng, P.-C. Maness, D.M. Blake, E.J. Wolfrum, S.L. Smolinski, W.A. Jacoby, Bactericidal mode of titanium dioxide photocatalysis, J. Photochem. Photobiol., A. 130 (2000) 163–170.

[41] J. Marugán, R. Van Grieken, C. Sordo, C. Cruz, Kinetics of the photocatalytic disinfection of *Escherichia coli* suspensions, Appl. Catal., B. 82 (2008) 27–36.

[42] W. Li, S. Liu, Bifunctional activated carbon with dual photocatalysis and adsorption capabilities for efficient phenol removal, Adsorption 18 (2012) 67–74.

[43] K.Y. Foo, B.H. Hameed, Decontamination of textile wastewater via TiO_2/activated carbon composite materials, Adv. Colloid Interface Sci. 159 (2010) 130–143.

[44] K. Seki, H. Yanagi, Y. Kobayashi, T. Ohta, T. Tani, UV photoemission study of dye/AgBr interfaces in relation to spectral sensitization, Phys. Rev. B. 49 (1994) 2760–2767.

[45] H. Huang, X. Li, Z. Kang, Y. Liu, H. Li, X. He, S. Lian, J. Liu, S.-T. Lee, Tuning metal@metal salt photocatalytic activities by different charged anions, Dalton Trans. 39 (2010) 10593–10597.

SECTION III: CARBON-DOPED TiO_2

[Editorial note: The following chapter consists of the first study performed chronologically. Methylene blue was used as a model organic pollutant for the quantification of photocatalytic activity of carbon-doped TiO_2, but was later abandoned for the Ag/AgX-AC studies due to its strong self-sensitization in the visible light region.]

Chapter 8:

Degradative and disinfective properties of carbon-doped anatase-rutile TiO_2 mixtures under visible light irradiation

Joanne Gamage McEvoy, Wenquan Cui, Zisheng Zhang

Catalysis Today, 207 (2012) 191–199.

Abstract

In this study, the high temperature annealing of TiC was studied to prepare carbon-doped TiO_2 with improved visible light response and photocatalytic activity. The anatase-rutile carbon-doped TiO_2 mixtures synthesized were characterized by X-ray diffraction (XRD), X-ray photoelectron spectroscopy (XPS), and ultraviolet-visible light diffuse reflectance spectrophotometry (UV-Vis). TiC was found to fully react at 400^{o}C, and transformation of the anatase to rutile phase of TiO_2 was observed since the latter form was more heat stable. XPS analysis revealed that carbon in C-TIO_2 was present as carbonate species. The UV-Vis spectra of the doped powders were red shifted compared to P25 TiO_2, and a band gap narrowing of 0.2 eV was observed. The photocatalytic activity of C-TiO_2 was quantified by the degradation of methylene blue under visible light irradiation. Langmuir-Hinshelwood kinetics were applied, and a maximum pseudo-first order degradation rate of 0.015 min^{-1} was observed using the carbon-doped titania annealed at 400^{o}C for 8 hours. Disinfection of *Escherichia coli* K-12 was investigated using the catalyst in an immobilized configuration under visible light, and up to 80% inactivation was achieved in 30 minutes, compared to the negligible inactivation using P25. A modified Hom disinfection kinetic model was used to describe the data.

Keywords: photocatalysis, carbon-doped TiO_2, methylene blue, *Escherichia coli*, oxidative annealing, TiC

8.1 Introduction

Interest in photocatalytic processes for environmental applications has spurred research in this area over the past 30 years [1–3]. Photocatalysis has been shown to be effective for the degradation of a wide range of organic pollutants, and is also capable of inactivating many microorganisms including various types of bacteria, fungi, viruses, and spores [4, 5]. Titanium dioxide (TiO_2) is often used as a photocatalyst because it is inexpensive, widely available, and nontoxic. However, a problem with the efficiency of TiO_2-mediated photocatalytic processes lies in the high required band gap energy (~3.2 eV) for excitation of this semiconductor, corresponding to short wavelength light in the ultraviolet (UV) range. Available energy from solar radiation at the surface of the earth consists of mainly longer wavelengths, with only 3–5% being UV. The ultimate goal of enhancing photonic efficiency of photocatalytic processes is to facilitate development of large scale solar-driven treatment processes. Efforts to this end can be grouped into two broad categories, namely: improving use of incoming UV radiation through reactor design and optimization (for example, using corrugated reactors [6, 7]), and enabling use of more abundant visible light by modifying TiO_2 to lower its band gap energy or by screening other classes of visible light active photocatalysts [8].

In regards to TiO_2-modification, doping techniques for improving visible light photoactivity involve the addition of metals, non-metals (most commonly, anionic species such as N, C, F, S), and dye-sensitizers [8, 9]. Carbon-doping of TiO_2 has been reported to improve its visible light response and photocatalytic activity, and has been shown to be more effective than nitrogen-doping [10–15]. Synthesis has been performed via many routes, including simple mixing of a carbon nanomaterial with TiO_2 [16], direct oxidation of Ti metal in a burner flame [10, 17, 18], sol-gel synthesis [19], hydrothermal synthesis [20], and deposition techniques such as physical vapour deposition (PVD), chemical vapour deposition (CVD), and electrophoretic deposition [21], among others.

Oxidative annealing of TiC can be used to obtain carbon-doped TiO_2, as first reported by Irie et al. using a two-step oxidation procedure [22]. Choi et al. used a variation of this synthesis

employing one-step oxidation of TiC in air to fabricate carbon-doped TiO_2 [23]. Shen et al. also used a one-step oxidative annealing of TiC in air to create carbon-doped TiO_2 powders that could degrade trichloroacetic acid under visible light irradiation [24].

The addition of dopants such as carbon, nitrogen, and sulfur can favour the crystal phase transformation from anatase to rutile in TiO_2 [25], while a synergistic effect between the anatase and rutile forms has been reported to increase the photocatalytic activity of such mixtures [26, 27]. Some carbon-doped mixed-phase titania powders have been reported in literature [25], however the emphasis in oxidative annealing methods has been on the production of a pure anatase carbon-doped powder. Therefore, the purpose of this study is to investigate the synthesis and characterization of these mixed-phase carbon-doped structures produced by oxidative annealing of TiC. The photoactivity of the prepared photocatalysts is quantified by the degradation of methylene blue (MB).

Additionally, few studies on the photocatalytic disinfection of bacteria using carbon-doped TiO_2 have been conducted [28–30]. Of these, none report disinfection using carbon-doped powders prepared from oxidative annealing. Since the synthesis method used for the preparation of doped TiO_2 has a strong effect on the final product and its corresponding photocatalytic activity [21], it is important to quantify disinfective effects of carbon-doped TiO_2 from TiC. The photocatalytic inactivation capabilities of these carbon-doped powders are studied in this work using *Escherichia coli* K-12 as a model microorganism.

8.2 Materials and methods

8.2.1 Sample preparation

Carbon-doped titanium dioxide (denoted CT###-h, where ### is the annealing temperature in °C, and h is the number of hours the sample was annealed for) was prepared by the oxidative annealing of titanium (IV) carbide (Sigma-Aldrich, < 4 μm, ≥ 95%). To prepare the powders, five grams of TiC in a crucible was oxidized in air in a Lindberg Blue M muffle furnace (ThermoFisher), equipped with a Yokogawa U150 temperature controller for various annealing temperatures and times. The powders were compared to standard Degussa

Aeroxide P25 TiO_2 (Evonik (Degussa), New Jersey; 90:10 wt% anatase: rutile determined by X-ray diffractometry (XRD)).

8.2.2 Characterization

XRD patterns for all prepared powders were collected using a Rigaku Ultima IV XRD apparatus with a Cu K(α) source. Differential scanning calorimetry (DSC) and thermogravimetric analysis (TGA) were studied on an SDT 2960 simultaneous DSC-TGA instrument under air flow with a heating rate of $3^oC\ min^{-1}$. X-ray photoelectron spectroscopy (XPS) was performed on a Kratos Analytical Axis Ultra DLD instrument, using monochromated Al X-rays at 140 W. Ultraviolet-visible (UV-Vis) light diffuse reflection spectra were recorded on a TU-1901 spectrophotometer.

8.2.3 Photocatalytic activity

8.2.3.1 Methylene blue degradation

To quantify photocatalytic degradation of methylene blue (MB) using the prepared C-TiO_2 powders, a slurry reactor was used in a constructed reflective housing to prevent outside light from entering the system. Illumination was provided by a 300 W ELH tungsten halide bulb (Ushio) with a UV filter (Kenko Zeta, $\lambda > 410$ nm, transmittance > 90%) at a distance of 10 cm from the beaker. The irradiation was measured using a quantum meter (Biospherical QSL-2100; 400 nm < λ < 700 nm), and was found to be approximately $4.7x10^{-3}$ Einstein $m^{-2}\ s^{-1}$. The sensor had a nominal sensitivity of 1 volt (or $1x10^{17}$ quanta = $1.66x10^{-7}$ Einstein) with a noise level typically less than 1 millivolt. Cooling was provided by an external cooling jacket, and the reaction temperature was controlled to $20^oC \pm 4$. A 200 mL solution containing 12 mg L^{-1} of reagent-grade methylene blue (Fisher Chemical) was allowed to equilibriate in the dark with 3 g L^{-1} of catalyst under constant magnetic stirring at 55 rpm for 30 minutes prior to each experiment. Photocatalytic degradation tests were then performed for 2 hours each, with samples drawn every 10 minutes. The samples were centrifuged at 8000 rpm for 5 minutes in an accuSpin Micro 17 (Fisher Scientific) microcentrifuge to remove the suspended catalyst, and the peak absorbance (at $\lambda = 665$ nm for MB) was measured using a Genysys 10-UV spectrophotometer (ThermoScientific). The absorbance was then correlated to concentration using the Beer-Lambert Law and a prepared standard

curve. Full spectrum UV-Vis wavescans of methylene blue samples were collected using a Biochrom Ultrospec 60 UV/Vis spectrophotomer. Controls were performed in the absence of light and catalyst, respectively, and all trials were performed in triplicate. The error was estimated as the standard deviation between triplicate runs.

8.2.3.2 *Escherichia coli* K-12 disinfection

For disinfection trials, the catalyst was immobilized on a stainless steel substrate. Sandblasted stainless steel discs (100 mm diameter) were loaded with the catalyst using a procedure adapted from Zhang et al. [31], where a 180 g L^{-1} slurry of catalyst powder suspended in 25% (v/v) aqueous methanol was used to coat the discs. A thin, opaque catalyst layer was applied using a paintbrush. The prepared catalyst film was then baked for 5 hours at 250^{o}C and cooled to room temperature prior to use. Film thickness measurements were made using a Vernier micrometer (Mitutoyo) and ranged from 3–21 μm.

Wild-type *Escherichia coli* K-12 (TG1 strain) were grown aerobically in Luria-Bertani (LB) medium overnight on a rotary shaker at 37^{o}C, corresponding to the stationary growth phase as determined by a prepared growth curve. The initial concentration from the overnight culture was quantified from a serial dilution and plating procedure, followed by bacterial enumeration using culturable cell counts. Disinfection studies were carried out using 50 mL of aqueous solution spiked with a predetermined concentration of bacteria in a 600 mL Pyrex beaker under irradiation using the 300 W light and UV filter. The aqueous *E. coli* suspension was prepared by centrifugation and washing of 1 mL of suspended bacterial culture three times at 8000 rpm and 5 minutes to remove the remaining growth media before inoculation into sterile distilled deionized water. The initial concentration of the prepared aqueous *E. coli* solution was controlled to ~10^{6} CFU mL^{-1}. During the disinfection trials, the temperature was maintained constant at 20^{o}C ± 4 using a water bath, and samples were collected periodically. These samples were then serially diluted and plated on solid LB plates using a standard spread plate method. The plates were spread in triplicate and incubated at 37^{o}C for 18 hours. Bacterial enumeration was performed using a standard plate count method, where counts in the range of 30 – 300 colony forming units per plate were considered statistically significant and were used to calculate cell concentration. For the disinfection studies, all

materials were sterilized for 20 minutes at 121°C prior to use. The disinfection trials were performed in triplicate. Estimation of kinetic constants in the disinfection model was performed using the Solver add-in in Microsoft Excel.

8.3 Results and discussion

8.3.1 Catalyst characterization

TGA-DSC analysis was performed to study the oxidation characteristics of TiC in air, as shown in Figure 8.1. Under these conditions, TiC began to oxidize at 350°C. The oxidation took place slowly until 450°C, and then occurred increasingly rapidly, reaching a maximum at 482°C, where an increased heat flow was observed. To perform a controlled oxidation, annealing in the slow oxidizing region was desirable. For this study, annealing temperatures in the range of 350 – 450°C were chosen.

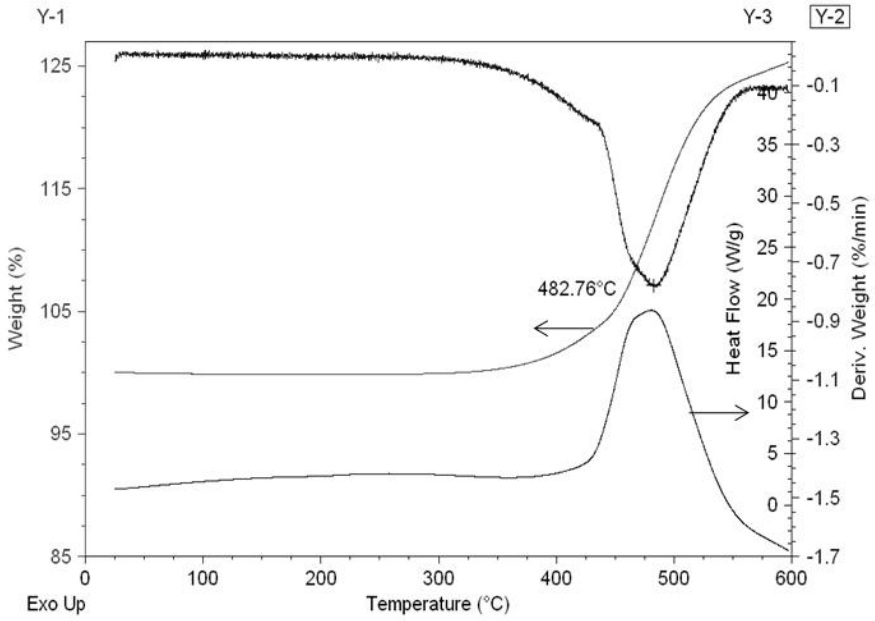

Figure 8.1: TGA-DSC analysis of TiC (bolded line refers to derivative weight)

XRD patterns for the photocatalysts annealed at different temperatures are shown in Figure 8.2. The crystalline phases of titania that could form during synthesis were anatase, rutile, and brookite. The anatase form was metastable and could irreversibly transform to the rutile phase upon heating, since the latter was the only stable phase in the bulk form [32].

The TiC phase diminished completely at an annealing temperature of 400^{o}C, and the anatase and rutile phases of TiO_2 were found to be present in all samples. The effect of annealing time at 400^{o}C on the powders was also studied, and XRD patterns for these prepared catalysts are shown in Figure 8.3. All of the powders annealed at 400^{o}C also displayed a mixed-phase crystal structure, as was observed by Choi et al. [23] and Shen et al. [24] and for annealing at this temperature.

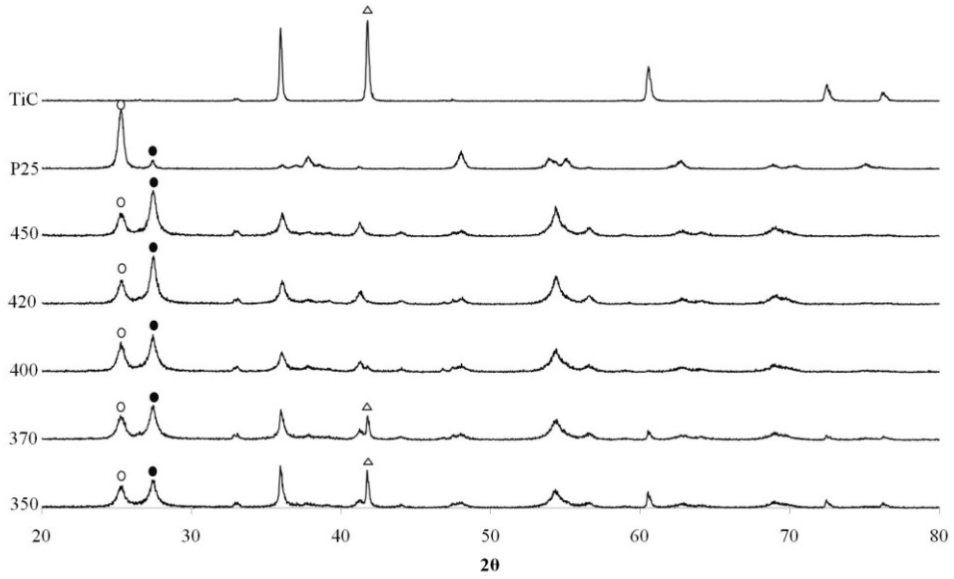

Figure 8.2: XRD patterns for prepared photocatalysts and reference materials (P25, TiC) (white circles refer to characteristic peaks for anatase, dark circles for rutile, and white triangles for TiC, respectively)

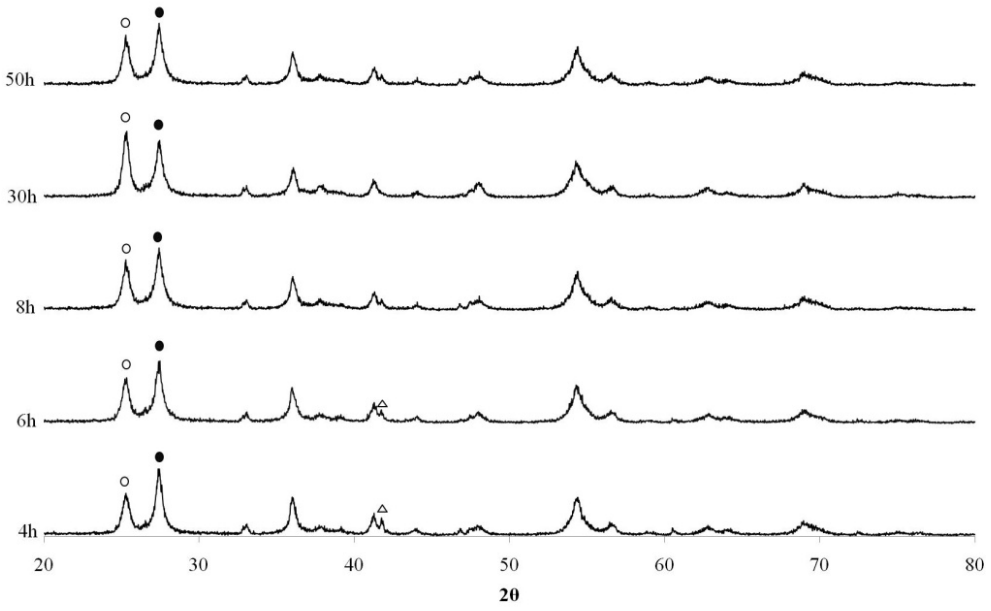

Figure 8.3: XRD patterns for prepared photocatalysts and reference materials (P25, TiC) (white circles refer to characteristic peaks for anatase, dark circles for rutile, and white triangles for TiC, respectively)

In this study, a low-temperature transformation from anatase to rutile was also observed, and was thought to be attributed to the presence of impurities in the starting material. The TiO_2 synthesized may have been more unstable due to existence of carbon in the crystal, which increased the transformation of the anatase phase into rutile [33].

The reference intensity ratio (RIR) method was used to estimate phase compositions from the data for samples containing TiC. For pure anatase/rutile mixtures obtained, the Spurr-Myers correlation was used [34], where the weight percent of anatase was given by:

$$x_A = (1+1.26*(I_R/I_A))^{-1} \qquad (8.1)$$

Where x denotes the weight fraction, I denotes the intensity of the strongest reflection, and the subscripts A and R denote the anatase and rutile phases, respectively. The rutile content was then determined by difference. The calculated weight percents are given in Table 8.1.

Table 8.1: Calculated weight percents of C-TiO_2 photocatalyst components

Catalyst	Anatase (wt%)	Rutile (wt%)	TiC (wt%)
CT350-8	46	34	20
CT370-8	55	35	10
CT400-8	41	59	-
CT420-8	29	71	-
CT450-8	29	71	-
CT400-4	33	64	3
CT400-6	34	64	2
CT400-30	48	52	-
CT400-50	43	57	-

From the estimated phase distributions at the initial annealing time of 8 hours, a large portion of unreacted TiC was observed at lower annealing temperatures (below 400^{o}C). This agreed with the result of Choi et al. (for annealing times less than 10 hours) [23]. At 400^{o}C, the anatase content reached a maximum, and then decreased at higher temperatures. This suggested that additional transformation of anatase to rutile at higher temperatures occurred, due to the decreased heat stability of the former crystal phase. The crystal structure changes were thought to be dominated by the annealing temperature, as changing annealing time did not have a distinguished effect on the phase distributions observed.

The Scherrer formula was used to estimate the grain size of the nanoparticles, where:

$$D = K_{sph}\,\lambda/(FWHM\cos\theta) \qquad (8.2)$$

Here, D is grain size (nm), λ is wavelength of X-ray radiation used (Cu Kα = 0.15418 nm), K_{sph} is the sphericity constant taken as 0.89, and FWHM is the line width at half-maximum peak height, after subtraction for equipment broadening. For the anatase-rutile photocatalyst mixtures, the average grain size was estimated considering the anatase (101) peak at 2θ = 25.4^o and the rutile (110) peak at 2θ = 27.5^o [35] according to the following relationship.

$$D_{avg} = D_A(I_A/(I_A+I_R)) + D_R(I_R/(I_A+I_R)) \qquad (8.3)$$

Where D refers to crystallite size (nm) and all other variables and subscripts are as previously described. The average grain size was between 15 and 17 nm for all of the prepared powders, and was 22 nm for P25 TiO_2. The observed grain sizes were found to increase with increasing temperature as expected due to agglomeration, but were in general

very similar.

To investigate the state of carbon in the doped photocatalyst, C1s core levels were measured using XPS, as shown in Figure 8.4. Two peaks were observed at 283.0 and 286.9 eV, respectively, and the former was assigned to adventitious carbon (considering peak shift due to the XPS apparatus used) [36]. The latter peak at ~287 was assigned to carbonate species [12]. The state of the carbon dopant was found in literature to be both a substitutional anion [10, 22, 23, 37, 38] and an interstitial cation [12, 39–42]. The anionic carbon peak was attributed to the -4 oxidation state in Ti-C bonds in carbides, with peaks in C1s spectra observed at low binding energy (~281.8 eV), while the cationic peak was due to the +4 state in the C–O bond in carbonates, as observed by Sakthivel and Kisch [12] and others with peaks at higher binding energies. It was suggested by Di Valentin et al. [43] based on density functional theory (DFT) calculations that in oxygen rich conditions, the formation of interstitial cations and/or substitution for titanium (i.e. C–O where carbon replaces Ti) can be favoured. In this study, carbon was present as a cationic species, possibly suggesting an oxygen-rich environment provided under the synthesis conditions used. The XPS results obtained also agreed with previous studies investigating the state of the carbon dopant in mixed-phase carbon-doped titania [44].

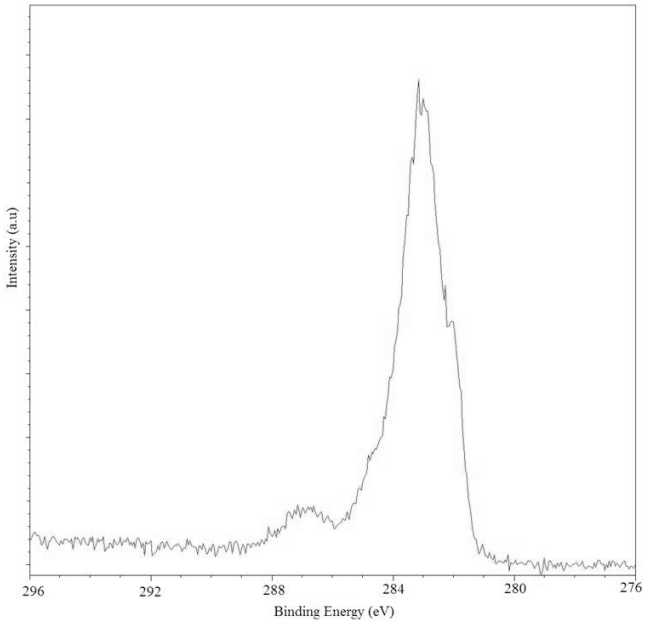

Figure 8.4: C1s XPS spectra for CT400-8

UV-Vis analysis was performed, and the absorbance spectrum of P25 TiO_2 was compared to that of CT400-8, as shown in Figure 8.5. The onset of the absorption spectrum for P25 was found to be ~387 nm, which corresponded well with the known band gap of the material (~3.2 eV), as it was found to be mostly anatase by XRD. For the carbon-doped TiO_2, the absorption spectrum red-shifted, and the edge was observed at ~415 nm. The associated band gap energy was found using Eq. (8.4).

$$E_{bg} = 1240/\lambda \quad (8.4)$$

The calculated band gap of 3.0 eV represented a decrease from the P25 band gap energy, and improved visible light absorption in the doped material. It should be noted that predominance of rutile phase in the carbon-doped powder may have also contributed to the decreased band gap energy (E_{bg}, rutile = 3.0 eV) [46]. However, C-TiO_2 exhibited an absorption tail, indicating improved visible light absorption from 400–700 nm over P25.

The role of cationic carbon in increasing visible light adsorption has been suggested by several studies. Di Valentin et al. [43] found that modest band gap variation and experimental red-shift in absorbed wavelengths could be attributed to carbon impurities in the material

inducing several intermediate states, as was also suggested by Wang and Lewis [38]. The mixing of C 2p and O 2p states causing mid-gap states was also reported elsewhere [11, 41, 47–49].

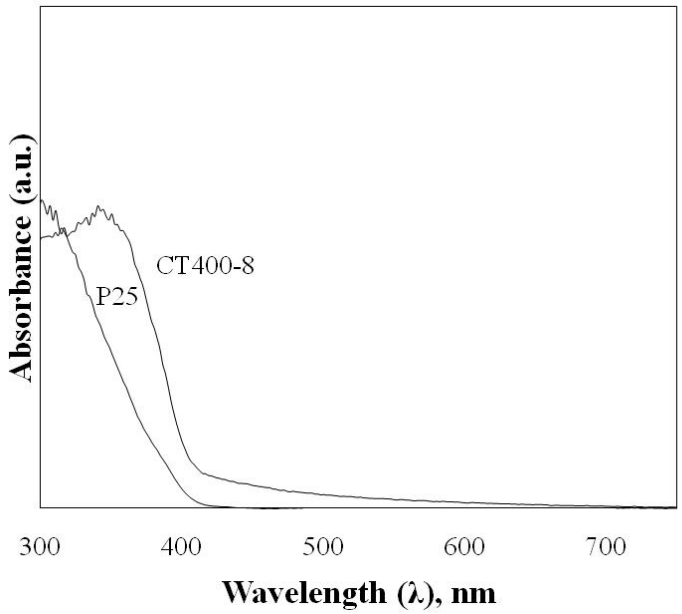

Figure 8.5: UV-Vis absorption spectra for carbon-doped powder and P25 TiO_2

8.3.2 Photocatalytic activity

8.3.2.1 MB degradation

The photocatalytic degradation of MB was studied using the prepared photocatalysts in slurry. MB is a heterocyclic aromatic compound having molecular formula $C_{16}H_{18}ClN_3S$, and is frequently used in analytical chemistry as a redox indicator, since MB solutions are blue in oxidizing environments, but are decoloured in the presence of reducing agents. It is employed in photocatalytic degradation studies as an indicator of the organic degradation capability of a certain catalyst. The results from control runs employing no catalyst and P25 TiO_2 are shown, respectively, along with a typical carbon-doped TiO_2 trial in Figure 8.6.

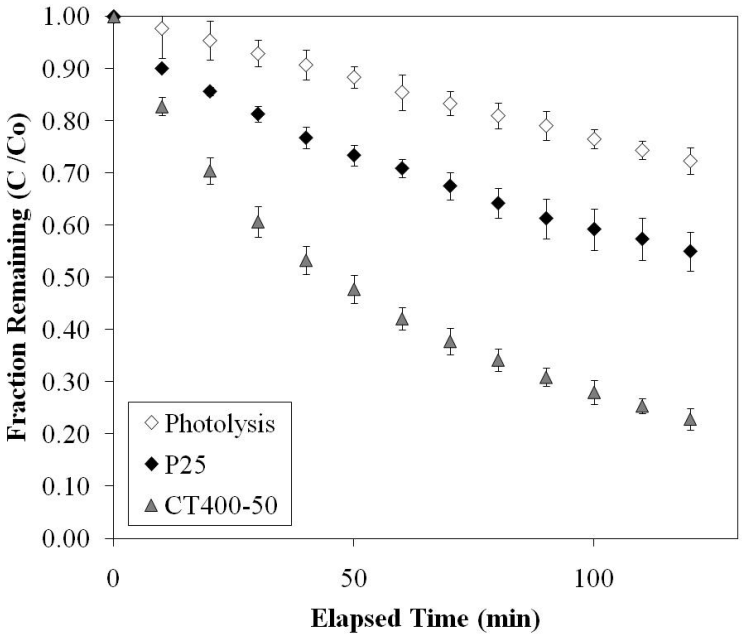

Figure 8.6: Degradation of MB using photolysis, P25 TiO_2, and carbon-doped TiO_2, respectively. (C_o = 12 mg L^{-1}, catalyst loading = 3 g L^{-1})

The self-degradation of MB in the absence of catalyst was observed due to photolysis, caused by absorbance of the molecule at long wavelengths (λ_{max} = 665 nm). This photolysis was able to effect up to 27% degradation of MB in 2 hours of irradiation. Using commercial P25, a degradation of 45% was observed. Sensitization of the TiO_2 catalyst by absorption of the dye molecules at higher wavelengths likely played a role in this degradation [50]. The results of a typical carbon-doped run, however, exhibited a marked increase in the performance of dye degradation compared to photolysis and P25, degrading up to 77% in 2 hours. This indicated that carbon-doped TiO_2 powders were comparatively more active than the traditional P25 catalyst under visible light irradiation. The enhanced activity was thought to result from a combination of improved visible light absorption and improved adsorption capability over P25.

Catalyst photosensitization by methylene blue occurred for both P25 and C-TiO_2, reacting according to the following scheme, where MB was directly excited by long-wavelength light:

$$MB^{+}_{ads} + \textit{visible light} \rightarrow MB^{*}_{ads} \qquad (8.5)$$

$$MB^{*}_{ads} + \text{C-}TiO_2 \rightarrow \text{C-}TiO_2\,(e) + MB^{+}_{ads} \qquad (8.6)$$

$$C\text{-}TiO_2\ (e) + O_2 \rightarrow C\text{-}TiO_2 + {}^{\bullet}O_2^- \qquad (8.7)$$

Reactions (8.5) – (8.7) also applied for TiO_2 when sensitized by MB. In this process, adsorbed MB was excited by visible light, and an electron from the excited dye was injected to the conduction band of the catalyst, where it could be scavenged by molecular oxygen. However, at lower wavelengths, direct excitation of the semiconductor could occur according to the following reactions:

$$C\text{-}TiO_2 + \textit{visible light} \rightarrow h^+ + e^- \qquad (8.8)$$

$$e^- + O_2 \rightarrow {}^{\bullet}O_2^- \qquad (8.9)$$

$$h^+ + H_2O \rightarrow {}^{\bullet}OH \qquad (8.10)$$

Due to improved visible light absorbance of the carbon-doped samples, and their reduced band gap compared to P25, direct excitation of these powders by lower wavelength light played a role in oxidation of MB dye, facilitating decolourization of the solution through a photocatalytic mechanism.

The enhanced photocatalytic activity observed with the carbon doped TiO_2 may have been due to the presence of interface states and/or interface defects caused by carbon in the mixed phase materials, which lowered their band gap [44]. The lower band gap energy and enhanced visible light absorption of the carbon-doped powders indicated that direct excitation could occur at lower wavelengths. This was not true for P25, since it could only be excited by UV, and this implied that the improved activity of P25 over photolysis alone may have been solely due to the photosensitization effect. The presence of photosensitization by MB was also supported by the fact that no disinfection using P25 was observed under visible light, as this process was dependent on direct excitation of the semiconductor to produce radicals and reactive species (as discussed in subsequent sections).

It has also been suggested that carbonaceous species such as adsorbed carbon detected by XPS may form a dense cokelike structure on the catalyst surface, which could act as a sensitizer responsible for the absorption tail in the visible light region [51]. This may also have affected the adsorption characteristics of carbon-doped powders compared to P25.

While the surface areas of the catalysts were not characterized, the adsorptive capabilities of the powders were studied by measuring the amount of MB adsorbed during the initial dark adsorption period of the degradation trials (30 minutes). The carbon doped powders were found to adsorb from 1.0 – 1.3x10^{-3} grams of MB per gram of catalyst, while P25 was only able to adsorb 0.16x10^{-3} grams MB per gram catalyst, an order of magnitude lower. The increased adsorption capability of the prepared powders over P25 indicated that a greater number of reaction sites on the surface of the catalyst may have also played a role in improving activity.

The decolourization of the dye using C-TiO_2 was indicated in the changes to absorption spectra with time, as shown in Figure 8.7. The decrease in intensity of the solution color was evidenced by the continual decrease in absorbance at the maximum absorption wavelength of MB with reaction time, and was attributable to the hypsochromic effect when all or parts of the auxochromic groups (methyl or methylamine in MB) were degraded. The methyl groups, being weak electron-donor substituents, facilitated attack on MB by the electrophilic species present in solution ($^{\bullet}$OH radicals and positive holes), causing demethylation. This apparent gradual blue-shift in the peak absorbance from 665 nm (initial) to ~625 nm (final) was earlier identified as being suggestive of a stepwise N-demethylization process [52]. This degradation mechanism was further evidenced in the current spectra by absorption bands of N-demethylated analogues of MB appearing in the visible range at 648–655 nm for Azure B, and at 620–634 nm for Azure A as the reaction proceeded [53].

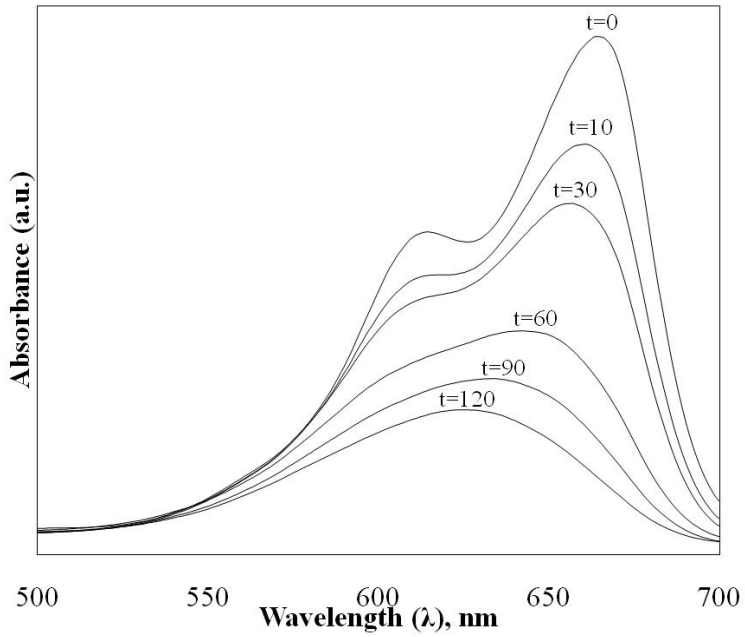

Figure 8.7: Changes to absorption spectra of methylene blue during the course of photocatalytic reaction. (C_o = 12 mg L^{-1}, catalyst loading = 3 g L^{-1})

A comparison of the powders prepared at different annealing temperatures and times are given in Figures 8.8 and 8.9, respectively. All samples prepared exhibited photocatalytic activity under visible light, and all had greater activity than P25 under these conditions. The maximum degradation observed was 82% for CT400-8 (corresponding to a final fractional concentration of 0.18). The data collected using the doped powders all exhibited similar trends in degradation, where the concentration decreased linearly for approximately 30 minutes, after which the decolourization process decelerated. Quantitative comparison between the data was made on the basis of Langmuir-Hinshelwood kinetic pseudo-first order rate constants.

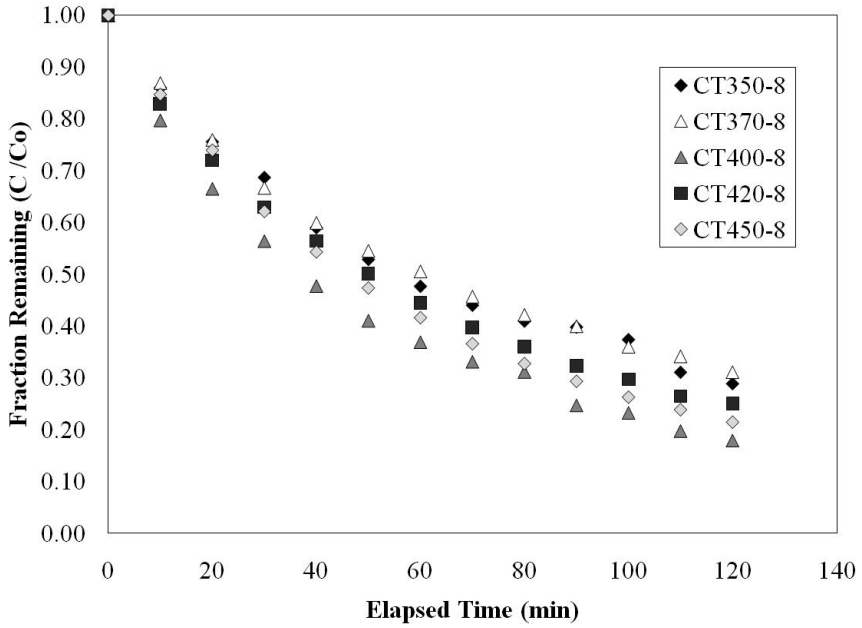

Figure 8.8: Degradation of MB using carbon-doped TiO_2 prepared at various annealing temperatures (8h). (catalyst loading = 3 g L^{-1}) – *error bars removed for clarity*

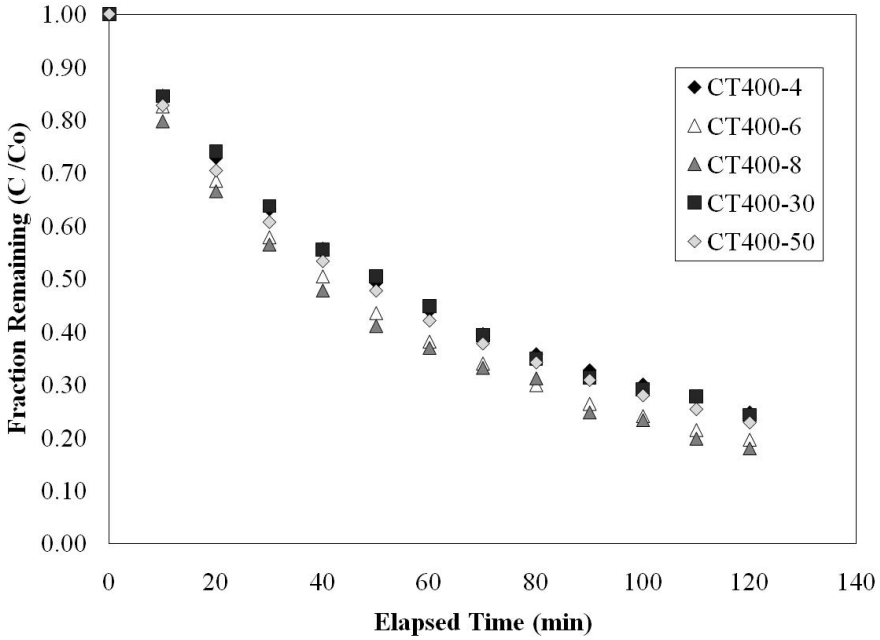

Figure 8.9: Degradation of MB using carbon-doped TiO_2 prepared at various annealing times (400°C). (catalyst loading = 3 g L^{-1}) – *error bars removed for clarity*

8.3.2.2 Langmuir-Hinshelwood kinetics

A Langmuir-Hinshelwood kinetic analysis can be applied for the degradation of MB, where:

$$-dC/dt = k_r KC/(1+KC) \qquad (8.11)$$

Where C is the concentration of reactant (mg L^{-1}), k_r is the reaction rate constant (mg L^{-1} min^{-1}), K is the adsorption coefficient of the reactant (L mg^{-1}), and t is the illumination time (min). This model assumes adsorption of reactants, surface reaction, and desorption of products, where the reaction is the rate limiting step. The expression can be rewritten and integrated to:

$$\ln(C_o/C) + K(C_o-C) = k_r Kt \qquad (8.12)$$

Where C_o is the initial concentration. It has been suggested that at very dilute concentrations (C_o <10^{-3} mol L^{-1}), KC becomes << 1, and the reaction is of apparent first order [54]. In this case, the concentration is sufficiently small (Co = $7.5x10^{-6}$), and so the approximation can be made, where the equation is simplified to:

$$ln(C_o/C) = k_r Kt = k't \qquad (8.13)$$

Where k' represents the pseudo-first order rate constant. A plot of $\ln(C_o/C)$ as a function of illumination time yields a straight line with slope corresponding to the first order constant. The pseudo-first order approximation was used as a basis for comparison of the activity of the catalysts. The rate constants were calculated and are given in Figure 8.10.

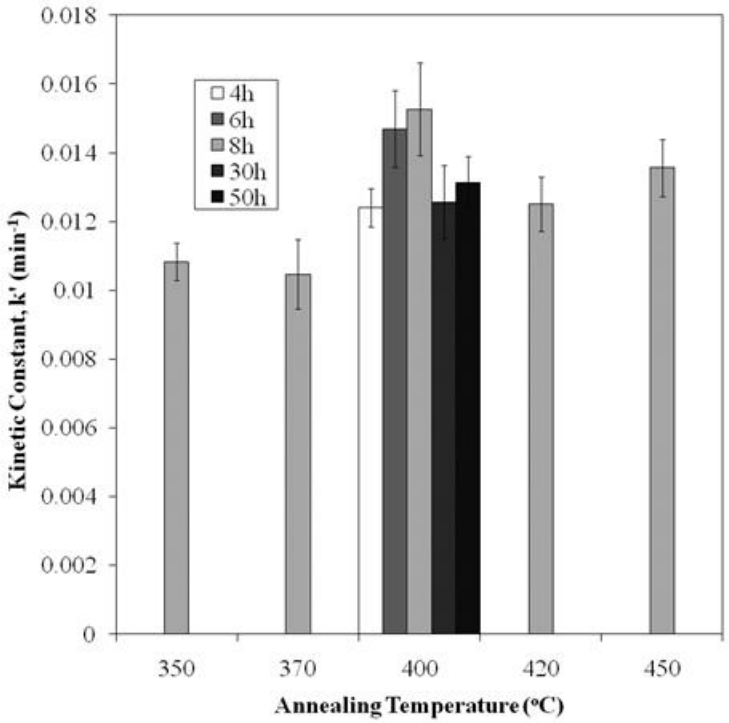

Figure 8.10: Pseudo-first order rate constants derived using Langmuir-Hinshelwood kinetics. (C_o = 12 mg L^{-1}, catalyst loading = 3 g L^{-1})

Statistical analysis was performed using a paired *t*-test with a 5% level of significance to quantify the differences between the activities observed. For the prepared powders containing TiC (CT350-8, CT370-8), a poorer photocatalytic performance was observed (k' = 0.010 & k' = 0.011 min^{-1}, respectively). This was due to the relatively large fraction of photocatalytically inactive TiC present. An optimum degradation rate of 0.015 min^{-1} was observed using the material annealed at 400^{o}C, while annealing at higher temperature did not significantly improve the final degradation. At higher temperatures, phase transformation from anatase to rutile resulted in decreased activity compared to CT400-8 (k' = 0.012 & k' = 0.013 for CT420-8 and CT450-8, respectively). This indicated that an optimum phase distribution was achieved when the sample was annealed at 400^{o}C for 8 hours.

The effect of annealing time on the powders calcined at 400^{o}C did not have a predictable influence on the phase distributions and photoactivities. This may indicate that differences in

activity with various annealing times may be influenced by not only the phase distribution, but also by other factors such as surface properties, defects, and quantity of incorporated carbons [56]. The values of kinetic constants obtained ranged from 0.012 to 0.015 min^{-1} for CT400-4 and CT400-8, respectively. A lack of trend in the influence of structure on the final photoactivity in carbon-containing mixed-phase powders was also observed by Treschev et al. [55].

8.3.2.3 Apparent photonic efficiency

The apparent photonic efficiency was used as an indicator of the utilization of delivered photons by various catalysts prepared in this study. This parameter is a ratio of the reaction rate to the incident light intensity, implying that under constant reaction conditions (illumination intensity and source, concentration of solution used, reaction temperature, etc.), the calculated photonic efficiency is proportional to the respective reaction rates [56]. The apparent photonic efficiency can be calculated by number of molecules transformed divided by number of delivered photons. In this study, the amount of delivered photons was quantified only in the range of 400–700 nm through the use of a quantum meter, while the actual photons to the reactor were in a broader range due to the type of illumination used. While this approximation allowed for relative comparison between the prepared catalysts, quantitative comparison of the obtained efficiency values with those reported in literature could not be made. Since the concentration was not linear with time, the photonic efficiency was also variable. However, at the initial stage of the reaction ($t \leq 30$ minutes), the concentration varied approximately linearly with time, so concentration at 30 minutes was used to calculate photonic efficiency. The expression for apparent photonic efficiency is given by:

$$\xi = V\Delta c/JA\Delta t \quad (8.14)$$

Where ξ is the apparent photonic efficiency (mol $Einstein^{-1}$), V is the volume of solution (L), Δc is the change in concentration (mol L^{-1}), J is the flux of photons (Einstein m^{-2} s^{-1}), A is the irradiated area (m^2), and Δt is the change in time (s). The results obtained are summarized in Table 8.2. The relative activities of the powders based on apparent photonic efficiencies were similar to those obtained through comparing the L-H kinetics. The maximum photonic

efficiency observed was 0.49% with CT400-8, and the minimum was 0.35% with CT350-8.

Table 8.2: Apparent photonic efficiencies for various C-TiO_2 photocatalysts

Catalyst	Apparent Photonic Efficiency, ξ (%)
CT350-8	0.35
CT370-8	0.38
CT400-8	0.49
CT420-8	0.42
CT450-8	0.43
CT400-4	0.42
CT400-6	0.48
CT400-30	0.41
CT400-50	0.44

8.3.3 *E. coli* K-12 inactivation

8.3.3.1 *E. coli* K-12 inactivation curves

The photocatalytic disinfection of *E. coli* was performed using the photocatalyst in an immobilized configuration. Hydroxyl radicals and other reactive oxygen species generated by photoexcitation of the catalyst are highly reactive and non-selective, so they can interfere with normal bacteriological processes to cause inactivation. A thin film was used in order to avoid the effects of cell inactivation by co-aggregation of cells and powder TiO_2 particles and cellular injury caused by phagocytosis of nanosized catalyst particles [57, 58]. In the case of a thin film, the cell survival was affected only by damage caused by photocatalysis [57].

In this study, the disinfective capabilities of the carbon-doped powders were quantified in comparison to those of undoped TiO_2 under visible light irradiation, and the results obtained are shown in Figure 8.11. Negligible inactivation was observed using P25, while an inactivation up to 80% was observed using the carbon-doped powders. This represented an improvement in activity of the prepared C-TiO_2 over P25 under visible light.

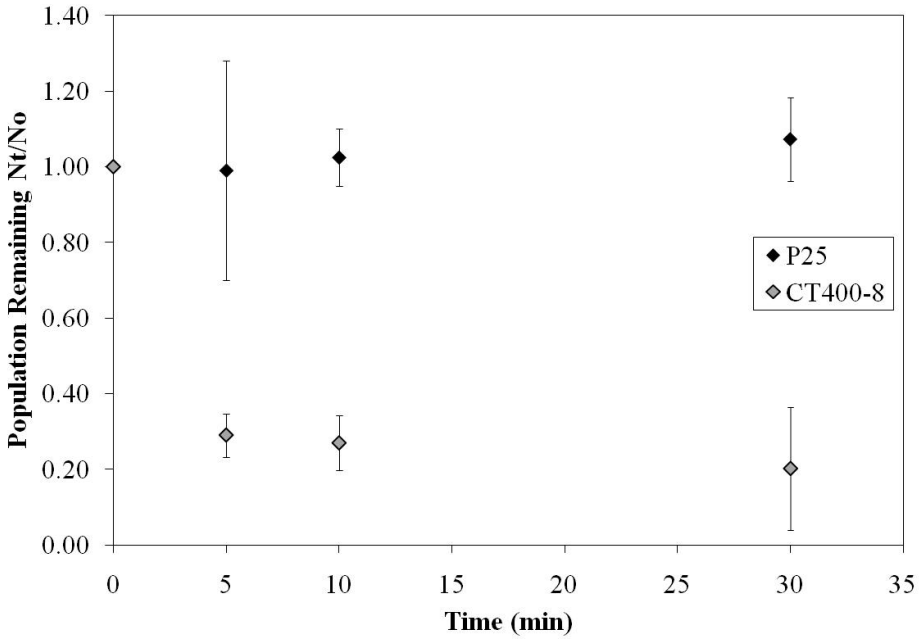

Figure 8.11: Inactivation of *E. coli* using immobilized P25 and carbon-doped TiO_2 catalyst. ($N_o = 10^6$ CFU mL^{-1})

A previous study on disinfection using carbon-doped TiO_2 by Wong et al. [28] indicated survival ratios (population remaining, Nt/No) higher than 70% after 25 minutes of irradiation in an immobilized catalyst configuration. However, due to differences in the irradiation volume used (μL in their case), level of irradiation provided, and method of preparation of the catalyst (ion-assisted electron-beam evaporation), quantitative comparison of the present results with the report from literature cannot be made.

The mechanism of bactericidal action of TiO_2 powders on *E. coli* has been proposed to be due to the action of radical oxidative species acting in concert to attack polyunsaturated phospholipids, where cell death is attributed to lipid peroxidation which causes a breakdown of the cell membrane [59]. It was also found that singlet oxygen ($^1O_2$) could be generated upon further oxidation of the superoxide oxygen anion ($^{\bullet}O_2^-$) under visible light in the presence of a non-metal doped visible-light active photocatalyst (N, S co-doped TiO_2) [60]. Since both $^{\bullet}O_2^-$ and $^1O_2$ are toxic to microorganisms [61, 62], they were found to be responsible for *E. coli* inactivation. The singlet oxygen generation on catalyst surfaces also interacted with the microenvironment of phospholipid membranes, causing lipid peroxidation reactions that led to cell death [63].

8.3.3.2 Kinetics of inactivation

Inactivation curves of *E. coli* under the photo-killing mechanism may exhibit any of three regions, namely: an initial delay or smooth decay at the beginning of reaction, called a "shoulder", a log-linear inactivation region that covers most of the reaction, and a deceleration process at the end of reaction, called a "tail". The "shoulder" is associated to an induction period where the production of radicals takes place, before the level of radicals produced becomes harmful to the bacteria, while the "tail" is associated to a decreasing inactivation rate caused by consumption of the radicals by both the living cells and the products of the lysis [30, 64]. Because of the complex mechanism associated with disinfection processes, kinetic analysis of photocatalytic bacterial inactivation is usually performed using empirical correlations. A model that can be used to describe kinetic data in the presence of any of the three regions is the modified Hom equation, applied to the case of constant concentration of disinfecting agent (such as in photocatalytic processes) [65]. The modified Hom equation is given by:

$$\log (N_t/N_o) = -k_1[1-\exp(-k_2 t)]^{k3} \qquad (8.15)$$

Where N is the bacterial population; k_1, k_2, and k_3 are kinetic constants, and all other parameters are as previously defined. The modified Hom equation was applied to the data and resulted in the following constants: $k_1 = 1.25$, $k_2 = 0.005$, and $k_3 = 0.273$. Model-predicted values were compared to the experimental data in Figure 8.12, and were observed to provide an appropriate fit.

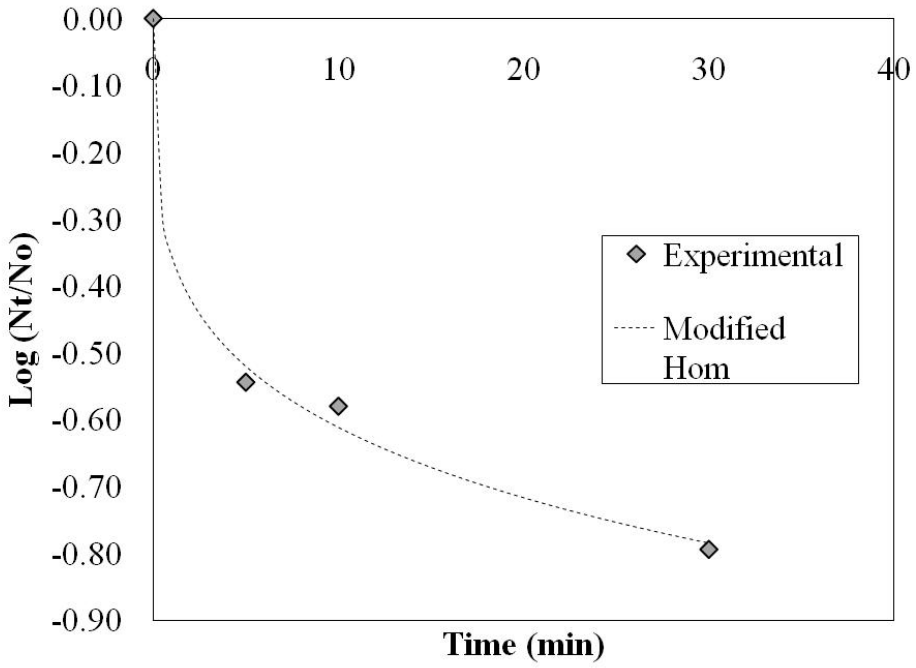

Figure 8.12: Disinfection kinetics: Comparison of experimental inactivation data and modified Hom model. ($N_o = 10^6$ CFU mL^{-1})

8.4 Conclusions and recommendations

Carbon doped anatase-rutile mixtures of TiO_2 were synthesized using high temperature oxidative annealing of TiC. Carbon was present in the form of carbonate species, and a red shift and absorption tail in the UV-Vis spectrum was observed, indicating improved visible light absorption of the prepared catalysts. The carbon doped TiO_2 powders were found to degrade methylene blue under visible light irradiation, achieving a maximum pseudo-first order kinetic constant of 0.015 min^{-1}. The sample annealed at 400^oC for 8 hours exhibited the highest photocatalytic activity. The prepared carbon doped TiO_2 was also used to inactivate *E. coli* K-12, and was able to facilitate an 80% photoinactivation in 30 minutes, while the undoped P25 did not show any disinfection activity. Future work involves the investigation of surface area and morphology of the samples. Additionally, suspension stability and surface charge data such as zeta potential should be explored, and their impact upon activity discerned. Since only the visible light activity of the catalyst was investigated in this work, further studies should be undertaken in order to characterize the photoactivity under real sun or solar simulated irradiation in order to confirm its applicability to solar water treatment.

8.5 Acknowledgments

The Natural Sciences and Engineering Research Council of Canada and the Canadian Federation of University Women are acknowledged for financial support. This work was also supported by the National Natural Science Foundation of China (Grant No. 50972037 and 51172063). The authors would like to acknowledge the Centre for Catalysis Research and Innovation and the Department of Earth Sciences (University of Ottawa) and Qi Yueli (College of Chemical Engineering at Hebei United University) for help with sample characterization.

8.6 References

[1] D.M. Blake, P.-C. Maness, Z. Huang, J. Wolfrum, J. Huang, W.A. Jacoby, Application of the photocatalytic chemistry of titanium dioxide to disinfection and the killing of cancer cells, Sep. Purif. Methods 28 (1999) 1–50.

[2] K. Yogo, M. Ishikawa, Recent progress in environmental catalytic technology, Catal. Surv. Jpn. 4 (2000) 83–90.

[3] D. Ljubas, Solar photocatalysis – a possible step in drinking water treatment, Energy 20 (2005) 1699–1710.

[4] C. McCullagh, J.M.C. Robertson, D.W. Bahnemann, P.K.J. Robertson, The application of TiO_2 photocatalysis for disinfection of water contaminated with pathogenic microorganisms: A review, Res. Chem. Intermed. 33 (2007) 359–375.

[5] J. Gamage, Z. Zhang, Applications of photocatalytic disinfection: A review, Int. J. Photoenergy 2010 (2010) Article ID 764871. *(also given in Appendix B)*

[6] S.M. Meunier, J. Gamage, Z. Duvnjak, Z. Zhang, Design and characterization of a novel rotating corrugated drum reactor for wastewater treatment, Int. J. Photoenergy, 2010 (2010) Article ID A146743.

[7] Z. Zhang, W.A. Anderson, M. Moo-Young, Modeling of corrugated plate photocatalytic reactors and experimental validation, Chem. Eng. Sci. 58 (2003) 911–914.

[8] A. Zaleska, Doped-TiO_2: A review, Recent Pat. Eng. 2 (2008) 157–164.

[9] U.I. Gaya, A.H. Abdullah, Heterogeneous photocatalytic degradation of organic contaminants over titanium dioxide: A review of fundamentals, progress, and problems, J. Photochem. Photobiol., C. 9 (2008) 1–12.

[10] S.U.M. Khan, M. Al-Shahry, W.B. Ingler, Efficient photochemical water splitting by a chemically modified n-TiO_2, Science 297 (2002) 2243–2245.

[11] J.H. Park, S. Kim, A.J. Bard, Novel carbon-doped TiO_2 nanotube arrays with high aspect ratios for efficiency solar water splitting, Nano Lett. 6 (2006) 24–28.

[12] S. Sakthivel, H. Kisch, Daylight photocatalysis by carbon-modified titanium dioxide, Angew. Chem. Int. Ed. 42 (2003) 4908–4911.

[13] D. Chen, Z. Jiang, J. Geng, Q. Wang, D. Yang, Carbon and nitrogen co-doped TiO_2 with enhanced visible-light photocatalytic activity, Ind. Eng. Chem. Res. 46 (2007) 2741–2746.

[14] F. Dong, H. Wang, Z. Wu, One-step "green" synthetic approach for mesoporous C-doped titanium dioxide with efficient visible light activity, J. Phys. Chem. C 113 (2009) 16717–16723.

[15] C. Xu, R. Killmeyer, M.L. Grey, S.U.M. Khan, Enhanced carbon doping of n-TiO_2 thin films for photoelectrochemical water splitting, Electrochem. Commun. 8 (2006) 1650–1654.

[16] Y. Yao, G. Li, S. Ciston, R.M. Lueptow, K.A. Gray, Photoreactive TiO_2/carbon nanotube composites: Synthesis and reactivity, Environ. Sci. Technol. 42 (2008) 4952–4957.

[17] K. Noworyta, J. Augustynski, Spectral photoresponses of carbon-doped TiO_2 film electrodes, Electrochem. Solid-State Lett. 7 (2004) E31–E33.

[18] A. Fujishima, K. Kohayakawa, K. Honda, Hydrogen production under sunlight with an electrochemical photocell, J. Electrochem. Soc. 122 (1975) 1487–1489.

[19] A. C. Pierre, Introduction to sol-gel processing, Kluwer, Boston, 1998.

[20] K. Byrappa, M. Yoshimura, Handbook of hydrothermal technology: A technology for crystal growth and materials processing, Norwich, New York, 2001.

[21] R. Leary, A. Westwood, Carbonaceous nanomaterials for the enhancement of TiO_2 photocatalysis, Carbon 49 (2011) 741–772.

[22] H. Irie, Y. Watanabe, K. Hashimoto, Carbon-doped anatase TiO_2 powders as a visible-light sensitive photocatalyst, Chem. Lett. 32 (2003) 772–773.

[23] Y. Choi, T. Umebayashi, M. Yoshikawa, Fabrication and characterization of C-doped anatase TiO_2 photocatalysts, J. Mater. Sci. 39 (2004) 18737–1839.

[24] M. Shen, Z. Wu, H. Huang, Y. Du, Z. Zou, P. Yang, Carbon-doped anatase TiO_2 obtained from TiC for photocatalysis under visible light irradiation, Mater. Lett. 60 (2006) 693–697.

[25] A. Chatterjee, S.-B. Wu, P.-W. Chou, M.-S. Wong, C.-L. Cheng, Observation of carbon-facilitated phase transformation of titanium dioxide forming mixed-phase titania by confocal Raman microscopy, Appl. Phys. Lett. 42 (2011) 1075–1080.

[26] J.M. Kroon, N.J. Bakker, J.P. Smit, P. Liska, K.R. Thampi, P. Wang, S.M. Zakeeruddin, M. Grätzel, A. Hinsch, S. Hore, U. Wurfel, R. Sastrawan, J.R. Durrant, E. Palomares, H. Pettersson, T. Gruszecki, J. Walter, K. Skupien, G.E. Tulloch, Nanocrystalline dye-sensitized solar cells having maximum performance, Prog. Photovoltaics Res. Appl. 15 (2007) 1–18.

[27] A. Kolmakov, M. Moskovits, Chemical sensing and catalysis by one-dimensional metal-oxide nanostructures, Annu. Rev. Mater. Res. 34 (2004) 151–180.

[28] M.-S. Wong, W.-C. Chu, D.-S. Sun, H.-S. Huang, J.-H. Chen, P.-J. Tsai, N.-T. Lin, M.-S. Yu, S.-F. Hsu, S.-L. Wang, H.-H. Chang, Visible-light-induced bactericidal activity of a nitrogen-doped titanium photocatalyst against human pathogens, Appl. Environ. Microbiol.

72 (2006) 6111–6116.

[29] G.-T. Lim, K.-H. Kim, J. Park, S.-H. Ohk, J.-H. Kim, D.L. Cho, Synthesis of carbon-doped photocatalytic TiO_2 nanopowders by AFD process, J. Ind. End. Chem. 16 (2010) 723–727.

[30] D. Mitoraj, A. Janczyk, M. Strus, H. Kisch, G. Stochel, P.B. Heczko, W. Macyk, Visible light inactivation of bacteria and fungi by modified titanium dioxide, Photochem. Photobiol. Sci. 6 (2007) 642–648.

[31] Z. Zhang, W.A. Anderson, M. Moo-Young, Experimental analysis of a corrugated plate photocatalytic reactor, Chem. Eng. J. 99 (2004) 145–152.

[32] A. Fujishima, K. Honda, Electrochemical photolysis of water at a semiconductor electrode, Nature 238 (1972) 37–38.

[33] Y.-H. Tseng, C.-S. Kuo, C.-H. Huang, Y.-Y. Li, P.-W. Chou, C.-L. Cheng, M.-S. Wong, Visible-light-responsive nano-TiO_2 with mixed crystal lattice and its photocatalytic activity, Nanotech. 17 (2006) 2490–2497.

[34] R.A. Spurr, H. Myers, Quantitative analysis of anatase-rutile mixtures with an X-ray diffractometer, Anal. Chem. 29 (1957) 760–762.

[35] T. Ihara, M. Miyoshi, Y. Iriyama, O. Matsumoto, S. Sugihara, Visible-light-active titanium oxide photocatalyst realized by an oxygen-deficient structure and by nitrogen doping, Appl. Catal., B. 42 (2003) 403–409.

[36] L. Zhang, R.V. Koka, A study on the oxidation and carbon diffusion of TiC in alumina-titanium carbide ceramics using XPS and Raman spectroscopy, Mater. Chem. Phys. 57 (1993) 23–32.

[37] S.-W. Hsu, T.-S.Tang, T.-K. Chen, M.-S. Wong, Ion-assisted electron-beam evaporation of carbon-doped titaniaum oxide films as visible-light photocatalyst, Thin Solid Films 515 (2007) 3521–3526.

[38] H. Wang, J.P. Lewis, Effects of dopant states on photoactivity in carbon-doped TiO_2, J. Phys. Condens. Matter 17 (2005) L209–L213.

[39] T. Ohno, T. Tsubota, K. Nishijima, Z. Miyamoto, Degradation of methylene blue on carbonate species-doped TiO_2 photocatalysts under visible light, Chem. Lett. 33 (2004) 750–751.

[40] W. Ren, Z. Ai, F. Jia, L. Zhang, X. Fan, Z. Zou, Low temperature preparation and visible light photocatalytic activity of mesoporous carbon-doped crystalline TiO_2, Appl. Catal., B. 69 (2007) 138–144.

[41] T. Tachikawa, S. Tojo, K. Kawai, M. Endo, M. Fujitsuka, T. Ohno, K. Nishijima, Z. Miyamoto, T. Majima, Photocatalytic oxidation reactivity of holes in the sulphur- and carbon-doped TiO_2 powders studied by time-resolved diffuse reflectance spectroscopy, J. Phys. Chem. B 108 (2004) 19299–19306.

[42] Y.M. Li, D.-S. Hwang, N.H. Lee, S.-J. Kim, Synthesis and characterization of carbon-doped titania as an artificial solar light sensitive photocatalyst, Chem Phys. Lett. 404 (2005)

25–29.

[43] C. Di Valentin, G. Pacchioni, A. Selloni, Theory of carbon doping of titanium dioxide, Chem. Mater. 17 (2005) 6656–6665.

[44] P.-W. Chou, S. Treschev, P.-H. Chung, C.-L. Cheng, Y.-H. Tseng, Y.-J. Cheng, M.-S. Wong, Observation of carbon-containing nanostructured mixed titania phases for visible-light photocatalysts, Appl. Phys. Lett. 89 (2006) 131919 (1)–131919 (3).

[45] M. Grätzel, Heterogeneous Photochemical Electron Transfer, CRC Press: Baton Rouge, FL, 1998.

[46] J. Pascual, J. Camassel, H. Mathieu, Fine structure in the intrinsic absorption edge of TiO_2, Phys. Rev. B. 18 (1978) 5606–5614.

[47] R. Asahi, T. Morikawa, T. Ohwaki, K. Aoki, Y. Taga, Visible-light photocatalysis in nitrogen-doped titanium oxides, Science 293 (2001) 269–271.

[48] H. Liu, A. Imanishi, Y. Nakato, Mechanisms for photooxidation reactions of water and organic compounds on carbon-doped titanium dioxide, as studied by photocurrent measurements, J. Phys. Chem. C 111 (2007) 8603–8610.

[49] Y. Park, W. Kim, H. Park, T. Tachikawa, T. Majima, W. Choi, Carbon–doped TiO_2 photocatalyst synthesized without using an external carbon precursor and the visible light activity, Appl. Catal., B. 91 (2009) 355–361.

[50] G.A. Epling, C. Lin, Photoassisted bleaching of dyes utilizing TiO_2 and visible light, Chemosphere 46 (2002) 561–570.

[51] M. Peressi, F. Favot, G. Cangiani, A. Baldereschi, Interface states at ZnSe/Ge heterojunctions: the role of atomic interdiffusion and disorder, Appl. Phys. Lett. 81 (2002) 5171–5173.

[52] T. Zhang, T. Oyama, A. Aoshima, H. Hidaka, J. Zhao, N. Serpone, Photooxidative N-demethylation of methylene blue in aqueous TiO_2 dispersions under UV irradiation, J. Photochem. Photobiol., A. 140 (2001) 163–172.

[53] M. Windholz, The Merck Index, 10^{th} edition, Merck & Co., Rahway, 1983.

[54] J.-M. Herrmann, Heterogeneous photocatalysis: fundamentals and applications to the removal of various types of aqueous pollutants, Catal. Today 53 (1999) 115–129.

[55] S.Y. Treschev, P.-W. Chou, Y.-H. Tseng, J-.B. Wang, E.V. Perevedentseva, C.-L. Cheng, Photoactivities of the visible-light-activated mixed-phase carbon-containing titanium dioxide: The effect of carbon incorporation , Appl. Catal., B. 79 (2008) 8–16.

[56] C. Baumanis, D.W. Bahnemann, TiO_2 thin film electrodes: Correlation between photocatalytic activity and electrochemical properties, J. Phys. Chem. C 112 (2008) 19097–19101.

[57] K. Sunada, T. Watanabe, K. Hashimoto, Studies on photokilling of bacteria on TiO_2 thin film, J. Photochem. Photobiol., A. 156 (2003) 227–233.

[58] Z. Huang, P.-C. Maness, D.M. Blake, E.J. Wolfrum, S.L. Smolinski, W.A. Jacoby, Bactericidal mode of titanium dioxide photocatalysis, J. Photochem. Photobiol., A. 130

(2000) 163–170.

[59] P.-C. Maness, S. Smolinski, D.-M. Blake, Z. Huang, E.J. Wolfrum, W.A. Jacoby, Bactericidal activity of photocatalytic TiO_2 reaction: Toward an understanding of its killing mechanism, Appl. Environ. Microbiol. 65 (1999) 4094–4098.

[60] J.A. Rengifo-Herrera, K. Pierzchala, A. Sienkiewicz, L. Forro, J. Kiwi, C. Pulgarin, Abatement of organics and *Escherichia coli* by N, S co-doped TiO_2 under UV and visible light: Implications of the formation of singlet oxygen ($^1O_2$) under visible light, Appl. Catal., B. 88 (2009) 398–406.

[61] Z. Cheng, Y. Li, What is responsible for the initiating chemistry of iron-mediated lipid peroxidation: An update, Chem. Rev. 107 (2007) 748–766.

[62] T.A. Dahl, W. R. Midden, P. E. Hartman, Pure singlet oxygen cytotoxicity for bacteria, Photochem. Photobiol. 46 (1987) 345–352.

[63] K. Hirakawa, T. Hirano, Singlet oxygen generation photocatalyzed by TiO_2 particles and its contribution to biomolecule damage, Chem. Lett. 35 (2006) 832–833.

[64] J. Marugán, R. van Grieken, C. Sordo, C. Cruz, Kinetics of the photocatalytic disinfection of *Escherichia coli* suspensions, Appl. Catal., B. 82 (2008) 27–36.

[65] M. Cho, H. Chung, J. Yoon, Disinfection of water containing natural organic matter using ozone-initiated radical reactions, Appl. Environ. Microbiol. 60 (2003) 2284–2291.

SECTION IV: CONCLUSIONS

Chapter 9:
General discussion and conclusions

9.1 Introduction

In order to better utilize solar irradiation as a driving force for photocatalysis reactions capable of degrading organic pollutants and inactivating microorganisms, and to improve the technical feasibility of this process for practical applications, enhanced photocatalytic functional materials are required. The need for appropriate photocatalysts that combine the desirable features of efficient visible light utilization, charge carrier separation, high surface area, acceptable activity for degradation and disinfection of a wide range of contaminants and microorganisms of interest, and suitable separability for post-use recovery has been raised as a relevant issue since the advent of the photocatalytic technique in the 1970's, as emphasized by various research efforts conducted along these streams. Although no single material is expected to meet all the needs of an ideal photocatalyst for every application, significant achievements have been made in improving photocatalytic process efficiencies and feasibilities through improving the photocatalyst itself, and therefore further research in pursuit of high performance functional materials is warranted. As an example of a modified

photocatalyst exhibiting increased functionality and improved efficiency, the commercialized photocatalytically-powered Hydrotect^{TM} product developed by TOTO Inc. utilizes metals-modified TiO_2 to initiate self-cleaning and antimicrobial mechanisms upon exposure to environmental humidity, rainwater, and solar irradiation, and can be applied as a thin layer on tiles or glass, or embedded into paint mixtures [1]. These surfaces may also be used for solar photocatalytic remediation of the negative impacts of outdoor NO_x air emissions on building facades. This example is one illustration of the potential contributions that materials development in photocatalysis can make in providing innovative solutions for environmental remediation and antimicrobial applications in practice.

9.2 General discussion

In this thesis, a number of novel photocatalysts were prepared based on various design strategies, and their visible light induced activities for detoxification and disinfection were investigated. The features and performances of these photocatalysts will be generally compared in this section.

The prepared photocatalysts could be grouped into two major classes of carbon-enhanced materials, namely activated carbon adsorbent photocatalysts and carbon-doped TiO_2. In the activated carbon based materials, the incorporated carbon was used as a structural support and mass transfer aid, which facilitated and enhanced photocatalysis through adsorptive processes promoting pollutant concentration and diffusion to active sites, as well as by intermediates retention. In contrast, in the carbon-doped TiO_2, carbon was thought to be intrinsically incorporated into the TiO_2 photocatalyst, affecting its band gap and consequent visible light absorption characteristics. Therefore, in the carbon-as-adsorbent case, the carbon indirectly influenced photocatalysis through the transfer of pollutants from solution to the solid sorbent phase, while in the carbon-as-dopant case, the carbon directly participated in the photoreactions that led to degradation and disinfection. This implied that in the former case, carbon acted mainly by mass transport mechanisms to facilitate pollutant transfer to active sites, while in the latter case, carbon acted mainly by photocatalytic mechanisms to facilitate chemical transformation of the pollutant through the photoinitiated process.

However, the role of carbon-as-adsorbent in facilitating pollutant removal from solution and promoting mass transfer to the supported photocatalytic sites was of great interest, since the faster pollutant removal rates associated to combined adsorption and photocatalysis over photocatalysis alone implied an overall more rapid treatment process, and synergistic mechanisms of adsorption and photocatalysis were possible. Therefore, the dynamic adsorption-photocatalysis was studied further. As identified in literature [2], development of adsorptive photocatalytic hybrid materials containing visible light active components is of current interest in photocatalysis, and as such, a surface plasmon resonance enhanced Ag/AgX (X = Cl, Br) was chosen as the photocatalytic component of an AC-photocatalyst composite. Plasmonic photocatalysts were implemented since they were previously found to possess photocatalytic reaction rates up to 8 times faster than doped TiO_2 due to improved visible light absorption and charge carrier separation mechanisms (as quantified for Ag/AgCl and N-TiO_2 on the degradation of methyl orange [3]). This reported increased visible light absorption agreed well with the results obtained in this work, based on comparison of UV-Vis spectra of the prepared Ag/AgX (X = Cl, Br), and C-TiO_2 (as seen in Figs. 3.7, 7.4, and 8.5, respectively). The developed Ag/AgX-AC composites represented novel SPR-enhanced adsorptive photocatalysts based on activated carbon, and combined two current streams of research in advanced photocatalytic materials. In addition, extension of these materials towards magnetic recovery techniques through incorporation of magnetic nanoparticles also hybridized previous research efforts made in SPR-enhanced photocatalysts, adsorbent photocatalysts based on activated carbon, and magnetic photocatalysts.

The Ag/AgCl-AC composites presented in Chapters 3–6 were unique due to their applicability as photoreactive AC materials that also possessed some degree of antibacterial activity. In particular, since silver-impregnated AC is already commercialized and of industrial significance for water treatment applications, and since chlorine has widespread user acceptance as a disinfection agent, the prepared Ag/AgCl-AC materials were thought to be of potential commercial relevance, since they possessed increased functionality (i.e. antimicrobial and photocatalytic mechanisms) over their antimicrobial counterparts alone. This research led to the further exploration of mechanistic considerations for other silver-

based antimicrobial photocatalysts reported in literature, in order to better characterize this emerging class of novel materials for disinfection applications. The results from this study were published as a critical review in a high-impact journal in chemistry, as given in Appendix A. For the adsorbent photocatalyst composites studied in this thesis, the antimicrobial and photocatalytic bifunctionality of the prepared materials may imply that a solar photocatalytic process can be used for the mineralization of adsorbed bacterial matter to regenerate the activated carbon surfaces. In addition, the composites prepared were of relevance to both photocatalytic detoxification and disinfection, and may be applied to polluted flows containing multiple sources of contamination.

Compared to Ag/AgCl-AC composites, the Ag/AgCl-magnetic AC prepared contained a more uniform structure and morphology, and the silica interlayer was thought to affect deposition behaviour of the photocatalyst onto AC. The photocatalytic activity for organics degradation was comparable to the nonmagnetic composite, although the disinfection efficiency was enhanced in both dark and light conditions, which was thought to be primarily due to an increased rate of silver ion elution from the magnetic composites compared to the pure Ag/AgCl-AC. In addition, the weight contribution of the heavy photocatalyst component made high magnetic nanoparticle loadings necessary, so future work should be performed in optimizing the nanoparticle to adsorbent to photocatalyst ratios to achieve the desired balance between magnetic, adsorptive, and photocatalytic behaviours of the composite.

The Ag/AgBr-AC composite prepared exhibited qualitatively higher visible light activity for the degradation of methyl orange than Ag/AgCl-AC, due to its dual visible light active components (semiconductor photocatalysis in AgBr, and SPR-enhanced Ag), which agreed well with the expected results from literature [4–7]. For the Ag/AgBr-AC composite, photocatalytic disinfection was thought to be dominated by photoreactive ROS generation, and the effect of eluted silver was less pronounced, since little inactivation was observed in the absence of irradiation. Notably, due to the fast rate of pollutant (MO) degradation relative to the rate of pollutant adsorption by Ag/AgBr-AC, the synergistic effects of adsorption and

photocatalytic degradation on pollutant removal could be observed directly via UV-Vis spectroscopy during the combined adsorption-photocatalytic process.

9.3 Conclusions

9.3.1 Project conclusions

Carbon-enhancement can be used as an effective strategy for the improvement of visible light induced photoactivity for detoxification and disinfection of organic and microbial pollutants in aqueous systems. Two classes of carbon-enhanced materials, namely plasmonic adsorbent photocatalyst composites based on activated carbon and carbon-doped TiO_2 were investigated in this project for the degradation of model organic pollutants (methylene blue, methyl orange, phenol) and the inactivation of a model microorganism (*E. coli* K-12) under visible light irradiation. The surface plasmon resonance enhanced photocatalysts (Ag/AgX; X = Cl, Br) possessed increased visible light absorption and improved photoactivity over doped TiO_2, in good agreement with literature [3]. The proposed Ag/AgCl-AC composites exhibited bifunctionality for organic pollutant adsorption and photodegradation, and the activated carbon adsorbent support was thought to enhance the photocatalytic reaction rate through mass transport mechanisms. Silica-coated iron oxide nanoparticles were introduced into the composite to prepare Ag/AgCl-magnetic AC, which was recoverable using an external magnetic field. The incorporated nanoparticles induced a change in the structure and morphology of the resulting composite, which also influenced the silver ion elution behaviour observed, increasing the overall antimicrobial activity. Ag/AgBr-AC was prepared in analogy to Ag/AgCl-AC, and exhibited a higher photocatalytic reaction rate for MO degradation due to the dual visible light absorption mechanisms present (SPR and semiconductor photocatalysis), however, the system suffered from a low photostability. Based on observations of the role of silver in the antimicrobial and photocatalytic disinfection activities of the composites, the behaviour of other silver-modified photocatalysts that act by various inactivation mechanisms under dark and light conditions, respectively, was described in detail.

9.3.2 Specific outcomes

The following specific outcomes were obtained with respect to the defined project objectives:

- **Novel SPR-enhanced visible light active adsorbent photocatalysts based on activated carbon, Ag/AgCl-AC composites, were developed and experimentally investigated.** The composites were synthesized and characterized, and the effect of photocatalyst to adsorbent ratio was studied for the removal of methyl orange and phenol model organic pollutants in aqueous solutions. The composites were shown to be effective as visible light active photocatalysts, and a mechanism for photocatalysis was proposed.
- **Adsorption and photocatalytic behaviours of the prepared Ag/AgCl-AC composites were experimentally investigated and modeled.** Dark adsorption of MO by the composites was studied, and appropriate models were applied to the removal behaviours observed. The adsorption mechanism was also investigated via the intraparticle diffusion model. Kinetics of MO removal under visible light were modeled considering adsorption and photocatalysis.
- **Photocatalytic *E. coli* K-12 inactivation using the prepared Ag/AgCl-AC composites was experimentally investigated.** Photocatalytic inactivation of a model microorganism, *E. coli* K-12, was investigated using the prepared composites, and the mechanism of inactivation was studied. Antibacterial and photocatalytic effects were described based on silver ion elution, photocatalytic reactive oxygen species generation, and bacterial adhesion.
- **The role of silver in the prepared Ag/AgCl-AC composites and other Ag-modified photocatalysts was elucidated.** The role of silver in silver-modified photocatalysts on antimicrobial and photocatalytic mechanisms in both dark and light conditions was discussed based on results from the materials developed in this thesis and from literature. The emergence of antibacterial photocatalysts as a novel class of disinfection materials was emphasized, and its implications for future use were highlighted.

- **Novel SPR-enhanced visible light active magnetic adsorbent photocatalysts, Ag/AgCl-magnetic AC composites, were developed and experimentally investigated.** The magnetic composites were prepared and characterized, and the effect of magnetic nanoparticles loading was studied. A method for the preparation of magnetic AC containing SiO_2-coated magnetite for use in photocatalytic applications was developed, which reduced the photodissociation of the magnetic components. The composites prepared exhibited quasi-superparamagnetic behaviour, and could be recovered after use via an external magnetic field. They were investigated for the degradation of methyl orange and phenol organic pollutants and the inactivation of *E. coli* K-12 under visible light, and the role of magnetic nanoparticles on the structure, morphology, and consequent photocatalytic activity of the composite was discussed.
- **A novel SPR-enhanced visible light active adsorbent photocatalyst, Ag/AgBr-AC, was developed and experimentally investigated.** The effect of the incorporated halide in Ag/AgX-AC composites was investigated, and an Ag/AgBr-AC adsorbent photocatalyst was prepared and characterized. The material was found to have good visible light activity due to band gap absorption in the visible light region by AgBr, and SPR-enhancement by Ag. Photoactivity for organics degradation and bacterial inactivation were investigated, and a mechanism of photocatalytic action was proposed.
- **Novel mixed-phase anatase-rutile carbon-doped TiO_2 photocatalysts were developed and experimentally investigated.** Mixed-phase anatase-rutile carbon-doped TiO_2 photocatalysts were prepared via oxidative annealing. The effect of annealing time and temperature were studied, and visible light activity for organics degradation and bacterial inactivation was investigated.

9.4 Publications

The work undertaken was shared with academic peers internationally and resulted in six publications in peer-reviewed journals, one refereed conference proceeding, and an additional two submitted manuscripts, as included in Chapters 3–8, and Appendices A–C in this thesis. In addition, six conference presentations were given in relation to the scope and results of this project.

9.5 Recommendations for future work

Based on the results obtained in this thesis, the following recommendations are proposed to further research in the topics discussed:

- Photocatalytic activity of the prepared Ag/AgCl should be increased in the AC composite to better optimize the dynamic adsorptive-photocatalytic behaviour and to realize the full potential of the designed material. This aspect can be studied by employing synthesis methods that better control Ag/AgCl sizes, shapes, morphologies, and consequent photocatalytic activities, such as through employing templated processes.
- Adding a regeneration cycle between degradation runs may be beneficial for improving the catalyst recyclability, such as through prolonged irradiation, or by washing and filtration.
- The effect of activated carbon structure should be further studied in the composites. For example, the use of carbons with shallow and wide pores may facilitate better pollutant diffusion to active sites and promote photoexcitation of catalyst contained inside the pore entrances.
- The silver ion elution behaviour with time during photocatalytic inactivation and during dark disinfection should be studied by using online ICP analysis, or by cyclic voltammetry. This would help better understand the role of silver ion elution on inactivation observed, and may also help clarify the fate of eluted silver in the photoreactive system, as discussed in Appendix A.
- Since ROS species can act as broad spectrum disinfectants, the inactivation of other microorganisms such as MS2 phage, a model virus, or other bacterial species such as *Pseudomonas putida* and *Bacillus subtilus* should be investigated.
- Structure and morphology of the reduced silver could be tuned in order to achieve a desirable and controlled ionic silver release rate in the dark, in order to optimize the antimicrobial properties of the photocatalyst in analogy to the continuous drug delivery paradigm discussed by Liu et al. [8]. This could also be studied in relation to photocatalytic activity of the host AgCl in order to develop antimicrobial photocatalytic materials with optimized inactivation capabilities in both dark and

light conditions.

- The magnetic nanoparticles synthesis could be further optimized to obtain smaller particle sizes and increased saturation magnetization values, resulting in improved superparamagnetic behaviour in the MAC composites. In addition, deposition of these nanoparticles within the very small micropores of the host AC may also be interesting to study, since these small pores were not used efficiently for the adsorption of larger molecules such as MO.
- Upon optimization of the plasmonic adsorbent photocatalysts, relevant studies should be undertaken to investigate the effects of process parameters such as light intensity in order to describe the activity observed with respect to practical solar applications.
- Mechanistic pathways for organics degradation mediated by the prepared catalysts should also be studied, and the total organic carbon during photocatalysis cycles monitored to ensure that mineralization is achieved and that the production and release of undesirable intermediates is minimized.

9.6 References

[1] TOTO USA, Inc. (2014), How Hydrotect Works, http://www.totousa.com/Green/Hydrotect/HowHydrotectWorks.aspx, 7 Jan 2014.

[2] T.-T. Lim, P.-S. Yap, M. Srinivasan, A.G. Fane, TiO_2/AC composites for synergistic adsorption-photocatalysis processes: Present challenges and further developments for water treatment and reclamation, Crit. Rev. Environ. Sci. Technol. 41, 13 (2011) 1173–1230.

[3] P. Wang, B. Huang, X. Qin, X. Zhang, Y. Dai, J. Wei, M.-H. Whangbo, Ag@AgCl: A highly efficient and stable photocatalyst active under visible light, Angew. Chem. Int. Ed. 47 (2008) 7931–7933.

[4] Z. Wang, J. Liu, W. Chen, Plasmonic Ag/AgBr nanohybrid: synergistic effect of SPR with photographic sensitivity for enhanced photocatalytic activity and stability, Dalton Trans. 41 (2012) 4866–4870.

[5] J. Jiang, H. Li, L. Zhang, New insight into daylight photocatalysis of AgBr @Ag: Synergistic effect between semiconductor photocatalysis and plasmonic photocatalysis, Chem. Eur. J. 18, 20 (2012) 6360–6369.

[6] P. Wang, B. Huang, X. Zhang, X. Qin, H. Jin, Y. Dai, Z. Wang, J. Wei, J. Zhan, S. Wang, J. Wang, M.-H. Whangbo, Highly efficient visible-light plasmonic photocatalyst Ag@AgBr, Chem. Eur. J. 15 (2009) 1821–1824.

[7] N. Kakuta, N. Goto, H. Ohwaki, T. Mizushima, Silver bromide as a photocatalyst for hydrogen generation from CH_3OH/H_2O solution, J. Phys. Chem. B 103 (1999) 5917–5919.

[8] J. Liu, D.A. Sonshine, S. Shervani, R.H. Hurt, Controlled release of biologically active silver from nanosilver surfaces, ACS Nano 4, 11 (2010) 6903–6913.

SECTION V: APPENDICES

Appendix A:
Antimicrobial and photocatalytic disinfection mechanisms in silver-modified photocatalysts under dark and light conditions

Joanne Gamage McEvoy, Zisheng Zhang

Journal of Photochemistry and Photobiology C: Photochemistry Reviews, 19 (2014) 62-75.

Abstract

The modification of photocatalysts by silver addition or deposition can be used to increase photocatalytic efficiencies by preventing photogenerated electron-hole recombination through electron trapping mechanisms, and by increasing visible light absorption of the composite material through the surface plasmon resonance enhancement of silver nanoparticles. Nanosilver also possesses excellent antimicrobial activity, and can be used as a biocidal agent when incorporated into TiO_2 photocatalysts. Alternatively, the host photocatalyst may also contribute to the antimicrobial activity observed in the absence of irradiation, such as for AgX (X = Cl, Br, I) and ZnO. These silver-modified composites represent a novel class of hybrid photocatalysts, which possess antibacterial and/or antiviral action in both dark and light conditions, and are discussed in detail in this review. In addition, other antimicrobial photocatalysts such as those based on copper are examined. Further work should be performed on these materials to distinguish the roles of acting mechanisms in the light-induced disinfection processes.

Keywords: antimicrobial, photocatalytic disinfection, silver-modified photocatalysts, electron-hole separation

A.1 Introduction

A.1.1 Photocatalytic disinfection

Disinfection plays an important role in the control of pathogens and microbial species in water, and can prevent waterborne epidemics and the spread of infectious disease. Adequate sterilization is also crucial to ensure the safety of medical instruments, food production processes, and environments such as health care facilities. Issues with conventional disinfectants such as chlorine, chloramines, and ozone have been recently identified, since these chemicals may be linked to the formation of harmful disinfection byproducts [1]. Additionally, highly resistant pathogens such as *Cryptosporidium* and *Giardia* cannot be effectively inactivated at normal dosages used for water treatment applications. Alternate disinfection methods using UV-induced processes have also been found to suffer from a lack of residual effect, highlighting the need for further development of appropriate disinfection techniques to address these shortcomings.

Since the discovery of the photocatalytic water splitting effect of titanium dioxide by Fujishima and Honda in 1972 [2], research in photocatalysis has been carried out to exploit this process for use in a wide variety of applications, including: hydrogen generation by solar water splitting [3], environmental remediation and purification of contaminated air, water, and soil [4, 5], self-cleaning applications [6], and photocatalysis-assisted organic chemical synthesis [7], among others. Matsunaga et al. first investigated the inactivation of microbial cells in water using photochemical sterilization, and they found the complete inactivation of *Lactobacillus acidophilus (L. acidophilus), Saccharomyces cerevisiae (S. cerevisiae),* and *Escherichia coli (E. coli)* could be achieved using Pt-TiO_2 under irradiation [8]. Photocatalytic disinfection has since been studied for a number of applications in the contexts of indoor air and environmental health, biological and medical applications, laboratory and hospital applications, pharmaceutical and food production, plant protection applications, wastewater and effluents treatment, and potable water production, as reviewed by Gamage and Zhang [9].

A.1.2 Challenges in TiO_2 photocatalysis

TiO_2 is the most widely used photocatalyst due to its availability, effectiveness, and low cost. TiO_2 can absorb electromagnetic radiation in the ultraviolet (UV) range, causing the photoexcitation of electrons in its valence band to be promoted to its conduction band, creating an electron-hole pair. This electron-hole pair can then undergo further reactions with dissolved oxygen and water to form reactive radical species. The process is often represented schematically for the degradation of a pollutant (ex. organic) according to Figure A.1. The generation of superoxide anions at the cathodic sites and of hydroxyl radicals at the anodic sites can also lead to the production of other reactive species such as hydrogen peroxide. Interaction of these photocatalysis-produced reactive oxygen species (ROS) with biological microorganisms can induce inactivation and cell death, for example, through ROS reaction with functional components in the microbial cell envelope in Gram-negative bacteria [10].

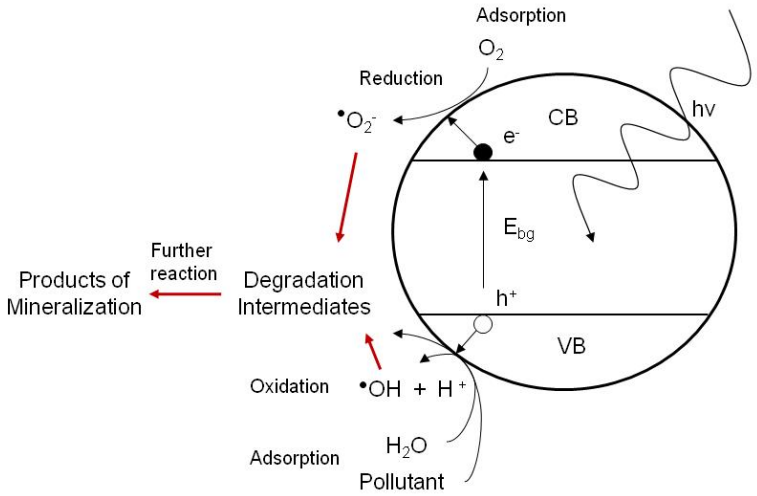

Figure A.1: Photocatalytic degradation by a semiconductor photocatalyst

A main issue arising in photocatalysis lies in the inability of TiO_2 to efficiently use solar light, which is composed of only 3–5% UV. However, solar irradiation consists of approximately 43% visible light, so more efficient utilization of this portion is desirable. Efforts to address this issue by increasing visible light absorption have been made through a number of catalyst modifications such as impurity doping [11–13], metals deposition [14–16], and sensitization [17, 18]. In addition, the rate of recombination of the photoexcited

electrons and holes is a major factor limiting the efficiency of photocatalytic processes [4, 19], and as such research in photocatalyst development has also been focused on the design and fabrication of photocatalysts possessing reduced recombination rates.

A.1.3 Silver-modified photocatalysts

One strategy for reducing electron-hole recombination and improving photocatalytic efficiency is through modifying the TiO_2 catalyst with metal nanoparticles such as Sn, Au, Pt, and Ag [20-24]. These metals have been found to efficiently promote electron-hole separation by forming a Schottky barrier at the metal-photocatalyst interface [25]. Silver is of particular interest in photocatalyst development, and has been cited to possess the following advantages when deposited on or incorporated into an oxide [26]: Ag can act as an electron trapping site to prevent recombination due to the formation of a Schottky barrier [14, 27], band gap narrowing may occur [28], and increased visible light absorption may also occur due to the plasmonic effect [29].

A.1.4 Silver-based disinfection

Silver-modified photocatalysts may also possess distinct advantages when used for disinfection. Silver is a well-known antibacterial agent in the absence of light, and nanosilver has been commercialized as a disinfectant for a number of applications, including use in consumer products such as clothing, respirators, cosmetics, detergents, socks, shoes, and cell phones. The mode of bactericidal action has been proposed to be due to the sorption of silver ions onto the negatively charged bacterial cell wall, causing deactivation of cellular enzymes, disruption of membrane permeability, leading to eventual cell lysis and death [30, 31]. The toxicity of Ag^+ ions at sub-micromolar concentrations has been linked to interaction with enzymes in the respiratory chain reaction, resulting in the uncoupling of respiration from synthesis of ATP [32]. The Ag^+ ion is also able to bind with transport proteins, leading to proton leakage and an induced collapse of proton motive force [33]. Silver ions have a high affinity for thiol groups present in cysteine residues existing from respiratory and transport proteins [32, 34, 35]. Cysteine is the only amino acid present to form hydrogen bonds during protein folding processes. Action on bacterial cells include the induction of morphological changes such as cytoplasm shrinkage and detachment of the cell wall membrane, DNA condensation and localization into electron-light regions in the centre of the

cell, and cell membrane degradation leading to the leakage of intracellular components [36–38].

A.1.5 Silver-modified photocatalysts as synergistic disinfection agents

Due to the possible presence of this inherent biocidal action of silver-modified photocatalysts in the dark, they are good candidates for photocatalytic disinfection processes, where the photo-induced disinfection and antimicrobial activity of the catalyst can act in concert to provide highly effective microbial inactivation under irradiation. It has also been suggested that, using such composites, the photocatalytic disinfection mechanism can compensate to kill silver-resistant microorganisms, which may be present in clinical [39] and environmental samples [40]. A baseline biocidal action due to the incorporated silver can prevent biofilm formation and biofouling on biocompatible host photocatalysts, such as TiO_2. Additionally, the biocidal activity provided by silver compounds can increase the applicability of photocatalyst composite materials, since they are usually limited to use under irradiation only [41]. In some cases, the photocatalytic host materials can also exhibit biocidal activity in the absence of irradiation, in addition to the antimicrobial action of the incorporated silver. Some examples of photocatalyst host materials that may exhibit biocidal activity are ZnO and AgX (X = Cl, Br, I), which also act photocatalytically under irradiation. In the light-induced reactions, the respective and synergistic roles of the silver and photocatalytic ROS-mediated processes should be further studied to gain an in-depth understanding of the overall inactivation observed.

In this review, synergistic disinfectants based on silver-modified photocatalysts are discussed and their modes of biocidal action in the presence and absence of light are examined, respectively. Particularly, Ag-modified catalysts based on TiO_2, silver halides (AgX), and ZnO are addressed. In addition, other antibacterial and/or antiviral photocatalytic materials such as those based on copper are briefly reviewed.

A.2 Silver-TiO_2

A.2.1 Silver-TiO_2 photocatalysts as synergistic disinfection agents

Crystalline TiO_2 of anatase or rutile structure is widely studied and used as an efficient and environmentally benign photocatalyst for the degradation of organic pollutants and disinfection of microorganisms [2, 42, 43]. The incorporation of silver into TiO_2 can improve the photocatalytic disinfection efficiencies observed. For example, the use of 1 wt% loading of Ag onto TiO_2 was found to reduce the reaction time required to completely inactivate 10^7 colony forming units (CFU) mL^{-1} of *E. coli* from 65 minutes to 16 minutes under UV light [44]. Sol-gel [16, 45], chemical vapour deposition [46–48], and physical vapour deposition [49] methods can be employed to prepare Ag-TiO_2 structures. In these composites, the silver nanoparticles are thought to enhance TiO_2 photoactivity by lowering the rate of recombination of photo-excited charge carriers by acting as electron traps [50, 51], and also by inducing visible light absorption through the surface plasmon resonance effect and subsequent electron transfer to TiO_2, resulting in charge separation [52, 53].

A.2.2 Mechanisms of photocatalytic enhancement

Modification of TiO_2 by introducing Ag deposits acts to alter the structure and mode of photocatalytic action because the silver can act as electron traps that enhance electron-hole separation, as shown in Figure A.2. The electrons can then be transferred to molecular oxygen to form superoxide and subsequently, other ROS. The electron trapping effect of Ag on TiO_2 was confirmed by photoluminescence studies for various Ag-TiO_2 materials including particles prepared by sol-gel synthesis [54, 55] and photodeposition [56], as well as for nanosilver-decorated titanium dioxide nanofibers [57], and it was found that silver on the TiO_2 surface decreased the electron-hole recombination by increasing the number of heterojunctions.

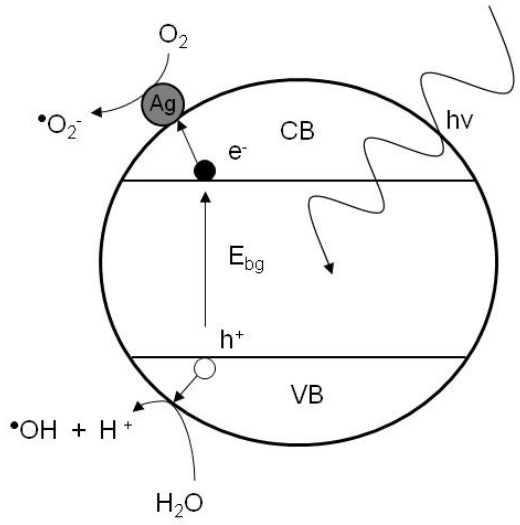

Figure A.2: Electron trapping in Ag-TiO_2

It should be noted that some disadvantages have been associated with silver deposition, including: reduction in access of radiation to TiO_2 surface due to excess coverage by silver deposits, blockage of TiO_2 active sites due to deposits, inhibition of role of oxygen due to increased electron transfer from TiO_2 to deposits [58, 59]. Therefore caution must be taken to avoid excessive silver loadings. Depending on the quantum size effects produced by the deposited silver, surface plasmon resonance may arise, causing increased visible light absorption by the composite catalyst. Surface plasmon resonance (SPR) is a phenomenon arising from the collective oscillation of conduction electrons of nanoscale noble metals upon interacting with electromagnetic radiation [60]. The shape, amplitude, and frequency of the maximum absorbance of this SPR is strongly dependent on the effective dielectric constant in the surrounding medium of the nanoparticles, and their respective morphologies and size distributions [61]. SPR can dramatically amplify visible light absorption for Ag-TiO_2 catalysts [29]. In the SPR-enhanced materials, surface electrons can be excited, and interfacial electron transfer can occur [14, 27, 62].

Table A.1: Results of select studies reporting enhancement of photocatalytic disinfection using Ag-modified photocatalysts

Photocatalyst	**Target Microorganism**	**Experimental**	**Results**	**Mechanistic Description**	**Reference**
Ag-TiO_2					
Ag-TiO_2	*E. coli*	1 wt% Ag-TiO_2 prepared by incipient wetness method; 0.75 g/L loading used under 250 W high pressure Hg irradiation	7-log inactivation achieved in 16 minutes under UV, 100 minutes in the absence of light	Electron-hole separation by incorporated Ag	[44]
TiO_2 thin films with deposited Ag on titanium plates	*E. coli*	TiO_2 films prepared by sol-gel spin-coating, $AgNO_3$ deposition and annealing used to deposit Ag; *E. coli* contacted with prepared films under 350 W Xe irradiation with UV filter	All prepared films exhibited > 80% inactivation in 30 minutes under dark conditions, and 100% inactivation in 15 minutes under irradiation	Electron-hole separation, bactericidal activity of Ag discussed	[63]
Ag-TiO_2 composite films	*E. coli*	Mesoporous TiO_2 films prepared by sol-gel spin-coating, $AgNO_3$ deposition and photoreduction used to deposit Ag into pores; *E. coli* contacted with prepared films under 5 mW/cm^2 UV for 5 minutes	Survival ratio was 9.2% in the dark, and complete inactivation was observed after 5 mins irradiation	Electron-hole separation, silver ion elution studied and found to influence bactericidal activity	[64]
Ag-TiO_2 nanocomposite layer deposited on Ag/TiO_2	*E. coli*	Anatase TiO_2 films prepared by sol-gel method followed by $AgNO_3$ deposition and photoreduction; films immersed in nutrient broth containing 10^5 CFU/mL *E. coli* under 10 W irradiation by white fluorescent light or outdoor solar irradiation (~ 1 mW/cm^2)	5-log reduction achieved in 110 and 90 min under visible and solar irradiation, respectively; compared to 140 min required in the dark	Silver ion release studied and found to influence bactericidal activity	[23]

Table A.1 (cont.): Results of select studies reporting enhancement of photocatalytic disinfection using Ag-modified photocatalysts

Photocatalyst	**Target Microorganism**	**Experimental**	**Result**	**Mechanistic Description**	**Reference**
TiO_2-Ag particles	*E. coli*	Particles prepared by micellar layer-by-layer strategy; 1 mg catalyst contacted with 7 mL bacteria, UV irradiation provided	Bactericidal efficiency of Ag-containing particles relative to TiO_2 increased from 45% to 51% in 1 h upon UV irradiation	Silver ion release studied and cited to be dominant bactericidal mechanism	[65]
Ag-TiO_2 nanoparticles	*Bacillus subtilus (B. subtilus), Pseudomonas putida (P. putida)*	Ag nanoparticles prepared on the surface of commercial TiO_2 by wet impregnation and chemical or UV reduction in a high-throughput cell viability assay	Ag-TiO_2 nanoparticles exerted stronger bactericidal effects in the dark than Ag nanoparticles, activity of Ag-P25 was intensified under UV light	Silver ion release and speciation with anionic ligands such as Cl^- studied, electron-trap mechanism of Ag discussed	[41]
Ag-TiO_2 nanoparticles	*Bacteriophage MS2*	Nanosized silver islands deposited onto commercial TiO_2 via photochemical reduction of silver nitrate; slurry photoreactor system using 100 mg/L catalyst studied under 2.5 mW/cm^2 UV irradiation	0.6 log removal of MS2 by adsorption and silver leaching in the dark, 5.95 log removal under irradiation	Silver ion release, charge separation, and increased bacterial adsorption of Ag-TiO_2 discussed	[66]
Ag/AgX-based materials					
Ag/AgCl/$W_{18}O_{49}$ nanorods	*Vibrio natriegens*	Deposition of $AgNO_3$ onto $W_{18}O_{49}$ nanorods and subsequent photoreduction; modified Kirby-Bauer disc diffusion assay used in dark and under 300 W Xe light	Zone of inhibition increased from 0.90 cm in the dark to 1.72 cm under irradiation	Silver ion release, visible light absorption due to plasmonic effect causing radical species generation cited	[67]

Table A.1 (cont.): Results of select studies reporting enhancement of photocatalytic disinfection using Ag-modified photocatalysts

Photocatalyst	Target Microorganism	Experimental	Result	Mechanistic Description	Reference
Ag/AgX-based materials					
Ag/AgBr/TiO_2	*E. coli*	AgBr/TiO_2 obtained via sol-gel route and solvothermal synthesis, Ag/AgBr/TiO_2 obtained by photoreduction; inactivation activity studied using 100 mL suspensions of 10^7 CFU/mL *E. coli* and 0.025 – 0.25 g/L photocatalyst under LED irradiation	Photocatalytic inactivation was <1 log in the dark, increased to 6-7 log reduction under irradiation	Ag ion release was found to be very low in the dark, activity under irradiation attributed to photocatalytic ROS production by plasmonic effect and subsequent charge injection to TiO_2	[68]
Zeolitic Ag/AgBr/TiO_2	*E. coli*	Zeolite-based photocatalysts prepared by sol-gel and deposition method; inactivation tests performed using 10^7 CFU/mL *E. coli*, 20 mg catalyst and 30 mL reaction fluid under 250 W Hg irradiation	~5.5 log reduction in dark conditions, 7 log reduction under irradiation	Ag ion release, radicals generation and charge separation mechanism of photocatalyst discussed	[69]
Ag-ZnO					
Ag-doped ZnO thin film	*E. coli*	Ag-doped ZnO thin films coated onto glass prepared by a sol-gel dip-coating method; 3 mL of $4.72x10^5$ CFU/mL exposed to thin film for irradiation under 3x15 W blacklight fluorescent UVA for 10, 20 and 30 minutes, respectively	Undoped ZnO exhibited some inactivation in the dark (<1 log) for 30 mins, increased to ~2 log under irradiation; for all Ag loadings (1–10 mol%), ~2 log inactivation observed in the dark for 30 mins, increased to 5-log inactivation after 20 minutes irradiation	Enhanced photocatalytic activity of Ag-doped ZnO, silver ion released (although leached Ag^+ was unquantifiably low)	[70]

A.2.3 Photocatalytic disinfection

The formation of active silver ions from metallic silver nanoparticles has also been reported to play a role in the inactivation mechanisms observed. The incorporation of silver onto TiO_2 increased the photocatalytic disinfection observed in a number of studies, and some representative results are highlighted in Table A.1. The studies discussed all report a baseline inactivation observed in the dark, and enhanced inactivation using the same material under irradiation.

A.2.4 Silver ion release behaviour

Silver ion release is an important factor in the evaluation of antimicrobial activity of silver-containing composite photocatalysts. Silver ions are mainly produced by irreversible oxidation of zerovalent metallic particles by reaction with oxygen, which is mediated by protons and other components of the surrounding fluid [71, 72]. Liberated silver ions strongly interact with the environment to which they are released, and can partition by binding with anionic ligands such as chloride (present in medium and saline in experimental studies) or biological thiol targets. AgCl precipitates formed can also undergo dissolution equilibrium between their dissolved complexes and solid forms to contribute to the total dissolved silver content. The formation of AgCl precipitates by silver-eluting samples is further complicated under irradiation, because a partial reduction might occur to generate Ag/AgCl species. Despite this, it was previously found through silver equilibrium speciation and pathway studies that, due to the high affinity binding of thiols ($K_{ads} \sim 10^{12}$), direct thiol transfer could occur at silver ion concentrations lower than the AgCl precipitation threshold and that the thiol targets were typically abundant enough in experimental studies to receive all of the free silver [73]. Additionally, the presence of silver at concentrations as low as 400 ppb may be effective against many bacterial species when used alone as a biocidal agent [74]. In practical applications, both a high antibacterial activity and low silver release are desirable for silver-based materials [23]. The slow release of silver leads to lengthening of antibacterial activity and facilitates controlled dosage [75]. Prolonged silver elution, or controlled release, is a desirable property for antibacterial materials and eukaryotic toxicity, and nanosilver has been compared analogously to a drug delivery system, where the silver nanoparticles contain a concentrated inventory of the active species (ionic silver and its

soluble complexes), which are transported to and released in the vicinity of biological sites such as thiol targets [73]. Therefore release of silver by silver-containing photocatalysts should be studied when their disinfection properties are under investigation.

For Ag-modified TiO_2 bactericidal photocatalysts, the release behaviour of silver ions was found to be mainly controlled by water diffusion characteristics in the silver-containing matrix [23, 25, 64, 76]. For example, silver-modified mesoporous TiO_2 quickly released Ag^+ ions in the first 30 minutes of use both in the dark and under UV [25], and this was attributed to the release from the Ag nanoparticles deposited on the external surface of mesoporous TiO_2. The slow rate of penetration of water molecules into the pores and subsequent diffusion of released Ag^+ ions out of the pores caused the decreased rate of silver release observed after the initial diffusion. This was also found with nanocomposite Ag-TiO_2/Ag/TiO_2 films, where TiO_2 acted as a barrier layer preventing free ion release by rapid water diffusion into the silver interlayer [23, 64], and on mesoporous Ag/TiO_2 films [64]. Accordingly, silver ion release can be slowed using silver immobilized on porous supports, promoting their effectiveness as antimicrobial materials for prolonged applications [77, 78].

A.2.5 Role of silver under irradiation

The role of silver under irradiation for antimicrobial photocatalysts has been discussed to a lesser extent. Under irradiation, system dynamics may be altered due to excitation of the TiO_2 photocatalyst to create photo-induced radicals and their interaction with ionic silver and silver nanoparticles. As indicated by van Grieken et al. [59], although many studies employ silver-modified TiO_2, only few groups have researched the lixiviation of silver to verify the stability of these deposits on the catalyst surface [79]. Using immobilized and slurry Ag-TiO_2 for bacterial inactivation, a negligible silver release and a consequent high stability of the surface silver deposits were found under irradiation. However, when a parallel experiment was performed in the dark, a significant amount of lixiviation occurred and resulted in greater inactivation than that observed in the presence of light. They attributed this inactivation to the antibacterial effect of soluble silver compounds, and it was concluded that radiation was important to assure the stability of the silver deposits. Radiation was thought to supply the necessary electrons to maintain the silver in its metallic state through

photocatalytic mechanisms, while re-oxidation occurred in the dark. Despite this, some silver ion release was observed in the photoirradiated system, where oxidation was thought to have taken place in the darker regions of the reaction system. Additionally, the photodegradation of methylene blue dye was investigated for comparison, and a decrease in activity was observed upon incorporation of silver, indicating that enhancement of *E. coli* inactivation was more likely due to the direct bactericidal action of silver and improved bacterial adhesion, as opposed to the electron-hole separation and interfacial charge transfer mechanisms, exclusively [59].

The use of methylene blue dye for photocatalytic comparison of disinfection activity was also performed by Srisitthiratkul et al. [57] for nanosilver-decorated TiO_2 nanofibers against *Staphylococcus aureus (S. aureus)* and *E. coli*, and they found an enhancement in the organic degradation with incorporation of silver at a sufficiently low loading (2%). This enhancement was confirmed to be due to electron-hole separation mechanisms, as probed by PL measurements. However, overloading of the photocatalyst with Ag was found to decrease photocatalytic efficiency.

In a non-photocatalytic system, the activity of silver ions in the form of dissolved $AgNO_3$ was enhanced under UV-A irradiation (300–400 nm) and visible light for the inactivation of *E. coli* and MS2 bacteriophage [80]. They attributed the observed enhancement to the photochemical reaction of silver-cysteine complexes that formed upon reaction of silver ions with thiol groups in structural or enzymatic proteins of the microorganisms, followed by photochemical reaction of these complexes to cause inactivation. According to the silver ion-thiol mechanism, silver ions generated in solution react with thiol in cysteine by replacement of a hydrogen atom in the –SH group to form a –S–Ag complex, destroying the enzymatic function of the protein [81–85]. Through spectrophotometric measurements, these cysteine complexes were found to absorb UV and visible irradiation up to 500 nm, and were thought to act photochemically according to the following scheme [80]:

$$R–SH + Ag^{+} \leftrightarrow R–S–Ag + H^{+} \quad (A.1)$$

$$R–S–Ag + h\nu \rightarrow R–S^{\bullet} + Ag \quad (A.2)$$

$$R–S^{\bullet} + R–S^{\bullet} \rightarrow R–S–S–R \qquad (A.3)$$

Reaction (A.1) was found to be reversible and dependent on the proton concentration in solution. Reaction (A.2) was thought to irreversibly generate zerovalent silver through abstraction of an electron in the chelated cysteine by a silver ion in the complex by ligand-to-metal charge transfer. In reaction (A.3), the cysteine-dimer was formed from the reaction of two monosulfide radicals and was identified as the photolyzed product of the silver-cysteine complex through mass spectrometry measurements.

These photochemical reactions reported for silver-cysteine complexes may play a role in the mechanism of inactivation using composite photocatalysts that release silver under irradiation. In such systems, photoproduced reactive species may also interact with the monosulfide radicals to form different reaction products. However, to probe such mechanisms, Okhaven [23] synthesized the reported Ag-TiO_2 film using SiO_2 instead to remove the effect of photocatalysis. In this control, no change in bactericidal activity was observed using the Ag-SiO_2 material in the dark or under irradiation for the inactivation of *E. coli*, indicating that the photochemical pathway reported for silver ion complexes was negligible in this case. Similarly, Liu et al. compared the antibacterial and photocatalytic activities of a mesoporous Ag/TiO_2 film on a silver-resistant strain of *E. coli* and on a normal strain [64]. They found the survival rate of silver-resistant *E. coli* to be much higher than that of normal *E. coli* in the dark, and the silver-resistant strain survival decreased significantly upon irradiation with UV light. The survival of this strain using Ag-TiO_2 under irradiation was lower than that observed using the pure TiO_2 photocatalytic material. Therefore, the silver nanoparticles incorporated into mesoporous TiO_2 were thought to act both antimicrobially and as an intensifier for photocatalysis through the charge-separation mechanism. In a study by Li et al., the inactivation of *B. subtilus* and *P. putida* was observed using Ag-TiO_2 (P25) in both dark and light conditions [41]. Inactivation using Ag-TiO_2 in the dark was found to be greater than the effects of pure silver nanoparticles in the dark. This may have been due to adsorption of bacteria onto the surface of TiO_2, inducing cell stress that could lead to mortality, as well as the influence of silver ion release. However, this ion release in the dark was lower than that observed for Ag nanoparticles and $AgNO_3$ salts, and

so the observed synergy was attributed to variation in dissolution and re-precipitation kinetic and equilibrium reactions between the pure Ag nanoparticles and Ag-TiO_2 nanoparticles. Under UV irradiation, the inactivation mechanism was found to be dominated by the effects of ROS generation.

The oxidation of silver nanoparticles in photoreactive systems has also been reported [29, 86]. As discussed with respect to photocatalytic and antibacterial activities of Ag-TiO_2 composites under irradiation [25], the redox potentials of the TiO_2 hole and the hydroxyl radical are +2.5 V and +1.9 V versus the normal hydrogen electrode (NHE), respectively [87]. This implies that the oxidation of metallic Ag to Ag^+ is thermodynamically favoured since Ag^o/Ag^+ = 0.7996 V vs. NHE, and this redox potential decreases with decreasing Ag particle size [88]. However, these oxidized silver ions may consume photogenerated electrons to reduce silver back to its metallic state [89]. Castro et al. probed the photocatalytic degradation of dichloroacetic acid (DCA) by Ag-TiO_2 under UV and visible light, and suggested that the photoproduced valence band holes were hindered from oxidizing DCA because they were consumed to oxidize Ag^o to Ag^+, implying that the electron-hole charge separation mechanism of the incorporated silver was negligible [90]. In their post-irradiation events studies, they found that a UV-treated Ag-TiO_2 sample exhibited increased inactivation efficiency in subsequent dark periods, and the activity was further promoted using the same sample again under visible light. It was postulated that the bacterial outer membrane acted as an electron donor to regenerate the Ag^o species necessary for subsequent photoactivation and ROS production under visible light. Therefore, for all silver-containing photocatalysts, clarification of the respective and synergistic roles of released silver and photo-generated ROS under irradiation should be studied to appropriately describe the relevant acting mechanisms.

A.2.6 Changes to bacterial adhesion properties

The modification of titania by silver can affect its bacterial adhesion properties, and influence the inactivation observed compared to the unmodified material. Ma et al. prepared silver-modified mesoporous TiO_2 and found that the electrostatic interactions between the particles and *E. coli* bacteria affected the inactivation efficiency obtained [25]. They

observed strong aggregation between Ag-TiO_2 particles and bacteria, and found that inactivated cells were encased by the particles after 30 minutes of mixing. Inactivation efficiency decreased when the positive charge on the particles increased, which was interesting because the bacteria carried a negative surface charge. Similarly, scanning electron microscope images of an immobilized Ag/TiO_2 surface prepared by dip-coating and photodeposition of Ag showed that the composite surface exhibited particulate nature and rough texture, and this topography was thought to be favourable for bacterial adhesion in *E. coli* inactivation [59]. In a study of MS2 bacteriophage inactivation using silver-doped TiO_2 reported by Liga et al. [66], an increased adsorptive removal was explained by the interactions of viral surface amino acids with silver, since there exist 183 cysteine residues exposed on the capsid surface of MS2 [91]. This increased adsorption was also noted to enhance the photocatalytic inactivation rate by causing the virus to come in close proximity to surface-bound and bulk generated $^{\bullet}OH$ radicals, while simultaneously increasing the likelihood of direct hole oxidation.

A.3 Silver-silver halides (Ag/AgX)

A.3.1 Overview of Ag/AgX photocatalysts

Another method of stabilizing highly reactive silver nanoparticles in photocatalytic systems is to incorporate them into silver/silver halide structures. Silver halides (AgX, X = Br, Cl, I) are photosensitive materials widely employed in photographic films. In photographic processes, silver halides absorb photons to liberate electron-hole pairs. The free electrons can combine with mobile interstitial silver ions to lead to separation of silver atoms, and upon continued absorption of photons, clusters of silver atoms are formed [89, 92, 93]. The critical size of silver clusters necessary to form a latent image is four silver atoms [93, 94]. Due to this instability under light, silver halides have not traditionally been used as photocatalysts.

However, when they are incorporated with silver nanoparticles, the two components act in concert as an efficient and stable visible light photocatalyst [95]. Silver/silver halides (mainly Ag/AgCl, Ag/AgBr) have been synthesized in literature using a variety of techniques such as deposition-precipitation-photoreduction [95–97], one-pot synthesis with poly(vinyl pyrrolidone) (PVP) and ethylene glycol at elevated temperature [98], ionic-liquid synthesis

using 1-octyl-3-methylimidazolium chloride as a chlorine source and reducing agent [99], double-jet method [100], and microwave-assisted non-aqueous growth [101]. In all cases, strong absorption in the visible light region was observed, due to SPR of the incorporated silver nanoparticles.

A.3.2 Mechanism of photocatalytic enhancement

In a system such as Ag/AgCl, a visible light photon can be absorbed by a silver nanoparticle, generating a hole and an electron. These can be effectively polarized by the surface plasmon resonance state of the silver, causing efficient separation of the hole and electron such that the electron is transferred to the silver surface furthest away from the interface with AgCl (because AgCl is terminated by Cl^- ions, and is negatively charged), and the hole transferred to the AgCl particle surface [95]. The stability of silver/silver halides has been attributed to this charge separation, which prevents the generated electron from being transferred to the Ag^+ ions of AgCl [99]. The electron is instead transferred to molecular oxygen present at the surface, forming active species such as the superoxide anion of oxygen, which can facilitate degradation of pollutants [102]. The positive hole generated can also oxidize Cl^- ions into Cl^o, which are themselves powerful oxidizing agents that can attack organic pollutants near the surface of the catalyst, and be reduced back to their ionic Cl^- state [95, 100]. In an Ag/AgBr system, visible light absorption by AgBr may also play a role in ROS generation in addition to SPR.

A.3.3 Photocatalytic disinfection

The disinfective capabilities of certain silver-based surface plasmon enhanced photocatalysts have been reported in literature. For example, $Ag/AgBr/TiO_2$ was investigated by Hu et al. [89] for inactivation of *E. coli* under visible light irradiation. They studied the mechanism of cell death through transmission electroscope microscopy, and confirmed inactivation to be caused by radical decomposition of the cell membrane. Hu et al. also confirmed the high photocatalytic inactivation efficiency of $AgBr/TiO_2$ and AgI/TiO_2 catalysts on *E. coli* and *S. aureus* under visible light irradiation [89, 103–106], and found that ROS species such as $HO_2^{\bullet}$, $^{\bullet}OH$, $^{\bullet}O_2^-$ and H_2O_2 were involved in bacterial inactivation. They reported that the electrostatic interactions between the bacteria and catalyst played a role in the inactivation

efficiency observed [89, 103, 107]. The mechanism of cell death was also studied by Zhang et al. [108], and a dominant role of diffusing hydroxyl radicals on photocatalytic disinfection of *E. coli* was found using Ag/AgBr/Bi_2WO_6 plasmonic nanojunction catalysts. Photocatalytic disinfection of *E. coli* was also reported by Elahifard et al. using apatite coated Ag/AgBr/TiO_2 [109], and by Wang et al. using Ag/AgBr/$WO_3 \cdot H_2O$ under visible light [110]. The plasmon-induced photocatalytic killing of enteric microorganisms *Shingella dysenteriae (S. dysenteriae)*, *E. coli*, and human rotavirus type 2 Wa under visible light was investigated using Ag-AgI/Al_2O_3 [105]. Interestingly, the silver halide alone has also been reported to possess antibacterial action, and studies have been performed without discussion of the material as a photocatalyst. For example, the bactericidal activity using AgCl only in the dark was reported [111–114], and the mechanism was attributed to the action of diffused Ag^+ ions. Similarly, nano-AgBr deposited on activated carbon filters were prepared by Pal et al. [115], and these composites were found to have a bactericidal effect on *E. coli* in the absence of photocatalytic mechanisms.

A.3.4 Ag/AgX as bactericidal and photocatalytic materials

Certain silver/silver halide materials have been discussed for their dual functions as bactericidal and photocatalytic materials in dark and light conditions, respectively. The results of select studies are shown in Table A.1, where there exists a baseline antimicrobial effect of the Ag/AgX- containing material in the dark, and an enhanced activity upon irradiation.

A.3.5 Silver ion release behaviour of antibacterial AgX

In Ag/AgX-type silver-modified photocatalysts, the contribution to inactivation by release of Ag^+ from metallic silver nanoparticles, and release due to the limited solubility of silver halides (ex. 10^{-5} solubility limit of AgCl) to form free silver (Ag^+) and soluble silver complexes (dissolved AgCl, $AgCl_x^{1-}$) in aqueous media should be considered when trying to quantify antibacterial activity [73]. To this end, silver release has been studied from AgCl materials used as bactericidal agents. Tuncer and Seker [116] investigated the antibacterial efficacies of silver and silver chloride-containing titania xerogels synthesized using single-step sol-gel methods against *E. coli*, and particularly, focused on the effect of silver chloride formation due to reaction of eluted Ag^+ ions with chloride present in the Mueller-Hinton

medium used for bacterial cultivation and for zone of inhibition studies. The local deposition of AgCl in the medium was described by the following equilibrium:

$$Ag^{+}_{(aq)} + Cl^{-}_{(aq)} \leftrightarrow AgCl_{(aq)} \qquad (A.4)$$

They observed high bactericidal activities with both the Ag-TiO_2 and AgCl-TiO_2 xerogels, but the release rate of silver ions from the latter was lower due to equilibrium dictated by equation (A.4). It was indicated that the controlled release of Ag^+ could be achieved when silver was present as AgCl crystallites, and that this was effective for antibacterial activity because bacterial growth could be inhibited at low silver concentrations, including at parts per billion levels [117]. It was also concluded that unnecessary release of silver occurred if silver was not present in the form of AgCl and that consideration of chloride ions present in the medium agar must be made to account for their interactions with diffused silver. In a study comparing the inhibitory effects of silver nanoparticles, silver ions, and silver chloride colloids on microbial growth of *E. coli* [112], it was noted that, depending on their size and bioavailability, the inhibition that could be caused by AgCl colloids (< 14 nm) could be as significant as pure Ag^+ ions introduced from bulk silver species ($AgNO_3$). The toxicity of Ag^+ ions was found to be dependent on the strength and amount of ligands present [118]. The effect of anionic ligands, namely chloride, was also studied in the characterization of silver release into wastewaters from commercially-available functional (nano)textiles after washing cycles [119]. Of the silver textiles studied, AgCl was the most frequently observed chemical form of silver in the washwater. The secondary formation of AgCl from Ag-containing textiles was found to occur during washing cycles, when the released free silver precipitated with chloride in the washwater. The release of silver from Ag nanoparticles is also size dependent, and is governed by the following relationship [120]:

$$2\,Ag_{(s)} + 0.5\,O_{2(aq)} + 2\,H^{+}_{(aq)} \rightarrow 2\,Ag^{+}_{(aq)} + H_2O_{(l)} \qquad (A.5)$$

Silver ion release from Ag nanoparticles is dependent on their prior oxidation, since metallic silver is insoluble in anaerobic conditions. Upon the formation of an oxide layer (Ag_2O) on the surface of the nanoparticle, release of silver cations ensues due to the high solubility of silver oxide [121]. An oxidant must be present for further dissolution to take place, and removing this source was found to completely inhibit the release of dissolved silver ions

[72]. From the silver ion release described in reaction (A.5), increasing the hydrogen concentration (by decreasing pH) in the presence of oxygen can increase the rate of silver oxide formation and dissolution. The dissolution rates of both Ag and AgCl are size-dependent, with smaller nanoparticles exhibiting faster release rates than larger particles.

A.3.6 Silver ion release behaviour of antibacterial and photocatalytic Ag/AgX in dark and light conditions

While the silver release and bactericidal activity for AgX materials is well documented, dynamics of oxidation and dissolution for Ag/AgX agents is discussed to a lesser extent. For example, some Ag/AgBr-modified semiconductors such as WO_3 [110], Bi_2WO_6 [104], and P25 TiO_2 [68] did not exhibit any bactericidal activity in the absence of light due to negligible silver ion release. However, Wang et al. reported bacterial inactivation of *E. coli* in the dark using Ag/AgBr-TiO_2 prepared by both sol-gel route and by solvothermal synthesis, respectively [68]. They attributed this dark biocidal activity to small amounts of silver ion release and the good dispersion of silver nanoparticles on the composite photocatalysts. The composites also showed high stability, and the silver ion release was found to be negligible under irradiation compared to that of a reference Ag/TiO_2 photocatalyst. The oxidation of silver nanoparticles in the composite Ag/AgBr-TiO_2 was thought to be prevented due to the surface plasmon-induced charge separation. In a study performed by Padervand et al. [69] on the antibacterial and visible light photocatalytic disinfection activities of Ag/AgBr/TiO_2/zeolite on *E. coli*, the observed antibacterial activity in the dark was also attributed to the presence of Ag^+ ions released to the medium. However, inactivation was enhanced under irradiation, and the silver ions were thought to act as an auxiliary factor contributing to bacterial inactivation in addition to photo-produced ROS.

Due to the high affinity of free ionic silver for anionic ligands, the formation of AgCl in the presence of saline or medium used in experimental studies or present in natural environments should be considered. The formation of AgCl shells on the surface of Ag nanoparticles, and the dissolution and formation of bioavailable $AgCl_x^{1-x}$ complexes in the presence of Cl^- complicate the toxicity kinetics from Ag nanoparticles and the silver release rate. Evidence has been provided for the precipitation of AgCl both as a separate phase and on the surface of

silver nanoparticles [122]. Possible complications under irradiation include the partial photoreduction some AgCl [73], and the subsequent photocatalytic action of the produced Ag/AgCl. In silver-modified photocatalysts releasing small quantities of Ag^+, the effects of AgCl formation are thought to be negligible, but may be more severe for highly Ag^+-eluting photocatalysts. Further research should be undertaken to clarify the role of the AgCl particulates formed, and especially their effect in photoreactive disinfection schemes.

A.4 Silver-ZnO

A.4.1 Overview of Ag-ZnO photocatalysts

ZnO is a wide bandgap semiconductor, and is considered as a suitable alternative to TiO_2 due to its nontoxicity and relatively lower preparation costs [123, 124]. Despite this, application of ZnO to photocatalysis has been limited because it exhibits a low photocatalytic activity and is susceptible to photocorrosion, which further degrades its activity in repeated cycles [125]. This corrosion is particularly problematic, and has been shown to occur to some extent in both dark and light conditions for ZnO coatings [126]. Efforts have been made towards improving the efficiency of ZnO photocatalysis, such as through decreasing ZnO particle sizes [127], tuning preparation procedures to develop films with high photocatalytic activity [128], increasing surface area through implementing hierarchical nanostructures [129], and optimizing the face- and morphology-dependent photocatalytic performance of hexagonal ZnO crystals [130–133].

Another strategy for improving the photocatalytic activity of ZnO is through combination with noble metal nanoparticles, such as Ag, Au, Pt, or Pd [134, 135]. These metal nanoparticles act as charge sinks [87] for photo-induced electrons in the host ZnO material to prevent recombination of the charge carriers by a similar mechanism as in noble metal nanoparticle deposited-TiO_2. Of the noble metals, silver is cited to be the cheapest [134]. Many attempts have been made to modify ZnO photocatalysts with Ag to improve photocatalytic activity [136–142], and photostability of the host ZnO may also improved upon introduction of the metal nanostructures [141].

A.4.2 Bactericidal activity of ZnO materials

ZnO has been investigated for its unique qualities as an antibacterial agent in the absence of light since before the 1950's [143], and has since been shown to be effective for the inactivation of *E. coli*, *Salmonella typhimurium (S. typhimurium), B. subtilis,* and *S. aureus*, among others [144–146]. Nano-sized ZnO (< 100 nm) has been found to be toxic to algae [147–150], crustaceans [151–153], fish [150], bacteria [154–158], nematodes [159], and plants [160, 161], to various extents. The antibacterial activity in all cases was dependent on the surface area and concentration, with increasing inactivation observed upon increasing these factors [162]. Additionally, smaller ZnO particles were found to exhibit higher bactericidal activity [156, 163, 164], and inactivation seemingly occurred on or near the particle surface [144]. Although still a controversial subject, the mechanism of antibacterial activity has been proposed to be due to a number of factors. Previous assessments attributed the biocidal action of nano-ZnO to H_2O_2 generation from the surface, inducing oxidative stress on bacterial species and causing eventual lysis [154–158, 165, 166]. However, many studies reported that the release of zinc ions from nano-ZnO was the main factor responsible for the observed toxicity [147, 149–152, 160, 161, 167, 168]. For example, the toxicity could be well-correlated to the concentration of free hydrated Zn^{2+} ions or labile zinc complexes [147, 169–172], although the attachment of ZnO nanoparticles and their aggregates to the microorganisms was also found to influence inactivation. The toxicity of nano-ZnO, bulk ZnO, and Zn^{2+} ions was the same at similar concentrations of dissolved zinc, so Zn^{2+} ions dissolved from ZnO were thought to be the main cause for ZnO ecotoxicity [147, 168]. The role of zinc ions released from dissolution of ZnO is not clear, although binding of the Zn^{2+} ion to the membranes of microorganisms has been suggested to prolong the lag phase of the microbial growth cycle [173]. Similar to Ag^+ speciation pathways and combination with anionic ligands previously discussed, the concentration of free ionic Zn^{2+} was found to be decreased in saline or nutrient media, due to the generation of precipitates and zinc complexes, which lowered the resulting toxicity observed [174].

A.4.3 Photocatalytic disinfection

Select studies have been performed investigating photocatalytic disinfection using Ag-modified ZnO materials. These materials are somewhat analogous to Ag/AgX photocatalysts, since the base (or host) photocatalyst possesses some antimicrobial activity. However, the mechanism and interaction of these compounds with microorganisms differ in dark and photoreactive systems. An example of an Ag-ZnO photocatalyst is provided in Table A.1, where there exists an antibacterial activity in the dark, which is enhanced upon irradiation due to the photocatalytic effect.

A.4.4 Silver ion release behaviour of antibacterial and photocatalytic Ag-ZnO materials

Investigation of the silver ion release behaviour of Ag-ZnO films prepared for photocatalytic inactivation of *E. coli* under both dark and light conditions indicated that the free silver concentration was very small, and was unquantifiable by inductively coupled plasma-mass spectrometry methods [70], although inactivation was observed in the dark using both the undoped ZnO material and the Ag-modified photocatalysts. Additionally, this activity was improved upon photoirradiation of the composites, and the authors attributed this to the effects of photo-induced radicals on bacterial inactivation. The activity in the dark was thought to be due to the antibacterial effects of ZnO and contact between silver nanoparticles on the thin film surface and the bacteria. The dynamics and speciation of released silver and zinc ions in both dark and photoreactive systems should be further investigated to gain an in-depth knowledge of this class of composite for both dark and light inactivation.

A.4.5 Changes to bacterial adhesion properties

The electrostatic forces between silver nanoparticles and bacteria have been reported to play a role in the antibacterial activity observed [175–177]. Similar to Ag-modified TiO_2 materials, changes to bacterial adhesion properties may occur upon the introduction of Ag into ZnO particles, which increase the bactericidal activity observed. For example, Lu et al. prepared Ag/ZnO nanocomposites that exhibited antibacterial activity on *E. coli* [178]. The Ag nanoparticles that were present in Ag/ZnO were highly positively charged compared to the pure Ag used for comparison. This was attributed to the transfer of electrons from Ag nanoparticles to ZnO nanorods, creating a strong interaction that was thought to enforce the

electrostatic attraction between the positively charged Ag and the negatively charged bacteria, increasing bactericidal activity observed.

A.5 Other antimicrobial photocatalysts

Similar to silver-modified photocatalysts, the development of other antibacterial photocatalytic materials possessing bifunctionality for applications in both dark and light conditions is also of interest for both the enhancement of photocatalytic activity of TiO_2 and other photocatalytic materials, and for the development of self-cleaning and self-disinfecting surfaces in public health-related settings such as hospitals, airports, metro stations, or schools [179], in addition to use in air and water purification systems. Some antimicrobial photocatalysts reported in literature are briefly reviewed in this section.

A.5.1 Copper-based materials

A.5.1.1 Copper-based disinfection

Copper and copper-based compounds have been known as disinfection agents since antiquity, with the earliest reports of their use in medicine described in the Smith Papyrus, an ancient Egyptian medical text, for the sterilization of chest wounds and drinking water [180]. The use of copper in various formulations continued throughout history, and became widespread in the 19^{th} and 20^{th} centuries for the treatment of diseases such as tubercular infections, lupus, syphilis, and anemia, until it was replaced by commercial antibiotics [180, 181]. However, current interest in copper-based antimicrobials is has been renewed to address problems associated to antibiotic resistance in bacterial communities, to develop of self-cleaning surfaces for use in hygiene-sensitive areas, and for applications to sterilizing bandages and textiles [181, 182]. Copper oxide (CuO) can be easily mixed with polymers and is chemically and physically stable. Additionally, CuO nanoparticles are cheaper than silver nanoparticles, although the latter exhibit stronger bactericidal activity in the dark [183]. Similar to silver, the antimicrobial effect of copper has been studied and explained with respect to its ionic forms, Cu^+ and Cu^{2+}. Specifically, the generation of reactive hydroxyl radicals is given in Eq. (A.6):

$$Cu^+ + H_2O_2 \rightarrow Cu^{2+} + OH^- + {}^{\bullet}OH \qquad (A.6)$$

These hydroxyl radicals can cause cellular damage through lipid and protein oxidation reactions [184]. Also similar to ionic silver, copper ions can interact with thiol groups in cysteines or glutathione [181], where the relevant reactions are given by eq. (A.7) and eq. (A.8):

$$2\ Cu^{2+} + 2\ RSSH \rightarrow 2\ Cu^{+} + RSSR + 2H^{+} \quad (A.7)$$

$$2\ Cu^{+} + 2\ H^{+} + O_2 \rightarrow 2\ Cu^{2+} + H_2O_2 \quad (A.8)$$

The toxicity of metallic copper is mainly ascribed to the reactions in equations (A.6) – (A.8), although alternative mechanisms involving iron displacement from iron-sulfur clusters [185] and the competition of copper ions with zinc and other metal ions on binding sites on proteins [186] are also possible.

A.5.1.2 Cupreous antimicrobial photocatalysts

Copper-modified or copper-containing photocatalysts with antibacterial capacities in the dark and enhanced photocatalytic activities under light have been reported in a number of studies, and may present a low-cost alternative to noble metal based biocidal photocatalysts. Similar to Ag in Ag-TiO_2 composites, the role of interfacial charge transfer between Cu and TiO_2 is emphasized as a photocatalysis-enhancing mechanism, which may contribute to photocatalytic inactivation in addition to the antibacterial and oligodynamic effects of incorporated copper. For example, Qiu et al. developed hybrid Cu_xO/TiO_2 nanocomposites composed of Cu^{+} and Cu^{2+} clusters grafted onto TiO_2 [179], and observed their efficient visible light induced photooxidation of volatile organic compounds (isopropanol, acetone, acetaldehyde) in air, as well as their inactivation of viruses (Qβ bacteriophage) and bacteria (*E. coli*, *S. aureus*) in both dark and light conditions. For organics mineralization, the improved visible light activity of the composite photocatalyst over pure TiO_2 was attributed to the role of Cu^{2+}, where valence band electrons from TiO_2 were excited to Cu^{2+} species in surface nanoclusters through interfacial charge transfer processes, resulting in high photocatalytic performance of the composite Cu_xO/TiO_2 system. With respect to antiviral and antibacterial effects, Cu^{+} species in the Cu_xO nanoclusters were found to be much more effective than Cu metal or Cu^{2+} species for enhancing the dark inactivation observed, emphasizing the need for careful optimization of valence states of the incorporated copper to

achieve the desired bifunctionality. This ratio was tuned to Cu^{+}/Cu^{2+} = 1.3, and although a dark disinfection was observed, the overall inactivation was increased in the presence of irradiation due to the combined role of biocidal copper and the effects of photocatalysis to damage outer membranes, proteins, DNA, and RNA of the viruses and bacteria studied [179].

Other relevant copper-TiO_2 materials reported in literature include TiO_2/Cu nanosurfaces for antibacterial photocatalytic films under weak visible light irradiation [187], which were also thought to act through interfacial charge transfer mechanisms and by oligodynamic copper ion release under irradiation. Similar observations were made for CuO/TiO_2 films prepared by chemical vapor deposition (CVD) against bacteriophage T4 and *E. coli* [188], and the possible role of photocatalysis in degrading dead cell mass to result in a cleaner surface for the penetration of UV light was discussed with respect to the higher observed activity of CuO/TiO_2 film over CuO film alone. Other Cu-TiO_2 co-deposited films prepared by CVD [189] exhibited a >5 log reduction of *E. coli* after 24 hours in dark conditions, and a >5 log reduction within 1 hour of UV irradiation, where the enhancement was thought to be due to the production of hydroxyl radicals via the photo-Fenton type reaction shown in Eq. (A.6). A Cu/TiO_2 system reported consisting of a TiO_2 film with photodeposited metallic copper (Cu^{o}) and copper ions (Cu^{+}, Cu^{2+}) was studied against copper-resistant *E. coli* [190], which possessed little porin protein on its outer membrane, losing the ability to transport the toxic copper ions into the cell [191–195]. A synergistic antibacterial and photocatalytic inactivation was observed under weak UV irradiation and was thought to occur in two steps, where the outer membrane of the bacteria was first attacked by ROS produced in TiO_2 photocatalysis, followed by the intrusion of copper ions into the cell [190]. This system illustrated the synergistic bifunctionality attainable in biocidal-photocatalytic systems, and highlights the need for further research in this stream.

A.5.2 Miscellaneous antimicrobial photocatalysts

Other approaches have been taken to enhance the antibacterial and antiviral activities of conventional photocatalysts. For example, Kong et al. prepared novel biocidal polymer-functionalized TiO_2 nanoparticles via a surface-initiated photopolymerization process using

titania as the initiator [196]. The resulting nanoparticles possessed a core/shell structure consisting of TiO_2/poly[2-(*tert*-butylamino)ethyl methacrylate-*co*-ethylene glycol dimethacrylate], and exhibited an antimicrobial efficiency of 95.7% against *S. aureus* in the dark. This observed efficiency increased to 99.9% in the presence of UV irradiation for 30 minutes, and was attributed to the synergistic effect of the biocidal polymer and the photocatalyst. Other materials such as multi-walled carbon nanotubes (CNTs) were also used to modify TiO_2 [197], and the prepared CNT-TiO_2 thin films possessed antibacterial activity against *E. coli* in the dark due to the antimicrobial effect of the incorporated nanotubes, and enhanced inactivation capacity under visible light irradiation, which was attributed to both the antibacterial activity of CNTs, and their role in improving charge transfer and optical absorption characteristics of the host TiO_2. Noble metal modified photocatalysts such as Au-TiO_2 [198] were also proposed and their antibacterial activity against *E. coli* confirmed in the absence of light. The use of this material as a photocatalyst was not discussed, although changes to the bacterial adhesion properties of pure TiO_2 due to the incorporated nanometal were suggested to contribute to the improved antibacterial activity observed, and were quantified by measuring zeta potentials of the pure and modified materials, respectively. It should be noted that Au-TiO_2 materials were previously reported and investigated as visible light active photocatalysts [199–202], due to surface plasmon resonance enhancement by the nanosized noble metal, and so further work should be performed on characterizing the mechanisms of combined antimicrobial and photocatalytic activities of these catalysts under irradiation.

A.6 Conclusions

The modification of TiO_2 by silver can be performed to create enhanced composite photocatalysts that exhibit high photocatalytic activity under dark and light conditions. The mechanisms of enhancement due to the incorporated silver are mainly due to antibacterial silver ion release in dark conditions, and promotion of photocatalysis by charge carrier separation under irradiation. In some cases, the photocatalytic disinfection can be enhanced by the action of released silver even under irradiation, but further work is needed to clarify the roles and fates of the silver species in photoreactive systems. Modification by silver can

also act to alter bacterial adhesion properties of the composite, and may improve its overall bactericidal and photocatalytic inactivation activities.

Ag/AgX (X = Cl, Br, I) photocatalysts also represent a class of silver-modified materials that can exhibit antimicrobial activity in both dark and light conditions. In this case, the photocatalytic enhancement is due to both increased visible light absorption and charge carrier separation by the surface plasmon resonance state of the nanosilver, as well as the generation of oxidative species from the host material, such as Cl^o or Br^o for Ag/AgCl and Ag/AgBr, respectively. The AgX support also prevents oxidation of nanosilver by a charge separation mechanism, which promotes the stability and long-term use of the catalyst. Although sparingly soluble, the AgX host material may contribute to the total dissolved silver species, playing a role in the inactivation observed in both dark and light conditions. Additionally, the formation of AgCl precipitates from the scavenging of ionic silver by anionic chloride ligands present in the reaction fluid may further complicate dynamics of photo-induced disinfection, since these AgCl precipitates may agglomerate and possibly be reduced; regenerating some Ag/AgCl species. The effect is thought to be more pronounced for highly Ag-eluting catalysts, but the extent to which this affects photocatalytic disinfection remains unknown.

Silver can also be used to modify ZnO materials, which are themselves biocidal, to improve the photocatalytic efficiency of the host material or to enhance the antimicrobial activity of the composite. Further research is needed to clarify the roles of silver and zinc ions in both the dark and photoreactive solutions, and to study mechanisms of inactivation using the composite materials.

Other approaches to improving photocatalytic activity of TiO_2 through addition of antimicrobial materials, such as by copper modification or by incorporation of carbon nanotubes, may also result in composite materials with both antimicrobial effects in the dark, and enhanced photocatalytic inactivation under irradiation. In addition to improving photocatalytic efficiencies, the development of bifunctional biocidal photocatalysts is also of

interest for preparing continuous-sterilizing surfaces that can act by different mechanisms in the presence and absence of irradiation, respectively. These systems should be carefully characterized in order to understand the role of acting mechanisms and their dynamic behaviour under various conditions to fully realize the potential of bifunctional antimicrobial photocatalytic materials for future use.

A.7 Acknowledgments

This work was supported by the Natural Sciences and Engineering Research Council of Canada.

A.8 References

[1] Q. Li, S. Mahendra, D.Y. Lyon, L. Brunet, M.V. Liga, D. Li, P.J.J. Alvarez, Antimicrobial nanomaterials for water disinfection and microbial control: Potential applications and implications, Water Res. 42 (2008) 4591–4602.

[2] A. Fujishima, K. Honda, Electrochemical photolysis of water at a semiconductor electrode, Nature 238 (1972) 37–38.

[3] Y. Tachibana, L. Vayssieres, J.R. Durrant, Artificial photosynthesis for solar water-splitting, Nat. Photonics 6 (2012) 511–518.

[4] M.R. Hoffman, S.T. Martin, W. Choi, D.W. Bahnemann, Environmental applications of semiconductor photocatalysis, Chem. Rev. 95 (1995) 69–96.

[5] A. Fujishima, T.N. Rao, D.A. Tryk, Titanium dioxide photocatalysis, J. Photochem. Photobiol., C. 1 (2000) 1–21.

[6] I.P. Parkin, R.G. Palgrave, Self cleaning coatings, J. Mater. Chem. 15 (2005) 1689–1695.

[7] T.P. Yoon, M.A. Ischay, J. Du, Visible light photocatalysis as a greener approach to photochemical synthesis, Nature Chem. 2 (2010) 527–532.

[8] T. Matsunaga, R. Tomoda, T. Nakajima, H. Wake, Photoelectrochemical sterilization of microbial cells by semiconductor powders, FEMS Microbiol. Lett. 29, 1–2 (1985) 211–214.

[9] J. Gamage, Z. Zhang, Applications of photocatalytic disinfection: A review, Int. J. Photoenergy, 2010 (2010) Article ID 764870. *(also given in Appendix B)*

[10] N.J. Sucher, M.C. Carles, J. Nowotny, T. Bak, Photocatalytic water disinfection on oxide semiconductors : Part 2 – structure, functional properties and reactivity of microbial agents, Adv. Appl. Ceram. 111, 1–2 (2012) 16–33.

[11] W.Y. Choi, A. Termin, M.R. Hoffmann, Role of metal-ion dopants in quantum-sized TiO_2 – correlation between photoreactivity and charge-carrier recombination dynamics, J. Phys. Chem. 98 (1994) 13669–13679.

[12] S. Sato, R. Nakamura, S. Abe, Visible-light sensitization of TiO_2 photocatalysts by wet-method N doping, Appl. Catal., A. 284, 1–2 (2012) 131–137.

[13] T. Umebayashi, T. Yamaki, H. Itoh, K. Asai, Analysis of electronic structures of 3D transition metal-doped TiO_2 based on band calculations, J. Phys. Chem. Solids 63 (2002) 1909–1920.

[14] G. Zhao, H. Kozuka, T. Yoko, Sol-gel preparation and photoelectrochemical properties of TiO_2 films containing Au and Ag metal particles, Thin Solid Films 277 (1996) 147–154.

[15] C.M. Wang, A. Heller, H. Gerischer, Palladium catalysis of O_2 reduction by electrons accumulated on TiO_2 particles during photoassisted oxidation of organic compounds, J. Am. Chem. Soc. 114 (1992) 5230–5234.

[16] I.M. Arabatzis, T. Stergiopoulos, M.C. Bernard, D. Labou, S.G. Neophytides, P. Falaras, Silver-modified titanium dioxide thin films for efficient photodegradation of methyl orange, Appl. Catal., B 42 (2003) 187–201.

[17] R. W. Fessenden, P.V. Kamat, Rate constants for charge injection from excited sensitizer into SnO_2, ZnO, and TiO_2 semiconductor nanocrystallites, J. Phys. Chem. 99 (1995) 12902–12906.

[18] J.M. Stipkala, F.N. Castellano, T.A. Heimer, C.A. Kelly, K.J.T. Livi, G.J. Meyer, Light-induced charge separation at sensitized sol-gel processed semiconductors, Chem. Mater. 99 (1997) 2341–2353.

[19] J. Hagen, 2006, Photocatalysis In: Industrial Catalysis: A practical approach, 2nd ed. Wiley-WCH Verlag GmbH & Co. KGaA, Weinheim, FRG.

[20] L.R. Quisenberry, L.H. Loetscher, J.E. Boyd, Catalytic inactivation of bacteria using Pd-modified titania, Catal. Commun. 10 (2009) 1417–1422.

[21] J. Liqiang, F. Honggang, W. Baiqi, W. Dejun, X. Baifu, L. Shudan, S. Jiazhong, Effects of Sn dopant on the photoinduced charge property and photocatalytic activity of TiO_2 nanoparticles, Appl. Catal., B. 62 (2006) 282–291.

[22] L. Armelao, D. Barreca, G. Bottaro, A. Gasparotto, C. Maccato, C. Maragno, E. Tondello, U.L. Štangar, M. Bergant, D. Mahne, Photocatalytic and antibacterial activity of TiO_2 and Au/TiO_2 nanosystems, Nanotechnol. 18 (2007) 375709.

[23] O. Akhavan, Lasting antibacterial activities of Ag-TiO_2/Ag/a-TiO_2 nanocomposite thin film -photocatalysts under solar light, J. Colloid Interface Sci. 336 (2009) 117–124.

[24] X. Wang, J.C. Yu, H.Y. Yip, L. Wu, P.K. Wong, S.Y. Lai, A mesoporous Pt/TiO_2 nanoarchitecture with catalytic and photocatalytic functions, Chem. Eur. J. 11 (2005) 2997–3004.

[25] J. Ma, Z. Xiong, T.D. Waite, W.J. Ng, X.S. Zhao, Enhanced inactivation of bacteria with silver-modified mesoporous TiO_2 under weak ultraviolet irradiation, Microporous Mesoporous Mater. 144 (2011) 97–104.

[26] J.H. Hsieh, R.B. Yu, Y.K. Chang, C. Li, Structural analysis of TiO_2 and TiO_2-Ag thin films and their antibacterial behaviours, J. Phys.: Conf. Ser. 339 (2012) 012012.

[27] J.-M. Herrmann, H. Tahiri, Y. Ait-Ichou, G. Lassaletta, A.R. González-Elipe, A. Fernández, Characterization and photocatalytic activity in aqueous medium of TiO_2 and Ag-TiO_2 coatings on quartz, Appl. Catal., B. 13 (1997) 219–228.

[28] K. Page, R.G. Palgrave, I.P. Parkin, M. Wilson, S.L.P. Savin, A.V. Chadwick, Titania and silver-titania composite films on glass – potent antimicrobial coatings, J. Mater. Chem. 17 (2007) 95–104.

[29] K. Awazu, M. Fujimaki, C. Rockstuhl, J. Tominaga, H. Murakami, Y. Ohki, N. Yoshida, T. Watanabe, A plasmonic photocatalyst consisting of silver nanoparticles embedded in titanium dioxide, J. Am. Chem. Soc. 130, 5 (2008) 1676–1680.

[30] H.T. Ratte, Bioaccumulation and toxicity of silver compounds: A review, Environ. Toxicol. Chem. 18, 1 (1999) 89–108.

[31] V. Sambhy, M.M. MacBride, B.R. Peterson, Silver bromide nanoparticle/polymer composites: Dual action tunable antimicrobial materials, J. Am. Chem. Soc. 128, 30 (2006) 9798–9808.

[32] K. Holt, A. Bard, Interaction of silver (I) ions with the respiratory chain of *Escherichia coli*: an electrochemical and scanning electrochemical study of the antimicrobial mechanism of micromolar Ag, Biochemistry 44 (2005) 13214–13223.

[33] C. Lok, C. Ho, R. Chen, Q. He, W. Yu, H. Sun, P. Tam, J. Chiu, C. Che, Proteomic analysis of the mode of antibacterial action of silver nanoparticles, J. Proteome Res. 5 (2006) 916–924.

[34] H. Petering, Pharmacology and toxicology of heavy-metal silver, Pharmacol. Ther. A. 1 (1976) 127–130.

[35] S. Liau, D. Read, W. Pugh, J. Furr, A. Russell, Interaction of silver nitrate with readily identifiable groups: relationship to the antibacterial action of silver ions, Lett. Appl. Microbiol. 25 (1997) 279–283.

[36] W. Jung, H. Koo, K. Kim, S. Shin, S. Kim, Y. Park, Antibacterial activity and mechanism of action of the silver ion in *Staphylococcus aureus* and *Escherichia coli*, Appl. Environ. Microbiol. 74 (2008) 2171–2178.

[37] Q. Fend, J. Wu, G. Chen, F. Cui, T. Kim, J. Kim, A mechanistic study of the antibacterial effect of silver ions on *Escherichia coli* and *Staphylococcus aureus*, J. Biomed. Mater. Res. 52 (2000) 662–668.

[38] Z.-M. Xiu, Q.-B. Zhang, H.L. Puppala, V.L. Colvin, P.J.J. Alvarez, Negligible particle-specific antibacterial activity of silver nanoparticles, Nano Lett. 12, 8 (2012) 4271–4275.

[39] A.T. Hendry, I.O. Stewart, Silver-resistant *Enterobacteriaceae* from hospital patients, Can. J. Microbiol. 25 (1979) 915–921.

[40] J.S. Grewal, R.P. Tiwari, Resistance to metal ions and antibiotics in *Escherichia coli* isolated from foodstuffs, J. Med. Microbiol. 32 (1990) 223–226.

[41] M. Li, M.E. Noriega-Trevino, N. Nino-Martinez, C. Marambio-Jones, J. Wang, R. Damoiseaux, F. Ruiz, E. M.V. Hoek, Synergistic bactericidal activity of Ag-TiO_2 nanoparticles in both light and dark conditions, Environ. Sci. Technol. 45 (2011) 8989–8995.

[42] B. O'Regan, M. Grätzel, A low-cost, high efficiency solar cell based on dye-sensitized colloidal TiO_2 films, Nature 353 (1991) 737–740.

[43] X. Chen, S.S. Mao, Titanium dioxide nanomaterials: Synthesis, properties, modifications, and applications, Chem. Rev. 107 (2007) 2891–2959.

[44] M. Pratap Reddy, A. Venugopal, M. Subrahmanyam, Hydroxyapatite-supported Ag-TiO_2 as *Escherichia coli* disinfection photocatalyst, Water Res. 41 (2007) 379–386.

[45] C. He, Y. Yu, X. Hu, A. Larbot, Influence of silver doping on the photocatalytic activity of titania films, Appl. Surf. Sci. 200 (2002) 239–247.

[46] L.A. Brook, P. Evans, H.A. Foster, M.E. Pemble, A. Steele, D.W. Sheel, H.M. Yates, Highly bioactive silver and silver/titania composite films grown by chemical vapour deposition, J. Photochem. Photobiol., A. 187 (2007) 53–63.

[47] X. Zhang, M. Zhou, L. Lei, Preparation of an Ag-TiO_2 photocatalyst coated on activated carbon by MOCVD, Mater. Chem. Phys. 91 (2005) 73–79.

[48] L.A. Brook, P. Evans, H.A. Foster, M.E. Pemble, D.W. Sheel, A. Steele, H.M. Yates, Novel multifunctional films, Surf. Coat. Technol. 201 (2007) 9373–9377.

[49] S.W. Yu, E. J. Kim, S.K. Ko, S. H. Hahn, Effect of calcinations on the structural and optical properties of M/TiO_2 thin films by RF magnetron co-sputtering, Mater. Lett. 58 (2004) 582–592.

[50] H.M. Sung-Suh, J. R. Choi, H.J. Hah, S.M. Koo, Y.C. Bae, Comparison of Ag deposition effects on the photocatalytic activity of the nanoparticulate TiO_2 under visible and UV light irradiation, J. Photochem. Photobiol., A. 163 (2004) 37–44.

[51] A. Sclafani, M.-N. Mozzanega, J.-M. Herrmann, Influence of silver deposits on the photocatalytic activity of titania, J. Catal. 168 (1997) 117–120.

[52] M.K. Seery, R. George, P. Floris, S.C. Pillai, Silver doped titanium dioxide nanomaterials for enhanced visible light photocatalysis, J. Photochem. Photobiol., A. 189 (2007) 258–263.

[53] Y. Tian, T. Tatsuma, Plasmon-induced photoelectrochemistry at metal nanoparticles supported on nanoporous TiO_2, Chem. Commun. 16 (2004) 1810–1811.

[54] B. Xin, L. Jing, Z. Ren, B. Wang, H. Fu, Effects of simultaneously doped and deposited Ag on the photocatalytic activity and surface states of TiO_2, J. Phys. Chem. B 109, 7 (2005) 2805–2809.

[55] J. Li, J. Xu, W.-L. Dai, K. Fan, Dependence of Ag deposition methods on the photocatalytic activity and surface state of TiO_2 with twist like helix structure, J. Phys. Chem. C 113 (2009) 8343–8349.

[56] H.W. Chen, Y. Ku, Y.L. Kuo, Photodegradation of *o*-cresol with Ag deposited on TiO_2 under visible and UV light irradiation, Chem. Eng. Technol. 30, 9 (2007) 1242–1247.

[57] C. Srisitthiratkul, V. Pongsorrarith, N. Intasanta, The potential use of nanosilver-decorated titanium dioxide nanofibers for toxin decomposition with antimicrobial and self-cleaning properties, Appl. Surf. Sci. 257 (2011) 8850–8856.

[58] H. Tran, J. Scott, K. Chiang, R. Amal, Clarifying the role of silver deposits on titania for the photocatalytic mineralisation of organic compounds, J. Photochem. Photobiol., A. 183 (2006) 41–52.

[59] R. van Grieken, J. Marugán, C. Sordo, P. Martinez, C. Pablos, Photocatalytic inactivation of bacteria in water using suspended and immobilized silver-TiO_2, Appl. Catal., B. 93 (2009) 112–118.

[60] X. Huang, I.H. El-Sayed, W. Qian, M.A. El-Sayed, Cancer cell imaging and photothermal therapy in the near-infrared region by using gold nanorods, J. Am. Chem. Soc. 128, 6 (2006) 2115–2129.

[61] K.L. Kelly, E. Coronado, L.L. Zhao, G.C. Schatz, The optical properties of metal nanoparticles: The influence of size, shape, and dielectric environment, J. Phys. Chem. B 107, 3 (2003) 668–677.

[62] G. Lassaletta, A.R. Gonzáles-Elipe, A. Justo, A. Fernández, F.J. Ager, M.A. Respaldiza, J.G. Soares, M.F. Da Silva, Thermal and photochemical methods for the preparation of thin films of cermet materials, J. Mater. Sci. 31 (1996) 2325–2332.

[63] L. Mai, D. Wang, S. Zhang, Y. Xie, C. Huang, Z. Zhang, Synthesis and bactericidal ability of Ag/TiO_2 composite films deposited on titanium plate, Appl. Surf. Sci. 257 (2010) 974–978.

[64] Y. Liu, X. Wang, F. Yang, X. Yang, Excellent antimicrobial properties of mesoporous anatase TiO_2 and Ag/TiO_2 composite films, Microporous Mesoporous Mater. 114 (2008) 431–439.

[65] W.-C. Lin, C.-N. Chen, T.-T. Tseng, M.-H. Wei, J.H. Hsieh, W.J. Tseng, Micellar layer-by-layer synthesis of TiO_2/Ag hybrid particles for bactericidal and photocatalytic activities, J. Eur. Ceram. Soc. 30 (2010) 2849–2857.

[66] M.V. Liga, E.L. Bryant, V.L. Colvin, Q. Li, Virus inactivation by silver doped titanium dioxide nanoparticles for drinking water treatment, Water Res. 45 (2011) 535–544.

[67] X. Chang, S. Sun, L. Dong, Y. Yin, Efficient synthesis of Ag/AgCl/$W_{18}O_{49}$ nanorods and their antibacterial activities, Mater. Lett. 83 (2012) 133–135.

[68] X. Wang, Y. Tang, Z. Chen, T.-T. Lim, Highly stable heterostructured Ag-AgBr/TiO_2 composite: a bifunctional visible-light active photocatalyst for destruction of ibuprofen and bacteria, J. Mater. Chem. 22 (2012) 23149–23158.

[69] M. Padervand, M.R. Elahifard, R. V. Meidanshahi, S. Ghasemi, S. Haghighi, M.R. Gholami, Investigation of the antibacterial and photocatalytic properties of the zeolitic nanosized AgBr/TiO_2 composites, Mater. Sci. Semicond. Process. 15 (2012) 73–79.

[70] K. Thongsuriwong, P. Amornpitoksuk, S. Suwanboon, Photocatalytic and antibacterial activities of Ag-doped ZnO thin films prepared by a sol-gel dip-coating method, J. Sol-Gel Sci. Technol. 62 (2012) 304–312.

[71] C. Lok, C. Ho, R. Chen, Q. He, W. Yu, H. Sun, P.K. Tam, J. Chiu, C. Che, Silver nanoparticles: Partial oxidation and antibacterial activities, J. Biol. Inorg. Chem. 12 (2007) 527–534.

[72] J. Liu, R.H. Hurt, Ion release kinetics and particle persistence in aqueous nanosilver colloids, Environ. Sci. Technol. 44 (2010) 2169–2175.

[73] J. Liu, D.A. Sonshine, S. Shervani, R.H. Hurt, Controlled release of biologically active silver from nanosilver surfaces, ACS Nano 4, 11 (2010) 6903–6913.

[74] M.N. Birmele, L.E. McCoy, M.S. Roberts, Disinfection of spacecraft potable water systems by passivation with ionic silver, NASA Technical Report; available at: http://ntrs.nasa.gov/archive/nasa/casi.ntrs.nasa.gov/20110014435_2011014957.pdf; accessed Dec. 10, 2012.

[75] Y.L. Wang, Y.Z. Wan, X.H. Dong, G.X. Chen, H.M. Tao, T.Y. Wen, Preparation and characterization of antibacterial viscose–based activated carbon fiber supporting silver, Carbon 36 (1998) 1567–1571.

[76] J. Keleher, J. Bashant, N. Heldt, L. Johnson, Y. Li, Photo-catalytic preparation ofsilver-coated TiO_2 particles for antibacterial applications, World J. Microbiol. Biotechnol. 18 (2002) 133–139

[77] Y.Z. Wan, Y.L. Wang, G.X. Cheng, H.L. Luo, X.H. Dong, Preparation and characterization of activated carbon fiber supporting silver-loaded mesoporous molecular sieves, Carbon 39 (2001) 1607–1610.

[78] S. Zhang, R. Fu, D. Wu, W. Xu, Q. Ye, Z. Chen, Preparation and characterization of antibacterial silver-dispersed activated carbon aerogels, Carbon 42 (2004) 3209–3216.

[79] A. Kubacka, M. Ferrer, A. Martínez-Arias, M. Fernández-García, Ag promotion of TiO_2-anatase disinfection capability: Study of *Escherichia coli* inactivation, Appl. Catal., B. 84 (2008) 87–93.

[80] J.Y. Kim, C. Lee, M. Cho, J. Yoon, Enhanced inactivation of *E. coli* and MS-2 phage by silver ions combined with UV-A and visible light irradiation, Water Res. 42 (2008) 356–362.

[81] P.D. Bragg, D.J. Rainnie, The effect of silver ion on the respiratory chain of *Escherichia coli*, Can. J. Microbiol. 20 (1973) 883–889.

[82] S.Y. Liau, D.C. Read, W.J. Pugh, J.R. Furr, A.D. Russell, Interaction of silver nitrate with readily identifiable groups: Relationship to the antibacterial action of silver ions, Lett. Appl. Microbiol. 25 (1997) 279–283.

[83] Y. Matsumura, K. Yoshikata, S. Kunisaki, T. Tshuchido, Mode of bactericidal action of silver zeolite and its comparison with that of silver nitrate, Appl. Environ. Microbiol. 69 (2003) 4278–4281.

[84] R.B. Thurman, C.P. Gerba, The molecular mechanisms of copper and silver ion disinfection of bacteria and viruses, CRC Crit. Rev. Environ. Control. 18 (1989) 295–315.

[85] A.D. Russell, W.B. Hugo, Antimicrobial activity and action of silver, Prog. Med. Chem. 31 (1994) 351–371.

[86] F. Liu, H. Liu, X. Li, H. Zhao, D. Zhu, Y. Zheng, C. Li, Nano-TiO_2@Ag/PVC film with enhanced antibacterial activities and photocatalytic properties, Appl. Surf. Sci, 258, 10 (2012) 4667–4671.

[87] V. Subramanian, E. Wolf, P.V. Kamat, Semiconductor-metal composite nanostrcutures. To what extent do metal nanoparticles improve the photocatalytic activity of TiO_2 films?, J. Phys. Chem. B 105, 46 (2001) 11439–11446.

[88] N.R. Jana, T.K. Sau, T. Pal, Growing small silver particle as redox catalyst, J. Phys. Chem. B 103 (1999) 115–121.

[89] C. Hu, Y. Lan, J. Qu, X. Hu, A. Wang, Ag/AgBr/TiO_2 visible light photocatalyst for destruction of azodyes and bacteria, J. Phys. Chem. B 110, 9 (2006) 4066–4072.

[90] C.A.Castro, P. Osorio, A. Sienkiewicz, C. Pulgarin, A. Centeno, S.A. Giraldo, Photocatalytic production of $^1O_2$ and $^{\bullet}OH$ mediated by silver oxidation during the photoinactivation of *Escherichia coli* with TiO_2, J. Hazard. Mater. 211–212 (2012) 172–181.

[91] W.M. Jou, M. Ysebaert, W. Fiers, G. Haegeman, Nucleotide sequence of gene coding for bacteriophasge MS2 coat protein, Nature 237, 5350 (1972) 82–88.

[92] N. Kakuta, N. Goto, H. Ohwaki, T. Mizushima, Silver bromide as a photocatalyst for hydrogen generation from CH_3OH/H_2O solution, J. Phys. Chem. B 103 (1999) 5917–5919.

[93] D. Schürch, A. Currao, S. Sarkar, G. Hodes, G. Calzaferri, The silver chloride photoanode in photoelectrochemical water splitting, J. Phys. Chem. B 106 (2002) 12764–12775.

[94] B. Tian, J. Zhang, Morphology-controlled synthesis and applications of silver halide photocatalytic materials, Catal. Surv. Asia 16, 4 (2012) 210–230.

[95] P. Wang, B. Huang, X. Qin, X. Zhang, Y. Dai, J. Wei, M.-H. Whangbo, Ag@AgCl: A highly efficient and stable photocatalyst active under visible light, Angew. Chem. Int. Ed. 47 (2008) 7931–7933.

[96] P. Wang, B. Huang, X. Zhang, X. Qin, H. Jin, Y. Dai, Z. Wang, J. Wei, J. Zhan, S. Wang, J. Wang, M.-H. Whangbo, Highly efficient visible-light plasmonic photocatalyst Ag@AgBr, Chem. Eur. J. 15 (2009) 1821–1824.

[97] H. Zhang, X. Fan, X. Quan, S. Chen, H. Yu, Graphene sheets grafted Ag@AgCl hybrid with enhanced photocatalytic activity under visible light, Environ. Sci. Technol. 45, 13 (2011) 573–5736.

[98] C. An, S. Pen, Y. Sun, Facile synthesis of sunlight-driven AgCl:Ag plasmonic nanophotocatalyst, Adv. Mater. 22, 23 (2010) 2570–2574.

[99] H. Xu, H. Li, J. Xia, S. Yin, Z. Luo, L. Liu, L. Xu, One-pot synthesis of visible-light-driven plasmonic photocatalyst Ag/AgCl in ionic liquid, ACS Appl. Mater. Interfaces 3, 1 (2011) 22–29.

[100] D. Wang, Y. Duan, Q. Luo, X. Li, L. Bao, Visible light photocatalytic activities of plasmonic Ag/AgBr particles synthesized by a double jet method, Desalination 270, 1–3 (2011) 174–180.

[101] J. Jiang, L. Zhang, Rapid microwave-assisted nonaqueous synthesis and growth mechanism of AgCl/Ag, and its daylight-driven plasmonic photocatalysis, Chem. Eur. J. 17, 13 (2011) 3710–3717.

[102] J. Yu, G. Dai, B. Huang, Fabrication and characterization of visible-light-driven plasmonic photocatalyst Ag/AgCl/TiO_2 nanotube arrays, J. Phys. Chem. C 113, 37 (2009) 16394–16401.

[103] C. Hu, J. Guo, J. Qu, X. Hu, Photocatalytic degradation of pathogenic bacteria with AgI/TiO_2 under visible light irradiation, Langmuir 23 (2007) 4982–4987.

[104] L.S. Zhang, K.H. Wong, H.Y. Yip, C. Hu, J.C. Yu, C.Y. Chan, P.K. Wong, Effective photocatalytic disinfection of *E. coli* K-12 using AgBr-Ag-Bi_2WO_6 nanojunction system irradiated by visible light: The role of diffusing hydroxyl radicals, Environ. Sci. Technol. 44 (2010) 1392–1398.

[105] C. Hu, T. Peng, X. Hu, Y. Nie, X. Zhou, J. Qu, H. He, Plasmon-induced photodegradation of toxic pollutants with Ag-AgI/Al_2O_3 under visible-light irradiation, J. Am. Chem. Soc. 132, 2 (2010) 857–862.

[106] X. Hu, C. Hu, T. Peng, X. Zhou, J. Qu, Plasmon-induced inactivation of enteric pathogenic microorganisms with Ag-AgI/Al_2O_3 under visible-light irradiation, Environ. Sci. Technol. 44 (2010) 7058–7062.

[107] A. Fujishima, X. Zhang, D.A. Tryk, TiO_2 photocatalysis and related surface phenomena, Surf. Sci. Rep. 63 (2008) 515–582.

[108] L. Zhang, K.-H. Wong, Z. Chen, J.C. Yu, J. Zhao, C. Hu, C.-Y. Chan, P.-K. Wong, AgBr-Ag-Bi_2WO_6 nanojunction system: A novel and efficient photocatalyst with double visible-light active components, Appl. Catal., A. 363, 1–2 (2009) 221–229.

[109] M.R. Elahifard, S. Rahimnejad, S. Haghighi, M.R. Gholami, Apatite-coated Ag/AgBr/TiO_2 visible-light photocatalyst for destruction of bacteria, J. Am. Chem. Soc. 129, 31 (2007) 9552–9553.

[110] P. Wang, B. Huang, X. Qin, X. Zhang, Y. Dai, M.-H. Whangbo, Ag/AgBr/$WO_3 \cdot H_2O$: Visible-light photocatalyst for bacteria destruction, Inorg. Chem. 48, 22 (2009) 10697–10702.

[111] M.A. Butkus, L. Edling, M.P. Labare, The efficacy of silver as a bactericidal agent: Advantages, limitations and considerations for future use, J. Water Supply Res. Technol. AQUA 52 (2003) 407–416.

[112] O. Choi, K.K. Deng, N.-J. Kim, L. Ross, R.Y. Surampalli, Z. Hu, The inhibitory effects of silver nanoparticles, silver ions, and silver chloride colloids on microbial growth, Water Res. 42, 12 (2008) 3066–3074.

[113] A.P. Adams, E.M. Santschi, M.A. Mellencamp, Antibacterial properties of a silver chloride-coated nylon wound dressing, Vet. Surg. 28 (1999) 219–225.

[114] S. Min, J. Yang, J.Y. Kim, Y. Kwon, Development of white antibacterial pigment based on silver chloride nanoparticles and mesoporous silica and its polymer composite, Microporous Mesoporous Mater. 128 (2010) 19–25.

[115] S. Pal, J. Joardar, J.M. Song, Removal of *E. coli* from water using surface-modified activated carbon filter media and its performance over an extended use, Environ. Sci. Technol. 20, 19 (2006) 6091–6097.

[116] M. Tuncer, E. Seker, Single step sol-gel made silver chloride on titania xerogels to inhibit *E. coli* bacteria growth: Effect of preparation and chloride ion on bactericidal activity, J. Sol-Gel Sci. Technol. 59 (2011) 304–310.

[117] M. Kawashita, S. Toda, H. Kim, T. Kokubo, N. Masuda, Preparation of antibacterial silver-doped silica glass microspheres, J. Biomed. Mater. Res. Part A 66 (2003) 266–274.

[118] H.T. Ratte, Bioaccumulation and toxicity of silver compounds: A review, Environ. Toxicol. Chem. 18 (1999) 89–108.

[119] C. Lorenz, L. Windler, N. von Goetz, R.P. Lehmann, M. Schuppler, K. Hungerbühler, M. Heuberger, B. Nowack, Characterization of silver release from commercially available functional (nano)textiles, Chemosphere 89 (2012) 817–824.

[120] C. Levard, E. Matt Hotze, G.V. Lowry, G.E. Brown, Environmental transformations of silver nanoparticles: Impact on stability and toxicity, Environ. Sci. Technol. 46, 13 (2012) 6900–6914.

[121] H.L. Johnston, F. Cuta, A.B. Garrett, The solubility of silver oxide in water, in alkali and in alkaline salt solutions – The amphoteric character of silver hydroxide, J. Am. Chem. Soc. 55 (1933) 2311–2325.

[122] C. Levard, F. M. Michel, Y. Wang, Y. Choi, P. Eng, G.E. Brown, Probing Ag nanoparticle surface oxidation in contact with (in)organics: An X-ray scattering and fluorescence yield approach, J. Synchrot. Radiat. 18, 6 (2011) 871–878.

[123] M.D. Hernández-Alonso, F. Fresno, S. Suárez, J.M. Coronado, Development of alternative photocatalysts to TiO_2: Challenges and opportunities, Energy Environ. Sci. 2 (2009) 1231–1257.

[124] J. Yu, X. Yu, Hydrothermal synthesis and photocatalytic activity of zinc oxide hollow spheres, Environ. Sci. Technol. 42 (2008) 4902–4907.

[125] A. van Dijken, A.H. Janssen, M.H.P. Smitsmans, D. Vanmaekelbergh, A. Meijerink, Size-selective photoetching of nanocrystalline semiconductor particles, Chem. Mater. 10 (1998) 3513–3522.

[126] P. Spathis, I. Poulios, The corrosion and photocorrosion of zinc and zinc oxide coatings, Corros. Sci. 37, 5 (1995) 673–680.

[127] G. Ramakrishna, H.N. Ghosh, Effect of particle size on the reactivity of quantum size ZnO nanoparticles and charge-transfer dynamics with adsorbed catechols, Langmuir 19 (2003) 3006–3012.

[128] N. Kaneva, I. Stambolova, V. Blaskov, Y. Dimitriev, S. Vassilev, C. Dushkin, Photocatalytic activity of nanostructured ZnO films prepared by two different methods for the photoinitiated decolorization of malachite green, J. Alloys Compd. 500 (2010) 252–258.

[129] F. Lu, W. Cai, Y. Zhang, ZnO hierarchical micro/nanoarchitectures: Solvothermal synthesis and structurally enhanced photocatalytic performance, Adv. Funct. Mater. 18 (2008) 1047–1056.

[130] E.S. Jang, J.H. Won, S.J. Hwang, J.H. Choy, Fine tuning of the face orientation of ZnO crystals to optimize their photocatalytic activity, Adv. Mater. 18 (2006) 3309–3312.

[131] A. McLaren, T. Valdes-Solis, G. Li, S.C. Tsang, Shape and size effects of ZnO nanocrystals on photocatalytic activity, J. Am. Chem. Soc. 131 (2009) 12540–12541.

[132] M.S. Mohajerani, A. Lak, A. Simchi, Effect of morphology on the solar photocatalytic behaviour of ZnO nanostructures, J. Alloys. Compd. 485 (2009) 616–620.

[133] X. Wang, Q. Zhang, Q. Wan, G. Dai, C. Zhou, B. Zou, Controllable ZnO architectures by ethanolamine-assisted hydrothermal reaction for enhanced photocatalytic activity, J. Phys. Chem. C 115 (2011) 2769–2775.

[134] C. Tian, Q. Zhang, B. Jiang, G. Tian, H. Fu, Glucose-mediated solution-solid route for easy synthesis of Ag/ZnO particles with superior photocatalytic activity and photostability, J. Alloys Cmpd. 509 (2011) 6935–6941.

[135] Y.N. Xia, Y.J. Xiong, B. Lim, S.E. Skrabalak, Shape-controlled synthesis of metal nanocrystals: Simple chemistry meets complex physics, Angew. Chem. Int. Ed. 48 (2009) 60–103.

[136] C. Pacholski, A. Kornowski, H. Weller, Nanomaterials: Site-specific photodeposition of silver on ZnO nanorods, Angew. Chem. Int. Ed. 43, 36 (2004) 4774–4777.

[137] J. Liqiang, W. Dejun, W. Baiqi, L. Shudan, X. Baifu, F. Honggang, S. Jiazhong, Effects of noble metal modification on surface oxygen composition, charge separation and photocatalytic activity of ZnO nanoparticles, J. Mol. Catal. A: Chem. 244 (2006) 193–200.

[138] C. Gu, C. Cheng, H. Huang, T. Wong, N. Wang, T.-Y. Zhang, Growth and photocatalytic activity of dendrite-like ZnO@Ag heterostructure nanocrystals, Cryst. Growth Des. 9 (2009) 3278–3285.

[139] Y. Zheng, C. Chen, Y. Zhan, X. Lin, Q. Zheng, K. Wei, J. Zhu, Photocatalytic activity of Ag/ZnO heterostructure nanocatalyst: Correlation between structure and property, J. Phys. Chem. C 112 (2008) 10773–10777.

[140] D. Lin, H. Wu, R. Zhang, W. Pan, Enhanced photocatalysis of electrospun Ag-ZnO heterostructured nanofibers, Chem. Mater. 21 (2009) 3479–3484.

[141] Y. Zheng, L. Zheng, Y. Zhan, X. Lin, Q. Zheng, K. Wei, Ag/ZnO heterostructure nanocrystals: Synthesis, characterization, and photocatalysis, J. Inorg. Chem. 46 (2007) 6980–6986.

[142] D. Zhang, X. Liu, X. Wang, Growth and photocatalytic activity of ZnO nanosheets stabilized by Ag nanoparticles, J. Alloys Compd. 509 (2011) 4972–4977.

[143] H.A. Bartels, The effect of eugenol and oil of cloves on the growth of microorganisms, Am. J. Orthod. Oral Surg. 33 (1947) 458–465.

[144] J. Sawai, H. Igarashi, A. Hashimoto, T. Kokugan, M. Shimizu, Evaluation of growth inhibitory effect of ceramics powder slurry on bacteria by conductance method, J. Chem. Eng. Jpn. 29 (1995) 288–293.

[145] J. Sawai, I. Saito, F. Kanou, H. Igarashi, A. Hasimoto, T. Kokugan, M. Shizimu, Mutagenicity test of ceramic powder which have growth inhibitory effect on bacteria, J. Chem. Eng. Jpn. 28 (1995) 352–354.

[146] L. Zhang, Y. Ding, M. Povey, D. York, ZnO nanofluids – A potential antibacterial agent, Prog. Nat. Sci. 18 (2008) 939–944.

[147] N.M. Franklin, N.J. Rogers, S.C. Apte, G.E. Batley, G.E. Gadd, P.S. Casey, Comparative toxicity of nanoparticulate ZnO, bulk ZnO, and $ZnCl_2$ to a freshwater microalgae (*Pseudokirchneriella subcapitata*): The importance of particle solubility, Environ. Sci. Technol. 41 (2007) 8484–8490.

[148] Y. Liu, L. He, A. Mustapha, H. Li, Z.Q. Hu, M. Lin, Antibacterial activities of zinc oxide nanoparticles against *Escherichia coli* O157:H7, J. Appl. Microbiol. 107 (2009) 1193–1201.

[149] V. Aruoja, H.C. Dubourguier, K. Kasemets, A. Kahru, Toxicity of nanoparticles of CuO, ZnO and TiO_2 to microalgae *Pseudokirchneriella subcapitata*, Sci. Total Environ. 407 (2009) 1461–1468.

[150] S.W.Y. Wong, P.T.Y. Leung, A.B. Djurišić, K.M.Y. Leung, Toxicities of nano zinc oxide to five marine organisms: Influences of aggregate size and ion solubility, Anal. Bioanal. Chem. 396 (2010) 609–618.

[151] M. Heinlaan, A. Ivask, I. Blinova, H.C. Dubourguier, A. Kahru, Toxicity of nanosized and bulk ZnO, CuO, and TiO_2 to bacteria *Vibrio fisheri* and crustaceans *Daphnia magna* and *Thamnocephalus platyurus*, Chemosphere 71 (2008) 1308–1316.

[152] I. Blinova, A. Ivask, M. Mortimer, A. Kahru, Ecotoxicity of nanoparticles of CuO and ZnO in natural water, Environ. Pollut. 158 (2010) 41–47.

[153] A. Kahru, H.C. Dubourguier, From ecotoxicology to nanoecotoxicology, Toxicolol. 269 (2010) 105–119.

[154] R. Brayner, R. Ferrari-Illiou, N. Brivois, S. Djediat, M.F. Benedetti, F. Fiévet, Toxicological impact studies based on *Escherichia coli* bacteria in ultrafine ZnO nanoparticles colloidal medium, Nano Lett. 6 (2006) 866–870.

[155] L.K. Adams, D. Y. Lyon, P.J.J. Alvarez, Comparative eco-toxicity of nanoscale TiO_2, SiO_2, and ZnO water suspensions, Water Res. 40 (2006) 3527–3532.

[156] L.L. Zhang, Y.H. Jiang, Y.L. Ding, M. Povey, D. York, Investigation into the antibacterial behaviour of suspensions of ZnO nanoparticles (ZnO nanofluids), J. Nanopart. Res. 9 (2007) 479–489.

[157] Z. Huang, X. Zheng, D. Yan, G. Yin, X. Liao, Y. Kang, Y. Yao, D. Huang, B. Hao, Toxicological effect of ZnO nanoparticles based on bacteria, Langmuir 24 (2008) 4140–4144.

[158] L.L. Zhang, Y.H. Jiang, Y.L. Ding, N. Daskalakis, L. Jeuken, M. Povey, D. York, Mechanistic investigation into antibacterial behaviour of suspensions of ZnO nanoparticles against *E. coli*, J. Nanopart. Res. 12 (2010) 1625–1636.

[159] H.H. Wang, R.L. Wick, B.S. Xing, Toxicity of nanoparticulate and bulk ZnO, Al_2O_3 and TiO_2 to the nematode *Caenorhabditis elegans*, Environ. Pollut. 157 (2009) 1171–1177.

[160] D.H. Lin, B.S. Xing, Phytotoxicity of nanoparticles: Inhibition of seed germination and root growth, Environ. Pollut. 150 (2007) 243–250.

[161] D.H. Lin, B.S. Xing, Root uptake and phytotoxicity of ZnO nanoparticles, Environ. Sci. Technol. 42 (2008) 5580–5585.

[162] O. Yamamoto, M. Hotta, J. Sawai, T. Sasamoto, H. Kojima, Influence of powder characteristic of ZnO on antibacterial activity – effect of specific surface area, J. Ceram. Soc. Jpn. 106, 10 (1998) 1007–11.

[163] J. Sawai, H. Igarashi, A. Hashimoto, T. Kokugan, M. Shimizu, Effect of particle size and heating temperature of ceramic powders on antibacterial activity of their slurries, J. Chem. Eng. Jpn. 29, 2 (1996) 251–256.

[164] S. Makhluf, R. Dror, Y. Nitzan, Y. Abramovich, R. Jelinek, A. Gedanken, Microwave-assisted synthesis of nanocrystalline MgO and its use as a bacteriocide, Adv. Funct. Mater. 15, 10 (2005) 1708–1715.

[165] J. Sawai, E. Kawada, F. Kanou, H. Igarashi, A. Hashimoto, T. Kokugan, M. Shimizu, Detection of active oxygen generated from ceramic powders having antibacterial activity, J. Chem. Eng. Jpn. 29 (1996) 627–633.

[166] Y. Xie, Y. He, P.L. Irwin, T. Jin, X. Shi, Antibacterial activity and mechanism of action of zinc oxide nanoparticles against *Campylobacter jejuni*, Appl. Environ. Microbiol. 77, 7 (2011) 2325–2331.

[167] T. Xia, M. Kovochich, M. Liong, L. Madler, B. Filbert, H.B. Shi, J.I. Yeh, J.I. Zink, A.E. Nel, Comparison of the mechanism of toxicity of zinc oxide and cerium oxide nanoparticles based on dissolution and oxidative stress properties, ACS Nano. 2 (2008) 2121–2134.

[168] B. Wu, Y. Wang, Y.H. Lee, A. Horst, Z.P. Wang, D.R. Chen, R. Sureshkumar, Y.J.J. Tang, Comparative eco-toxicities or nano-ZnO particles under aquatic and aerosol exposure modes, Environ. Sci. Technol. 44 (2010) 1484–1489.

[169] W. Bai, Z.Y. Zhang, W.J. Tian, X. He, Y.H. Ma, Y.L. Zhao, Z.F. Chai, Toxicity of zinc oxide nanoparticles to zebrafish embryo: A physicochemical study of toxicity mechanism, J. Nanopart. Res. 12 (2010) 1645–1654.

[170] A.L. Neal, What can be inferred from bacterium – nanoparticle interactions about the potential consequences of environmental exposure to nanoparticles?, Ecotoxicol. 17 (2008) 362–371.

[171] S. Nair, A. Sasidharan, V.V. Divya Rani, D. Menon, S. Nair, K. Manzoor, S. Raina, Role of size-scale of ZnO nanoparticles and microparticles on toxicity toward bacteria and osteoblast cancer cells, J. Mater. Sci. Mater. Med. 20, Suppl. 1 (2009) 235–241.

[172] W. Jiang, H. Mashayekhi, B.S. Xing, Bacterial toxicity comparison between nano- and micro-scaled oxide particles, Environ. Pollut. 157 (2009) 1619–1625.

[173] S. Atmaca, K. Gul, R. Clcek, The effect of zinc on microbial growth, Turkish J. Med. Sci. 28 (1998) 595–597.

[174] M. Li, L. Zhu, D. Lin, Toxicity of ZnO nanoparticles to *Escherichia coli*: Mechanism and the influence of medium components, Environ. Sci. Technol. 45, 5 (2011) 1977–1983.

[175] S. Shrivastava, T. Bera, A. Roy, G. Singh, P. Ramachandrarao, D. Dash, Characterization of enhanced antibacterial effects of novel silver nanoparticles, Nanotechnol. 19 (2007) Article ID 225103.

[176] J. Thiel, L. Pakstis, S. Buzby, M. Raffi, C. Ni, D.J. Pochan, S. Ismat Shah, Antibacterial properties of silver-doped titania, Small 3 (2007) 799–803.

[177] J.R. Morones, J.L. Elechiguerra, A. Camacho, K. Holt, J.B. Kouri, J.T. Ramírezm M.J. Yacaman, The bactericidal effect of silver nanoparticles, Nanotechnol. 16 (2005) 2346–2353.

[178] W. Lu, G. Liu, S. Gao, S. Xing, J. Wang, Tyrosine-assisted preparation of Ag/ZnO nanocomposites with enhanced photocatalytic performance and synergistic antibacterial activities, Nanotechnol. 19 (2008) 445711.

[179] X. Qiu, M. Miyauchi, K. Sunada, M. Minoshima, M. Liu, Y. Lu, D. Li, Y. Shimodaira, Y. Hosogi, Y. Kuroda, K. Hashimoto, Hybrid Cu_xO/TiO_2 nanocomposites as risk-reduction materials in indoor environments, ACS Nano 6, 2 (2012) 1609–1618.

[180] H.H.A. Dollwet, J.R.J. Sorenson, Historic uses of copper compounds in medicine, Trace Elem. Med. 2 (1985) 80–87.

[181] G. Grass, C. Rensing, M. Solioz, Metallic copper as an antimicrobial surface, Appl. Environ. Microbiol. 77, 5 (2011) 1541–1547.

[182] L. Perelshtein, G. Applerot, N. Perkas, E. Wehrschuetz-Sigl, A. Hasmann, G. Guebitz, A. Gedanken, CuO-cotton nanocomposite: Formation, morphology, and antibacterial activity, Surf. Coat. Tech. 204 (2009) 54–57.

[183] I.M. Hamouda, Current perspectives of nanoparticles in medical and dental biomaterials, J. Biomed. Res. 26, 3 (2012) 143–151.

[184] Y.S. Yoshida, S. Furuta, E. Niki, Effects of metal chelating agents on the oxidation of lipids induced by copper and iron, Biochim. Biophys. Acta 1210 (1993) 81–88.

[185] L. Macomber, J.A. Imlay, The iron-sulfer clusters of dehydratases are primary intracellular targets of copper toxicity, Proc. Natl. Acad. Sci. U.S.A. 106 (2009) 8344–8349.

[186] Y.-N. Chang, M. Zhang, L. Xia, J. Zhang, G. Xing, The toxic effects and mechanisms of CuO and ZnO nanoparticles, Mater. 5 (2012) 2850–2871.

[187] O. Baghriche, S. Rtimi, C. Pulgarin, R. Sanjines, J. Kiwi, Innovative TiO_2/Cu nanosurfaces inactivating bacteria in the minute range under low-intensity actinic light, ACS Appl. Mat. Interfaces 4 (2012) 5234–5240.

[188] I.B. Ditta, A. Steele, C. Liptrot, J. Tobin, H. Tyler, H.M. Yates, D. W. Sheel, H.A. Foster, Photocatalytic antimicrobial activity of thin surface films of TiO_2, CuO, and TiO_2/CuO dual layers on *Escherichia coli* and bacteriophage T4, Appl. Microbiol. Biotechnol. 79 (2008) 127–133.

[189] H.A. Foster, D.W. Sheel, P. Sheel, P. Evans, S. Varghese, N. Rutschke, H.M. Yates, Antimicrobial activity of titania/silver and titania/copper films prepared by CVD, J. Photochem. Photobiol., A. 216 (2010) 283–289.

[190] K. Sunada, T. Watanabe, K. Hashimoto, Bactericidal activity of copper-deposited TiO_2 thin film under weak UV light illumination, Environ. Sci. Technol. 37 (2003) 4785–4789.

[191] J.F. Lutkenhaus, Role of a major outer membrane protein in *Escherichia coli*, J. Bacteriol. 131, 2 (1977) 631–637.

[192] H. Nikaido, E.Y. Rosenberg, Porin channels in *Escherichia coli*: Studies with liposomes reconstituted from purified proteins, J. Bacteriol. 153, 1 (1983) 241–252.

[193] R. Benz, A. Schmid, R.E.W. Hancock, Ion selectivity of Gram-negative bacterial porins, J. Bacteriol. 162, 2 (1985) 722–727.

[194] R. Nakae, T. Nakae, Diffusion of aminoglycoside antibiotics across the outer membrane of *Escherichia coli*, Antimicrob. Agent. Chemother. 22, 4 (1982) 554–559.

[195] T. Nakae, Outer-membrane permeability of bacteria, Crit. Rev. Microbiol. 13, 1 (1986) 1–62.

[196] H. Kong, J. Song, J. Jang, Photocatalytic antibacterial capabilities of TiO_2-biocidal polymer nanocomposites synthesized by a surface-initiated photopolymerization, Environ. Sci. Technol. 44 (2010) 5672–5676.

[197] O. Akhavan, R. Azimirad, S. Safa, M.M. Larijani, Visible light photo-induced antibacterial activity of CNT-doped TiO_2 thin films with various CNT contents, J. Mater. Chem. 20 (2010) 7386–7392.

[198] S.F. Chen, J.P. Li, K. Qian, W.P. Xu, Y. Lu, W. X. Huang, S. H. Yu, Large scale photochemical synthesis of M@TiO_2 nanocomposites (M = Ag, Pd, Au, Pt) and their optical properties, CO oxidation performance, and antibacterial effect, Nano. Res. 3 (2010) 244–255.

[199] R.S. Sonawane, M.K. Dongare, Sol-gel synthesis of Au/TiO_2 thin films for photocatalytic degradation of phenol in sunlight, J. Mol. Catal. A: Chem. 243 (2006) 68–76.

[200] H. Li, Z. Bian, J. Zhu, Y. Huo, H. Li, Y. Lu, Mesoporous Au/TiO_2 nanocomposites with enhanced photocatalytic activity, J. Am. Chem. Soc. 129 (2007) 4538–4539.

[201] Z. Zheng, B. Huang, X. Qin, X. Zhang, Y. Dai, M.-H. Whangbo, Facile *in situ* synthesis of visible-light plasmonic photocatalysts M@TiO_2 (M = Au, Pt, Ag) and evaluation of their photocatalytic oxidation of benzene to phenol, J. Mater. Chem. 21 (2011) 9079–9087.

[202] I.M. Arabatzis, T. Stergiopoulos, D. Andreeva, S. Kitova, S.G. Neophytides, P. Falaras, Characterization and photocatalytic activity of Au/TiO_2 thin films for azo-dye degradation, J.

Catal. 220 (2003) 127–135.

Appendix B:
Applications of photocatalytic disinfection: A review

Joanne Gamage, Zisheng Zhang

International Journal of Photoenergy, Volume 2010 (2010) Article ID 764870.

Abstract

Due to the ability of photocatalysis to inactivate a wide range of microorganisms, it is being examined as a viable alternative to traditional disinfection methods such as chlorination, which can produce harmful byproducts. Photocatalysis is a versatile and effective process that can be adapted for use in many disinfection applications in both air and water matrices. Additionally, photocatalytic surfaces are being developed and tested for use in the context of "self-disinfecting" materials. Studies on the photocatalytic technique for disinfection demonstrate that this process possesses potential for widespread applications in indoor air and environmental health, biological and medical applications, laboratory and hospital applications, pharmaceutical and food industry, plant protection applications, wastewater and effluents treatment, and drinking water disinfection. Studies on photocatalytic disinfection using a variety of techniques and test organisms are reviewed, with emphasis on end-use application of developed technologies and methods.

B.1 Introduction

Photocatalytic processes are recognized as potentially viable solutions to environmental problems [1–3]. Disinfection of microorganisms is of particular importance, because traditional methods such as chlorination are chemical intensive and have many associated disadvantages. For example, in water treatment applications, chlorine used for disinfection can react with organic material to generate chloro-organic compounds that are highly carcinogenic [4, 5]. Furthermore, some pathogens such as viruses, bacteria such as *Legionella*, and protozoans such as *Cryptosporidium* and *Giardia lamblia* (*G. lamblia*) cysts are known to be resistant to chlorine disinfection [6, 7]. Other treatment alternatives such as ozonation and irradiation using germicidal lamps (254 nm) have their own problems and limitations, such as the lack of residual effect [8] and generation of small colony variants [9] for the latter and production of toxic disinfection byproducts for the former [10].

In comparison, the TiO_2 semiconductor commonly used in photocatalytic processes is nontoxic, chemically stable, available at a reasonable cost, and capable of repeated use without substantial loss of catalytic ability [11]. Heterogeneous photocatalysis using titanium dioxide is a safe, nonhazardous, and ecofriendly process that ideally does not produce any harmful byproducts. Extensive research in this field has been performed in the area of photocatalytic removal of organic, inorganic, and microbial pollutants [12, 13].

The mechanism of bactericidal action of photocatalysis, as reported by Sunada et al. is attributed to the combination of cell membrane damage and further oxidative attack of internal cellular components, ultimately resulting in cell death [14].

Since the work of Matsunaga et al. in 1985 reporting the application of photocatalysis for the destruction of *Lactobacillus acidophilus* (*L. acidophilus*), *Saccharomyces cerevisiae* (*S. cerevisiae)*, and *Escherichia coli* (*E. coli*) using platinum-loaded TiO_2 [15], there has been much interest in biological applications of this process. A comprehensive review of the application of photocatalysis for water disinfection is given by McCullagh et al. [16], with many others available in the literature [17–21].

Research in the field of photocatalytic disinfection has been very diverse, with the TiO_2/UV process shown to successfully inactivate many microorganisms including bacteria such as *E. coli* [22–24], *L. acidophilus* [15], *Pseudodomonas stutzeri* (*P. stutzeri*) [25], *Bacillus pumilus* (*B. pumilus*) [26], *Streptococcus mutans* (*S. mutans*) [1], yeasts such as *S. cerevisiae* [15], algae such as *Chlorella vulgaris* (*C. vulgaris*) [15], viruses such as phage MS2 [15, 27, 28], *B. fragilis* bacteriophage [15, 27], Poliovirus I [28], and protozoans such as *Cryptosporidium parvum* (*C. parvum*) [29], and *G. intestinalis* [30].

Research efforts are being made to improve the efficiency of the TiO_2 catalyst by means of doping with various metals [31–33] and nonmetals [34, 35]. Other parameters that can be varied in photocatalytic processes, such as the source of irradiation [18] and factors affecting process efficiency [36] have also been under investigation. Additionally, there are many reactor designs and configurations [37, 38] used to exploit photocatalytic disinfection for a wide range of applications, as this process can be used in both water and air matrices [39]. The current review will focus on developments in photocatalytic disinfection for application in the following contexts: indoor air and environmental health, biological and medical applications, laboratory and hospital applications, pharmaceutical and food industry, plant protection applications, wastewater and effluents treatment, and drinking water disinfection.

B.2 Indoor air and environmental health

The photocatalytic process is well recognized for the removal of organic pollutants in the gaseous phase such as volatile organic compounds (VOCs), and as such is applicable to contaminant control in indoor environments such as residences, office buildings, factories, aircrafts, and spacecrafts [40, 41].

To increase the scope of the photocatalytic process in application to indoor air treatment, the disinfection capabilities of this technique are also under investigation [39]. Disinfection is of importance in indoor air applications because of the risk of exposure to harmful airborne contaminants. Bioaerosols are a major contributor to indoor air pollution, and more than 60 bacteria, viruses, and fungi have been documented as infectious airborne pathogens. Diseases

transmitted via bioaerosols include tuberculosis, Legionaries, influenza, colds, mumps, measles, rubella, small pox, aspergillosis, pneumonia, meningitis, diphtheria, and scarlet fever [42]. Traditional technologies to clean indoor air include the use of activated charcoal filters, HEPA filters, ozonation, air ionization, and bioguard filters, although none of these technologies is completely effective [20].

In the pioneering work by Goswami et al. [43] investigating the disinfection of indoor air by photocatalysis, a recirculating duct facility was developed to inactivate biological contaminants with photocatalytic techniques. Experiments using *Serratia marcescens* (*S. marcascens*) in air resulted in 100% destruction of microorganisms using a recirculating loop in 600 minutes [43]. This time was reduced to less than 3 minutes in later experiments [44].

Photocatalytic oxidation can also inactivate infectious microorganisms that can be used as airborne bioterrorism weapons, such as *B. anthracis* (Anthrax) [45–47]. A photocatalytic system was investigated by Knight in 2003 to reduce the spread of severe acute respiratory syndrome (SARS) on flights [48], following outbreak of the disease. Similarly, in 2007, the avian influenza virus A/H5N2 was shown to be inactivated from the gaseous phase using a photocatalytic prototype system [39].

Inactivation of various Gram-positive and Gram-negative bacteria using visible light and a doped catalyst [49], as well as fluorescent light irradiation similar to that used in indoor environments was studied [50].

It was also shown that *E. coli* could be completely mineralized on a TiO_2 coated surface in air [42]. Carbon mass balance and kinetic data for complete oxidation of *E. coli*, *Aspergillus niger* (*A. niger*), *Micrococcus luteus (M. luteus)*, and *B. subtilis* cells and spores were subsequently presented [51]. A comprehensive mechanism and detailed description of the photokilling of *E. coli* on TiO_2 coated surfaces in air was extensively studied in order to quantify the kinetics of *E. coli* immobilization and abatement via photocatalysis, by monitoring FTIR, AFM, and CFU as a function of time and observing peroxidation of the

membrane cell walls [52–56].

Novel photoreactors and photo-assisted catalytic systems for air disinfection applications such as those using polyester supports for the catalyst [57], carbon nanotubes [58], combination with other disinfection systems [59], membrane systems [60], silver bactericidal agents in cotton textiles for the abatement of *E. coli* [61–63], high surface area CuO catalysts [64], and structured silica surfaces [65] have also been reported.

In terms of environmental health, the antifungal capability of photocatalysis against mould fungi on coated wood boards used in buildings was confirmed [66] using *A. niger* as a test microbe under UVA irradiation.

B.3 Biological and medical applications

Due to the disinfective properties of photocatalytic processes, they are being explored for use in medical applications. Studies have been performed using coatings on bioimplants to implement photocatalysis for antibacterial purposes [46, 67, 68]. Shiraishi et al. explored the photocatalytic inactivation of *S. aureus*, a common pathogenic bacterium in implant-related infection, using TiO_2 film on stainless steel and titanium substrates [69]. The bactericidal effect of the coating was confirmed upon UV irradiation, and the use of these coated photocatalytic substrates presented a useful strategy for the control of infections associated with biomedical implants.

Photocatalysis is also able to kill animal cells, and the antitumor activity was studied using subcutaneous titania injection onto skin tumours followed by 40 minutes of UV illumination [70]. This procedure produced a tenfold tumour volume reduction after three weeks, where the catalyst and light alone controls exhibited tumour increases in volume by factors of 30 – 50. The use of photocatalysis for cancer cell treatment has also been documented elsewhere [1, 71].

As previously alluded to in air-disinfection strategies, photocatalysis can be employed to

remove harmful airborne biological threats such as Anthrax [47,72]. In this sense, it can be an effective technique for combating bioterror.

B.4 Laboratory and hospital applications

Particularly in microbiological laboratories and in areas of intensive medical use, frequent and thorough disinfection of surfaces is needed in order to reduce the concentration of bacteria and to prevent bacterial transmission. Conventional methods of disinfection with wiping are not effective long-term, and are staff and time intensive. These methods also involve the use of harsh and aggressive chemicals. Disinfection with hard ultraviolet light (UVC) is usually unsatisfactory, since the depth of penetration is inadequate and there are occupational health risks involved [73].

Photocatalytic oxidation on surfaces coated with titanium dioxide offers an alternative to traditional methods of surface disinfection. Research has been performed on the biocidal activity of thin films of titania anchored to solid surfaces [73–75]. The effectiveness of this process was demonstrated using bacteria relevant to hygiene such as *E. coli*, *P. aeruginosa*, *S. aureus*, and *E. faecium* [73]. The inactivation of *E. coli* (ATCC8739) cells deposited on TiO_2 membrane filters upon irradiation with fluorescent light was also shown as an application of self-disinfecting surfaces [76].

Thin films deposited on stainless steel using a novel flame-assisted CVD technique were also tested for antimicrobial activity on *E. coli* [68]. There is a wide range of applications for this self-disinfecting material because of the desirable mechanical properties and resistance to corrosion of stainless steel. Transparent TiO_2 films on this substrate were also shown to be effective for sterilization of *B. pumilus* [77].

Titania photocatalysts doped with CuO were coated on surfaces and their biocidal activity evaluated [78]. This investigation also explored the synergistic effect of photocatalysis and toxicity of copper to inactivate bacteriophage T4 and *E. coli*.

Enhanced photocatalysis using nitrogen-doped TiO_2 was also reported for its visible light-induced bactericidal activity against human pathogens [79]. It was proposed in this study that photocatalytic disinfection using visible light can offer a means of continuous disinfection for surfaces constantly in contact with humans, such as door handles and push buttons. Visible light-induced inactivation of *E. coli* was also studied using titania codoped with nitrogen and sulfur [80–83]. This introduces new disinfectant opportunities in public environments, such as public toilets, schools, hospitals, metro stations, airports, hotels, or public transportation, which are ideal places for the transmission of pathogens [84, 85].

Photocatalysis has also been investigated for the inactivation of prions, the infectious agents of a family of transmissible, fatal, neurodegenerative disorders affecting both humans and animals [86]. These prions may be transmitted via ingestion of contaminated food or during medical treatments with contaminated biological materials or surgical tools. The effectiveness of photocatalytic oxidation for inactivating prions can help reduce the risk of spread and demonstrates the practical applications of this technology for disinfection of contaminated surfaces and inanimate objects.

Another application of photocatalysis in hospital settings is for the control of Legionnaire's disease, which is associated to hot water distribution systems containing bacteria of the *Legionella* species [87]. In laboratory scale studies, photocatalytic oxidation using TiO_2/UV was shown to mineralize the cells of four strains of *L. pneumophilia* serogroup 1 (strain 977, strain 1009, strain 1004, and ATCC 33153) upon prolonged treatment. This implied that the process used might be a viable alternative to traditional disinfection processes for the control of *Legionella* bacteria in hospital hot water systems, such as thermal eradication and hyperchlorination [88].

B.5 Pharmaceutical and food industries

Due to the antibacterial applications of TiO_2-mediated photooxidation, this process shows promise for the elimination of microorganisms in areas where the use of chemical cleaning agents or biocides is ineffective or is restricted by regulations, for example in the

pharmaceutical and food industries [33]. TiO_2 is nontoxic and has been approved by the American Food and Drug Administration for use in human food, drugs, cosmetics, and food contact materials [89].

TiO_2 powder-coated packaging film was shown to inactivate *E. coli* (ATCC 11775) *in vitro* when irradiated with UVA light [89]. Actual tests on cut lettuce stored in a TiO_2-coated film bag under UVA irradiation also showed this method to be effective for the reduction of *E. coli* colonies, indicating that the coated film could reduce microbial contamination on the surfaces of solid food products and reduce the risk of microbial growth in food packaging. TiO_2 photocatalysis has also been shown to be effective for the inactivation of other foodborne bacteria such as *Salmonella chloraesuis* (*S. chlroaesuis*), *Vibrio parahaemolyticus* (*V. parahaemolyticus*), and *Listeria monocytogenes* (*L. monocytogenes*) [68].

Surface disinfection is also of importance in food processing, as foodborne infections can be caused by the proliferation and resistance to cleaning procedures of pathogenic germs on surfaces of the production equipment in such industries. Studies with *E. coli* strains (PHL 1273) [90] synthesizing curli, a type of appendage that allows the bacteria to stick to surfaces and form biofilms, demonstrated the inactivation of this organism using titania and various types of UV irradiation. In dark events studies following the bacterial inactivation, no bacterial cultivability was recovered after 48 hours, indicating that the durability of disinfection was adequate. Nitrogen doping of the titania photocatalyst was also reported in a separate study [91] with the use of visible light to inactivate *E. coli* and biofilm bacteria. Disinfection of *E. coli* using TiO_2-containing paper and UV fluorescent irradiation was also investigated [92].

B.6 Plant protection applications

Photocatalytic disinfection may also be useful for the control and inactivation of pathogenic species present in nutritive solutions used in circulating hydroponic agricultures [93]. Many plant pathogens can be transmitted by irrigation and recycled waters used in hydroponic agriculture. Conventional bactericidal methods often apply chemical pesticides to disinfect

these pathogens, but these can be harmful to animals, humans, and the environment due to their residual toxicity [94]. Photocatalytic disinfection of these plant pathogens using TiO_2 may therefore be used as a novel tool for plant protection and as an alternative to the use of harsh chemicals.

Using TiO_2 thin films on glass substrates and UVA irradiation, *Enterobacter cloacae* (*E. cloaecae)* SM1 and *Erwinia carotovora subsp. caratovora* ZL1, phytopathogenic enterobacteria that cause basal rot and soft rot in a variety of vegetable crops, were efficiently inactivated [94]. Subsequent studies investigated the effects of doping the titania catalyst with various photosensitive dyes and using visible light irradiation [95]. From these studies, the disinfection of phytopathogenic bacteria causing basal and soft rot could be efficiently achieved under visible light.

Solar photocatalytic disinfection using batch process reactors and titania photocatalysts was also shown to be effective for the disinfection of five wild strains of the *Fusarium* genus (*F. equiseti*, *F. oxysporum*, *F. anthophilum*, *F. verticilloides*, and *F. solani*), which are common plant pathogens [96]. In these studies, natural solar radiation was used and the photocatalytic solar disinfection was compared to solar-only disinfection for the fungi, and the photocatalytic process was found to be faster than solar-only disinfection in all trials.

The disinfection capability of titania photocatalyst films was also tested on pathogens of mushroom diseases: *Trichoderma harzianum*, *Cladobotryum varium*, *Spicellum roseum*, and *P. tolaasi*. The disinfection of these species was confirmed by experiments conducted in mushroom-growing rooms under black light and white light irradiation, respectively [97].

B.7 Wastewater and effluents

The use of photocatalysis for water and wastewater treatment is a topic well-documented in the literature, especially with respect to solar photocatalysis [17–21, 98–101]. Due to the ability of photocatalysis to mineralize many organic pollutants, it has been used for remediation of contaminated groundwaters via various solar concentrating reactors.

Photocatalysis has been used in engineering scale for solar photocatalytic treatment of industrial nonbiodegradable persistent chlorinated water contaminants [21], and in field scale for treatment of effluents from a resins factory [102]. This process has also shown to be effective for treatment of wastewaters from a 5-fluororacil (cancer drug) manufacturing plant [103], distillery wastewater [104], pulp and paper mill wastewater [105], dyehouse wastewater [17], and oilfield produced water [35].

However, the disinfection capabilities of photocatalytic processes have not thoroughly been exploited for treatment of wastewaters. Wastewater reclamation and reuse is of growing importance, especially in areas where the freshwater supply is limited, and so effective disinfection of wastewaters is necessary. Any technical means of sewage reuse is limited by persistent organic pollutants and microorganisms that are not removed by the conventional mechanical and biological treatment train [106]. Additional treatment is therefore necessary before any reuse can take place.

Early work on photocatalytic disinfection of municipal secondary wastewater effluents showed inactivation of coliform bacteria and poliovirus I using suspensions of titanium dioxide and fluorescent and sunlight irradiation, respectively [28]. Photocatalysis is also useful for disinfection of sewage containing organisms that are highly resistant to traditional disinfection methods, such as *C. parvum* [107] and noroviruses [108].

Municipal wastewater effluents from a sewage disposal plant in Hannover, Germany were treated in a TiO_2 slurry reactor under UVA irradiation to simultaneously detoxify and disinfect the samples [109]. The photocatalytic treatment was able to diminish the concentration of dissolved organic pollutants (indicated by TOC and COD), and as well inactivate pathogenic microorganisms (indicated by *E. coli*). A similar result was obtained from studies monitoring faecal S*treptococci* and total coliforms using slurry systems with UVA lamps and solar irradiation, respectively [110].

The investigation of a bacterial consortia of *E. coli* and *Enterococcus* species present in real

wastewaters from a biological wastewater treatment plant in Lausanne (Switzerland) [111] indicated that the *Enterococcus* species were less sensitive to photocatalytic treatment than coliforms and other Gram-negative bacteria. Additionally, the effects of temperature, turbidity, and various other physical parameters of the samples on the photocatalytic inactivation of *E. coli* were investigated [112].

Other research explored enhanced photocatalysis to improve the efficiency of disinfection of wastewaters for reuse, for example, by employing titania-activated carbon catalyst mixtures [113], and through the development of nanocrystalline photocatalytic membranes [114]. The latter is of particular importance in aeronautical applications, as it combines membrane separation technologies with advanced oxidation technologies to create hybrid photocatalytic composite membranes designed for the treatment and reuse of water on long-duration space missions [115].

An inexpensive approach to synthesizing a novel nitrogen-doped photocatalyst was also developed [116], which possessed improved efficiency of visible light induced disinfection of wastewaters, introducing a new generation of catalysts for this application.

B.8 Drinking water disinfection

Titania photocatalysis has been proven to be effective in the removal of chemical compounds and microbiological pathogens from water. A thorough review by McCullagh et al. [16] of the application of photocatalysis for the removal of biological species in this context examines the results of studies investigating the disinfective effects of TiO_2 suspensions, effect of additives and pH, respectively, on the photocatalytic abilities and of TiO_2 thin films, and the effect of electrochemically applied potential on the photobactericidal effect of TiO_2 thin films. The current discussion will focus on the various applications of photocatalytic drinking water disinfection.

B.8.1 Drinking water production in developing countries

In 2004, it was estimated that about 15% of the world's population, mostly living in the less-favoured regions of the planet, did not have access to enough fresh water to satisfy their daily

needs, and this number was expected to double by 2015 [117]. This represents a serious public health issue since waterborne, water-washed, and water-based diseases are associated with lack of improvement in domestic water supply and adequate sanitation [118]. Development of cost-effective methods for removal of pollutants from water supplies can help alleviate this problem. Especially in rural communities, water disinfection must have sufficiently low operational costs. Alternative technologies to traditional chlorination are currently being considered for household use [119].

Solar disinfection (SODIS) is a simple technology that is capable of inactivating many waterborne pathogenic bacteria using the combined effect of solar UVA radiation and temperature [120–123]. This method is low cost and does not produce toxic byproducts, however, limits the volume of water subject to treatment (typically 2 L per exposed water bottle) and has a disadvantageously long processing time associated (typically 2 day exposure for complete inactivation) [118].

The combination of sunlight and photocatalyst is a promising option for water treatment in areas with insufficient infrastructure but high yearly sunshine. The use of compound parabolic reactors as an efficient technology to collect and focus diffuse and direct solar radiation onto a transparent pipe containing contaminated water was demonstrated for the disinfection of water using TiO_2 suspensions [124–126].

The European Union International Cooperation program (INCO) has sponsored initiatives for developing a solar photocatalysis-based cost-effective technology for water decontamination and disinfection in rural areas of developing countries, named the SOLWATER and AQUACAT projects, respectively [93]. These projects were aimed at developing a solar reactor to decontaminate and disinfect small volumes of water, and field tests with the final prototypes were carried out to validate operation under real conditions [126].

The final SOLWATER prototype was composed of two tubes containing Ahlstrom paper impregnated with titanium dioxide, and two tubes containing a supported photosensitizer [93]. These tubes were placed on a compound parabolic concentrating collector and run in series, where the electricity was provided by a solar panel (Figure B.1).

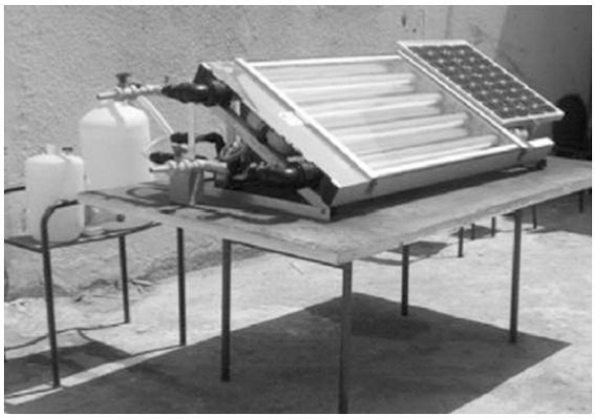

Figure B.1: Final SOLWATER and AQUACAT (solar photocatalytic) water disinfection system installed at École Supérieure de Technologie de Fès, Morroco [93]

Field tests using the SOLWATER prototype placed in the yard of a shanty house in Los Pereyra, Tucumán, Argentina studied the removal of bacterial contamination during three months of testing using natural water contaminated with coliforms, *E. faecalis*, and *P. aeruginosa*, as well as high levels of natural organic matter and variable inorganic pollutants [126]. The SOLWATER reactor was shown to be effective for this application. Similar tests were performed in photoreactors installed in various geographic regions, including Egypt, France, Greece, Mexico, Morocco, Peru, Spain, Switzerland, and Tunisia [93].

Other research in the field of potable water production in developing countries includes the development of affordable and efficient technology in the form of batch borosilicate glass and PET plastic SODIS reactors fitted with flexible plastic inserts coated with TiO_2 powder [127]. These were shown to be 20 and 25% more effective, respectively, than SODIS alone for the inactivation of *E. coli* K-12. This novel system was also able to reduce the concentration of *C. parvum* oocysts present [128]. It should be also noted that there has also

been significant research done regarding the solar disinfection of this highly resistant organism using SODIS alone [122, 129, 130].

B.8.2 Surface water treatment

While the majority of photocatalytic disinfection studies reported are carried out with distilled water or buffer solutions [16], there have been attempts to quantify the effects of the chemical constituents of natural surface waters on photocatalysis [131, 132]. It has been shown, using surface water samples, that the presence of inorganic ions and humic acids decreases the rate of photocatalytic disinfection of *E. coli* [132].

Other efforts have been made to evaluate photocatalysis using real waters [133–137]. For example, the integration of photocatalysis into traditional water treatment processes for the removal of organic matter, present in variable levels during the year, was studied in the UK using three surface water samples [135].

Natural water samples from the Cauca River in Cali, Columbia showed a drastic increase in *E. coli* culturable cell concentration 24 hours after stopping irradiation [134]. This was not observed for the control experiment using an *E. coli* suspension in distilled water. It was concluded that caution should be taken when making predictions based on simple models as they are not necessarily representative of natural crude water samples.

The effect of pH, inorganic ions, organic matter, and H_2O_2 on *E. coli* photocatalytic inactivation by TiO_2 was studied by simulating natural and environmental conditions of these parameters using distilled and tap water samples [131]. The results of this study and others [132] confirmed that laboratory results using ultrapure water samples are not representative of the real application in natural waters.

In studies performed on surface water samples by Ireland et al. [133], it was concluded that inorganic-radical scavengers can have a major negative impact on the efficacy of the photocatalytic process, and the presence of organic matter in the water samples also reduces *E. coli* inactivation kinetics.

Using a field-scale compound parabolic collector at the Swiss Federal Institute of Technology, in Lausanne, natural water from the Leman Lake was used to suspend *E. coli* in the presence of TiO_2 and irradiation under solar conditions [125]. From studies on the postirradiation period, the effective disinfection time (EDT) was defined as the time necessary to avoid bacterial regrowth after 24h (or 48h) in the dark after stopping phototreatment. It was suggested that the necessary EDT should be used as an indicator of the impact of solar photocatalytic processes on bacteria instead of the UV dose required to achieve a certain level of disinfection.

B.8.3 Eutrophic water treatment

Another application of photocatalytic disinfection is in the treatment of eutrophic water. Control of algal blooms in eutrophic water is important because toxic cyanobacterial blooms in drinking water supplies may cause human health problems [136]. Copper-based algaecides can be used for these purposes, however this may introduce secondary environmental problems [137].

Photocatalytic inactivation of three species of algae: *Anabaena, Microcystis,* and *Melosira*, was studied using TiO_2-coated glass beads and UV-light irradiation [137]. Complete photocatalytic inactivation of *Anabaena* and *Microcystis* was obtained in about 30 minutes, while the inactivation efficiency for *Melosira* was somewhat lower due to the inorganic siliceous wall surrounding the cells.

Floating TiO_2-coated hollow glass beads were introduced into a mesocosm installed at the Nakdong River in Kimhae, Korea [137]. This mesocosm was a 25 m^2 and 2 m deep semipermeable membrane. The concentrations of chlorophyll-a were measured for one month, and it was shown that more than 50% of the chlorophyll-a concentration could be reduced using TiO_2 photocatalysts and natural solar radiation. A picture of the experimental mesocosm is shown in Figure B.2.

Figure B.2: Experimental mesocosm used in the Nakdong River, Korea [137]

B.8.4 Groundwater treatment

The ability of photocatalysis to break down and detoxify harmful organic chemicals has been exploited for groundwater treatment, as shown by engineering scale demonstrations using solar photocatalysis to remediate groundwater contaminated from leaking underground storage tanks [138].

The disinfective abilities of photocatalytic processes for application to treating groundwater contaminated with microorganisms such as *F. solani* [139] was also investigated and shown to be effective for the removal of such microorganisms. The study of natural well water containing *F. solani* species and CPCs employing solar illumination was also explored as a process configuration for this application [140].

B.9 Conclusions

The photocatalytic technique is a versatile and effective disinfection process capable of inactivating a wide range of harmful microorganisms in various media. It is a safe, nontoxic, and relatively inexpensive disinfection method whose adaptability allows it to be used for many purposes. Research in the field of photocatalytic disinfection is very diverse, covering a broad range of applications.

Particularly, the use of photocatalysis was shown to be effective for various air-cleaning

applications to inactivate harmful airborne microbial pathogens, or to combat airborne bioterror threats, such as Anthrax. Photocatalytic thin films on various substrates were also shown to have potential application for "self-disinfecting" surfaces and materials, which can be used for medical implants, surgical tools and surfaces in laboratory and hospital settings, and equipment in the pharmaceutical and food industries. Photocatalytic food packaging was shown to be a potential tool for the reduction of risk of foodborne illnesses in cut lettuce and other packaged foods. In terms of plant protection, photocatalysis was investigated for use in hydroponic agricultures as an alternative to harsh pesticides. For water treatment applications, photocatalytic disinfection was studied and implemented for drinking water production using novel reactors and solar irradiation. Eutrophic waters containing algal blooms were also shown to be effectively treated using TiO_2-coated hollow beads and solar irradiation.

The effectiveness of photocatalytic disinfection for inactivating microorganisms of concern for each of these applications was presented, highlighting key studies and research efforts conducted. While the performance of this technology should still be optimized for specific applications, based on the literature presented, it is evident that photocatalysis may be considered as a viable alternative to traditional disinfection methods in some cases.

In a move towards a more environmentally friendly world, traditional solutions to classic problems, such as the production of safe drinking water, must shift towards more sustainable alternatives. Photocatalytic disinfection may present a replacement technology for traditional methods in traditional applications, as well as a novel approach for solving other disinfection problems, such as the control of bioterror threats. In this sense, the strength of photocatalytic disinfection lies in its versatility for use in many different applications.

B.10 References

[1] D.M. Blake, P.-C. Maness, Z. Huang, E.J. Wolfrum, J. Huang, W.A. Jacoby, Application of the photocatalytic chemistry of titanium dioxide to disinfection and the killing of cancer cells, Sep. Purif. Methods 28, 1 (1999) 1–50.

[2] K. Yogo, M. Ishikawa, Recent progress in environmental catalytic technology, Catal.

Surv. Jpn. 4, 1 (2000) 83–90.

[3] D. Ljubas, Solar photocatalysis – a possible step in drinking water treatment, Energy 30, 10 (2005) 1699–1710.

[4] H.J. Kool, C.F. Keijl, J. Hrubec, Water Chlorination: Chemistry, Environmental Impact and Health Effects, Lewis, Chelsea, Mich, USA, 1985.

[5] P.S.M. Dunlop, J.A. Byrne, N. Manga, B.R. Eggins, The photocatalytic removal of bacterial pollutants from drinking water, J. Photochem. Photobiol., A. 148, 1–3 (2002) 355–363.

[6] F.W. Pontis, Ed., Water Quality and Treatment, A Handbook of Community Water Supplies, McGraw Hill, New York, NY, USA, 4th edition, 1990.

[7] S. Regli, Disinfection requirements to control for microbial contamination, in: Regulating Drinking Water Quality, C. E. Gilbert and E. J. Calabrese, Eds., Lewis, MI, USA, 1992.

[8] W.J. Masschelin, Ultraviolet Light in Water and Wastewater Sanitation, Lewis, Boca Raton, FL, USA, 2002.

[9] J.M.C. Robertson, P.K.J. Robertson, L.A. Lawton, A comparison of the effectiveness of TiO_2 photocatalysis and UVA photolysis for the destruction of three pathogenic micro-organisms, J. Photochem. Photobiol., A. 175, 1 (2005) 51–56.

[10] W.-J. Huang, G.-C. Fang, C.-C. Wang, The determination and fate of disinfection by-products from ozonation of polluted raw water, Sci. Total Environ. 345, 1–3, (2005) 261–272.

[11] M.A. Fox, C.C. Chen, K. Park, J.N. Younathan, in: Organic Transformations in Non-Homogeneous Media, M. A. Fox, Ed., ACS Symposium Series, 1985.

[12] A. Fujishima, T.N. Rao, D.A. Tryk, Titanium dioxide photocatalysis, J. Photochem. Photobiol., C. 1, 1 (2000) 1–21.

[13] A.-G. Rincón, C. Pulgarin, Use of coaxial photocatalytic reactor (CAPHORE) in the TiO_2 photo-assisted treatment of mixed *E. coli* and *Bacillus* sp. and bacterial community present in wastewater, Catal. Today, 101, 3–4 (2005) 331–344.

[14] K. Sunada, T. Watanabe, K. Hashimoto, Studies on photokilling of bacteria on TiO_2 thin film, J. Photochem. Photobiol., A. 156, 1–3 (2003) 227–233.

[15] T. Matsunaga, R. Tomoda, T. Nakajima, H. Wake, Photoelectrochemical sterilization of microbial cells by semiconductor powders, FEMS Microbiol. Lett. 29, 1–2 (1985) 211–214.

[16] C. McCullagh, J.M.C. Robertson, D.W. Bahnemann, P.K.J. Robertson, The application of TiO_2 photocatalysis for disinfection of water contaminated with pathogenic micro-organisms: a review, Res. Chem. Intermed. 33, 3–5 (2007) 359–375.

[17] D.Y. Goswami, D.M. Blake, Cleaning up with sunshine, Mech. Eng. 118, 8 (1996) 56–59.

[18] D.Y. Goswami, A review of engineering developments of aqueous phase solar photocatalytic detoxification and disinfection processes, J. Sol. Energy Eng. – T. ASME 119, 2 (1997) 101–107.

[19] M. Romero, J. Blanco, B. Sánchez, A. Vidal, S. Malato, A.I. Cardona, E. Garcia, Solar photocatalytic degradation of water and air pollutants: challenges and perspectives, Sol. Energy 66, 2 (1999) 169–182.

[20] D.Y. Goswami, S. Vijayaraghavan, S. Lu, G. Tamm, New and emerging developments in solar energy, Sol. Energy 76, 1–3 (2004) 33–43.

[21] S. Malato, J. Blanco, D.C. Alarcón, M.I. Maldonado, P. Fernández-Ibáñez, W. Gernjak, Photocatalytic decontamination and disinfection of water with solar collectors, Catal. Today 122, 1–2 (2007) 137–149.

[22] S.S. Block, D.Y. Goswami, Chemical enhanced sunlight for killing bacteria, Proc. Int. Sol. Energy Conf. 1 (1995) 431–437.

[23] R. Armon, N. Laot, N. Narkis, I. Neeman, Photocatalytic inactivation of different bacteria and bacteriophages in drinking water at different TiO_2 concentration with or without exposure to O_2, J. Adv. Oxid. Technol. 3 (1998) 145–150.

[24] A.T. Cooper, D.Y. Goswami, S.S. Block, Solar photochemical detoxification and disinfection for water treatment in tropical developing countries, J. Adv. Oxid. Technol. 3, 2 (1998) 151–154.

[25] M. Biguzzi, G. Shama, Effect of titanium dioxide concentration on the survival of *Pseudomonas stutzeri* during irradiation with near ultraviolet light, Lett. Appl. Microbiol. 19, 6 (1994) 458–460.

[26] H.N. Pham, T. McDowell, E. Wilkins, Photocatalytically-mediated disinfection of water using TiO_2 as a catalyst and spore-forming *Bacillus pumilus* as a model, J. Environ. Sci. Health Part A. 30, 3 (1995) 627–636.

[27] J.C. Sjogren, R.A. Sierka, Inactivation of phage MS2 by iron-aided titanium dioxide photocatalysis, Appl. Environ. Microbiol. 60, 1 (1994) 344–347.

[28] R.J. Watts, S. Kong, M.P. Orr, G.C. Miller, B.E. Henry, Photocatalytic inactivation of coliform bacteria and viruses in secondary wastewater effluent, Water Res. 29, 1 (1995) 95–100.

[29] H. Ryu, D. Gerrity, J.C. Crittenden, M. Abbaszadegan, Photocatalytic inactivation of *Cryptosporidium parvum* with TiO_2 and low-pressure ultraviolet irradiation, Water Res. 42, 6–7 (2008) 1523–1530.

[30] M. Sökmen, S. Değerli, A. Aslan, Photocatalytic disinfection of *Giardia intestinalis* and *Acanthamoeba castellani* cysts in water, Exp. Parasitol. 119, 1 (2008) 44–48.

[31] S.M. Karvinen, The effects of trace element doping on the optical properties and photocatalytic activity of nanostructured titanium dioxide, Ind. Eng. Chem. Res. 42, 5 (2003) 1035–1043.

[32] A. Vohra, D.Y. Goswami, D.A. Deshpande, S.S. Block, Enhanced photocatalytic inactivation of bacterial spores on surfaces in air, J. Ind. Microbiol. Biotechnol. 32, 8 (2005) 364–370.

[33] E.V. Skorb, L.I. Antonouskaya, N.A. Belyasova, D.G. Shchukin, H. Möhwald, D.V.

Sviridov, Antibacterial activity of thin-film photocatalysts based on metal-modified TiO_2 and TiO_2:In_2O_3 nanocomposite, Appl. Catal., B. 84, 1–2 (2008) 94–99.

[34] J.C. Yu, W. Ho, J. Yu, H. Yip, K. W. Po, J. Zhao, Efficient visible-light-induced photocatalytic disinfection on sulfur-doped nanocrystalline titania, Environ. Sci. Technol. 39, 4 (2005) 1175–1179.

[35] G. Li, T. An, X. Nie, G. Sheng, X. Zeng, J. Fu, Z. Lin, E.Y. Zeng, Mutagenicity assessment of produced water during photoelectrocatalytic degradation, Environ. Toxicol. Chem. 26, 3 (2007) 416–423.

[36] T.P.T. Cushnie, P.K.J. Robertson, S. Officer, P.M. Pollard, C. McCullagh, J.M.C. Robertson, Variables to be considered when assessing the photocatalytic destruction of bacterial pathogens, Chemosphere 74, 10 (2009) 1374–1378.

[37] Y.-S. Choi, B.-W. Kim, Photocatalytic disinfection of *E. coli* in a UV/TiO_2-immobilised optical-fibre reactor, J. Chem. Technol. Biotechnol. 75, 12 (2000) 1145–1150.

[38] M. Subrahmanyam, P. Boule, V.D. Kumari, D.N. Kumar, M. Sancelme, A. Rachel, Pumice stone supported titanium dioxide for removal of pathogen in drinking water and recalcitrant in wastewater, Sol. Energy 82, 12 (2008) 1099–1106.

[39] C. Guillard, T.-H. Bui, C. Felix, V. Moules, B. Lina, P. Lejeune, Microbiological disinfection of water and air by photocatalysis, Comptes Rendus Chimie, 11, 1–2 (2008) 107–113.

[40] D.T. Tompkins, W.A. Zeitner, B.J. Lawnicki, M.A. Anderson, Evaluation of photocatalysis for gas-phase air cleaning - part 1: process, technical, and sizing considerations, ASHRAE Trans. 111, 2 (2005) 60–84.

[41] D.F. Ollis, Photocatalytic purification and remediation of contaminated air and water, Comptes Rendus de l'Academie des Sciences IIC 3, 3, 6 (2000) 405–411.

[42] W.A. Jacoby, P.C. Maness, E.J. Wolfrum, D.M. Blake, J.A. Fennell, Mineralization of bacterial cell mass on a photocatalytic surface in air, Environ. Sci. Technol. 32, 17 (1998) 2650–2653.

[43] D.Y. Goswami, D.M. Trivedi, S.S. Block, Photocatalytic disinfection of indoor air, J. Sol. Energy Eng. – T. ASME 119, 1 (1997), 92–96.

[44] T.K. Goswami, S. Hingorani, H. Griest, D.Y. Goswami, S.S. Block, Photocatalytic system to destroy bioaerosols in air, J. Adv. Oxid. Technol. 4, 2 (1999) 185–188.

[45] H.T. Griest, S.K. Hingorani, K. Kelly, D.Y. Goswami, Using scanning electron microscopy to visualize the photocatalytic mineralization of airborne microorganisms, in Proceedings of the 9th International Conference on Indoor Air Quality and Climate, Processing of the Indoor Air, pp. 712–717, Monterey, CA, USA, 2002.

[46] C. Lee, H. Choi, C. Lee, H. Kim, Photocatalytic properties of nano-structured TiO_2 plasma sprayed coating, Surf. Coat. Technol. 173, 2–3 (2003) 192–200.

[47] J.-H. Kau, D.-S. Sun, H.-H. Huang, M.-S. Wong, H.-C. Lin, H.-H. Chang, Role of visible light-activated photocatalyst on the reduction of anthrax spore-induced mortality in

mice, PLoS ONE 4, 1 (2009) 1–8.

[48] H. Knight, Sars wars, Engineer 292 (2003) 27–35.

[49] D. Mitoraj, A. Jańczyk, M. Strus, H. Kisch, G. Stochel, P.B. Heczko, W. Macyk, Visible light inactivation of bacteria and fungi by modified titanium dioxide, Photochem. Photobiol. Sci. 6, 6 (2007) 642–648.

[50] A. Pal, S.O. Pehkonen, L.E. Yu, M.B. Ray, Photocatalytic inactivation of Gram-positive and Gram-negative bacteria using fluorescent light, J. Photochem. Photobiol., A. 186, 2–3 (2007) 335–341.

[51] E.J. Wolfrum, J. Huang, D.M. Blake, P.-C. Maness, Z. Huang, J. Fiest, Photocatalytic oxidation of bacteria, bacterial and fungal spores, and model biofilm components to carbon dioxide on titanium dioxide-coated surfaces, Environ. Sci. Technol. 36, 15 (2002) 3412–3419.

[52] J. Kiwi, V. Nadtochenko, New evidence for TiO_2 photocatalysis during bilayer lipid peroxidation, J. Phys. Chem. B 108, 45 (2004) 17675–17684.

[53] R. Basca, J. Kiwi, T. Ohno, P. Albers, V. Nadtochenko, Preparation, testing and characterization of doped TiO_2 able to transform biomolecules under visible light irradiation by peroxidation/oxidation, J. Phys. Chem. B 109 (2005) 5994–6003.

[54] J. Kiwi, V. Nadtochenko, Evidence for the mechanism of photocatalytic degradation of the bacterial wall membrane at the TiO_2 interface by ATR-FTIR and laser kinetic spectroscopy, Langmuir 21, 10 (2005) 4631–4641.

[55] V.A. Nadtochenko, A.G. Rincon, S.E. Stanca, J. Kiwi, Dynamics of E. coli membrane cell peroxidation during TiO_2 photocatalysis studied by ATR-FTIR spectroscopy and AFM microscopy, J. Photochem. Photobiol., A. 169, 2 (2005) 131–137.

[56] V. Nadtochenko, C. Pulgarin, P. Bowen, J. Kiwi, Laser spectroscopy of the interaction of bacterial wall membranes and E. coli with TiO_2, J. Photochem. Photobiol., A. 181 (2006) 401–404.

[57] M.P. Paschoalino, W.F. Jardim, Indoor air disinfection using a polyester supported TiO_2 photo-reactor, Indoor Air 18, 6 (2008) 473–479.

[58] V. Krishna, S. Pumprueg, S.-H. Lee, J. Zhao. W. Sigmund, B. Koopman, B.M. Moudgil, Photocatalytic disinfection with titanium dioxide coated multi-wall carbon nanotubes, Process Saf. Environ. Prot. 83, 4B (2005) 393–397.

[59] S.A. Grinshpun, A. Adhikari, T. Honda, K.Y. Kim, M. Toivola, K.S. Rao, T. Reponen, Control of aerosol contaminants in indoor air: combining the particle concentration reduction with microbial inactivation, Environ. Sci. Technol. 41, 2 (2007) 606–612.

[60] A. Pal, X. Mint, L.E. Yu, S.O. Pehkonen, M.B. Ray, Photocatalytic inactivation of bioaerosols by TiO_2 coated membrane, Int. J. Chem. Reactor Eng. 3 (2005) A45.

[61] T. Yuranova, A.G. Rincon, A. Bozzi, S. Parra, C. Pulgarin, P. Albers, J. Kiwi, Antibacterial textiles prepared by RF-plasma and vacuum-UV mediated deposition of silver, J. Photochem. Photobiol., A. 161, 1 (2003) 27–34.

[62] T. Yuranova, A.G. Rincon, C. Pulgarin, D. Laub, N. Xantopoulos, H.-J. Mathieu, Bactericide cotton textiles active in *E. coli* abatement prepared under mild preparation conditions, J. Photochem. Photobiol., A. 181 (2006) 363–369.

[63] M.I. Mejia, G. Restrepo, J.M. Marin, R. Sanjines, C. Pulgarin, E. Mielczarski, Magnetron-sputtered Ag surfaces: New evidence for the nature of the Ag ions intervening in bacterial inactivation, ACS Appl. Mater. Interfaces 2 (2010) 230–235.

[64] M. Paschoalino, N.C. Guedes, W. Jardim, E. Mielczarski, K. Mielczarski, P. Bowen, Photo-assisted inactivation of *E. coli* by high surface area CuO under light irradiation (>360 nm), J. Photochem. Photobiol., A. 199 (2008) 105–111.

[65] A. Moncayo-Lasso, R.A. Torres-Palma, J. Kiwi, N. Benítez, C. Pulgarin, Bacterial inactivation and organic oxidation via immobilized photo-Fenton reagent on structured silica surfaces, Appl. Catal., B. 84, 3–4 (2008) 577–583.

[66] F. Chen, X. Yang, Q. Wu, Antifungal capability of TiO_2 coated film on moist wood, Build. Environ. 44, 5 (2009) 1088–1093.

[67] P. Kern, P. Schwaller, J. Michler, Electrolytic deposition of titania films as interference coatings on biomedical implants: microstructure, chemistry and nano-mechanical properties, Thin Solid Films 494, 1–2 (2006) 279–286.

[68] P. Evans, D.W. Sheel, Photoactive and antibacterial TiO_2 thin films on stainless steel, Surf. Coat. Technol. 201, 22–23 (2007) 9319–9324.

[69] K. Shiraishi, H. Koseki, T. Tsurumoto, K. Baba, M. Naito, K. Nakayama, H. Shindo, Antibacterial metal implant with a TiO_2-conferred photocatalytic bactericidal effect against *Staphylococcus aureus*, Surf. Interface Anal. 41, 1 (2009) 17–22.

[70] Y. Kubota, T. Shuin, C. Kawasaki, M. Hosaka, H. Kitamura, R. Cai, H. Sakai, K. Hashimoto, A. Fujishima, Photokilling of T-24 human bladder cancer cells with titanium dioxide, Br. J. Cancer 70, 6 (1994) 1107–1111.

[71] H. Irie, K. Sunada, K. Hashimoto, Recent developments in TiO_2 photocatalysis: novel applications to interior ecology materials and energy saving systems, Electrochem. 72, 12 (2004) 807–812.

[72] S.-H. Lee, S. Pumprueg, B. Moudgil, W. Sigmund, Inactivation of bacterial endospores by photocatalytic nanocomposites, Colloids Surf., B. 40, 2 (2005) 93–98.

[73] K.P. Kühn, I.F. Chaberny, K. Massholder, M. Stickler, V.W. Benz, H.-G. Sonntag, L. Erdinger, Disinfection of surfaces by photocatalytic oxidation with titanium dioxide and UVA light, Chemosphere 53, 1 (2003) 71–77.

[74] Y. Kikuchi, K. Sunada, T. Iyoda, K. Hashimoto, A. Fujishima, Photocatalytic bactericidal effect of TiO_2 thin films: dynamic view of the active oxygen species responsible for the effect, J. Photochem. Photobiol., A. 106, 1–3 (1997) 51–56.

[75] P. Evans, T. English, D. Hammond, M.E. Pemble, D.W. Sheel, The role of SiO_2 barrier layers in determining the structure and photocatalytic activity of TiO_2 films deposited on stainless steel, Appl. Catal., A. 321, 2 (2007) 140–146.

[76] L. Caballero, K.A. Whitehead, N.S. Allen, J. Verran, Inactivation of *Escherichia coli* on immobilized TiO_2 using fluorescent light, J. Photochem. Photobiol., A. 202, 2–3 (2009) 92–98.

[77] J.C. Yu, W. Ho, J. Lin, H. Yip, P.K. Wong, Photocatalytic activity, antibacterial effect, and photoinduced hydrophilicity of TiO_2 films coated on a stainless steel substrate, Environ. Sci. Technol. 37, 10 (2003) 2296–2301.

[78] K. Sunada, T. Watanabe, K. Hashimoto, Bactericidal activity of copper-deposited TiO_2 thin film under weak UV light illumination, Environ. Sci. Technol. 37, 20 (2003), 4785–4789.

[79] M.-S. Wong, W.-C. Chu, D.-S. Sun, H.-H. Huang, J.-H. Chen, P.-J. Tsai, N.-T. Lin, M.-S. Yu, S.-F. Hsu, S.-L. Wang, H.-H. Chang, Visible-light-induced bactericidal activity of a nitrogen-doped titanium photocatalyst against human pathogens, Appl. Environ. Microbiol. 72, 9 (2006) 6111–6116.

[80] J.A. Rengifo-Herrera, E. Mielczarski, J. Mielczarski, N.C. Castillo, J. Kiwi, C. Pulgarin, *Escherichia coli* inactivation by N, S co-doped commercial TiO_2 powders under UV and visible light, Appl. Catal., B. 84, 3–4 (2008) 448–456.

[81] J.A. Rengifo-Herrera, K. Pierzchała, A. Sienkiewicz, L. Forró, J. Kiwi, C. Pulgarin, Abatement of organics and *Escherichia coli* by N, S co-doped TiO_2 under UV and visible light. Implications of the formation of singlet oxygen (1O2) under visible light, Appl. Catal., B. 88, 3–4 (2009) 398–406.

[82] J.A. Rengifo-Herrera, J. Kiwi, C. Pulgarin, N, S co-doped and N-doped Degussa P-25 powders with visible light response prepared by mechanical mixing of thiourea and urea. Reactivity towards *E. coli* inactivation and phenol oxidation, J. Photochem. Photobiol., A. 205, 2–3 (2009) 109–115.

[83] J.A. Rengifo-Herrera, K. Pierzchala, A. Sienkiewicz, L. Forró, J. Kiwi, J. E. Moser, C. Pulgarin, Synthesis, characterization, and photocatalytic activities of nanoparticulate N,S-codoped TiO_2 having different surface-to-volume ratios, J. Phys. Chem. C 114 (2010) 2717–2723.

[84] B.A. Walther, P.W. Ewald, Pathogen survival in the external environment and the evolution of virulence, Biol. Rev. Camb. Philos. 79, 4 (2004) 849–869.

[85] K.-T. Chen, P.-Y. Chen, R.-B. Tang, Y.F. Huang, P.I. Lee, J.Y. Yang, H.Y. Chen, J. Bresee, E. Hummelman, R. Glass, Sentinel hospital surveillance for rotavirus diarrhea in Taiwan, 2001-2003, J. Infect. Dis. 192, 1 (2005) S44–S48.

[86] N. Laot, N. Narkis, I. Neeman, R. Armon, TiO_2 photocatalytic inactivation of selected microorganisms under various conditions: sunlight, intermittent and variable irradiation intensity, CdS supplementation and entrapment of TiO_2 into sol-gel, J. Adv. Oxid. Technol. 4 (1999) 97–102.

[87] Y.W. Cheng, R.C.Y. Chan, P.K. Wong, Disinfection of *Legionella pneumophila* by photocatalytic oxidation, Water Res. 41, 4 (2007) 842–852.

[88] Center for Disease Control and Prevention, Hospital Control Practices Advisory

Committee, Guidelines for prevention of nosocomial pneumonia, CDC's Morbidity and Mortality Weekly Reporter, 46 (1997) 1–79.

[89] C. Chawengkijwanich, Y. Hayata, Development of TiO_2 powder-coated food packaging film and its ability to inactivate *Escherichia coli* in vitro and in actual tests, Int. J. Food Microbiol. 123, 3 (2008) 288–292.

[90] A.K. Benabbou, Z. Derriche, C. Felix, P. Lejeune, C. Guillard, Photocatalytic inactivation of *Escherichia coli*: Effect of concentration of TiO_2 and microorganism, nature, and intensity of UV irradiation, Appl. Catal., B. 76, 3–4 (2007) 257–263.

[91] Y. Liu, J. Li, X. Qiu, C. Burda, Bactericidal activity of nitrogen-doped metal oxide nanocatalysts and the influence of bacterial extracellular polymeric substances (EPS), J. Photochem. Photobiol., A. 190, 1 (2007) 94–100.

[92] H. Matsubara, M. Takada, S. Koyama, Research on application of photoactive TiO_2 to paper, Kinoshi Kenkyu Kaishi 34 (1996) 36–39.

[93] J. Blanco, S. Malato, P. Fernández-Ibañez, D. Alarcón, W. Gernjak, M.I. Maldonado, Review of feasible solar energy applications to water processes, Renewable Sustainable Energy Rev. 13, 6–7 (2009) 1437–1445.

[94] K.S. Yao, D.Y. Wang, W.Y. Ho, J.J. Yan, K.C. Tzeng, Photocatalytic bactericidal effect of TiO_2 thin film on plant pathogens, Surf. Coat. Technol. 201, 15 (2007) 6886–6888.

[95] K.S. Yao, D.Y. Wang, C.Y. Chang, K.W. Weng, L.Y. Yang, S.J. Lee, T.C. Cheng, C.C. Hwang, Photocatalytic disinfection of phytopathogenic bacteria by dye-sensitized TiO_2 thin film activated by visible light, Surf. Coat. Technol. 202, 4–7 (2007) 1329–1332.

[96] C. Sichel, M. de Cara, J. Tello, J. Blanco, P. Fernández-Ibáñez, Solar photocatalytic disinfection of agricultural pathogenic fungi: *Fusarium* species, Appl. Catal., B. 74, 1–2 (2007) 152–160.

[97] D. Sawada, M. Ohmasa, M. Fukuda, K. Masuno, H. Koide, S. Tsunoda, K. Nakamura, Disinfection of some pathogens of mushroom cultivation by photocatalytic treatment, Mycosci. 46, 1 (2005) 54–60.

[98] R. Dillert, S. Vollmer, M. Schober, J. Theurich, D. Bahnemann, H.-J. Arntz, K. Pahlmann, J. Wienefeld, T. Schmedding, G. Sager, Pilot plant studies on the photocatalytic oxidation of a pretreated industrial wastewater, GWF Wasser Abwasser 140, 4 (1999) 293–297.

[99] R. Dillert, S. Vollmer, E. Gross, M. Schober, D. Bahnemann, J. Wienefeld, K. Pahlmann, T. Schmedding, H.-J. Arntz, G. Sager, Solar-catalytic treatment of an industrial wastewater, Zeitschrift fur Physikalische Chemie 213, 2 (1999) 141–147.

[100] R. Dillert, S. Vollmer, M. Schober, J. Theurich, D. Bahnemann, H.-J. Arntz, K. Pahlmann, J. Wienefield, T. Schmedding, G. Sager, Photokatalytische behandlung eines industriabwassers im stegdoppelplattenreaktor, Chemie Ingenieur Tecnik 71 (1999) 396–399.

[101] D. Bahnemann, Photocatalytic water treatment: solar energy applications, Sol. Energy 77, 5 (2004) 445–459.

[102] J. Blanco, S. Malato, Solar photocatalytic mineralization of real hazardous waste water at pre-industrial level, in Proceedings of the ASME/JSME/JSES International Solar Energy Conference, D. E. Klett, R. E. Hogan, and T. Tanaka, Eds., pp. 103–109, San Francisco, CA, USA, 1994.

[103] M. Anhegen, D.Y. Goswami, G. Svedberg, Photocatalytic treatment of wastewater from 5-fluoracil manufacturing, in Proceedings of the ASME/JSME/JSES International Solar Energy Conference, Maui, HI, 1995.

[104] A.H. Zaidi, D.Y. Goswami, A.C. Wilkie, Solar photocatalytic post-treatment of anaerobically digested distillery effluent, in Proceedings of the American Solar Energy Society Annual Conference, pp. 51–56, Minneapolis, MN, USA, 1995.

[105] C.S. Turchi, L. Edmunson, D.F. Ollis, Application of heterogeneous photocatalysis for the destruction of organic contaminants from a paper mill alkali extraction process, in Proceedings of the TAPPI 5th International Symposium on Wood and Pulping Chemistry, Raleigh, NC, USA, 1989.

[106] O. Seven, B. Dindar, S. Aydemir, D. Metin, M.A. Ozinel, S. Icli, Solar photocalytic disinfection of a group of bacteria and fungi aqueous suspensions with TiO_2, ZnO and sahara desert dust, J. Photochem. Photobiol., A. 165, 1–3 (2004) 103–107.

[107] M. Otaki, T. Hirata, S. Ohgaki, Aqueous microorganisms inactivation by photocatalytic reaction, Water Sci. Technol. 42, 3–4 (2000) 103–108.

[108] T. Kato, T. Shibata, H. Tohma, M. Tamura, O. Miki, Degredation of norovirus in sewage treatment water by photocatalytic ultraviolent disinfection, Nippon Steel Technical Report, pp. 41–44, 1992.

[109] R. Dillert, U. Siemon, D. Bahnemann, Photocatalytic disinfection of municipal wastewater, Chem. Eng. Technol. 21, 4 (1998) 356–358.

[110] J.A. Herrera Melián, J.M. Doña Rodríguez, A. Viera Suárez, E. Tello Rendón, C. Valdés do Campo, J. Arana, J. Pérez Peña, The photocatalytic disinfection of urban waste waters, Chemosphere 41, 3 (2000) 323–327.

[111] A.G. Rincón, C. Pulgarin, Bactericidal action of illuminated TiO_2 on pure *Escherichia coli* and natural bacterial consortia: post-irradiation events in the dark and assessment of the effective disinfection time, Appl. Catal., B. 49, 2 (2004) 99–112.

[112] A.G. Rincón, C. Pulgarin, Photocatalytical inactivation of *E. coli*: effect of (continuous-intermittent) light intensity and of (suspended-fixed) TiO_2 concentration, Appl. Catal., B. 44, 3 (2003) 263–284.

[113] Y. Li, M. Ma, X. Wang, X. Wang, Inactivated properties of activated carbon-supported TiO_2 nanoparticles for bacteria and kinetic study, J. Environ. Sci. 20, 12 (2008) 1527–1533.

[114] H. Choi, A.C. Sofranko, D.D. Dionysiou, Nanocrystalline TiO_2 photocatalytic membranes with a hierarchical mesoporous multilayer structure: synthesis, characterization, and multifunction, Adv. Funct. Mater. 16, 8 (2006) 1067–1074.

[115] H. Choi, E. Stathatos, D.D. Dionysiou, Photocatalytic TiO_2 films and membranes for the development of efficient wastewater treatment and reuse systems, Desalination 202, 1–3

(2007) 199–206.

[116] Y. Liu, J. Li, X. Qiu, C. Burda, Novel TiO_2 nanocatalysts for wastewater purification: tapping energy from the sun, Water Sci. Technol. 54, 8 (2006) 47–54.

[117] P.H. Gleick, World's Water 2004–2005, Island Press, Washington, DC, USA, 2004.

[118] L. Villen, F. Manjon, D. Garcia-Fresnadillo, G. Orellana, Solar water disinfection by photocatalytic singlet oxygen production in heterogeneous medium, Appl. Catal., B. 69 (2006) 1–9.

[119] I. Najm, R.R. Trussel, New and emerging drinking water treatment technologies, in: Identifying Future Drinking Water Contaminants, National Academy, Washington, DC, USA, 1999.

[120] M. Boyle, C. Sichel, P. Fernández-Ibáñez, G.B. Arias-Quiroz, M. Iriarte-Puña, A. Mercado, E. Ubomba-Jaswa, K.G. McGuigan, Bactericidal effect of solar water disinfection under real sunlight conditions, Appl. Environ. Microbiol. 74, 10 (2008) 2997–3001.

[121] E. Ubomba-Jaswa, C. Navntoft, I. Polo-López, P. Fernández-Ibáñez, K. G. McGuigan, Solar disinfection of drinking water (SODIS): an investigation of the effect of UVA dose on inactivation efficiency, Photochem. Photobiol. Sci. 8, 5 (2009) 587–595.

[122] H. Gómez-Couso, M. Fontán-Saínz, C. Sichel, P. Fernández-Ibáñez, E. Ares-Mazás, Solar disinfection of turbid waters experimentally contaminated with *Cryptosporidium parvum* oocysts under real field conditions, Trop. Med. Int. Health 14, 6 (2009) 1–9.

[123] E. Ubomba-Jaswa, P. Fernández-Ibáñez, C. Navntoft, M. Inmaculada Polo-López, K. G. McGuigana, Investigating the microbial inactivation efficiency of a 25 L batch solar disinfection (SODIS) reactor enhanced with a compound parabolic collector (CPC) for household use, J. Chem. Technol. Biotechnol. 85, 8 (2010) 1028–1037.

[124] O.A. McLoughlin, P. Fernández-Ibáñez, W. Gernjak, S. Malato Rodriguez, L.W. Gill, Photocatalytic disinfection of water using low cost compound parabolic collectors, Sol. Energy 77, 5 (2004) 625–633.

[125] A.-G. Rincón, C. Pulgarin, Field solar *E. coli* inactivation in the absence and presence of TiO_2: is UV solar dose an appropriate parameter for standardization of water solar disinfection? Sol. Energy 77, 5 (2004) 635–648.

[126] C. Navntoft, P. Araujo, M.I. Litter, M.C. Apella, D. Fernández, M.E. Puchulu, M. del V. Hidalgo, M.A. Blesa, Field tests of the solar water detoxification SOLWATER reactor in Los Pereyra, Tucumán, Argentina, J. Sol. Energy Eng. – T. ASME 129, 1 (2007) 127–134.

[127] E.F. Duffy, F. Al Touati, S.C. Kehoe, O.A. McLoughlin, L.W. Gill, W. Gernjak, I. Oller, M.I. Maldonado, S. Malato, J. Cassidy, R.H. Reed, K.G. McGuigan, A novel TiO_2-assisted solar photocatalytic batch-process disinfection reactor for the treatment of biological and chemical contaminants in domestic drinking water in developing countries, Sol. Energy, 77, 5 (2004) 649–655.

[128] F. Méndez-Hermida, E. Ares-Mazás, K.G. McGuigan, M. Boyle, C. Sichel, P. Fernández-Ibáñez, Disinfection of drinking water contaminated with *Cryptosporidium parvum* oocysts under natural sunlight and using the photocatalyst TiO_2, J. Photochem.

Photobiol., B. 88, 2–3 (2007) 105–111.

[129] H. Gómez-Couso, M. Fontán-Sainz, J. Fernández-Alonso, E. Ares-Mazás, Excystation of *Cryptosporidium parvum* at temperatures that are reached during solar water disinfection, Parasitol.136, 4 (2009) 393–399.

[130] K.G. McGuigan, F. Méndez-Hermida, J.A. Castro-Hermida, E. Ares-Mazás, S.C. Kehoe, M. Boyle, C. Sichel, P. Fernández-Ibáñez, B.P. Meyer, S. Ramalingham, E.A. Meyer, Batch solar disinfection inactivates oocysts of *Cryptosporidium parvum* and cysts of *Giardia muris* in drinking water, J. Appl. Microbiol. 101, 2 (2006) 453–463.

[131] A.G. Rincón, C. Pulgarin, Effect of pH, inorganic ions, organic matter and H_2O_2 on *E. coli* K12 photocatalytic inactivation by TiO_2: implications in solar water disinfection, Appl. Catal., B. 51, 4 (2004) 283–302.

[132] J. Marugán, R. van Grieken, C. Sordo, C. Cruz, Kinetics of the photocatalytic disinfection of *Escherichia coli* suspensions, Appl. Catal., B. 82, 1–2 (2008) 27–36.

[133] J.C. Ireland, P. Klostermann, E.W. Rice, R.M. Clark, Inactivation of *Escherichia coli* by titanium dioxide photocatalytic oxidation, Appl. Environ. Microbiol. 59, 5 (1993) 1668–1670.

[134] J. Wist, J. Sanabria, C. Dierolf, W. Torres, C. Pulgarin, Evaluation of photocatalytic disinfection of crude water for drinking-water production, J. Photochem. Photobiol., A. 147, 3 (2002) 241–246.

[135] C.A. Murray, E.H. Goslan, S.A. Parsons, TiO_2/UV: single stage drinking water treatment for NOM removal? J. Environ. Eng. Sci. 6, 3 (2007) 311–317.

[136] S.-C. Kim, D.-K. Lee, Inactivation of algal blooms in eutrophic water of drinking water supplies with the photocatalysis of TiO_2 thin film on hollow glass beads, Water Sci. Technol. 52, 9 (2005) 145–152.

[137] A.J. Feitz, T.D. Waite, G.J. Jones, B.H. Boyden, P.T. Orr, Photocatalytic degradation of the blue-green algal toxin Microcystin-LR in a natural organic-aqueous matrix, Environ. Sci. Technol. 33, 2 (1999) 243–249.

[138] D.Y. Goswami, J. Klausner, G.D. Mathur, A. Martin, K. Schanze, P. Wyness, C. Turchi, E. Marchand, Solar photocatalytic treatment of groundwater at Tyndall AFB, field test results, in: Proceedings of the American Solar Energy Society Annual Conference, Washington, DC, USA, 1993.

[139] P. Fernández-Ibáñez, C. Sichel, M.I. Polo-López, M. de Cara-García, J.C. Tello, Photocatalytic disinfection of natural well water contaminated by *Fusarium solani* using TiO_2 slurry in solar CPC photo-reactors, Catal. Today 144, 1-2 (2009) 62–68.

[140] M.I. Polo-López, P. Fernández-Ibáñez, I. García-Fernández, I. Oller, I. Salgado-Tránsito, C. Sichel, Resistance of *Fusarium sp* spores to solar TiO_2 photocatalysis: influence of spore type and water (scaling-up results), J. Chem. Technol. Biotechnol. 85 (2010) 1038–1048.

Appendix C:
Visible light induced degradation and disinfection using multifunctional Ag/AgCl-AC composite photocatalysts

Joanne Gamage McEvoy, Wenquan Cui, Zisheng Zhang

Proceedings of the 2013 American Institute of Chemical Engineers Annual Meeting,
Applied Environmental Catalysis Session, paper 405g.

C.1 Introduction

Photocatalysis is a process where a material is excited by light to produce electron-hole pairs that can initiate a series of reduction and oxidation reactions causing the degradation and eventual mineralization of organic pollutants in the presence of oxygen and water. The reactive radicals may also interact with biological species to cause their inactivation [1]. Photocatalysis suffers low solar efficiencies due to the traditional use of TiO_2 catalyst, which is only excited by ultraviolet light not abundant in solar radiation. One strategy proposed for improving visible light-induced photocatalytic efficiency is through the use of silver/silver halide materials (Ag/AgX; X = Cl, Br) [2, 3], which act through surface plasmon resonance-enhanced light absorption and charge carrier separation mechanisms. The photocatalyst efficiencies can also be increased by immobilization onto activated carbon (AC), where a common contact interface between solids allows the pollutants to be adsorbed by AC, and migrate continuously to the supported photocatalyst [4]. In this study, novel visible light active adsorptive photocatalyst Ag/AgCl-activated carbon (AC) composites are prepared and investigated for their degradative and disinfective capabilities under visible light. These composites combine the enhanced visible light absorption and photocatalytic efficiency gained using plasmonic nanostructures on silver halides with the synergy of adsorption by incorporation with an AC matrix to create hybrid photocatalysts.

C.2 Experimental

Synthesis of Ag/AgCl-AC composites

Ag/AgCl-AC composites were prepared by an impregnation-precipitation-photoreduction method. In a typical synthesis, 1 g of unmodified Darco G60 activated carbon (100 mesh, Sigma-Aldrich) was impregnated with 20 mL of aqueous $AgNO_3$ (ACS grade, MP Biomedicals Inc.) of a certain concentration. The mixture was sonicated for 10 minutes, and stirred magnetically for 6 hours. 20 mL of HCl (reagent-grade, Fisher Scientific) was then added dropwise in a 50% stoichiometric excess, and the mixture was magnetically stirred for 2 hours. The reduction of some AgCl was then carried out via irradiation by a 300 W UV-Vis light source (Ushio ELH) for 1 hour. The obtained composite was filtered and dried in air overnight. The prepared Ag/AgCl-AC composite powders were gently ground in an agate

mortar before use. The samples were denoted by weight ratio of Ag to AC (Ag: AC), calculated as if all of the AgCl was reduced to Ag. Reference Ag/AgCl was prepared using the same procedures but omitting the AC impregnation step, and AgCl was prepared similarly without the photoreduction step.

Characterization

X-ray diffraction (XRD) patterns of all prepared powders were collected using a Rigaku Ultima IV XRD with a Cu K(α) source (λ = 0.15418 nm) operating at 40 kV and 44 mA. The morphology of the samples (coated in Au/Pd alloy using an Anatech Hummer VII sputter coater) was studied using Tescan VegaII XMU field emission scanning electron microscope (SEM). Ultraviolet-visible (UV-Vis) diffuse reflectance spectra were measured using a UV-Vis spectrophotometer (Puxi, UV 1901) equipped with an integrating sphere attachment and on a Thermo Evolution 300 spectrophotometer equipped with a Praying Mantis diffuse reflectance accessory over the range of 230 – 800 nm.

Photocatalytic degradation

To quantify the photocatalytic degradation of methyl orange using the composite powders, a slurry reactor was set up in a reflective housing to prevent outside light from entering the system. Illumination was provided by a 300 W ELH tungsten halide bulb (Ushio) with a UV filter (Kenko Zeta, λ > 410 nm, transmittance > 90%) at a 10 cm distance from the beaker. Cooling was provided by an external cooling jacket, and the temperature of the reaction was controlled to $20^{o}C \pm 2$. For the photodegradation tests, 200 mL of MO solution was allowed to equilibriate in the dark with 0.5 g L^{-1} of catalyst under constant magnetic stirring at 180 rpm for 2 hours prior to each experiment. After the pseudo-equilibrium was reached, irradiation was supplied and the photocatalytic degradation was then studied for 2.5 hours. For all tests, samples were drawn periodically and were centrifuged and the supernatant analyzed using a spectrophometer (Genesys 10UV, ThermoScientific). The peak absorbance used for MO was λ = 463 nm. The removal efficiency was calculated according to:

$$Removal\ Efficiency\ (\%) = (C_o - C_t)/C_o \times 100 \qquad (C.1)$$

Where C_o denotes the initial pollutant concentration (mg L^{-1}), and C_t is the concentration at

time t (mg L^{-1}). C_o was taken as the adsorption equilibrium concentration after the dark adsorption time. The error associated to the experiments was estimated as the standard deviation between triplicate runs.

Photocatalytic disinfection

Wild-type *Escherichia coli* K-12 (TG1 strain) was used as a standard strain for all the bacterial inactivation studies. *E. coli* K-12 was chosen because it is known to be non-pathogenic and is a common model used in laboratory experiments. It was obtained from Dr. Christopher Q. Lan in the Department of Chemical and Biological Engineering at the University of Ottawa, and was maintained as a laboratory strain.

All inactivation trials were performed in triplicate, and all materials were sterilized for 20 minutes at 121^{o}C prior to use. For the disinfection studies, inactivation was measured by loss of culturability of the bacteria. Cultures were prepared by growing *E. coli* K-12 (TG1) aerobically in Luria-Bertani medium (Difco LB broth, Miller; containing 10 g L^{-1} tryptone, 5 g L^{-1} yeast extract, and 10 g L^{-1} NaCl) medium on a rotary shaker at 37^{o}C until the stationary phase was reached. The initial concentration from the overnight culture was determined from a serial dilution and plating procedure using a plated volume of 25 µL. Aliquots were spread in triplicate on LB agar plates for each dilution, and incubated at 37^{o}C for 18 hours. Bacterial enumeration was performed using standard plate counts (for viable and cultivable bacteria), where counts in the range of 30 – 300 colony forming units per plate were considered statistically significant and were used to calculate the cell concentration.

The temporal course of inactivation was studied using 50 mL of saline solution spiked with bacteria in a 100 mL Pyrex beaker. The initial bacterial suspension was prepared by centrifugation at 14 800 rpm for 5 minutes and resuspension in saline. This centrifugation and washing procedure was repeated three times to remove the growth media from the bacterial pellet. The initial concentration of the prepared *E. coli* in the reaction medium was controlled to ~10^6 colony forming units (CFU) mL^{-1}. The catalyst was added to the bacterial suspension at a loading of 5 g L^{-1}, and the mixture was magnetically stirred at 160 rpm under

irradiation. During disinfection, the temperature was maintained constant at 20^{o}C ± 2 using a water bath, and samples were collected periodically. The samples were serially diluted in saline and then spread onto LB agar plates using aliquot volumes ranging from 25 – 100 µL. The plates were incubated and bacteria enumerated using the standard plate count method. The diffusion of silver ions (Ag^{+}) from the prepared photocatalyst was measured using inductively coupled plasma mass spectrometry (ICP-MS) on an Agilent HP 4500. For the diffusion tests, 5 g L^{-1} of prepared catalyst in distilled deionized water was magnetically stirred at 160 rpm in the dark for 7 days, and 1 mL samples were withdrawn periodically. The samples were centrifuged and acidified before analysis of the supernatant. For all ICP measurements, the analyses were performed for triplicate samples.

C.3 Results and discussion

Photocatalyst characterization

The phase structure and crystallinity of the prepared samples were investigated by XRD. Comparison of the obtained patterns for the prepared composites and for pure AC and Ag/AgCl are shown in Figure C.1. The prepared composites exhibited similar patterns and crystallinities to pure Ag/AgCl, as indicated by the peak positions and intensities. The diffraction peaks were indexed to face centered cubic AgCl (JCPDS card # 31-1238) with lattice constants of a = 5.545 – 5.549 Å. The major diffraction peaks for the (111) plane at 38.1^{o} and for the (200) plane at 44.3^{o} for metallic Ag (JCPDS card #01-087-0597) were observed for the pure Ag/AgCl material, implying that *in situ* reduction was able to induce the transformation of some AgCl to Ag. However, the peaks associated to metallic silver could not be observed in Ag/AgCl-AC composites, which may have been due to their low content, small particle sizes, and high dispersion of on the surface of Ag/AgCl-AC [5].

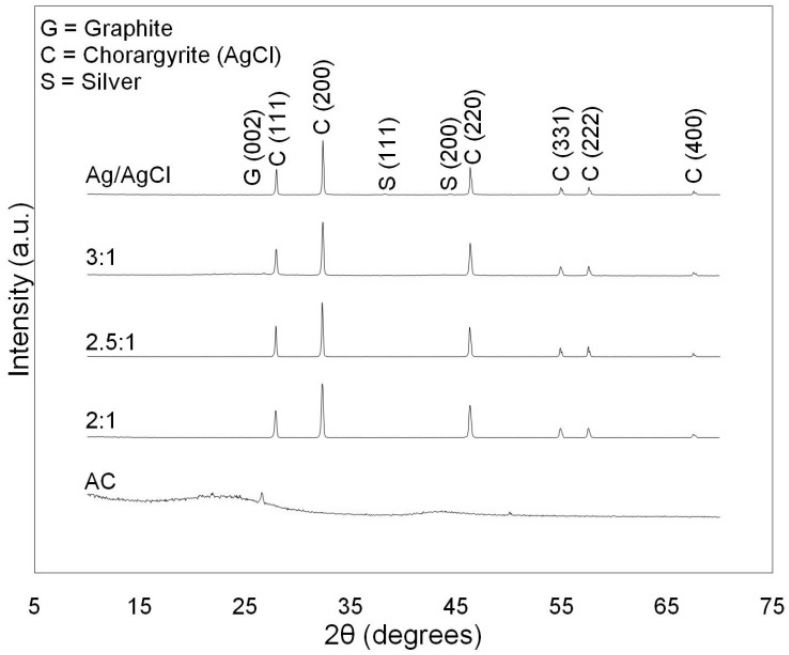

Figure C.1: XRD patterns for AC, Ag/AgCl, and various compositions of Ag/AgCl-AC

To further investigate the morphology of Ag/AgCl-AC, SEM imaging was performed, and the results are presented in Figure C.2. The deposition of Ag/AgCl was found to form clusters resulting in high coverage of AC, although some exposed surfaces of the textured carbon host material were observed. The AgCl particles in Ag/AgCl-AC were found by SEM to range from 470 nm to 1.06 μm, and the reduced Ag particles were approximately 110 nm to 150 nm. The photochemical reduction *in situ* has been reported to generate Ag atoms that aggregate to form silver nanograins that deposit on the surface of AgCl particles [6], in good agreement with the results obtained in this study.

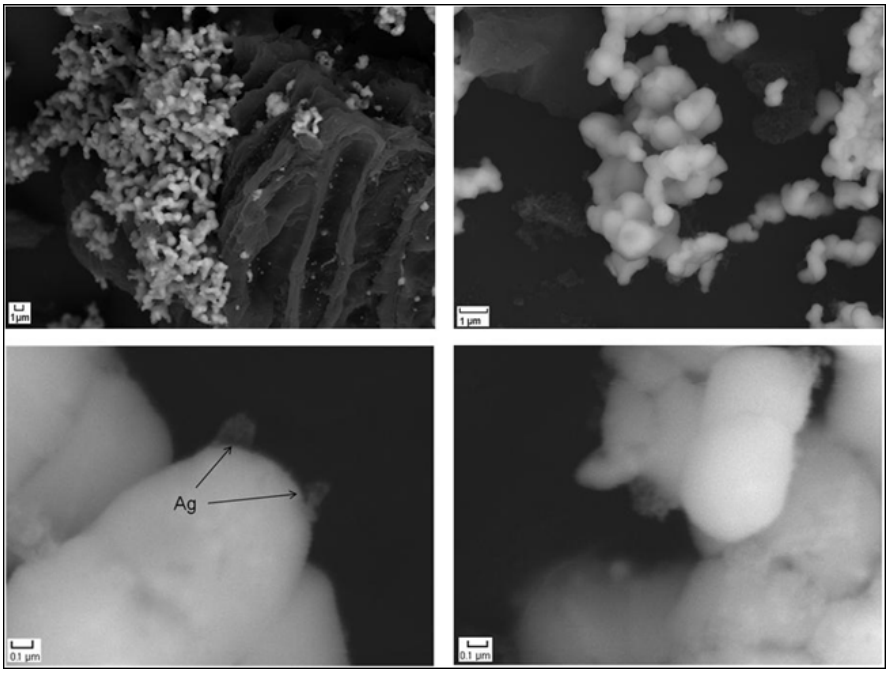

Figure C.2: SEM images of prepared Ag/AgCl-AC composite (2.5:1)

The UV-Vis absorption data for a representative Ag/AgCl-AC composite (2.5:1), as-prepared Ag/AgCl, and unreduced AgCl are given in Figure C.3. For all the samples, an absorbance edge at ~385 nm was observed due to the band gap absorption of AgCl. Compared to unreduced AgCl, the prepared Ag/AgCl catalyst also showed a broad absorption band in the range of 400–800 nm, which was thought to be due to the surface plasmon resonance of Ag NPs produced during photoreduction. The broadness of the peak was attributed to multiple plasmonic oscillation frequencies present because of variation in shapes and diameters of Ag NP clusters formed [3]. The Ag/AgCl-AC composite also showed broad, strong absorbance in the visible light region, which indicated that it possessed good applicability as a visible light active photocatalyst.

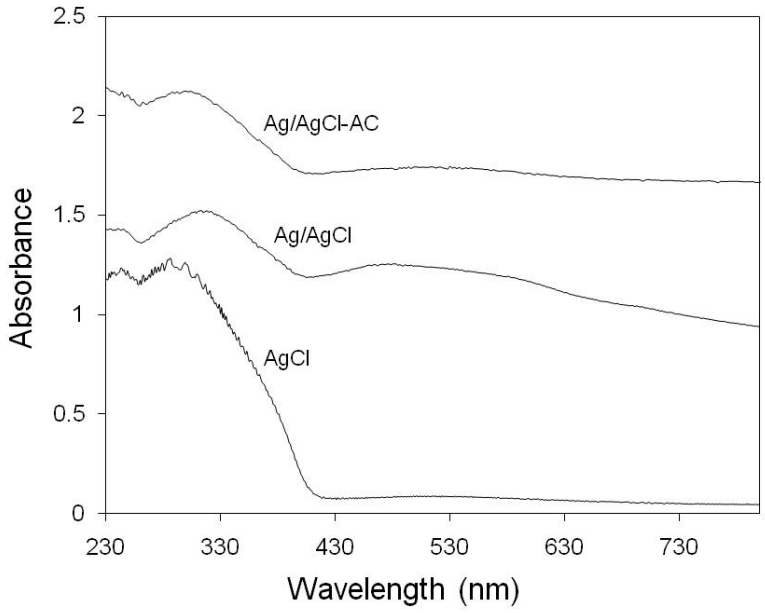

Figure C.3: UV-Vis absorption spectra of 2.5:1 Ag/AgCl-AC composite, as-prepared Ag/AgCl, and unreduced AgCl, respectively

Photocatalytic degradation of MO

To investigate the photocatalytic activity of the Ag/AgCl-AC composites, degradation runs were carried out using a 2 hour dark adsorption time, followed by visible light irradiation. The results obtained are shown in Figure C.4, as amount of MO removed from solution per weight of catalyst used. The composite catalysts exhibited a sharp change in the removal rate of MO upon illumination, after adsorption pseudo-equilibrium was reached. This was thought to be due to visible light absorption and consequent photocatalytic effect in the composites, removing the MO pollutant by degradation. The results also suggested that the prepared Ag/AgCl-AC was able to remove MO from solution by a dynamic adsorption-photocatalysis mechanism under visible light.

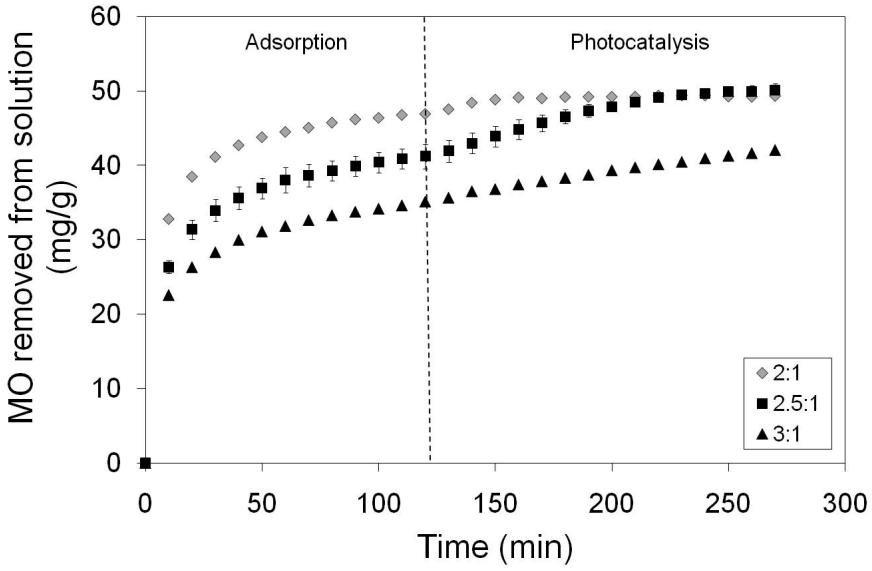

Figure C.4: Adsorption and subsequent photocatalysis using 2:1, 2.5:1, and 3:1 Ag/AgCl-AC composites. (C_o = 25 mg L^{-1}, loading = 0.5 g L^{-1}) – *representative error bars shown*

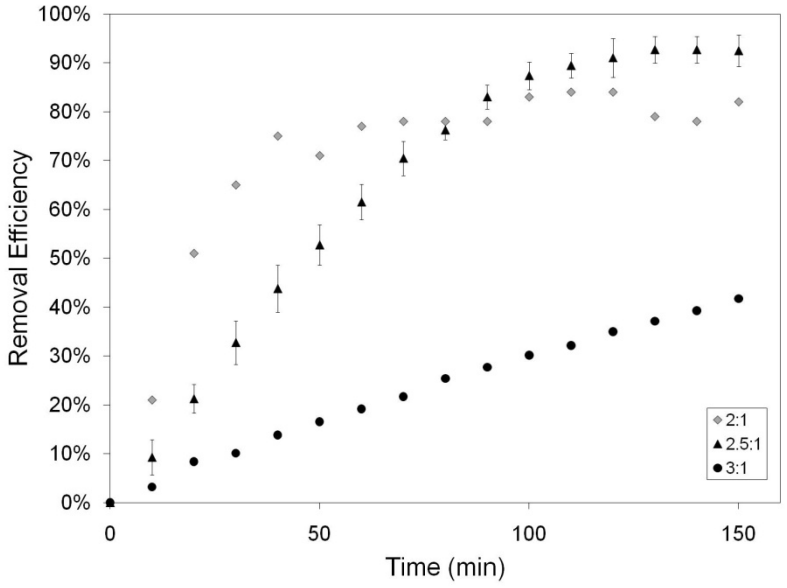

Figure C.5: Photocatalytic removal efficiency as a function of time for 2:1, 2.5:1, and 3:1 Ag/AgCl-AC composites, respectively. (C_o = 25 mg L^{-1}, loading = 0.5 g L^{-1}) – *representative error bars shown*

The data from the prolonged adsorption-photocatalysis studies shown in Figure C.4 were normalized using the concentrations at the end of dark adsorption as the initial concentrations

for photocatalytic reaction, and the calculated temporal removal efficiencies for photocatalysis are given in Figure C.5. The Langmuir-Hinshelwood kinetic expression for heterogeneous surface reactions was used to describe the experimental data, where the reaction rate is given by the following expression:

$$-dC/dt = K_{ads}\, k_{LH}\, C/(1+K_{ads}C) \quad \text{(C.2a)}$$

Where K_{ads} is the Langmuir Hinshelwood adsorption coefficient (L mg^{-1}), and k_{LH} is the reaction rate constant (mg L^{-1} min^{-1}). The Langmuir Hinshelwood constants were calculated by minimization of the sum of square errors function, and the results are given in Table C.1 for the 2.5:1 and 3:1 composites, respectively.

Table C.1: Calculated Langmuir-Hinshelwood kinetic parameters for Ag/AgCl-AC composites

Ag/AgCl:AC Ratio	**k_{LH} (L mg^{-1})**	**K_{ads} (mg L^{-1} min^{-1})**	**SSE**	**R^2**
2.5:1	0.039	0.523	0.238	0.981
3:1	0.117	0.0695	0.0357	0.998

The obtained Langmuir-Hinshelwood kinetic constants suggested that as the proportion of photocatalyst was increased, the photocatalytic reaction rate increased. However, the adsorption rate simultaneously decreased, which was thought to be due to the loss of surface area caused by pore-blocking from excessive photocatalyst loading. Therefore, an appropriate balance between adsorptive and photocatalytic capabilities should be considered to achieve acceptable dynamic behaviour in the photosystem. As a preliminary optimum, the 2.5:1 composite was selected for further study.

***Photocatalytic disinfection of E. coli* K-12**

The antibacterial and photocatalytic inactivation properties of Ag/AgCl-AC were evaluated using Gram-negative *E. coli* as a model microorganism, since it is an indicator of faecal contamination [1]. To evaluate the temporal course of inactivation due to photocatalysis, a standard plate count method was used to quantify changes to viable and cultivable bacterial concentrations during the experiment. A comparison of inactivation curves for photolysis (no catalyst), AC equivalent, dark control (no light), and the prepared Ag/AgCl-AC composite

are given in Figure C.6, with the final survival ratios obtained shown inset. The final survival ratios were calculated as the ratio of Nt/No, where Nt represents the bacterial concentration after the total inactivation time, t (t = 60) and No is the initial concentration (t = 0).

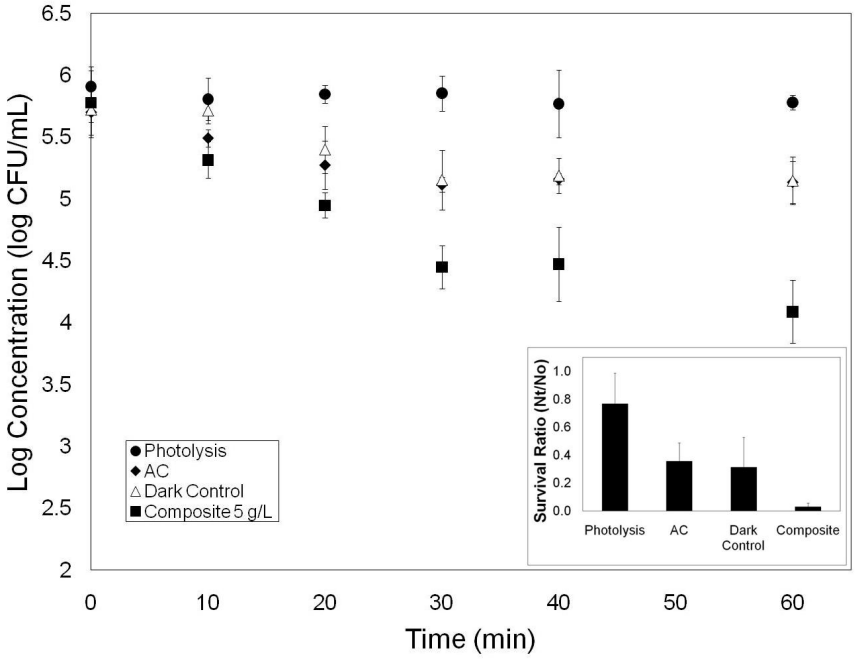

Figure C.6: Inactivation curves for photolysis, dark control, AC, and irradiated composite, final survival ratios shown inset. (composite loading = 5 g L^{-1}, pH = 5.5)

The photolysis run illustrated cell death in the absence of any adsorptive, antibacterial, or photocatalytic phenomena. The contribution of the visible light source in inactivating bacteria was found to be negligible, and a final survival ratio of 0.77 ± 0.22 was observed after 60 minutes. The AC trial, performed using an equivalent of AC as that in the 2.5:1 composite, indicated some adsorption of the bacteria onto the AC substrate, decreasing the population in solution (where concentration was quantified). For the AC-only process, a final survival ratio of 0.36 ± 0.13 was calculated. The adsorption was found to proceed gradually for the first 30 minutes, after which its effects were negligible. The dark control, which was performed using the composite in the absence of light, showed a similar temporal course as AC, with a final survival ratio of 0.31 ± 0.22. However, using the non-irradiated composite, both the biocidal effect of the Ag/AgCl and adsorption were possible mechanisms that played a role in decreasing concentration.

In terms of adsorption, the photocatalyst-adsorbent composites were thought to possess "egg-shell" structures, where photocatalyst occupied mainly the outside surface of AC, effectively decreasing total surface area by pore-blocking. Darco G60 AC possesses a high degree of porosity, and has a pore size distribution in the range of 5–30 nm [7]. Due to the average length of 2–4 μm and average diameter 0.5–1 μm for rod-shaped *E. coli*, the bacteria were thought to be mainly adsorbed on the outer surface of both the AC and the composite used in this study, and could not diffuse into the pores.

It was also reported previously that Ag/AgCl carried a mainly negative surface charge due to termination by chlorine ions, and polarization of the metallic Ag electron distribution relative to the AgCl interface [2], while unmodified AC was expected to carry a positive charge at the slightly acidic solution pH used (~5.5). The Gram-negative bacteria also would have had a negative charge at this pH. This implied that, although the AC adsorption trials contained equivalent mass loadings to those used in the composite, electrostatic interactions between the bacteria and photocatalytic materials may have been different between the two sets of data (AC and composite, respectively) due to the presence of photocatalyst on the outer surface of AC in the Ag/AgCl-AC composite. This difference was thought to affect the adsorption dynamics observed. Although adsorption behaviour was not expected to be similar between the AC and Ag/AgCl-AC trials, it was also difficult to confirm the presence of biocidal action of Ag/AgCl in the dark. However, it was suspected to play a role, where the biocidal action was thought to be attributable to the effects of silver contained in the composite catalyst.

The mechanism of biocidal action for silver nanoparticles and for silver-containing compounds has been linked primarily to the release of silver in its ionic form (Ag^+) [8]. The toxicity of Ag^+ ions at sub-micromolar concentrations is related to its interaction with enzymes in the respiratory chain reaction, resulting in uncoupling respiration from the synthesis of ATP [9]. Ag^+ is also able to bind with transport proteins, leading to proton leakage and induced collapse of proton motive force [10].

To probe the diffusion of silver ions from the composite catalyst in the dark in the slurry system, samples were analyzed using ICP-MS. The non-cumulative release of silver ions into 50 mL distilled deionized water under stirring in the dark was recorded, and the concentration was found to be 531 ± 93 ppb, 320 ± 81 ppb, and 121 ± 40 ppb after 1h, 24 h, and 7 days immersion, respectively. These values represented upper limits on the free silver ion concentration in solution, since ion release was tested in the absence of anionic ligands such as chlorine or organosulfur compounds such as thiols (–SH). In the experimental inactivation studies, the dissolved silver ion concentration from the Ag/AgCl-AC catalyst was attributable to contributions of the irreversible oxidation of metallic Ag to Ag (I), followed by its speciation, as well as the limited solubility of the AgCl itself (10^{-5} solubility limit). It was previously found through silver equilibrium speciation and pathway studies that, due to the high affinity binding of thiols ($K_{ads} \sim 10^{12}$), direct thiol transfer could occur at silver ion concentrations lower than the AgCl precipitation threshold and that thiol targets were typically abundant enough in experimental studies to receive all of the free silver [11]. Therefore, based on the toxicity of silver ions and the release behaviour observed, the contribution of ionic silver was thought to play some role in the biocidal activity of the photocatalyst.

There was an improved rate of bacterial inactivation upon irradiation of the composite photocatalyst, and a final survival ratio of 0.03 ± 0.025 was observed, corresponding to inactivation of 97 ± 2.5% of bacteria. This increased loss of bacterial cultivability was thought to be due to photocatalytic action on the bacteria when the photocatalyst was irradiated with visible light. Photons in the visible light region were absorbed by the photocatalyst and used to generate electron-hole pairs in the metallic silver. The photogenerated electrons and holes could then undergo further reaction with dissolved oxygen and water to form ROS species, which could interact with *E. coli* bacteria. The inactivation of *E. coli* K-12 using a similar plasmon-enhanced photocatalyst Ag/AgBr-Bi_2WO_6 under visible light was previously attributed mainly to the role of diffusing $^{\bullet}OH$ radical species produced [12]. Cell death due to the action of ROS species has been linked

to the peroxidation of functional groups in the cell wall bilayers leading to an increase in bilayer wall disorder. This increases fluidity of the cell wall, and causes eventual lysis through free efflux of intracellular components [13].

C.4 Conclusions

Composite photocatalysts based on Ag/AgCl and activated carbon were synthesized with various compositions by an impregnation-precipitation-photoreduction method. The prepared composites were thought to possess an "egg-shell" composite structure, and were able to absorb visible light due to surface plasmon resonance of the incorporated silver. The composites exhibited good photocatalytic activity for MO degradation and for *E. coli* K-12 inactivation.

C.5 References

[1] J. Marugán, R. van Grieken, C. Pablos, C. Sordo, Analogies and differences between photocatalytic oxidation of chemicals and photocatalytic inactivation of microorganisms, Water Res. 44, 3 (2010) 789–796.

[2] P. Wang, B. Huang, X. Qin, X. Zhang, Y. Dai, J. Wei, M.-H. Whangbo, Ag@AgCl: A highly efficient and stable photocatalyst active under visible light, Angew. Chem. Int. Ed. 47 (2008) 7931–7933.

[3] P. Wang, B. Huang, X. Zhang, X. Qin, H. Jin, Y. Dai, Z. Wang, J. Wei, J. Zhan, S. Wang, J. Wang, M.-H. Whangbo, Highly efficient visible-light plasmonic photocatalyst Ag@AgBr, Chem. Eur. J. 15 (2009) 1821–1824.

[4] J. Matos, J. Laine, J.-M. Herrmann, Synergy effect in the photocatalytic degradation of phenol on a suspended mixture of titania and activated carbon, Appl. Catal., B. 18 (1998) 281–291.

[5] C. Hu, T. Peng, X. Hu, Y. Nie, X. Zhou, J. Qu, H. He, Plasmon-induced photodegradation of toxic pollutants with Ag-AgI/Al_2O_3 under visible-light irradiation, J. Am. Chem. Soc. 132 (2010) 857–862.

[6] H. Zhang, X. Fan, X. Quan, S. Chen, H. Yu, Graphene sheets grafted Ag@AgCl hybrid with enhanced plasmonic photocatalytic activity under visible light, Environ. Sci. Technol. 45 (2011) 5731–5736.

[7] B. Gao, P.S. Yap, T.M. Lim, T.–T. Lim, Adsorption-photocatalytic degradation of Acid Red 88 supported TiO_2: Effect of activated carbon support and aqueous anions, Chem. Eng. J. 171 (2011) 1098–1107.

[8] Z. Xiu, Q. Zhang, H.L. Puppala, V.L. Colvin, P.J.J. Alvarez, Negligible particle-specific antibacterial activity of silver nanoparticles, Nano Lett. 12, 8 (2012) 4271–4275.

[9] K.B. Holt, A.J. Bard, Interaction of silver (I) ions with the respiratory chain of *Escherichia coli*: an electrochemical and scanning electrochemical study of the antimicrobial mechanism of micromolar Ag, Biochemistry 44 (2005) 13214–13223.

[10] C.-N. Lok, C.-M. Ho, R. Chen, Q.-Y. He, W.-Y. Yu, H. Sun, P.K.-H. Tam, J.-F. Chiu, C.-M. Che, Proteomic analysis of the mode of antibacterial action of silver nanoparticles, J. Proteome Res. 5 (2006) 916–924.

[11] J. Liu, D.A. Sonshine, S. Shervani, R. H. Hurt, Controlled release of biologically active silver from nanosilver surfaces, ACS Nano 4, 11 (2010) 6903–6913.

[12] L.-S. Zhang, K.-H. Wong, H.-Y. Yip, C. Hu, J.C. Yu, C.-Y. Chan, P.-K. Wong, Effective photocatalytic disinfection of *E. coli* K-12 using AgBr-Ag-Bi_2WO_6 nanojunction system irradiated by visible light: The role of diffusing hydroxyl radicals, Environ. Sci. Technol. 44 (2010) 1392–1398.

[13] C. Pulgarin, J. Kiwi, V.A. Nadtochenko, Mechanism of photocatalytic bacterial inactivation on TiO_2 films involving cell-wall damage and lysis, Appl. Catal., B. 128 (2012) 179–183.

Appendix D:
Scholarly contributions

The following scholarly contributions were made by the PhD candidate during the course of this graduate work.

D.1 Refereed journal articles (published or accepted)

[1] J. Gamage McEvoy, Z. Zhang, "Synthesis and characterization of magnetically separable Ag/AgCl-magnetic activated carbon composites for visible light induced photocatalytic detoxification and disinfection", *Applied Catalysis B: Environmental*, **2014**, in press.

[2] J. Gamage McEvoy, Z. Zhang, "Antimicrobial and photocatalytic disinfection mechanisms in silver-modified photocatalysts under dark and light conditions", *Journal of Photochemistry and Photobiology C: Photochemistry Reviews*, **2014**, 19, 62.

[3] Y. Liang, S. Lin, J. Hu, L. Liu, J. Gamage McEvoy, W. Cui, "Facile hydrothermal synthesis of nanocomposites Ag@AgCl/$K_2Ti_4O_9$ and photocatalytic degradation under visible light irradiation", *Journal of Molecular Catalysis A: Chemical*, **2014**, 383–384, 231.

[4] J. Gamage McEvoy, W. Cui, Z. Zhang, "Synthesis and characterization of Ag/AgCl-activated carbon composites for enhanced visible light photocatalysis", *Applied Catalysis B: Environmental*, **2014**, 144, 702.

[5] Y. Liang, M. Shao, L. Liu, J. Gamage McEvoy, J. Hu, W. Cui, "Synthesis of Cu_2S@$K_4Nb_6O_{17}$ composite and its photocatalytic activity for hydrogen production", *Catalysis Communications*, **2014**, 46, 10, 128.

[6] W. Cui, H. Wang, L. Liu, Y. Liang, J. Gamage McEvoy, "Plasmonic Ag@AgCl-intercalated $K_4Nb_6O_{17}$ composite for enhanced photocatalytic degradation of Rhodamine B under visible light", *Applied Surface Science*, **2013**, 283, 820.

[7] J. Gamage McEvoy, D.A. Bilodeau, W. Cui, Z. Zhang, "Visible-light-driven inactivation of *Escherichia coli* K-12 using an Ag/AgCl-activated carbon composite photocatalyst", *Journal of Photochemistry & Photobiology A: Chemistry,* **2013**, 267, 25.

[8] W. Cui, S. Ma, L. Liu, Y. Liang, J. Gamage McEvoy, "Photocatalytic activity of $Cd_{1-x}Zn_xS/K_2Ti_4O_9$ for Rhodamine B degradation under visible light illumination", *Applied Surface Science*, **2013**, 271, 171.

[9] Y. Liang, M. Shao, W. Cui, J. Gamage McEvoy, "Photocatalytic degradation of Rhodamine B by CdS-loaded $K_4Nb_6O_{17}$ nanocomposites prepared via reverse microemulsion", *Journal of Molecular Catalysis A: Chemical*, **2013**, 370, 87.

[10] A.A. Donaldson, A. Ye, J. Gamage McEvoy, Z. Zhang, "Rotating corrugated photoreactor design: Experimental and computational analysis of TiO_2-based photocatalysis", *American Institute of Chemical Engineers Journal*, **2012**, 59, 2, 560.

[11] J. Gamage McEvoy, W. Cui, Z. Zhang, "Degradative and disinfective properties of carbon-doped anatase-rutile TiO_2 mixtures under visible light irradiation", *Catalysis Today*, **2012**, 207, 191.

[12] P. Plouffe*, J. Gamage McEvoy*, R. Ball*, E.J. Anthony*, "Object-oriented simulation of an Endex reactor for separation of carbon dioxide from flue emissions", *Computers and Chemical Engineering*, **2012**, 40, 213. (*all authors contributed equally)

[13] Y. Wang, J. Gamage, Z. Zhang, "Extraction of taxanes from *Taxus canadensis* using dynamic pressurized liquid extraction", *Biotechnology and Bioprocess Engineering*, **2011**, 16, 4, 769.

[14] N. Ho, J. Gamage, Z. Zhang, "Photocatalytic degradation of eriochrome black dye in a rotating corrugated drum photocatalytic reactor", *International Journal of Chemical Reactor Engineering*, **2010**, 8, Article #A155.

[15] S.M. Meunier, J. Gamage, Z. Duvnjak, Z. Zhang, "Design and characterization of a novel rotating corrugated drum reactor for wastewater treatment", *International Journal of Photoenergy*, **2010**, Article ID 146743.

[16] J. Gamage, Z. Zhang, "Applications of photocatalytic disinfection: A review", *International Journal of Photoenergy*, **2010**, Article ID 764870.

D.2 Refereed conference proceedings

[17] J. Gamage McEvoy, W. Cui, Z. Zhang, "Visible light induced degradation and disinfection using multifunctional Ag/AgCl activated carbon composite photocatalysts", *Proceedings of the 2013 American Institute of Chemical Engineers Annual Meeting*, San Francisco, CA, Nov. 3–8, **2013**, paper 405g.

[18] Y. Liang, H. Wang, W. Cui, L. Liu, J. Gamage McEvoy, Z. Zhang, "Microwave-assisted synthesis of extra-fine Ag@AgI photocatalyst with high activity under visible light irradiation", *Proceedings of the 2013 American Institute of Chemical Engineers Annual Meeting*, San Francisco, CA, Nov. 3–8, **2013**, paper 22f.

D.3 Conference presentations

* presenting author

[19] J. Gamage McEvoy*, W. Cui, Z. Zhang, "Visible light induced degradation and disinfection using multifunctional Ag/AgCl activated carbon composite photocatalysts", *2013 American Institute of Chemical Engineers Annual Meeting*, San Francisco, CA, Nov. 3–8, **2013**.

[20] Y. Liang, H. Wang, W. Cui, L. Liu, J. Gamage McEvoy*, Z. Zhang, "Microwave-assisted synthesis of extra-fine Ag@AgI photocatalyst with high activity under visible light irradiation", *2013 American Institute of Chemical Engineers Annual Meeting*, San Francisco, CA, Nov. 3–8, **2013**.

[21] J. Gamage McEvoy*, W. Cui, Z. Zhang, "Degradation of methyl orange by a plasmonic photocatalyst-adsorbent: Ag/AgCl on activated carbon", *7th International Conference on Environmental Catalysis*, Lyon, France, Sept. 2–6, **2012**.

[22] W. Cui, S. Ma, J. Gamage McEvoy*, L. Liu, Y. Liang, Z. Zhang, "PbS-sensitized $K_2Ti_4O_9$ composite: Photocatalytic activity for hydrogen production under visible light", *7th International Conference on Environmental Catalysis*, Lyon, France, Sept. 2–6, **2012**.

[23] W. Cui, S. Ma, J. Gamage McEvoy*, L. Liu, Y. Liang, Z. Zhang, "CdS-sensitized $K_2Ti_4O_9$ composite for photocatalytic activity for hydrogen production under visible light", *7th International Conference on Environmental Catalysis*, Lyon, France, Sept. 2–6, **2012**.

[24] J. Gamage McEvoy, D.A. Bilodeau*, W. Cui, Z. Zhang, "Photocatalytic inactivation of *Escherichia coli* K12 using Ag/AgCl-AC under visible light", *14th Canadian Society for Chemical Engineering Ontario-Québec Biotechnology Meeting*, Ottawa, ON, May 30–31, **2012**.

[25] A.A. Donaldson, J. Gamage McEvoy*, A. Ye, Z. Zhang, "Modeling and validation of a rotating corrugated drum reactor utilizing novel photocatalyst for wastewater treatment", *61st Canadian Chemical Engineering Conference*, London, ON, Oct. 23–26, **2011**.

[26] J. Gamage McEvoy*, T. Comeau, Z. Zhang, "Visible-light photocatalysis using carbon-doped TiO_2", *61st Canadian Chemical Engineering Conference*, London, ON, Oct. 23–26, **2011**.

[27] J. Gamage McEvoy*, T. Comeau, Z. Zhang, "Visible-light photocatalysis using carbon-modified TiO_2: Disinfection of *Escherichia coli*", *13th Canadian Society for Chemical Engineering Ontario-Québec Biotechnology Meeting*, Kingston, ON, May 12–13, **2011**.

[28] J. Gamage McEvoy*, T. Comeau, Z. Zhang, "Visible-light photocatalysis using carbon-modified TiO_2: Degradation of methylene blue model wastewater", *International Conference on Environmental Pollution and Remediation*, Ottawa, ON, Aug. 17–19, **2011**.

[29] Y. Wang, J. Gamage, Z. Zhang*, "Solute distribution model and its application to separation of different components from biomass", *International Conference on Biomass and Energy Technologies*, Beijing, China, Aug. 20–22, **2010**.

[30] Z. Zhang*, N. Ho, J. Gamage, "Photocatalytic degradation of color compounds in wastewater", *19th International Congress of Chemical and Process Engineering*, Prague, Czech Republic, Aug. 28–Sept. 1, **2010**.

D.4 Invited presentations and seminars

[31] J. Gamage McEvoy, "Multifunctional silver/silver halide-activated carbon composites for photocatalytic detoxification and disinfection", *University of Ottawa Department of Chemical and Biological Engineering Graduate Seminar Series*, Mar. **2014.**

[32] J. Gamage McEvoy, "Multifunctional Ag/AgCl-activated carbon composites for photocatalytic detoxification and disinfection", *University of Ottawa Centre for Catalysis Research and Innovation Seminar Series*, May **2013**.

[33] J. Gamage McEvoy, "Research on photocatalytic water treatment", *Canadian Federation of University Women, Kanata Chapter Meeting*, Nov. **2012**.